

Understanding the Interface Chemistry of TiO₂/Fe₂O₃ Composite Photocatalyst-Sorbent Materials for the Treatment of Arsenic(III) Contaminated Waters

Jay Calum Bullen

2020

A thesis submitted for the degree of Doctor of Philosophy

Department of Earth Science and Engineering

Department of Chemistry

Centre for Doctoral Training in the Advanced Characterisation of Materials

Imperial College London

I declare that the research presented in this thesis is my own work and that all other sources have been appropriately referenced.

The copyright of this thesis rests with the author. Unless otherwise indicated, its contents are licensed under a Creative Commons Attribution-Non Commercial 4.0 International Licence (CC BY-NC). Under this licence, you may copy and redistribute the material in any medium or format. You may also create and distribute modified versions of the work. This is on the condition that: you credit the author and do not use it, or any derivative works, for a commercial purpose. When reusing or sharing this work, ensure you make the licence terms clear to others by naming the licence and linking to the licence text. Where a work has been adapted, you should indicate that the work has been changed and describe those changes. Please seek permission from the copyright holder for uses of this work that are not included in this licence or permitted under UK Copyright Law.

Abstract

Over one hundred million people worldwide are exposed to arsenic contaminated groundwaters. In oxygenated environments arsenic is found in the +5 oxidation state and is readily removed through adsorption onto iron oxides. However, in South Asia, where arsenic exposure is most severe, arsenic is found in the +3 oxidation state. This species is both more toxic and more difficult to remove than As(V). The current generation of arsenic treatment plants often fail to meet the World Health Organisation's $10 \mu\text{g L}^{-1}$ guideline limit, and the oxidation of As(III) to As(V) is therefore necessary to achieve effective removal of arsenic in South Asia.

Multifunctional photocatalyst-sorbents are an attractive solution, as a single material can be used to both oxidise As(III) and adsorb As(V). Whilst multifunctional behaviour is often achieved by coupling different materials into new composite forms, our understanding of how material coupling influences the behaviour of each component (i.e. photocatalytic oxidation and adsorption) remains limited.

This thesis investigated a mesoporous $\text{TiO}_2/\text{Fe}_2\text{O}_3$ composite. This work found that monolayer adsorption of As(V) is component additive, with TiO_2 and Fe_2O_3 surface components behaving independently of one another. Multilayer adsorption of As(III) is not component additive, due to differences between the surface morphology of meso- $\text{TiO}_2/\text{Fe}_2\text{O}_3$ and single-phase reference samples. Coupling TiO_2 with Fe_2O_3 significantly reduced photocatalytic activity, due to parasitic absorption of ultraviolet light by the Fe_2O_3 phase. The kinetic mechanism also changed after coupling, from a reactive oxygen species (ROS) mediated pathway to direct surface oxidation. This work considered the balance between the high sorbent concentrations needed for long filter device life-times, and the low photocatalyst concentrations needed to achieve effective light penetration through TiO_2 suspensions. Kinetic adsorption modelling predicted that at least 10 g L^{-1} material is required for effective arsenic removal, presenting constraints on how this technology can be engineered.

Table of contents

Abstract	3
Table of contents	4
List of tables	7
List of figures	8
1. Introduction	13
2. Background	17
2.1. Arsenic contaminated groundwaters worldwide	17
2.2. The toxicology of arsenic	19
2.3. Epidemic exposure to arsenic in South Asia	20
2.4. Remediation and its challenges	26
2.5. Advanced oxidation processes	30
2.6. Emerging materials in water treatment	34
2.7. Mesoporous TiO ₂ /Fe ₂ O ₃ : A bifunctional sorbent for arsenic remediation	39
2.8. Surface Complexation Modelling	45
2.9. Research aims and objectives	46
3. Experimental	53
3.1. Reagents and Materials	53
3.2. Materials Characterisation	60
3.3. Analytical determination of arsenic	65
3.4. Development of analytical techniques for the quantitative speciation of inorganic arsenic	67
3.5. Adsorption at equilibrium: Experimental and modelling	70
3.6. Photocatalytic oxidation: Characterisation of ultraviolet absorption and kinetic experiments	73
3.7. Modelling adsorption kinetics: Arsenic treatment plant design	84
4. Development of analytical techniques for quantitative arsenic speciation: As(V)-selective chemisorbent resins and electrochemistry	91
4.1. Introduction	91
4.2. Optimising electrochemical speciation for the arsenic-contaminated groundwaters of South Asia	98
4.3. Method development: Arsenic speciation using an As(V)-selective chemisorbent	104

4.4. Case studies for the validation of analytical methods	107
4.5. Cross-comparison of ImpAs with anodic stripping voltammetry for the rapid, reliable and portable speciation of arsenic	115
4.6. Conclusions	117
5. Characterisation of meso-TiO ₂ /FeO ₃ and reference samples	119
5.1. Introduction	119
5.2. Understanding the structure and composition of meso-TiO ₂ /Fe ₂ O ₃	121
5.3. Surface charge and the point of zero charge	137
5.4. ATR-FTIR baseline spectra before adsorption of arsenic	142
5.5. Implications	146
6. Developing an accurate surface complexation model of arsenic adsorption onto meso-TiO ₂ /Fe ₂ O ₃ using surface-sensitive analytical techniques	149
6.1. Introduction	149
6.2. Testing component additivity at the meso-TiO ₂ /Fe ₂ O ₃ surface	152
6.3. Identifying surface complexes for modelling	159
6.4. Surface Complexation Modelling	167
6.5. Conclusions	186
7. A mechanistic explanation for different arsenic(III) oxidation rates using single-component TiO ₂ and composite TiO ₂ /Fe ₂ O ₃ photocatalysts	189
7.1. Introduction	189
7.2. Optical characterisation to understand the ultraviolet absorption of meso-TiO ₂ /Fe ₂ O ₃	193
7.3. Verifying that composite photocatalyst-sorbents improve total arsenic removal under environmentally relevant conditions	196
7.4. Establishing the order of reaction: Analysis of initial rates	199
7.5. New rate equations reconcile discrepancies between initial rates and serial data	205
7.6. A mechanistic account for changes in photocatalytic oxidation kinetics after coupling meso-TiO ₂ with Fe ₂ O ₃	215
7.7. Conclusions	217
8. Design of an arsenic treatment plant: Insights from a kinetic adsorption model	221
8.1. Introduction	221
8.2. Developing a kinetic model sensitive to changes in the initial sorbate and sorbent concentration	224

8.3. Modelling an arsenic treatment plant to inform the design of photocatalyst-sorbent remediation	240
8.4. Future work: Integrating desorption rates	253
8.5. Conclusions	261
9. Conclusions and evaluation	263
9.1. Summary of key findings	263
9.2. New concepts and innovations	265
9.3. The future of the TiO ₂ /Fe ₂ O ₃ multifunctional sorbent	267
9.4. The future for the combined photocatalytic oxidation-adsorption approach towards the remediation of arsenic(III)	268
Acknowledgements	271
List of publications	272
Selected presentations	273
References	274
10. Appendix	301
10.1. Literature search	301
10.2. Reagents	304
10.3. Removal of arsenic(V) using ImpAs and shaking by hand	305
10.4. Anodic stripping voltammetry	306
10.5. Differences between synthetic batches of meso-TiO ₂ /Fe ₂ O ₃	310
10.6. XPS spectra of samples before adsorption of arsenic	316
10.7. Unsuccessful application of the potentiometric mass titration technique	319
10.8. Surface complexation modelling	322
10.9. FITEQL codes for surface complexation modelling	330
10.10. Set up of photooxidation kinetic experiments	347
10.11. Langmuir-Hinshelwood kinetics partially capture the adsorption-controlled kinetics of meso-TiO ₂ /Fe ₂ O ₃	352
10.12. Surface complexation modelling for the kinetic analysis of As(III) photocatalytic oxidation	356
10.13. Natural waters and the influence of media on the photocatalytic oxidation of As(III)	361
10.14. Transient absorption spectroscopy (TAS)	365
10.15. Data used to reduce the conditionality of the pseudo-second order kinetic adsorption model	377
10.16. MATLAB codes used to model an arsenic treatment plant	388

List of tables

Table 2.1: The inorganic composition of groundwaters in the Bengal Basin of South Asia.	23
Table 3.1: Arsenic concentrations detected in the West Bengal groundwater samples.	55
Table 3.2: Characterisation of the waters used in this work.	56
Table 3.3: ETLM parameters used for surface complexation modelling in Visual MINTEQ.	83
Table 4.1: Verifying that total As detection is equally sensitive towards As(III) and As(V).	99
Table 4.2: ASV operating parameters.	103
Table 4.3: The ability of each ligand to complex zinc.	114
Table 5.1: The main impurities detected using XRF, reported as mass percent.	123
Table 5.2: BET-surface area and pore sizes determined from N ₂ adsorption-desorption isotherms.	125
Table 5.3: Surface charge: A summary of the results obtained from dynamic light scattering (DLS) analysis (particle size and zeta potential) and potentiometric titration of mineral samples.	141
Table 5.4: FTIR peak assignment for blank samples, prior to adsorption.	144
Table 5.5: Materials characterisation: a compiled table of the most significant results used in the subsequent experimental work.	146
Table 6.1: Adsorption isotherm parameters.	155
Table 6.2: The assignment of new IR peaks after adsorption of arsenic.	164
Table 6.3: All adsorption reactions modelled in this work, and equations governing the conversion of equilibrium constants between the site-occupancy standard stand at the 1.0 M hypothetical standard state.	168
Table 6.4: Surface complexation modelling parameters for the ETLM.	177
Table 6.5: Comparison of ETLM parameters for surface protonation and electrolyte adsorption.	178
Table 6.6: Comparison of ETLM parameters for the adsorption of As(V).	179
Table 6.7: Comparison of ETLM parameters for the adsorption of As(III).	180
Table 6.8: A comparison of the accuracy of the CA-SCM when components are weighted by XRF (bulk), XPS (near surface) and LEIS (outermost surface) analysis.	183
Table 8.1: A selection of kinetic models used to describe adsorption.	226
Table 8.2: Parameters used to model selected data sets using the PSO model and the new rate equation, using a single rate constant to model all kinetic experiments in a given data set, where C ₀ or C _s was varied.	239
Table 8.3: Experimentally determined parameters for the adsorption capacity and kinetics of the As(III)/TiO ₂ -Fe ₂ O ₃ system at pH 7 (10 mM HEPES buffer) using experimental data from Lapinee ²⁵² .	240
Table 8.4: Parameters used for modelling an arsenic treatment plant.	242
Table 8.5: Parameters used to model experimental adsorption kinetic data, using a combination of monodentate and bidentate surface complexes.	260
	377

List of figures

Figure 2.1: A rural arsenic treatment plant in West Bengal, India, based on membrane technology.	27
Figure 2.2: Example of a well-head arsenic removal unit, typical for rural communities in India.	29
Figure 2.3: Generation of charge carriers in a heterogeneous photocatalyst.	32
Figure 2.4: A comparison of publications in general water treatment versus arsenic remediation more specifically.	33
Figure 2.5: The type-II staggered heterojunction, where photoexcited electrons and holes transfer in opposite directions. e ⁻ and h ⁺ denote electrons and holes respectively, cb and cv denote the conduction and valence bands respectively.	37
Figure 2.6: Research papers published each year on arsenic remediation using composite materials.	39
Figure 2.7: Illustration of the type-I heterojunction possible at the interface between anatase TiO ₂ and Fe ₂ O ₃ .	47
Figure 2.8: An initial idea of how meso-TiO ₂ /Fe ₂ O ₃ might be incorporated into an arsenic treatment plant, considering a pre-treatment with sorbent media to remove As(V), phosphate and other species which might interfere with the photocatalytic oxidation.	48
Figure 3.1: Sampling sites for field work.	55
Figure 3.2: Preparation of meso-TiO ₂ (batch 1).	57
Figure 3.3: Preparation of meso-TiO ₂ /Fe ₂ O ₃ (batch 2) from meso-TiO ₂ .	58
Figure 3.4: Meso-TiO ₂ /Fe ₂ O ₃ (batch 1). The material (a) before and (b) after initial calcination (300 °C, 10 minutes), and (c) before and (d) after the final calcination (300 °C, 6 hours).	59
Figure 3.5: The progress of mineral washing, looking for convergence in the electrode potential as a sign of a clean surface.	59
Figure 3.6: An example of the hysteresis observed between forwards (addition of base, solid lines) and reverse (addition of acid, dashed lines) titrations.	64
Figure 3.7: The recovery of internal standards was used to monitor changes in the sensitivity of ICP-MS detection, and thus better calibrate total arsenic concentrations.	66
Figure 3.8: The portable PDV6000 ultra potentiostat used in this work.	67
Figure 3.9: Photoreactor design.	78
Figure 3.10: Characterisation of light intensity.	78
Figure 3.11: Illustration of how calculation of initial rates using the slope between the first two data points of q _t as a function of t gives a systematically lower result than when fitting the PSO model, using the linearised plot of t/q _t as a function of t.	86
Figure 4.1: A concept schematic for arsenic speciation as performed by the two methods used in this study.	97
Figure 4.2: The influence of deposition voltage on As stripping peak intensity. (a) As(III) determination at pH 2 (40 µM hydrazine), and (b) total As determination at pH 1, both systems acidified with HCl.	98
Figure 4.3: The influence of iron on the electrochemical detection of arsenic.	100

Figure 4.4: The influence of (a) EDTA and (b) hydrazine on As stripping peaks during total As determination ($5 \mu\text{g L}^{-1}$ As(V), pH 1).	101
Figure 4.5: The influence of inorganic groundwater species on the electrochemical detection of arsenic.	102
Figure 4.6: ImpAs method development: arsenic speciation using batch treatment.	105
Figure 4.7: The syringes loaded with 0.2, 0.4 and 1.0 gram ImpAs used in this work.	105
Figure 4.8: ImpAs method development: arsenic speciation using syringe devices for a column treatment.	106
Figure 4.9: Case study 1: Determination of photooxidation rate constants in synthetic solutions.	108
Figure 4.10: Case study 2: Speciation in natural media.	110
Figure 4.11: Current limitations of speciation using ImpAs.	111
Figure 4.12: Multi-element analysis using ICP-MS reveals the influence of EDTA on the speciation of arsenic using ImpAs.	112
Figure 4.13: Leaching of zinc from the ImpAs receptor (bottom) due to complexation of zinc by EDTA (top).	113
Figure 4.14: The comparison of arsenic speciation determined using the developed ImpAs/ICP-MS and ASV methods in (a) synthetic and (b) natural samples.	115
Figure 5.1: XRD confirmation of the crystal phase of synthesised powders.	121
Figure 5.2: N ₂ -adsorption/desorption isotherms used to determine the BET-specific surface area of washed mineral samples.	124
Figure 5.3: Optical microscopy of Fe ₂ O ₃ , meso-TiO ₂ and meso-TiO ₂ /Fe ₂ O ₃ (both from batch 2) and FeOOH samples.	128
Figure 5.4: SEM images showing meso-TiO ₂ /Fe ₂ O ₃ (batch 1) particles as agglomerates of smaller structures.	129
Figure 5.5: TEM image showing lattice planes in the crystalline surface of meso-TiO ₂ /Fe ₂ O ₃ particles.	130
Figure 5.6: TEM (top) and fast Fourier transforms (bottom) used to measure crystallite dimensions. Each spot in the FFT was assigned a crystal structure and miller index using literature XRD patterns from the PANalytical software. The above TEM shows nanoscale mixing of the TiO ₂ and Fe ₂ O ₃ crystallites, demonstrating a heterogeneous surface structure. Colour overlays correspond to anatase (green) and hematite (blue) crystallites.	131
Figure 5.7: STEM-EDS analysis of three meso-TiO ₂ /Fe ₂ O ₃ particles (batch 2).	133
Figure 5.8: Quantifying the relative abundance of meso-TiO ₂ and Fe ₂ O ₃ phases within the meso-TiO ₂ /Fe ₂ O ₃ bulk material.	135
Figure 5.9: (a) LEIS depth profile of meso-TiO ₂ /Fe ₂ O ₃ and reference samples and (b) determination of the outermost surface composition by peak integration and a linear combination of end-member reference samples.	136
Figure 5.10: Mineral composition as a sample of probing depth	136
Figure 5.11: Identification of the point of zero salt effect (pzse) by potentiometric titration, for (a) Fe ₂ O ₃ , (b) meso-TiO ₂ , (c) meso-TiO ₂ /Fe ₂ O ₃ , and (d) FeOOH.	138

Figure 5.12: Identifying the isoelectric point (iep).	140
Figure 5.13: A visual comparison of the point of charge, determined from potentiometric titrations (red bars) and zeta potential analysis (blue bars).	141
Figure 5.14: ATR-FTIR spectra for mineral samples before adsorption of arsenic.	142
Figure 5.15: The influence of anatase:rutile ratio on the adsorption of arsenic to TiO ₂ .	147
Figure 6.1: Component additivity in surface charge as measured by potentiometric titration.	153
Figure 6.2: Full comparison of As(V) and As(III) adsorption isotherms modelled by the Langmuir and Freundlich models.	156
Figure 6.3: Theoretical verification that bulk precipitation did not occur in the adsorption isotherms.	157
Figure 6.4: The component additivity of arsenic adsorption isotherms.	158
Figure 6.5: The influence of arsenic adsorption on zeta potential.	160
Figure 6.6: The influence of arsenic adsorption on infrared absorption.	161
Figure 6.7: Identifying appropriate surface complexes: FTIR spectra in the v(As-O) stretching mode region, after adsorption of (a) As(V), and (b) As(III).	162
Figure 6.8: The surface complexes and corresponding reactions used in the surface complexation model (sketched in Jmol). Colours correspond to arsenic (purple), oxygen (red), hydrogen (white) and titanium/iron (brown).	163
Figure 6.9: ETLM parameter determination using potentiometric titration surface charge curves.	170
Figure 6.10: Determination of C ₁ and optimisation of logK _{0M} and logK _{0L} for (a) FeOOH, (b) Fe ₂ O ₃ , and (c) meso-TiO ₂ .	171
Figure 6.11: Determination of As(V) surface complexation constants using the pH adsorption edges of (a) FeOOH, (b) Fe ₂ O ₃ , and (c) meso-TiO ₂ .	172
Figure 6.12: Determination of As(III) surface complexation constants using the pH adsorption edges of (a) FeOOH, (b) Fe ₂ O ₃ , and (c) meso-TiO ₂ .	173
Figure 6.13: Validation of the As(V) surface complexation model. As(V) adsorption isotherms were predicted by the SCM (black lines) and validated against experimental results (black squares) for (a) FeOOH, (b) Fe ₂ O ₃ , and (c) meso-TiO ₂ .	174
Figure 6.14: Fitting multilayer As(III) adsorption constants to adsorption isotherms.	176
Figure 6.15: A comparison of adsorption isotherms predicted by the component additive surface complexation model (CA-SCM) with experimental results.	182
Figure 6.16: The shared EDL CA-SCM, where a single electrical double layer is used to calculate the electrostatic work done in the adsorption of arsenic to both Fe ₂ O ₃ and meso-TiO ₂ surface components.	185
Figure 6.17: Values of the coefficient of determination (R^2) calculated to determine the goodness of fit between meso-TiO ₂ /Fe ₂ O ₃ experimental data and the component additive predictions, using components weighting according to XRF, XPS and LEIS analysis. Values of R^2 were calculated for surface charge (potentiometric titration), As(V) adsorption isotherms (modelled with both the Langmuir adsorption isotherm and the CA-SCM), and As(III) adsorption isotherms (both the Freundlich adsorption isotherm and the CA-SCM).	187

Figure 7.1: Characterisation of UV-Vis absorption. (a) UV-Vis absorbance of meso-TiO ₂ , meso-TiO ₂ /Fe ₂ O ₃ , and Fe ₂ O ₃ powders (0.1 g L ⁻¹ suspended in Milli-Q water).	194
Figure 7.2: Probing heterojunction effects in the composite meso-TiO ₂ /Fe ₂ O ₃ photocatalyst using transient absorption spectroscopy (TAS).	195
Figure 7.3: A comparison of total arsenic removed before (lightly shaded bars) and after (heavily shaded bars) photooxidation using meso-TiO ₂ and meso-TiO ₂ /Fe ₂ O ₃ as photocatalyst-sorbents in a variety of media.	197
Figure 7.4: The influence of light intensity on the initial rate of As(III) photocatalytic oxidation in the presence of (a) meso-TiO ₂ and (b) meso-TiO ₂ /Fe ₂ O ₃ photocatalysts. (c) The comparison of initial rates.	200
Figure 7.5: The influence of As(III) concentration on the rate of photocatalytic oxidation in the presence of (a) meso-TiO ₂ and (b) meso-TiO ₂ /Fe ₂ O ₃ photocatalysts.	202
Figure 7.6: The influence of phosphate (10 mg L ⁻¹) on the photocatalytic oxidation of As(III).	203
Figure 7.7: Linearisation of serial data using pseudo first-order kinetics.	206
Figure 7.8: Application of the As(V) deactivation kinetics given in Equation 3.29 to explain the disguised zero-order kinetics of meso-TiO ₂ .	208
Figure 7.9: The SCM-constrained As(V) deactivation model for the photocatalytic oxidation of As(III) in the presence of meso-TiO ₂ .	210
Figure 7.10: The SCM-predicted partitioning of As(III) between adsorbed and aqueous phases for (a) meso-TiO ₂ and (b) meso-TiO ₂ /Fe ₂ O ₃ , with different total arsenic concentrations, as photocatalytic oxidation progresses.	212
Figure 7.11: The partitioning of As(III) between aqueous and adsorbed phases predicted by the Langmuir adsorption isotherm as photocatalytic oxidation of As(III) increases, with (a) meso-TiO ₂ and (b) meso-TiO ₂ /Fe ₂ O ₃ .	213
Figure 7.12: The SCM-constrained As(III) kinetic model, fitted to serial data in the form ln(C _t /C ₀).	213
Figure 7.13: A comparison of the SCM-constrained As(III) kinetic model with pseudo first-order (PFO) and Langmuir-Hinshelwood (LH) kinetics.	214
Figure 7.14: A mechanistic account for the observed differences between the rates of photocatalytic oxidation of As(III) in the presence of meso-TiO ₂ and meso-TiO ₂ /Fe ₂ O ₃ .	216
Figure 8.1: The initial rate of adsorption as a function of (a) initial sorbate concentration (C ₀) and (b) sorbent concentration (C _s).	228
Figure 8.2: Pseudo-second order (PSO) rate constant k ₂ as a function of (a) initial sorbate concentration (C ₀) and (b) sorbent concentration (C _s).	229
Figure 8.3: Demonstrating the lack of predictive capability in the PSO model due to the C ₀ and C _s conditionality of k ₂ .	233
Figure 8.4: Mathematical demonstration of the reduced sensitivity towards C ₀ and C _s in the new rate constant k' compared with k ₂ .	235
Figure 8.5: Adsorption isotherms were fit using experimental data and then used to recalculate q _e at each point in time when modelling kinetic experiments using the modified form of the pseudo-second order rate equation.	236

Figure 8.6: Modelling adsorption kinetics using the new kinetic model.	237
Figure 8.7: Calibration curves between the experimentally observed q_t and q_t values predicted by the original PSO and modified kinetic models in (a) absolute form and (b) logarithmic form.	238
Figure 8.8: Comparison of the modified adsorption kinetic model with the unmodified PSO.	241
Figure 8.9: Modelling batch treatments.	243
Figure 8.10: Modelling continuous-flow treatment.	245
Figure 8.11: Comparison of simulated results for the batch (blue squares) and continuous-flow (red circles) models.	246
Figure 8.12: Kinetic adsorption modelling: batch treatment using the same sorbent for 365 days.	248
Figure 8.13: Comparison of 365-day sorbent deployments simulated using batch and continuous-flow configurations.	250
Figure 8.14: Sorbent efficiency (mg g ⁻¹ adsorbed at the end of year or at breakthrough, whichever occurs soonest).	251
Figure 8.15: The mass of sorbent required per household per year using the continuous-flow configuration divided by the mass of sorbent required in the batch treatment, with an initial concentration of 500 µg L ⁻¹ As(III).	251
Figure 8.16: An adsorption-desorption model using a single type of surface complex.	255
Figure 8.17: Demonstration of adsorption kinetic data fitting using an adsorption-desorption model with monodentate and bidentate surface complexes.	258
Figure 8.18: Recreating PSO kinetics using first-order adsorption and desorption rates, with monodentate and bidentate surface complexes.	259
Figure 8.19: Recreating PSO kinetics using first-order adsorption and desorption rates, with monodentate and bidentate surface complexes, where the proportion of available adsorption capacity remaining is weighted via $q_{\text{weighted}} = q_{\text{mono2}} + q_{\text{bi}}$. $k_{\text{ads}} = 0.123 \text{ L g}^{-1} \text{ min}^{-1}$; $k_{\text{des}} = 0.44 \text{ min}^{-1}$, $k_{\text{bi} \rightarrow \text{mono}} = 0.17$ (unitless); $k_{\text{mono} \rightarrow \text{bi}} = 0.065$ (min ⁻¹).	259

1. Introduction

The arsenic treatment plants developed for South Asia often fail to provide safe drinking water¹. A study in rural Uttar Pradesh, India, found that after 10 years, only 34 out of 200 treatment plants were still in operation. Of these 34, only one plant was delivering water below the 10 µg L⁻¹ World Health Organisation guideline limit¹. The remaining 97% of treatment plants were providing unsafe water to the community. One major difficulty in providing safe water within South Asia is the presence of the arsenic(III) species H₃AsO₃, released under anoxic, reducing groundwater conditions². Removal of As(III) using conventional approaches such as adsorption is ineffective due to the neutral charge of this species³.

Pre-oxidation of arsenite, As(III), to the more strongly adsorbing, negatively charged arsenate, As(V), oxyanions (i.e. H₂AsO₄⁻ and HAsO₄²⁻ at neutral pH) is thus important to achieve effective arsenic removal⁴. Whilst oxidation of As(III) can be achieved through application of conventional chemical oxidants such as chlorine, permanganate, ozone, and Fenton's reagent^{5 6}, this approach (a) incurs running costs due to the consumption of chemical reagents^{7 8}, and (b) risks the formation of toxic disinfection by-products (DBPs), such as the carcinogenic trihalomethanes formed by Cl₂⁶. DBPs are increasingly likely in South Asia due to the high levels of dissolved organic matter present in arsenic-contaminated groundwaters⁹. Oxidation using heterogeneous photocatalysts such as TiO₂ reduces the risk of DBPs¹⁰. Mixed mineral TiO₂/Fe₂O₃ composites are especially attractive: these multifunctional materials combine photocatalytic oxidation of As(III) to As(V), using the TiO₂ phase, with effective adsorption of As(V) to the Fe₂O₃ phase^{11 12 13}.

To design an arsenic treatment plant based on photocatalyst-sorbent technology, we need to know the adsorption capacity, adsorption kinetics, and photocatalytic activity of our media. However, our understanding of how coupling materials into new composite forms affects adsorption and catalysis is limited, with few systematic studies reported in the literature. Does each component continue to function independently, or does new behaviour arise?

Adsorption capacity is best described using surface complexation models (SCM), which offer sensitivity to environmental conditions missing from the more widely used Langmuir and Freundlich models ¹⁴. Component additive (CA) models describe a composite sorbent, such as TiO₂/Fe₂O₃, as a collection of distinct surface components, such as pure TiO₂ and Fe₂O₃ ¹⁵. CA-SCMs are desirable tools, firstly to understand how arsenic partitions between the TiO₂ and Fe₂O₃ surfaces, and secondly to quickly predict the adsorption capacity of new synthetic sorbents. However, the CA-SCMs developed for composite sorbents have often failed to accurately predict experimental observations, with errors between model and experiment as large as 300% ^{16 1 17}. These errors have been attributed both to behavioural changes after coupling, such as site blocking ¹⁷ and surface charge effects ¹⁸, and to inaccuracies when calculating of the relative abundance of each surface phase ¹⁵. Currently, there is no CA-SCM available to model adsorption of arsenic onto TiO₂/Fe₂O₃ composites ¹⁹. This thesis fills the gap, by introducing surface-sensitive techniques for more accurate CA-SCM component-weighting, developing a CA-SCM for meso-TiO₂/Fe₂O₃ and probing how coupling TiO₂ and Fe₂O₃ influences the adsorption of As(III) and As(V).

The effects of Fe₂O₃-coupling on the photocatalytic oxidation of As(III) using TiO₂ must also be understood, to optimise the synthesis of TiO₂/Fe₂O₃ composites and to design appropriate reactors. Despite numerous recent studies investigating remediation of As(III) using titania-iron oxide composites, the effects of iron oxide-coupling have not been investigated mechanistically ^{20 21 22 23 11}. Coupling TiO₂ with Fe₂O₃ has two potential effects, enhancing and suppressing photocatalytic activity respectively. Firstly, mixed semiconductor photocatalysts often show superior photocatalytic activity due to heterojunction effects that reduce electron-hole recombination rates ²⁴. Secondly, iron oxides, such as Fe₂O₃, have small bandgaps (2.2 eV versus 3.2 eV for anatase TiO₂) and will theoretically reduce the excitation of TiO₂ by parasitic absorption of ultraviolet light, suppressing photocatalytic activity. This thesis determines the kinetics of photocatalytic oxidation of As(III) using a TiO₂/Fe₂O₃ composite and mechanistically explains the significant changes when TiO₂ is coupled with Fe₂O₃.

To date, photocatalyst-sorbent materials remain untested for real-life applications in As(III) remediation. No study has considered how we will reconcile low photocatalyst concentrations with high sorbent concentrations. Photocatalysts are typically been used in low concentrations (<1 g L⁻¹) to achieve effective light penetration through the system ^{25 26 26 27 28 29}. However, sorbent materials are needed in high concentrations to achieve long device lifetimes. Sorbent life-time is a major factor determining the success or failure of arsenic mitigation schemes in South Asia: users often fail to replace or regenerate saturated sorbent media due to lack of expertise ³⁰ or lack of confidence ³¹, and replacement media can be expensive ³⁰. This thesis therefore develops a kinetic adsorption model which is used to identify the range of TiO₂/Fe₂O₃

concentrations under which a combined photocatalytic oxidation-adsorption treatment is viable.

This thesis aims to understand the chemistry of the meso-TiO₂/Fe₂O₃ composite system, for the remediation of As(III) using a combined photocatalytic oxidation-adsorption approach. The primary objectives were as follows:

- To develop the use of surface-sensitive analytical techniques for the accurate weighting of components within CA-SCM, so that the adsorption of arsenic onto meso-TiO₂/Fe₂O₃ can be accurately modelled.
- To determine the effects of Fe₂O₃-coupling on the photocatalytic oxidation of As(III) using meso-TiO₂/Fe₂O₃, so that treatments can be better engineered and composite photocatalyst-sorbents better synthesised.
- To develop a kinetic adsorption model and determine the minimum concentration of meso-TiO₂/Fe₂O₃ needed for an arsenic treatment plant, to inform future engineering studies.

The thesis is structured as follows:

- Chapter 2 provides a background to As(III) contamination in the groundwaters of South Asia, the limitations in current remediation technologies, and current interest in using bifunctional photocatalyst-sorbent composite materials.
- Chapter 3 provides a description of the experimental techniques and methods.
- Chapter 4 develops and optimises analytical techniques for the speciation of arsenic, considering both the need to monitor As(III) oxidation kinetics in this work, and the need to achieve large scale speciation in future groundwater surveys.
- Chapter 5 characterises the meso-TiO₂/Fe₂O₃ composite material studied in this thesis.
- Chapter 6 demonstrates the application of surface-sensitive analytic techniques for accurate component-weighting within component additive surface complexation models (CA-SCM), developing an accurate model for the adsorption of arsenic onto meso-TiO₂/Fe₂O₃.
- Chapter 7 identifies the major mechanisms by which Fe₂O₃-coupling affects the photocatalytic oxidation of As(III) using meso-TiO₂, explaining the observed differences in reaction rates after meso-TiO₂ and Fe₂O₃ are coupled.
- Chapter 8 establishes the minimum concentrations of meso-TiO₂/Fe₂O₃ needed for an arsenic treatment plant, considering differences between the typical material concentrations used for photocatalytic and sorbent applications. This chapter develops

a kinetic adsorption model, which is used to assess the influence of reactor design, e.g. the choice of batch versus continuous-flow reactor, and treatment times.

- Chapter 9 concludes by discussing the new insights provided by this thesis into a combined photocatalytic oxidation-adsorption approach towards the remediation of As(III) using meso-TiO₂/Fe₂O₃. A vision for future work is outlined.

2. Background

2.1. Arsenic contaminated groundwaters worldwide

Groundwater is an invaluable source of freshwater globally, contributing over one hundred times more to the global freshwater supply than surface waters^{32 33}. Whilst the overwhelming majority of water extracted is used for irrigation (around 70% globally³⁴, and 89% and 86% in India and Bangladesh respectively³⁵), groundwater is also vital for domestic uses such as drinking, cleaning and sanitation³⁵. Consequently, any contamination of our groundwater supply is a major concern.

Arsenic is a toxic Group 1 carcinogen³⁶, and over 100 million people worldwide are at risk from arsenic-contaminated groundwaters³⁷. The list of countries affected includes Argentina, China, Bangladesh, India, Peru, Taiwan, the USA, Vietnam and the UK (Cornwall)^{38 39 40 41 42}. The World Health Organisation (WHO) guideline limit for arsenic in drinking water is just 10 µg L⁻¹, however groundwater arsenic concentrations can reach as high as 3 mg L⁻¹ (USA) and 7.5 mg L⁻¹ (Argentina)⁴³. Groundwater decontamination becomes challenging with as little as 100 µg L⁻¹ arsenic⁴⁴.

Arsenic is known as a 'Silent Killer,' since it is colourless, odourless, and tasteless⁴⁵, and symptoms may not appear for over a decade⁴³. Consequently, identifying exposed communities is challenging, haphazard, and slow. Despite Bangladesh making a significant move away from surface water and towards groundwater for domestic consumption in the 1970s, it was only in the 1990s that arsenic exposure was identified⁴⁴. Similar public health crises were identified in Taiwan (in the 1960s), Chile (1970s), and Mexico (1980s)⁴⁴. New cases of public exposure to arsenic-contaminated groundwaters continue to be identified, for instance more recent studies have identified exposed communities in Pakistan⁴⁶. However, arsenic exposure in Bangladesh and West Bengal, India, remains the most significant public health threat to date⁴⁴.

Since most arsenic contamination is geogenic and thus natural, high, middle and low-income countries are all affected. The US Environmental Protection Agency have set their Maximum Contaminant Level (MCL) for arsenic at 10 µg L⁻¹ (matching the WHO's guideline limit). One survey by the United States Geological Survey (USGS) found that 7% of wells tested in the US contained more than 10 µg L⁻¹ arsenic ⁴⁷. Another study found that 9% of wells tested exceeded the MCL, rising to 45% when considering only the methanogenic aquifers ⁴⁸.

Arsenic contaminated groundwaters are caused by a variety of reasons. Reducing aquifers in the sediment basins of South Asia lead to the release of As(III) through microbially-mediated reductive dissolution of iron (hydr)oxides ⁴⁹. In the arid regions of Mexico, the US and Chile, As(V) is released through oxidation of pyrite ⁴⁹. Mining activity is the principal route to anthropogenic arsenic contamination of groundwaters, as in Burkina Faso, the US and the UK ⁵⁰. Geothermal waters have also contaminated groundwaters in the USA and New Zealand ⁵⁰.

Arsenic contaminated waters vary in pH, redox conditions, presence of organic matter/bacteria, and the concentration of inorganic anions (bicarbonate, phosphate, sulphate) and cations (Fe(II) and Mn(II)), precipitating once exposed to air). It is consequently not surprising that arsenic can be found in a range of chemical forms, with different redox states, protonation states, and the possibility of incorporating organic functional groups ⁵¹.

The typical pH range of groundwaters is pH 5-8, where As(III) ("arsenite") is present as the protonated H₃AsO₃ species, and As(V) ("arsenate") is present as a mixture of negatively charged H₂AsO₄⁻ and HAsO₄²⁻ oxyanions. Because H₃AsO₃ is neutrally charged at circumneutral pH, it is difficult to remove efficiently using typical water treatment processes such as coagulation-flocculation or adsorption (discussed thoroughly in section 2.4) ⁶. Whilst inorganic As(V) and As(III) are the thermodynamically favourable species in oxic (with oxygen) and anoxic (without oxygen) groundwaters respectively, the redox transformation between the two oxidation states is slow ⁵². Consequently, the arsenic pumped to the surface from anoxic groundwaters may persist in the +3 oxidation state for significant durations.

Factors exacerbating the risk of arsenic exposure include poor groundwater management. For instance, groundwater over-abstraction leads to land subsidence, which is well documented in cities such as Mexico City and Jakarta ⁵³. Subsidence can induce arsenic contamination by altering the directions of aquifer flow and introducing air into the aquifer ⁵⁴, and the arid regions of California and Mexico currently face enhanced arsenic risk due to over-abstraction ⁵⁵. Over-abstraction of groundwater in Kolkata, India is similarly inducing land subsidence ⁵³, and aquifers are expected to become contaminated with arsenic in the coming decades ⁵⁶. Over-abstraction will naturally increase in the near future, due to increasing agricultural, industrial and public demands. Poor groundwater management also enhances the risk of arsenic

contamination through mechanisms such as the contamination of agricultural land when using arsenic-contaminated groundwaters to irrigate crops⁵⁷, and the enhanced microbe-mediated arsenic release when organic matter is allowed to reach aquifers (e.g. from landfill waste)⁴⁸.

Since most arsenic contamination of groundwaters is geogenic, the areas affected are often very large. Consequently, removing arsenic at the source, i.e. within the aquifer, is normally an inefficient solution⁴⁸. It is easier to treat groundwater once it has been pumped to the surface. However, centralised water treatment plants are expensive: in the US, arsenic clean-up programs have costed millions of dollars to establish⁵⁸. The problem of arsenic contaminated groundwater is thus widespread, expensive, and challenging.

2.2. The toxicology of arsenic

Arsenic is the highest ranked toxic substance on the ATSDR Substance Priority List⁵⁹ and it is rated a Group 1 carcinogen by the International Agency for Research on Cancer³⁶. The symptoms presented by acute and chronic arsenic poisoning (arsenicosis) are markedly different. The toxicity of arsenic also depends on its chemical form, i.e. inorganic As(III) versus As(V), and inorganic As versus organic As.

Acute poisoning normally occurs due to the ingestion of pesticides or insecticides³⁹. Fatal doses are reported in various forms: in absolute mass terms (100 to 300 mg), as a daily intake normalised to body mass ($0.6 \text{ mg kg}^{-1} \text{ day}^{-1}$), or as a concentration (above 60 mg L^{-1})^{39 60}. Mortality can take as long as eight days to occur³⁹. Ingestion of smaller amounts, such as up to 5 mg, or from $300 \mu\text{g L}^{-1}$ to 30 mg L^{-1} causes stomach and intestinal problems, vomiting or diarrhoea for up to twelve hours^{39 60}. Other conditions include peripheral neuropathy: a form of nerve damage with tingling sensations, numbness and muscle weakness^{39 61}. Peripheral neuropathy may persist for years³⁹, and was exhibited in many victims of Manchester's arsenic-in-beer crisis of 1900-1901⁶².

Chronic arsenicosis presents different symptoms, with various levels of severity and varying durations before onset. Chronic arsenic exposure causes skin lesions such as keratoses (non-cancerous skin growths, potentially debilitating) after around 10 years of exposure, and arsenic-induced skin cancers after 20 years⁴³. Dose-dependent studies in Taiwan indicated that habitual drinking of water contaminated with $500 \mu\text{g L}^{-1}$ arsenic presents a 10% lifetime risk of arsenic-induced mortality (and a 1% risk at $50 \mu\text{g L}^{-1}$)⁴³. Exposure to similar concentrations of arsenic in Chile similarly showed a 5 to 10% risk of contracting fatal internal cancers⁴³. Chronic arsenic exposure has also been linked to miscarriage⁶⁰.

Arsenic toxicity increases in the order: oAs(V)<iAs(V)<iAs(III)<oAs(III) (where *i* and *o* denote inorganic and organic species respectively)^{63 64}. Inorganic As(V) behaves as a chemical analogue to phosphate (PO₃⁴⁻), replacing phosphate within adenosine triphosphate (ATP) and thus disrupting metabolic pathways in animals, bacteria and plants^{39 65}. As As(V) is taken up into cells by phosphate transport proteins, As(V) can also disrupt cellular phosphate cycling⁶⁵. Inorganic As(III) interacts with dithiol groups causing inactivation of enzymes⁶⁵. As(III) also increases the risk of cancer through inhibiting the autophagy response (the process by which damaged cells are removed and recycled)⁶⁶. It is believed that inorganic arsenic does not directly interact with DNA, but increases the risk of other DNA damaging species⁶⁷. For instance, the presence of arsenic causes hypomethylation of DNA, disrupting gene expression^{68 69}. On the other hand organic As(III) (mono- and di-methylated species) do appear to damage DNA⁶⁷. Finally, arsenic is also believed to cause cell damage through oxidative stress⁷⁰, due to the formation of reactive intermediates during intracellular arsenic redox cycling³⁹.

2.3. Epidemic exposure to arsenic in South Asia

“The worst mass poisoning in history.”

(World Health Organisation, 2000⁴³)

In the 1970s, UNICEF aimed to supply clean and safe drinking water across Bangladesh to reduce the high infant mortality rates due to cholera and diarrhoea⁷¹. Thousands of tube wells were dug, providing groundwater as a safe alternative to the microbe-contaminated surface waters⁴³. With government support this campaign was incredibly successful: three million wells were installed by 1998⁷², and 8.6 million as of 2008⁷³. Currently, 97% of the rural population of Bangladesh relies on tube wells as the primary source of drinking water⁷⁴. Whether due to changing water supply or other factors, infant mortality has steadily decreased from 148 deaths per 1000 births to just 31, between 1972 and 2015^{75 76}.

Tragically however, the groundwater extracted by these tube wells was contaminated with arsenic. Since the skin lesions and cancers caused by chronic arsenic poisoning take years-to-decades to develop, it was not until 1993-1994 that the public health crisis was identified⁴³. Large scale testing was conducted, and by 2008 it was determined that 31% of wells failed to meet the local 50 µg L⁻¹ limit for arsenic, with 20-35 million people at risk^{73 77}. The lower WHO limit of 10 µg L⁻¹ painted a bleaker picture, with 57 million people exposed⁷⁷. Other calculations

have been higher still, estimating there to be 80 million people at risk in Bangladesh, and 50 million people at risk in neighbouring West Bengal, India³⁹.

2.3.1. The source and mechanism for arsenic release

Nickson et al. (1999) demonstrated that in the Bengal Basin of South Asia, arsenic is released under reducing conditions, and not through the oxidation of pyrite as was previously thought². In anoxic groundwaters, microbes starved of oxygen reductively dissolve iron oxides in order to metabolise the organic matter that is prevalent in the aquifer sediments. Consequently, the arsenic that had previously adsorbed to these iron oxides is released as inorganic As(III).

The arsenic is believed to have originated in the Himalayas, where the weathering of arsenic-containing rocks during heavy rainfall in our current Holocene geological period (especially prior to 1000 BCE) released material that was transported downstream⁷⁸. This silt contained fine iron hydroxides, to which mobilised arsenic bound, before becoming buried as a sediment in the Bengal Basin delta². Corresponding with this theory, arsenic-contaminated groundwaters can be found in all countries fed by rivers sourced from the Himalayas. This includes Nepal⁷⁹, Pakistan⁴⁶, Tibet⁸⁰, China⁸¹, Myanmar⁸¹, Thailand⁸¹, Cambodia⁸² and Vietnam⁸². A notable exception is Bhutan, since its high altitude positions it outside of the affected river basins⁸³. With slow groundwater flows, aquifer recharge and discharge can take thousands of years, explaining why this ancient source of arsenic persists⁸⁴.

2.3.2. The composition of South Asia's groundwaters

Previously published data on the inorganic composition of arsenic-contaminated groundwaters in South Asia (Bangladesh and West Bengal, India) is presented in Table 2.1. The pH of these groundwaters is generally close to neutral. Arsenic(III) contaminated waters are anoxic, with <20% saturation of dissolved oxygen² and negative redox potentials⁸². Calcium and carbonate are normally the dominant cation and anion respectively, though sodium and chloride can dominate⁸⁵. Calculations using published data give an ionic strength of approximately 0.018 ± 0.003 M⁸⁶, which is significantly increased by the presence of NaCl (e.g. 0.046 ± 0.036 M⁸⁷ and 0.088 ± 0.028 M⁸⁵). At circumneutral pH, adsorption of arsenic onto soils (especially As(V)) increases as the ionic strength is increased from 0.01 to 0.6 M⁸⁸.

A significant influence on the adsorption of arsenic is the presence of competitor anions, especially phosphate^{6 89 50}, which is normally an order of magnitude more concentrated than arsenic (Table 2.1). Sulphate anions are around two orders of magnitude more concentrated than arsenic, and sulphate is known to interfere with adsorption processes, being a well-known foulant of anion exchange resins⁹⁰. The groundwater aquifers of South Asia are anoxic and reducing, leading to high concentrations of dissolved iron and manganese (Table 2.1). Once exposed to air, Fe(II) and Mn(II) ions typically precipitate out quickly, within minutes or hours. This often leads to the concentration of arsenic and other anions decreasing once anoxic groundwater is pumped to the surface, due to anions co-precipitating with (and adsorbing onto) Fe and Mn oxides^{40 91}. Groundwaters in South Asia typically contain high concentrations of dissolved organic matter, such as humic and fulvic acids⁹¹. These are known to hinder adsorption⁹², and interfere with photocatalysis (e.g. by scavenging oxidants)⁹³.

2.3.1. The impact of arsenic exposure

In Bangladesh, arsenic poisoning is estimated as the cause for 1 in every 18 deaths. This is equivalent to 43 000 deaths per year⁷⁴. It is little wonder that many consider the arsenic crisis across Bangladesh and West Bengal to be the “worst mass poisoning in history”^{94 95 96}. Those most at risk are those living in rural communities with lower incomes⁹⁷ and beyond the obvious health impacts, arsenic poisoning has significant social and economic ramifications. For instance, those presenting visible symptoms are often ostracised from society, especially women⁹⁸. Economically, painful and debilitating skin lesions often prevent the afflicted from continuing work, and it is common for many to stop work to better care for a family member⁷⁴. A 2012 report by the WHO into the arsenic crisis in Bangladesh estimated an economic cost of over \$US 12 billion over twenty years⁷⁴. The report further claimed that the crisis might be eliminated within twenty years (by 2030) through appropriate government spending⁷⁴. However, many claim that to date, the programs aiming to combat arsenic contaminated groundwater have failed due to poor implementation, monitoring and quality control⁹⁹.

Table 2.1: The inorganic composition of groundwaters in the Bengal Basin of South Asia. Columns labelled ‘±’ indicate the standard deviation in averaged measurements, and N indicates the number of data points. The final average, median and standard deviation results were calculated using an even weighting of each literature source. Blank cells indicate where a parameter was not reported. Literature sources are as follows: [1] Joypur, Adrivok and Moynar villages in West Bengal, India, reported by McArthur et al. ⁸⁶; [2] Bangladesh, reported by Hug and Leupin ⁴⁰ with data from the British Geological Survey ¹⁰⁰; [3] Kushtia district, Western Bangladesh, reported by Munir and Rasul ¹⁰¹; [4] Southwest Bangladesh, reported by Ayers et al. ⁸⁵; [5] Bangladesh, reported by Aggarwal et al. ⁸⁷. Total As indicates the total concentration of dissolved arsenic, i.e. inorganic As(V) and As(III), as well as dissolved organic arsenic species. Total As was determined using [1] graphite-furnace AAS ⁸⁶, [2] ICP-MS [3] ICP-AES ¹⁰¹, [4] ICP-OES ⁸⁵, and [5] ICP-MS ⁸⁷.

Property	Source								average	median	±		
	[1] ⁸⁶	± (N=25)	[2] ^{40 100}	± (N>30)	[3] ¹⁰¹ (N=2)	[4] ⁸⁵	± (N=71)	[5] ⁸⁷					
pH	6.96	0.06	7	0.2	7.05	6.91	0.4	8.32	0.58	7.25	7	0.6	
Concentration (mg L ⁻¹)	Total As	0.226	0.165	0.301	0.2	0.08	0.072	0.065	-	-	0.17	0.15	0.11
	Na ⁺	41.9	6.7	-	-	19.3	1430	940	742	1210	557	392	670
	K ⁺	2.58	1.56	-	-	2.17	35.9	16.6	38	45	20	19	20
	Ca ²⁺	135	8	-	-	114	175	104	104	48	106	114	65
	Mg ²⁺	37.8	1.3	-	-	22.3	143	89	74.1	53.6	56	38	56
	Sr(II)	0.586	0.041	-	-	0.289	1.31	0.8	-	-	0.73	0.59	0.53
	Ba(II)	0.194	0.045	-	-	0.166	0.572	0.5	-	-	0.31	0.19	0.23
	Fe(II)	3.45	0.57	4.2	3.8	6.98	2.55	3.4	4.36	5.08	4.3	4.2	1.7
	Mn(II)	1	0.6	0.5	0.6	0.715	0.231	0.271	0.132	0.046	0.52	0.5	0.36
	NH ₄ ⁺	25	118	-	-	-	-	-	-	-	25.4	25.4	-
	HCO ₃ ⁻	601	63	-	-	708	766	206	320	90	599	655	198
	Cl ⁻	54.7	9.3	-	-	3.27	2080	1370	1080	1740	804	569	983
	SO ₄ ²⁻	14.2	18.4	-	-	0.424	19.3	31.8	-	-	11	14	9.8
	NO ₃ ⁻	0.621	0.899	-	-	1.45	0.334	0.4	-	-	0.8	0.62	0.58
	PO ₄ ³⁻	1.05	0.57	1.9	1.8	0.023	2.32	1.8	-	-	1.3	1.5	1
	H ₄ SiO ₄	64.7	3	19	5	-	21.6	7.3	-	-	35	22	26

2.3.2. Mitigation efforts undertaken to date

There are two approaches available to mitigating arsenic exposure: (a) changing to a non-contaminated water source, or (b) removing arsenic from the contaminated source. Due to pathogenic contamination of surface waters, the best solution to sourcing arsenic-free water is the installation of new deep wells, tapping aquifers with low arsenic concentrations. Removal of arsenic from contaminated waters can be carried out at both the household and the community level. This section discusses the progress and challenges faced by these different approaches.

2.3.2.1. Switching to arsenic-free groundwater sources

Arsenic levels across Bangladesh were mapped out in 2001 by the British Geological Survey (BGS)¹⁰². The survey illustrated the high variance of arsenic concentrations at short distances, with huge differences even between neighbouring tube wells¹⁰⁰. This effect arises because tube wells tap into different aquifers, depending on how deep they are drilled. Most tube wells in Bangladesh are shallow, tapping into the aquifer at ~40 metres from the surface. This is the arsenic-contaminated aquifer¹⁰³. Deep wells, extending more than 150 metres below the surface, normally tap into low-arsenic aquifers and therefore provide water that is arsenic-free and safe to drink¹⁰³.

However, switching from shallow wells to deep wells has had many challenges. Firstly, the installation of deep wells is too expensive to provide perfect coverage for all communities at risk. Secondly, despite a good understanding of the mechanism of arsenic release and the associated geology (with mapping and models available), interventions are still often targeted at the wrong communities¹⁰⁴. For instance, multiple deep wells are often provided to low-risk communities¹⁰⁵, whilst many at-risk villages remain without a single low-arsenic well¹⁰⁶. Thirdly, elite capture, wherein privileged members of society claim a public resource for their own, prevents many vulnerable people from accessing deep wells^{106 107}. Additionally, families will continue to use a shallow well if it is closer¹⁰⁸. Finally, deep wells are often not tested for arsenic during installation¹⁰⁵, and even when they are, deep wells can become contaminated with continuous use, due to recharge of the deep well aquifer from neighbouring arsenic-contaminated aquifers. Consequently, without regular monitoring, the safety of the deep well cannot be verified.

2.3.2.2. Remediation of arsenic-contaminated groundwater sources

Other mitigation schemes have considered technologies to remove arsenic from the contaminated shallow aquifers. These approaches normally use sorbent media in a filtration design. The best-known product is the Sono household filter^{101 109}. One 2016 study reports that this product has found a niche for treating arsenic-contaminated waters when deep wells are unavailable, however the technology has limited success¹¹⁰. A 2010 study of household filtration devices found that after two years, one quarter of households had stopped using the technology, and that for those who continued to use the devices, 10% failed to provide safe drinking water³⁰. All sorbent media eventually becomes saturated and ceases to function, however adequate monitoring is missing from the current generation of small-scale filtration programs³⁰. When the media is saturated, it must be cleaned or replaced. High dropout rates are explained by users not understanding how to clean the media, or not understanding the importance of cleaning the media, as well as the prohibitive costs of replacing media (\$33-65 USD)³⁰. Additionally, the public often distrusts or dislikes arsenic-free water (whether from deep wells or treated water sourced from the shallow aquifer) since consumers are used to, and prefer, the taste of arsenic-contaminated shallow aquifer water³⁰.

2.3.3. Future arsenic exposure

Increased public awareness and various mitigation programs have been successful in reducing public exposure to arsenic¹⁰⁴. However, many millions of people are still at risk, and factors including groundwater over-abstraction risk increasing our exposure to arsenic in the future. Economic and population growth both lead to an increased demand for water that is threatening to contaminate previously safe supplies. In rural areas, groundwater consumption is increasing due to the demand for irrigation¹¹¹. Increased groundwater pumping brings the surface waters rich in organic matter down into the aquifer, increasing microbial dissolution of iron oxides and enhancing the release of arsenic¹¹². This increases both the prevalence and severity of arsenic contamination¹¹¹. In urban areas such as Kolkata, India, rapid urbanisation has dramatically increased both public and industrial demand for water⁵³. Studies predict that groundwater over-abstraction will lead to contamination of urban aquifers in the next 50 years, due to the aquifers that are currently safe recharging from arsenic-contaminated sources⁵⁶.

Further efforts are needed to minimise public exposure to arsenic, be it greater public awareness; improved governance and expanded mitigation schemes; new technology; or a combination of all three. The work presented in this thesis focuses on South Asia, due to (a)

the number of people exposed, and (b) the health and economic consequences. Remediation of arsenic in South Asia is especially challenging, given the neutral charge of As(III). This thesis therefore focuses on the technological aspects of arsenic remediation, and the following sections provide a review of previous efforts to treat As(III)-contaminated waters.

2.4. Remediation and its challenges

When the extent of arsenic exposure in South Asia was revealed in 1993-1994, a significant effort was made to design and engineer new remediation techniques, with a boom in research on the remediation of arsenic (publication rates are presented in the Appendix). Research into the remediation of arsenic continues to show growth year on year. Several in-depth reviews have been published discussing technologies for the remediation of arsenic ^{113 114 115}. This section highlights the main approaches and their limited effectiveness for the removal of As(III).

2.4.1. Flocculation-coagulation

Flocculation-coagulation is a routine treatment carried out by centralised water treatment plants worldwide. A coagulating agent is added to the contaminated water (commonly ferric chloride, FeCl₃, or alum, Al₂(SO₄)₃) ¹¹³. These salts trap contaminants with opposing charge (e.g. As(V) oxyanions are trapped by Fe²⁺ and Al³⁺). A floc is formed which then coagulates and precipitates out of solution. The coagulated sludge is then physically separated from the treated water. In the best case scenario, flocculation-coagulation is 50% less effective for removal of As(III) compared with As(V) due to the neutral charge of H₃AsO₃ ¹¹³. In the worst case scenario As(III) is not removed at all ¹¹³. A further problem is the generation of large volumes of arsenic-rich sludge, which is expensive to detoxify ¹¹³.

2.4.2. Membrane technologies

Membrane technologies work by size or charge exclusion. Using microfiltration and ultrafiltration technologies (with 0.1-10 µm and 2-100 nm pore sizes respectively) solvated arsenic cannot be excluded by size. Consequently, addition of a coagulant media is necessary to incorporate the arsenic into colloidal forms ¹¹³. Whilst nanofiltration (1-10 nm pore sizes) and reverse osmosis have been used to remove As(V), the remediation of As(III) using

membrane technologies remains limited, and this technique is often unable to meet guideline limits¹¹³. Additionally, membrane technologies have high capital and running costs¹¹⁶. These approaches are energy intensive and require a power source to pressurise the feedstock waters, limiting applications in rural off-grid settings. An example of the current membrane-based arsenic treatment plants developed for rural India is presented in Figure 2.1.



Figure 2.1: A rural arsenic treatment plant in West Bengal, India, based on membrane technology. (Left) The influent is mixed with air and media for oxidation and incorporation of dissolved arsenic into colloidal forms. (Right) Ceramic membranes are used to filter out colloidal arsenic. Source: the author, 2018.

2.4.3. Co-precipitation

Co-precipitation is a low-cost option for water treatment. Arsenic is removed from solution via the formation of an insoluble product, such as ferric arsenate, AsFeO_4 ^{117 118}. The precipitated solids are then separated from the clean water. Co-precipitation is also used by the mineral processing industry to detoxify wastewater effluents^{97 118}. The effectiveness of co-precipitation depends on the water quality. Ho Chi Minh City in Vietnam, is situated on a large delta, like Bangladesh. Many of the eleven million inhabitants rely on tube wells for drinking water, of which 20% are contaminated by arsenic above the WHO $10 \mu\text{g L}^{-1}$ guideline limit⁴⁰. The groundwater has high concentrations of dissolved iron and therefore co-precipitation is an effective treatment for arsenic removal, where the arsenic-rich precipitates are collected in the sediment of sand filters used to remove iron⁴⁰. Unfortunately, co-precipitation is much less effective in South Asia as these groundwaters have (a) less dissolved Fe, and (b) more phosphate. Phosphate outcompetes As(III) for incorporation into, and adsorption onto the iron (hydr)oxide precipitates^{6 40}. Whilst As(III) will oxidise to As(V) under ambient conditions, photocatalysed by sunlight, and then co-precipitate with any remaining Fe(III), the process is slow and the treated water often remains unsafe to drink⁴⁰.

2.4.4. Less established technologies

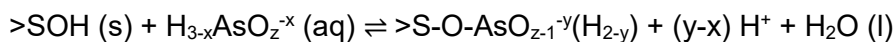
Other methods used to remove arsenic from water include ion exchange resins. Again, this technique relies on electrostatic interactions (e.g. exchange of As(V) for chloride or acetate anions), with limited ability to remove As(III)¹¹⁹. Electrocoagulation has been investigated for improved As(III) removal, however, given the energy input needed, its economic efficiency has not been established¹¹⁹. Treatments using solar energy have also been investigated. This includes a co-precipitation-filtration technique, using an electrolytic cell to produce chlorine, which oxidises As(III), enhancing removal via co-precipitation¹²⁰. This autonomous plant successfully reduced an influent arsenic concentration of 190 µg L⁻¹ to 10 ±4 µg L⁻¹ during a ten month deployment¹²⁰. Given the high density of arsenic (despite being a metalloid, arsenic is classed as a *heavy metal*), distillation using low cost methods such as solar stills offer further possibilities towards achieving arsenic remediation using sustainable energy^{121 122}.

2.4.5. Adsorption

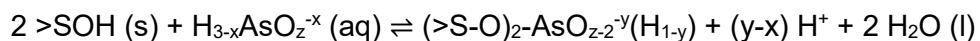
Adsorption has received more attention than any other technology when it comes arsenic remediation (publication rates are presented in the Appendix). Adsorption is the process whereby a dissolved *sorbate* binds to the surface of a solid *sorbent* material. Adsorption is an effective solution for oxygenated waters due to the strong covalent bonds formed between As(V) and the surface hydroxyls of mineral sorbents such as iron oxides. Filling a filter device with sorbent media provides a simple, low-cost solution to As(V) removal¹¹⁶. Adsorption reactions include chemisorption (where covalent bonds are formed between the sorbate and the sorbent), physisorption (where the sorbate and sorbent bind due to electrostatic attractions), and capillary condensation¹²³. Adsorption offers advantages for developing countries and rural areas through its low cost, simple implementation, and high efficiency³.

Activated carbon and charcoal are popular and established sorbents for the removal of toxic organic compounds (and are also used to improve aesthetics, namely taste and odour)¹²⁴. Activated carbons show incredibly high surface areas, typically above 1000 m² g⁻¹, providing high adsorption capacities¹²³. Whilst activated carbon is an effective sorbent for metal cation sorbates (such as Cd²⁺ and Pb²⁺) which bond with the sorbent's aromatic π-electrons¹²⁵, activated carbon has no specific mechanism for the adsorption of arsenic. Activated carbon is therefore a poor arsenic sorbent, though it can be used as a high surface area support for further functionalisation^{126 127 128}.

In contrast, mineral oxides such as goethite (FeOOH), magnetite (Fe_3O_4), hematite ($\alpha\text{-Fe}_2\text{O}_3$) and aluminium oxide (Al_2O_3) are effective As(V) sorbents⁹⁷ (despite having lower surface areas than activated carbon, typically around $100 \text{ m}^2 \text{ g}^{-1}$ ¹²³). Inorganic arsenic adsorbs to minerals primarily through a condensation reaction between the hydroxyl groups of the mineral surface and the arsenic sorbate. This reaction is represented through the generic equations:



Equation 2.1



Equation 2.2

for monodentate and bidentate adsorption respectively, where $>\text{S}$ denotes a surface metal atom, x and y are zero or positive integers, and z is 3 or 4. The removal of As(V) using iron oxides is especially effective owing to the electrostatic attraction between the positive mineral surface (at circumneutral pH) and the negative charge of the oxyanion surface complex^{129 130}.

The Sono-3-Kolshi filter is designed for household remediation using adsorption, and this product has gained traction in Bangladesh. The filter uses gravity to pass the influent water through two buckets filled with (1) cast iron turnings covered with sand, and (2) wood charcoal mixed with sand¹⁰¹. It is claimed that this product can serve a family of five for five months at a cost of around \$USD 5¹⁰¹. However, one study found that the success of Sono filters was limited by factors including the need to dispose of toxic sludge by-products when the sorbent is saturated³¹.

Community-scale devices also suffer from problems when the sorbent is saturated. Figure 2.2 shows a community-scale arsenic removal device used in Uttar Pradesh, India, typical of the technology offered to rural communities (in this case using Al_2O_3 as the sorbent)¹. One study assessed 34 plants after 10 years of operation, and found that most plants were failing to remove any arsenic at all¹. These units fail when the sorbent media becomes saturated and arsenic breaks through into the effluent. Since users often fail to replace or regenerate saturated sorbent media due to lack of expertise³⁰ or lack of confidence³¹, sorbent life-time is a major factor determining the success or failure of arsenic mitigation schemes in South Asia built around adsorption technology. As(III) forms weaker

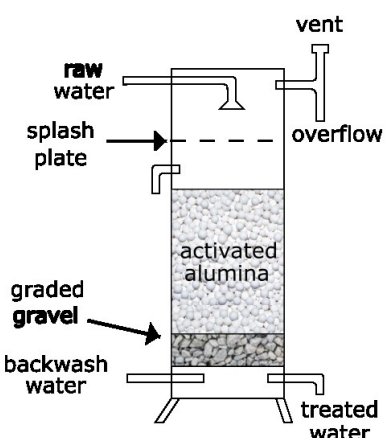


Figure 2.2: Example of a well-head arsenic removal unit, typical for rural communities in India. This diagram was re-drawn for clarity from another source¹.

bonds to the sorbent than As(V), and is thus more easily displaced by competitor ions such as phosphate and sulphate oxyanions ¹³¹, reducing sorbent lifetimes.

2.4.6. The need to oxidise

In all of the technologies discussed removal of As(III) is more challenging than removal of As(V). This is even true for adsorption, perhaps the favoured technique for removal of arsenic. Oxidation of As(III) to As(V) therefore offers a solution towards increasing the effectiveness of arsenic remediation ^{132 133}. In the case of adsorption, oxidation should increase sorbent media lifetimes, reducing the frequency that media needs to be replaced or generated. Longer lived sorbent media reduces the costs of replacing saturated media, and reduces the problem of toxic sludge disposal ³⁰. However, as Figure 2.2 shows, oxidation typically incorporated into typical arsenic removal units through an ‘aerial oxidation’ step, which mixes the influent water with air from the atmosphere ¹³⁴. (In this example, water is passed through a showerhead-type sprinkler). Unfortunately, oxidation of As(III) using air is slow. Studies of in-situ oxidation (pumping air underground) have shown that several days treatment is often required ¹³⁵. Consequently, a more involved pre-treatment to oxidise As(III) to As(V) is needed to achieve effective removal of As(III), and increase the lifetimes of arsenic removal units ⁹⁷.

2.5. Advanced oxidation processes

This section provides an overview of the various approaches towards achieving oxidation of As(III): chemical oxidation, *in situ* photooxidation, and the application of heterogeneous photocatalysts.

2.5.1. Chemical oxidation

For all conventional water treatments, removal of the neutral As(III) species (H_3AsO_3) is a major challenge. Many studies have considered oxidative pre-treatments to convert neutral As(III) to the negatively charged As(V) oxyanions, $HAsO_4^{2-}$ and $H_2AsO_4^-$ ^{136 137 138}. Not only is the inorganic As(V) more easily removed, but it is less toxic (see section 2.1).

Oxidation of drinking water is typically achieved through the addition of chlorine (ClO_2 , HOCl or ClO^-), permanganate (MnO_4^-), ozone (O_3) or Fenton's reagent ($\text{H}_2\text{O}_2/\text{Fe}^{2+}$), typically for disinfection by degrading microbial life (this is especially important for surface waters where faecal contamination is always a risk)¹³⁹. Excess chlorine is often added to help preserve standing water before consumption, and this is known as the chlorine residual¹⁴⁰. The term 'advanced oxidation process' (AOP) refers to water treatments that use the *in situ* generation of highly reactive hydroxyl radical ($\cdot\text{OH}$) oxidants¹⁴¹, such as treatments using H_2O_2 or O_3 .

Chemical oxidants can also be used to oxidise As(III)^{5 6}, however chemical oxidation has at least three limitations: (a) a chemical feedstock is needed, (b) there is a trade-off between achieving a chlorine residual and providing good taste, and (c) there is a risk of forming disinfection by-products (DBPs) such as trihalomethanes, which are their selves carcinogenic⁹. Presently water, sanitation and hygiene (WASH) practitioners are looking towards automated chlorine dosing at the point of use, whether mechanical or electrical, to ensure the necessary chlorine residual is achieved¹⁴⁰. Whilst such technology could be used to oxidise As(III), automated dosing has not yet been widely adopted¹⁴⁰. Additionally, both surface and groundwaters in the Bengal Basin contain high concentrations of dissolved organic matter, increasing the risk of toxic DBPs^{9 6}.

2.5.2. Aqueous-phase photooxidation

Oxidation catalysed by ultraviolet (UV) light has been used for water disinfection since the 20th century¹²⁴, where the reactive free radicals produced by UV excitation of dissolved oxygen interrupt cell metabolism and degrade cell structures. Solar disinfection harnesses the freely available ultraviolet light radiating from the sun, whilst UV lamps can be used when there is access to electricity. UV Waterworks was a product aimed for providing ultraviolet water disinfection to developing countries on a household scale. UV Waterworks claimed to be able to deliver water free from microbes at a cost of just 5 cents per person per year, with a capital cost of \$US 300¹⁴².

Direct photooxidation of As(III) in the absence of any heterogeneous photocatalyst can be achieved. Ryu et al. demonstrated than at pH 7, in equilibrium with air, $750 \mu\text{g L}^{-1}$ As(III) was oxidised in 90 minutes, upon irradiation with a 240 nm ultraviolet light source (hard UV)¹⁴³. Photooxidation rates can be improved by creating a more oxidising environment, e.g. adding excess dissolved oxygen¹⁴³, or photoexcited intermediates such as the sulphate radical ($\text{SO}_4^{\cdot-}$)¹⁴⁴. However, other species naturally occurring in the groundwaters of South Asia, such as dissolved organic carbon, are known to reduce photooxidation rates through oxidant

scavenging⁹³. Many groups have therefore looked towards heterogeneous photocatalysts to improve reaction rates in the photooxidation of As(III) and thereby reduce treatment times and energy costs.

2.5.3. Photocatalytic oxidation

Photooxidation kinetics can be improved by addition of a heterogeneous photocatalyst. Photocatalytic activity was first identified in 1938, when TiO₂ (nowadays our best-known solid-state photocatalyst) was observed to induce the photobleaching of dyes¹⁴⁵. TiO₂ found subsequent applications in water splitting (photoelectrolysis, generating H₂ and O₂ gas) in the 1960's¹⁴⁶, and continues to be the benchmark photocatalyst for many reactions.

TiO₂ is a semi-conductor material, wherein valence electrons occupy a band of molecular orbitals delocalised across the material¹⁴⁷. Upon irradiation by light with sufficient energy, photons are absorbed with the subsequent promotion of an electron from the valence band to the conduction band (Figure 2.3). The energy of the photon must be equal or greater to the difference between the highest occupied molecular orbital (HOMO) of the valence band and the lowest unoccupied molecular orbital (LUMO) of the conduction band, and this energy difference is the *band gap*¹⁴⁷. The photoexcited electron occupies a quantum state in the conduction band, and the unoccupied quantum state left behind in the valence band is known as a *hole*. This photoexcited electron-hole pair is termed an *exciton*, and these charge carrier pairs are responsible for photocatalytic and photovoltaic behaviour. To catalyse a redox reaction photoexcitons must migrate to the solid surface, where electrons and holes may reduce and oxidise substrates respectively. The vast majority of charge carriers recombine, emitting heat, and the major challenge for photocatalyst design is improving the collection of charge carriers at the surface.

In water treatment, TiO₂ has already found applications in the photocatalytic degradation of chlorophenols (toxic pesticides and wood preservatives)¹⁴⁸, and organic dyes in wastewater effluents from the industrial manufacture of textiles, paints, food stuffs and cosmetics¹⁴⁸.

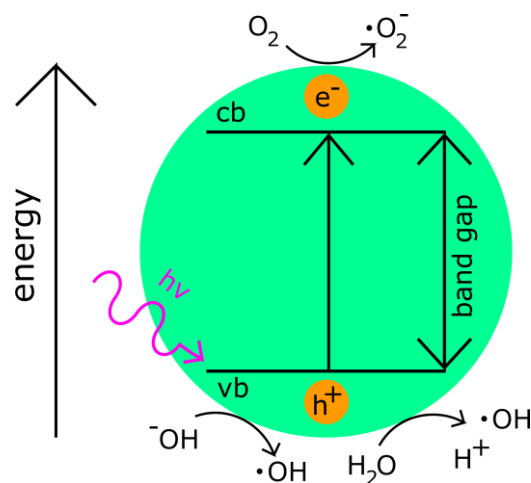


Figure 2.3: Generation of charge carriers in a heterogeneous photocatalyst. e^- and h^+ denote the excited electrons and holes respectively, cb and vb denote the conduction and valence bands respectively, and hv denotes the energy of the absorbed photon (where h is the Planck constant, and v is the frequency of the photon).

However, the application of heterogeneous photocatalysts for water remediation is not as established as other advanced oxidation processes.

2.5.4. As(III) remediation using heterogeneous photocatalysts

It is only since the turn of the millennium that both adsorption and photocatalysis have received significant research interest, and both are now in a period of exponential growth (Figure 2.4a). For adsorption, this recent growth is likely due to recognition of the toxicity of heavy metal contaminants and new efforts to remove them (other contaminants such as harmful pathogens are best removed by established treatments such as size exclusion and chlorination, of which neither process is appropriate for the removal of heavy metals). The main drivers for research in water treatment using heterogeneous photocatalysts are disinfection (destruction of pathogens) and degradation of large molecular organic contaminants¹⁴⁹.

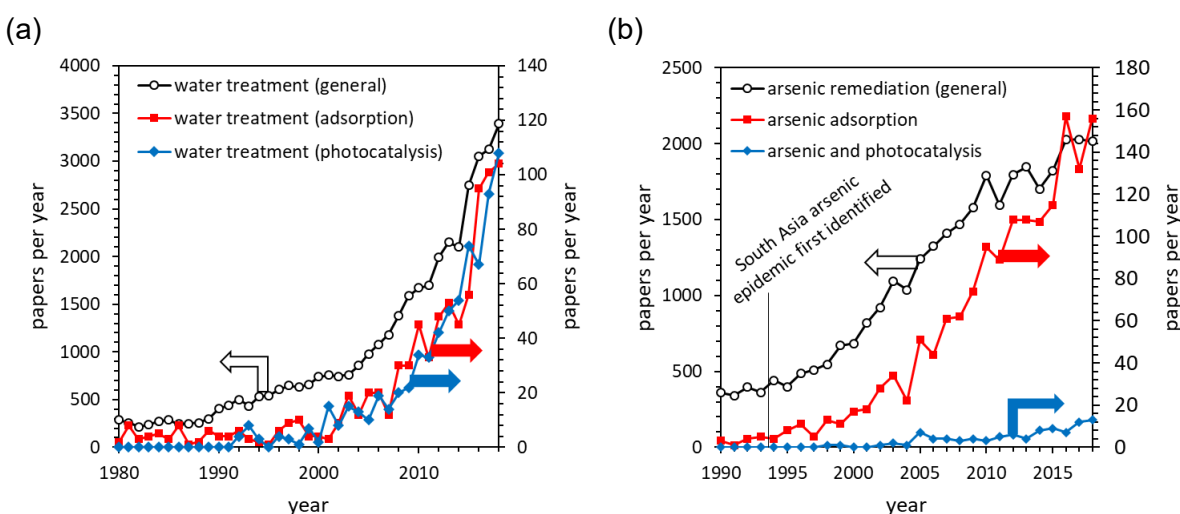


Figure 2.4: A comparison of publications in general water treatment versus arsenic remediation more specifically. (a) presents publications in water treatment: in general (open circles with black lines), specifically mentioning adsorption (red squares), and specifically mentioning photocatalysis (blue diamonds). (b) presents publications in arsenic remediation (open circles with black lines), arsenic adsorption (red squares), and arsenic photocatalysis (blue diamonds). The line at 1993 indicates when epidemic exposure to arsenic within South Asia was first identified⁴³. Arrows are used indicate to which y-axis each data series belongs. A description of the methodology and the search terms used is given in the Appendix.

The situation is very different however if we consider technologies for the more specific aim of arsenic remediation. Figure 2.4b shows that whilst research into sorbents for arsenic remediation has grown rapidly since the South Asia arsenic crisis was first identified (1993–1994), studies on the application of photocatalysis for the remediation of arsenic only really began in 2005, most notably with the study of Dutta et al.²⁸. A few earlier publications demonstrated the photocatalytic oxidation of As(III) in the presence of UV-irradiated TiO₂:

Foster et al. (1998) and Yang et al. (1999)^{150 151}. Whilst publications in arsenic removal via adsorption has increased from 5 per year (1993) to 156 (2018), photocatalysis for arsenic remediation has only increased from 7 per year (2005) to 13 (2018) (Figure 2.4b). This suggests that the field of arsenic remediation via photocatalysis may be underdeveloped at present.

Studies have considered TiO₂ for the photocatalytic oxidation of As(III) both by itself, and in the presence of additional reagents, such as hydrogen peroxide, H₂O₂¹³². There are, however, very few studies considering alternative heterogeneous photocatalysts¹⁴¹. The few alternatives considered include WO₃¹⁵², ZrO₂¹⁵², graphitic carbon nitride¹⁵³, and CuO/ZnO composites¹⁵⁴. To date, despite many papers demonstrating successful photocatalytic oxidation of As(III), few studies have implemented photocatalysis in any kind of practical design: whilst a few column studies are reported^{132 155}, no study demonstrates the real-life application of heterogeneous photocatalysis for the remediation of arsenic.

2.6. Emerging materials in water treatment

This section presents an overview of emerging areas in water treatment: nanomaterials, multifunctional materials (e.g. the combined photocatalyst-sorbent system), composite materials (often synthesised with the aim of achieving multifunctional behaviour), and enhanced photocatalytic activity using heterojunctions at semi-conductor interfaces.

2.6.1. Nanomaterials: Superior activity

Since around 2005, there has been a boom in publications concerning nanotechnology for water treatment, and at present nearly one in ten water treatment papers involves nanotechnology in some way (figures in the Appendix). Nanomaterials are defined as materials which have one (nanosheets), two (nanorods and nanotubes) or three (nanoparticles) spatial dimensions confined to less than 100 nm. Nanoparticles exhibit high surface areas ($>100 \text{ m}^2 \text{ g}^{-1}$), yielding high adsorption capacities. Nanomaterials are often highly reactive, given that atoms located at edges and corners have high potential energy¹²³. Nanomaterials have found uses as (a) sorbents, thanks to their high surface areas and large adsorption capacities¹⁵⁶, and (b) photocatalysts, thanks to their high surface areas and the short distances between photogenerated charge carriers and the surface¹⁵⁷, and ©

membranes for nanofiltration, since small nanopores improve size exclusion and charge exclusion^{158 159}. Nanomaterials for water treatment are likely to continue their exponential rise into the foreseeable future (Appendix, Figure 10.1).

2.6.2. Multifunctional sorbents: Secondary properties

When identifying the best candidate nanomaterial for applications as a sorbent or photocatalyst, it is necessary to look beyond surface area and reactivity, and to consider other properties such as dispersion/colloidal stability¹⁶⁰, chemical stability, toxicity¹⁶¹ and whether the material exhibits any other behaviour, such as magnetism¹⁶². Materials offering beneficial secondary capabilities are becoming widely investigated in contemporary water research¹⁶³. In some instances, the term ‘multifunctional’ is used to describe materials which offer several potential applications¹⁶⁴. In this thesis, ‘multifunctional’ describes materials which show more than one useful active property for the purposes of remediating contaminated water.

Examples of multifunctional materials include magnetite (Fe_3O_4), which, in addition to being a good sorbent for heavy metal removal, is also magnetic¹⁶². This magnetism facilitates the removal of toxic sludge from treated water. TiO_2 is another example of a multifunctional material, where its photocatalytic activity is combined with reasonable affinity towards the adsorption of a variety of heavy metal contaminants¹⁶⁵. Studies may also aim to expand the selectivity of a sorbent towards additional contaminants (e.g. increasing sorbent functionality), through impregnating the sorbent with minority sorbent phases, selective towards particular contaminants¹²³. Research in water treatment using multifunctional materials for adsorption and photocatalysis only really began around the year 2010, however continued growth in the field looks likely (Appendix).

2.6.3. Composite materials: Introducing new properties

Some materials exhibit multifunctional behaviour with a single component, or after impregnation/doping minority components into the bulk material. In other cases, multifunctional behaviour is acquired by combining multiple materials into a new composite form, creating a material with two or more discrete solid phases. Whilst TiO_2 is a reasonable sorbent for contaminants including arsenic^{166 167 168 169}, it has a significantly lower adsorption capacity than iron oxides¹⁶⁶, and evidence suggests that this adsorption capacity can actually lead to deactivation of TiO_2 as a photocatalyst¹⁷⁰.

Vaiano et al. claimed that their observations of incomplete photocatalytic oxidation of As(III) in the presence of TiO₂ were due to the photocatalyst surface becoming increasingly blocked by the As(V) produced ¹⁷⁰. Blocking of surface sites is known to suppress photocatalytic activity ¹⁷¹. When TiO₂ was combined with molybdenum oxide as a new composite material, As(III) photooxidation proceeded to completion. The authors claimed that this was due to the MoO_x phase adsorbing the As(V) product and thus preventing the TiO₂ surface from becoming blocked ¹⁷⁰. In this case, coupling TiO₂ with MoO_x appears to have created a multifunctional material, where the two components behave synergistically. Coupling TiO₂ with a second material that has a greater affinity for the adsorption of As(V) might therefore improve As(III) remediation by (a) increasing adsorption capacity and (b) removing As(V) and other anions which would otherwise block the TiO₂ surface and suppress photocatalytic activity. Composite photocatalysts often also exhibit improved photocatalytic properties through heterojunction effects (discussed in section 2.6.4).

Other examples of multifunctional composite materials used for the remediation of As(III) include Chi et al. (2016) and Pincus et al. (2019). Chi et al. used a g-C₃N₄/Fe₃O₄ composite, with graphitic carbon nitride (g-C₃N₄) acting as a visible light photocatalyst, and magnetite (Fe₃O₄) acting as a magnetic sorbent ¹⁵³. Pincus et al. used a chitosan composite, impregnated with TiO₂ and loaded with Cu. In this material TiO₂ acts as photocatalyst, and chitosan (functionalised with amine groups) acts as a support for cross-linked Cu, which acts as an As(V)-selective sorption site ¹⁶³.

Synthesis of new composite materials is not always done with the intention of introducing new functionality. For instance, grafting or impregnating metal oxides such as Fe₃O₄ onto high surface area activated carbon, biochar or graphene is a popular way to (a) immobilise metal oxide sorbents for easy removal from treated water, (b) increase surface areas, and (c) improve stability (e.g. preventing Fe₃O₄ from oxidation and leaching during application) ^{172 173}. Alternatively, a number of studies have coated or impregnated metal oxides onto cheap, bulk supports for use in fixed bed reactors and for ease of post-treatment. This includes arsenic removal by iron oxide coated sand ^{174 175 176}, arsenic removal by TiO₂-impregnated chitosan beads ¹⁷³, and removal of Cu(II) and Ni(II) using chitosan supported on alumina ¹⁷⁷. Recent research has also considered the use of composite and multifunctional sorbents for other purposes, such as removal of Cr(III) by iron oxide-silica ¹⁷⁸, Pb²⁺ by hydroxyapatite-chitosan ¹⁷⁹, Cu²⁺, Pb²⁺ and Cd²⁺ by phosphonate-organosilica ¹⁸⁰ and Th⁴⁺ by polyacrylamide-aluminosilicate ¹⁸¹.

2.6.4. Heterojunctions: Improving photocatalytic activity

Heterojunctions are important phenomena in composite photocatalysts, arising when an interface is formed between semi-conductors with dissimilar conduction and valence band energies²⁴. The major challenge in photocatalysis is collecting photoexcitons at the catalyst surface. As excitons are inherently unstable, electron-hole recombination is more probable than charge carriers successfully reaching the catalyst surface and interacting with the substrate. When two semi-conductors with staggered bandgaps are brought to an interface, a potential energy field is created (*band bending*)¹⁸². This field encourages photoexcited electrons to migrate from the semiconductor with the highest conduction band energy to the lowest, and encourages positive holes to migrate from the semiconductor with the lowest valence band energy to the highest¹⁸³. The transferral of charge carriers across the interface reduces recombination rates and so increases photocatalytic activity¹⁸³. In fact Degussa P25, the best known commercial TiO₂ product, is itself a composite of 80% anatase TiO₂ and 20% rutile TiO₂ with the resulting heterojunction conferring the effective charge separation which gives P25 its excellent photocatalytic properties¹⁸⁴.

The ideal situation is the type-II staggered heterojunction (Figure 2.5), where both conduction and valence bands of one semiconductor phase are more positive than the other²⁴. In this heterojunction, photoexcited electrons and holes will transfer in opposite directions, decreasing recombination rates. In a type-I heterojunction, the conduction and valence bands of one semi-conductor phase are more positive and negative, respectively, than the other²⁴. In the type-I heterojunction, electrons and holes transfer in the same direction as one another, and consequently beneficial heterojunction effects may be limited if electrons and holes transfer between semi-conductors at similar rates²⁴.

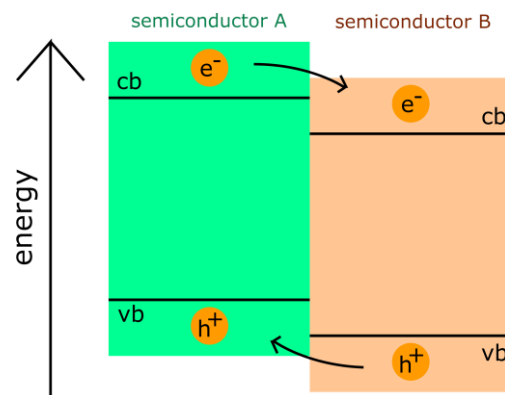


Figure 2.5: The type-II staggered heterojunction, where photoexcited electrons and holes transfer in opposite directions. e⁻ and h⁺ denote electrons and holes respectively, cb and cv denote the conduction and valence bands respectively.

A variety of mixed semi-conductor photocatalysts have been investigated for applications in water remediation, for instance TiO₂, Cu₂O and Bi₂WO₆ have all been grafted onto graphene¹⁷². Grafting semi-conductors onto graphene both (a) facilitates charge carrier separation (thereby reducing electron-hole recombination rates) and (b) immobilises metal oxide nanoparticles (so that the photocatalyst can be separated more easily from the treated water).

On the other hand, Beydoun et al. (2000) claimed that the unfavourable heterojunction between TiO₂ and Fe₃O₄ (a type-I staggered heterojunction) actually increased the rate of electron-hole recombination leading to worse performance ¹⁸⁵.

There are only a few publications where heterojunction behaviour has been discussed specifically in relation to the photocatalytic oxidation of As(III). Fausey et al. (2019) found that within their nanofiber matt composites, reduced graphene oxide acted as an electron acceptor to TiO₂, preventing charge carrier recombination, increasing the concentration of generated hydroxyl radicals, and thereby improving As(III) photooxidation rates ¹⁸⁶. Similarly, improved removal of As(III) has been observed when graphitic carbon nitride (g-C₃N₄) was coupled with Fe₂O₃ ¹⁸⁷ and Fe₃O₄ ¹⁵³ and assigned to the heterojunction effect.

2.6.5. Multifunctionality and As(III)

Adsorption is the favoured method for the separation of arsenic from contaminated water, and the interactions between arsenic and a wide range of single-component sorbent materials has been well characterised. Much recent sorbent development thus focuses on composite, multifunctional materials, wherein the advantageous properties of multiple single-phase materials may be combined. For instance, there are now numerous examples of composite photocatalyst-sorbents, used to provide a photocatalytic pre-treatment, e.g. oxidation of As(III) ¹⁸⁸, reduction of Cr(VI) ¹⁸⁹, or degradation of organic contaminants ²³, producing products that are safer and more readily removed through subsequent adsorption.

Several groups have combined photocatalytic and sorbent materials into bifunctional composite forms for the remediation of As(III). There are potential advantages to incorporating both capabilities into a single material: a single reactor can be more easily engineered, the operator needs only use a single media within the arsenic treatment plant or treatment device, and there is the possibility of synergistic effects, wherein coupling different components may enhance either photocatalytic oxidation or adsorption. Figure 2.6 shows that whilst adsorption of arsenic has been widely studied ever since arsenic exposure in South Asia was identified in 1993, the application of composite sorbent materials has only been investigated since 2008, though the publication rate is now climbing. On the other hand, research into composite photocatalysts for the remediation of arsenic is rare, and the combined photocatalytic oxidation-adsorption approach has only received continuous attention since 2015. The application of composite and multifunctional materials for arsenic remediation is clearly an emerging area, and the field is likely to receive increased attention in the near future.

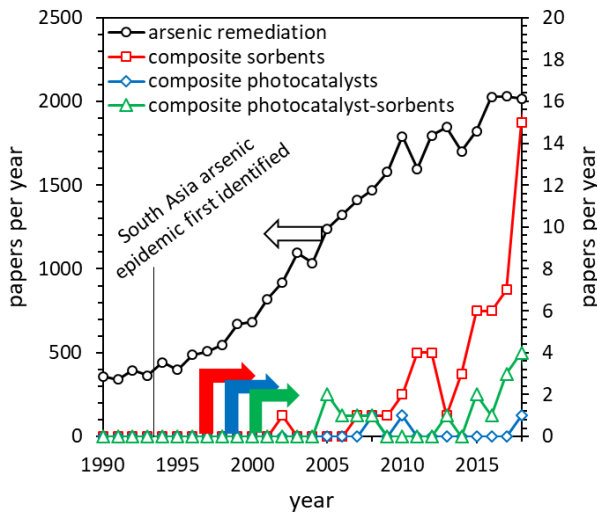


Figure 2.6: Research papers published each year on arsenic remediation using composite materials. A description of the methodology and the search terms used is given in the Appendix. Arrows are used indicate to which y-axis each data series belongs.

2.7. Mesoporous $\text{TiO}_2/\text{Fe}_2\text{O}_3$: A bifunctional sorbent for arsenic remediation

This thesis considers a composite photocatalyst-sorbent material based upon TiO_2 and Fe_2O_3 crystalline phases for the remediation of As(III)-contaminated waters. This section presents an overview of what is currently known concerning photocatalytic oxidation of As(III) in the presence of TiO_2 , and adsorption of arsenic onto iron oxides such as Fe_2O_3 . This section then covers previous work on the titania-iron oxide composite system, including the meso- $\text{TiO}_2/\text{Fe}_2\text{O}_3$ composite studied in this work. The knowledge gap pertaining to single-component TiO_2 and Fe_2O_3 systems, and the composite $\text{TiO}_2/\text{Fe}_2\text{O}_3$ system is identified and discussed.

2.7.1. TiO_2 : The benchmark photocatalyst for As(III) oxidation

The majority of literature concerning the application of heterogeneous photocatalysts for the oxidation of As(III) considers TiO_2 , with only a handful of studies exploring other photocatalytic materials^{152 153 154}. TiO_2 is clearly considered the benchmark material for investigating the photocatalytic oxidation of As(III), however contradictory results concerning kinetic laws and the underlying reaction mechanisms have often been reported.

2.7.1.1. The mechanism of heterogeneous photocatalytic oxidation of As(III)

The mechanism of TiO₂-catalysed As(III) photooxidation has been heavily disputed over the past twenty years, with ·OH hydroxyl radical mediated^{151 28 190}, O₂·⁻ superoxide radical mediated^{191 192}, and direct positive hole oxidation¹⁴¹ all considered to be potential pathways for As(III) oxidation by different authors.

Yang et al. (1999) observed that degassing suspensions with N₂ suppressed As(III) photooxidation in the presence of TiO₂ (pH 9)¹⁵¹. The authors concluded that since oxygen scavenges electrons from the TiO₂ conduction band (increasing hole life-times), As(III) must be oxidised directly by holes or via the ·OH hydroxyl radical intermediate, and not by the superoxide radical, O₂·⁻. Lee and Choi (2002) also observed faster reactions in the presence of O₂, however addition of *t*-butanol as a hydroxyl scavenger had no observable effect (except when humic acid was also present) and the authors thus argued that As(III) oxidation used a superoxide-mediated pathway¹⁹¹. Dutta et al. (2005) argued against the O₂·⁻ intermediate²⁸. In this study, benzoic acid (a hydroxyl scavenger) was found to suppress reaction rates, leading the authors to argue for a hydroxyl-mediated pathway. Whilst Bissen et al. (2001) found no significant influence of pH on the kinetic rate between pH 5-9, Zhang and Itoh (2006) found high kinetic rates at either pH extreme when using an iron oxide-titanium composite material, suggesting hydroxyl and superoxide radical-mediated pathways taking dominance depending on the concentration of acidic protons and hydroxide ions¹⁹³. Yoon et al. (2009) observed that when using formic acid as a hole or hydroxyl scavenger, As(III) oxidation rates were suppressed whilst H₂O₂ was generated¹⁹⁰. Since H₂O₂ is produced by superoxide radicals, Yoon et al. used this evidence to argue that hydroxyl radicals or valence band holes drive As(III) photooxidation. Addition of methanol as a surface hydroxyl radical scavenger significantly but incompletely suppressed As(III) photooxidation leading the authors to conclude that both valence band holes and hydroxyl radicals are intermediates in As(III) photooxidation.

Choi et al. (2010) claimed to have indisputable evidence for the superoxide-mediated pathway¹⁹². In this study, transient absorption spectroscopy (TAS) showed that the change in optical density at 700 nm after excitation with a 355 nm laser pulse was decreased upon addition of As(III). The authors claimed that since the signal from electrons trapped in the conduction band occurs at 550-800 nm, As(III) must increase the scavenging of trapped electrons, indicating the superoxide-mediated pathway. Other studies have suggested that the electron signal is actually centred at much higher wavelengths (850 nm in anatase TiO₂), with hole signals identified at 460 nm in anatase and 590 nm in rutile¹⁸⁴. Neither the position of the hole

signal nor the actual life-time of the transient absorption were discussed in the study of Choi et al. The reported data also showed that the electron signal at high wavelengths is greater than the hole signal after addition of As(III) (see their Figure 2, inset), suggesting that holes are scavenged in the presence of As(III) rather than electrons¹⁹². According to Marinho et al. (2019) the identity of the principle photooxidant in As(III)/TiO₂ systems has still not been resolved¹⁴¹.

To date, no study has identified whether the oxidation of As(III) in the presence of a heterogeneous photocatalyst such as TiO₂ occurs at the surface or in solution, e.g. in their proposed superoxide-mediated mechanism, Choi et al. raise the possibility of both surface and solution oxidation but no further discussion is provided¹⁹².

2.7.1.2. Understanding the rate laws

Much remains unknown about the kinetics of the photocatalytic oxidation of As(III) using TiO₂. Full kinetic rate equations, e.g. including the concentration of intermediate oxidants, have not been developed. Instead, previous studies have focused on determining the order of reaction with respect to the concentration of aqueous As(III). Bissen et al. identified first-order kinetics, with respect to aqueous As(III), in the oxidation of 50 µg L⁻¹ As(III) using Degussa P25 TiO₂ (0.001-0.05 g L⁻¹) at pH 5-9¹³⁹. In contrast, Dutta et al. found zero-order kinetics in the oxidation of 3-25 mg L⁻¹ As(III), using Degussa P25 TiO₂ (0.1 g L⁻¹) at pH 9²⁸. Examples of other kinetic laws, such as the adsorption-controlled Langmuir-Hinshelwood kinetics, are rare¹⁹⁴. Causes for zero-order photooxidation kinetics include (a) saturation of the photocatalyst surface with the substrate, (b) limited photon supply, or (c) limited supply of other reactants such as oxygen¹⁹⁵. Initial rate analysis is recommended as a superior method to determine rate laws, compared with analysis of serial data¹⁹⁵, but most data reported in the literature focuses on the integral analysis of serial data rather than initial rates.

2.7.1.3. The influence of media

The nature of the background media can influence photocatalysis through a variety of mechanisms, including (a) adsorption of both inorganic and organic species blocking the photocatalyst surface¹⁷¹; (b) absorption of incident photons by dissolved organic carbon, such as humic acids, reducing the rate of photoexcitation within the photocatalyst¹⁷¹; (c) the scavenging of radical intermediates, e.g. dissolved organic carbon scavenging oxidant

species⁹³. Groundwaters in South Asia are notably high in concentrations of dissolved organic carbon, phosphate, carbonate and dissolved iron (Table 2.1). In the absence of photocatalysts, humic acid promotes the oxidation of As(III) under soft UV irradiation¹⁹⁶, however as humic acid absorbs at wavelengths <400 nm¹⁹⁷, humic acid will suppress excitation of heterogeneous photocatalysts. Humic acid can also block sites and scavenge radical intermediates and holes¹⁷¹. Phosphate influences photocatalytic oxidation in a number of ways, including suppressing oxidation by blocking access to the catalyst surface, or facilitating photooxidation either by drawing positive holes to the surface (H₂PO₄⁻ anions are negatively charged at pH 7) or by forming hydrogen-bonded complexes with H₂O, facilitating charge transfer and subsequent generation of radical intermediates¹⁷¹. Carbonate is known to form the radical intermediate CO₃²⁻¹⁹⁸, which has been observed to inhibit photocatalytic water splitting¹⁹⁹. There are thus a wide range of mechanisms by which the species present in the groundwaters of South Asia might suppress or enhance photocatalytic oxidation of As(III).

Only a limited number of studies have investigated the influence of background media on the kinetics of As(III) photooxidation²⁰⁰. Lee and Choi (2002) found that both Fe³⁺ ions and humic acid increased reaction kinetics at pH 3, providing evidence for the viability of UV/TiO₂ treatment for arsenic contaminated groundwater¹⁹¹. However, Tsimas et al. (2009) found that humic acid suppressed photooxidation of As(III) in their system²⁰¹. Xu et al. (2008) observed significant suppression in the photodegradation of monomethylarsonic acid when carbonate was added²⁰². Ferguson et al. (2005) saw no significant effect between addition of phosphate and As(III) photocatalytic oxidation kinetics²⁰³. Lescano et al. (2015) found that when they added hydrogen peroxide, H₂O₂, as a co-oxidant in their two-column photocatalytic oxidation-adsorption system, arsenic breakthrough occurred twice as quickly, which they suggested was due to the adsorption of hydrogen peroxide onto TiO₂¹³². Lescano et al. also found that the oxidation of As(III) to As(V) in their column system decreased from 93% to 60% when replacing ultrapure water with natural Argentinian groundwater as the media¹³². It is not clear if any investigations in the photocatalytic oxidation of As(III) have been performed using real groundwaters collected from the arsenic-contaminated regions of South Asia.

2.7.1.4. The influence of crystal polymorphs

Studies show that increasing the temperature of TiO₂ calcination increases the rate of photocatalytic hydroxyl radical generation, due to the introduction of surface defects, up to a point, beyond which the rate decreases. The decreasing rate is attributed to the change in titania crystal phases from anatase to rutile²⁰⁴. Despite the band gap of anatase being greater

than that of rutile (3.20 to 3.03 eV), anatase generally performs better as a photocatalyst^{204 205}. This may be due to anatase having better charge carrier transport, from bulk material to the surface²⁰⁵. However, this alone does not account for the study by Tryba et al. (2007) wherein methylene blue decomposition rates drop off whilst hydroxyl radical formation rates continue to increase above 700°C. It has been suggested that this effect is due to a difference in mechanistic pathways, with (a) anatase-photogenerated hydroxyl radicals reacting both at the surface and in solution, but (b) rutile-photogenerated hydroxyl radicals being trapped at the rutile surface, and therefore only degrading adsorbed substrates²⁰⁶.

2.7.2. Iron oxides: Established arsenic sorbents

Iron oxides are amongst the best arsenic sorbents. The goethite formulation *Bayoxide E33* is a product marketed specifically for arsenic remediation, and is considered to be the benchmark arsenic sorbent^{4 89 92 176 207 208 209 210 211 212}. Iron oxides are non-toxic, cheap, and can be produced in large quantities²¹³. Adsorption of inorganic As(III) and As(V) to iron oxides is well characterised, with a wealth of experimental data covering hematite ($\alpha\text{-Fe}_2\text{O}_3$)^{214 215 216}, maghemite ($\gamma\text{-Fe}_2\text{O}_3$)^{217 218}, magnetite (Fe_3O_4)^{214 219 166 220}, goethite (FeOOH)^{214 221 222 223 224 225}, ferrihydrite ($(\text{Fe}^{3+})_2\text{O}_3 \cdot 0.5\text{H}_2\text{O}$)^{226 227 228 227}, and amorphous iron oxides^{229 230}.

Crystalline iron oxides can be readily synthesised with surface areas of 100-200 m² g⁻¹ and As(V) adsorption capacities of up to 100 mg g⁻¹²¹³. Amorphous iron oxides can be prepared with higher surface areas, up to 600 m² g⁻¹, and capacities of up to 400 mg g⁻¹²³⁰ (though these amorphous materials are less stable than crystalline iron oxides²³¹). pH is perhaps the most significant variable controlling adsorption of As(V) onto iron oxide surfaces²³², being more favourable at acidic pH owing to (a) the electrostatic attraction between the negative As(V) oxyanion and positively charged mineral surface, and (b) the availability of acidic protons as reactants for surface complexation. As(III) adsorption, in comparison, is far less pH dependent, and adsorption maxima occur at circumneutral pH, between pH 6²³³ and pH 8²³⁰.

2.7.2.1. Surface complexes

The majority of X-ray absorption spectroscopy (XAS) studies have concluded that both As(V) and As(III) form predominantly bidentate surface complexes on hematite^{234 235}, goethite^{236 224 235} and other iron oxides^{237 237 235 238}, as well as titania^{239 240}. These are typically identified as binuclear corner-sharing complexes, however mononuclear edge-sharing^{234 235} and

monodentate corner-sharing²²⁴ binding modes are often said to also be present. The prevalence of bidentate complexes over monodentate complexes is also suggested through density functional theory (DFT) simulations^{239 241}, and infrared (IR) spectroscopy^{229 242 243}. However, there are doubts concerning the accuracy of these conclusions, most notably the study of Loring et al. (2009) who through a combination of XAS and IR experiments concluded that As(V) binds to goethite through monodentate complexation²⁴⁴.

As(III) outer-sphere surface complexes are often detected alongside inner-sphere complexes²⁴⁵. Outer-sphere complexes, where the sorbate retains its solvation sphere and binds to the sorbate through non-covalent electrostatic interactions, are much weaker compared with the bidentate inner-sphere complex and its two covalent bonds. These weaker outer-sphere surface complexes may partially explain why adsorption of As(III) is so much more influenced by the presence of competitor ions such as phosphate, sulphate and carbonate than As(V)²²⁵.

2.7.3. Meso-TiO₂/Fe₂O₃: A model bifunctional composite

Titania-iron oxide composites are the most popular bifunctional materials investigated for As(III) remediation through a combined photocatalytic oxidation-adsorption approach. TiO₂ is the popular benchmark photocatalyst²⁴⁶, being abundant, cheap and chemically stable¹⁷². Meanwhile, iron oxides are considered amongst the most effective As(V) sorbents, with well-established commercial products⁹². The principal disadvantage in this system is the relatively large band gap of TiO₂ (3.0-3.2 eV) which limits photocatalytic activity to the ultraviolet region. Subsequently, performance under solar irradiation is poor¹⁷².

Examples of titania-iron oxide composites developed for arsenic remediation include:

- iron oxide-TiO₂ loaded iron slag (2006)¹⁹³
- Fe₂O₃ precipitated over commercial TiO₂ (2011)²³
- γ-Fe₂O₃-TiO₂ nanoparticles (2013)¹²
- Fe₂O₃ precipitated over Degussa P25 (2014)²⁴⁷
- hierarchical α-Fe₂O₃/TiO₂ hollow spheres (2016)²¹
- Fe₃O₄-TiO₂ nanoparticles (2016)²⁴⁸
- reduced graphene oxide supported mesoporous Fe₂O₃/TiO₂ nanoparticles (2016)²²
- Fe₂O₃-TiO₂ porous ceramic beads (2017)¹³
- TiO₂ nanoparticles anchored on Fe₃O₄ nanosheets (2019)²⁴⁹

Previous work within our group screened several synthetic routes towards producing $\text{TiO}_2\text{-Fe}_2\text{O}_3$ composite materials. Part of this work was published by D'Arcy et al., where hematite (Fe_2O_3) was precipitated over a commercial TiO_2 anatase support²³. The group explored further synthetic routes towards achieving $\text{TiO}_2/\text{Fe}_2\text{O}_3$ composite powders, including (a) bimetallic sol-gel products, (b) TiO_2 and Fe_2O_3 bound using tetraethyl orthosilicate, (c) “organic precursor hydrolysis”, (d) precipitating Fe_2O_3 onto a commercial anatase, and (e) precipitating Fe_2O_3 onto a mesoporous titania support^{250 251}.

Out of the synthetic routes investigated, the sol-gel and coprecipitation products were the most promising in terms of their cost and adsorption capacity²⁵⁰. This included the mesoporous $\text{TiO}_2/\text{Fe}_2\text{O}_3$ developed by Zhou et al.¹¹, which also offered the best photooxidation kinetics²⁵¹. This meso- $\text{TiO}_2/\text{Fe}_2\text{O}_3$ composite is synthesised by following a procedure of wet impregnation of iron into an anatase TiO_2 mesoporous support prepared by a sol-gel synthesis. Zhou et al. successfully used this material to oxidise and adsorb arsenic, regenerating the material through hot cycles in basic solution¹¹. The meso- $\text{TiO}_2/\text{Fe}_2\text{O}_3$ powders synthesised previously elsewhere have individual crystallite diameters of around 10 nm¹¹, with crystallites aggregated into large, size-disperse particles, with diameters of between 0.5 and 50 μm ^{11 251}. This material theoretically couples optimal crystallite diameters for efficient extraction of photogenerated charge carriers (~ 10 nm)¹⁵⁷ with a larger overall particle structure to minimise the risk of the material leaching into the treated water and inducing toxicity through endocytosis.

2.8. Surface Complexation Modelling

The primary mechanism by which metals and metalloids adsorb onto a mineral surface, e.g. adsorption of As(III) onto Fe_2O_3 , is through surface complexation. These reactions are analogous to aqueous phase complexation reactions, with hydroxyl groups on the mineral surface acting as the ligands that complex with the metal sorbate²⁵². Just as aqueous phase complexation reactions are described by equilibrium constants, so are surface complexation reactions. The notable feature of surface complexation, however, is that the equilibrium position is influenced not just by the activities of the sorbate and concentrations of the surface hydroxyls, but also by the electrostatic work involved in bringing a charged sorbate ion to a charged sorbent surface. Surface complexation models (SCM) often, but not always, incorporate corrections for these electrostatic interactions.

SCMs predict adsorption as a function of pH, ionic strength, and the presence of competitor ions. This helps us to predict adsorption under different environmental conditions, with

sensitivity that is missing in the more widely used Langmuir and Freundlich adsorption isotherm models ¹⁴. Composite sorbents can be modelled using two approaches: the generalised component (GC) and component additive (CA) methods. The GC method approximates and models the heterogeneous sorbent as a single-phase solid with a homogeneous surface ^{15 253}, whilst the CA method describes the heterogeneous sorbent as a combination of chemically distinct surfaces, each with its own adsorption equilibrium constants.

A CA-SCM for adsorption of arsenic onto meso-TiO₂/Fe₂O₃ is a desirable tool for two reasons. Firstly, adsorption of arsenic onto these materials is poorly understood, e.g. whether the TiO₂ and Fe₂O₃ surfaces behave independently, or whether new chemistry arises once the materials are coupled. Previous work on understanding arsenic adsorption in mixed sorbent systems is limited to one previous CA-SCM study on arsenic groundwater mobility ²⁵⁴. Developing new models will improve our understanding of how arsenic partitions across the composite sorbent surface. Secondly, an accurate CA model will predict arsenic adsorption as a function of the surface composition (i.e. the TiO₂:Fe₂O₃ ratio). This information can help optimise synthetic procedures, improving the performance of TiO₂/Fe₂O₃ composites.

A range of surface complexation models exist, primarily differing in their description of the electrical double layer. Constant capacitance (CCM), diffuse double layer (DDL), basic Stern layer (BSL) and triple layer (TLM) models differ in how many planes of charge are considered, whether outer-sphere complexation is included (physisorption of a sorbate, with an intact solvation sphere), and whether electrolyte adsorption is included. A brief explanation of surface complexation modelling theory is provided in the Appendix, followed by a discussion of the extended triple layer model (ETLM) that was used in this thesis.

2.9. Research aims and objectives

As highlighted in section 2.7.3, composite photocatalyst-sorbents, especially where TiO₂ is coupled with iron oxides, are increasingly investigated for applications in arsenic(III) remediation. However, there is a lack of understanding over how the chemistry of each constituent material is influenced by coupling into new composite forms. A number of questions remain unanswered for the TiO₂/Fe₂O₃ composite system, which must be addressed in order to understand how an arsenic treatment based on this technology might function, and how the treatment might be engineered.

2.9.1. The knowledge gap

Firstly, most studies report adsorption capacities of composite materials normalised to mass (i.e. milligrams of arsenic adsorbed per gram of material)^{11 163 255}. This tells us nothing about the chemistry of adsorption, which depends on the surface area rather than the total mass. Whilst adsorption is generally considered a monolayer process, for which TiO₂ and Fe₂O₃ surface phases can be considered as discrete entities, multilayer adsorption of arsenic is often observed^{256 245 257}. Multilayer adsorption is influenced by pore morphology^{258 259}, and the surface morphology of composite materials is often different to that of its constituent materials, being influenced by the synthetic procedure^{260 261 262}. To date, no study has answered the question of whether adsorption of arsenic onto TiO₂/Fe₂O₃ proceeds via component additivity. That is to say, whether the adsorption of arsenic onto TiO₂/Fe₂O₃ proceeds as a combination of arsenic adsorption onto individual TiO₂ and Fe₂O₃ surfaces, or whether new behaviour arises¹⁵.

Secondly, previous studies on the application of composite photocatalyst-sorbent materials for As(III) remediation have typically lacked the control experiments, using single-component photocatalysts, that are needed to establish (a) baseline rates and determine whether TiO₂/Fe₂O₃ composite materials provide better or worse photocatalytic activity, and (b) the mechanisms responsible for any observed differences. Iron oxides are poor photocatalysts owing due to fast electron-hole recombination kinetics²⁶³, and pure Fe₂O₃ shows negligible photocatalytic activity towards the oxidation of As(III)¹⁸⁷. However, with a bandgap of just 2.2 eV¹⁷¹, Fe₂O₃ absorbs soft ultraviolet photons more strongly than TiO₂, which could significantly reduce photooxidation kinetics¹⁷¹. On the other hand, if a favourable heterojunction is formed at the interface between TiO₂ and Fe₂O₃ crystal phases, photooxidation might be improved through better charge carrier separation. An illustration of the type-I heterojunction between TiO₂ and Fe₂O₃ is presented in Figure 2.7. There is also the possibility of As(V) deactivating the photocatalyst by blocking access to photocatalyst surface sites and, which the Fe₂O₃ sorbent phase might help prevent¹⁷⁰. As with adsorption, we must ask whether the photocatalytic oxidation of As(III) in the presence of meso-TiO₂/Fe₂O₃ proceeds as per the single-component TiO₂ photocatalyst, or whether the presence of the

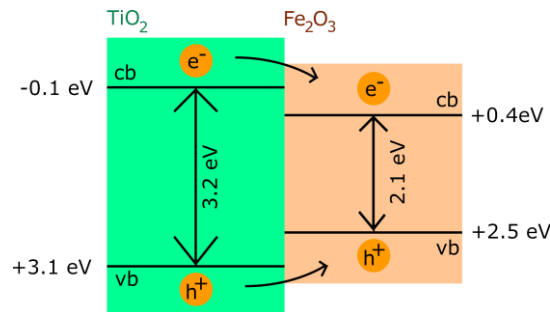


Figure 2.7: Illustration of the type-I heterojunction possible at the interface between anatase TiO₂ and Fe₂O₃. Conduction and valence band potentials at pH 0 versus the normal hydrogen electrode were taken from Tamirat et al., where the range of conduction and valence band potentials for Fe₂O₃ is given as +0.3 to +0.6 and +2.4 to +2.7 eV respectively⁴⁷⁵.

Fe₂O₃ phase alters the photocatalytic activity. To date, no study has identified the mechanisms influencing photocatalytic oxidation of As(III) using titania-iron oxide composites.

Thirdly, photocatalyst-sorbent materials remain untested for real-life applications in As(III) remediation. An important yet unanswered question when engineering the photocatalyst-sorbent system is how much material we should use. Low concentrations of suspended photocatalysts (<1 g L⁻¹) are typically used for As(III) photooxidation to achieve effective light penetration through the system^{25 26 26 27 28 29}. Whilst linear relationships between TiO₂ concentrations and reaction rates are often observed at low catalyst concentrations, at high catalyst concentrations reaction rates become limited by the supply of photons or by light scattering effects²⁷. Reaction rates may even decrease when excess photocatalyst is added²⁶⁴. However, low sorbent concentrations lead to low adsorption capacities and thus limited filter lifetimes before spent sorbent media (i.e. with no adsorption capacity left) must be replaced or regenerated. This work therefore aims to identify the approximate concentration of meso-TiO₂/Fe₂O₃ that should be used in an arsenic treatment plant, by considering the minimum concentration that provides sufficient adsorption capacity with fast treatment times.

Despite the attention given to TiO₂/Fe₂O₃ composites, much remains unknown about how the process of coupling TiO₂ with Fe₂O₃ influences the adsorption of arsenic and the photocatalytic oxidation of As(III). The following discussion identifies the three main research questions needed to better understand arsenic remediation using the meso-TiO₂/Fe₂O₃ system.

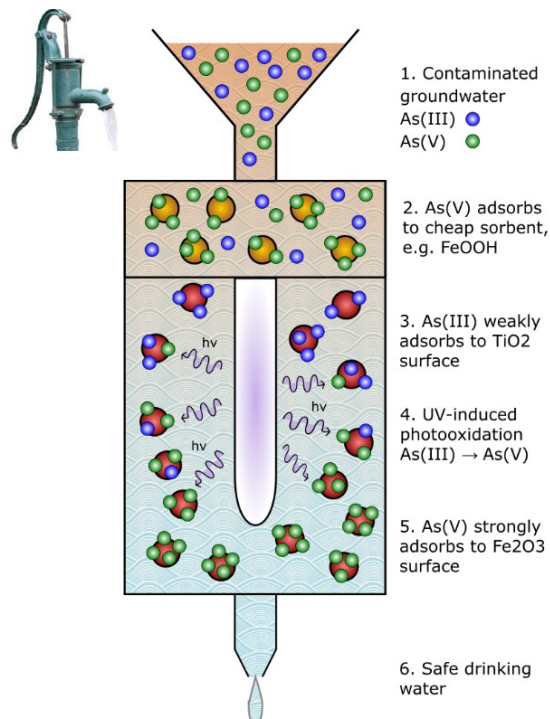


Figure 2.8: An initial idea of how meso-TiO₂/Fe₂O₃ might be incorporated into an arsenic treatment plant, considering a pre-treatment with sorbent media to remove As(V), phosphate and other species which might interfere with the photocatalytic oxidation.

2.9.2. Accurate adsorption modelling: Is adsorption of arsenic onto meso-TiO₂/Fe₂O₃ component additive?

The adsorption of contaminants onto composite sorbents is poorly understood. For instance, component additive surface complexation models (CA-SCM) have failed to accurately predict experimental observations for many sorbate-sorbent systems^{16 18 17}. In most cases, CA-SCMs have been developed using the mass ratio of solid phases in the material bulk to represent the ratio of solid phases at the sorbent surface^{16 18 265 266 267 268 269}. This assumption leads to errors in scenarios where (a) particles of one sorbent component are smaller than the other and thus exhibit a higher surface area-to-mass ratio, or (b) one sorbent component is a surface coating, blocking adsorption onto the second component¹⁵.

Published studies concerning the adsorption of arsenic onto composite sorbents using the CA approach are limited to a single paper, where CA-SCM was used to investigate groundwater arsenic mobility²⁵⁴. (It is unclear whether this is a true CA-SCM, as only a single sorbent component (hydrous ferric oxide) appears to have been used). There are no examples of CA-SCM being used to investigate the influence that sorbent coupling has on the adsorption of arsenic.

This thesis therefore aims to develop an accurate CA-SCM for two reasons. Firstly, an accurate CA-SCM enables us to identify whether arsenic adsorption is component additive or whether adsorption is influenced by sorbent coupling. We can therefore improve our mechanistic understanding of how arsenic adsorbs onto the TiO₂/Fe₂O₃ composite sorbent. Secondly, an accurate CA-SCM allows us to predict the adsorption capacity of new TiO₂-iron oxide composite materials when prepared under different synthetic routes. By understanding the influence of the TiO₂:Fe₂O₃ surface area ratio, and the sorbent morphology, we can better engineer the next generation of composite photocatalyst-sorbents. From an initial outlook, adsorption is a process occurring at an atomic-scale interface between solution and the suspended solid. The hypothesis was therefore that coupling TiO₂ with Fe₂O₃ into a new composite material would not influence the chemistry of each sorbent surface, and that arsenic adsorption would be successfully predicted using the CA approach. This work is discussed in chapter 6.

2.9.3. Understanding photocatalytic rates: How does Fe₂O₃-coupling influence the photocatalytic oxidation of arsenic(III) using meso-TiO₂?

As highlighted in section 2.9.1, the presence of Fe₂O₃ can influence the photocatalytic oxidation of As(III) in the presence of TiO₂ in a number of ways. Photooxidation can be suppressed due to the Fe₂O₃ phase absorbing incident photons, limiting the rate of TiO₂ photoexcitation¹⁷¹, or due to precipitation of Fe₂O₃ reducing the surface area of exposed TiO₂ due to pore filling or formation of an iron oxide surface-coating¹¹. Alternatively, photooxidation can be enhanced, either through formation of a heterojunction²⁴⁷, or due to Fe₂O₃ adsorbing anions and thus preventing blockage of the TiO₂ surface¹⁷⁰. To understand the scenarios in which TiO₂/Fe₂O₃ composites will out-perform single-phase TiO₂ and Fe₂O₃, it is therefore necessary to understand the photocatalytic chemistry of coupled TiO₂/Fe₂O₃ composites.

This thesis therefore aims to determine how coupling the TiO₂ photocatalyst with an Fe₂O₃ sorbent phase affects the chemistry of As(III) remediation through photocatalytic oxidation (chapter 7). The hypothesis was that significant differences would be observed between the activity of pure meso-TiO₂ and coupled meso-TiO₂/Fe₂O₃, with photooxidation rates either being enhanced through heterojunction effects, or suppressed due to parasitic light absorption by Fe₂O₃. To investigate this hypothesis, the optical properties of meso-TiO₂/Fe₂O₃ were investigated using spectroscopic techniques (UV-Vis spectroscopy and transient absorption spectroscopy, TAS) and modelled using the component additive approach. The kinetics of meso-TiO₂ and meso-TiO₂/Fe₂O₃ were determined and rate models were developed. This combination of optical characterisation and kinetic analysis was used to identify the dominant modes by which Fe₂O₃-coupling influences the photocatalytic oxidation of As(III).

2.9.4. Treatment plant design: How do we choose the concentration of meso-TiO₂/Fe₂O₃ that balances photocatalysis and adsorption?

As discussed in section 2.4, the life-time of the media in arsenic treatment plants and household filters is a major factor limiting the success of mitigation efforts. The life-time of a sorbent filter is easily improved by increasing the quantity of sorbent media used. However, photocatalytic activity is lost when excess photocatalyst concentrations are added to the reactor ²⁶⁴. The ideal reactor based upon a multifunctional photocatalyst-sorbent material would therefore use the minimum concentration of media needed to provide the desired sorbent lifetime.

This thesis therefore aimed to determine the minimum concentration of meso-TiO₂/Fe₂O₃ needed to achieve effective remediation of As(III) using adsorption only, and to compare this against the typical range of photocatalyst concentrations (chapter 8). The hypothesis was that in order to achieve long reactor lifetimes, meso-TiO₂/Fe₂O₃ would be required in concentrations far greater than the <1 g L⁻¹ TiO₂ that is typically used in photocatalytic reactors. The research question was answered by developing a kinetic adsorption model from experimental and literature data, as an initial illustration to inform the design of future engineering experiments.

The life-time of the sorbent depends not just on the concentrations of sorbent and sorbate, but also on how it is used, e.g. the reactor design (batch versus continuous flow) and the treatment time ²⁷⁰. Consequently, equilibrium adsorption data is insufficient, and a kinetic adsorption model must be developed. Currently, the kinetic models used to describe adsorption, such as the widely-used pseudo-second order (PSO) model, are conditional to the specific experimental conditions used ²⁷¹ ²⁷². This means that there is no predictive capacity for changes in sorbent concentration and sorbate concentration. Whilst sensitivity is offered in models such as the Integrated Kinetic Langmuir (IKL) model ²⁷³, simpler models with no such sensitivity (such as the PSO model) are better understood and more widely used ²⁷¹. Consequently, before simulating the arsenic treatment plant, this thesis develops the PSO model towards achieving realistic sensitivity towards changes in sorbent and sorbate concentration. The new model is used to predict treatment plant performance using different reactor designs and different sorbent concentrations, and an illustration of how this model can be improved in the future, through integration of adsorption-desorption kinetics and photocatalytic oxidation kinetics, is also provided.

3. Experimental

3.1. Reagents and Materials

All chemicals used were at least reagent grade or analytical grade (as detailed in the Appendix). Stock solutions (1000 mg L^{-1} , 13.3 mM) of As(V) and As(III) were prepared from $\text{Na}_2\text{HAsO}_4 \cdot 7\text{H}_2\text{O}$ and As_2O_3 respectively. Stock solutions were calibrated against a standard solution of arsenic (Fluka, $1000 \pm 4 \text{ mg L}^{-1}$, traceCERT) and lab solutions were kept refrigerated. As(III) solutions were contained within opaque containers to prevent photooxidation (As(III) is stable in the dark, even when adsorbed to TiO_2 ^{191 203 240}).

Solutions of 0.01 M NaCl were prepared from NaCl salt. Solutions of 0.01 M 4-(2-hydroxyethyl)-1-piperazineethanesulfonic acid (HEPES) were prepared from HEPES free acid and adjusted to pH 7.44 using small volumes of 1 M NaOH. Solutions of 0.01 M carbonate were prepared from NaHCO_3 and adjusted to pH 7.2 using small volumes of 1 M HCl. A stock solution of 1000 mg L^{-1} phosphate was prepared from $\text{NaHPO}_4 \cdot 7\text{H}_2\text{O}$. Stock solutions of 24 mM aqueous hydrazine were prepared from hydrazine hydrate or hydrazinium sulphate salt. Stock solutions of 0.5 M ethylenediaminetetraacetic acid (EDTA) were prepared from EDTA tetrasodium salt, acidified to pH 8. A stock solution of 60 mM Fe(II) (pH 2.1) was prepared from $\text{FeSO}_4 \cdot 7\text{H}_2\text{O}$. A stock solution of 10 mM Mn(II) was prepared from $\text{MnCl}_2 \cdot 4\text{H}_2\text{O}$. All solutions were made up to volume using Milli-Q water.

The As(V)-selective resin *ImpAs* was obtained, having been prepared as previously reported²¹², with improvements in the synthesis increasing As(V) chemisorption capacity from 10 to 16 mg g^{-1} . Bayoxide E33 (a commercially synthesised goethite (FeOOH) powder^{210 89}) was obtained commercially.

3.1. Groundwater samples

3.1.1.1. Synthetic groundwaters

Synthetic groundwaters CW (pH 7.42), SGW-1 (pH 7.09) and SGW-2 (pH 8.32) were prepared to the concentrations given in Table 3.2 as follows. Challenge Water (CW) was prepared by purging 1 L Milli-Q water with nitrogen gas for 1 hour to which was added Na₂SiO₃ (0.04 g) and NaHCO₃ (0.25 g). The pH was adjusted to pH 7.5 with a small amount of 1 M HCl. Separately, NaNO₃ (1.2 g), NaF (0.22 g) and HNa₂PO₄.7H₂O (0.035 g) were added to 100 mL of Milli-Q. An aliquot of this solution (1 mL) was added to the 1 L stock. To the 1 L stock solution was added CaCl₂.H₂O (0.15 g). The pH was adjusted to 7.47 with addition of a small volume of 1 M HCl. Synthetic groundwater SGW-1 was prepared by purging 1 L Milli-Q water with nitrogen gas for 1 hour, to which Na₂SiO₃ (0.08 g), NaHCO₃ (0.8 g) and MgSO₄.7H₂O (0.037 g) were added. In a separate volumetric flask, NaNO₃ (0.085 g), HNa₂PO₄.7H₂O (0.3 g) and KHCO₃ (0.7 g) were dissolved in 100 mL Milli-Q water. An aliquot of this solution (1 mL) was added to the 1 L stock, followed by CaCl₂.2H₂O (0.11 g), MgCl₂.6H₂O (0.28 g) and MnCl₂.4H₂O (0.004 g). The pH was adjusted to 7.1. Synthetic ground water SGW-2 was prepared by purging 1 L Milli-Q water with nitrogen gas for 1 hour, to which NaHCO₃ (0.9 g) and MgCl₂.6H₂O (0.3 g) were added. KH₂PO₄ (0.1 g), Ca(NO₃)₂ (0.15 g), MgSO₄.7H₂O (1.5 g) and NH₄Cl (4 g) were then dissolved in N₂-purged Milli-Q water (50 mL) and 1 mL of this solution was added to the 1 L stock solution. The pH of SGW-2 was 8.32.

3.1.1.2. Natural waters

Three oxic waters were sourced from Europe. Groundwater was collected from a natural spring sourced from granite bedrock in Cornwall, UK, and surface water was collected from a stream feeding into the River Kennal, also in Cornwall. Bottled mineral water from a French volcanic spring was purchased. These samples were filtered using a 0.45 µm nylon membrane.

Anoxic groundwaters were also collected from West Bengal, India. Well 3 (deep well, 400 feet), well 4 (shallow well), STN13 (shallow well, 70 feet) were located in the village of Sahispur (23°04'16.9"N 88°36'33.4"E), and STN5 (deep well, 480 feet) and STN2 were both in the village of Chakudanga (23°04'57.7"N 88°36'09.0"E). Both villages are in the Nadia district of West Bengal, known for their arsenic contaminated groundwaters. The sampling procedure was based on that of Gibbon-Walsh et al.⁹¹. Tube wells were pumped continuously for 6-15

minutes, before collecting samples in opaque plastic bottles to prevent photooxidation of As(III). Samples were immediately spiked with either HCl (to pH 2) or 10 mM EDTA to prevent iron precipitation. Samples were filtered to remove solid particulates and bacteria. The location of the villages and photographs of two of the tube wells sampled are presented in Figure 3.1.



Figure 3.1: Sampling sites for field work. (a) Location of field site at Sahispur village (red) within the Bengal Basin, and photos of (b) well 3 and (c) well 4. Chakudanga is located around 2.5 km North East of Sahispur.

Natural samples were characterised for pH, inorganic content (ICP-MS multielement analysis) and absorbance at 254 nm. Absorbance at 254 nm is an indicator of humic acid, a major form of dissolved organic carbon in the Bengal Basin²⁷⁴. The concentrations and speciation of arsenic in the Indian groundwater samples is presented in Table 3.1, where values of total As determined using anodic stripping voltammetry (ASV) closely agree with inductively coupled plasma mass spectrometry (ICP-MS). ASV indicates that As(III) was the major oxidation state of arsenic in these groundwaters. Further characterisation of all water samples is presented in Table 3.2.

Table 3.1: Arsenic concentrations detected in the West Bengal groundwater samples.

Source		Well 3	Well 4	STN13	STN5	STN2
Well type		Deep	Shallow	Shallow	Deep	-
pH		7.3	7.2	8.2	8.4	-
ICP-MS	As ($\mu\text{g L}^{-1}$)	9.9 ± 1.4	53.3 ± 2.7	-	100.3 ± 2.6	16.3 ± 5.2
ASV	As(III) ($\mu\text{g L}^{-1}$)	10	52	190	95	-
	Total As ($\mu\text{g L}^{-1}$)	12	63	180	110	-
	% As(III)	86	84	~100	86	-

Table 3.2: Characterisation of the waters used in this work. Synthetic groundwater compositions were determined from the mass of reagents used. The composition of natural waters was determined by ICP-MS using a multi-element standard. Blank cells indicate where a species was not added to solution or was not detected. '<LoD' refers to species that were under the detection limit.

a : SGW-1 and SGW-2 were both based on data from McArthur et al., 2004. SGW-1 was used for ImpAs experiments in London, whilst SGW-2 was used for electrochemistry experiments in Liverpool.

b : Since SGW-2 was used for optimisation of ASV conditions, this sample was always acidified to pH 1 or 2 during analysis.

The uncertainty in pH was determined from the sensitivity of the two different pH meters used in the lab and in the field.

Ion	Concentration (mg L ⁻¹)										
	Synthetic media			Natural media							
	SGW-1 (ImpAs tests)	SGW-2 (ASV tests)	CW	bottled mineral water	Cornish ground-water	Cornish surface water	well 3 (West Bengal deep well)	well 4 (West Bengal shallow well)	STN13 (West Bengal shallow well)	STN5 (West Bengal deep well)	STN2 (West Bengal deep well)
HCO ₃ ⁻	590	650	180	-	-	-	-	-	-	-	-
Ca ²⁺	34	1.5	47	2.5	2.5	2.1	16	14	18	19	22
Na ⁺	250	250	88	9.8	9.8	11	990	860	139	68	1041
Mg ²⁺	37	39	13	9.0	3.9	3.1	29	19	17	16	32
Cl ⁻	160	160	82	-	-	-	-	-	-	-	-
NH ₄ ⁺	-	27	-	-	-	-	-	-	-	-	-
H ₄ SiO ₄	63	-	31	-	-	-	-	-	-	-	-
SO ₄ ²⁻	14	12	50	-	-	-	-	-	-	-	-
K ⁺	2.7	0.57	-	6.7	3.0	2.7	4.1	2.1	9.0	9.1	4.3
Fe ²⁺	-	0 or 3.4 added	-	<LoD	<LoD	<LoD	1.8	5.0	4.3	13	4.8
Mn ²⁺	0.97	-	-	0.0002	0.021	0.0002	0.13	0.14	0.3	0.3	0.49
HPO ₄ ²⁻	1.1	1.4	0.13	-	-	-	-	-	-	-	-
NO ₃ ⁻	0.62	4.5	8.8	-	-	-	-	-	-	-	-
Sr ²⁺	-	-	-	0.057	0.060	0.047	0.49	0.27	0.37	0.35	0.20
Ba ²⁺	-	-	-	<LoD	0.007	0.006	0.12	0.17	0.23	0.20	0.17
F ⁻	-	-	1	-	-	-	-	-	-	-	-
pH	7.09 ± 0.02	8.32 ± 0.02 ^b	7.42 ± 0.02	7.39 ± 0.02	6.52 ± 0.02	7.55 ± 0.02	7.3 ± 0.1	7.2 ± 0.1	8.2 ± 0.1	8.4 ± 0.1	-
absorbance at 254 nm (cm ⁻¹)	-	-	-	0.023	0.025	0.105	-	0.046	0.022	0.044	-

3.1.2. Synthesis of meso-TiO₂/Fe₂O₃ and reference samples

Meso-TiO₂ and meso-TiO₂/Fe₂O₃ was synthesised according to the method previously published by Liu et al.¹⁵⁷ and Zhou et al.¹¹. Previous studies by our research group had established that this method produced a TiO₂/Fe₂O₃ composite which combined high adsorption capacity with good photocatalytic oxidation kinetics, compared with other synthetic products²⁵¹.

Meso-TiO₂ and meso-TiO₂/Fe₂O₃ were synthesised in two batches: a small-scale test batch, and a larger second batch with sufficient quantity for all adsorption experiments. The two batches differed in the antase:rutile ratio of the TiO₂ component: the first batch was primarily anatase, whilst the second batch was primarily rutile (this is discussed in the Appendix). Since the original meso-TiO₂/Fe₂O₃ composite reported by Zhou et al. was based upon the anatase polymorph of TiO₂¹¹ and anatase is generally the superior photocatalyst²⁷⁵, the first batch was used for all photocatalytic oxidation experiments, and the second batch was used for all adsorption experiments.

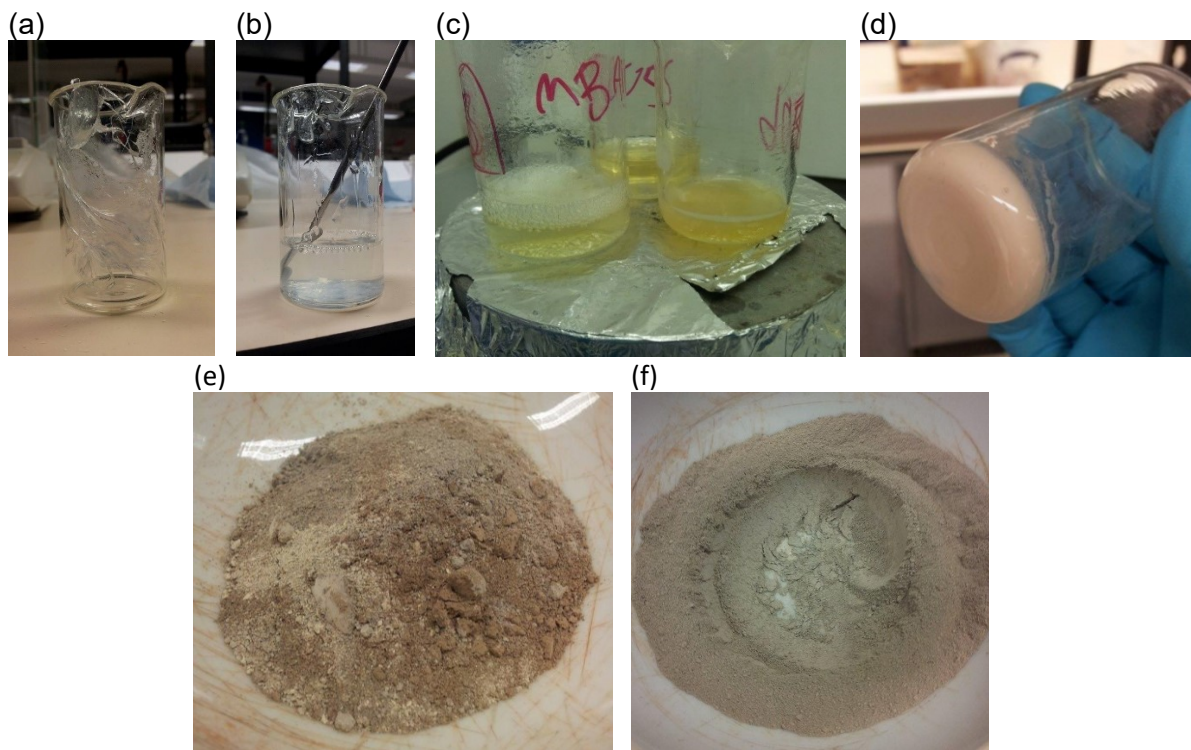


Figure 3.2: Preparation of meso-TiO₂ (batch 1). (a, b) Pluronic P123 is dissolved in ethanol, (c) which is slowly mixed with acidified Ti(OBu)₄, (d) producing a solid white foam. (e) A heterogeneous powder is obtained after calcination, yielding a homogeneous powder once crushed.

The mesoporous TiO₂ powder was first prepared following a sol-gel procedure (Figure 3.2)¹⁵⁷. P123 (an organic polymer with hydrophilic tails and a hydrophobic centre, 1 gram) was dissolved in ethanol (12 g). This solution was then added slowly to a second solution, consisting of Ti(IV) n-butoxide (2.7 g) in 37% hydrochloric acid (3.2 g)¹⁵⁷. The mixture was then aged at room temperature¹⁵⁷. A solid powder was obtained after calcination (350 °C, 4 hours, 1 °C min⁻¹ ramping) and crushing. An aliquot of the meso-TiO₂ powder was kept as a reference sample, and the remainder was coupled with Fe₂O₃.



Figure 3.3: Preparation of meso-TiO₂/Fe₂O₃ (batch 2) from meso-TiO₂. (a) A solution of ethanolic ferric nitrate solution (right hand beakers) was prepared. (b) meso-TiO₂ was added, stirred for 30 minutes, and sonicated for 30 minutes. The green circle highlights that not all meso-TiO₂ was well mixed during stirring. (c) and (d) show beakers before and after evaporation of the solvent. (e) shows the product, (f) which was collected and then (g) crushed into a homogeneous powder.

In the second stage of the synthesis, a 0.60 M $\text{Fe}(\text{NO}_3)_3$ solution was prepared by dissolving $\text{Fe}(\text{NO}_3)_3 \cdot 9\text{H}_2\text{O}$ (7.25 g) in ethanol (30 mL), as illustrated in Figure 3.3¹¹. Meso-TiO₂ (1.5 g) was added to the solution, stirred magnetically (30 minutes), and then sonicated (30 minutes)¹¹. During both these steps, a significant mass of meso-TiO₂ was not suspended, due to insufficient mixing. The solvent was evaporated in the oven (50 °C) and the dry solid was crushed to a homogeneous powder. No new XRD peaks were observed in the XRD patterns of the yellow product formed after ferric nitrate precipitation, indicating that no iron precipitates were crystalline before calcination.

The product was calcinated at 300 °C for 10 minutes, crushed, and calcinated again at 300°C for 6 hours¹¹ (Figure 3.4)¹¹. After the first 10 minutes of calcination, the powder developed a dark ruby colour, but a lighter yellow-orange powder was obtained after crushing. After the final calcination, a red powder with an intermediate brightness was obtained.

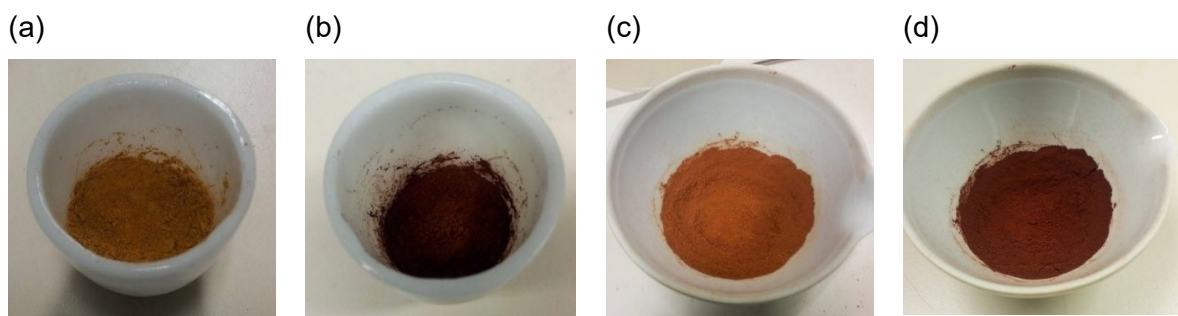


Figure 3.4: Meso-TiO₂/Fe₂O₃ (batch 1). The material (a) before and (b) after initial calcination (300 °C, 10 minutes), and (c) before and (d) after the final calcination (300 °C, 6 hours).

A reference sample of Fe₂O₃ was prepared, following the conditions used for the second stage of meso-TiO₂/Fe₂O₃ synthesis. A solution of ethanolic $\text{Fe}(\text{NO}_3)_3$ (0.60 M) was prepared by dissolving $\text{Fe}(\text{NO}_3)_3 \cdot 9\text{H}_2\text{O}$ (7.25 g) in ethanol (30 mL). This solution was dried in the oven at 50°C until all solvent had evaporated. The product was calcinated 300°C for 6 hours, then crushed into a homogeneous powder.

All materials were washed before conducting adsorption experiments, to remove acidic and basic impurities, as well as other adsorbed contaminants. Meso-TiO₂, Fe₂O₃ and their composite were all washed using dialysis

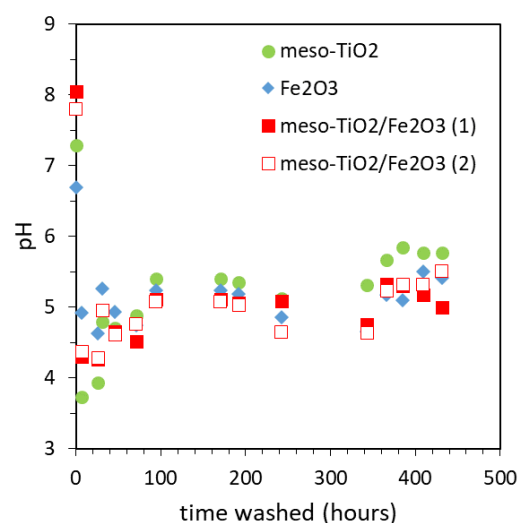


Figure 3.5: The progress of mineral washing, looking for convergence in the electrode potential as a sign of a clean surface. Meso-TiO₂/Fe₂O₃ (1) and meso-TiO₂/Fe₂O₃ (2) labels correspond to two separate dialysis tubes prepared with meso-TiO₂/Fe₂O₃ (batch 2) as the total sample mass was too large for a single tube.

tubing (Spectrum Labs Spectra/Por 6 1000 D MWCO Standard RC). Here, osmosis across a semipermeable membrane was used to remove soluble impurities from the material surface. The molecular weight cut-off (MWCO) of the dialysis tubing was 1 kD (i.e. the membrane is permeable to solutes with a molecular weight of under 1000 atomic mass units). Samples were washed for over two weeks, by which point pH readings had stabilised, indicating the removal of acidic impurities (Figure 3.5). Bayoxide E33 had been previously washed using a different procedure: one wash in 0.1 mM HCl, one wash in 10 mM NaOH, and repeat washes in Milli-Q water until pH readings had stabilised.

3.2. Materials Characterisation

3.2.1. X-ray diffraction

X-ray diffraction (XRD) was used to identify the crystalline phases within each mineral oxide sample. XRD patterns were recorded using the PANalytical MPD X-ray diffractometer. A background was fit to each XRD pattern and peaks were identified using ‘search and match’ in High Score Plus. Bragg’s law relates the angle of diffracted X-rays to the lattice spacing (the distance between crystal planes), allowing crystalline phases to be identified from their XRD patterns using the peak library within High Score Plus. Bragg’s is written as:

$$n\lambda = 2d_{hkl}\sin\theta$$

Equation 3.1

where n is a positive integer (corresponding to the whole number of wavelengths travelled by constructively interfering X-rays), λ is the X-ray wavelength (\AA), d_{hkl} is the lattice spacing (\AA), and θ is the angle of the diffracted X-rays ($^\circ$)²⁷⁶.

XRD patterns were also used to estimate average crystallite diameters using the Scherrer equation. The Scherrer equation (1918) describes the relationship between the broadening of an XRD peak and the size of the diffracting crystallite (perpendicular to the direction of the lattice planes)^{277 278}. The equation can be used to determine crystallite sizes up to ~100 nm, and the equation is written as:

$$t = \frac{K\lambda}{\beta \cos(\theta)}$$

Equation 3.2

where t is the crystallite size (\AA), K is the shape factor, λ is the X-ray wavelength (\AA), β is peak broadening (i.e. the full width at half maximum, FWHM) in radians, and θ is the Bragg angle ($^\circ$). The X-ray wavelength, λ , was set as the 50:50 average of the copper $\text{K}\alpha_1$ and $\text{K}\alpha_2$ lines (1.541874 \AA). The shape factor was set to 0.94 (assuming spherical crystallites with cubic symmetry). Peak broadening due to the instrument was set as 0.09 ($2^\circ\theta$) and subtracted from the FWHM when determining β . Above 100 or 200 nm the accuracy of the equation diminishes, as the peak narrows and the FWHM becomes increasingly defined by factors other than crystallite size, such as the quality of the instrument²⁷⁸.

To investigate the influence of temperature on the distribution of anatase and rutile crystal phases within meso-TiO₂, high temperature XRD was performed using an Anton Parr environmental heating chamber. The temperature was increased from 400 °C to 800 °C with a stepped increase of 25 °C every 51.4 minutes.

3.2.2. Electron microscopy

Powder samples were studied by scanning electron microscopy (SEM) using the LEO Gemini 1525 FEGSEM. The constituent crystallites of powder samples were studied by transmission electron microscopy (TEM) and scanning transmission electron microscopy coupled with energy dispersive X-ray spectroscopy (STEM-EDS) using the JEOL JEM-2100F.

3.2.3. Surface area and porosity

N₂ adsorption-desorption isotherms were obtained using the Quantachrome Autosorb iQ, after outgassing FeOOH at 100 °C and all other samples at 200 °C, for 20 hours. The BET-specific surface area was determined by multipoint analysis of the N₂ adsorption branch in the region of $P/P_0=0.05-0.35$. The total pore volume was determined using the total volume of N₂ gas adsorbed at the highest value of P/P_0 (0.995). The pore size distribution was determined using the desorption branch of the N₂ isotherm with Barrett-Joyner-Halenda (BJH) analysis.

3.2.4. Quantifying the material composition

The relative abundance of meso-TiO₂ and Fe₂O₃ within the meso-TiO₂/Fe₂O₃ composite was quantified by (1) X-ray fluorescence (XRF, for the bulk composition) using the PANalytical Epsilon 3 XLE, (2) X-ray photoelectron spectroscopy (XPS, for the near surface composition) using the Thermo Scientific K-alpha, and (3) low energy ion scattering (LEIS) using the combined IONTOF TOF.SIMS⁵-Qtac¹⁰⁰ LEIS instrument (for the outermost surface composition). XRF analysis was carried out under the standard Omnia settings (PANalytical Omnia software). For XPS analysis, samples were oven dried overnight (70 °C for FeOOH and 200 °C for all other samples) to remove adsorbed water and carbonate. Spectra were taken for the C1s, O1s, Fe2p and Ti2p regions, using the Al K α line at 1486.6 eV with a line-width of 0.85 eV and a spot size of 400 μm², with the flood gun switched on. XPS data was analysed using Thermo Avantage software, with the C1s adventitious carbon peak normalised to 284.8 eV. For LEIS analysis, samples were pumped down to vacuum overnight to remove water. LEIS survey spectra were obtained using He⁺ 3 keV and Ne⁺ 5 keV primary beams, rastering over a 1 mm² area. A LEIS depth profile was performed to remove adsorbed organic carbon which obscured the metal peaks (particularly Ti). Depth profiling was conducted using an Ar⁺ sputter gun (0.5 keV, 100 nA, 2 mm², 15 s) with a one second pause for the flood gun. Depth profiling was performed until surface impurities had been removed and the area of the metal peaks had reached a maximum.

For each technique, the composition of meso-TiO₂ and Fe₂O₃ phases within meso-TiO₂/Fe₂O₃ was determined using single-component meso-TiO₂ and Fe₂O₃ powders as reference samples. The calculation is written as:

$$m(a)_{\text{composite}} = \frac{I(a)_{\text{composite}}}{I(a)_a} \div \left(\frac{I(a)_{\text{composite}}}{I(a)_a} + \frac{I(b)_{\text{composite}}}{I(b)_b} \right)$$

Equation 3.3

where *a* is the component of interest (e.g. Fe₂O₃) and *b* is the second component (e.g. meso-TiO₂), *m(a)* is the mass fraction of component *a*, and *I(i)* is the intensity (counts) of component *i*, where *i* is component *a* or *b*. The right-hand term in brackets ensures that the combined mass fractions of all components equals unity. For ternary systems, further quotients for components C, D, E, etc. can simply be added inside the brackets of the denominator.

For XRF the impurities were <1% of the total atomic weight. For XPS, Fe and Ti peaks were scaled up to account for absorption of the incident beam by impurities (carbon, nitrogen and chlorine) which varied across samples. No impurity correction was calculated for LEIS.

Errors were calculated as the difference between the combined intensity fractions of Fe and Ti peaks in the meso-TiO₂/Fe₂O₃ composite, minus the theoretical combined intensity fractions (theoretically the combined intensity fractions add up to units). The equation is expressed as:

$$\text{relative error (\%)} = \left| 100 \times \left(\frac{I(a)_{\text{composite}}}{I(a)_a} + \frac{I(b)_{\text{composite}}}{I(b)_b} - 1 \right) \right|$$

Equation 3.4

XRF analysis required 30 minutes per sample, XPS analysis required 30-60 minutes per sample, and a single day of LEIS analysis was sufficient for depth profiling meso-TiO₂/Fe₂O₃ and the two reference samples (meso-TiO₂ and Fe₂O₃).

3.2.5. Zeta potential and particle size

Mineral powders (1 g L⁻¹) were suspended in 0.01 M NaCl and the pH was adjusted using small additions of 1 and 0.01 M HCl and NaOH. Suspensions were shaken for two days to achieve equilibrium before the final pH was recorded. Zeta potential and particle size measurements were made using the Malvern Zetasizer Nano. The isoelectric point (iep) was determined as the pH wherein samples exhibited zero zeta potential.

3.2.6. Determination of surface charge

A titration procedure was developed in line with the recommended conditions of Lützenkirchen et al.²⁷⁹ using the Metrohm 888 Titrando and pH electrode. Potentiometric titrations of mineral suspensions (10 g L⁻¹) were carried out in 0.01, 0.05 and 0.1 M NaCl to identify the point of zero salt effect (pzse) as a primary measure of the point of zero charge (pzc). Suspensions were first acidified to pH 3-4 with 0.1 M HCl and bubbled with N₂ gas for two hours to purge the system of carbonate. Suspensions were titrated forwards to pH 10-11 with 0.1 M NaOH followed by a reverse titration with 0.1 M HCl to check for hysteresis. Titrations were carried out over 7 hours in both forwards (base) and reverse (acid) directions, which showed good reversibility with low hysteresis (Figure 3.6). The electrode potential (mV) was converted to pH using a 4-point calibration curve with buffer solutions at pH 4, 7, 10 and 13 (Sigma Aldrich). Mineral suspensions and buffer solutions were kept at 25.0 °C using a water bath. Titrant strength was calibrated against a standard solution of 1.000 M HCl. For titrations in 0.1 M NaCl, ionic strength dropped by ~3% over the course of the forward titration. In 0.01 M NaCl,

ionic strength increased by up to 14% during the forward titration. This was accounted for in the modelling by explicitly defining the ionic strength at each titration step, then using the Davies equation (valid up to 0.5 M ionic strength) to determine activity coefficients²⁵². The surface area of sorbent in the vessel was generally above 30 m² in line with Lützenkirchen's recommendations²⁷⁹. The pzse was determined as the intersection of titration curves in 0.01, 0.05 and 0.1 M NaCl. Surface charge was determined as the proton excess via the equation:

$$Q = c(a)-c(b)-[H^+]-[OH^-]$$

Equation 3.5

where Q is surface charge (as the net proton excess, mol L⁻¹), c(a) and c(b) are the total amounts of acid and base added to the system respectively (M), and [H⁺] and [OH⁻] (M) were determined from the measured pH. Acidic impurities were subtracted from Q before surface charge was modelled in the SCM.

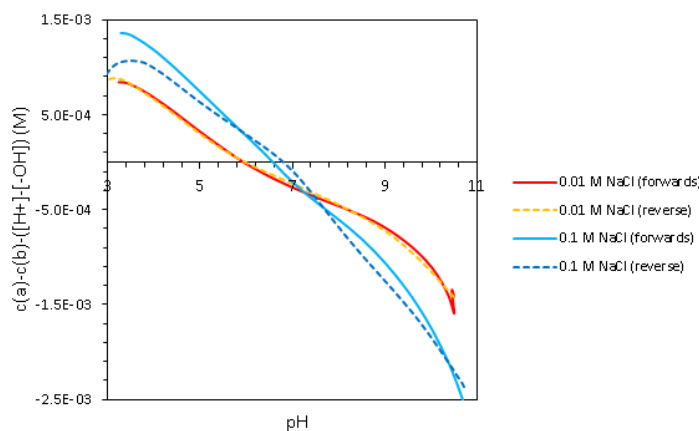


Figure 3.6: An example of the hysteresis observed between forwards (addition of base, solid lines) and reverse (addition of acid, dashed lines) titrations. In this case 10 g L⁻¹ meso-TiO₂/Fe₂O₃ in 0.01 and 0.1 M NaCl (red and blue respectively) was purged with N₂ for two hours at pH 3 and then titrated with 0.1 M NaOH and 0.1 M HCl. Hysteresis in potentiometric titration of mineral suspensions is typically caused by carbonate impurities.

Potentiometric mass titrations were also carried out in 0.1 M NaCl with typically 5, 10 and 15 g L⁻¹ mass loading to identify the point of zero mass effect (pzme) to further confirm that the point of zero charge (pzc) had been identified (Appendix).

3.3. Analytical determination of arsenic

3.3.1. Anodic stripping voltammetry

For all photocatalytic oxidation experiments, concentrations of As(III) and total As were determined by square wave anodic stripping voltammetry (SWASV), using the Metrohm 663 VA Stand, the IME663 interface and the General Purpose Electrochemical System (GPES) software. Detection was made using a vibrating 25 µm diameter gold microwire working electrode, iridium wire auxiliary electrode, and a silver-silver chloride reference electrode (Ag/AgCl//NaNO₃(1M)) ²⁸⁰. The working electrode was conditioned at the start of each day using cyclic voltammetry (CV) in 0.5 M H₂SO₄. The electrode was conditioned at -2.5 V for 30 seconds, before 5 scans were performed, with a linear sweep between -0.2 and +1.5 V at a rate of 1 V s⁻¹. The CV scan was used to detect faulty electrodes and contaminated electrolytes.

Detection of As(III) was made at pH 2 (samples were acidified by addition of 6 M HCl), in the presence of 40 µM hydrazine, acting as a sacrificial oxidant to prevent oxidation of As(III) ²⁸¹. The solution was purged of oxygen by bubbling nitrogen gas for several minutes prior to addition of the sample. Detection of total As was made at pH 1 (samples were acidified by addition of 6 M HCl), without addition of hydrazine and without a nitrogen purge. In both analytical procedures, the working electrode was first conditioned, vibrating at +0.7 V for 5 seconds. Deposition was made at -0.7 V for detection of As(III) and -1.3 V for total As, for 20 seconds in both cases. Anodic stripping was made using a sweep between -0.5 and +0.7 V, superimposed with a square wave profile with a step potential of 8 mV, an amplitude of 50 mV, and a frequency of 50 Hz.

For detection of both As(III) and total As, each analytical scan was followed by a background scan, using the same deposition potential and the same stripping profile, but reducing the deposition time to 1 second only, limiting the deposition of arsenic. The background voltammogram was subtracted from the analytical voltammogram to minimise the interference of charging current. The peak derivative was used as the measure of peak intensity, giving better precision than peak height and peak area.

Uncertainties for arsenic determination made using ASV with the method of standard additions were calculated with the following formula:

$$\frac{s_y}{|m|} \sqrt{\frac{1}{n} + \frac{\bar{y}^2}{m^2 \sum(x_i - \bar{x})^2}}$$

Equation 3.6

where s_y is the standard deviation in peak height across all data points, m is the slope, n is the number of data points, \bar{y} is the average peak height across all data points, x_i is the concentration of arsenic for data point i , and \bar{x} is the average concentration of arsenic across all data points ²⁸². In this work, detection using ASV often gave a variability between repeat measurements of the sample higher than the uncertainty given using the above formula. In cases where repeat measurements gave a standard error greater than the uncertainty of each individual measurement, the standard error is reported.

3.3.2. Inductively Coupled Plasma Mass Spectrometry (ICP-MS)

Samples were acidified to 2% (v/v) HNO₃ and analysed using the Agilent 7900 quadrupole ICP-MS with a helium collision cell. Calibration curves of at least 5 points were obtained both with a single element arsenic standard (Fluka, 1000 ± 4 mg L⁻¹, traceCERT) and a multi-element standard (Inorganic Ventures, 10 µg mL⁻¹, NIST-traceable standard). Measurements were also normalised to internal standards (primarily yttrium) to correct for changes in sensitivity of the detector during analysis. The most significant effect was the decrease in sensitivity for samples with high concentrations of total dissolved solids, e.g. the samples prepared in 0.01 M HEPES (with a high molar mass of 238 g mol⁻¹).

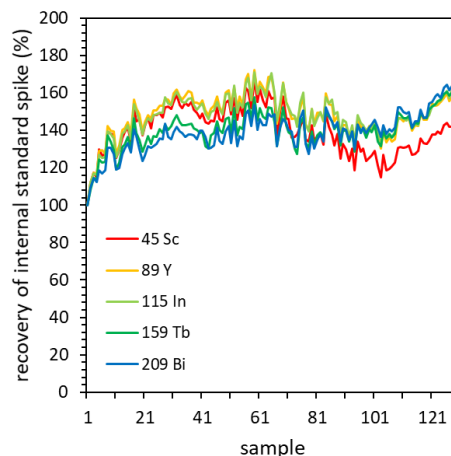


Figure 3.7: The recovery of internal standards was used to monitor changes in the sensitivity of ICP-MS detection, and thus better calibrate total arsenic concentrations.

3.4. Development of analytical techniques for the quantitative speciation of inorganic arsenic

The following section describes the experiments used to (a) optimise the electrochemical speciation of arsenic using a portable voltammeter, and (b) develop a new solid phase extraction (SPE) technique for the speciation of arsenic using an As(V)-selective chemisorbent resin. The results are presented and discussed in chapter 4.

3.4.1. Optimisation of electrochemical speciation using a portable voltammeter

As(III) and total As were determined by ASV using a portable PDV6000 Ultra potentiostat (Modern Water – UK) powered by 4x1.5 V AA batteries and equipped with the associated reference electrode ($\text{Ag}/\text{AgCl}/\text{KCl}(3\text{M})$) and auxiliary platinum electrode (Figure 3.8). The working electrode was a 30 μm diameter, 5 mm long gold microwire. The final operating parameters are summarised in chapter 4. Detection was made by linear scan ASV (LSASV), scanning from -0.4 V to +0.7 V with a 4 or 8 V s^{-1} scan rate and a 1.6 mV step. The solution was stirred during the deposition step and then held for 10 seconds at -0.4 V before the stripping scan took place. All measurements were made in the presence of dissolved oxygen.

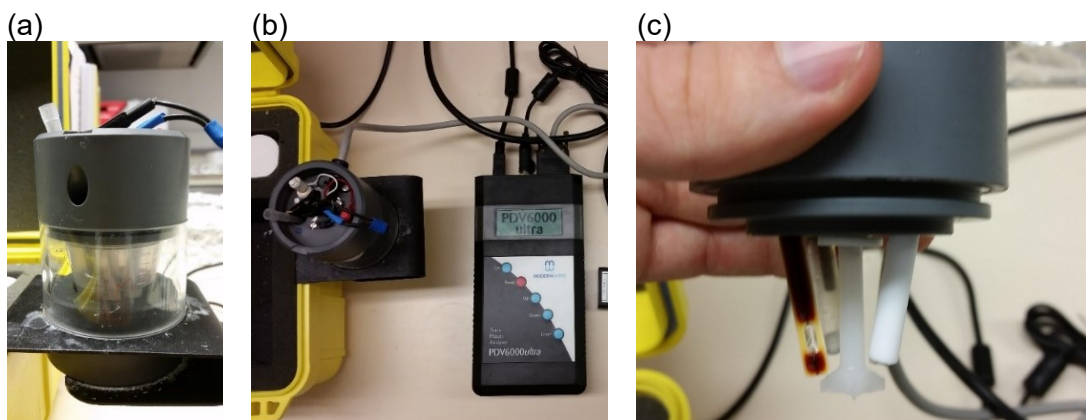


Figure 3.8: The portable PDV6000 ultra potentiostat used in this work. Shown are the portable potentiostat (top left), sample cell (top right) and the electrode configuration (bottom). The PDV6000 ultra was equipped with a built 30 μm gold microwire electrode (bottom left), $\text{Ag}/\text{AgCl}/\text{KCl}(3\text{M})$ reference electrode (bottom middle, behind the rotor) and platinum auxiliary electrode (bottom right).

As(III) was determined after addition of 0.01 M HCl and 10-20 µM hydrazine to prevent oxidation of As(III)²⁸³, using a deposition potential of -0.7 V for 15 seconds. Total As was determined in 0.1 M HCl, using a deposition potential of -1.3 V for 15 seconds. In these conditions of acidity and pH, immediate oxidation of As(III) to As(V) by the oxidant produced at the auxiliary electrode ensures that all arsenic in the voltammetric is present as As(V)²⁸³. The blank electrolyte prior to addition of the sample was used for background subtraction. The As stripping peak was located at ca. +180 mV in 0.01 M HCl and ca. +230 mV in 0.1 M HCl. Peak height was used for quantification. As(III) and total As were determined by the method of standard additions, with a minimum of 2 additions of As in each case⁹¹.

The working electrode was cleaned in 0.5 M H₂SO₄ by imposing a potential of -2.5 V for 30 seconds followed by a CV scan between -0.2 and +1.5 V at a scan rate of 1 V s⁻¹²⁸¹. Electrodes were cleaned at the start of each day, and sometimes between measurements if electrode sensitivity appeared diminished (i.e. after analysis of very high iron content synthetic waters).

3.4.2. Development of a solid phase extraction technique using an As(V)-selective chemisorbent

A method for the speciation of inorganic arsenic using an As(V)-selective chemisorbent resin was developed, according to the following experiments.

3.4.2.1. Batch experiments to verify the selectivity of ImpAs

To verify that ImpAs does not remove As(III) from solution, batch experiments under equilibrium conditions were carried out. Three background media were used: 10 mM HEPES, CW, and SGW-1. Solutions of 1 mg L⁻¹ total As (13 µM) in ratios of 0:100, 25:75, 50:50, 75:25 and 100:0 As(III) to As(V) were prepared in each media using 100 mg L⁻¹ (1.3 mM) As(III) and As(V) stock solutions. To each solution, 0, 1 or 20 g L⁻¹ ImpAs was added. Solutions were kept wrapped in aluminium foil to prevent photooxidation of As(III) and shaken overnight in an incubated shaker at 25°C and filtered gravimetrically to remove ImpAs. Total As was determined by ICP-MS.

3.4.2.2. Syringe experiments and development of a quick and portable device

As a prototype portable device for high sample throughput, disposable plastic syringes (5 mL volume) were loaded with ImpAs. To investigate the influence of mass loading, 0.2, 0.4 and 1 g ImpAs was used, giving path lengths of 2.5, 5 and 12 mm respectively. Solutions of 1 mg L^{-1} As(V) (13 μM) in 10 mM HEPES, CW or SGW-1 were prepared (total volume 50 mL). Each treatment consisted of loading aliquots (5 mL) of the arsenic-spiked water into the top of the syringe by pipette, collecting the effluent as the aliquot was passed through the syringe, and repeating until the total 50 mL sample had been processed. This treatment was repeated, with 1 mL of the effluent collected after each treatment for determination of total As by ICP-MS. The flow rate was controlled by hand, with solutions passed through the syringes dropwise (1 drop per second, ca. 1 minute per 5 mL aliquot). The effluent solution was collected directly, without discarding the first portion. Experiments were performed with and without prior conditioning of ImpAs. Without conditioning, ImpAs was used dry. When conditioned, the background media was passed through ImpAs several times and care was taken to ensure that air space in the top of the syringe did not re-aerate and thus dry out the resin. Conditioning took 30-60 seconds. A single syringe was prepared for each mass of ImpAs, and these three syringes were reused for all synthetic groundwater experiments. A control experiment was performed in duplicate, with 1 mg L^{-1} As(III) (10 mM HEPES) replacing the 1 mg L^{-1} As(V) influent sample, and [As(III) (aq)] was determined by ASV to verify that As(III) was neither removed nor oxidised during treatment with ImpAs.

3.4.3. Case study 1: Determining rate constants for the photocatalytic oxidation of As(III)

Suspensions of 0.1 g L^{-1} Degussa P25 (TiO_2) and 10 mg L^{-1} As(III) (133 μM) were prepared in 10 mM HEPES (total volume 100 mL) and stirred overnight in the dark to achieve equilibrium adsorption. Beginning at $t=0$, suspensions were irradiated with UV light ($\lambda=368 \text{ nm}$) with a light intensity of 13.7 mW cm^{-2} . Aliquots were taken at regular intervals, with TiO_2 removed using a 0.45 μm nylon syringe filter (VWR 28145-489). Each aliquot was (a) analysed for total As by ICP-MS, (b) diluted from 1 mL to 10 mL with Milli-Q water and passed three times through a conditioned ImpAs syringe, then analysed by ICP-MS for “As(III)”, and (c) speciated by ASV. A single ImpAs syringe was used for all experiments. For each time series, the value of k and

its uncertainty were calculated as the slope of the linear regression and its standard error. Experiments were performed in duplicate to give a final average, and the final uncertainty was calculated as the difference between the maximum and average values of k.

3.4.4. Case study 2: The speciation of natural waters

Acidified samples were pH neutralised by addition of NaOH before conducting the arsenic spiking experiment, since ImpAs performs poorly under acidic conditions (due to protonation of the pyridine groups ($pK_a = 5.2$) disrupting the ImpAs metal-organic receptor)²¹². Natural samples were subdivided and spiked with arsenic stock solutions to give a wide range of As(III):As(V) ratios. The first half of each subsample was collected without further treatment (for determination of As(III) and total As by ASV, and total As by ICP-MS), whilst the second half was passed through a syringe loaded with ImpAs (1 g) for determination of “As(III)”, with the results labelled as *ImpAs/ICP-MS*. Using ASV, As(III) was determined within 24 hours of sampling and total As within 48 hours. Samples were diluted at least 5 times with Milli-Q water during measurement by ASV to minimise matrix effects and the most concentrated samples were diluted 60-100 times to ensure analysis was made within the linear range of the method. Three ImpAs syringes were used to treat all samples, separated into (a) oxic waters, (b) anoxic waters without addition of EDTA, and (c) anoxic samples with addition of EDTA.

3.5. Adsorption at equilibrium: Experimental and modelling

3.5.1. Adsorption isotherms and pH edges

Arsenic adsorption batch experiments were conducted with 1 g L⁻¹ sorbent powder suspended in 0.01 M NaCl. The pH was adjusted with small additions of 0.01 and 1 M HCl and NaOH. Suspensions were shaken for two hours to condition the surface before being spiked with As(V) or As(III) (50 mL total volume). For the pH adsorption edge, total As was fixed at 0.3 mM and the pH was varied between 3 and 11, whilst for the adsorption isotherm the pH was fixed at 7.0±0.1 and [As (aq)] was varied between 0.1 and 700 µM. The pH was adjusted over the course of several days with small aliquots of 0.01 and 1 M HCl and NaOH, and suspensions

were equilibrated for 5 days before a final pH measurement was taken^{225 23}. Aliquots of each suspension were filtered (0.45 µm, nylon mesh) and the aqueous phase was kept for ICP-MS determination of total As. Blank electrolyte, blank mineral suspensions, and matrix-matched arsenic control samples were analysed by ICP-MS in parallel with each experiment.

Arsenic adsorption isotherms were modelled using the Langmuir equation:

$$Q_e = Q_{\max}(K_L C_e / (1 + K_L C_e))$$

Equation 3.7

and Freundlich equation:

$$Q_e = K_F C_e^{1/n}$$

Equation 3.8

where Q_e is the equilibrium concentration of adsorbed arsenic (µmol m⁻²), Q_{\max} is the amount of arsenic adsorbed at monolayer coverage (µmol m⁻²), C_e is the equilibrium concentration of aqueous arsenic (µM), and K_L (µM⁻¹), K_F (µmol m⁻² µM^{-1/n}) and n (dimensionless) are all experimentally determined constants²³.

Arsenic adsorption isotherms were not conducted under N₂ gas purging, in-line with previous work where environmental carbonate contamination was not thought to significantly influence arsenic sorption under the experimental conditions used^{230 284 211}.

3.5.2. Characterisation of arsenic-sorbed minerals

Suspensions of mineral powders (1 g L⁻¹, 0.01 M NaCl, pH 7.0±0.1 fixed with 0.01 and 1 M HCl and NaOH) were spiked with 0-700 µM As(III) or As(V) (0-53 mg L⁻¹). Suspensions were equilibrated for five days. Aliquots were taken for determination of zeta potential using the Malvern Zetasizer Nano. Suspensions were also filtered gravimetrically, and oven dried at 70 °C to minimise the amount of adsorbed water. ATR-FTIR spectra of the blank and arsenic-sorbed powders were collected between 400 and 4000 cm⁻¹ (Perkin Elmer Spectrum Two FT-IR Spectrometer). Spectra were normalised to the intensity of the metal oxide lattice excitation peaks (as these vibrations were expected to be little changed after adsorption, and much more intense than peaks corresponding to ν(As-O) stretching vibrations). A blank subtraction was made using the arsenic-free samples to provide better resolution of new peaks emerging post-arsenic sorption.

3.5.3. Surface complexation modelling

In this work, FITEQL 2.0 was used to optimise surface complexation constants. FITEQL was chosen as (a) the software is well established and widely used^{285 254 230 286}, and (b) it is compatible with the triple layer model electrostatics that are used in the more sophisticated, contemporary SCMs^{287 245 288 289}. The electrical double layer model used in this work was the extended triple layer model (ETLM) developed by Sverjensky, Fukushi et al.^{290 290 245}.

Surface complexation constants for the ETLM were obtained following the method used by Kanematsu et al. (explained in the supplementary information of their paper)⁸⁹, wherein (i) the site density of each mineral (surface hydroxyls per nanometre square) is chosen from the literature, (ii) surface acidity constants are predicted using Sverjensky's empirical formula²⁹¹, (iii) electrolyte adsorption constants (and the inner-sphere capacitance (C_1) are determined by fitting potentiometric titration data, and (iv) arsenic surface complexation (adsorption) constants are determined by fitting pH adsorption edges^{284 89}. The model was then validated by predicting experimental adsorption isotherms²²⁵.

Examples of the codes used in FITEQL are provided in the Appendix and are also available elsewhere²⁹². When modelling potentiometric titrations, (1) the free concentration of H⁺, (2) the total concentration of H⁺, (3) the ionic strength and (4) the dilution factor were all input as serial data (i.e. experimental data points). The free concentration of H⁺ signifies the concentration of aqueous protons, determined from the experimental pH reading, whilst the total concentration of H⁺ denotes the total proton excess (c(a)-c(b)) provided by the addition of titrant to the suspension. The ionic strength was calculated at each point in the titration using the Davies equation. The dilution factor was included to account for increases in the volume of the suspension as titrant was added over the course of each titration. Electrolyte adsorption constants were optimised, but surface acidity constants and the total concentration of surface sites were not.

To obtain surface complexation constants for the adsorption of arsenic, first, the concentration of free H₃AsO₃ or H₃AsO₄ was calculated for each point in the experimental pH adsorption edge. This was achieved by entering (1) the pH and (2) the total concentration of aqueous arsenic that remained after adsorption at each experimental data point, as input variables, and then calculating the speciation of As(III) and As(V) in the absence of any sorbent. The pH adsorption edge was then modelled using (1) the total concentration of surface hydroxyls, (2) the total concentration of arsenic, (3) the free concentration of H₃AsO₃ or H₃AsO₄ (calculated as just discussed), and (4) the free concentration of H⁺, as serial data inputs. The total concentration of surface hydroxyls and the total concentration of arsenic were both included

as serial data, given the slight variations in the quantities of sorbent and sorbate that were added to each batch experiment (the amount added of each was calculated using a mass balance for accuracy and precision).

To obtain an equilibrium constant for the surface precipitation of As(III), the following reaction was included:



Equation 3.9

where $>\text{SOH}$ denotes a surface hydroxyl, X is either a proton or a single negative charge, the mass action is equal to the product of the activity of As(OH)_3 (aq) and the sum of the activities of $(>\text{SO})_2\text{AsO}^-$ and $(>\text{SO})_2\text{AsOH}$ surface complexes, and the mass balance is equal to As(OH)_3 (aq) only (i.e. there is no net consumption of surface complexes, they act to catalyse the process of precipitation). Equilibrium constants for this reaction were obtained by fitting the SCM to the experimental adsorption isotherms. The monodentate H-bonded complex did not provide sites for surface precipitation within this model.

3.6. Photocatalytic oxidation: Characterisation of ultraviolet absorption and kinetic experiments

3.6.1. UV-Vis spectroscopy

UV-visible transmission and reflection spectra were measured using a Shimadzu UV-2700 spectrophotometer, equipped with an integrating sphere, in the wavelength range of 190–1400 nm. Dry powders were measured in reflectance mode, being held between glass slides, and referenced against BaSO_4 . Powders suspended in Milli-Q water ($0.01\text{--}10 \text{ g L}^{-1}$) were measured in both transmission and reflectance modes using a 2 mm cuvette (QC). Transmission and reflectance spectra were referenced against an air-filled cuvette. The reflectance and transmission spectra of water blanks were subtracted during data processing.

The absorbance of suspended powders is calculated using the proportion of incident light transmitted through the sample:

$$A = -\log\left(\frac{I_t}{I_0}\right)$$

Equation 3.10

where I_t is the intensity of the transmitted light and I_0 is the intensity of the incident light. To account for diffuse reflection from the suspended powders, Equation 3.10 was modified to give the following:

$$A = -\log\left(\frac{I_t + I_r}{1 - I_{\text{blank}-r}}\right)$$

Equation 3.11

where I_t is the proportion of transmitted light, I_r is the proportion of reflected light, and $I_{\text{blank}-r}$ is the proportion of incident light reflected by the blank cuvette filled with water.

Absorption coefficients were then determined using the Beer-Lambert law:

$$A = \varepsilon cl$$

Equation 3.12

where A is absorbance (dimensionless), ε is the wavelength-dependent absorption coefficient ($\text{L g}^{-1} \text{cm}^{-1}$), c is the powder concentration (g L^{-1}), and l is the path length (cm)¹⁴⁷.

The component additive prediction of absorbance (A) for meso-TiO₂/Fe₂O₃ suspensions was calculated using a linear combination of meso-TiO₂ and Fe₂O₃ spectra¹⁵, weighted according to the mass fraction of each component (as calculated using XRF):

$$A_{\text{comp}} = m_a A_b + m_b A_a$$

Equation 3.13

where comp denotes the composite photocatalyst, a and b denote the two individual component reference samples (i.e. meso-TiO₂ and Fe₂O₃), A_{comp} is the predicted absorbance of the composite photocatalyst, m_i is the mass fraction of component i within the composite photocatalyst (calculated using XRF), and A_i is the experimentally observed absorbance of the single-component reference sample i .

The component additive prediction of the absorption coefficient (ϵ) was calculated similarly:

$$\epsilon_{\text{comp}} = m_a \epsilon_a + m_b \epsilon_b$$

Equation 3.14

where ϵ_i is the experimentally calculated absorption coefficient of the single-component reference sample i ($\text{L g}^{-1} \text{ cm}^{-1}$). The proportion of incident photons absorbed by each component (meso-TiO₂ or Fe₂O₃) within the composite was then estimated using the equation:

$$\theta_i = \frac{m_i A_i}{A_{\text{comp}}}$$

Equation 3.15

where θ_a represents the fraction of photons (at the given wavelength) absorbed by the composite photocatalyst that are absorbed by component i .

The band-gap of dry powders was determined using the Tauc plot, by plotting $(F(R_\infty)hv)^{1/2}$ as a function of photon energy (eV), and identifying where the band edge intercepts the background²⁹³. $F(R_\infty)$ is the Kubelka-Munk function, and is expressed as:

$$F(R_\infty) = \frac{(1 - R_\infty)^2}{2R_\infty}$$

Equation 3.16

where R_∞ is the absolute reflectance of an infinitely thick layer of sample, i.e. the diffuse reflectance measured²⁹⁴. Photon energy, hv (eV), was calculated using:

$$hv = \frac{hc}{\lambda} \cdot 1.602 \cdot 10^{-19}$$

Equation 3.17

where h is Planck's constant ($6.626 \times 10^{-34} \text{ m}^2 \text{ kg}^{-1} \text{ s}^{-1}$), v is frequency (s^{-1}), c is the speed of light ($2.998 \times 10^8 \text{ m s}^{-1}$), λ is photon wavelength (m) and $1.602 \cdot 10^{-19}$ is the conversion factor between joules and electron volts.

3.6.2. Transient absorption spectroscopy

Transient absorption spectroscopy (TAS) measures the change in absorbance, or *optical density*, as a function of time, after a sample is excited by a laser pulse. The experimental set-up and method was based upon that reported by Jiamprasertboon et al.²⁹⁵, using a 355 nm laser, however several changes were made. (1) The frequency of the laser pulse was increased to 0.8-1 Hz. (2) The diffuse reflectance was measured at between 600 and 1000 nm, in 100 nm increments. (3) Each kinetic trace was calculated from the average of 100 laser pulses, except for experiments in As(III) suspensions. Here, in order to minimise the systematic error of progressive As(III) photooxidation under the laser pulse, an average of 10 pulses was collected at each wavelength (in a randomised order), with triplicate measurements (a total of 30 pulses at each wavelength). (4) Samples were measured (a) in air, (b) in methanol and in 2 mM aqueous AgNO₃ and (c) in 10 mM HEPES (pH 7.3±0.1) with 0-50 mg L⁻¹ As(III) and 0 or 50 mg L⁻¹ phosphate.

$\Delta OD(t, \lambda)$ is the change in optical density at time t, and wavelength λ , and is related to the change in the intensity of transmitted or reflected light through the expression:

$$\Delta OD(t, \lambda) = -\log\left(1 + \frac{\Delta I(t, \lambda)}{I_0(\lambda)}\right)$$

Equation 3.18

where $\Delta I(t, \lambda)$ is the change in the intensity of transmitted or reflected light at time t, and at wavelength λ , and $I_0(\lambda)$ is the intensity of transmitted or reflected light at wavelength λ before the laser pulse²⁹⁶.

A component additive prediction, treating meso-TiO₂ and Fe₂O₃ phases within the composite photocatalyst as non-interacting components, was calculated to probe heterojunction behaviour after coupling TiO₂ with Fe₂O₃. First, transient absorption decay curves were modelled using a power-law decay function with the equation:

$$[h^+]_t = At^{-\alpha}$$

Equation 3.19

where $[h^+]_t$ is the concentration of holes at time t (represented by ΔOD), t is time (seconds), and A and α are fitting parameters²⁹⁷. Parameters A and α were calculated in Origin by optimising the goodness of fit (R^2) between the model and experimental data. Data before 0.1 ms and after 100 ms were excluded from data fitting, due to interference from the laser pulse and loss of suspension respectively.

The modelled transient absorption decay was then normalised to unity at t=100 µs. The normalised value of A ($A_{\text{normalised}}$) was calculated using:

$$A_{\text{normalised}} = \frac{1}{0.0001^{-\alpha}}$$

Equation 3.20

The transient absorption half-life ($t_{1/2}$) was then calculated using the formula:

$$t_{1/2} = \left(\frac{1}{2} \cdot \frac{1}{A_{\text{normalised}}} \right)^{-\frac{1}{\alpha}}$$

Equation 3.21

The transient absorption of meso-TiO₂/Fe₂O₃ was then modelled under component additivity, using a linear combination of the power law decay curves of meso-TiO₂ and Fe₂O₃. First, the distribution of the absorbed laser pulse between meso-TiO₂ and Fe₂O₃ components was estimated as the product of each component's optical density at $\lambda=355$ nm and its mass fraction. This was calculated using Equation 3.15, albeit the absorbance of meso-TiO₂ and Fe₂O₃ was calculated from the intensity of light reflected from the dry powders (UV-Vis reflectance spectroscopy), rather than the intensity of light absorbed by suspended powders. The component additive prediction of transient absorption decay was then calculated using the formula:

$$\Delta OD(t, \lambda)_{\text{comp}} = \theta(0,355 \text{ nm})_a \Delta OD(t, \lambda)_a + \theta(0,355 \text{ nm})_b \Delta OD(t, \lambda)_b$$

Equation 3.22

where $\Delta OD(t, \lambda)_{\text{comp}}$ is the change in optical density (i.e. the transient absorption) of the composite photocatalyst at time t and wavelength λ , $\theta(0,355 \text{ nm})_i$ is the proportion of the laser pulse absorbed by component i (Equation 3.15), and $\Delta OD(t, \lambda)_i$ is the experimentally observed transient absorption of component i at time t and wavelength λ (calculated using the power-law decay function).

3.6.3. Photoreactor design and set-up

In this thesis, the reactor used to explore the photocatalytic oxidation kinetics of As(III) was a 100 mL beaker sited on top of a magnetic stirrer, illuminated overhead by a horizontal ultraviolet lamp ($\lambda = 368$ nm, 18 mW). The design is illustrated in Figure 3.9. The light intensity across the sample surface area was measured using a power meter (PM 100, S120 UV,

Thorlabs) connected to a power sensor (S120UV, Thorlabs). The photoreactor was housed within an opaque black plastic box. A UV-transparent fused-silica lid was used to prevent evaporation.

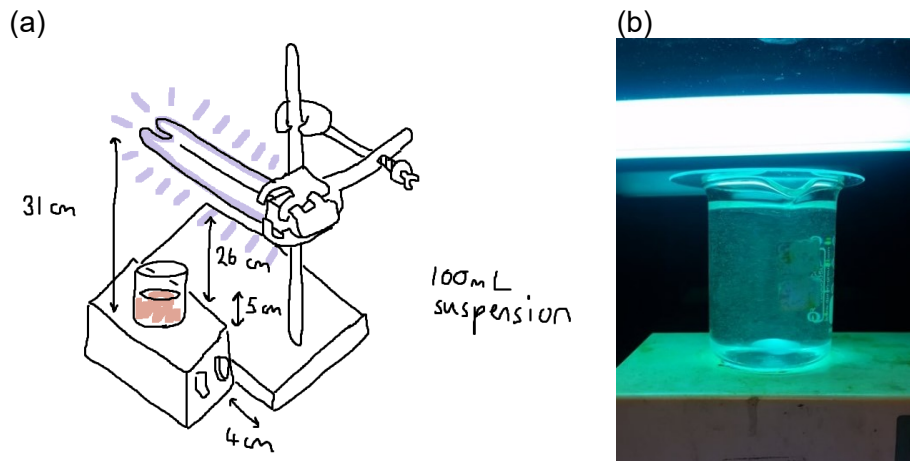


Figure 3.9: Photoreactor design. (a) A sketch of the photoreactor used in this work, with distance between lamp and suspension adjusted by means of a retort stand, with the entire apparatus housed within a black box. (b) The photoreactor in operation, with the lamp fixed 2 cm above the suspension surface, the photocatalyst suspended using a magnetic stirrer, and a fused-silica glass lid preventing water loss due to evaporation.

The variance in the light intensity delivered by the lamp across the surface of the suspension was <1% (at a distance of 2.5 cm) (Figure 3.10a). The exponential decrease in light intensity with the increasing distance between the lamp and the surface of the suspension after 2 cm (Figure 3.10), indicates that the lamp can be approximated as a point source irradiating the suspension from above, ignoring lateral irradiation. This data was used to constrain the light intensity in the photocatalytic oxidation experiments.

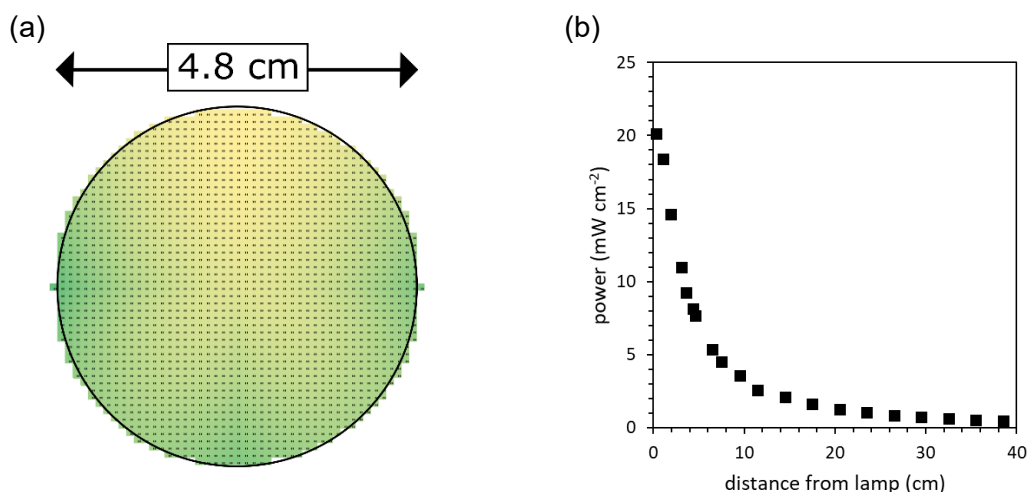


Figure 3.10: Characterisation of light intensity. (a) The light intensity was measured at five points across the surface of the suspension (four evenly spaced points along the circumference of the beaker and one in the centre) with the lamp located 2.5 cm above the beaker. The light intensity between these points was interpolated using a polynomial function, and the results suggested that the variance in light intensity was <1%. (b) The intensity of the light delivered to the suspension was measured as a function of the distance between the lamp and the surface of the beaker. Linear interpolation between data points was used to calculate the light intensity in each photocatalytic oxidation experiment.

Initial experiments fixed the lamp in place with a retort stand, to facilitate adjustment of the distance between lamp and suspension, so that photon flux could be varied. When a power series had been established, the lamp was fixed in place with a UV-opaque plastic box. As UV absorbance heated suspensions to around 30 °C, evaporation became significant on the hours-days timescale, both lowering the height of suspension (increasing the distance between the lamp and solution surface) and concentrating the arsenic (denser than water). Evaporation was prevented by a sheet of fused silica glass, which unlike regular borate glass is transparent at 368 nm.

3.6.4. Photooxidation kinetic experiments

Powders were suspended (0.1 g L^{-1}) in 100 mL media (10 mM HEPES, with or without addition of 10 mg L^{-1} phosphate) and spiked with As(III) ($500 \mu\text{g L}^{-1}$ to 10 mg L^{-1}). Suspensions were adjusted to pH 7.3 ± 0.1 through addition of small volumes of 0.01 and 1 M HCl and NaOH and mixed by magnetic stirring. Suspensions were stirred overnight in the dark to achieve equilibrium adsorption before irradiation. The UV lamp was warmed up for ten minutes before the sample was irradiated. The time at which the suspension was first irradiated was designated t=0. At regular time intervals, aliquots of the suspension (1 mL) were extracted and size filtered using a $0.45 \mu\text{m}$ nylon membrane syringe filter (VWR 28145-489) to remove the photocatalyst powder. The beaker was periodically raised above the magnetic stirrer on plastic sheets to keep the surface of the suspension at a constant distance from the lamp, since sequential sampling reduced the volume of the suspension by up to 20%. Samples were kept in the dark prior to analysis to prevent further photooxidation. The concentration of As(III) remaining was determined using anodic stripping voltammetry (ASV).

3.6.5. Kinetic analysis of photocatalytic oxidation

The kinetics of As(III) photocatalytic oxidation in the presence of meso-TiO₂ and meso-TiO₂/Fe₂O₃ were investigated using two methods for corroboration: both the method of initial rates and analysis of serial data ²⁹⁸.

Initial rates were calculated by fitting a linear regression to the initial linear region of [As(III) (aq)] versus time.

Pseudo first-order (PFO) kinetics follow the rate equation:

$$\frac{dC}{dt} = -k_1 C_t$$

Equation 3.23

Where C is the concentration of aqueous As(III) (i.e. [As(III) (aq)]), t is time (min), k₁ is the pseudo first-order rate constant (min⁻¹) and C_t is the concentration of aqueous As(III) at time t²⁹⁹.

The integrated solution to this equation can be rearranged into the linear form:

$$\ln\left(\frac{C_t}{C_0}\right) = -k_1 t$$

Equation 3.24

where C₀ is the concentration of aqueous As(III) at t=0. The PFO rate constant, k₁, was calculated from the slope of ln(C_t/C₀) as a function of time.

The Langmuir-Hinshelwood rate equation is first order to the concentration of adsorbed substrate. The concentration of adsorbed substrate is calculated using the Langmuir adsorption isotherm. Given that a significant proportion of total As(III) is adsorbed to the photocatalyst surface at any given time, Langmuir-Hinshelwood kinetics were used to calculate the rate of change in the total concentration of As(III) remaining (rather than the rate of change in aqueous As(III) only), with the following rate equation:

$$\frac{d[\text{total As(III)}]}{dt} = k \frac{K_L C_t}{1 + (K_L C_t)}$$

Equation 3.25

where [total As(III)] is the sum of aqueous and adsorbed As(III) (mg L⁻¹), k (mg L⁻¹ min⁻¹) is the rate constant, and K_L is the Langmuir constant (L mg⁻¹)³⁰⁰. The parameter k is a convolution of the Langmuir-Hinshelwood rate constant, k_{LH} (min⁻¹), and the monolayer adsorption capacity, Q_{max} (mg g⁻¹). The rate constant k_{LH} is obtained through the equation:

$$k_{LH} = \frac{k}{Q_{\max} C_s}$$

Equation 3.26

where C_s is the concentration of suspended photocatalyst (0.1 g L^{-1}). K_L and Q_{\max} were calculated in this work by fitting the adsorption isotherms reported in chapter 6, in the range of $C_e=0-11 \text{ mg L}^{-1}$ (i.e. before significant multilayer adsorption of As(III) occurs).

The concentration of total As(III) in Equation 3.25 was calculated at each point of time using the mass balancing equation:

$$[\text{total As(III)}]_t = [\text{As(III) (aq)}]_t + [\text{As(III) (ads)}]_t$$

Equation 3.27

where $[\text{As(III)} (\text{ads})]_t$ is calculated at each point in time using the Langmuir adsorption isotherm:

$$[\text{As(III)} (\text{ads})]_t = Q_{\max} C_s \frac{K_L C_t}{1 + (K_L C_t)}$$

Equation 3.28

Two different kinetic models were investigated to explain possible As(V) deactivation of meso-TiO₂ were investigated. The first model (As(V) deactivation model (1)) is derived within chapter 7, and uses the rate equation:

$$\frac{dC}{dt} = k^\ddagger \left(1 - \left(1 - \frac{C_t}{C_0} \right) \right)$$

Equation 3.29

where C is the concentration of aqueous As(III), k^\ddagger is the rate constant ($\mu\text{g L}^{-1} \text{ min}^{-1}$), and C_t and C_0 are the concentrations of aqueous As(III) at time t and $t=0$ respectively. This equation reduces to:

$$\frac{dC}{dt} = k^\ddagger \left(\frac{C_t}{C_0} \right)$$

Equation 3.30

and consequently, relates to the original pseudo-first order rate equation through the expression:

$$k^\ddagger = k C_0$$

Equation 3.31

The second model (the SCM-constrained As(V) model) uses the rate equation:

$$\frac{d[\text{As(III) (total)}]}{dt} = k^\ddagger (1 - j[\text{As(V) (ads)}]_t)$$

Equation 3.32

where k^\ddagger is the rate constant ($\mu\text{g L}^{-1} \text{min}^{-1}$), j is a sensitivity factor reflecting the extent to which the presence of As(V) suppresses the reaction (g mg^{-1}), and $[\text{As(V)} \text{ (ads)}]$ is the concentration of adsorbed As(V) at time t (mg g^{-1}). The concentration of adsorbed As(V) at each point in time was calculated using the surface complexation model (SCM) developed in chapter 6. The concentration of aqueous phase As(III) was also calculated using the SCM and used to calculate $\frac{C_t}{C_0}$.

The SCM was also used to improve the sensitivity of Langmuir-Hinshelwood kinetics to the competitive adsorption of As(V). The rate equation of the SCM-constrained As(III) model was:

$$\frac{d[\text{total As(III)}]}{dt} = k_{\text{SCM}} [\text{As(III)} \text{ (ads)}]_t$$

Equation 3.33

where k_{SCM} is the rate constant (min^{-1}), and $[\text{As(III)} \text{ (ads)}]_t$ is the concentration of adsorbed As(III) at time t (mg L^{-1}), calculated by the SCM.

New equilibrium constants for the competitive adsorption of phosphate were calculated by fitting pH adsorption edges reported in the literature^{301 302}, and the fitting of the model to the experimental data is presented in the Appendix. SCM calculations were performed using Visual MINTEQ 3.1, as the sweep function allows sequential calculations to be performed and the data collected more quickly than in FITEQL 2.0.

The values of k_{LH} , k^\dagger , k^\ddagger , and k_{SCM} were calculated by non-linear regression, minimising the sum of squares between experimental and modelled values of $\ln(C_t/C_0)$. The model was fit to $\ln(C_t/C_0)$ rather than C_t/C_0 to ensure that the model captured the observed kinetics at low values of C_t as well as at high values of C_t .

Uncertainties in the initial rate were calculated from the standard error in the slope of the linear regression that was fitted to the initial linear region of each kinetics experiment. Uncertainties in the rate constants calculated using the integral method were calculated using the standard error of the slope of the linear regression used to calculate each rate constant. Uncertainties in the rate constants calculated by non-linear regression were estimated from the uncertainties in the initial rate.

Table 3.3: ETLM parameters used for surface complexation modelling in Visual MINTEQ. All parameters were calculated in this work through experiment and modelling, as discussed in chapter 6, except for the phosphate surface complexation equilibrium constants, which were calculated by fitting the pH adsorption edges reported elsewhere^{301 302}. Log(K0) values are reported for each surface complexation reaction, along with the charge in surface potential. Total arsenic was varied between 0.5 and 10 mg L⁻¹, as per the experimental work. The distribution of As(III) and As(V) was varied between 100% As(III) and 100% As(V) in 1% increments.

Property/reaction	Value		$\Delta\psi$
pH	7		-
Ionic strength (M)	0.01		-
NaCl (M)	0.01		-
	Fe ₂ O ₃	Meso-TiO ₂	
Surface area (m ² g ⁻¹)	103.4	110.1	-
Concentration of solid (g L ⁻¹)	0.068	0.032	-
Site density (sites nm ⁻²)	4.0	3.0	-
Concentration of sites (μM)	46.7	17.5	-
Inner capacitance, C ₁ (F m ⁻²)	0.8	1.3	-
Outer capacitance, C ₂ (F m ⁻²)	0.2	0.2	-
>SOH + H ⁺ = >SOH ₂ ⁺	5.48	1.50	$\psi_0 - \psi_\beta$
>SOH = >SO ⁻ + H ⁺	-12.3	-8.10	$-\psi_0 + \psi_\beta$
>SOH + H ⁺ + Cl ⁻ = >SOH ₂ ⁺ ---Cl ⁻	8.98	4.63	$\psi_0 - \psi_\beta$
>SOH + Na ⁺ = >SO ⁻ ---Na ⁺ + H ⁺	-9.3	-5.5	$-\psi_0 + \psi_\beta$
2 >SOH + H ₃ AsO ₃ = (>SO) ₂ AsOH + 2H ₂ O	5.3	-	0
2 >SOH + H ₃ AsO ₃ = (>SO) ₂ AsO ⁻ + H ⁺ + 2H ₂ O	-0.5	3.0	$-\psi_\beta$
>SOH + H ₃ AsO ₃ = >SOH ₂ ⁺ ---AsO(OH) ₂ ⁻	5.7	4.0	$\psi_0 - \psi_\beta$
2 >SOH + AsO ₄ ³⁻ + 3H ⁺ = (>SO) ₂ AsO ₂ H + 2H ₂ O	29.6	-	0
2 >SOH + AsO ₄ ³⁻ + 2H ⁺ = (>SO) ₂ AsO ₂ ⁻ + 2H ₂ O	27.8	28.7	$-\psi_\beta$
>SOH + AsO ₄ ³⁻ + H ⁺ = >SOAsO ₃ ²⁻	24.0	26.6	$-2\psi_\beta$
2 >SOH + PO ₄ ³⁻ + 3H ⁺ = (>SO) ₂ PO ₂ H + 2H ₂ O	29.7	26.7	0
2 >SOH + PO ₄ ³⁻ + 2H ⁺ = (>SO) ₂ PO ₂ ⁻ + 2H ₂ O	28.7	28.9	$-\psi_\beta$
>SOH + PO ₄ ³⁻ + H ⁺ = >SOPO ₃ ²⁻	22.9	22.7	$-2\psi_\beta$

3.6.6. Calculating the quantum yield

The quantum yield (Φ) was calculated by dividing the incident light intensity by the initial rate, using the equation:

$$\Phi = \left(\frac{jSA}{V} \cdot \frac{\lambda}{hc} \cdot \frac{1}{A} \right) \div \left(\frac{\text{initial rate}}{74.9 \text{ g mol}^{-1} \cdot 10^6} \right)$$

Equation 3.34

where j is the lamp power (J cm⁻² s⁻¹), SA is the surface area of the beaker (cm²), V is the volume of the beaker (L), λ is the wavelength of the incident photons (m), h is the Planck constant (6.63×10^{-3} m² kg⁻¹ s⁻¹), c is the speed of light (3.00×10^8 m² s⁻¹), A is the Avogadro constant (6.02×10^{23} mol⁻¹), and the initial rate is given in $\mu\text{g L}^{-1} \text{s}^{-1}$. In this study j was varied between 2.4 and 14.3 mW cm⁻² (0.0024 to 0.0143 J cm⁻² s⁻¹); SA was 21 cm²; V was 0.1 L; and λ was 368 nm (3.68×10^{-7} m).

3.7. Modelling adsorption kinetics: Arsenic treatment plant design

3.7.1. Developing an adsorption kinetic model sensitive to changes in initial sorbate and sorbent concentration

Currently, the pseudo-second order (PSO) model is the most popular method for describing adsorption kinetics²⁷¹. The PSO rate equation is:

$$\frac{dq}{dt} = k_2(q_e - q_t)^2$$

Equation 3.35

where q is the concentration of adsorbed sorbate (mg g⁻¹), q_t and q_e are values of q at time t and at equilibrium respectively, and k_2 is the pseudo-second order rate constant (g mg⁻¹ min⁻¹).

Integration of Equation 3.35 yields the linear equation:

$$\frac{t}{q_t} = \frac{1}{k_2 q_e^2} + \left(\frac{1}{q_e}\right)t$$

Equation 3.36

By plotting $(\frac{t}{q_t})$ as a function of time t , the adsorption capacity q_e and pseudo-second order rate constant, k_2 , were calculated from the slope and intercept respectively.

Since the pseudo second-order (PSO) kinetics popularly used to describe adsorption of arsenic onto TiO₂ and Fe₂O₃ sorbents do not offer sensitivity towards changes in sorbate and sorbent concentration, the PSO was modified to reduce experimental conditionality and allow the influence of sorbate and sorbent concentrations on adsorption kinetics to be better predicted. Literature data was compiled and used to investigate how changing sorbate and sorbent concentrations typically influences the observed kinetics.

3.7.1.1. Collecting data sets from the literature

Literature sources that experimentally investigated the influence of C₀, C_s or particle size upon adsorption kinetics were compiled (and are presented in the Appendix). Studies using

oxyanions, metal cations and organic dyes as the sorbate were all included, to ensure the findings would be general and non-sorbate-specific. Both mineral sorbents and organic sorbents (activated carbon and chitosan) were included, however zeolites and metal-organic frameworks (MOFs) were not, since the sorption mechanism of sorbate trapping within cages might present inconsistent results. None of the literature sources found gave any mechanistic account or mathematical explanation for observed differences in adsorption kinetics due to varying C_0 , C_s or particle size. Most literature sources used the pseudo second-order (PSO) model to describe adsorption kinetics.

In total 79 literature sources with around 200 kinetic experiments were collected. To investigate the influence of initial sorbate concentration, 11 literature sources with a combined 43 kinetic experiments were collected. For initial sorbent concentration, 11 literature sources with 43 experiments were collected. For particle size, 15 data sets from 6 literature sources, with a combined 47 experiments were collected. A data set was considered to be all kinetic experiments using the same sorbate-sorbent system within a single literature source.

3.7.1.2. Calculation of initial rates

To investigate the dependency of adsorption kinetics on C_0 , C_s and particle radius, the method of initial rates was used²⁹⁹. Experimental kinetic data from the literature was tabulated and initial reaction rates were calculated. Many data sets lacked good resolution for the initial stages of adsorption, e.g. in ~30% of all experiments reaction progress had already exceeded 50% when the first data point after mixing sorbent with sorbate was collected. Consequently, calculating the initial rate (the rate of reaction at $t=0$) using the slope of q_t versus time at the earliest data points would lead to a systematic under-calculation of the initial reaction rate, as early curvature in adsorption kinetics would be missed (Figure 3.11). This error becomes increasingly significant the later that initial adsorption data is collected. Determination of initial adsorption kinetics using the slope of q_t versus t would also give a random error associated with calculating rates from two data points only.

To provide a better estimation of the initial rate, each data set was fit with the PSO model, which was then used to calculate the rate at $t=0$. PSO parameters (k_2 and q_e) were determined using the linearised form of the PSO rate equation (Equation 3.36). Adsorption kinetic profiles were plotted as $\frac{t}{q_t}$ against t and the linear regression was obtained using the LINEST function in Microsoft Excel. q_e was obtained via the relationship $q_e = \frac{1}{m}$ where m is the gradient of the

linear regression, and k_2 was obtained via $k_2 = cq_e^2$, where c is the y-intercept. The initial rate of adsorption was calculated by simplifying Equation 3.35, giving:

$$\text{initial rate} = \frac{dq}{dt} = k_2 q_e^2$$

Equation 3.37

All literature data sets were normalised to the same units for ease of comparison: $k_2 - \text{g mg}^{-1} \text{min}^{-1}$; $q_e - \text{mg g}^{-1}$; and initial rate – $\text{mg g}^{-1} \text{min}^{-1}$. The advantages in determining the initial rate of adsorption using the PSO model compared with the initial slope of q_t versus time are demonstrated in Figure 3.11. In the example, the initial rate was three times greater when calculated using the PSO model compared with the initial slope (4.4 versus $1.3 \text{ mg g}^{-1} \text{ min}^{-1}$). In this experiment, the first data point collected after mixing gave a value of $q_t = 4 \text{ mg g}^{-1}$. Given that $q_e = 5.4 \text{ mg g}^{-1}$, adsorption progress had already reached 75% completion when the first data was collected, and it is therefore not surprising that the slope of q_t versus time gives a significantly lower initial rate compared with the PSO model: the PSO includes curvature within its interpolation of early adsorption kinetics (interpolating between t=0 and 3 minutes). Not only are systematic errors reduced, but the PSO method also reduces the random error due to uncertainties in determination of sorbate concentrations, since most kinetic experiments gave at least 5 data points with which to fit the PSO parameters, rather than just two data points used in the initial slope method.

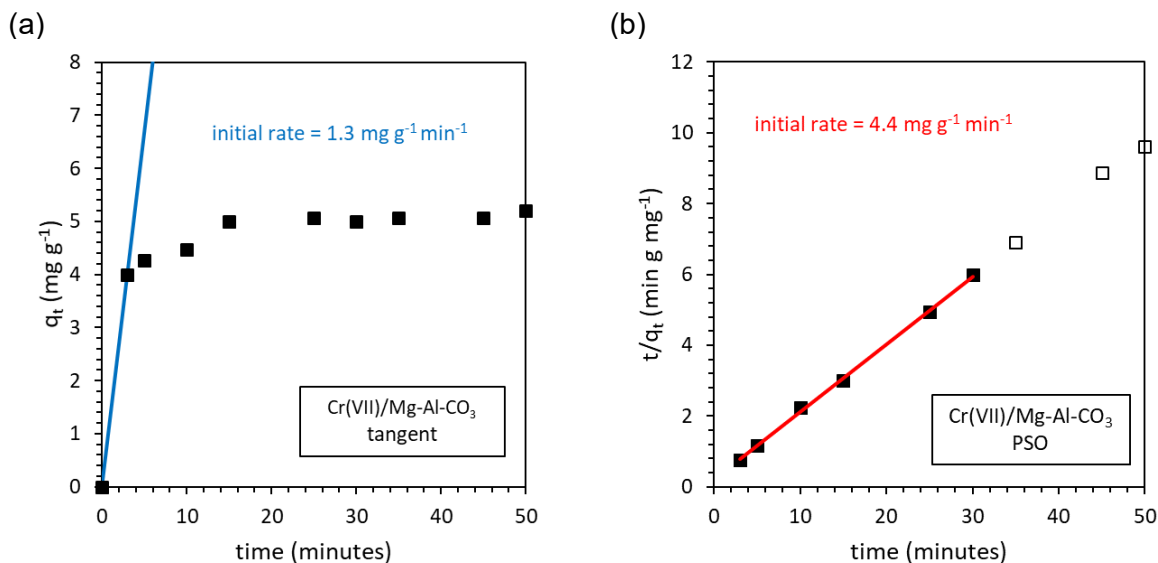


Figure 3.11: Illustration of how calculation of initial rates using the slope between the first two data points of q_t as a function of t gives a systematically lower result than when fitting the PSO model, using the linearised plot of t/q_t as a function of t . The data presented is from the Cr(VII)/Mg-Al-CO₃ data set with 10 mg L^{-1} sorbate and 1.5 g L^{-1} sorbent.³⁰³ The initial rate was calculated to be $8.5 \text{ mg g}^{-1} \text{ min}^{-1}$ when using the PSO method with only the first two data points.

3.7.1.3. Determining the order of reaction

The order of reaction with respect to C_0 , C_s or particle radius (r) was determined by using linear regression to calculate the gradient of $\log(\text{initial rate})$ versus $\log(\text{independent variable})$ ²⁹⁹, where each data point plotted represents a single kinetic experiment within a given literature study. This is expressed as:

$$\text{order of reaction} = \frac{\Delta \log(\text{initial rate})}{\Delta \log(C_0, C_s \text{ or } r)}$$

Equation 3.38

For each data set, the order of reaction with respect to the independent variable was calculated using the LINEST formula in Microsoft Excel. The error of each data set was calculated using the standard error of the slope. A generalised order of reaction was calculated as the average (mean, \bar{x}) and median (\tilde{x}) order of reaction between all data sets was collected. The errors reported are the standard deviation between all data sets. The dependencies of k_2 and k' upon C_0 , C_s and r were determined using the same method, substituting initial rates for k_2 or k' .

3.7.1.4. Kinetic modelling using the modified rate equation

As the new rate equation derived in chapter 8 (section 8.2) was not easily linearised, this new model was simulated using Microsoft Excel. The quantity of sorbate adsorbed at the n^{th} data point was calculated using the following formula:

$$q_n = q_{n-1} + \left((t_n - t_{n-1}) \cdot \left(k' C_{t(n-1)} \left(1 - \frac{q_{n-1}}{q_e} \right)^2 \right) \right)$$

Equation 3.39

with the concentration of aqueous sorbate remaining, C_t , decreasing according to the following equation:

$$C_{t(n)} = C_{t(n-1)} - C_s \cdot (q_n - q_{n-1})$$

Equation 3.40

The time interval between data points, $(t_n - t_{n-1})$ or Δt , was minimised until the magnitude of Δt had no significance on the observed kinetics.

3.7.2. Modelling an arsenic treatment plant based on meso-TiO₂/Fe₂O₃

A third batch of the meso-TiO₂/Fe₂O₃ composite had been synthesised elsewhere, and the adsorption capacity and kinetic parameters determined ²⁵¹. These results were used as input parameters for the kinetic adsorption model of the arsenic treatment plant.

3.7.2.1. Modelling batch treatments

The batch reactor design was modelled using the new rate equation, i.e.:

$$\frac{dq}{dt} = k' C_t \left(1 - \frac{q_e}{q_t}\right)^2$$

Equation 3.41

where t is time (minutes), q_t and q_e are the concentrations of As(III) adsorbed at time t and at equilibrium, respectively, C_t is the concentration of aqueous As(III) at time t, and

$$k' = \frac{k_2 q_e^{\dagger 2}}{C_0^{\dagger}}$$

Equation 3.42

where k₂ denotes the PSO rate constant, and q_e[†] and C₀[†] denote the values of q_e and C₀ in the original experiment ³⁰⁴. The expression for second-order dependence of adsorption kinetics upon the relative amount of available adsorption capacity remaining, $(1 - \frac{q_e}{q_t})^2$, is the same expression seen in the Integrated Kinetic Langmuir (IKL) model ²⁷³. In the new kinetic model derived in this thesis, q_e was calculated at each point in time using the experimentally determined Freundlich adsorption isotherm. It has been shown that use of adsorption isotherms to calculate the PSO parameter q_e outside of equilibrium, at each point in time, gives a better account of initial adsorption kinetics than when using the fixed term q_e determined from the linearised form of the PSO model ³⁰⁵.

3.7.2.2. Modelling continuous-flow treatments

The continuous flow reactor design was modelled through the modification of Equation 3.41 yielding:

$$\frac{dC}{dt} = jC_{influent} - C_s k' C_t \left(1 - \frac{q_e}{q_t}\right)^2 - jC_t$$

Equation 3.43

where j is the reactor turnover rate (bed volumes min^{-1}) used as a proxy for the flow rate, and $C_{influent}$ is the sorbate concentration of influent As(III) (mg L^{-1}). The term $jC_{influent}$ reflects the increase in C_t due to influx of influent, whilst jC_t represents the extraction of effluent. Continuous flow reactors were modelled with C_s varied between 0.01 and 10 000 g L^{-1} and C_0 was set at 0.5, 1 and 2 mg L^{-1} . j was varied between 0.001 and 1 min^{-1} to reflect residence times (i.e. treatment times) between one minute and one day.

3.7.2.3. Modelling 365 days of treatment

To model 365 days of sequential batch treatments using the same mass of sorbent, a reactor operated once per day on a single volume of water was considered, as per the study of Colombo and Ashokkumar ²⁶⁴. 365 consecutive simulations were conducted, each one representing a single day: in each simulation the initial value of q_t was made equal to the final value of q_t from the previous simulation, to reflect increasing saturation of the sorbent with each passing day. The size of the reactor was set as 40 L household^{-1} to meet clean water requirements, and the quantity of sorbent needed per household calculated using:

$$\text{mass of sorbent } (\text{g household}^{-1}) = V (40 \text{ L household}^{-1}) \cdot C_s (\text{g L}^{-1})$$

Equation 3.44

To model the continuous-flow system, (a) the number of bed volumes successfully treated in 365 days was calculated, using the equation:

$$\text{bed volumes treated } (\text{year}^{-1}) = j (\text{min}^{-1}) \cdot 525\,600 (\text{min year}^{-1})$$

Equation 3.45

and (b) the number of bed volumes treated before breakthrough was calculated, and the lesser of the two results was used as a measure of the volume of safe water produced in 365 days.

The size of the reactor was calculated as the minimum size required to provide 40 L⁻¹ household⁻¹ day⁻¹, using the equation:

$$V \text{ (L)} = 40 \text{ (L household}^{-1} \text{ day}^{-1}) \cdot j \text{ (min}^{-1}) \cdot 1440 \text{ (min day}^{-1})$$

Equation 3.46

In both systems, the sorbent efficiency (mg g⁻¹) was determined as the concentration of As(III) either (a) adsorbed at breakthrough or (b) after 365 days (whichever came sooner). The average residence time (min) was calculated as the inverse of turnover rate.

3.7.2.4. Simulating the arsenic treatment plant using MATLAB

A MATLAB program was written in order to solve the differential equations (Equation 3.40 and Equation 3.43) governing the adsorption kinetics of the theoretical arsenic treatment plant. The codes are provided in the Appendix and also available elsewhere³⁰⁶. For each simulation, the input parameters were C₀, C_s, C_{influent}, j, k', K_F, n and q₀ (where q₀ is the initial concentration of adsorbed As(III), being only non-zero when simulating 365 days of batch treatment). The end-point of each simulation was 1440 minutes for the batch system and calculated as a product of C_{influent} and $\frac{1}{j}$ for the continuous-flow system. 2000 data points were collected, with shorter time intervals during the initial stages of reaction (where C_t and q_t are fastest to change), giving a better resolution. The differential equations were solved using ODE15s and ODE45 functions with the output saved to a .txt file.

For both systems, As(III) concentrations of 500 and 2000 µg L⁻¹ were considered, representing the most severe arsenic contamination observed in South Asia³⁰⁷. The model was simplified by not including phosphate and sulphate anions which would compete with arsenic for sorbent binding sites. Due to a 10% difference between the concentrations of adsorbed As(III) at C_e=23 mg L⁻¹ measured using adsorption isotherm and adsorption kinetic experiments, the value of the experimentally determined K_F was increased by 10% to better fit the kinetic data.

4. Development of analytical techniques for quantitative arsenic speciation: As(V)-selective chemisorbent resins and electrochemistry

4.1. Introduction

Investigating the kinetics of As(III) photocatalytic oxidation requires the analytical capacity to measure As(III) and As(V) species separately from one another. The first aim in this thesis was to identify and develop a suitable approach towards analytical speciation. The requirements for this method were:

- Accuracy
 - Kinetic serial data must be accurate to provide precise rate constants, allowing the influence of experimental conditions upon photocatalytic rates to be assessed. Commercial field test kits are notoriously inaccurate, offering only semi-quantitative results³⁰⁸.
- Low detection limits
 - Low limits of detection (LoD) are needed to minimise the volume of sample needed. During kinetic experiments with sequential sampling, each aliquot reduces the volume of the system, both increasing the distance between lamp and solution (thereby reducing the incident light intensity) and changing the concentration of photocatalyst (if the suspension is unevenly mixed). By reducing the aliquot volume, the impact of measurement upon the system being observed is minimised.
- High sample throughput
 - To ensure photocatalytic oxidation kinetics were captured at a good resolution, a minimum of 10 data points were collected. At least five experiments were

needed to mathematically investigate the relationship between photocatalytic oxidation kinetics and (a) photon flux and (b) initial As(III) concentrations.

Performing these experiments with two different photocatalysts (meso-TiO₂ and meso-TiO₂/Fe₂O₃) corresponds a minimum of 200 samples before control experiments and experiments in different media are considered.

- Low cost
 - Low measurement costs per sample were required due to the large number of samples collected.

An additional requirement was that the technique should be portable. A significant problem with arsenic remediation is that the quality of the treated water produced by household-scale filters and community-scale treatment plants is rarely monitored³⁰. Reliable, low-cost methods for the online detection of arsenic are far from being realised³⁰⁹. In lieu of permanent online techniques, portable arsenic speciation is the best option, especially given that the areas affected by arsenic contamination are geographically large, and the most affected communities are rural populations. For arsenic treatment plants utilising advanced oxidation processes, monitoring As(III) at both influent and effluent points could have significant advantages, allowing processes to be optimised by adjusting treatment time, the concentration of oxidants, or the intensity of ultraviolet radiation³¹⁰.

Within the wider community, analytical speciation of arsenic is needed both in the assessment of contaminated groundwaters, and for studying the fundamental chemistry of arsenic in the laboratory. Knowing the speciation of arsenic within groundwaters is important for two reasons. Firstly, As(III) is up to 60 times more toxic than As(V), an important consideration if we want to provide accurate public health risk assessments^{311 312}. Secondly, knowledge of the speciation can help understand the cycling of arsenic within the environment³¹³. Reliable, low-cost and easy-to-use analytical techniques are also needed for the speciation of arsenic in synthetic media. Besides photocatalytic oxidation, many research groups are investigating processes such as chemical oxidation (e.g. Fenton's reagent)¹³⁸ and the competitive adsorption between As(III) and As(V)³¹⁴.

While arsenic speciation is now routinely achieved using hyphenated techniques such as high-performance liquid chromatography mass spectrometry (HPLC-ICP-MS)³¹⁵, these techniques fail to meet the low-cost requirement (e.g. tens of thousands of dollars total³¹⁶, and at least \$10 per sample³¹⁷). Furthermore, where samples are to be collected on-site, for instance at the tube well source or at the arsenic treatment plant, on-site speciation is preferable in order to avoid problems of sample storage: most importantly the progressive oxidation of As(III) on an hours-to-days timescale⁹¹. Unfortunately, field speciation continues to be a specialist

pursuit and groundwater contamination continues to be assessed on the basis of total arsenic only. This includes the five million tube wells tested in Bangladesh between 2000 and 2003³¹⁸ as well as more recent studies^{319 320 321}.

Portable and low-cost arsenic speciation has been achieved by various techniques, including colorimetric and electrochemical methods. Due to evolution of toxic arsine gas (AsH_3) and problems of reliability, the Gutzeit method has been superseded by molybdenum blue for colorimetric determination of arsenic^{322 323}. The molybdenum blue method involves formation of a blue colour-complex between molybdate and As(V). The concentration of arsenic is then estimated from the intensity of the colour evolved³²⁴ or better yet quantified by use of a spectrophotometer³²⁵, of which portable models are available³²⁶. Since the molybdenum blue method is As(V) selective, speciation can be achieved, with total As determined by addition of a chemical oxidant before analysis^{325 324 327}. Unfortunately, the molybdenum blue method suffers from a well-known phosphate interference. This is a major problem since the arsenic contaminated groundwaters of South Asia contain ten times more phosphate than arsenic^{86 40}. Colorimetric speciation therefore necessitates a number of chemical pre-treatments to remove phosphate and interconvert As(III) and As(V), complicating field analysis³²⁵.

4.1.1. Electrochemical detection

Electrochemistry is lower cost than ICP-MS³²⁸ and often portable, allowing on-site analysis of field samples⁹¹. Unlike ICP-MS, electrochemical detection is less sensitive towards organic arsenic such as monomethylarsonic acid (MMA) and dimethylarsonic acid (DMA) compared with inorganic arsenic⁹¹. This is not necessarily a problem, given that the environmentally stable organic forms of arsenic are less toxic than inorganic arsenic species, and so less important to monitor³²⁹. Electrochemical detection does not suffer from phosphate interference, unlike colorimetric detection using the molybdenum blue method. However, historically the perceived lack of “reliability, selectivity and sensitivity” has prevented the wider use of electrochemistry to detect arsenic³³⁰ and commercial uptake remains limited³³¹. This is most likely since electrochemistry suffers from issues related to sensor stability and its need for an expert eye, preventing its wider use by non-experts.

A range of electrochemical techniques can be used to detect arsenic: anodic stripping voltammetry (ASV)⁹¹, cathodic stripping voltammetry (CSV)³³², and chronoamperometry³³³. A selection of publications on the electrochemical detection of arsenic is presented in the Appendix. Voltammetric techniques impose a potential voltage on the working electrode, and

the current generated by the oxidation or reduction of the analyte is measured. The signal of the analyte is separated from interfering species based on differences between redox potentials²⁸². Trace analytes, such as environmental arsenic, are difficult to detect using cyclic voltammetry (CV), so a preconcentration step is normally needed²⁸²: either the anodic deposition of As(0) onto the electrode surface or the cathodic adsorption of arsenic oxyanions.

Anodic stripping voltammetry is currently the most widely used technique for electrochemical detection of arsenic. A negative voltage is imposed at the working electrode, and the reduction of aqueous As(III) or As(V) leads to deposition of solid As(0). As(0) is then stripped by sweeping the electrode from low to high potentials, and the oxidation of solid As(0) to aqueous As(III) produces a measurable current. The stripping reaction is:



Equation 4.1³³³

Arsenic has also been successfully detected at neutral pH using CSV. In CSV, a cathodic preconcentration step adsorbs arsenic onto the electrode surface. During the stripping step, a sweep from high to low potential reduces adsorbed As(III), producing solid As(0) and a measurable current³³².

The sensitivity of stripping voltammetry is improved by:

- Increasing the deposition time²⁸².
- Changing the profile of the potential sweep used to strip arsenic from a linear sweep to a sampled stepped profile, where current is measured at the end of each potential step. This minimises the interference from the charging current (electrolyte ions not participating in redox reactions), since charging current decays faster than faradaic current (the current generated by the redox reactions of interest)²⁸².
- Superimposing high frequency oscillations onto the stripping profile, such as a square wave signal. The oscillating potential causes rapid switching between oxidation and reduction reactions, amplifying the signal of the analyte³³⁴. Square wave stripping voltammetry (SWSV) has three advantages over sampled current voltammetry: (i) up to 100 times lower detection limits, (ii) up to four times improved peak resolution, and (iii) quicker measurements with greater sample throughput²⁸².
- Use of low surface area microelectrodes, allowing a good coverage of analyte over the electrode to be achieved even with very dilute samples²⁸². Microelectrodes also reduce the electrical double layer capacitance, reducing charging current²⁸².

Both liquid mercury and solid-state electrodes have been used for the electrochemical detection of arsenic, and previously published methods are compiled in the Appendix. Hanging

drop mercury electrodes (HDME) are not appropriate for ASV detection of arsenic³³⁵ since the HDME has a low operating potential range: mercury is oxidised at just +0.25 V (with the potential decreasing in the presence of chloride²⁸²). This is approximately the same potential as the oxidation of As(0) to As(III)²⁸². Arsenic can be detected with the HDME using CSV, upon addition of Cu(II) ions to form a copper arsenide amalgam in the deposition step (Cu_3As_2). During the stripping step, arsenic is reduced to arsine (AsH_3), which is unfortunately a toxic gas³³⁶. The HDME is also a poor choice for on-site detection, given the hazards of using toxic mercury in the field³³⁷.

The electrochemical speciation of arsenic is best achieved using solid electrodes, and gold³³⁸ is preferred over silver and platinum³³⁹. Efforts to optimise the detection of arsenic using gold electrodes are ongoing²⁸². Whilst detection of As(III) is easily achieved, detection of As(V) is challenging due to its low electroactivity under mild conditions. As(V) is normally reduced to As(III) using a reductive pretreatment prior to analysis, and the concentration of As(V) is determined through subtraction of As(III) from total As^{336 91 283}. However, chemical reduction steps are inconvenient for field analysis⁹¹. Alternatively, a strong negative potential (e.g. below -1 V) can be applied during deposition, evolving hydrogen gas at the working electrode and oxygen and chlorine at the auxiliary electrode. These react to give hypochlorous acid (HClO) which rapidly oxidises As(III) to As(V)²⁸⁰. As(V) is then directly deposited onto the working electrode using the strong reducing potential^{280 283}.

Despite the portability of electrochemistry and its ability to cope with high phosphate concentrations, there are few examples of this technique being used in the arsenic-contaminated groundwaters of South Asia⁹¹. This work therefore optimised electrochemical speciation of arsenic using the portable PDV6000 ultra potentiostat for the groundwaters of South Asia. The optimised method was then tested in parallel with speciation using an As(V)-selective chemisorbent resin, firstly to determine photocatalytic oxidation kinetics, and secondly to speciate arsenic in natural samples collected from arsenic-contaminated regions.

4.1.2. Selective chemisorbent resins

An alternative method is to separate As(III) and As(V) immediately at the time of sampling for later detection under laboratory conditions^{340 341 342}. This can be achieved by passing the solution through a sorbent that is selective to As(V) but leaves As(III) unaffected, for which chloride and acetate anion exchange resins can be used (solid phase extraction, SPE)^{343 344}. By measuring total As before and after treatment, the inorganic speciation can be determined. There are two potential drawbacks to ion-exchange resins. Firstly, these resins are selective

to a wide range of anions besides As(V). In South Asia groundwaters phosphate, sulphate and carbonate are 1, 2, and 4 orders of magnitude more prevalent than arsenic^{86 85} and much adsorption capacity will be lost to competing anions (particularly sulphate)⁹⁰. Consequently, resins will reach saturation more quickly than intended³⁴⁵. Secondly, exchanged ions are leached into the effluent which may interfere with subsequent analysis, particularly chloride, since the polyatomic ⁴⁰Ar³⁵Cl⁺ ion has historically been an interference with the ⁷⁵As peak during ICP-MS analysis³⁴⁶ (although modern instruments with collision cells counter this problem³⁴⁷). Finally, SPE often requires additional elution steps to remove sorbed As(III)³⁴⁸

349 350

To date, no study has considered the application of arsenic-selective chemisorbent materials towards the analytical speciation of arsenic. ImpAs is a recently reported chemisorbent material, consisting of an As(V)-selective receptor immobilised onto polymeric beads, with a high affinity for arsenate (patent number US 2017/0113949 A1)²¹². The active component of ImpAs is a metal-organic complex containing two Zn(II) centres to which As(V) oxyanions coordinate. ImpAs shows the greatest affinity towards As(V) at pH 6-8 and is thus suitable for most global groundwaters²¹². Chemisorbent resins could offer an exciting new route towards arsenic speciation, as their high selectivity will theoretically reduce interference from other anions, for better results in the most challenging waters, and if the material is non-selective towards As(III), then additional elution steps are not required.

4.1.3. Aims and objectives

The aim of this chapter was to develop (a) ASV using a portable potentiostat and (b) solid phase extraction using the ImpAs chemisorbent as two analytical techniques for the speciation of arsenic. These techniques were investigated (1) for determining photocatalytic oxidation kinetics, needed later in this thesis, and (2) for more general applications, e.g. on-site speciation of contaminated groundwaters.

To achieve this aim, the objectives were:

- To optimise electrochemical speciation of arsenic for the groundwater chemistry of South Asia, using a portable potentiostat.
- To test and verify the ability of ImpAs to separate As(V) from As(III), both in buffer solutions and in synthetic groundwaters. Buffer solutions were used to match the experimental conditions of the photocatalytic oxidation kinetics determined in chapter

7, and synthetic groundwaters were used to represent the arsenic contaminated groundwaters of South Asia.

- To conduct a cross-comparison of the two analytical techniques, with two case studies. The first study involved the determination of rate constants for the photocatalytic oxidation of As(III) using Degussa P25 (a commercial TiO₂ powder), and the second study considered the speciation of arsenic in natural waters from arsenic-contaminated regions (West Bengal, India and Cornwall, UK).
- To identify an appropriate analytical technique for the rest of this thesis.

The methodology of this chapter is illustrated in Figure 4.1.

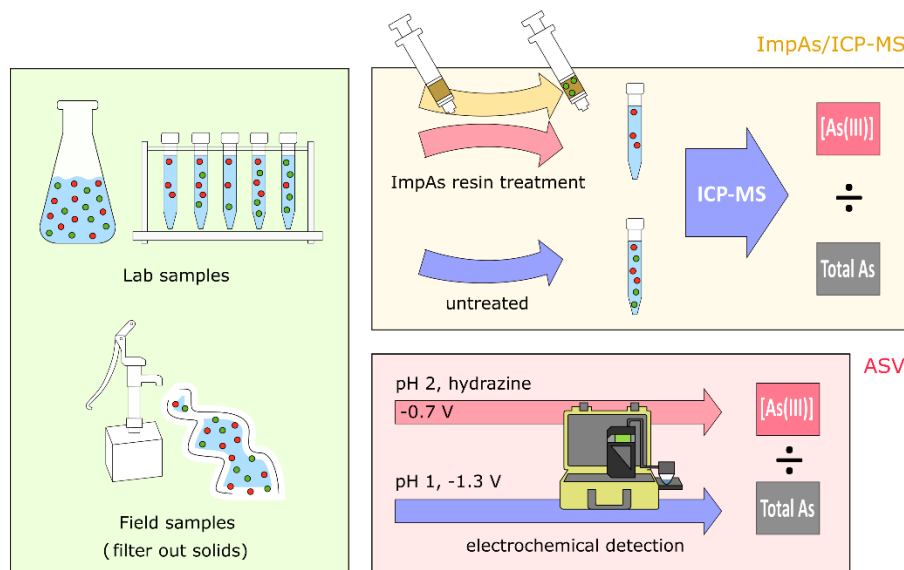


Figure 4.1: A concept schematic for arsenic speciation as performed by the two methods used in this study. As(III) is represented in red, and As(V) in green. Blue arrows denote determination of total As, whilst red arrows denote determination of As(III). Speciation is reported as the percentage of total As which is As(III).

4.2. Optimising electrochemical speciation for the arsenic-contaminated groundwaters of South Asia

The objective of this section was to optimise the portable voltammetric system for arsenic speciation in the challenging arsenic-contaminated waters of South Asia ³⁵¹. In Bangladesh and West Bengal, India, concentrations of 60 µM Fe(II) (approximately 3.3 mg L⁻¹) and 20 µM Mn(II) (1.1 mg L⁻¹) are typical for arsenic contaminated groundwaters ^{86 40 85}. There are only a few papers dealing with the electrochemical speciation of arsenic in the groundwaters of South Asia ^{352 353 91} and they all differ in their methods and/or apparatus. This section therefore systematically investigates the influence of synthetic groundwaters with high concentrations of Fe and Mn, EDTA and hydrazine, on the speciation of arsenic under acidic conditions, using fast linear scan ASV (with a scan rate of 4-8 V s⁻¹).

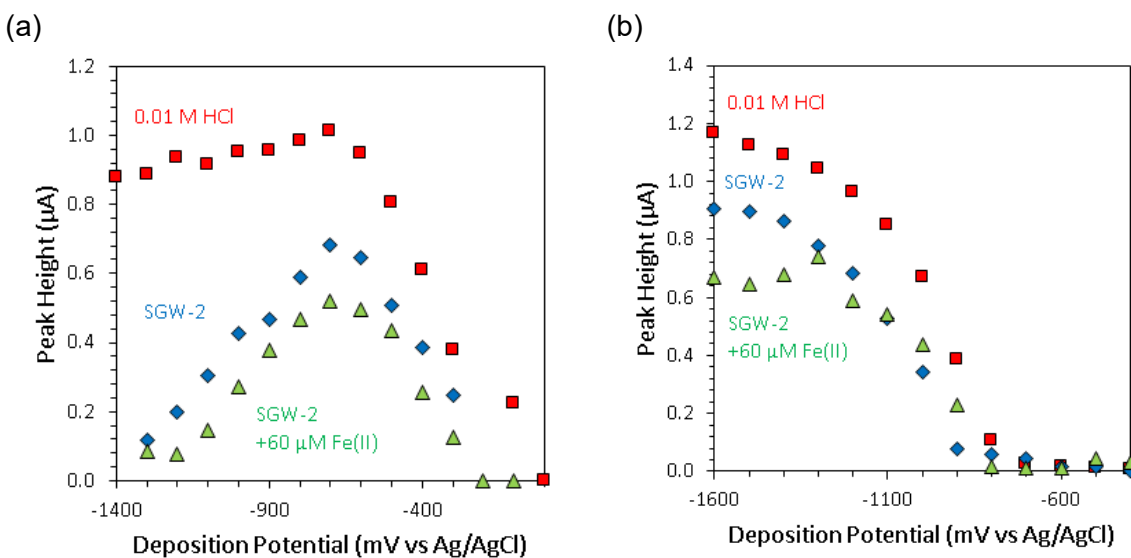


Figure 4.2: The influence of deposition voltage on As stripping peak intensity. (a) As(III) determination at pH 2 (40 µM hydrazine), and (b) total As determination at pH 1, both systems acidified with HCl. Media used were blank HCl (red squares), SGW-2 (blue diamonds) and SGW-2 +60 µM Fe(II) (green triangles). 15 seconds deposition, 10 seconds hold at ≤0.4 V (no more negative than the deposition potential), stripping at 4 V s⁻¹. As(III) detection was made in the presence of 5 µg L⁻¹ As(III), and total As detection was made in the presence of 5 µg L⁻¹ As(V).

The As stripping peak was located at ca. +180 mV in 0.01 M HCl and ca. +230 mV in 0.1 M HCl. The optimum deposition potential for detection of As(III) was -0.7 V, whether in 0.01 M HCl or synthetic groundwater acidified to pH 2 (Figure 4.2a). At more negative deposition potentials, the height of the As peak in the synthetic groundwaters decayed, disappearing at

around -1.3 V, whilst the arsenic peak remained stable in 0.01 M HCl. This was consistent in repeat experiments. For total As determination at pH 1, no peak was seen until deposition at -0.8 V. Peak height then increased until -1.3 or -1.4 V, after which the peak height plateaued (Figure 4.2b). Linear sweep performed well with the PDV6000 ultra potentiostat, so oscillating sweep profiles such as square wave stripping voltammetry were not needed.

The method used to detect total As gave equal sensitivity towards As(III) and As(V). This was verified by comparing spike recoveries using (a) the 1 mg L⁻¹ As(V) stock solution as the analyte and the 1 mg L⁻¹ As(III) stock solution as the standard, and (b) the As(III) stock as the analyte and the As(V) stock solution as the standard. All results were within error of 100% spike recovery (Table 4.1).

Table 4.1: Verifying that total As detection is equally sensitive towards As(III) and As(V). 1 mg L⁻¹ As(V) standard solution calibrated against 1 mg L⁻¹ As(III) standard solution. Conditions were 0.1 M HCl, -1.3 V deposition (15 seconds), linear sweep (8 V s⁻¹).

Analyte	Standard	Measurement	Result (µg L ⁻¹)	Relative uncertainty (%)
1 mg L ⁻¹ As(V)	1 mg L ⁻¹ As(III)	1	1013 ± 54	5
		2	1062 ± 60	6
1 mg L ⁻¹ As(III)	1 mg L ⁻¹ As(III)	1	1080 ± 26	2
		2	945 ± 47	5

Additions of high concentrations of Fe(II) generally resulted in a decrease of the As(III) signal (Figure 4.3a, b). For example, a loss of ca. 40% was observed after the addition of 120 µM Fe(II) (6.6 mg L⁻¹). Even at 300 µM Fe(II), the arsenic peak was still well shaped and standard additions could be used for reliable arsenic determination. A peak at ca. +0.6 V whose intensity increased linearly with Fe additions was present on the stripping scan. The potential of this peak was significantly more positive than that of arsenic, and consequently this peak did not interfere with the As peak. During determination of total As, no significant decrease of the As peak was observed during addition of up to 300 µM Fe(II) (16.5 mg L⁻¹) (Figure 4.3c, d). Peaks corresponding to environmentally present copper did not interfere with either method, being small and being separated from the arsenic peak by +200 mV (Figure 4.3). Addition of up 100 µM Mn(II) (5.5 mg L⁻¹) affected neither the As(III) nor the As(V) peak (Appendix). No new peak was observed in after addition of Mn(II), indicating that Mn(II) is not electroactive under these conditions.

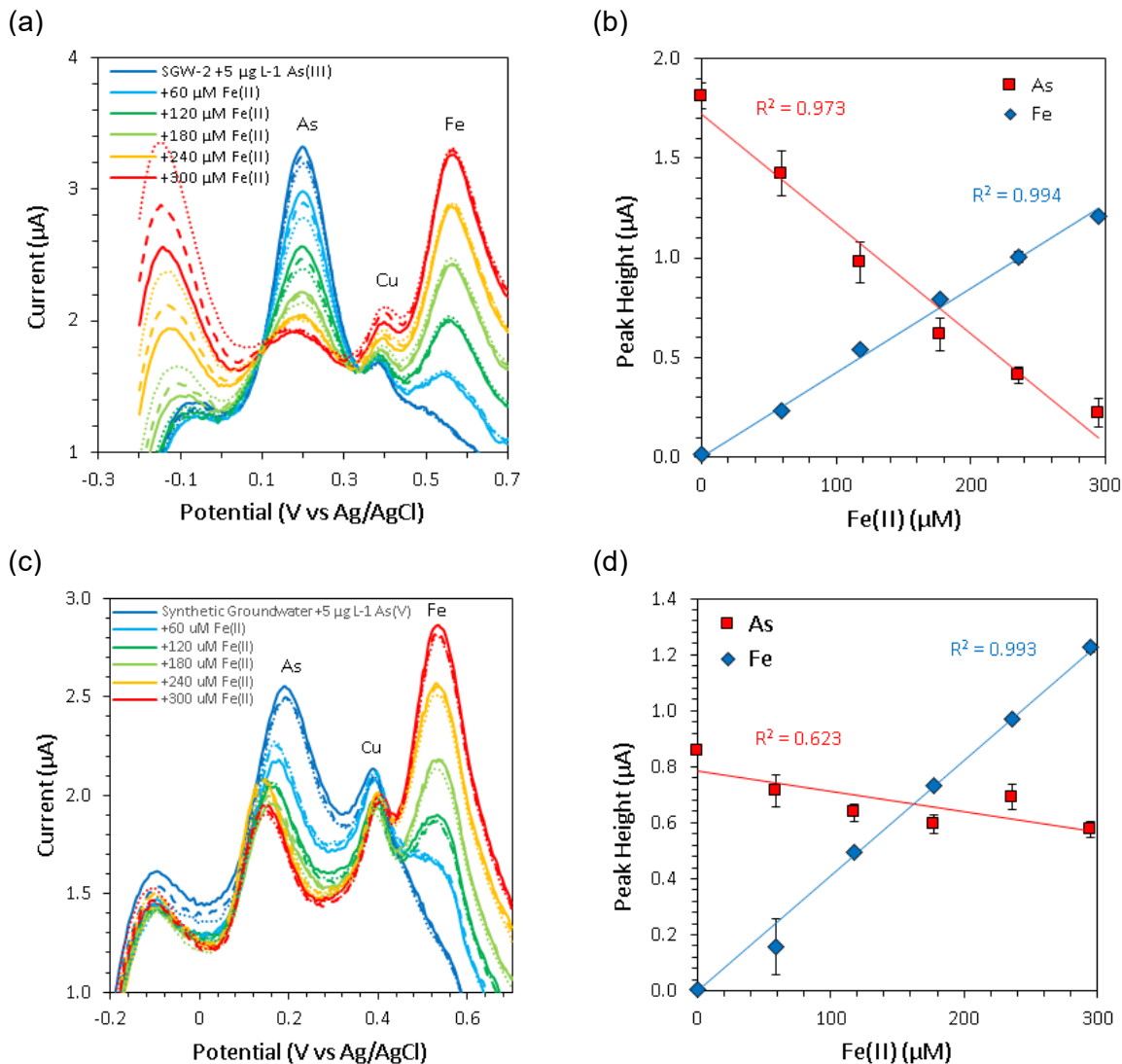


Figure 4.3: The influence of iron on the electrochemical detection of arsenic. (a) and (b) show the influence of Fe(II) on the detection of As(III) at pH 2 (5 $\mu\text{g L}^{-1}$ or 67 nM As(III)). (c) and (d) show the influence of Fe(II) on the detection of total As at pH 1 (5 $\mu\text{g L}^{-1}$ or 67 nM As(V)). In West Bengal and Bangladesh, concentrations of around 60 μM Fe(II) (3.3 mg L^{-1}) are commonplace for arsenic contaminated groundwaters.^{86, 40, 85} Error bars represent the standard deviation between the three repeat scans made after each addition of Fe(II). LSASV conditions were 15s deposition at -1.3 V (total As) or -0.7 V (As(III)), 10s hold at -400 mV, stripping from -400mV to +700mV at 4 V s^{-1} . Detection was made at pH 2 with 20 μM hydrazine for As(III) and pH 1 with no hydrazine for total As.

The chelating agent EDTA was used in this work to preserve natural samples, preventing the loss of arsenic due to the precipitation of iron (initiated by the oxidation of Fe(II) to Fe(III)). The influence of EDTA on the As peak during the detection of total As was investigated (Figure 4.4a). A well formed As peak was observed with addition of up to 25 mM EDTA (7.5 g L^{-1}), after which the peak was rapidly lost. A signal attributed to EDTA (at +600 mV) was observed, increasing at a rate approximately equal to the rate at which the As peak decreased. Field samples were preserved with addition of 10 mM EDTA (2.9 mg L^{-1}), which is below the threshold identified for As peak instability (25 mM, 7.5 g L^{-1}).

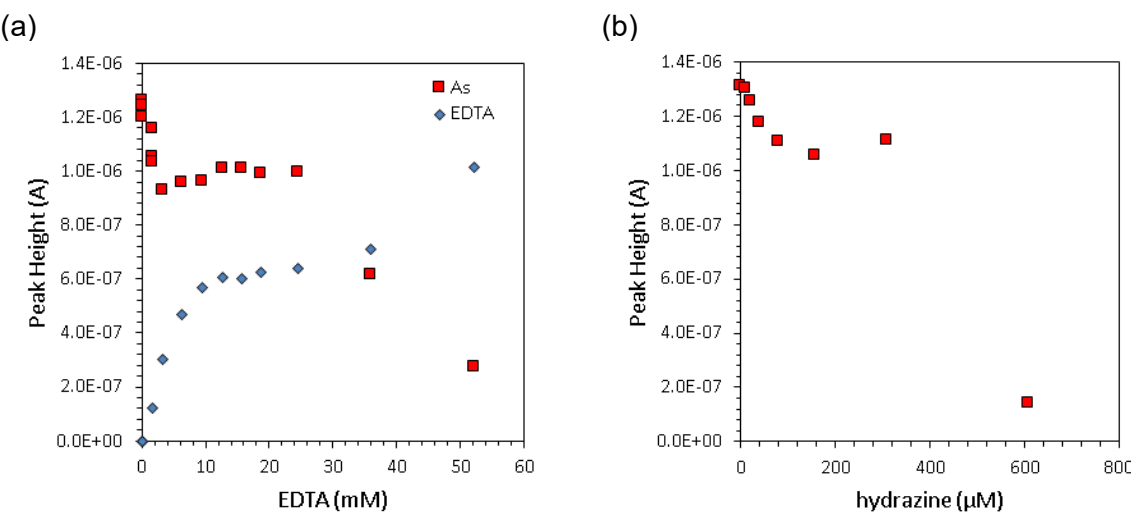


Figure 4.4: The influence of (a) EDTA and (b) hydrazine on As stripping peaks during total As determination ($5 \mu\text{g L}^{-1}$ As(V), pH 1). The data series labelled 'EDTA' indicates a second peak that appeared at ca. +600 mV. LSASV parameters were 15s at -1.3 V, 10s hold at -400 mV, stripping from -400mV to +700mV at 4 V s^{-1} . Arsenic peaks remained stable with up to 25 mM EDTA, beyond which peak current fell towards zero. Addition of excess hydrazine (sometimes as low as 40 μM) was accompanied with an increase in background current at positive stripping potentials, which increased in magnitude and shifted toward negative potentials with repeat scans, eventually obscuring the As peak. 20 μM hydrazine was identified as ideal. For total As determination, arsenic could be detected with up to 300 μM hydrazine, far beyond the concentrations used for sample preservation.

During detection of As(III), peaks can be unstable when depositing at potentials below -0.5 V. This is likely due to oxidation of As(III) to As(V) via HClO formed at the auxiliary electrode during deposition²⁸³. Hydrazine (N_2H_4) has been used since the 1980's to preserve samples and prevent the oxidation of As(III)³³⁶. In this work hydrazine was introduced during detection of As(III), as a sacrificial oxidant to stabilise the arsenic peak (ascorbic acid is also sometimes used to prevent oxidation of As(III)²⁸³). In this work, As(III) could not be detected without addition of hydrazine. However, voltammograms were often unstable with 40 μM hydrazine: a peak appeared at ca. +350 mV, increasing with repeat scans and obscuring the As peak. Addition of 10-20 μM hydrazine gave good stability and was used in the final procedure. Since field samples were preserved with hydrazine, the influence of hydrazine on detection of total As was also assessed. As peaks were stable with addition of up to 300 μM hydrazine (9.6 mg L^{-1}), beyond which signal from the As peak was significantly lost (Figure 4.4b). This was far beyond the 20 μM hydrazine used to preserve samples in this work.

The sensitivity and linear range of each procedure was similar regardless to whether the electrolyte was 10 mM HCl or synthetic groundwater (SGW-2) (Figure 4.5). However, detection limits were higher in synthetic groundwater than in blank HCl. During determination of total As, the LoD increased from 0.06 to 0.4 $\mu\text{g L}^{-1}$ (0.8 to 5 nM) when the blank HCl electrolyte was replaced with synthetic groundwater, and during determination of As(III) the LoD increased from 0.1 to 0.3 $\mu\text{g L}^{-1}$ (1 to 4 nM). Within the linear range, the average

uncertainty of measurement via the method of standard additions was $\pm 6\%$ (propagated from the standard error of the slope in the linear regression). In all cases detection limits were $<1 \mu\text{g L}^{-1}$ indicating that arsenic-contaminated waters can be speciated. This work shows that the inorganic ions commonly encountered in South Asia, including natural levels of Fe(II) and Mn(II), do not significantly impact arsenic analysis by the method of standard additions under this voltammetric procedure. The final operating conditions and detection limits of the optimised procedure are presented in Table 4.2.

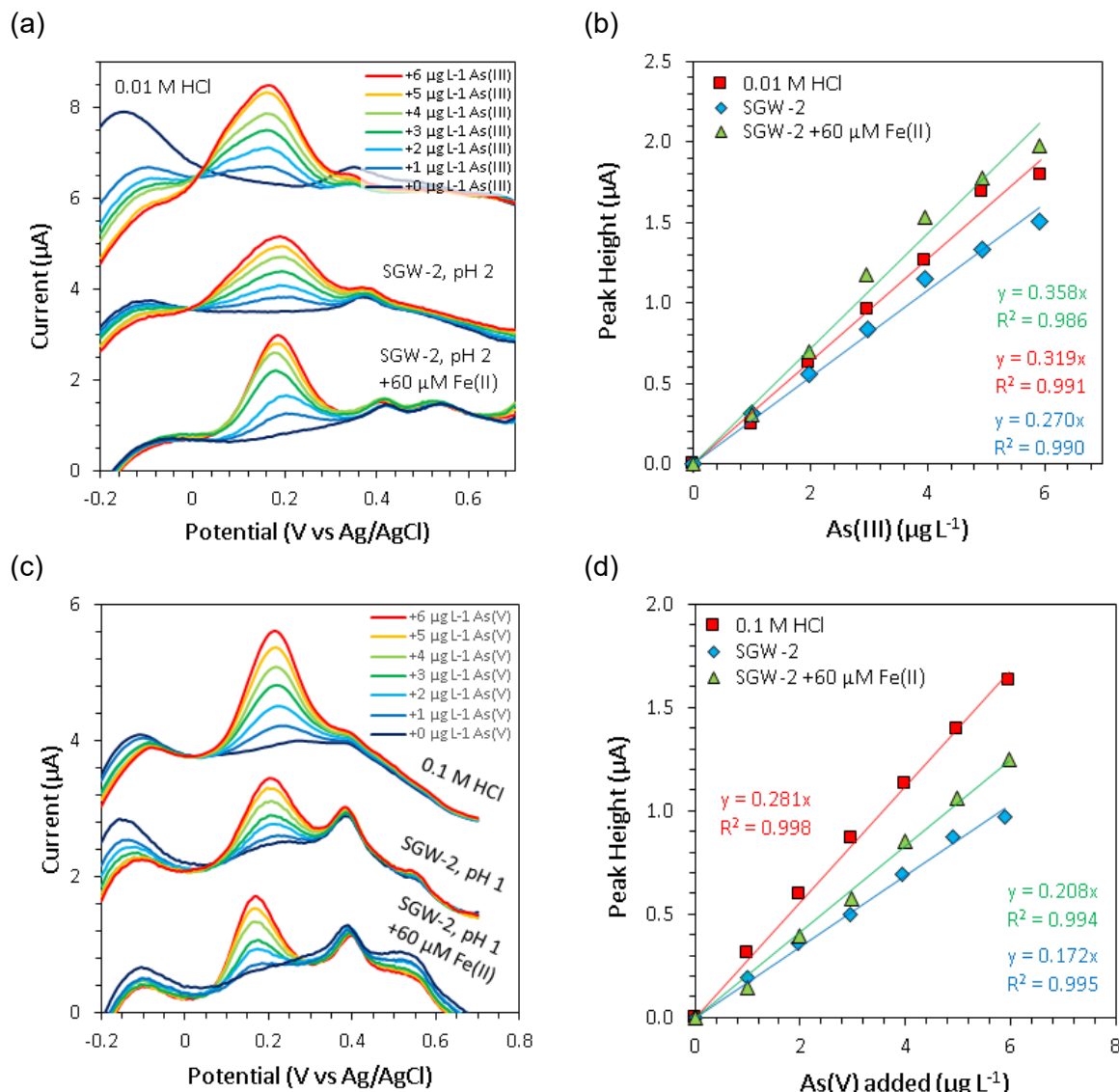


Figure 4.5: The influence of inorganic groundwater species on the electrochemical detection of arsenic. (a) and (b) show the As(III) stripping peaks ($5 \mu\text{g L}^{-1}$ or 67nM As(III)) in synthetic waters with increasing additions of As(III). (c) and (d) show total As stripping peaks ($5 \mu\text{g L}^{-1}$ or 67nM As(V)) with increasing As(III). LSASV conditions were 15s at -1.3 V (total As) or -0.7 V (As(III)), 10s hold at -400 mV , stripping from -400 mV to $+700 \text{ mV}$ at 4 V s^{-1} . Detection was made at pH 2 with $20 \mu\text{M}$ hydrazine for As(III) and pH 1 with no hydrazine for total As.

Table 4.2: ASV operating parameters. The limits of detection (LoD) and limits of quantification (LoQ) are reported for both blank HCl and acidified SGW-2 media. LoD and LoQ were calculated respectively as 3 and 10 times the standard deviation (σ) of seven repeat scans of the lowest concentration of standard added. Further information is provided in the Appendix - Figure 10.5.

Potentiostat		PDV6000ultra	
Determination		As(III)	Total As
pH (in HCl)		2	1
Hydrazine (μM)		20	None
N_2 purge			None
Rest		+600 mV	
Deposition		-700 mV (15 s)	-1300 mV (15 s)
Hold		+400 mV (10 s)	
Stripping	Start potential	-400 mV	
	Final potential	+700 mV	
	Profile	Linear sweep	
	Sweep rate	8 V s^{-1}	
Cleaning		+700 mV (2 s)	
LoD (3σ) ($\mu\text{g L}^{-1}$)	HCl	0.095	0.058
	SGW-2	0.34	0.44
LoQ (10σ) ($\mu\text{g L}^{-1}$)	HCl	0.32	0.19
	SGW-2	1.1	1.5
Linear range ($\mu\text{g L}^{-1}$)		6	6

4.3. Method development: Arsenic speciation using an As(V)-selective chemisorbent

4.3.1. Speciation under equilibrium conditions

ImpAs is a polystyrene-based material functionalised with a metal-organic receptor that has a very high affinity towards chemisorption of As(V)²¹². The objective of this section was to investigate whether ImpAs can separate As(III) and As(V) from synthetic waters. Batch reactions under equilibrium conditions were used to verify that As(V)-selective ImpAs does not remove As(III) from solution, even after overnight shaking (in 10 mM HEPES). Since separation of As(III) and As(V) fails when the sorbent is saturated, ImpAs was kept in excess. The concentrations of total As in samples with and without addition of ImpAs (where addition of ImpAs is referred to as a “treatment”) were determined by ICP-MS. As(III) concentrations were unaffected by addition of ImpAs (Figure 4.6a). The speciation of each sample, expressed as the percentage of total As that is As(III), was determined using the equation:

$$\text{speciation (\% As(III))} = 100 \times \frac{[\text{Total As (ImpAs treated)}]}{[\text{Total As (untreated)}]}$$

Equation 4.2

The comparison of observed versus expected results is presented in Figure 4.6b. When 1 g L⁻¹ ImpAs was used to treat each sample, the linear regression gave a slope of 0.952 ±0.049 (within 5% of the expected one-to-one calibration curve) with R² = 0.992. Equation 4.2 gave a speciation of 2.9 ±0.3% and 94.3 ±2.2% As(III) when As(III) mixing fractions were 0% and 100% As(III) respectively. Similar results were obtained when using a high excess of 20 g L⁻¹ ImpAs: a calibration curve with a slope of 0.887 ±0.022, with 3.5 and 92.6 % As(III) calculated when As(III) mixing fractions were 0 and 100% respectively. These results indicate that ImpAs does not remove As(III) from solution, and that quantitative removal of As(V) and separation from As(III) was achieved within ±7%.

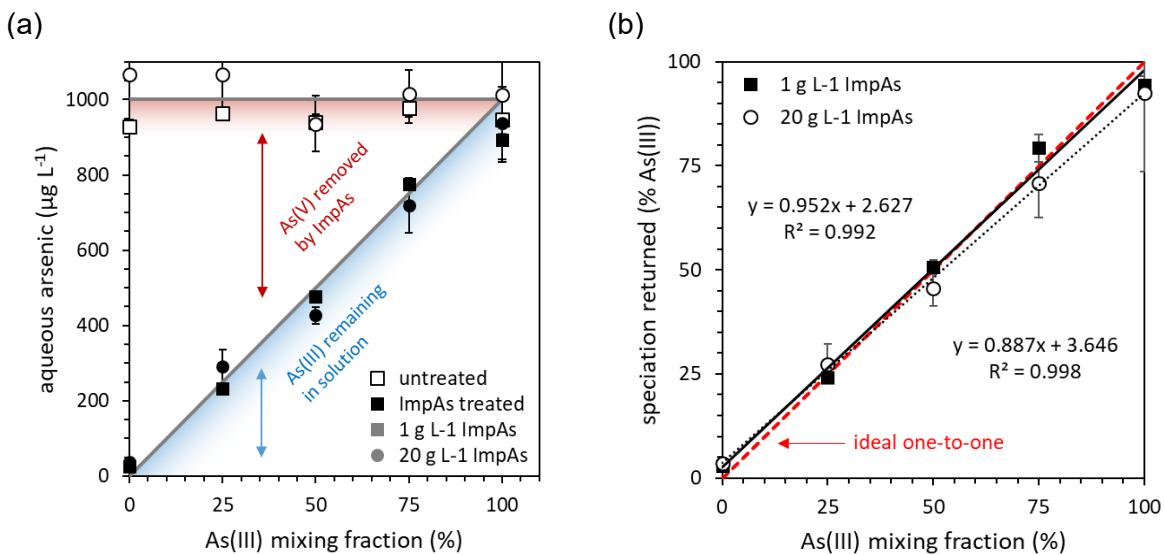


Figure 4.6: ImpAs method development: arsenic speciation using batch treatment. (a) The concentration of total As that remains in solution with and without addition of ImpAs as a function of the As(III):As(V) mixing ratio, and (b) the resulting calibration curves.

4.3.2. Implementation as an easy-to-use, portable device

Having verified that ImpAs can speciate arsenic under equilibrium kinetics, ImpAs was loaded into syringes to (a) provide a rapid and high throughput device for laboratory applications, and (b) to provide portability for on-site applications. (Simply shaking ImpAs suspensions by hand to remove As(V) was too slow, taking at least 20 minutes, as shown in the Appendix). Syringes were first tested for As(V) removal in 10 mM HEPES with and without prior conditioning (i.e. resin wetting). Here, the aim was to identify the appropriate amount of ImpAs for 5 mL plastic syringes, balancing efficient removal with low material consumption. Since As(V) sorption is a function of contact time between sorbent and sample, syringes were prepared with 0.2 g (2.5 mm path length), 0.4 g (5 mm) and 1.0 g (12 mm) ImpAs (Figure 4.7).



Figure 4.7: The syringes loaded with 0.2, 0.4 and 1.0 gram ImpAs used in this work. Column path lengths were 2.5, 5 and 12 mm respectively.

Without prior conditioning, As(V) removal was limited and the 1 g ImpAs syringe only removed $57.9 \pm 2.0\%$ As(V) in a single pass (Figure 4.8a). This is likely due to pore channelling between resin beads, offering paths of least resistance through which influent contact with ImpAs is limited. However, when ImpAs was conditioned first, it demonstrated very efficient removal of As(V) ($98.0 \pm 1.8\%$ with a single pass, using 1 g ImpAs). When conditioned, increasing the mass of ImpAs also increased As(V) removal due to increased contact (Figure 4.8a). In all cases ImpAs was unsaturated and so incomplete As(V) removal was due to kinetic limitations rather than insufficient sorption capacity. Cross-contamination due to carry over was only identified for a single data point in Figure 4.8a. Control experiments ($N=2$) demonstrated that As(III) was neither removed nor oxidised when passed through the syringe (Figure 4.8c, grey diamonds).

Having established efficient As(V) removal using ImpAs syringes in HEPES buffer solutions, more complex media were considered. Challenge Water (CW) is a synthetic groundwater used to test the performance of arsenic removal units ³⁵⁴ and synthetic groundwaters SGW-1 and SGW-2 were formulated based upon the composition of arsenic-contaminated groundwaters in West Bengal, India (Table 3.2) ⁸⁶. CW was high in sulphate, which is known to interfere with anion exchange resins ⁹⁰, whilst SGW-1 was high in phosphate, a known competitor of As(V) for ImpAs binding sites ²¹². ImpAs was effective in both CW and SGW-1 with 92.9 ± 1.1 ($N = 2$) and $96.9 \pm 0.7\%$ ($N = 2$) As(V) removed in a single pass (Figure 4.8b), demonstrating that ImpAs-loaded syringes can speciate arsenic in the presence of inorganic groundwater species.

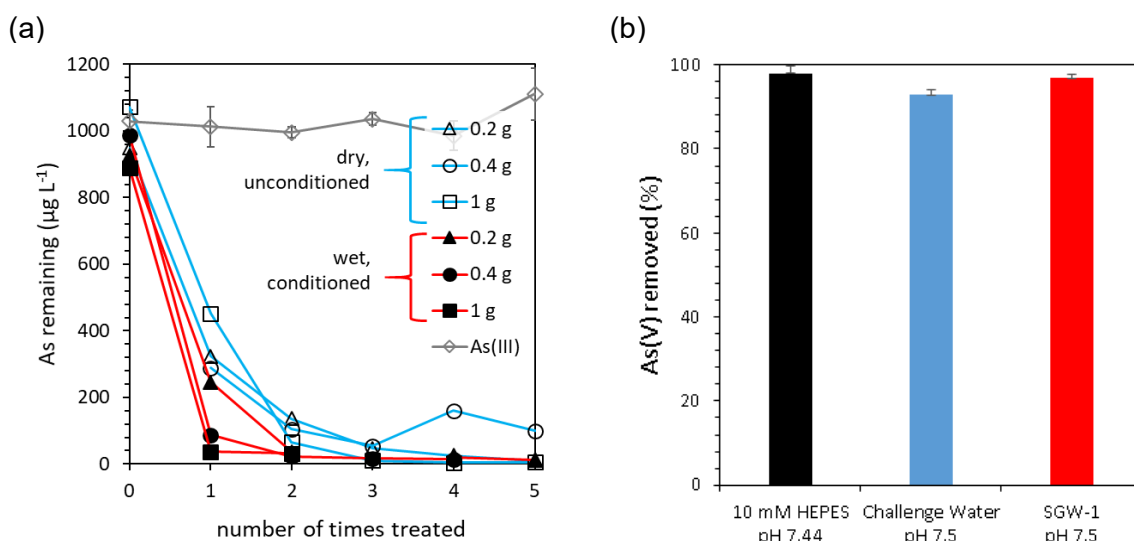


Figure 4.8: ImpAs method development: arsenic speciation using syringe devices for a column treatment. (a) The removal of As(V) with sequential passes through syringes loaded with different masses of ImpAs. (b) As(V) removal efficiency in different media after a single pass through a syringe loaded with 1 g ImpAs ($N=2$). Experimental conditions were 1 mg L^{-1} As(V) in HEPES (pH 7.4). The data series labelled "As(III)" (grey diamonds), indicates a control experiment where 1 mg L^{-1} As(III) in HEPES was treated using the 1 g ImpAs syringe, and As(III) detected using ASV to verify that As(III) was neither oxidised nor removed during treatment.

4.4. Case studies for the validation of analytical methods

Two case studies were used to cross-validate the two analytical procedures: (1) speciation of arsenic using the optimised ASV procedure, and (2) speciation of arsenic using ImpAs-loaded syringes followed by ICP-MS detection. The first case study was the determination of photocatalytic oxidation kinetics, since this was the major driver for developing analytical speciation techniques within this thesis. The second case study was the speciation of arsenic in natural waters, due to the limitations of current portable techniques discussed within the introduction to this chapter.

4.4.1. Case study 1: Determination of photooxidation rate constants in synthetic solutions

The photooxidation of As(III) using Degussa P25 TiO₂ as a photocatalyst was investigated, using both analytical techniques to monitor the reaction kinetics (Figure 4.9a). The reaction was modelled using pseudo-first order kinetics, with the rate equation:

$$-\frac{d[\text{As(III)}]}{dt} = k[\text{As(III)}]$$

Equation 4.3

where $d[\text{As(III)}]/dt$ is the rate of change in the concentration of As(III) with respect to time, and k is the pseudo-first order rate constant (min^{-1}). The integrated solution to this equation can be rearranged into the linear form

$$\ln\left(\frac{[\text{As(III)}]_t}{[\text{As(III)}]_0}\right) = -kt$$

Equation 4.4

where $[\text{As(III)}]_t$ and $[\text{As(III)}]_0$ are the concentrations of As(III) at time t and $t=0$ respectively. Plotting Equation 4.4 in the linear form $y=mx+c$ indicated pseudo-first order kinetics, with $R^2=0.937\pm0.006$ using ASV measurements, and $R^2=0.981$ using ImpAs/ICP-MS (Figure 4.9b). (Identical R^2 values were obtained in the two repeat experiments using ImpAs/ICP-MS

analysis). In each repeat experiment the values of k determined using the two different analytical procedures were within error of one another (Figure 4.9c). Taking an average of the two repeat experiments gave $k=0.0710\pm 0.0019 \text{ min}^{-1}$ when As(III) concentrations were detected using ASV, and $k=0.0725\pm 0.0061 \text{ min}^{-1}$ when ImpAs/ICP-MS was used (Figure 4.9c). Again, the values of k obtained by the two analytical methods were within error of one another. Since the two analytical techniques captured the same kinetics as one another, both techniques are valid for the determination of arsenic speciation in synthetic media.

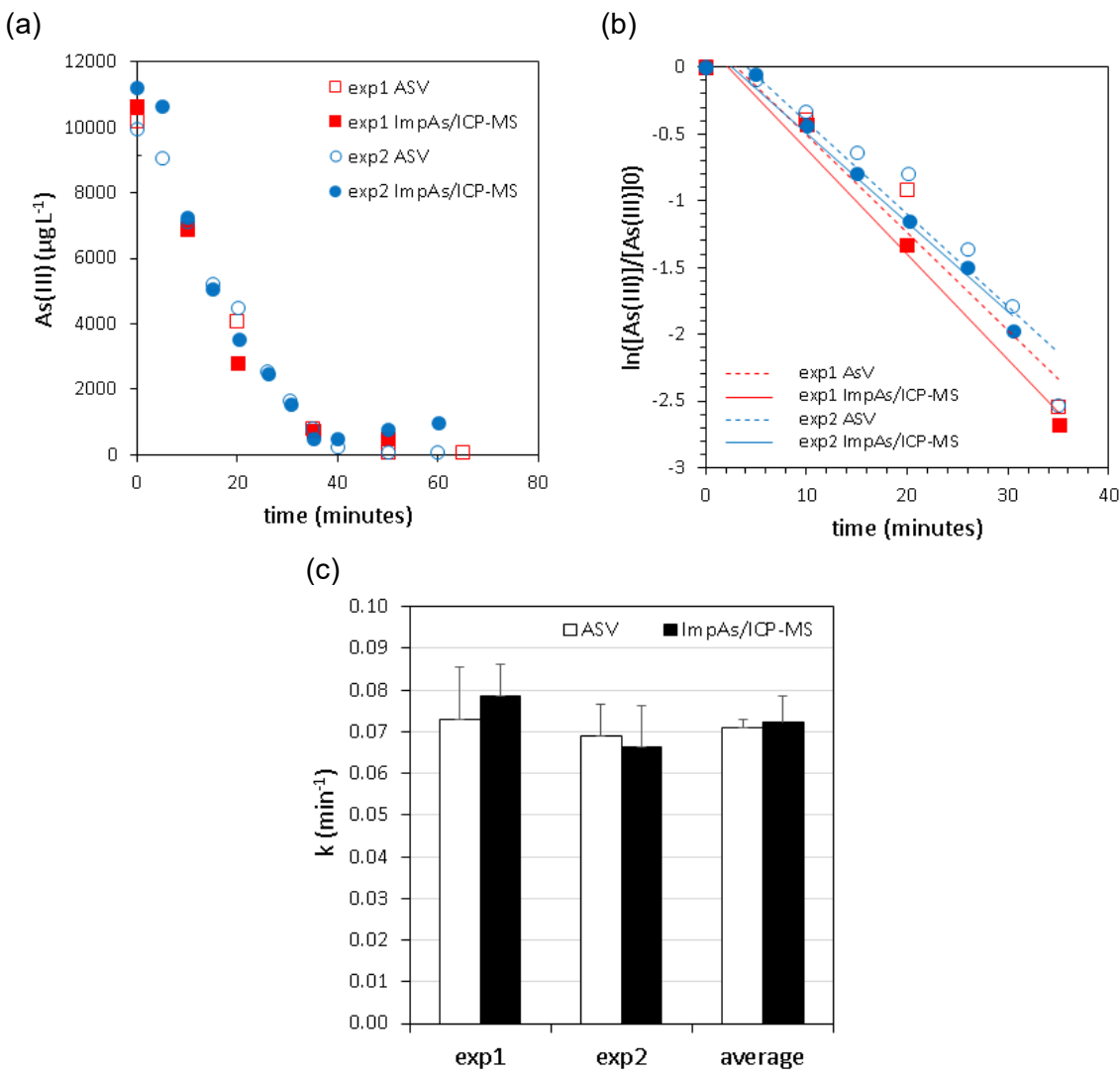


Figure 4.9: Case study 1: Determination of photooxidation rate constants in synthetic solutions. Experimental conditions were 10 mg L^{-1} initial As(III), 0.1 g L^{-1} Degussa P25 TiO₂, suspended in 10 mM HEPES (pH 7.44). (a) The time series for the photocatalytic oxidation of As(III) (two repeat experiments). (b) Experimental data was fitted to the pseudo-first order kinetic model. (c) The comparison of rate constant, k , as determined using the two analytical methods. ASV measurements are shown as unfilled shapes, ImpAs/ICP-MS measurements are filled. Red squares indicate the first repeat experiment, and blue circles indicate the second repeat experiment. Solid lines and dashed lines indicate the linear best fit for ImpAs/ICP-MS and ASV results respectively.

4.4.2. Case study 2: Speciation of natural waters

Spike recovery experiments were used to verify that both analytical techniques work in natural waters. This was particularly important given that the selectivity of ImpAs had not been previously tested for removal of As(V) in the presence of dissolved organic matter.

4.4.2.1. Spike recovery experiment

Groundwater from a spring and surface water from a stream (both from Cornwall, UK) were chosen as representative oxic waters, alongside commercial bottled mineral water from France. Four groundwater samples were also collected and tested from tube wells in West Bengal, India, being examples of anoxic and reducing waters. These samples showed high concentrations of dissolved iron (and are characterised in Table 3.2). After filtration to remove solids, clear groundwater samples from West Bengal required immediate acidification to pH 2 (using HCl), or spiking with 10mM EDTA, to prevent the formation of yellow-brown iron precipitates within a matter of minutes.

Samples were spiked with arsenic to provide a mix of As(III):As(V) ratios. The samples were then speciated using the developed ASV and ImpAs/ICP-MS methods. Speciation of arsenic in three of these natural waters is presented in Figure 4.10. For untreated samples, ICP-MS showed that 100% of the As(V) spike added was recovered by total As determination. Treatment using ImpAs removed all of the As(V) spike added. This indicated that speciation using ImpAs was successful. Similar results were achieved using ASV, since total As detection provided full spike recovery, whilst As(III) detection was unaffected by the addition of As(V). Similar results were obtained for waters from both oxic and anoxic environments. Despite the ImpAs resin becoming coated with a dark precipitate after treating large volumes of the West Bengal samples (Figure 4.11a), the aqueous samples did not develop colour during the course of the experiment, indicating that iron precipitation was not a problem.

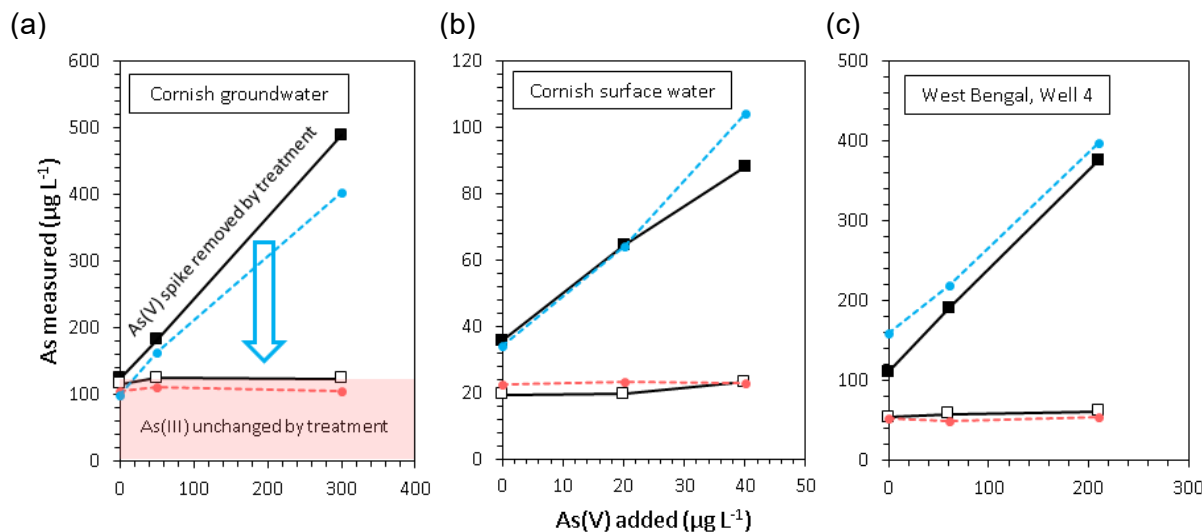


Figure 4.10: Case study 2: Speciation in natural media. Samples were spiked with arsenic to obtain a mix of As(III) and As(V), and an ImpAs-loaded syringe was used to remove As(V). By determining total As by ICP-MS before treatment with ImpAs (black filled squares) and after treatment (white squares) the speciation was determined. ASV determination is also given for comparison (dashed lines) with total As (blue) and As(III) (red).

4.4.2.2. Limitations

Samples preserved by acidification must be pH neutralised before treatment with ImpAs, to prevent disruption of the metal-organic receptor. Unlike the other West Bengal groundwaters, STN5 showed rapid iron precipitation both (i) immediately after sampling the water (before acidification) and (ii) within minutes of pH neutralisation. This sample had the highest high iron concentration (13 mg L^{-1} versus $\leq 5.0 \text{ mg L}^{-1}$ for all other samples, Table 3.2), and 99% of all arsenic present had been oxidised during storage. During the course of the STN5 spike experiment, the observed total As failed to match the quantity of the As(V) spike added (Figure 4.11b) owing to the loss of arsenic associated with iron precipitation. The concentration of As(III) was more stable, suggesting that the loss of arsenic was due to adsorption and co-precipitation of As(V), in line with previous findings⁹¹. Besides acidification, the chelating agent EDTA can be used to prevent iron precipitation. Whilst addition of EDTA prevented loss of iron both in standing samples and during ImpAs treatment, EDTA presented a new problem: EDTA limited the ability of ImpAs to remove As(V) from solution (Figure 4.11c).

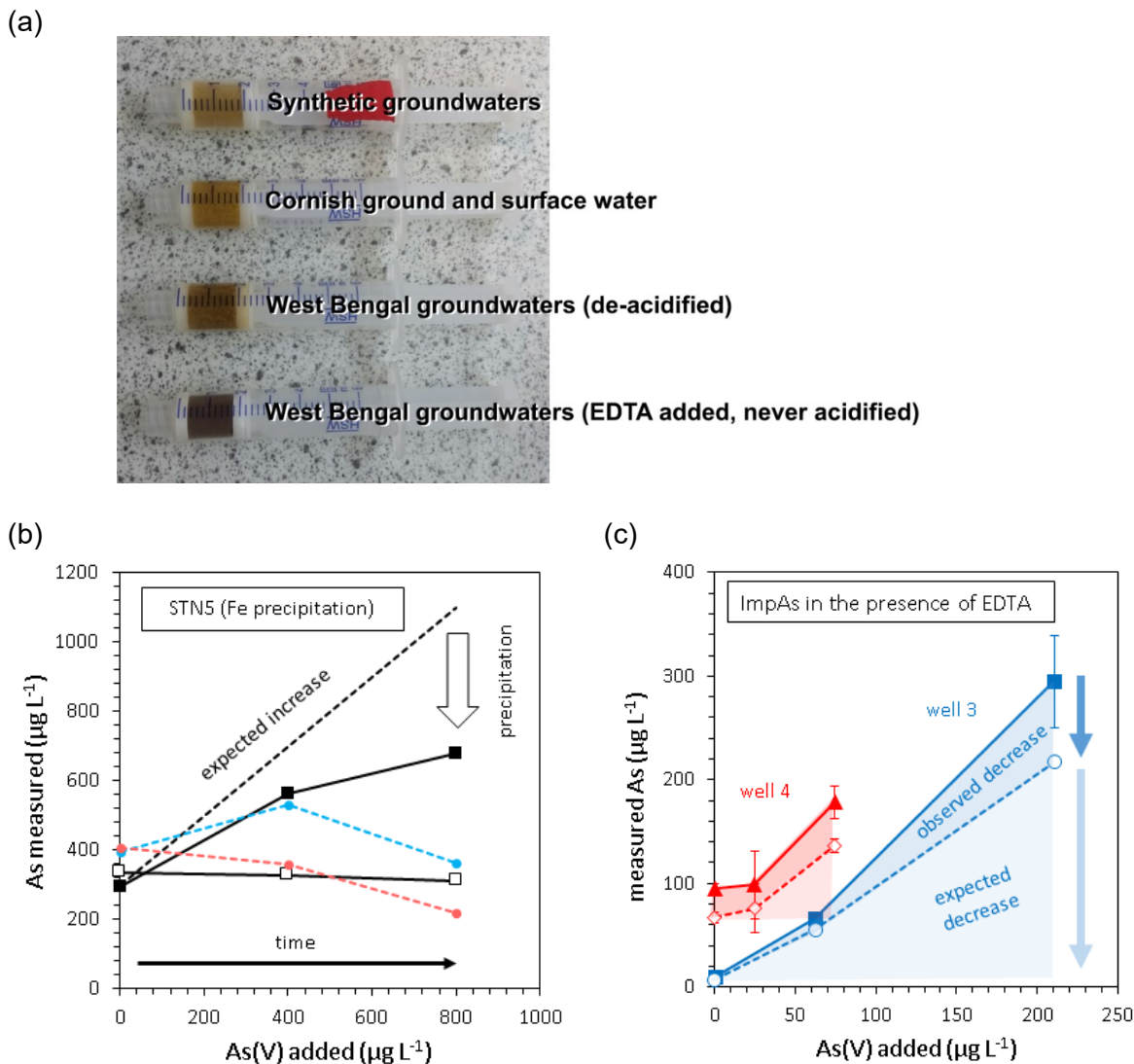


Figure 4.11: Current limitations of speciation using ImpAs. (a) The colour change in ImpAs due to precipitation of iron within the syringe, especially when used for West Bengal groundwaters with high concentrations of dissolved iron. Whilst EDTA reduced the rate of iron precipitation during ImpAs treatment of West Bengal groundwaters, the final colour of the resin is darker than for the ImpAs syringe used to treat de-acidified West Bengal groundwaters. This can be explained by the darker syringe having been used to treat many more samples. (b) The precipitation of iron during analysis of STN5 samples was associated with a loss of total As. (c) In the presence of 10 mM EDTA, ImpAs failed to remove all the As(V) spike, resulting in an overestimation of the proportion of As(III) present in the total As.

Multi-element ICP-MS analysis revealed that whilst EDTA slowed the rate of iron (and manganese) precipitation during ImpAs treatment (Figure 4.12a and b), the presence of EDTA was associated with the leaching of zinc from the syringe (Figure 4.12c). Zinc is an essential component of the ImpAs metal-organic As(V) receptor and the loss of Zn would therefore explain the failure of ImpAs to remove As(V) in the presence of EDTA^{355 356}. This mechanism is illustrated in Figure 4.13.

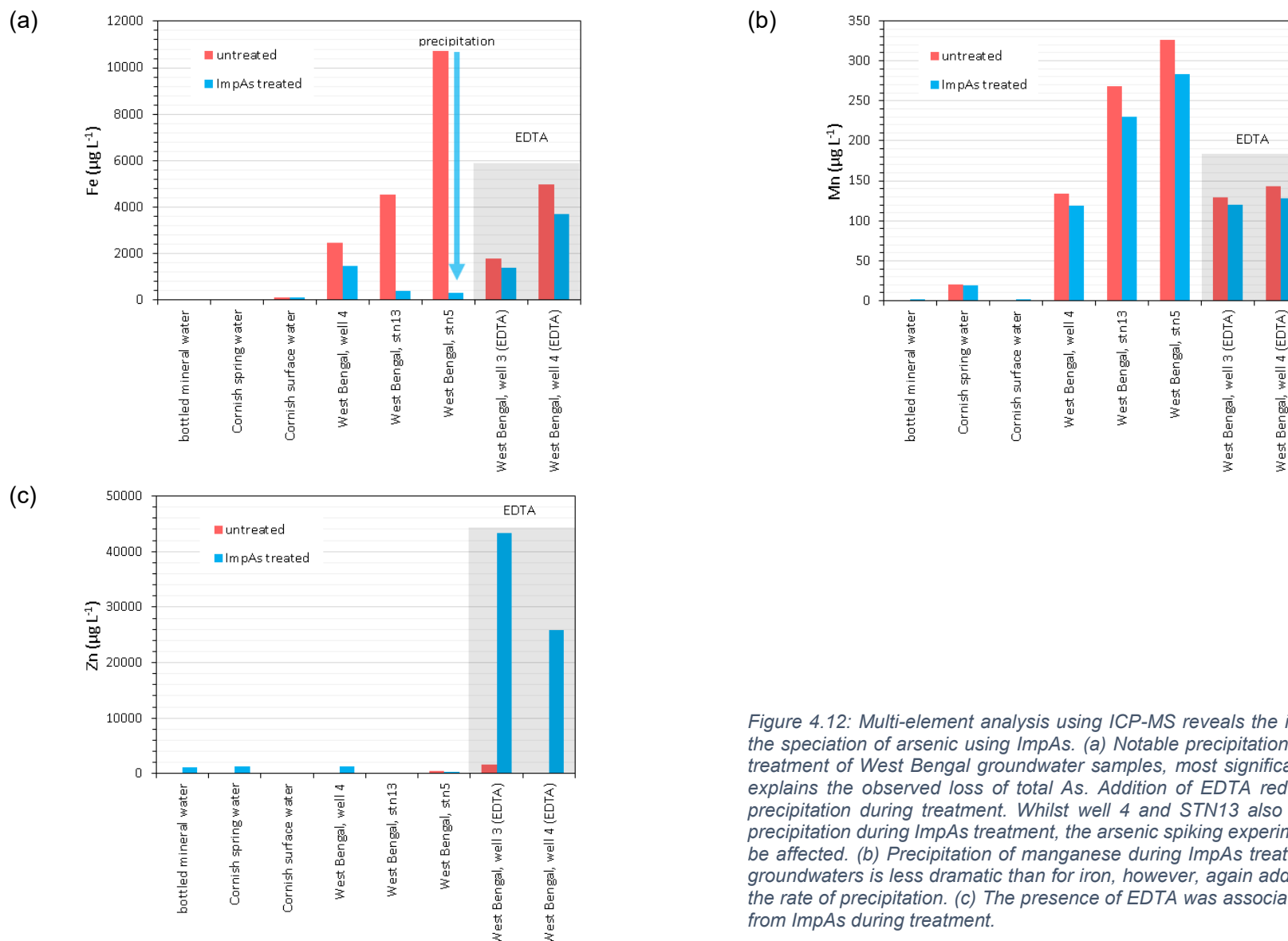


Figure 4.12: Multi-element analysis using ICP-MS reveals the influence of EDTA on the speciation of arsenic using ImpAs. (a) Notable precipitation of iron during ImpAs treatment of West Bengal groundwater samples, most significantly for STN5, which explains the observed loss of total As. Addition of EDTA reduces the rate of iron precipitation during treatment. Whilst well 4 and STN13 also show significant iron precipitation during ImpAs treatment, the arsenic spiking experiment did not appear to be affected. (b) Precipitation of manganese during ImpAs treatment of West Bengal groundwaters is less dramatic than for iron, however, again addition of EDTA slowed the rate of precipitation. (c) The presence of EDTA was associated with zinc leaching from ImpAs during treatment.

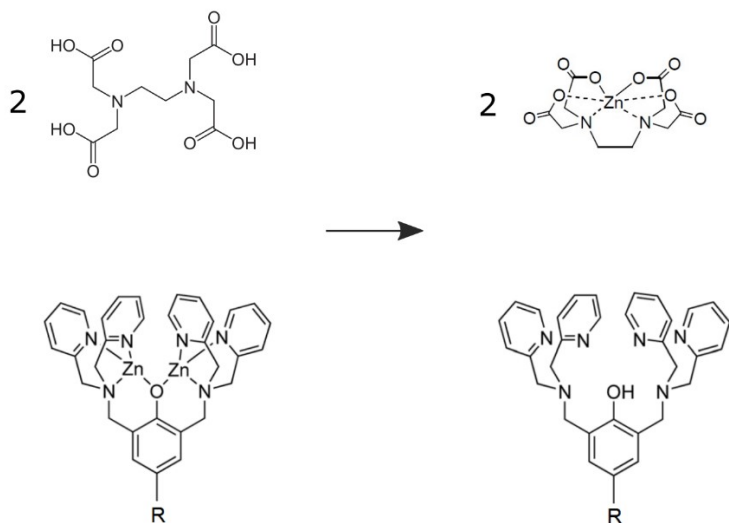


Figure 4.13: Leaching of zinc from the ImpAs receptor (bottom) due to complexation of zinc by EDTA (top).

Dissolved organic carbon (DOC), e.g. humic and fulvic acids, are also known to complex with Zn^{2+} ^{357 358} however ImpAs removal of the As(V) was successful for Cornish surface water, Well 4 and STN13, which all showed significant concentrations of humic-like content (detected by increased ultraviolet absorbance at 254 nm³⁵⁹, with results presented in Table 3.2). The stability of the ImpAs metal-organic receptor in the presence of natural DOC and its instability in the presence of EDTA can be explained by considering the equilibrium between the free and complexed states of zinc. For a 1:1 zinc-to-ligand complex, we can express the complexation between zinc and the ligand as:

$$K'_{ZnL} = \frac{[ZnL]}{[Zn][L]}$$

Equation 4.5

where K'_{ZnL} is the conditional complexation constant, and $[ZnL]$, $[Zn]$ and $[L]$ are the concentrations of the zinc-ligand complex, zinc, and the ligand respectively. In this simplified equation, activity coefficients are ignored and charges are omitted.

The concentration of all ligands was at least two orders of magnitude greater than the concentration of Zn (Table 4.3), so the decrease in $[L]$ at equilibrium is negligible. Equation 4.5 can thus be rearranged to give:

$$K'_{ZnL}[L_{init}] = \frac{[ZnL]}{[Zn]}$$

Equation 4.6

where [L_{init}] represent the initial (or total) concentration of the ligand. Calculations of K'ZnL[L_{init}] (Table 4.3) indicate that EDTA both has a sufficiently strong complexation constant, and is present in sufficient concentrations, to leach zinc from ImpAs (for ImpAs, K_{ZnL}[L_{init}]=3.51, whilst for EDTA, K_{ZnL}[L_{init}]=13.8). This agrees with the experimental observations. The disruption of the metal-organic receptor due to zinc leaching results in a loss in the ability of ImpAs to retain As(V). In contrast, calculations of K'ZnL[L_{init}] show that at the concentrations typical in natural waters, humic and fulvic acids are too weakly complexing to induce zinc leaching. These findings indicate that when ImpAs is used to treat samples with high dissolved iron concentrations, acid should be used as the sample preservative rather than EDTA. However, samples must be pH neutralised prior to analysis, since ImpAs shows less affinity towards As(V) at low pH, due to protonation of the pyridine groups which coordinate to zinc ²¹².

In contrast, ASV was seemingly unaffected by the concentrations of EDTA used in this study (section 4.2). The sensitivity of ASV decreased with decreasing sample dilution. However, once this was taken into consideration, no significant difference was observed in the sensitivity of ASV towards the natural samples containing organic matter, and the synthetic samples without organic matter (Appendix). This indicates that the ASV technique did not suffer from organic matter interference.

Table 4.3: The ability of each ligand to complex zinc.

^a : $K'_{ZnL}[L_{init}] = [ZnL]/[Zn]$

^b : Moffat et al. ²¹², ^c : Cvetkovic et al. ³⁵⁷, ^d : Hirata et al. ³⁵⁸, ^e : Bojja et al. ³⁶⁰.

^f : the pore volume of ImpAs resin is approximately 1 cm³ g⁻¹, and the ligand concentration taken to be 16 mg g⁻¹ based upon the adsorption data.

^g : these figures were calculated using the high literature DOC for Bengal Basin of 50 mg L⁻¹ ^{361 85}, and assuming all is either humic acid (25 meq g⁻¹) or fulvic acid (9 meq g⁻¹) with high concentrations of functional groups ^{362 358}.

ligand	log K'ZnL	[L _{init}] (M)	log(K'ZnL[L _{init}]) ^a
ImpAs	4.18 ^b	0.21 ^f	3.51
humic acid	2.25 ^c	0.0013 ^g	-0.65
fulvic acid	5.66 ^d	0.00045 ^g	2.31
EDTA	15.8 ^e	0.010	13.8

4.5. Cross-comparison of ImpAs with anodic stripping voltammetry for the rapid, reliable and portable speciation of arsenic

In the speciation of synthetic waters, results obtained using ImpAs/ICP-MS and ASV were in close agreement of one another, generally within error (Figure 4.14a). The goodness of fit in the cross-calibration was $R^2=0.967$. In the first case study, differences between photooxidation rate constants determined by ASV and ImpAs/ICP-MS were statistically insignificant: the difference of 2.0% was within error bounds, suggesting that both techniques were accurate and equally valid. The precision of rate constants determined in duplicate by ImpAs/ICP-MS was slightly lower than those obtained by ASV ($\pm 8.4\%$ versus $\pm 2.7\%$).

In the speciation of natural waters (using HCl as the sample preservative) ImpAs/ICP-MS and ASV also agreed with one another, albeit with greater variance ($R^2 = 0.902$) (Figure 4.14b). Importantly, there was no significant difference between oxic and anoxic water samples, suggesting both techniques are valid in both environments (providing that iron precipitation in the ImpAs treatment of anoxic samples is mitigated).

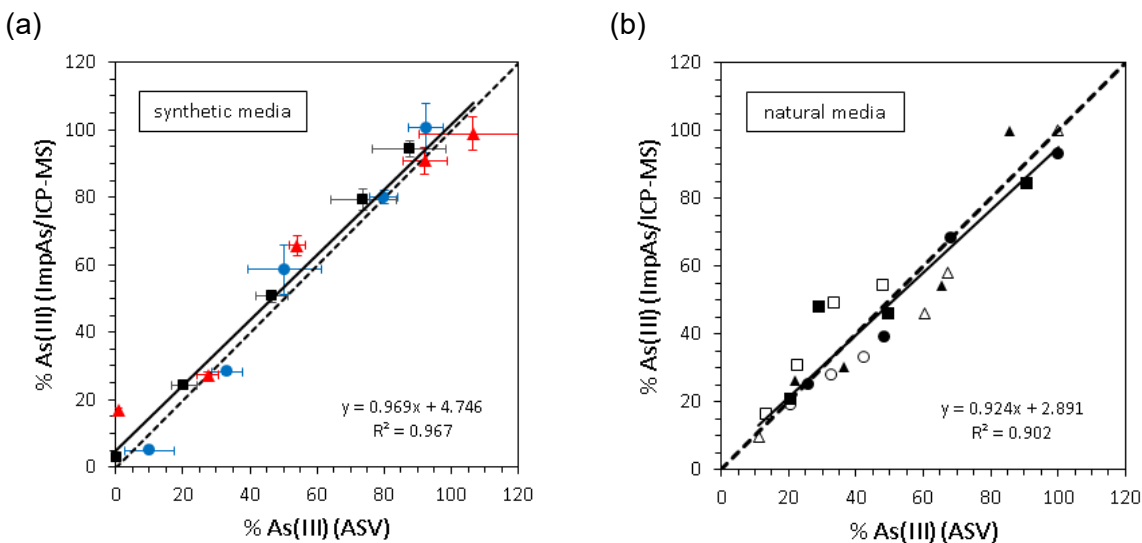


Figure 4.14: The comparison of arsenic speciation determined using the developed ImpAs/ICP-MS and ASV methods in (a) synthetic and (b) natural samples. (a) Cross-calibration of arsenic speciation in 10 mM HEPES (black squares), CW (blue circles) and SGW-1 (red triangles). Error bars indicate the propagated uncertainty of each measurement. (b) The cross-calibration of arsenic speciation in natural media. Data points correspond to bottled mineral water (black squares), Cornish groundwater (black circles) and surface water (black triangles), and West Bengal groundwater samples Well 4 (white squares), STN13 (white circles) and STN5 (white triangles). Dashed lines indicate the ideal one-to-one cross-calibration, and solid black lines indicate the linear best fit.

Speciation using the ImpAs/ICP-MS technique was much more time effective than ASV, requiring 30-60 seconds to condition the resin and one minute to filter 5 mL of sample, plus 3 minutes of analysis using ICP-MS. Meanwhile, ASV required approximately 20 minutes experimental work to measure one sample in duplicate (35 seconds per scan, 15 scans to measure background, sample and 2 additions in triplicate). This highlights how chemisorbents such as ImpAs might offer a route to achieving high throughput speciation. With a maximum As(V) capacity of 16 mg g⁻¹, a single syringe with 1.0 g ImpAs can theoretically treat a maximum 16 L water contaminated with 1000 µg L⁻¹ As(V). This allows the resin to be reused for many samples. Just three syringes were used to treat nearly all the samples in this work. These syringes were separated for treatment of (a) all synthetic media samples (at 1.0 grams loading), (b) all natural oxic waters, and (c) all natural de-acidified West Bengal groundwaters. Little trace of cross-contamination between samples was observed.

Speciation using handheld syringes loaded with ImpAs is highly portable, especially since a single syringe can treat many samples. Unlike ASV, no hardware, batteries or additional reagents are required. If coupled with a fast laboratory detection method (e.g. ICP-MS), high sample throughput can be achieved. In contrast, although ASV gives lower sample throughput and requires more manual operation, ASV provides an immediate answer for on-site analysis and for near real-time monitoring of oxidation experiments. Anodic stripping voltammetry is currently easier to use for natural samples with high iron levels (> 5 mg L⁻¹), where acidification or EDTA can be used to avoid precipitation.

In analysis costs, ASV is far cheaper in capital and consumable costs due to the cost of detectors such as ICP-MS. Portable potentiostats are priced between £2000 and £6000. The main consumable when using ASV is the gold microwire electrode. These cost between £1 to £30 each, and can perform around 100 measurements, giving a cost of <£1 per sample. On the other hand, running ICP-MS instrumentation costs tens of thousands of dollars, and around \$10 per sample³¹⁷. Speciation using ImpAs could be made more economical if a cheaper detector were used. For small scale testing, ASV is more economical as a handful of samples can be measured at low cost, whilst ImpAs/ICP-MS will be more appropriate for large scale surveys where high throughput is required.

4.6. Conclusions

This chapter aimed to develop the application of (a) ASV using a portable potentiostat, and (b) the As(V)-selective chemisorbent material ImpAs as analytical methods for the speciation of arsenic. These methods were considered for applications in (i) determining photooxidation kinetics within this thesis, and (ii) other applications such as field surveys and monitoring As(III) oxidation within arsenic treatment plants.

For the purposes of determining photooxidation kinetics within this thesis, ASV was chosen as the analytical technique. Whilst being demanding of the operator's time and requiring more technical expertise, ASV offers near real-time results, which ultimately allow the experimental procedure to be quickly adjusted and optimised. For instance, the time resolution can be adjusted within the experiment to better capture the time-scale of interest. Additionally, the cost per sample of ASV is lower (with dozens of samples measured using a single electrode costing approximately £30), which allowed a much larger data set to be collected.

When it comes to monitoring As(III) oxidation in arsenic treatment plants, ASV would be an excellent technique, offering cheaper online options than ImpAs coupled with ICP-MS or another detector. Unfortunately, low-cost electrochemical systems for online detection of arsenic are currently limited³⁰⁹. However, for spot sampling applications, such as water quality surveys, ImpAs coupled with a laboratory-based technique such as ICP-MS or AAS is the superior option. Little technical expertise is needed to use the ImpAs syringe, whilst the capacity of analytical laboratories running ICP-MS or atomic absorption spectroscopy (AAS) is much greater than the capacity of electrochemical laboratories³⁶³, opening up the possibility for achieving arsenic speciation in future large-scale field campaigns.

5. Characterisation of meso-TiO₂/FeO₃ and reference samples

5.1. Introduction

A range of materials characterisation techniques were used in this work (a) to achieve quality control, (b) to provide constraints for data normalisation and cross-comparison between different materials, and (c) to better understand the mechanisms of arsenic remediation using the composite meso-TiO₂/Fe₂O₃ material.

The physical properties of the composite surface (namely the surface area and the relative abundance of Fe₂O₃ to meso-TiO₂) are vital parameters to understand both adsorption of arsenic and photooxidation. For instance, it is well established that iron oxides are superior arsenic sorbents than TiO₂. Adsorption is a surface process, and hence for the most effective adsorption it is desirable to maximise Fe₂O₃:TiO₂ surface ratio. However, photocatalytic oxidation of As(III) also involves surface processes, whether the reaction mechanism is direct oxidation of As(III) using positive holes trapped at the catalyst surface, or the generation of radical intermediates at the photocatalyst surface followed by oxidation of As(III) in solution. Whilst the influence of the Fe₂O₃:TiO₂ surface area ratio on photocatalysis is not as predictable as the influence of the surface ratio on adsorption is, one could hypothesis that high TiO₂ surface areas will provide the best performance. Whilst we can predict the bulk composition of our composite product from the concentrations of reagents and precursors used, the bulk composition is often different to surface composition ¹⁵. This was especially true in this work, considering that the synthesis procedure calls for the iron oxide phase to be precipitated onto a pre-existing solid mesoscale TiO₂ powder. It was therefore anticipated that a higher Fe:Ti ratio would be found at the material surface when compared with the bulk, and that this would influence the observed adsorption and photooxidation of arsenic in subsequent experiments.

Another important aspect of materials characterisation was to assess the influence of Fe₂O₃ on the absorption of ultraviolet light by meso-TiO₂. At low photon flux, photocatalytic activity is typically proportional to the photon flux²⁷. It follows that any competitive absorption of incident photons by the Fe₂O₃ component of meso-TiO₂/Fe₂O₃ will decrease the photocatalytic activity of meso-TiO₂. This is explored in chapter 7.

The aims of this chapter were thus:

- To achieve quality control, ensuring that the synthesis produced the desired materials, and to evaluate the significance of any differences between each synthetic batch of meso-TiO₂/Fe₂O₃. This was achieved using XRD, and impurities were assessed using XRF, XPS, ATR-FTIR and potentiometric titrations.
- To determine the parameters needed to normalise experimental results, e.g. determining the surface area to normalise arsenic adsorption capacities and determining the surface charge to normalise surface complexation constants (in the extended triple layer model). The BET-specific surface area was determined using N₂ adsorption isotherms, and the point of zero charge was determined using potentiometric titrations and electrophoretic measurements (zeta potential).
- To determine the hierarchy of the composite structure of meso-TiO₂/Fe₂O₃, and quantitatively determine the surface composition, so that arsenic adsorption might be assessed on the basis of component additivity. Crystallite aggregation was investigated using STEM-EDS. Changes in material composition from the bulk to the outermost surface were investigated and quantified using a combination of XRF, XPS and LEIS. The absorption of light by meso-TiO₂ and Fe₂O₃ components was assessed by UV-Vis spectroscopy (and is discussed in chapter 7).

5.2. Understanding the structure and composition of meso-TiO₂/Fe₂O₃

5.2.1. Identification of crystal phases

XRD patterns were analysed to identify the crystal phases present in each sample (Figure 5.1). Only one batch of Fe₂O₃ was prepared in this work, so the same XRD pattern is shown in both figure panels. The Fe₂O₃ reference sample was confirmed as being α-Fe₂O₃ (hematite) with no peaks corresponding to other crystalline solids observed. XRD peaks corresponding to crystalline anatase and rutile phases of TiO₂ were identified in both batches of meso-TiO₂, with no other peaks observed. In the first batch of products, the primary anatase peak ({101} at 25.35°) was several times greater in intensity than the principal rutile peak ({110} at 27.38°) in both the intermediate meso-TiO₂ and final meso-TiO₂/Fe₂O₃ products. In the second batch of products, the rutile peak was approximately twice as intense as the anatase peak. This indicates significant differences between the two batches of products. As copper Kα₁ and Kα₂ lines were used as the X-ray source, a high background was observed for all iron-containing samples due to iron fluorescence. All XRD peaks displayed significant peak broadening, indicating nanoscale crystallites (discussed in section 5.2.6).

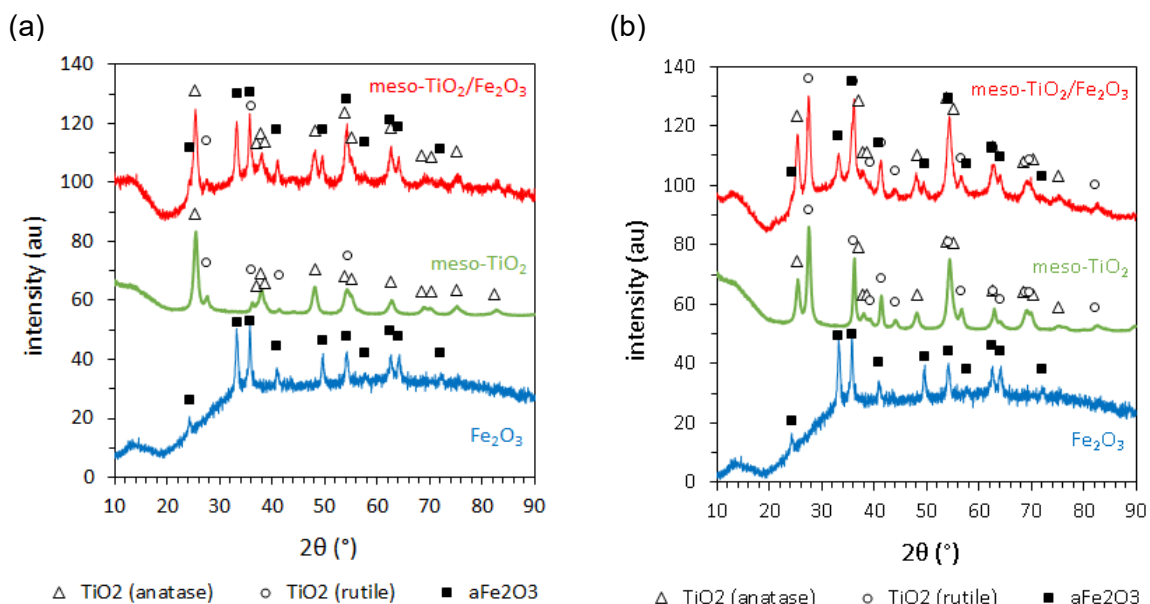


Figure 5.1: XRD confirmation of the crystal phase of synthesised powders. XRD patterns of meso-TiO₂/Fe₂O₃ and reference samples are presented for (a) batch 1 and (b) batch 2. Peaks are labelled according to the following crystal phases: hematite (black squares), rutile (open circles) and anatase (open triangles). ‘au’ stands for arbitrary units and XRD patterns have been shifted in the y-axis for clarity.

In the absence of pure anatase and rutile TiO₂ samples to provide reference XRD patterns, the ratio of anatase to rutile in the two batches was calculated using the Spurr and Myers equation^{364 365}. This empirical equation is expressed as:

$$f = \frac{1}{1 + 1.26 \frac{I(r)}{I(a)}}$$

Equation 5.1

where f is the intensity function, equivalent to the mass fraction of anatase in the sample, and I(r) and I(a) are the peak intensities (integrated areas) of the rutile {110} and anatase {101} diffraction peaks at 27.38° and 27.38° respectively^{364 365}. The Spurr and Myers equation demonstrated that anatase was the dominant phase in the first batch of meso-TiO₂ (84% anatase, 16% rutile), whilst rutile was the dominant phase in the second batch (28% anatase, 72% rutile). This distribution of TiO₂ between anatase and rutile crystal phases was maintained after the Fe₂O₃-coupling procedure: the first batch of meso-TiO₂/Fe₂O₃ was 86% anatase and 14% rutile, whilst the second batch was 28% anatase and 72% rutile. An investigation into the causes for this difference between the two synthetic batches of meso-TiO₂/Fe₂O₃ is provided in the Appendix.

5.2.2. Impurities

Since impurities influence both potentiometric titration²⁷⁹ and adsorption experiments³⁶⁶, the identity and concentration of impurities was assessed using X-ray fluorescence (XRF). The results indicated that all synthesised materials contained between 0.54 and 1.0% impurities by mass. Surprisingly, the commercial FeOOH samples contained the most impurities: 1.3% by mass, decreasing to 1.0% after washing. In both batches of meso-TiO₂, chlorine was the main impurity. This is most likely due to residual chloride from the hydrochloric acid reagent. After coupling meso-TiO₂ with Fe₂O₃, the amount of chlorine decreased by ~50%. After washing the samples, the amount of chlorine detected in meso-TiO₂/Fe₂O₃ decreased by ~40% whilst other impurities remained constant. Mineral washing was also successful in reducing the net acidic impurities (section 5.3). FeOOH showed comparatively very little chlorine, and no net acidic impurities were observed with or without mineral washing (section 5.3). These results suggest that the net acidic impurities identified using potentiometric titrations were associated with the residual chlorine. Vanadium was the dominant contaminant in both batches of the composite material, despite not being detected for any of the reference

samples. As vanadium was not detected for the Fe_2O_3 reference sample, this impurity cannot be attributed to contaminated reagents and its source remains unidentified.

Table 5.1: The main impurities detected using XRF, reported as mass percent. The colour shading of each cell indicates the abundance of the impurity, with red and orange indicating that more of the impurity was detected compared with green and yellow cells. The limit of detection is abbreviated as LoD.

sample	Fe_2O_3	meso- TiO_2		meso- $\text{TiO}_2/\text{Fe}_2\text{O}_3$			FeOOH	
notes	unwashed	batch 1, unwashed	batch 2, unwashed	batch 1, unwashed	batch 2, unwashed	batch 2, washed	unwashed	washed
element	mass %							
Fe	97.9	<0.1	<0.1	51.5	48	54.1	80.1	94.6
Ti	<LoD	77.5	78.8	32.5	36.2	34.5	<LoD	<LoD
Cl	0.0149	0.432	0.252	0.203	0.131	0.0937	0.0383	0.0226
V	<LoD	<LoD	<LoD	0.284	0.304	0.295	<LoD	<LoD
Ca	0.0528	0.0819	0.0429	0.0771	0.0575	0.0596	0.190	0.145
P	0.0848	0.0728	0.0681	0.0796	0.0859	0.0865	0.087	0.0877
Si	0.055	0.0588	0.0559	0.0646	0.0616	0.0657	0.0448	0.0534
Mn	<LoD	<LoD	<LoD	0.0005	<LoD	<LoD	0.200	0.247
total impurities	0.5442	0.9907	0.6949	0.9553	0.8710	0.7987	1.2948	0.9937

5.2.3. Surface area and pore volume

For meso- TiO_2 , Fe_2O_3 and meso- $\text{TiO}_2/\text{Fe}_2\text{O}_3$, N_2 adsorption-desorption isotherms showed IUPAC Type II adsorption branches with H3 hysteresis loops (Figure 5.2)³⁶⁷. The hysteresis loops in the mid P/P_0 range reflect condensation within mesopores (2-50 nm diameter), and nitrogen uptake at low P/P_0 represents the presence of some microporosity (<2 nm)³⁶⁸.

Of the materials synthesised in this work, meso- TiO_2 had the highest surface area (Table 5.2), with $146 \text{ m}^2 \text{ g}^{-1}$ for the first batch and $106 \text{ m}^2 \text{ g}^{-1}$ for the second batch. The BET-specific surface area decreased after coupling meso- TiO_2 with Fe_2O_3 ($116 \text{ m}^2 \text{ g}^{-1}$ for batch 1 and $100 \text{ m}^2 \text{ g}^{-1}$ for batch 2). For batch 2, this is less than the surface area of the Fe_2O_3 reference sample ($103 \text{ m}^2 \text{ g}^{-1}$) suggesting that iron oxide precipitation fills the pores of the meso- TiO_2 precursor. The BJH average pore diameter also increased after coupling meso- TiO_2 with Fe_2O_3 in the second batch synthesis (from 7.8 to 8.6 nm in batch 2). This also suggests that the smaller pores of meso- TiO_2 are filled during iron oxide precipitation. Higher surface areas for both meso- TiO_2 and composite meso- $\text{TiO}_2/\text{Fe}_2\text{O}_3$ were achieved compared with previous work^{11 251}. FeOOH had the largest surface area at $127 \text{ m}^2 \text{ g}^{-1}$, a large pore diameter at 21 nm, no significant hysteresis, and little uptake at low P/P_0 , suggesting a lack of micropores and mesopores³⁶⁸.

Mineral washing had little effect on the surface area indicating that the dialysis tubing successfully retained even the smallest material particles.

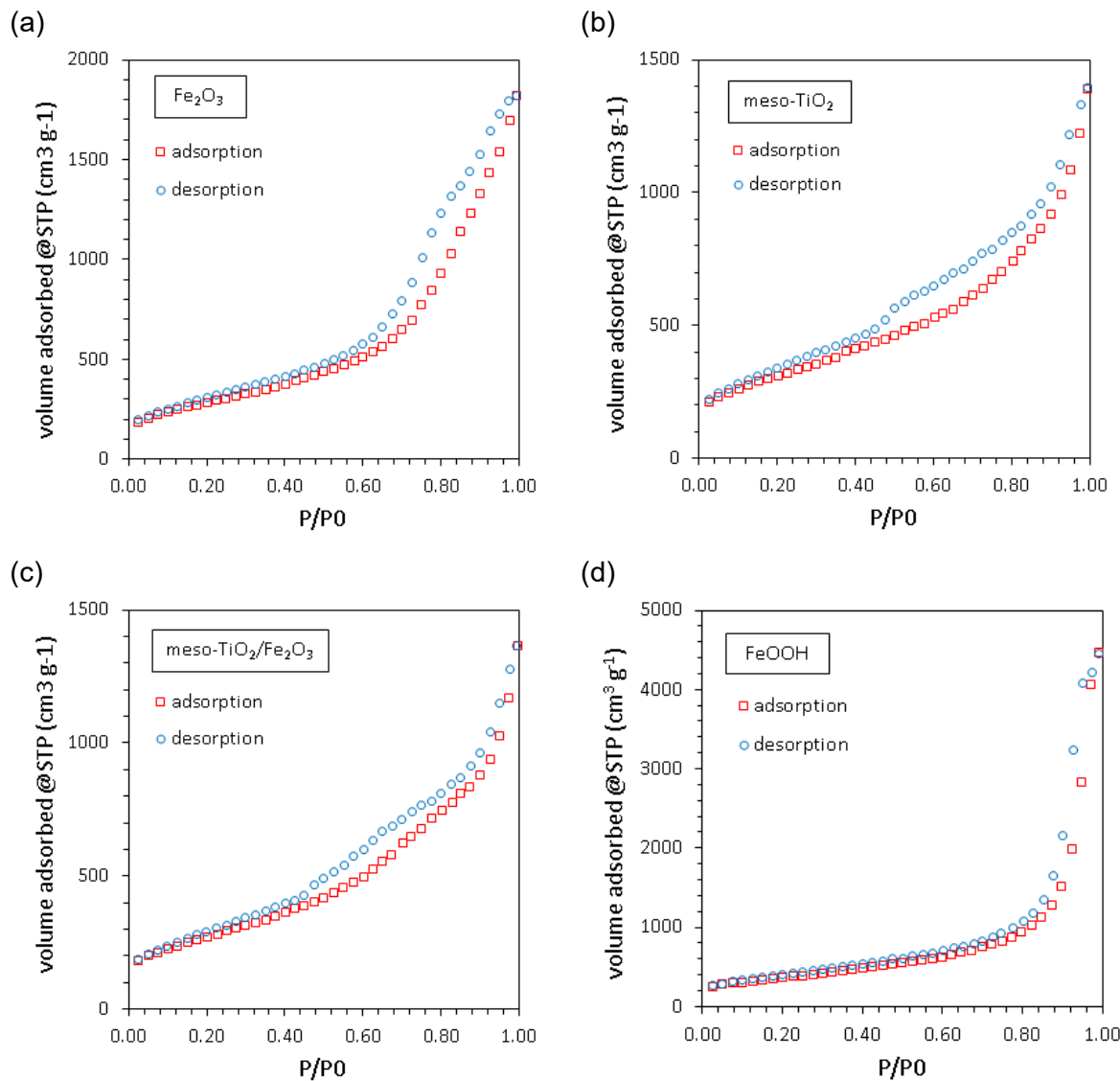


Figure 5.2: N₂-adsorption/desorption isotherms used to determine the BET-specific surface area of washed mineral samples. The products of synthesis batch 2 are presented, and similar results were obtained for batch 1. Mesopore hysteresis loops can be identified, particularly for meso-TiO₂ and meso-TiO₂/Fe₂O₃.

Table 5.2: BET-surface area and pore sizes determined from N_2 adsorption-desorption isotherms. In this work all samples were outgassed at 200 °C except for FeOOH which was outgassed at 100 °C. In this work the average pore size was determined by BJH analysis of desorption isotherms.

Study	Material	Notes	multipoint BET-specific surface area ($\text{m}^2 \text{ g}^{-1}$)	total pore volume ($\text{cm}^3 \text{ g}^{-1}$)	average pore size (nm)
This work	Fe_2O_3	unwashed	109	0.30	11.1
		washed	103	0.23	8.9
	meso-TiO ₂ (batch 1)	unwashed	146	0.32	8.8
	meso-TiO ₂ /Fe ₂ O ₃ (batch 1)	unwashed	116	0.25	8.7
	meso-TiO ₂ (batch 2)	unwashed	106	0.32	6.7
		washed	110	0.22	7.8
	meso-TiO ₂ /Fe ₂ O ₃ (batch 2)	unwashed	96	0.37	7.0
		washed	100	0.22	8.6
	FeOOH (Bayoxide E33)	unwashed	130	0.64	9.8
		washed	127	0.69	21.2
Lapinee ²⁵¹	meso-TiO ₂	unwashed	113	0.22	7.7
	meso-TiO ₂ /Fe ₂ O ₃	unwashed	63	0.16	10.1
Zhou et al. ¹¹	meso-TiO ₂	washed in ethanol	135	-	~10
	meso-TiO ₂ /Fe ₂ O ₃	washed in ethanol	95	-	~10
Md Hanif et al. (unpublished)	FeOOH (lab synthesised)	unwashed	41	0.20	-

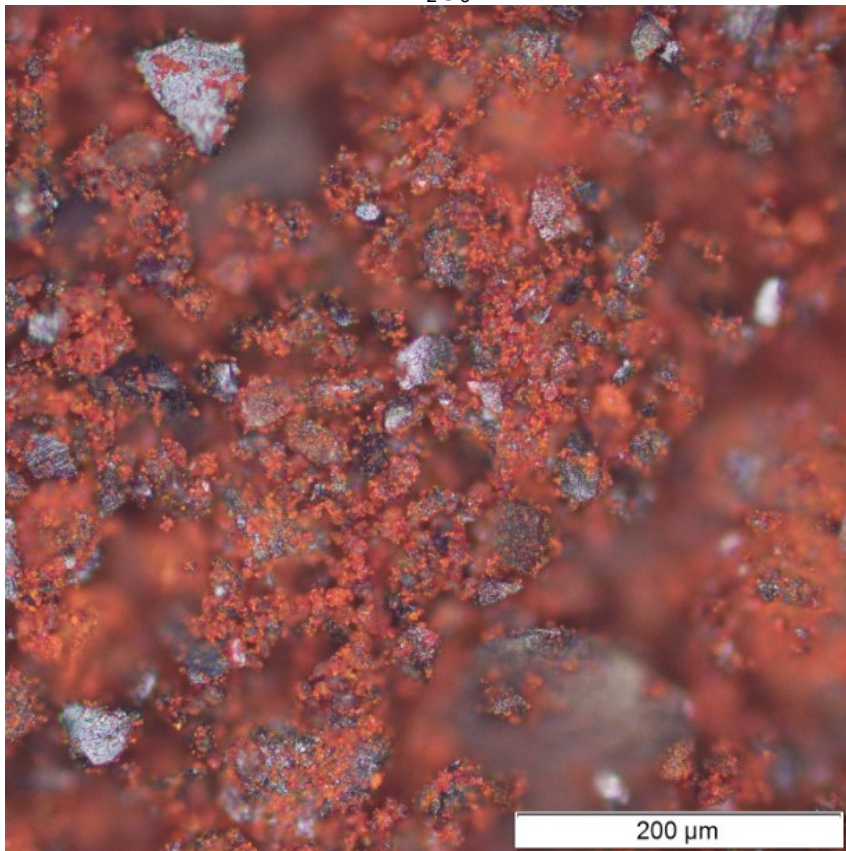
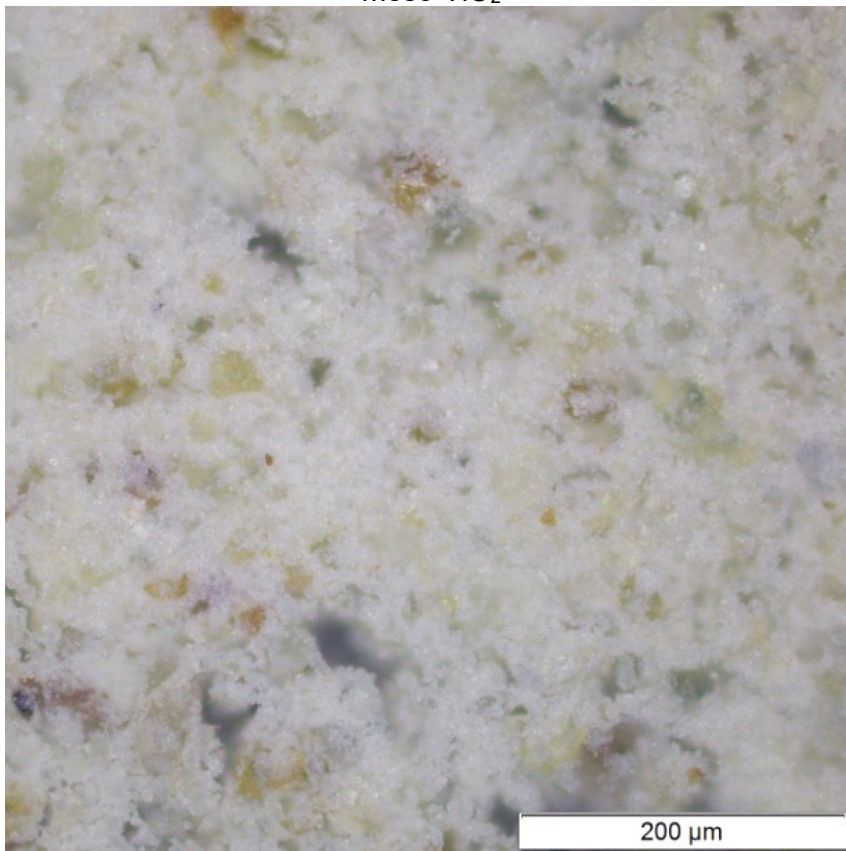
5.2.4. Colour and macroscale particle size

To the eye, meso-TiO₂, meso-TiO₂/Fe₂O₃, Fe₂O₃ and FeOOH samples were grey, red, dark red and brown respectively. All final products were finely powdered with diffuse (rather than specular) reflectance. Optical microscopy revealed significant variation within each powder sample at the micrometre scale (Figure 5.3). Fe₂O₃ consisted of a mix between (a) large, reflective, dark blue-black particles with angular edges between 10 and 100 µm in size and (b) smaller red particles, mostly <10 µm in size. Meso-TiO₂ was primarily composed of white particles <10 µm in size, interspersed with larger particles, with colours ranging between yellow, green and brown, with sizes up to ~40 µm. The meso-TiO₂/Fe₂O₃ composite material consisted primarily of red particles <10 µm in size, however some of the larger dark, reflective particles seen in the Fe₂O₃ reference sample were also present. Unlike meso-TiO₂, no white coloured particles were observed. FeOOH was the most homogeneous sample, with a consistent yellow colour and all particles <10 µm in size. These results indicate that both meso-TiO₂ and Fe₂O₃ reference samples were highly heterogeneous at the micrometre scale.

For Fe₂O₃, the small red particles likely correspond to fast crystallisation kinetics with rapid nucleation and the nanoscale crystallites observed using XRD, whilst the larger particles would correspond to slow crystal growth. A possible explanation is that crystal growth is slow during the initial stages of solvent evaporation, producing larger crystallites, whilst rapid nucleation of the remaining ethanolic Fe(II) ions when total solvent evaporation is approached yields the smaller nanocrystallites.

The small white particles observed in the meso-TiO₂ powder are expected to be the desired anatase product from a successful sol-gel synthesis. The larger, coloured particles may be material which has failed to complete the sol-gel process. Whilst single crystal TiO₂ is normally colourless, crystals may appear blue due to free carrier absorption, or yellow due to oxygen vacancies when prepared under reducing conditions ³⁶⁹. Heat treatment of rutile TiO₂ (above 400 °C) leads to red shifting of the UV-Vis absorbance, giving a yellow colour ³⁷⁰. Coloured TiO₂ often displays enhanced photocatalytic properties due to the associated Ti(III) defect sites ³⁷¹. Other possible causes for the formation of coloured particles include inclusion of chlorine impurities (which were identified by XRF in section 5.2.2), which are known to red shift the absorbance of TiO₂ ³⁷², or simply residual titanium butoxide (perhaps unlikely given the high temperatures of calcination).

The homogeneous red colour observed for the majority of the meso-TiO₂/Fe₂O₃ powder suggests that the meso-TiO₂ precursor has been coated with iron oxide. The large (>10 µm) dark blue particles are less abundant in the meso-TiO₂/Fe₂O₃ powder than in the Fe₂O₃ reference sample, suggesting that the presence of meso-TiO₂ influenced iron oxide precipitation. Meso-TiO₂ likely provides surface sites for the nucleation of Fe₂O₃ crystal growth, thereby constraining Fe₂O₃ to smaller particle sizes (in agreement with the reduced surface area of meso-TiO₂/Fe₂O₃ compared with meso-TiO₂ and Fe₂O₃ that is discussed in section 5.2.3).

Fe_2O_3 meso- TiO_2 

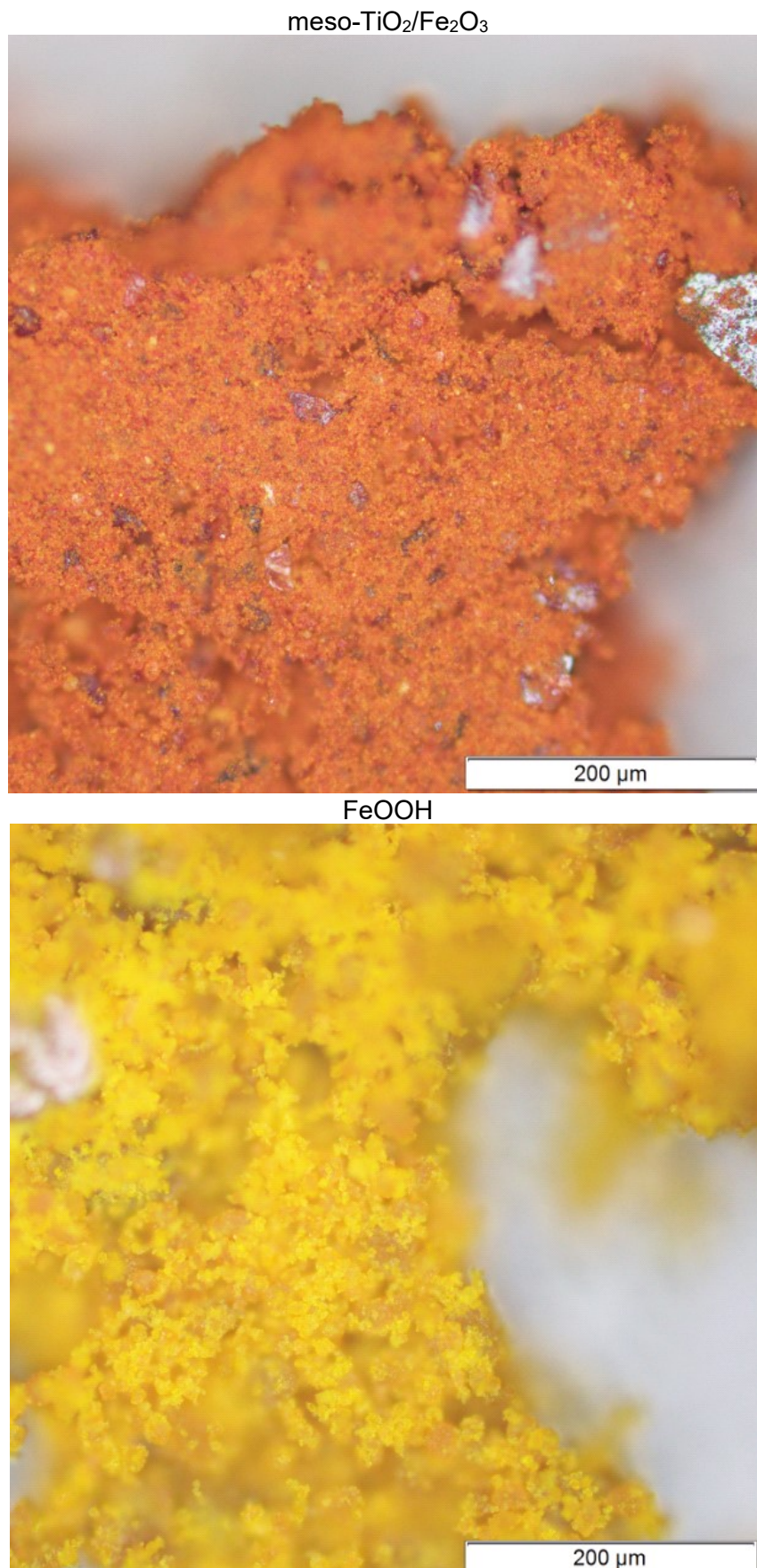


Figure 5.3: Optical microscopy of Fe₂O₃, meso-TiO₂ and meso-TiO₂/Fe₂O₃ (both from batch 2) and FeOOH samples.

5.2.5. Particle size at the microscale

Particle size was estimated using two techniques for comparison: (a) scanning electron microscopy (SEM) and (b) dynamic light scattering (DLS). SEM images of meso-TiO₂/Fe₂O₃ showed a heterogeneous distribution of particle sizes, typically between 0.5 and 50 µm, each in turn composed of features that were tens of nanometres wide, providing a very rough surface (Figure 5.4). The well-defined, concaved, 10 nm diameter pores observed previously in meso-TiO₂ thin-films produced by dip-coating slides into the same synthetic reagents ¹⁵⁷ were not observed. The contrast of SEM is given by differences in electron density, and the brighter regions of meso-TiO₂/Fe₂O₃ correspond to the iron oxide. SEM indicated that the morphology of Fe₂O₃ was much less structured than that of meso-TiO₂.

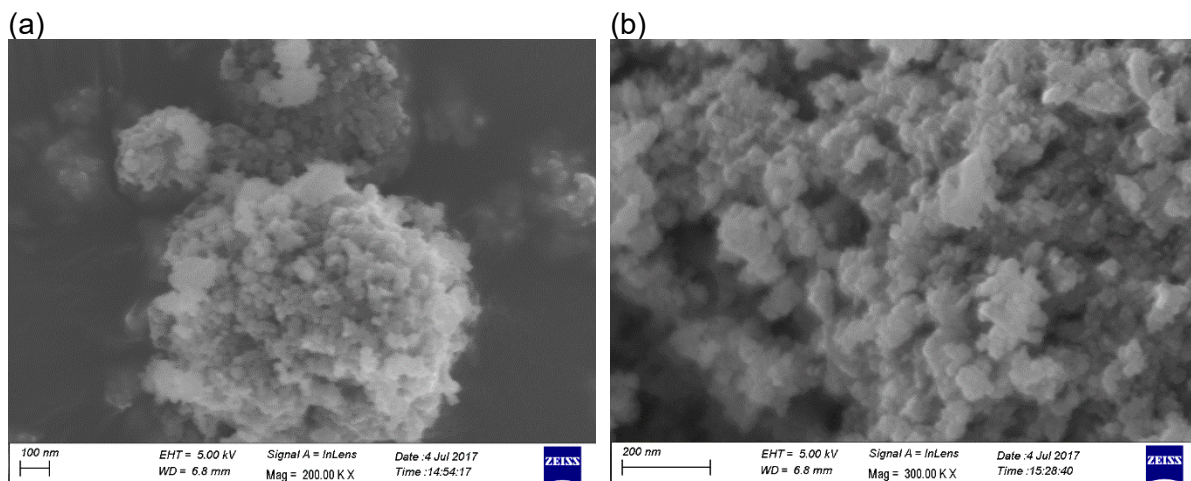


Figure 5.4: SEM images showing meso-TiO₂/Fe₂O₃ (batch 1) particles as agglomerates of smaller structures. The less well-defined, brighter areas of the SEM images indicate higher electron density and can therefore be assigned to the iron oxide precipitate formed on top of the meso-TiO₂ support.

Particles size as a function of pH was measured using dynamic light scattering (DLS) and is presented along with zeta potential measurements in section 5.3. The smallest particle size of meso-TiO₂/Fe₂O₃ calculated using DLS was 400 nm, in good agreement to the particle sizes observed using SEM (~500 nm). The largest particle size observed using DLS was 2.4 µm, which is significantly smaller than the 50 µm observed using SEM. The maximum particle size observed by DLS occurred at the isoelectric point (iep) where suspensions are least stable. The agglomeration and sedimentation of larger particles, which cannot be measured using DLS, are the likely the reason for this difference between the maximum particle sizes measured using SEM and DLS. Fe₂O₃ and meso-TiO₂ showed similar particle sizes (DLS), with 0.4-2.0 µm for Fe₂O₃ and 0.3-2.8 µm for meso-TiO₂. FeOOH showed both the smallest

and largest particle sizes as determined by DLS, with a minimum of 250 nm and maximum of 4.4 µm. The low minimum particle size is due to the fine nanopowder nature of the FeOOH sample, as opposed to aggregated mesoscale particles. The high maximum particle size is likely due to the material having a homogeneous surface resulting in strong aggregation of nanocrystallites at the iep.

5.2.6. Crystallite size

Crystallite size was estimated using two techniques: (a) transmission electron microscopy (TEM) and (b) application of the Scherrer equation to XRD patterns. TEM analysis of meso-TiO₂/Fe₂O₃ (batch 2) revealed the presence of well-formed crystallites with distinct lattice planes (Figure 5.5). Crystallite diameters were measured and fast Fourier transforms (FFT) were used to identify the crystal phase. (Figure 5.6). The average diameter of hematite (α -Fe₂O₃) crystallites was 15.9 ± 3.3 nm (N=10 crystallites counted), whilst the average diameter of anatase TiO₂ crystallites was 14.7 ± 3.5 nm (N=6). Rutile crystallites were not identified in the selection of TEM images obtained.

Application of the Scherrer equation to the XRD pattern of meso-TiO₂/Fe₂O₃ (batch 2) gave an average crystallite size of 14.3 ± 4.0 nm for α -Fe₂O₃, 13.6 ± 2.2 nm for rutile TiO₂ and 12.0 ± 1.0 nm for anatase TiO₂. (The errors indicate the standard deviation between the crystallite sizes calculated for all XRD peaks between $2\theta = 5-90^\circ$ in a given crystal phase). All sizes were within error of the TEM results. TiO₂ crystallite sizes were in line with the literature for meso-TiO₂, where synthetic conditions had been tuned to yield crystallite sizes of 10 nm. It is reported that this corresponds to the mean free path length of photoexcitons, and is thus anticipated to yield efficient photocatalysis ¹⁵⁷.

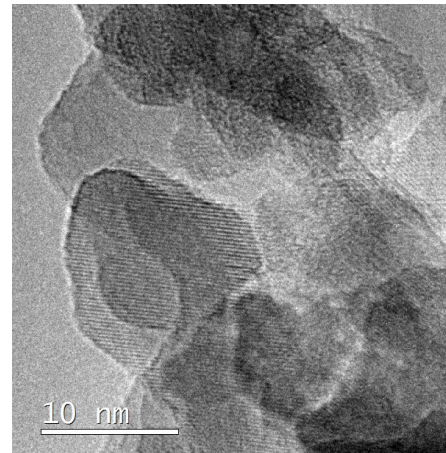


Figure 5.5: TEM image showing lattice planes in the crystalline surface of meso-TiO₂/Fe₂O₃ particles. All crystal lattice planes observed in this image were assigned to hematite on the basis of d-spacing parameters, calculated from the fast Fourier transform.

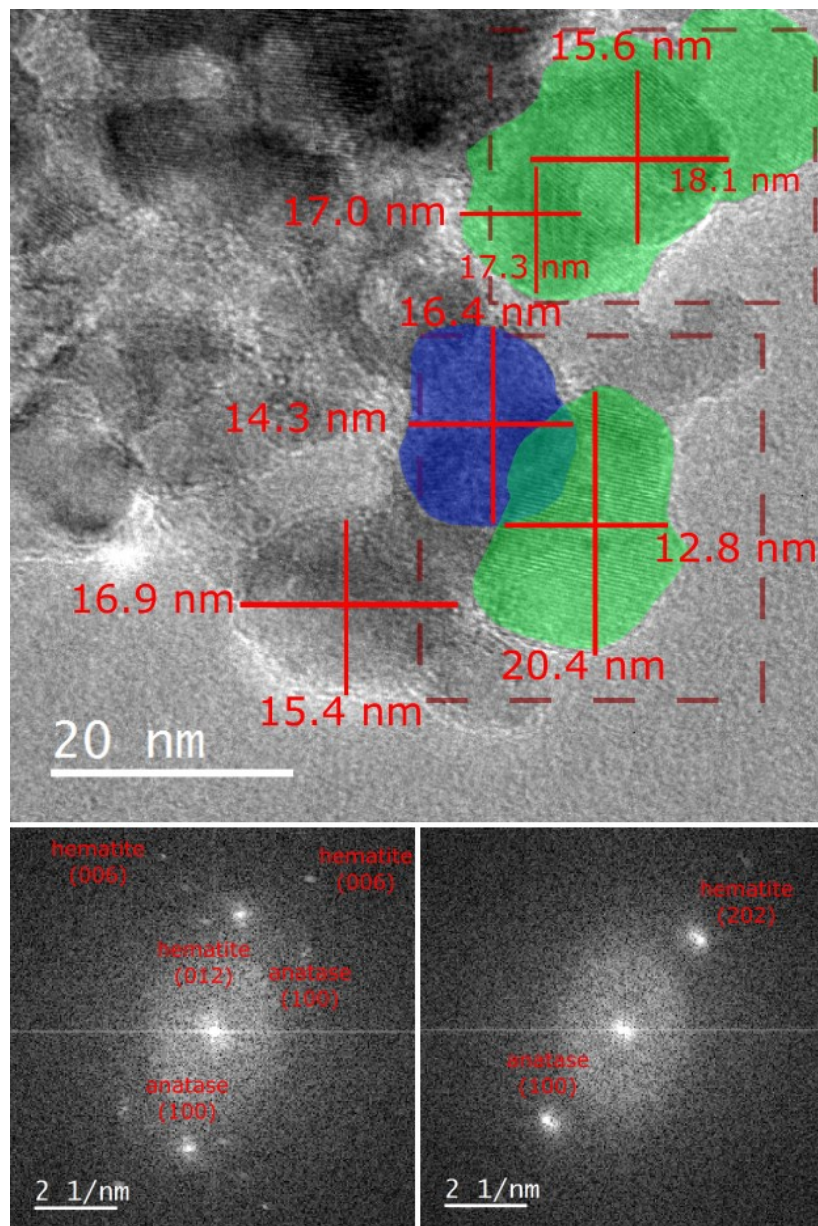


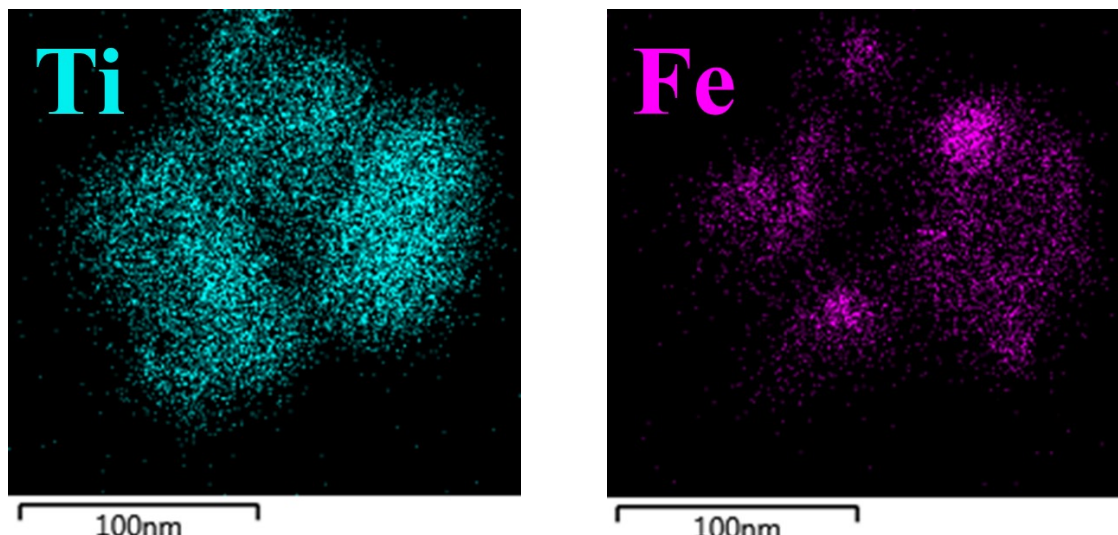
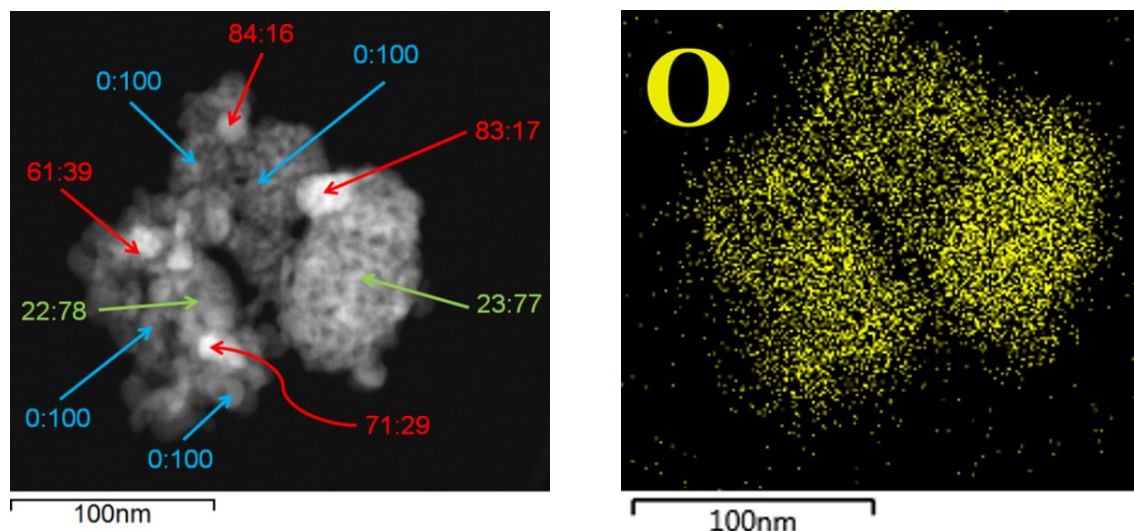
Figure 5.6: TEM (top) and fast Fourier transforms (bottom) used to measure crystallite dimensions. Each spot in the FFT was assigned a crystal structure and miller index using literature XRD patterns from the PANalytical software. The above TEM shows nanoscale mixing of the TiO_2 and Fe_2O_3 crystallites, demonstrating a heterogeneous surface structure. Colour overlays correspond to anatase (green) and hematite (blue) crystallites.

5.2.7. Structural hierarchy of the composite material

Meso- TiO_2/Fe_2O_3 was analysed using STEM-EDS to identify the hierarchy of the composite structure, i.e. how meso- TiO_2 and Fe_2O_3 components interrelate to one another. Three particles were analysed by STEM-EDS mapping (Figure 5.7). Particle A (~150 nm in diameter) showed

Ti present across the entire cross-section of the particle with constant intensity. Fe was detected across most of the particle, with more iron detected in the bright, electron dense regions of the STEM image. For the largest particle, particle B (~750 nm in diameter), STEM-EDS detected Fe across the entire particle, but Ti was only detected in limited regions. The Ti detected in particle B was poorly defined in shape, suggesting that it may be part of an underlying feature, i.e. a TiO₂ core particle about which iron has precipitated. STEM-EDS detected Fe and Ti simultaneously for most regions of the median sized particle C (~400 nm in diameter) with one 100 nm-sized region being primarily Fe (top left) and another primarily Ti (bottom left). For all particles, oxygen was detected across the entire particle with similar intensity between Fe-majority and Ti-majority regions.

Particle A



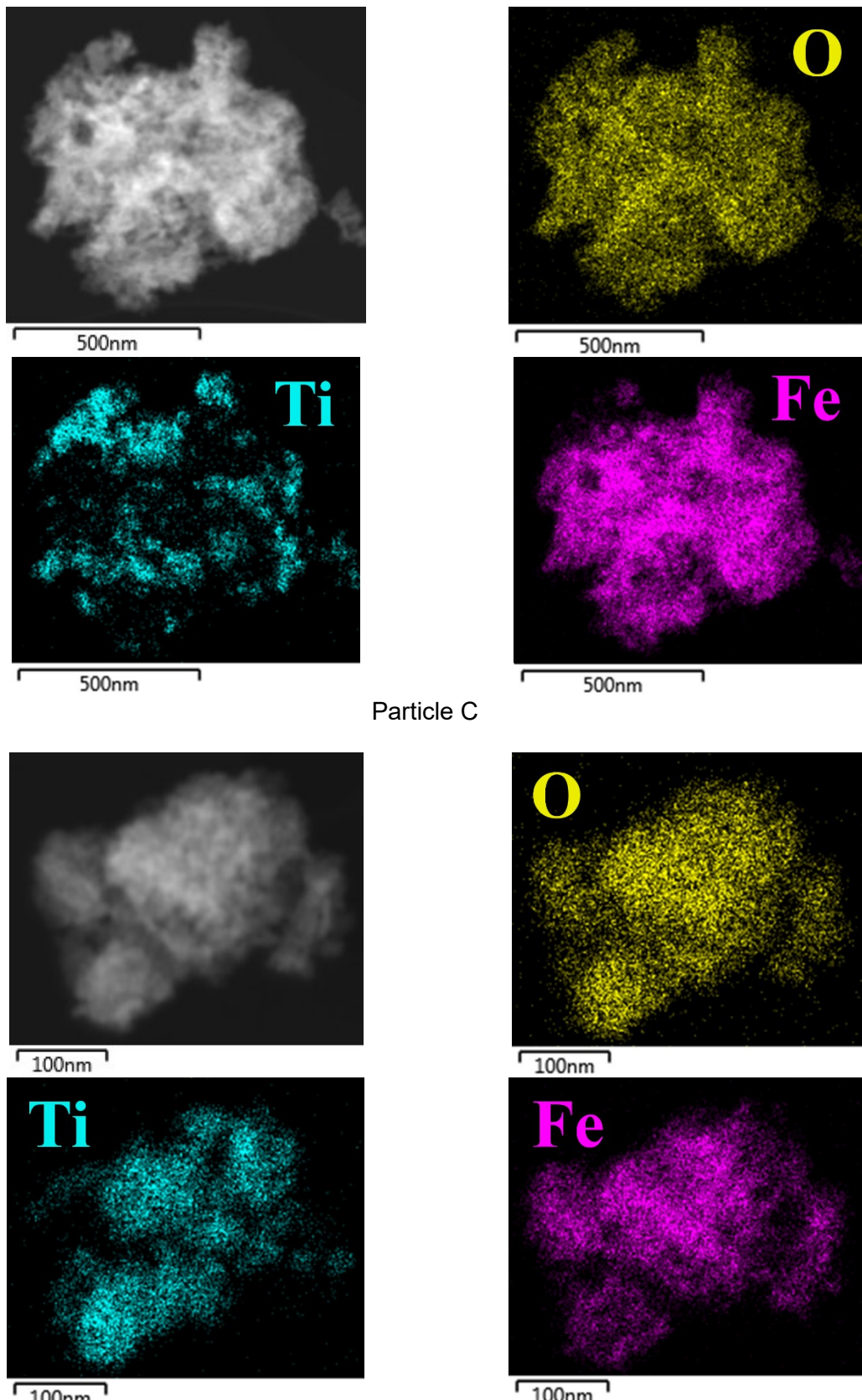


Figure 5.7: STEM-EDS analysis of three meso-TiO₂/Fe₂O₃ particles (batch 2). Top left panels present the STEM image. Top right, bottom left and bottom right panels show the STEM-EDS mapping of oxygen, titanium and iron respectively. For particle A, Fe:Ti ratios were determined by STEM-EDS point analysis. Red labels denote Fe-majority regions, green labels denote Ti-majority regions and blue labels denote Ti-only regions.

STEM-EDS point analysis of particle A was used to quantify the ratio between Fe and Ti at a number of different features, which were aligned with three categories (Figure 5.7, first panel). (1) STEM-EDS point analysis revealed a number of areas where Ti was present without Fe, i.e. exposed TiO₂. (2) Large areas of particle A were predominantly Ti with a low amount of Fe and as these features were <100 nm in size, it is believed that the Fe must correspond to a thin coating on the TiO₂ surface, rather than particulate/granular Fe₂O₃ precipitates. In these regions the presence of mesopores (on the ~10 nm diameter scale) can be identified in the STEM-EDS image as dark spots, most clearly on the righthand side of the image. (3) Bright areas (i.e. high electron density) in the STEM-EDS image all corresponded to Fe rich regions and can therefore be assigned to Fe₂O₃ precipitates with more of a particulate/granular structure than the iron oxide coating previously discussed.

These results suggest that the aggregate meso-TiO₂/Fe₂O₃ particles are typically composed of a TiO₂ core with (a) an incomplete iron oxide coating, leaving some TiO₂ exposed at the surface, plus (b) more discrete Fe₂O₃ precipitates (which would correspond to the bright, electron dense amorphous regions previously observed in the SEM discussion, section 5.2.5).

5.2.8. Material composition as a function of probing depth

A quantitative description of the composition of meso-TiO₂ and Fe₂O₃ components within the composite meso-TiO₂/Fe₂O₃ was needed for component additive adsorption modelling (chapter 6). XRF, XPS and LEIS were chosen for quantitative characterisation, owing to their different penetration depths. XRF has a probing depth in the order of micrometres, and therefore corresponds to a bulk analysis for these meso-scale particles (equivalent to the mass ratio)³⁷³. XPS probes the near surface, with a penetration depth of 1-10 nm, whilst LEIS is sensitive to the outermost surface (i.e. atomic-scale sensitivity)³⁷³.

XRF analysis, using meso-TiO₂ and Fe₂O₃ as end-member reference samples, gave a bulk composition of 51.6 ±2.6% Fe₂O₃ and 48.4 ±2.4% meso-TiO₂ (weight percent) for the meso-TiO₂/Fe₂O₃ composite (Figure 5.8a). This is in close agreement to the quantities of reagents used (a theoretical 50:50 mass balance of Fe₂O₃-to-TiO₂). Whilst XRD patterns are not normally used for quantification of crystal phase abundance, requiring good quality reference samples, XRD has been used to quantify the composition of a material in other adsorption studies^{374 375 376}. In this work, XRD patterns were combined to verify the XRF quantification of bulk material composition, using the intensity of the rutile TiO₂ peak at 27.38° and the α-Fe₂O₃ peak at 33.12° (Figure 5.8b). This gave a bulk composition of 47% Fe₂O₃ and 53%

meso-TiO₂. This is within error of the XRF results. Interestingly, the XRD-weighted linear combination of Fe₂O₃ and meso-TiO₂ XRD patterns faithfully reproduced the intensity of all other peaks observed in the meso-TiO₂/Fe₂O₃ XRD pattern, and even reproduced the intensity of the background arising from the fluorescence of iron under the copper K α_1 and K α_2 lines.

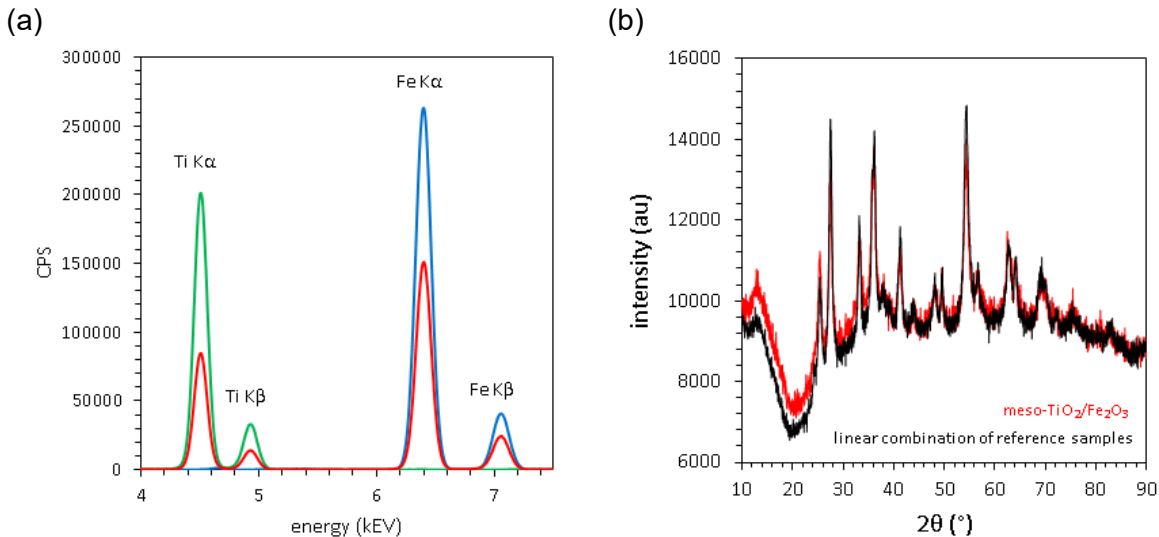


Figure 5.8: Quantifying the relative abundance of meso-TiO₂ and Fe₂O₃ phases within the meso-TiO₂/Fe₂O₃ bulk material. (a) XRF spectra (Fe₂O₃ reference sample in blue, meso-TiO₂ in green, and meso-TiO₂/Fe₂O₃ in red), and (b) determination by XRD, showing the XRD pattern for the composite (red), and the weighted linear combination of Fe₂O₃ and meso-TiO₂ reference samples (black), fitted according to the most intense peak from each reference pattern. Both X-ray techniques gave similar results, with XRF indicating 51.6% Fe₂O₃ and 48.4% meso-TiO₂, whilst XRD suggested that the sample contained 47% Fe₂O₃ and 53% meso-TiO₂.

XPS spectra are presented in the Appendix. By comparing the intensity of Fe2p^{3/2} and Ti2p^{3/2} peaks with reference samples as end-members, XPS gave a near surface composition of 58.7 ± 2.6% Fe₂O₃ and 41.3 ± 1.8% meso-TiO₂ for the meso-TiO₂/Fe₂O₃ composite. This indicated that the near surface contained significantly more Fe₂O₃ and significantly less meso-TiO₂ than the bulk material.

During LEIS analysis, a depth profile was used to remove the influence of adsorbed organics. The intensity (area) of Fe and Ti peaks came to a plateau with a dose of 2-4 × 10¹⁵ ions cm⁻², corresponding to a sputter depth of 1-2 Å (Figure 5.9a). This distance is little more than one atomic layer. Using reference samples as end members, LEIS spectra indicated that the outermost surface of meso-TiO₂/Fe₂O₃ was composed of 68.0 ± 0.7% Fe₂O₃ and just 32.0 ± 0.3% meso-TiO₂ for (Figure 5.9b). This indicated that the outermost surface contained significantly more Fe₂O₃ and significantly less meso-TiO₂ than both the bulk material and the near surface.

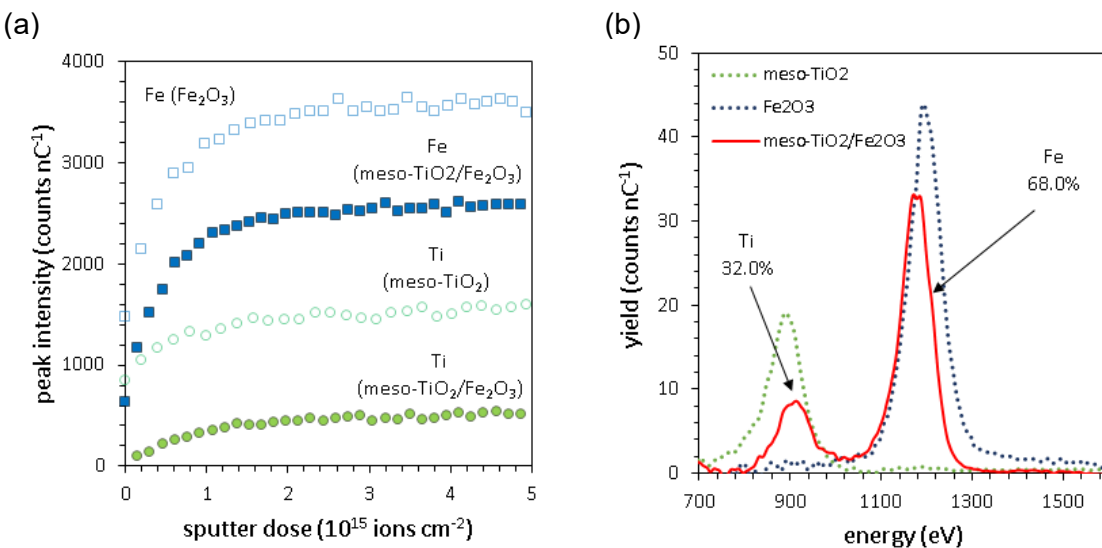


Figure 5.9: (a) LEIS depth profile of meso-TiO₂/Fe₂O₃ and reference samples and (b) determination of the outermost surface composition by peak integration and a linear combination of end-member reference samples.

The results from XRF, XPS and LEIS analysis agree with the STEM-EDS analysis and demonstrate that the surface of meso-TiO₂/Fe₂O₃ was enriched in iron oxide relative to the bulk material (Figure 5.10). This iron oxide enrichment is analogous to the fine surface coatings encountered in natural sediments which have caused previous problems in accurate adsorption modelling using the component additive approach¹⁵. Since Fe₂O₃ was precipitated from aqueous phase over a solid meso-TiO₂ support, the observed surface enrichment of iron oxide is not surprising. It is interesting to note that despite being sensitive to the near surface, XPS only partially captured the degree of iron oxide surface enrichment that was observed using LEIS. Since the penetration depth of XPS is on the same scale as the crystallite diameter (~12-14 nm), this suggests that much of the iron oxide surface coating is very thin (<10 nm). Quantification using XRF, XPS and LEIS analysis was precise, as all errors were less than 3%.

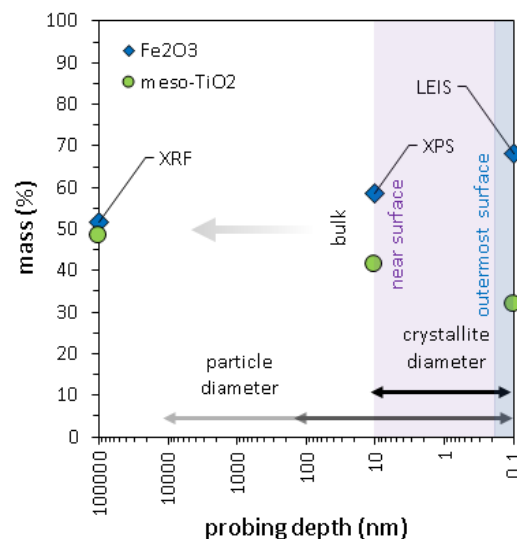


Figure 5.10: Mineral composition as a sample of probing depth. The composition of the outermost and near surfaces is compared with the bulk composition using different characterisation techniques.

5.3. Surface charge and the point of zero charge

The point of zero charge (pzc) is a very useful property for characterising different mineral surfaces and understanding how they adsorb charged species. At pH values below the pzc, a mineral surface is positively charged due to a net excess of protonated surface hydroxyl groups, promoting the adsorption of anionic sorbates due to electrostatic attraction, whilst repelling cationic sorbates²⁵². In contrast, at pH values above the pzc a negative surface charge develops, promoting the adsorption of cations and suppressing the adsorption of anions. Most surface complexation models include surface charge effects to improve their chemical description of adsorption, and so improve accuracy and sensitivity³⁷⁷. Iron oxides have high pzc values and are positively charged at pH 7-8 (as per South Asian groundwaters), whilst TiO₂ has a low pzc value and is negatively charged in the same waters³⁷⁸. It is therefore important to understand the surface charge of meso-TiO₂/Fe₂O₃ and accurately incorporate electrostatic effects into surface complexation models. Surface charge was also used as a surface property with which to probe component additivity in chapter 6.

5.3.1. Potentiometric titrations and the point of zero salt effect

The most established method for determining the point of zero charge of a mineral sample is to perform a number of potentiometric titrations at different ionic strengths and then identify the common intersection point (cip) between them. During a potentiometric titration, the pH is measured as a function of the quantity of acid or base titrant added. The (de)protonation of surface hydroxyls (also referred to as surface acidity) buffers the change in pH. The total amount of titrant added is equivalent to the term $c(a)-c(b)$, corresponding to the net concentration of acid added to the total system (split between the aqueous phase and the solid-solution interface). By subtracting the term $([H^+]-[OH^-])$ from $c(a)-c(b)$, corresponding to the concentration of protons in solution, we obtain a term for the net surface proton excess, i.e. we obtain a measure of surface charge.

Unfortunately, the pzc is not necessarily equivalent to where the plot of Q or $c(a)-c(b)-([H^+]-[OH^-])$ versus pH intercepts the x-axis, as any acid or base impurities irreversibly consumed during titration will shift the titration curve down or up (respectively) in the y-axis. The cip method does not suffer from this problem. As ionic strength is increased, the capacitance of the electrical double layer is increased, and more charge can be stored at the solid-solution interface. Subsequently, the slope of the titration curve increases. However, at the pzc there

is no net surface charge and therefore increasing ionic strength does not influence the value of Q at the pzc (to an approximation). Identifying the cip of titrations at different ionic strengths therefore provides one measure of the pzc, termed the point of zero salt effect (pzse).

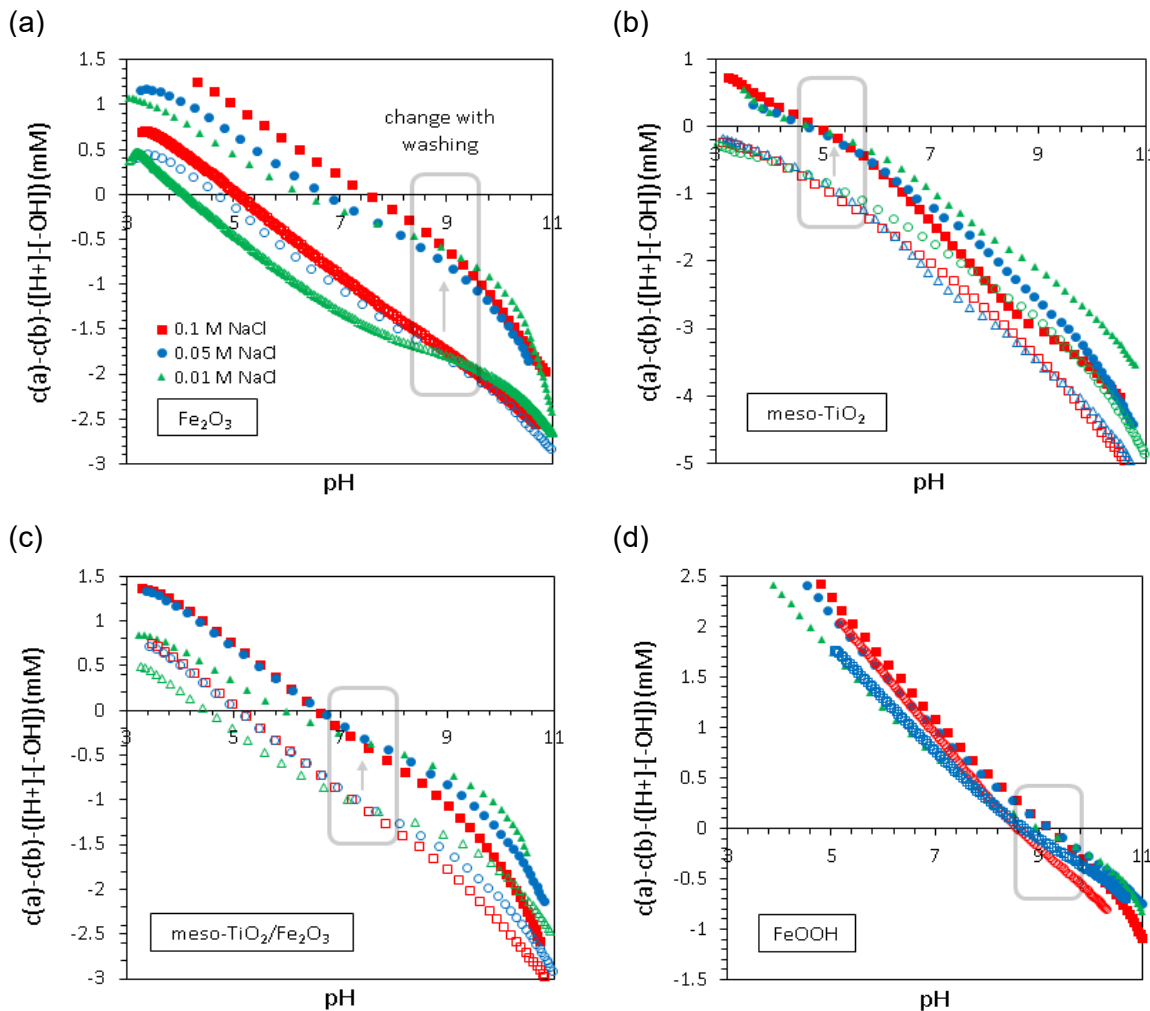


Figure 5.11: Identification of the point of zero salt effect (pzse) by potentiometric titration, for (a) Fe₂O₃, (b) meso-TiO₂, (c) meso-TiO₂/Fe₂O₃, and (d) FeOOH. Shown are titration curves for both washed samples (solid shapes), and unwashed samples (open shapes). Titrations were carried out in 0.01 M NaCl (green triangles), 0.05 M NaCl (blue circles) and 0.1 M NaCl (red squares). All titrations used 10 g L⁻¹ of mineral, 0.1 M HCl and 0.1 M NaOH. Grey boxes highlight where the pzse was found, whilst arrows highlight the removal of acidic impurities after washing in dialysis tubing in all samples except for FeOOH, which had negligible impurities even before washing.

Identification of the pzse for unwashed minerals revealed significant acidic impurities in all synthesised samples (Figure 5.11). Net acidic impurities were approximately 0.2, 0.1 and 0.1 mmol g⁻¹ for Fe₂O₃, meso-TiO₂ and meso-TiO₂/Fe₂O₃ respectively. For Fe₂O₃ this was equivalent to two thirds of the total change in Q across the entire titration curve. To mitigate any errors that might arise from acidic impurities, and to provide a surface with fewer impurities for subsequent adsorption studies, all minerals were washed using dialysis tubing. Mineral

washing was successful, reducing net acidic impurities by 60-80% (Figure 3.5). For FeOOH (the commercial product), net acidic impurities were negligible both before and after washing. Mineral washing had no significant change on the pzse for all samples. Values of the pzse are reported in Table 5.3.

5.3.2. Zeta potential and the isoelectric point

When identified using the potentiometric titration cip method, the point of zero charge is then commonly verified using a second technique³⁷⁸. In this thesis, potentiometric mass titrations (PMT)^{379 380} were originally used as a second technique, however large uncertainties were achieved using this method (particularly due to the acidic impurities present in the synthesised samples) as discussed in the Appendix.

Instead, the pzc was verified by measuring the zeta potential at different pH values. The isoelectric point (iep) is the term given to the pH at which zeta potential (ζ) is equal to zero. Zeta potential is the potential at the slipping plane (or “shear plane”) of a suspended solid. Inside the slipping plane there is sufficient attraction between solvent and solid that solvent molecules are stationary relative to the solid, and travel through solution with the suspended solid. In the absence of charged sorbates, the iep will approximately occur at the same pH as the pzse. Knowledge of the zeta potential is additionally useful as it indicates how well suspended and how well dispersed the sorbent is: at the iep there is no net repulsive electrostatic force to prevent solid particles aggregating due to attractive van der Waals interactions³⁸¹. At zeta potential extremes, particles are better suspended due to electrostatic repulsion. For adsorption and photocatalysis good dispersion is desirable, increasing the surface area available to the substrate.

Zeta potential as a function of pH is presented in Figure 5.12, with the average particle size determined using DLS overlaid. The maximum particle size coincided with the iep for iron oxides FeOOH and Fe₂O₃, with particle agglomeration occurring within a narrow pH window. DLS detected large (>1 µm) meso-TiO₂ and meso-TiO₂/Fe₂O₃ particles across a much wider pH window. This suggests either that the sol-gel TiO₂ particle aggregates are bulkier than the iron oxides, or that the surface is less homogeneous.

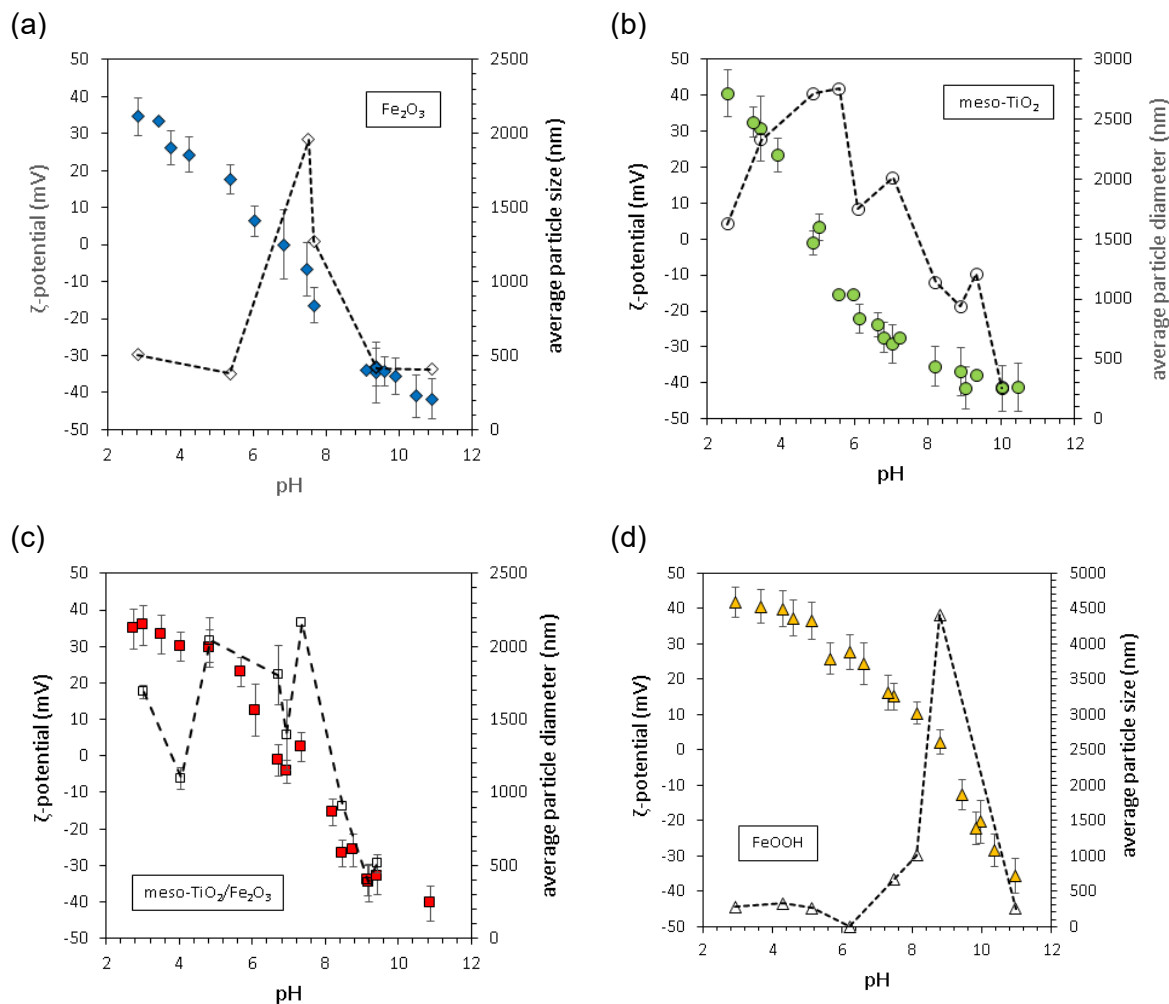


Figure 5.12: Identifying the isoelectric point (iep). This figure demonstrates the influence of pH on zeta potential (filled shapes) and the mean size of suspended particles (open shapes with dashed lines). Error bars indicate the zeta potential deviation reported by the Zetasizer application. The experimental conditions were 0.01 M NaCl, 1 g L⁻¹ mineral loading, and pH 7.0 ± 0.1.

5.3.3. The point of zero charge

The final pzc values determined in this work are presented in Table 5.3 and highlighted in Figure 5.13. For meso-TiO₂, meso-TiO₂/Fe₂O₃ and FeOOH, pzse and iep values were within error of one another. The iep of Fe₂O₃ was 6.8±0.4. This was 2.1 pH units lower than the pzse value of 8.88±0.16. This difference may be due to the presence of carbonate, as unlike during potentiometric titration, samples were not acidified and then purged with N₂ gas before zeta potential analysis. The zeta potential of mineral suspensions is known to decrease in the presence of carbonate ³⁸². Mechanisms for this decrease in zeta potential include (a) negatively charged monodentate surface complexes ³⁸³ [$>\text{SOCO}_2^-$, where $>\text{S}$ denotes the mineral surface, although the neutral ($>\text{SO}$)₂CO species is probably more prevalent ³⁸⁴], (b) outer-sphere surface complexes ³⁸⁴, and (c) the build-up of CO₃²⁻ in the electrical double layer, within the slipping plane ³⁸³. Adsorbed carbonate was also observed in the ATR-FTIR spectra of all samples, most significantly in the iron-containing samples (section 5.4).

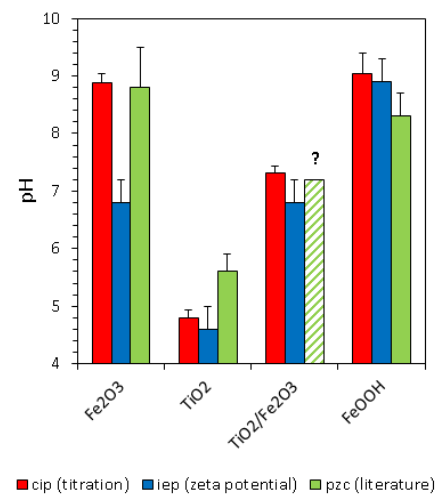


Figure 5.13: A visual comparison of the point of charge, determined from potentiometric titrations (red bars) and zeta potential analysis (blue bars). Error bars indicate the uncertainty, determined for potentiometric titrations as the difference between maximum and minimum possible pH values for the common intersection point between titration curves and the central cip location taken forwards, whilst uncertainties in the iep were determined as the uncertainty in where zeta potential crossed 0 mV. Literature values are from Kosmulski ³⁷⁸ ³⁸⁵ and error bars represent the variance in reported results where both pzse and iep were in agreement. The question mark highlights that we would expect the pzc of a TiO₂/Fe₂O₃ composite to lie between the values reported in the literature for pure TiO₂ and Fe₂O₃.

Table 5.3: Surface charge: A summary of the results obtained from dynamic light scattering (DLS) analysis (particle size and zeta potential) and potentiometric titration of mineral samples.

sample	meso-TiO ₂	Fe ₂ O ₃	meso-TiO ₂ /Fe ₂ O ₃	FeOOH
smallest particle size peak (nm)	91	81	88	60
largest particle size peak (nm)	5435	1958	5503	4409
pH of largest particle size	5.58	7.52	8.20	8.80
pzse (titration)	4.80±0.14	8.88±0.16	7.32±0.12	9.05±0.35
iep (zeta potential)	4.6±0.4	6.8±0.4	6.8±0.4	8.9±0.4
pzc (literature)	5.4-5.9 (or 5.2-6.8) ³⁸⁵ ³⁷⁸	8.3-9.5 ³⁷⁸	not available	7.9-8.7 for synthetic goethite ³⁷⁸

5.4. ATR-FTIR baseline spectra before adsorption of arsenic

Attenuated total reflectance Fourier-transform infrared (ATR-FTIR) spectra were obtained (a) to check for the presence of chemical impurities (e.g. organics not detected by XRF and other surface contaminants), but more importantly (b) to provide a baseline for detecting new vibrations after adsorption of arsenic (chapter 6).

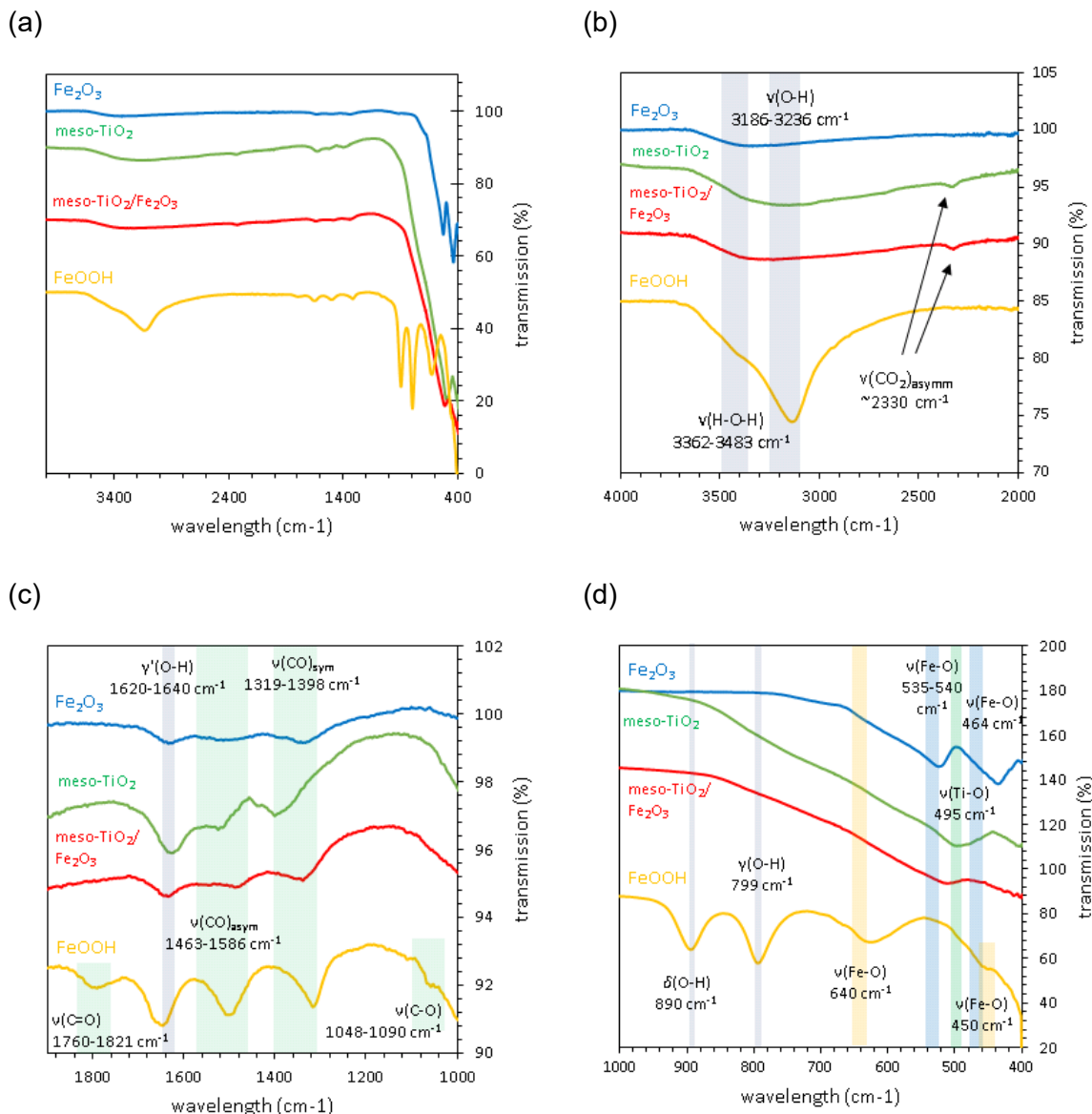


Figure 5.14: ATR-FTIR spectra for mineral samples before adsorption of arsenic. (a) The full spectrum of each sample, between 400 and 4000 cm⁻¹. (b) The hydroxyl stretching region. (c) The hydroxyl deformation and carbonate stretching region. (d) The lattice stretching vibration region. Each peak is labelled with the literature wavenumbers (cm⁻¹) used to assign each peak. Spectra have been shifted in the y-axis for clarity.

The ATR-FTIR spectra of samples before adsorption of arsenic are presented in Figure 5.14. ATR-FTIR peaks were assigned to vibrational modes using literature data as presented in Table 5.4. All samples demonstrated the typical features of mineral oxides: metal-oxygen bonds (M-O) and surface hydroxyl groups (S-O-H, where S is a surface metal ion), with little trace of impurities besides adsorbed carbonate. FeOOH demonstrated the strongest hydroxyl stretching peaks, $\nu(\text{O}-\text{H})$, and hydroxyl deformation, $\delta(\text{O}-\text{H})$, since whilst all mineral samples contained surface hydroxyl groups (which serve as active sites for the adsorption of arsenic), only FeOOH contained hydroxyl groups within the crystal lattice. The $\nu(\text{O}-\text{H})$ peaks of FeOOH were better defined, as whilst surface hydroxyls are present in a wide variety of local environments (e.g. interactions with adsorbed water and carbonate) giving a broad peak shape, hydroxyl groups inside the FeOOH crystal lattice are all held in the same environment. FeOOH exhibited an additional peak at 890 cm^{-1} corresponding to the deformation of hydroxyl groups, $\delta(\text{O}-\text{H})$, within the crystal lattice.

Peaks corresponding to the symmetric and antisymmetric stretching vibrations of carbonate, $\nu(\text{CO})_{\text{sym}}$ and $\nu(\text{CO})_{\text{asym}}$, were observed in all samples, which is unsurprising given that carbonate is formed by the dissolution of atmospheric CO_2 according to Henry's constant. Again, these peaks were most intense for FeOOH. This may indicate a greater quantity of adsorbed carbonate due to the high surface area and high point of zero charge of this sample. The $\nu(\text{CO}_2)$ peak at 2330 cm^{-1} may indicate CO_2 trapped within the porous structure of meso-TiO₂. The position of the $\nu(\text{C}-\text{O})$ peaks in the spectrum of meso-TiO₂/Fe₂O₃ were closer in position to the $\nu(\text{C}-\text{O})$ peaks of Fe₂O₃ than meso-TiO₂, suggesting that the majority of carbonate is adsorbed on the Fe₂O₃ surface component, rather than the meso-TiO₂ phase. This is logical since Fe₂O₃ has the higher point of zero charge, and thus an electrostatic attraction between the positive mineral surface and carbonate anions. This is a small piece of evidence suggesting that adsorption of anions, including arsenic(V), is dominated by the Fe₂O₃ phase, rather than by meso-TiO₂. Adsorbed carbonate was also identified in the XPS spectra of mineral samples through the presence of C=O and C-O peaks in the C1s region (Appendix).

Table 5.4: FTIR peak assignment for blank samples, prior to adsorption. Parentheses indicate other minerals, where no direct match was found. Weak and very weak peaks are labelled w and vw respectively.

Vibration			Position (cm ⁻¹) and intensity						
			Literature			Experimental			
Label	Description	Category	Goethite	Hematite	Titania	FeOOH	Fe ₂ O ₃	Meso-TiO ₂	Meso-TiO ₂ /Fe ₂ O ₃
v(H-O-H)	v1 hydroxyl stretch	Mineral	3407 ³⁸⁶	3483-3470 ³⁸⁷	3432 ³⁸⁸ 3362 ³⁸⁹	3410	3355	3234	3333
v(O-H)	v2 hydroxyl stretch	Mineral	3236-3206 ³⁸⁷	3186 ³⁸⁷	3216 ³⁸⁹	3137			
v(CO ₂) _{asym}	CO ₂ asymmetric stretch (not carbonate)	CO ₂	2345 - 2325 ³⁹⁰ (copper benzoate) 2343 (montmorillonite) ³⁹¹ 2350 (anatase) ³⁹²			-	-	2333 w	2325 w
v(C=O)	C=O stretch (bond order 2)	Carbonate	1777 (carbonate glass) ³⁹³ 1748 (MgCO ₃ -K ₂ CO ₃) ³⁹³ 1800 (propylene carbonate) ³⁹⁴ 1790 (diphenyl carbonate) ³⁹⁵ 1790 (CHO ₃) ³⁹⁶ 1821 (CHO ₃) ³⁹⁷	1798 (calcite) ³⁹⁸ 1760 v(CO ₃) overtone ³⁸³ 1786, 1768 v(C-O) asymm mono/bide nate mononucle ar ³⁸³	1802, bidentate carbonate ³⁹²	1798	-	-	-
v'(O-H)	O-H bend (hydroxyl and adsorbed water)	Mineral and water	1637 ³⁸⁷	1633 ³⁹⁹ 1623 (Fe ₃ O ₄) ⁴⁰⁰ 1640 ³⁸³	1630 ¹⁶⁰ 1620 ⁴⁰¹	1650	1640	1632	1639
v(CO) _{asym}	Bicarbonate asymmetric stretch	Carbonate	1620 ⁴⁰²	1610 (Fe ₃ O ₄) ⁴⁰⁰	1625-1656 ³⁹²				
v(CO) _{asym}	O-C-O asymmetric stretch	Carbonate	1490 ⁴⁰²	1463 ²⁴² 1562-1552 ³⁸³ 1530 ³⁸³ 1477 ³⁸³ 1545 (Fe ₃ O ₄) ⁴⁰³ ~1550 ³⁸³	1586 ³⁹² 1562 ⁴⁰⁴	1501	1504	1528	-
v(C-O) _{sym}	O-C-O symmetric stretch	Carbonate	1335 ⁴⁰²	1357 ²⁴² 1356-1358 and 1321-1319 ³⁸³ 1335 (Fe ₃ O ₄) ⁴⁰³ 1393 (Fe ₃ O ₄) ⁴⁰⁰ ~1350 ³⁸³	1398 ⁴⁰⁴ 1376, 1316 ³⁹² 1392, 1378 ³⁹²	1317	1388, 1337	1398	1340

Vibration			Position (cm^{-1}) and intensity						
			Literature			Experimental			
Label	Description	Category	Goethite	Hematite	Titania	FeOOH	Fe_2O_3	Meso- TiO_2	Meso- $\text{TiO}_2/\text{Fe}_2\text{O}_3$
v(C-O)	C-O (symmetric) stretch (bond order 1)	Carbonate	1010 ⁴⁰² C- OH stretch 1050 ³⁸³ (propylene carbonate) ³⁹⁴ 957 (CHO ₃) ³⁹⁶ 1090 (CHO ₃) ³⁹⁷	1050, 1150 ³⁸⁸ 1070 (Fe ₃ O ₄) ⁴⁰³ 1070 (HFO) ⁴⁰⁵ ⁴⁰⁶	1080 ³⁸⁸ 1048, 1052 ³⁹² “O-C-O symmetric stretch”	1060	1059 vw	-	-
$\delta(\text{O-H})$	Hydroxyl deformation	Mineral	890 ³⁸⁶	-	-	896	-	-	-
$\gamma(\text{O-H})$	Hydroxyl deformation	Mineral	799 ³⁸⁶	-	-	797	-	-	-
v(Fe-O)	FeO ₆ lattice	Mineral	640 ³⁸⁶	-	-	629	-	-	-
v(Fe-O)	Fe-O stretch	Mineral	-	540 ³⁹⁹ 535 ⁴⁰⁷	-	-	526	-	512
v(Ti-O)	Ti-O stretch	Mineral	-	-	800-450 ³⁸⁸ 500 ²⁶¹ 400-700 Ti-O stretch and Ti-O- Ti bridging ⁴⁰¹	-	-	495	-
v(Fe-O)	FeO ₆ lattice	Mineral	450 ³⁸⁶	464 ⁴⁰⁷	-	454	437	-	-

5.5. Implications

This chapter achieved three major outcomes. Firstly, crystal phases were confirmed and the structure of meso-TiO₂/Fe₂O₃ was determined. A quantitative assessment of impurities was achieved, and acidic impurities were successfully reduced through mineral washing, offering a measure of quality control. Secondly, all data necessary to constrain and normalise experimental results in subsequent adsorption and photocatalysis studies was collected. Thirdly, an understanding of the composite structure of meso-TiO₂/Fe₂O₃ was achieved, with the composition quantitatively determined at three different probing depths. The most important properties, discussed in subsequent chapters, are presented in Table 5.5.

Table 5.5: Materials characterisation: a compiled table of the most significant results used in the subsequent experimental work. pH_{pzc} indicates the pH at the point of zero charge. All experiment results pertain to the second batch of meso-TiO₂ and meso-TiO₂/Fe₂O₃ except where explicitly stated.

Sample	FeOOH	Fe ₂ O ₃	meso-TiO ₂	meso-TiO ₂ /Fe ₂ O ₃
Crystal phase	α-FeOOH	αFe ₂ O ₃	rutile anatase	α-Fe ₂ O ₃ rutile anatase
BET-specific surface area (m ² g ⁻¹)	127	103	146 (batch 1) 110 (batch 2)	116 (batch 1) 100 (batch 2)
Total pore volume (cm ³ g ⁻¹)	0.69	0.23	0.22	0.22
BJH average pore size (nm)	21	8.9	7.8	8.6
Crystallite diameter (Scherrer equation)	15.8±7.3	20.5±5	17±3.8 (rutile) 13.6±2.5 anatase)	14.3±4 (hematite) 13.6±2.2 (rutile) 12.0±1.0 anatase)
Crystallite diameter (TEM)	---	---	---	15.9±3.3 (hematite) (N=10) 14.7±3.5 (anatase) (N=6)
Particle size (DLS)	250 nm – 4.4 μm	400 nm – 2.0 μm	300 nm – 2.8 μm	400 nm – 2.4 μm
Particle size (SEM)	---	---	---	500 nm - 50 μm
pH _{pzc} (pzse)	9.05±0.35	8.88±0.16	4.80±0.14	7.32±0.12
pH _{pzc} (iep)	8.9±0.4	6.8±0.4	4.6±0.4	6.8±0.4
pH _{pzc} (literature)	7.9 – 8.7 ³⁷⁸	8.3-9.5 ³⁷⁸	5.2-6.8 ^{385 378}	N/A

Whilst the surface area of meso-TiO₂ decreases once coupled with Fe₂O₃, the surface area is roughly equal to that of the Fe₂O₃ reference sample, offering a similar concentration of surface sites for adsorption. Investigating the structure of meso-TiO₂/Fe₂O₃, a thin, incomplete iron oxide surface coating was identified, on top of the meso-TiO₂ support, which limits the amount of exposed TiO₂ surface. Since adsorption is an atomic-scale process, it can be anticipated

that this coating may exhibit a strong influence over the adsorption of arsenic. Whilst more discrete, particle-like Fe_2O_3 features on the surface of the composite material were also identified, the presence of meso- TiO_2 during precipitation of iron oxide appears to have constrained Fe_2O_3 crystal growth to smaller sizes.

Significant differences were observed between the anatase:rutile ratio of the meso- TiO_2 component in the two synthetic batches. Batch 1 was primarily anatase, whilst batch 2 was primarily rutile. Only the second batch contained sufficient material for the adsorption experiments, whilst the first batch was best suited for photooxidation kinetics, since anatase is considered the superior photocatalytic phase²⁰⁵. Using the anatase-dominated batch 1 for photocatalytic oxidation experiments also facilitates comparison with previous studies^{11 21 23}.

To investigate whether arsenic adsorption data collected using the second batch of meso- TiO_2 and composite meso- $\text{TiO}_2/\text{Fe}_2\text{O}_3$, with its high rutile content, can be used to model the anatase-based first batch of meso- $\text{TiO}_2/\text{Fe}_2\text{O}_3$, the study of Gupta et al. was considered. In this study, multiple samples with different anatase:rutile ratios were prepared and used as arsenic sorbents³⁶⁵. Plotting the amount of arsenic adsorbed (normalised to surface area) as a function of the anatase weight fraction indicated that samples with higher anatase mass fractions exhibit greater As(V) and As(III) adsorption (Figure 5.15a). Using linear regression, this study predicts that meso- TiO_2 batch 1 (84% anatase) would adsorb 89% more arsenic than batch 2 (28% anatase), potentially a very significant source of error. However, the goodness of fit as measured by the coefficient of determination was only 0.605.

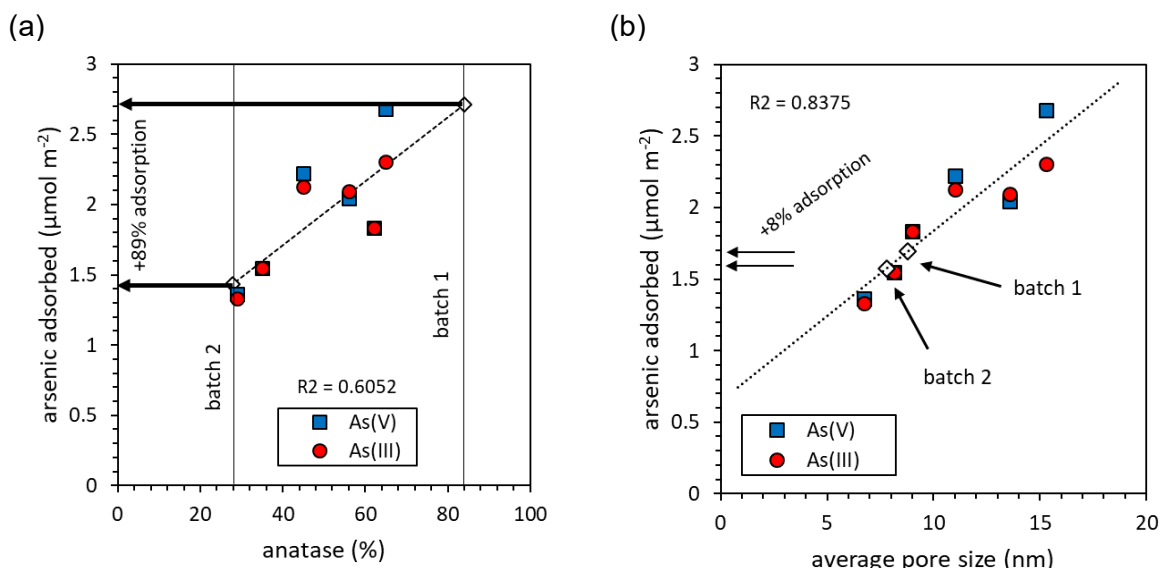


Figure 5.15: The influence of anatase:rutile ratio on the adsorption of arsenic to TiO_2 . Data was taken from Gupta et al.³⁶⁵ and normalised to (a) the surface area, and (b) the pore size reported for each sample. The experimental conditions were $0.3 \text{ g L}^{-1} \text{ TiO}_2$, 10 mg L^{-1} total As concentration and equilibration for 1 day. Diamonds denote the quantities of arsenic adsorbed to meso- TiO_2 batch 1 and batch 2 respectively as predicted by the linear regression.

A far stronger relationship was found between the quantity of arsenic adsorbed and the average pore size (Figure 5.15b), with $R^2 = 0.8375$ for the 6 samples. This suggests that the differences observed in the study of Gupta et al. were primarily due to differences in surface morphology, and not the anatase:rutile ratio. The importance of surface morphology on arsenic adsorption is discussed in chapter 6. As the average pore sizes of both meso-TiO₂ batches were very similar (8.8 and 7.8 nm for the washed products of batch 1 and batch 2 respectively), the difference in adsorption predicted by the linear regression is much smaller, at just 8%. This suggests that the use of adsorption data collected for the rutile-majority batch 2 samples can reasonably be used to predict adsorption of arsenic onto the anatase-majority batch 1 samples with an error of less than 10%.

6. Developing an accurate surface complexation model of arsenic adsorption onto meso-TiO₂/Fe₂O₃ using surface-sensitive analytical techniques

6.1. Introduction

Surface complexation models (SCMs) are powerful tools to help us understand the behaviour of sorbents. These models predict adsorption as a function of pH, ionic strength, and the presence of competitor ions, thereby offering a realistic sensitivity to environmental conditions that is typically lacking in the better-known Langmuir and Freundlich adsorption isotherm models ¹⁴. Whilst SCMs are well established for single-component systems, there are two contrasting approaches towards modelling heterogeneous systems: the Generalised Component (GC) and Component Additive (CA) methods.

The GC method approximates and models a heterogeneous sorbent as a homogeneous surface ^{15 253}. This approach is more common in the literature than CA, but has notable limitations, including (a) the equilibrium constants for the surface reactions must be experimentally determined for each new heterogeneous surface, i.e. there is no capacity to predict how changing the surface composition will influence adsorption ¹⁵, and (b) adsorption across multiple surfaces is convoluted, and this limits our mechanistic insight into how the sorbate partitions across the different surface components that make up the overall sorbent surface ⁴⁰⁸.

In contrast, the CA approach describes the total sorbent assemblage as a combination of single-component surfaces ¹⁵. Equilibrium constants are obtained using reference samples to represent each of the surface components in the CA model. Component additive modelling has advantages over the GC approach since (a) it is easily adjusted to predict the behaviour

of new composite formulations with different surface compositions (e.g. if meso-TiO₂/Fe₂O₃ is synthesised with a different ratio of reagents), and (b) since adsorption is deconvoluted, CA modelling provides insights into how the sorbate partitions between the surface components (e.g. identifying whether meso-TiO₂ or Fe₂O₃ controls the observed adsorption)⁴⁰⁹.

A component additive surface complexation model (CA-SCM) that accurately predicts the adsorption of arsenic onto meso-TiO₂/Fe₂O₃ is a desirable tool for two reasons. Firstly, an accurate CA-SCM enables us to assess whether arsenic adsorption is component additive or if it is influenced by sorbent coupling. Secondly, an accurate CA-SCM offers a tool allowing arsenic adsorption onto TiO₂-iron oxide composite materials, prepared by different synthetic routes, to be predicted. This can help us to better engineer the next generation of composite photocatalyst-sorbents.

However, the CA-SCM approach has had variable success in describing experimental data, with the main challenge being the need to accurately quantify the abundance of each component at the sorbent surface¹⁵. Different approaches have been used to weight the contribution of each component to the overall adsorption. The mass ratio of the bulk material is most commonly used^{16 18 265 266 267 268 269}. The major problem with weighting according to the bulk mass ratio is that the bulk composition does not necessarily reflect the material composition at the surface¹⁵. Examples include (a) where one component has a particularly high surface area-to-mass ratio, and (b) where one component comprises the material bulk, and the second comprises a thin surface coating. (Secondary minerals such as amorphous iron and aluminium (hydr)oxides are examples of prevalent, naturally occurring, high surface area surface coatings¹⁵). Consequently, in many cases CA models weighted by mass ratios of the bulk material fail to describe the extent of experimentally observed adsorption^{16 17 18}. X-ray diffraction (XRD) has also been used for CA-SCM weighting^{374 375 376}. However, XRD probes the bulk material and therefore has all the limitations just discussed.

Currently only a few techniques have been used to characterise the surface and better weight components within CA-SCMs. These are chemical extractions^{15 410} and the fitting of experimental adsorption isotherms against single-component reference isotherms⁴¹¹. Chemical extractions can be used to quantify the abundance of a surface coating when the solid phase is different to the bulk material. However, this technique has poor surface sensitivity, especially for thick coatings, and the technique is inaccurate when strong treatments dissolve the bulk material¹⁵. Meanwhile, whilst providing a very good CA-SCM fit for the adsorption of uranium(VI) onto natural sediments, Dong and Wan⁴¹¹ noted that their approach of quantifying surface composition using end-member adsorption isotherms is limited to binary CA models, and more complex ternary systems cannot be weighted in this

way. Previous authors have commented on how new surface characterisation techniques are needed to improve the predictions made through component additive modelling^{253 410}.

These limitations can be overcome through the use of surface-sensitive analytical techniques. X-ray photoelectron spectroscopy (XPS) is now routinely used to investigate the near-surface (1-10 nm^{412 413}) of materials before and after adsorption, however there are no examples of XPS being used for the weighting of components within CA modelling. Another technique, less widely used, is low energy ion scattering (LEIS). This is a quantitative, spectroscopic technique sensitive to the outermost atomic surface^{373 414 415}. XPS resolves elements on the basis of electron binding energy, whilst LEIS resolves elements on the basis of mass^{416 417}. Consequently, unlike the fitting of adsorption isotherms, both XPS and LEIS could find applications in the CA modelling of ternary composite materials⁴¹⁸. To date, no study has used LEIS for multicomponent adsorption modelling. This chapter therefore investigates whether the accuracy of CA-SCMs can be improved through choice of more appropriate materials characterisation techniques, namely LEIS.

6.1.1. Aims and objectives

The aim of this chapter was to develop a CA-SCM that accurately describes adsorption of arsenic onto meso-TiO₂/Fe₂O₃. Chapter 5 identified that the surface of this material is significantly enriched in iron oxide relative to the bulk material. Since surface coatings are expected to be responsible for the failings of many previous CA-SCM studies, the adsorption of arsenic onto meso-TiO₂/Fe₂O₃ was studied using XRF, XPS and LEIS data to weight the meso-TiO₂ and Fe₂O₃ surface components within the CA model. XRF was used to reflect the bulk mass ratio used in most previous CA-SCM studies. LEIS was used, since it offers the best surface sensitivity. XPS was used as an example of a more widely available surface-sensitive technique. This chapter considered the hypothesis that CA predictions would be most accurate when LEIS is used to weight each component, owing to the excellent surface sensitivity of this technique. This chapter investigates component additivity in three different chemical properties: (i) surface charge (potentiometric titration), (ii) arsenic(V) adsorption (using the Langmuir isotherm), and (iii) arsenic(III) adsorption (using the Freundlich isotherm). Bayoxide E33, a commercial goethite sorbent (FeOOH), was used throughout this chapter for two reasons: firstly, it is a benchmark As(V) sorbent, and secondly, an accurate single-component SCM was previously developed to describe the adsorption of As(V) and As(III) onto Bayoxide E33, offering a useful resource for developing the meso-TiO₂ and Fe₂O₃ single-component SCMs^{225 89}.

6.2. Testing component additivity at the meso-TiO₂/Fe₂O₃ surface

The component additive description of a composite sorbent assumes that the observed adsorption is equal to the weighted linear combination of each sorbent phase ¹⁵. This can be expressed as:

$$P_{\text{composite}} = m_A P_A + m_B P_B$$

Equation 6.1

where P_i represents the chemical property of material i under a given set of experimental conditions (pH, ionic strength, aqueous arsenic concentration), and m_i represents the relative abundance (mass fraction) of component i . The chemical properties investigated using the component additive approach were (a) net proton excess/surface charge, (b) the concentration of As(V) adsorbed, and (c) the concentration of As(III) adsorbed. For all chemical properties, linear combinations were calculated using XRF-, XPS- and LEIS-weighted values of m_i . Ternary composites can be easily modelled by incorporation of further $m_i P_i$ terms where i corresponds to components C, D, E... etc.

6.2.1. Surface charge

The surface charge of meso-TiO₂/Fe₂O₃ and the reference samples was determined using potentiometric titrations, presented in Figure 6.1a. Characterisation of the point of zero charge was previously discussed in chapter 5. The positioning of the pzc of meso-TiO₂/Fe₂O₃ between meso-TiO₂ and Fe₂O₃ indicates that both TiO₂ and Fe₂O₃ were exposed at the material surface. This agreed with STEM-EDS analysis (chapter 5).

To investigate whether the surface acidity of meso-TiO₂/Fe₂O₃ could be predicted under the CA approach, the surface charge profiles of meso-TiO₂/Fe₂O₃ were reconstructed through a linear combination of reference samples, with meso-TiO₂ and Fe₂O₃ considered to be end-members (Equation 6.1). The contribution of meso-TiO₂ and Fe₂O₃ reference titrations was weighted according to the material compositions recorded at the bulk, near surface and outermost surface (i.e. using XRF, XPS and LEIS analysis).

The results are presented in Figure 6.1b-d. The accuracy of surface charge predictions increased in the order XRF < XPS < LEIS, demonstrating that surface protonation of meso-TiO₂/Fe₂O₃ is most accurately modelled under the CA approach when using the composition of the outermost surface. This highlights the importance that the iron oxide surface coating (identified by STEM-EDS and the three spectroscopic techniques in section 5.2) has upon the surface chemistry of the meso-TiO₂/Fe₂O₃ composite.

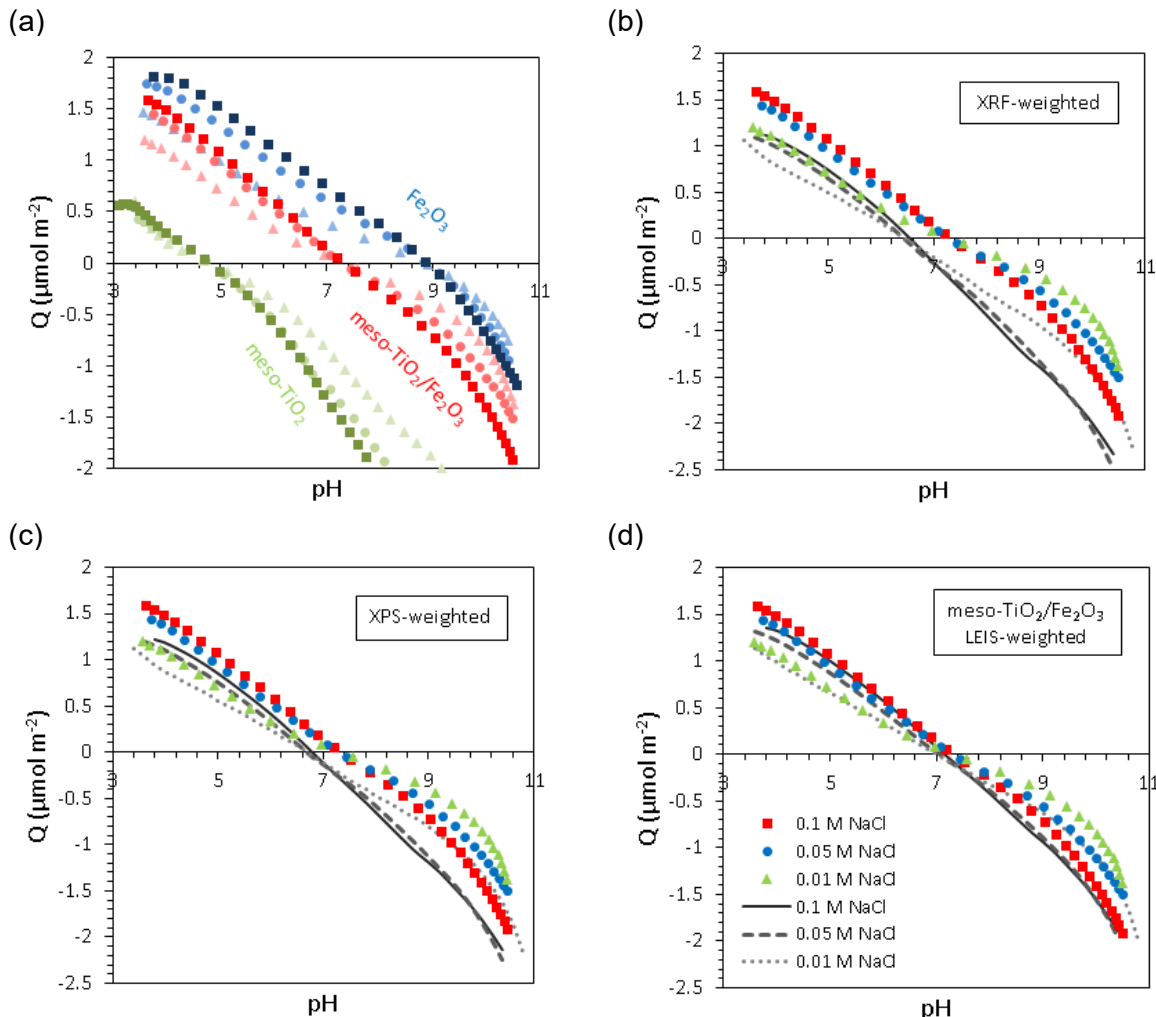


Figure 6.1: Component additivity in surface charge as measured by potentiometric titration. (a) Meso-TiO₂/Fe₂O₃ and reference samples, and surface charge predicted as a linear combination of end members weighted by (a) XRF bulk composition, (b) XPS near-surface composition and (c) LEIS outermost surface composition. Titrations were carried out in 0.1 M NaCl (squares), 0.05 M NaCl (circles) and 0.01 M NaCl (triangles). All experiments were conducted with 10 g L⁻¹ sorbent loading. All data shown is from forwards titrations using 0.1 M NaOH.

6.2.2. Adsorption of arsenic

Adsorption isotherms were obtained in order to (a) determine the adsorption mechanism, and (b) determine whether the component additive prediction of arsenic adsorption onto meso-

TiO₂/Fe₂O₃ would also show the best accuracy using LEIS-quantification of the outermost surface, and (c) to provide unseen data with which to validate the SCM.

6.2.2.1. Comparison of adsorption isotherm models

Langmuir and Freundlich adsorption isotherms were used to assess component additivity of arsenic adsorption, since they involve fewer fitting parameters than a SCM. These isotherms also allowed the adsorption mechanism to be investigated. The Langmuir model describes a sorbate binding to a limited number of (homogeneous) surface sites: the sorbent is saturated and further sorption ceases once a monolayer of sorbate has been adsorbed. In contrast, the Freundlich isotherm has no upper limit to adsorption and so can fit monolayer adsorption (to a heterogeneous surface)⁴¹⁹ or multilayer sorption⁴²⁰. pH 7 was chosen, representative of the arsenic contaminated groundwaters of South Asia, and 0.01 M NaCl was used as the electrolyte, representing the typical ionic strength of these groundwaters⁸⁶. Adsorption isotherms are presented in Figure 6.2 and Langmuir and Freundlich parameters are presented in Table 6.1.

For As(V), differences in the goodness of fit between Langmuir and Freundlich models were not significant (the average value of R² and its standard deviation was 0.749 ±0.093 for the Langmuir isotherm and 0.757 ±0.235 for the Freundlich isotherm). However, the plateau in the adsorption of As(V) at high [As(V) (aq)] suggested that As(V) primarily binds by monolayer adsorption, as per the Langmuir adsorption isotherm. Contrastingly, for As(III), the Freundlich adsorption isotherm gave a significantly better fit (R²=0.867 ±0.079 and 0.990 ±0.007 for the Langmuir and Freundlich isotherms respectively). There was no plateau in the adsorption of As(III) at high sorbate concentrations. This suggests that adsorption of As(III) proceeded either via monolayer binding to a heterogeneous surface or multilayer formation. As the Langmuir model successfully fitted As(V) adsorption isotherms, suggesting homogeneous binding sites for arsenic, the Freundlich adsorption isotherm suggests multilayer adsorption of As(III), e.g. the surface precipitation or surface polymerisation of As(III) over all samples at pH 7.0 ±0.1.

This is in agreement with multiple authors who have identified that As(III) forms surface precipitates or undergoes surface polymerisation over iron oxides, starting at coverages between 1 and 10 µmol m⁻²^{256 245 257}. The strongest evidence for As(III) surface precipitation onto iron oxides is a study using high resolution transmission electron microscopy (HR-TEM) and extended X-ray absorption fine structure (EXAFS) spectroscopy, which observed an amorphous arsenic-rich coating on Fe₃O₄ nanoparticles when As(III) adsorption exceeded 2

$\mu\text{mol m}^{-2}$. This coating was up to 10 nm thick (pH 7.2, 0.15 μM to 10 mM As(III) (aq), 0.1 M NaCl)²⁵⁷.

Surface precipitation of As(V) is less frequently observed, explaining why the Langmuir model provides a good fit in this work. Mamindy-Pajany et al. observed surface precipitation behaviour for As(V) adsorption onto Fe_2O_3 (when $[\text{As(V)} \text{ (aq)}] > 100 \mu\text{M}$ and $[\text{As(V)} \text{ (ads)}] > 3 \mu\text{mol m}^{-2}$) but not for FeOOH (pH 6, 0.01 M NaNO₃)⁴²¹. In contrast, the adsorption isotherms reported by Jeong et al. show As(V) surface precipitation behaviour over Al₂O₃ ($[\text{As(V)} \text{ (aq)}] > 5.3 \mu\text{M}$ and $[\text{As(V)} \text{ (ads)}] > 2.4 \mu\text{mol m}^{-2}$) but not for Fe_2O_3 (with a coverage of only 1.6 $\mu\text{mol m}^{-2}$ reached) (pH 5-9, no specific electrolyte)⁴²². Jia et al. identified formation of As(V) surface precipitates using XRD. This study found an amorphous ferric arsenate (AsFeO₄) or scorodite ($\text{FeAsO}_4 \cdot 2\text{H}_2\text{O}$) formed on iron hydroxides at acidic pH, but not at pH 8⁴²³. There was no evidence for multilayer As(V) sorption in our work (i.e. Langmuir behaviour with a plateau to adsorption). At pH 7.0 ± 0.1 , As(V) oxyanions have a repulsive negative charge towards other As(V) oxyanions, which makes surface precipitation less likely than with neutral H₃AsO₃). As well as pH, kinetic limitations may influence the inconsistent observations of arsenic surface precipitation, since surface precipitation is a slower process than monolayer adsorption via surface complexation⁴²⁴. Bulk precipitation of As(V) or As(III) was not observed in control experiments or in PHREEQC modelling (Figure 6.3).

Table 6.1: Adsorption isotherm parameters. Parameters were calculated using C_e in μM and Q_e and Q_{\max} in $\mu\text{mol mol}^{-2}$ for easier comparison with literature sorbents differing in surface area. Adsorption isotherm parameters were calculated using 7-12 experimental data points, and uncertainties (expressed as one standard deviation, or 1σ) were determined using a nonlinear regression Monte Carlo method⁴²⁵.

Sample	FeOOH	Fe_2O_3	meso-TiO ₂	meso-TiO ₂ /Fe ₂ O ₃
BET-specific surface area ($\text{m}^2 \text{ g}^{-1}$)	127	103	110	100
BJH-specific average pore diameter (nm)	21.2	8.9	7.8	8.6
BJH total pore volume ($\text{cm}^3 \text{ g}^{-1}$)	0.69	0.23	0.22	0.22
Langmuir isotherm, As(V) adsorption				
$K_L (\mu\text{M}^{-1})$	0.961 ± 0.232	0.126 ± 0.030	0.0536 ± 0.009	0.070 ± 0.015
$Q_{\max} (\mu\text{mol m}^{-2})$	1.97 ± 0.08	2.08 ± 0.07	1.21 ± 0.04	1.81 ± 0.05
R^2 (linear form)	1.000	0.999	0.999	0.991
R^2 (C_e vs q_e)	0.623	0.763	0.849	0.654
Q_{\max} (mg g ⁻¹)	18.7 ± 0.8	16.1 ± 0.5	9.62 ± 0.3	13.6 ± 0.4
Freundlich isotherm, As(III) adsorption				
n	5.71 ± 0.28	4.26 ± 0.26	3.61 ± 0.19	3.51 ± 0.11
$K_F (\mu\text{mol m}^{-2} \mu\text{M}^{-1/n})$	1.11 ± 0.08	1.19 ± 0.08	0.49 ± 0.04	0.69 ± 0.03
R^2 (linear form)	0.975	0.988	0.977	0.994
R^2 (C_e vs q_e)	0.907	0.979	0.992	0.996

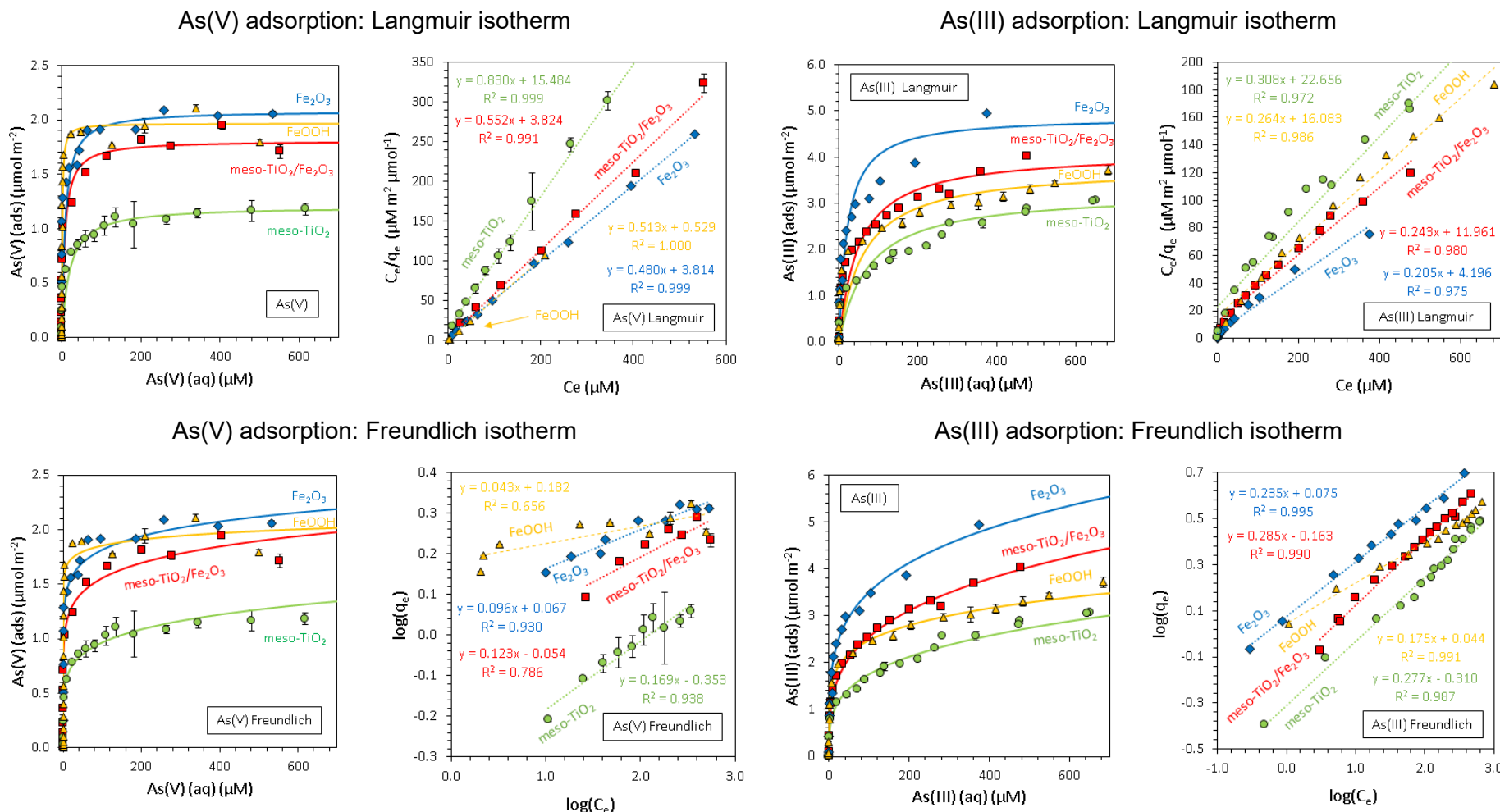


Figure 6.2: Full comparison of As(V) and As(III) adsorption isotherms modelled by the Langmuir and Freundlich models. Experimental conditions were 1 g L⁻¹ mineral, 0.01 M NaCl, pH adjusted to 7.0±0.1, 50 mL total volume. Here we see that As(V) adsorption over these minerals was best described by the Langmuir adsorption isotherm (i.e. monolayer adsorption), whilst As(III) adsorption was best described by the Freundlich adsorption isotherm (i.e. multilayer adsorption). The Langmuir adsorption isotherm failed to fit the adsorption of As(III), whilst the Freundlich adsorption isotherm failed to provide the adsorption plateau observed experimentally at high As(V) concentrations. Shapes indicate experimental points, whilst lines indicate the isotherm model. Shown are Fe₂O₃ (blue diamonds), meso-TiO₂ (green circles), meso-TiO₂/Fe₂O₃ (red squares) and FeOOH (yellow triangles).

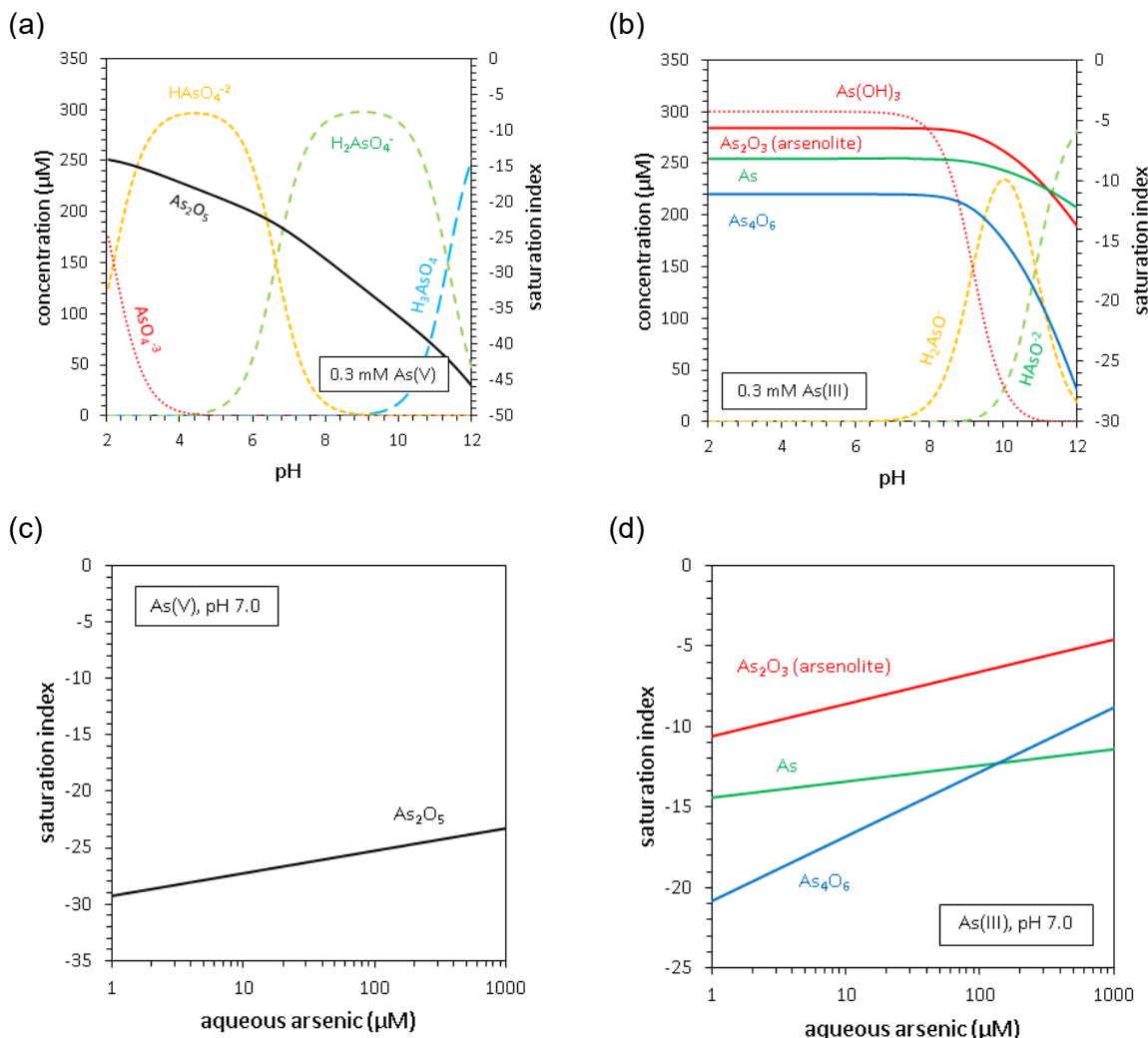


Figure 6.3: Theoretical verification that bulk precipitation did not occur in the adsorption isotherms. Saturation indices were calculated in PHREEQC for (a) As(V) and (b) As(III) pH adsorption edges, and (c) As(V) and (d) As(III) adsorption isotherms. Solid lines denote saturation indices for solid phases, whilst dashed lines denote the concentrations of aqueous arsenic species. The electrolyte was 0.01 M NaCl and the system was modelled in equilibrium with H_2 (g) to achieve a pe of 0 at pH 7, using the LLNL.DAT database. As_4O_6 denotes the cubic arsenolite and monoclinic claudetite As(III) precipitates in the LLNL.DAT database, whilst As denotes the reduced elemental $\text{As}(0)$. Across all conditions in this study, As(III) was closer to precipitation than As(V) but saturation indices never reached zero. The only arsenic-iron precipitate in the LLNL.DAT database is arsenopyrite (FeAsS), which requires the presence of sulphur.

6.2.2.2. Component additivity of arsenic adsorption

A linear combination of meso-TiO₂ and Fe₂O₃ adsorption isotherms, weighted according to material composition at the bulk, near surface and outermost surface was used to give CA predictions for the adsorption of arsenic onto meso-TiO₂/Fe₂O₃ (Equation 6.1). As with surface charge, the most accurate component additive prediction for adsorption of As(V) onto meso-TiO₂/Fe₂O₃ was achieved when using LEIS-weighting for the linear combination of reference samples (Figure 6.4a). The R² values were 0.482, 0.582 and 0.680 for the XRF-, XPS- and LEIS-weighted linear combinations of As(V) Langmuir adsorption isotherms respectively.

However, LEIS-weighting gave the worst CA prediction of the As(III) adsorption isotherm, compared with XPS- and XRF-weighted combinations, overestimating the experimentally observed adsorption (Figure 6.4b). The R² values were 0.976, 0.947 and 0.861 for XRF-, XPS- and LEIS-weighted linear combinations of As(III) Freundlich adsorption isotherms respectively. This effect could be due to differences in surface morphology between the composite and reference samples influencing multilayer sorption, as discussed in section 6.4.3.

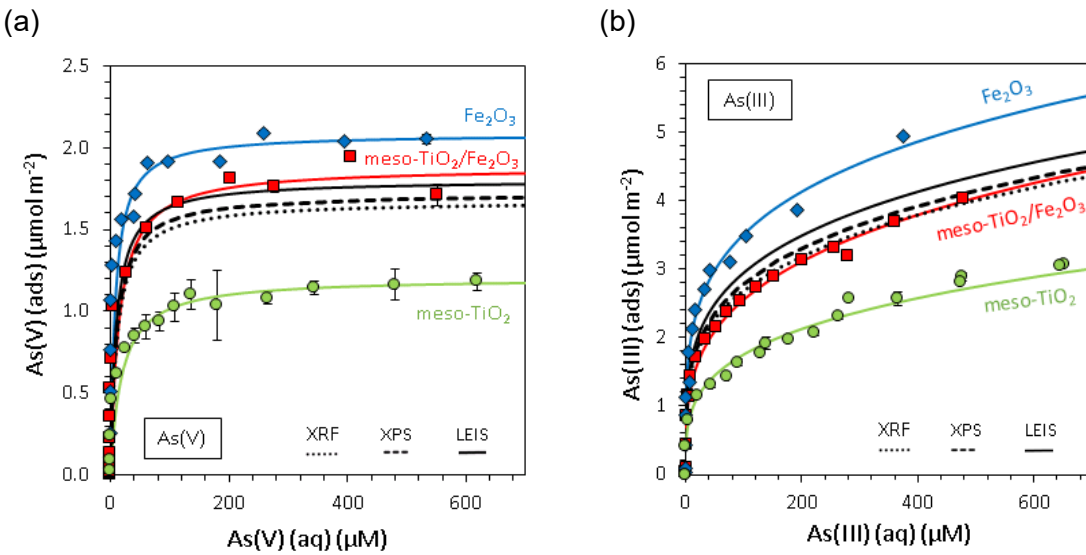


Figure 6.4: The component additivity of arsenic adsorption isotherms. Adsorption isotherms are presented for meso-TiO₂/Fe₂O₃ (red squares), meso-TiO₂ (green circles) and Fe₂O₃ (blue diamonds). Solid coloured lines indicate the results of adsorption isotherm fitting, whilst predictions are shown for the LEIS- (black solid lines), XPS- (dashed lines) and XRF- (dotted lines) weighted linear combination of end-member reference sample isotherms. (a) shows the Langmuir fit for As(V) adsorption, whilst (c) shows the Freundlich fit for As(III) adsorption. All experiments were conducted in 0.01 M NaCl, 1 g L⁻¹ sorbent loading, and pH 7.0 ± 0.1.

6.2.3. Using LEIS to more accurately weight surface components

Unlike monolayer surface protonation and As(V) adsorption reactions, multilayer As(III) adsorption was the only case where using LEIS to weight each component failed to provide the most accurate CA model. Unlike monolayer adsorption, multilayer processes are influenced by sorbent morphology, e.g. pore size and surface roughness^{426 427 428}, and differences between the surface morphology of the reference samples and composite meso-TiO₂/Fe₂O₃ may explain the failure of LEIS to provide the most accurate CA prediction of As(III) adsorption, discussed in section 6.4.3. The improved accuracy using LEIS, in the CA predictions of surface charge and As(V) adsorption, highlights the importance of identifying and quantifying surface coatings. It is likely that in many previous cases where CA models

have failed, a major cause was inappropriate component weighting, such as using mass ratios, and a failure to identify surfaces enriched in certain components.

6.3. Identifying surface complexes for modelling

In this section, evidence was gathered to identify the most important arsenic surface complexes for the SCM, as experimental constraints. As a starting point, X-ray absorption spectroscopy (XAS) data was considered to determine whether the SCM should focus on bidentate or monodentate surface complexes. The majority of spectroscopic studies have concluded that both As(V) and As(III) predominantly form bidentate complexes on titania²³⁹²⁴⁰, hematite²³⁴²³⁵, goethite²³⁶²²⁴²³⁵ and other iron oxides²³⁷²³⁷²³⁵²³⁸. These are typically identified as binuclear corner-sharing complexes, however mononuclear edge-sharing²³⁴²³⁵ and monodentate corner-sharing²²⁴ binding modes are often also said to be present. The prevalence of bidentate complexes on TiO₂ and on iron oxides is further supported by theoretical simulations using density functional theory (DFT)²³⁹²⁴¹, and experimentally by infrared (IR) spectroscopy²⁴²²²⁹²⁴³. The predominance of bidentate complexation over monodentate is not universally supported however, most notably in the study of Loring et al., who through a combination of XAS and IR experiments concluded that As(V) bound to goethite through monodentate complexation²⁴⁴.

Pena et al. used a combination of FTIR and zeta potential measurements as evidence that, unlike aqueous arsenite, bidentate As(III)-TiO₂ surface complexes were deprotonated between pH 5.5 and 9, i.e. the complexes were of the form (>SO)₂AsO⁻, where >S denotes the metal oxide surface²⁴⁰. In this thesis, the suspensions prepared for the adsorption isotherm experiments were also analysed for zeta potential (at pH 7.0 ± 0.1), and dried arsenic-sorbed powders were analysed by ATR-FTIR, to help identify the charge and protonation state of arsenic adsorbed on the mineral samples. Caution must be taken as drying samples can change the binding mode⁴²⁹, however the surface complexes chosen ultimately agreed with the literature²⁴⁰, and with the complexes used in previous SCMs²²⁵²⁴⁵.

6.3.1. Changes in zeta potential as evidence for the charge on arsenic surface complexes

The zeta potential of all samples decreased with increasing adsorption of both As(V) and As(III) (Figure 6.5a, b). However, zeta potential was much more sensitive to As(V) than As(III), with a 4-to-5 times larger decrease in zeta potential for the same increase in surface coverage. Since the maximum negative charge of adsorbed As(V) is -2 (for a monodentate complex), this suggests that complexed As(III) is likely a combination of -1 and neutrally charged species.

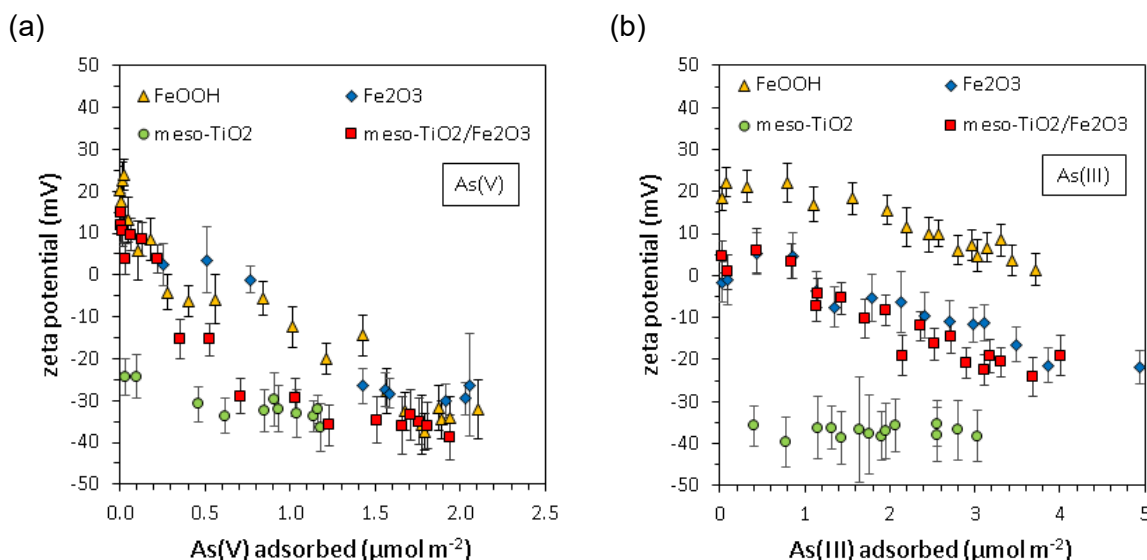


Figure 6.5: The influence of arsenic adsorption on zeta potential. Zeta potential is presented as a function of (a) adsorbed As(V), and (b) adsorbed As(III). Data is presented for FeOOH (yellow triangles), Fe₂O₃ (blue diamonds), meso-TiO₂ (green circles) and meso-TiO₂/Fe₂O₃ (red squares). Experimental conditions were 0.01 M NaCl, 1 g L⁻¹ sorbent, pH 7.0 ± 0.1.

6.3.2. Infrared spectroscopy as evidence for the protonation state of arsenic surface complexes

The infrared absorption peaks that appeared after adsorption of arsenic are reported in Table 6.2. After adsorption of As(III), FeOOH, Fe₂O₃ and meso-TiO₂/Fe₂O₃ all showed new IR peaks corresponding to hydroxyl stretching vibrations between 2850 and 2990 cm⁻¹ (Figure 6.6a). Meso-TiO₂ did not show increased absorption in this region. The presence of O-H stretching vibrations was accompanied by bond deformation modes at 1380-1470, 1100-1255 and 1030-1070 cm⁻¹ (Figure 6.6b). As(V)-sorbed samples showed only the weakest signs of hydroxyl stretching vibrations. These peaks were therefore assigned to AsO-H stretching and

deformation modes from adsorbed As(III). This suggests that As(V) surface complexes were predominantly deprotonated at pH 7. In the literature, hydroxyl stretching peaks at the same wavenumber can be observed for As(V)-sorbed Fe_2O_3 at low pH, indicating protonation of As(V) surface complexes under acidic conditions (see Figure 7c in Wang et al.⁴³⁰).

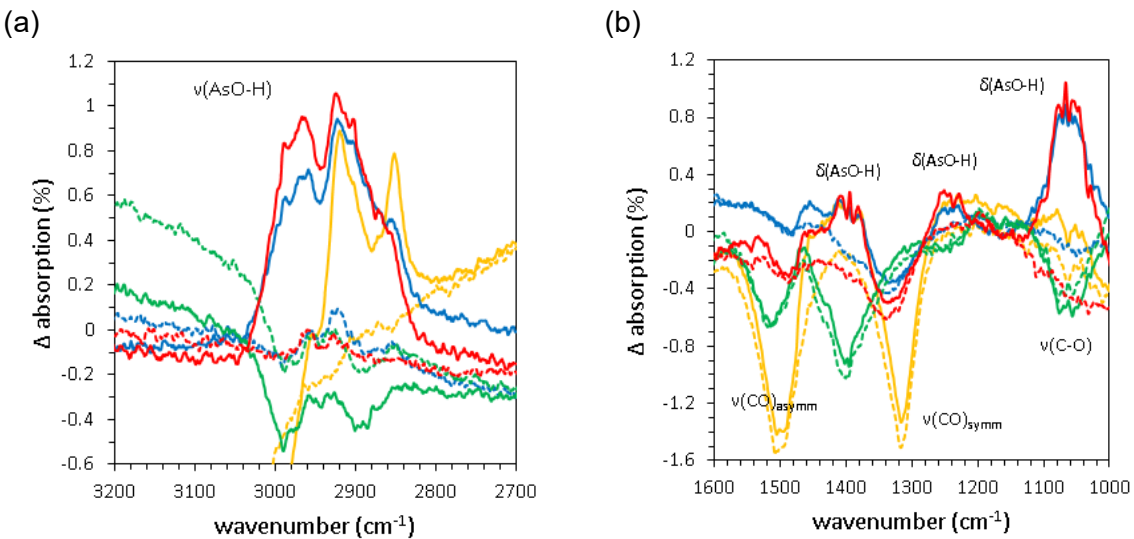


Figure 6.6: The influence of arsenic adsorption on infrared absorption. FTIR spectra are presented after adsorption of As(V) (dashed lines), and As(III) (solid lines). The spectra recorded for each sample before adsorption of arsenic were subtracted from the spectra after adsorption of arsenic to improve peak resolution. Data is presented for FeOOH (yellow), Fe_2O_3 (blue), meso-TiO₂ (green) and meso-TiO₂/Fe₂O₃ (red). Experimental conditions were 0.01 M NaCl, 1 g L⁻¹ sorbent, pH 7.0 ± 0.1.

For a protonated bidentate As(V) surface complex, the As=O bond is strongest, with the highest frequency stretching excitation. In contrast, the As-OH bond is weaker, with lower frequency excitations. As-OM bonds, where M is a metal (such as those found in surface complexes) are intermediate in energy and excitation frequency. Myneni et al., Goldberg and Johnston, Pena et al., have all identified dominant arsenic surface complexes by comparing the position of $v(\text{As-O})$ absorption bands against IR spectra for aqueous arsenic species at different pH, for which the speciation is well known^{431 229 240}. The $v(\text{As-OH})$ stretching region was examined for all samples besides FeOOH, where strong lattice vibrations overlapped with $v(\text{As-OH})$ and prevented analysis.

For As(V), a strong absorption at ~805-808 cm^{-1} was observed corresponding to $v(\text{As-OM})$, i.e. where the oxygen is complexed to the surface (Figure 6.7a)^{431 240}. Since no As(V) hydroxyl vibrations were detected, any monodentate surface complexes should be deprotonated and of the form $>\text{SOAsO}_3^{2-}$. The delocalised charge across three As-O bonds lowers the excitation frequency for uncomplexed As-O, and as such the highest frequency band should be positioned at <855 cm^{-1} ⁴³¹. However, experimental spectra showed that the $v(\text{As-O})$ absorption band extended to >890 cm^{-1} corresponding to electron delocalisation across only

two As-O bonds. Two uncomplexed oxygen atoms and an absence of As hydroxyls suggests the presence of bidentate complexes of the form $(>\text{SO})_2\text{AsO}_2^-$, in agreement with the XAS literature. In the case of meso-TiO₂, increased absorption was also observed at 690 cm⁻¹, corresponding to $\nu(\text{As-OH})$ vibrations (however, due to the absence of $\nu(\text{AsO-H})$ vibrations this observation is inconclusive). Bidentate $(>\text{SO})_2\text{AsO}_2^-$ was subsequently chosen as the major As(V) surface complex at pH 7, as a modelling constraint.

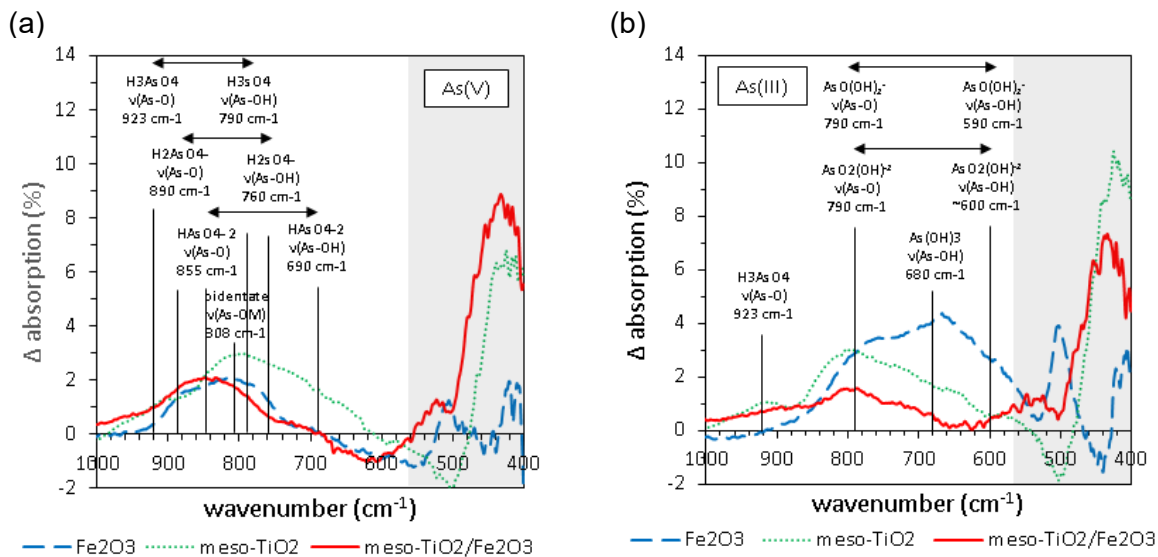


Figure 6.7: Identifying appropriate surface complexes: FTIR spectra in the $\nu(\text{As-O})$ stretching mode region, after adsorption of (a) As(V), and (b) As(III). Spectra recorded for each sample before adsorption of arsenic were subtracted from the post-adsorption spectra to improve peak resolution. Data is presented for Fe₂O₃ (blue dashed lines), meso-TiO₂ (green dotted lines) and meso-TiO₂/Fe₂O₃ (red solid lines). The area shaded grey indicates where the intense M-O lattice vibrations made the background subtraction unreliable. Spectra for FeOOH are not shown, as the lattice vibrations overlapped with $\nu(\text{As-O})$ stretching modes which were too strong to perform a background subtraction. Experimental conditions were 0.01 M NaCl, 1 g L⁻¹ sorbent, pH 7.0 ± 0.1.

For As(III), all three samples showed increased absorption at 790 cm⁻¹ corresponding to uncomplexed oxygen (Figure 6.7b) ⁴³². This reinforces the evidence from zeta potential measurements that the As(III) surface complexes are negatively charged. The strong absorption at 680 cm⁻¹ for Fe₂O₃ corresponds to $\nu(\text{As-OH})$, and could either indicate a significant amount of protonated surface complexes, or a significant amount of surface precipitate. Meso-TiO₂ showed a small peak at 920 cm⁻¹, corresponding to uncomplexed As(V) $\nu(\text{As-O})$ stretching vibrations. This suggests that some As(III) had been oxidised, which is not unexpected due to the photocatalytic activity of TiO₂. No insight into the coordination order of As(III) (i.e. monodentate versus bidentate) could be gained from the ATR-FTIR data. As zeta potential data suggests a mix of -1 and neutrally charged complexes, and the literature identifies bidentate binding modes, a mixture of $(>\text{SO})_2\text{AsO}_2^-$ and $(>\text{SO})_2\text{AsOH}$ were chosen as the major As(III) surface complexes at pH 7, as modelling constraints. The following section discusses the final selection of surface complexes used in the SCM, as well as the equations relating the hypothetical 1.0 M equilibrium constants (optimised in FITEQL 2.0) to the ETLM site-occupancy standard-state constants.

6.3.3. The surface complexation reactions modelled

The surface complexes identified as the most major As(V) and As(III) species are presented in Figure 6.8, in the non-shaded cells. These complexes were used as constraints, ensuring that the SCM fits to experimental pH adsorption edges featured these surface complexes as the dominant forms of adsorbed arsenic at pH 7. As the speciation of adsorbed arsenic changes with pH, additional surface complexes were required to fit the experimental pH adsorption edges. These additional surface complexes were chosen from those successfully used by Kanematsu et al. in the extended triple layer modelling of the adsorption of arsenic onto Bayoxide E33²²⁵. These complexes are shown in the grey-shaded cells. pH edges were constrained by ensuring that these additional complexes were minority species at pH 7. $\Delta\psi$ indicates the change in surface potential upon the formation of each surface complex, where ψ_0 and ψ_β denote the surface potential at the 0-plane and β -plane respectively, within the extended triple layer model.

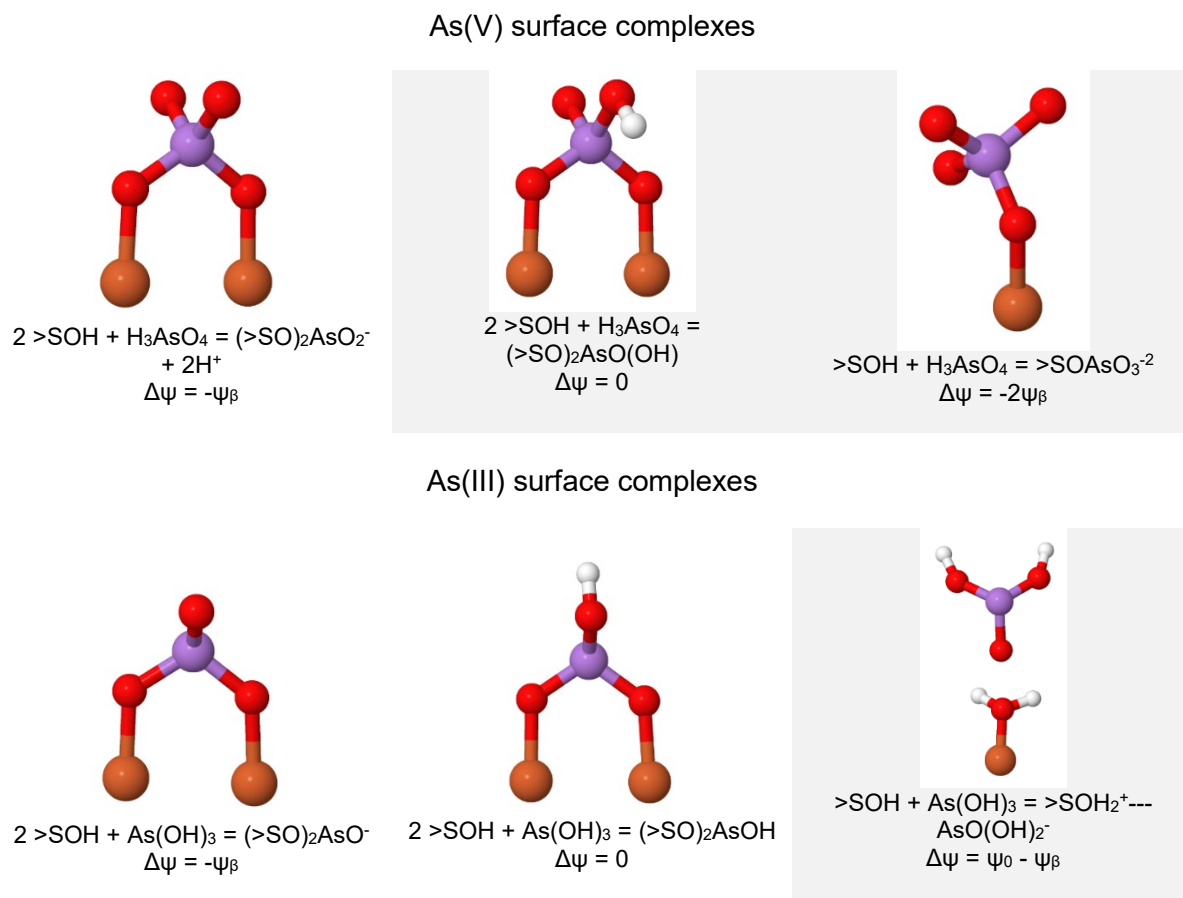


Figure 6.8: Surface complexes and corresponding reactions modelled (sketched in Jmol). Colours correspond to arsenic (purple), oxygen (red), hydrogen (white) and titanium/iron (brown). Top: As(V) surface complexes, bottom: As(III) surface complexes, including the H-bonded ‘outer-sphere’ complex. The principal species identified using zeta potential measurements and ATR-FTIR in the main text are shown with a white background, whilst the additional surface complexes added in accordance with the literature and used to fit the pH adsorption edges at low and high pH are highlighted in grey. (Neither of the protonated forms of bidentate As(V) nor As(III) surface complexes were used for modelling adsorption of arsenic onto meso-TiO₂ as they gave no improvement to the fit).

Table 6.2: The assignment of new IR peaks after adsorption of arsenic. The cell shading in the first two columns are used to group together peaks assigned to similar vibration modes. Green and red fonts denote samples containing As(V) and As(III) respectively. In the literature column w, vw, s and vs denote weak, very weak, strong and very strong peaks respectively. Negatively charged arsenic oxyanion are labelled “-ve”. Antisymmetric vibrations are labelled “as”. Bidentate binuclear surface complexes are labelled “BB”.

Vibration		Wavenumber (cm ⁻¹)						
		Literature			Peaks observed experimentally			
Label	Description	Adsorbed As	Mineralised/compound As	Aqueous As	FeOOH	Meso-TiO ₂ /Fe ₂ O ₃	Meso-TiO ₂	Meso-TiO ₂ /Fe ₂ O ₃
v(O-H)	O-H stretch These high wavenumber peaks correspond to hydroxyls without H-bonding. They don't necessarily involve arsenic	3671, 3618, 3542 ettringite ⁴³³ 3678, 3602 ferrihydrite ²⁴¹ 3708, 3713, 3596 ferrihydrite ²⁴¹	3650 legrandite ⁴³⁴ 3484 Na ₂ AsO _{4.7} H ₂ O ⁴³⁵	3520 As(OH) ₃ ⁴³⁶	-	3661 As(III) and As(V)	-	3662 As(III) only
v(O-H)	O-H stretch	3350, 3011 ettringite ⁴³³	3217 Na ₂ AsO _{4.7} H ₂ O ⁴³⁵	-	-	-	-	-
v(AsO-H)	AsO-H stretch	3052, 3027 As(III) ²⁴¹ 3010 As(V) ²⁴¹	2955 vladimirite ⁴³⁷	3000 HAsO ₄ ²⁻ ⁴³³	2990 As(III) only	-	-	-
v(AsO-H)	AsO-H stretch	-	2950 As ₂ O ₃ ⁴³⁸	-	2958 As(III) only	2964 As(III) and As(V)	2955 As(III) and As(V)	2970 As(III) only
v(AsO-H)	AsO-H stretch	2873 As(III) ²⁴¹	2900 adamite ⁴³⁴	-	2920 As(III) only	2916 As(III) and As(V)	2915 As(III) and As(V)	2920 As(III) only
v(AsO-H)	AsO-H stretch	2855 As(III) ²⁴¹	2880 As ₂ O ₃ ⁴³⁸	-	2851 As(III) only	2850 As(III) only	2850 As(III) and As(V)	2861 As(III) only
v(O-H)	H-bonded OH in AsO ₃ OH or H ₂ O ⁴³⁷	-	2337 Na ₂ AsO _{4.7} H ₂ O ⁴³⁵ 2342, 2256 vladimirite ⁴³⁷	-	-	(hint of a peak already)	(already a peak here)	(already a peak here)
δ(H ₂ O)	Deformation of water	-	1690, 1647 Na ₂ AsO _{4.7} H ₂ O ⁴³⁵ 1679 NaAsO ₂ ⁴³⁵ 1650 legrandite, adamite, austinite ⁴³⁴ 1689, 1658, 1664 pharmacolite, vladimirite ⁴³⁷	-	C癱ides with the mineral (O-H) deformation peak already present			
δ(H ₂ O)		-	1625, 1566 pharmacolite, vladimirite ⁴³⁷	-	-	1526 As(III) and As(V)	1575 As(V) only	1561, 1540 vw As(III)
δ(AsO-H)	As-O-H deformation	-	1442 NaAsO ₂ ⁴³⁵	-	1462 As(III) only	1461 As(III) and As(V)	1463 As(III) and As(V)	1466 As(III) only
δ(AsO-H)	As-O-H deformation	-	1409 NaAsO ₂ ⁴³⁵ 1423 vladimirite ⁴³⁷	-	1409 As(III) only	1405 As(III) only	-	1406 As(III) only
δ(AsO-H)	As-O-H deformation	1400 CO ₃ ²⁻ v3 asymmetric ⁴⁰²	1400 As ₂ O ₃ ⁴³⁸	-	1394 As(III) only	1394 As(III) and As(V)	1394 As(III) only	1394 As(III) only
δ(AsO-H)	As-O-H deformation	1361 CO ₃ ²⁻ 1373 SO-H bending ⁴³⁹ 1381 As(III) ⁴⁴⁰	1375 As ₂ O ₃ ⁴³⁸	1375 H ₃ AsO ₃ ⁴⁴¹	1378 As(III) only	1380 As(III) only	1366 As(III) and As(V)	1382 As(III) only
δ(AsOH)	As-O-H deformation	-	1283 Na ₂ AsO _{4.7} H ₂ O ⁴³⁵ 1303 vladimirite ⁴³⁷ 1253 picropharmacolite ⁴³⁷	1250 As(OH) ₃ ⁴³⁶	1254 As(III) only	1254 As(III) 1243 As(V)	-	1255 As(III) only

Vibration		Wavenumber (cm ⁻¹)						
		Literature			Peaks observed experimentally			
δ(AsOH)	As-O-H deformation	1230 HCO ₃ ⁻ bound to dry oxides ⁴⁰²	-	-	1230 As(III) only	1222 As(III) 1214 As(V)	-	1230 As(III) 1212 As(V) only
δ(AsOH)	As-O-H deformation	-	1179 Na ₂ HAsO ₄ .7H ₂ O ⁴³⁵ 1142, 1175 pharmacolite, picropharmacolite ⁴³⁷	-	-	1152 As(III) 1184 As(V)	1198-1096 As(III) and As(V)	-
δ(AsOH)	As-O-H deformation	-	1117, 1101 pharmacolite, vladimirite ⁴³⁷	-	1074 As(III) only	1070 As(III) only	-	1074 As(III) only
δ(AsOH)	As-O-H deformation	-	-	-	1066 As(III) only	-	-	1065 As(III) only
δ(AsOH)	As-O-H deformation	-	1040 As ₂ O ₃ ⁴³⁸ 1050 legrandite ⁴³⁴ 1040 vv As ₂ O ₃ ⁴³⁶ 1040 As ₄ O ₆ ⁴⁴²	-	1048 As(III) only	1045 As(III) only	-	1051 As(III) only
δ(AsOH)	As-O-H deformation	1037, 1008 AlO ₂ -AsO ₂ (H ₂ O) ₄ v(As-O) ⁴³¹	1030 arsenate mineral ⁴³⁴ 969 Na ₂ HAsO ₄ .7H ₂ O ⁴³⁵ 1015 picropharmacolite ⁴³⁷	1041 H ₂ AsO ₄ ⁻ v(As-O) ⁴³¹	-	-	-	1028 As(III) only
v(As-O)	-	947 v(As-O) ettringite (-ve) ⁴³³	-	-	-	-	-	-
v(As-O)	Stretching vibration of As(V) with one uncoordinated oxygen	900 v(As-O) ettringite (-ve) ⁴³³	-	923 H ₃ AsO ₄ ⁻ v(As-O) ⁴³¹	-	-	910 As(V) 920 As(III)	-
v(As-O)	Stretching vibration of As(V) with two uncoordinated oxygens	884 v(As-O) ferrihydrite (BB protonated) ⁴³²	886 (as) ceruleite v(As-O) 4 ⁴⁴³	915-875 (as, s) H ₂ AsO ₄ ⁻ v(As-O) ⁴³¹	-	890 As(V) only	-	(900-860) As(V) only
v(As-O)	Stretching vibration of As(V) with three uncoordinated oxygens	860 v(As-OFe) ferrihydrite ⁴³² (BB deprotonated) 872 v(As-OFe) siderite ⁴⁰⁷	869, 836 (as) tsumcorite v(As-O) ⁴⁴⁴ 860 adamite v(As-O) ⁴³⁴ 845 austinite v(As-O) ⁴³⁴	866-838 (as, s) HAsO ₄ ⁻² v(As-O) ⁴³¹	-	-	-	860 As(V) only
v(As-OM)	v(As-OM) for adsorbed As(V)	830 (TiO ₂) v(As-O) (BB -ve) ²⁴⁰ 842 v(As-O) (ettringite) (-ve) ⁴³³ 830 v(As-OFe) ferrihydrite (BB protonated) ⁴³²	827 (as) ceruleite ⁴⁴³ 825 legrandite v(As-O) ⁴³⁴	-	830 As(III) and As(V)	-	-	-
v(As-OM)	(also present for aqueous As(V) with four uncoordinated oxygens)	808 TiO ₂ v(As-OTi) (BB -ve) ²⁴⁰ 808, 787 v(As-OCa) Ettringite (-ve) ⁴³³ 804 v(As-OFe) ferrihydrite (BB -ve) ⁴³²	787 (as) ceruleite v(As-O) ⁴⁴³ 790 legrandite v(As-O) ⁴³⁴ 800, 820 adamite v(As-O) ⁴³⁴ 800 austinite v(As-O) ⁴³⁴ 803 As ₂ O ₃ ⁴³⁶ v(As-O)	818-791 (s, as) AsO ₄ ⁻³ v(As-O) ⁴³¹ 808-769 (s) H ₂ AsO ₄ ⁻ v(As-OH) ⁴³¹	-	805 As(V) only	805 As(V) 800 As(III)	(860-720) As(V) only
v(As-OH) v(As-O)	AsO-H stretch for As(V) As-O ⁻ stretch for As(III)	787 v(As-OFe) siderite ⁴⁰⁷ 780 v(As-O) TiO ₂ (BB -ve) ²⁴⁰	774, 747 NaAsO ₂ v(As-O) ⁴³⁵	765-745 (as, s) H ₂ AsO ₄ ⁻ v(As-OH) ⁴³¹ 790 AsO(OH) ⁻² v(As-O) ⁴³⁶	770 As(III) and As(V)	770 As(III) only	800-620 As(III) and As(V)	790 As(III) only

Vibration		Wavenumber (cm ⁻¹)						
		Literature			Peaks observed experimentally			
v(As-OH)	As-OM stretch for adsorbed As(III) will lie between v(As-O ⁺) and v(As-OH) excitation frequencies	-	-	707 HAsO ₄ ²⁻ v(As-OH) ⁴³¹ 710 (s) As(OH) ₃ v(As-OH) ⁴³⁶ 752 (s) AsO ₃ ⁻ v(As-O) ⁴³⁶	-	-	800-620 As(III) only	-
v(As-OH)	-	-	730 legrandite v(As-OH) ⁴³⁴	690 As(OH) ₃ v(As-OH) ⁴³⁶ 655 (s) As(OH) ₃ v(As-OH) ⁴³⁶ 680 (s) AsO ₃ ⁻ v(As-O) ⁴³⁶	650 As(III) and As(V)	660 As(III) only	800-620 As(III) only	-
v(As-OH)	-	-	-	610,570 (as, s) AsO(OH) ²⁻ v(As-OH) ⁴³⁶	-	-	-	-
v(As-OH)	As-OH symmetric stretch	-	-	540, 570 (H ₂ AsO ₃ ²⁻) ⁴⁴⁵	Unresolved due to interference from lattice vibrations			
v(M-O)	M-O bond in arsenate mineral	-	520 legrandite ⁴³⁴ 515, 535 adamite ⁴³⁴ 525 austenite ⁴³⁴ 555 As ₄ O ₆ ⁴⁴²	-				
δ(As-O)	As-O bend	-	474-401 tsumcorite ⁴⁴⁴ 349 As ₄ O ₆ ⁴⁴²	-				
δ(As-O)	As-O bend	-	370-294 tsumcorite ⁴⁴⁴	-				

6.4. Surface Complexation Modelling

A range of SCMs exist, primarily differing in their description of the electrical double layer. Constant capacitance (CCM), diffuse double layer (DDL), basic stern (BSL) and triple layer models (TLM) differ in (a) how many planes of charge are considered, (b) whether outer-sphere complexation is included as well as inner-sphere, and (c) in the incorporation of electrolyte adsorption. In this thesis, the extended triple layer model (ETLM) was chosen. This surface complexation model was developed principally by Sverjensky and Fukushi^{290 245}. The ETLM is consistent with spectroscopic data⁴⁴⁶ and provides very good fits for the adsorption of arsenic onto mineral oxides including Bayoxide E33, the commercial goethite (FeOOH) arsenic sorbent²²⁵.

The ETLM differs from other triple layer models since (i) the negative charge of inner-sphere arsenic complexes is located in the β -plane⁴⁴⁷, and (ii) the site-occupancy standard state is introduced²⁹¹. In the ETLM, the negative charge of inner-sphere deprotonated arsenic surface complexes is distributed to the β -plane, providing better fits to experimental data than when this charge is located in the 0-plane²³⁴. This has been assigned to either charge distribution²³⁴ or the release of water dipoles from the adsorption site⁴⁴⁷. With the ETLM site-occupancy standard state, surface complexation constants are normalised to account for differences in the pzc, surface area, and site density across the literature, with the aim of improving the cross-compatibility of published data⁴⁴⁶. Whilst SCM equations typically take equilibrium constants in the hypothetical 1.0 M standard state, the ETLM site-occupancy standard state re-normalises equilibrium constants for a hypothetical sorbent with 10 sites nm^{-2} and 10 $\text{m}^2 \text{g}^{-1}$ (arbitrarily chosen)⁴⁴⁶. The ETLM is claimed to be more spectroscopically consistent than the CD-MUSIC model (another contemporary TLM), as the ETLM produces the experimentally observed influence of ionic strength upon the distribution between inner and outer-sphere complexes⁴⁴⁷. The authors also comment that the ETLM has fewer fitting parameters than the CD-MUSIC model, given that the ETLM does not have a charge splitting factor⁴⁴⁷.

Surface complexation constants for the ETLM were obtained following the method used by Kanematsu et al. (2010, discussed within their supplementary information⁸⁹). In this method (i) the site density of each mineral (surface hydroxyls per nanometre square) is chosen from the literature, (ii) surface acidity constants are predicted using Sverjensky's empirical formula²⁸⁸, (iii) electrolyte adsorption constants (and the inner-sphere capacitance, C_1) are determined by fitting potentiometric titration data, and (iv) arsenic surface complexation constants are determined by fitting pH adsorption edges^{284 89}. The model was then validated by predicting unseen experimental adsorption isotherms.

Table 6.3: All adsorption reactions modelled in this work, and equations governing the conversion of equilibrium constants between the site-occupancy standard stand at the 1.0 M hypothetical standard state. θ denotes equilibrium constants for the site-occupancy standard state, and 0 denotes the hypothetical 1.0 M standard state equilibrium constants entered into FITEQL²⁹¹.

Label	Reaction	$\Delta\psi$	Conversion between standard states
Surface acidity			
K ₁	$>\text{SOH} + \text{H}^+ \rightleftharpoons >\text{SOH}_2^+$	+ ψ_0	$\log K\theta 1 = \text{pH}_{\text{pzc}} - \Delta pK\theta/2$ $\log K01 = \log K\theta 1 - \log(N_S A_S / N^\ddagger A^\ddagger)$
K ₂	$>\text{SOH} \rightleftharpoons >\text{SO}^- + \text{H}^+$	- ψ_0	$\log K\theta 2 = \text{pH}_{\text{pzc}} + \Delta pK\theta/2$ $\log K01 = \log K\theta 1 - \log(N_S A_S / N^\ddagger A^\ddagger)$
Electrolyte adsorption			
K _M	$>\text{SOH} + \text{Na}^+ \rightleftharpoons >\text{SO}^- - \text{Na}^+ + \text{H}^+$	- $\psi_0 + \psi_\beta$	$\log K\theta M = \log K0M + \text{pH}_{\text{pzc}} + \Delta pK\theta/2 + \log(N_S A_S / N^\ddagger A^\ddagger)$
K _L	$>\text{SOH} + \text{H}^+ + \text{Cl}^- \rightleftharpoons >\text{SOH}_2^+ - \text{Cl}^-$	$\psi_0 - \psi_\beta$	$\log K\theta L = \log K0L - \text{pH}_{\text{pzc}} + \Delta pK\theta/2 + \log(N_S A_S / N^\ddagger A^\ddagger)$
As(V) adsorption			
K _{(>SO)2AsO2-}	$2>\text{SOH} + \text{H}_3\text{AsO}_4 \rightleftharpoons (>\text{SO})_2\text{AsO}_2^- + \text{H}^+ + 2\text{H}_2\text{O}$	- ψ_β	$\log K\theta = \log K0 - 2\text{pH}_{\text{pzc}} + \Delta pK\theta + \log((N_S A_S)^2 C_S / N^\ddagger A^\ddagger)$
K _{(>SO)2AsO2H}	$2>\text{SOH} + \text{H}_3\text{AsO}_4 \rightleftharpoons (>\text{SO})_2\text{AsO}_2\text{H} + 2\text{H}_2\text{O}$	0	$\log K\theta = \log K0 - 2\text{pH}_{\text{pzc}} + \Delta pK\theta + \log((N_S A_S)^2 C_S / N^\ddagger A^\ddagger)$
K _{>SOAsO3-2}	$>\text{SOH} + \text{H}_3\text{AsO}_4 \rightleftharpoons >\text{SOAsO}_3^{2-} + 2\text{H}^+ + \text{H}_2\text{O}$	-2 ψ_β	$\log K\theta = \log K0 - \text{pH}_{\text{pzc}} + \Delta pK\theta/2 + \log(N_S A_S / N^\ddagger A^\ddagger)$
As(III) adsorption and surface precipitation			
K _{(>SO)2AsO-}	$2>\text{SOH} + \text{As(OH)}_3 \rightleftharpoons (>\text{SO})_2\text{AsO}^- + \text{H}^+ + 2\text{H}_2\text{O}$	- ψ_β	$\log K\theta = \log K0 - 2\text{pH}_{\text{pzc}} + \Delta pK\theta + \log((N_S A_S)^2 C_S / N^\ddagger A^\ddagger)$
K _{(>SO)2AsOH}	$2>\text{SOH} + \text{As(OH)}_3 \rightleftharpoons (>\text{SO})_2\text{AsOH} + 2\text{H}_2\text{O}$	0	$\log K\theta = \log K0 - 2\text{pH}_{\text{pzc}} + \Delta pK\theta + \log((N_S A_S)^2 C_S / N^\ddagger A^\ddagger)$
K _{>SOH2+-AsO(OH)2-}	$>\text{SOH} + \text{As(OH)}_3 \rightleftharpoons >\text{SOH}_2^+ - \text{AsO(OH)}_2^-$	+ $\psi_0 . \psi_\beta$	$\log K\theta = \log K0 - \log(N_S A_S / N^\ddagger A^\ddagger)$
K _{ppt}	$(>\text{SO})_2\text{AsOX} + \text{As(OH)}_3 \text{ (aq)} \rightleftharpoons \frac{1}{2} \text{As}_2\text{O}_3 \text{ (s)} + (>\text{SO})_2\text{AsOX} + 3/2 \text{ H}_2\text{O} \text{ (l)}$	0	-

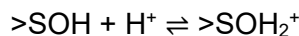
All of the adsorption reactions modelled, and the equations governing the conversion between the site-occupancy standard state and the 1.0 M hypothetical standard state, are presented in Table 6.3.

6.4.1. Modelling surface charge using potentiometric titrations

Since Fe_2O_3 showed a maximum As(V) adsorption capacity similar to that of FeOOH (when normalised to surface area), the site density of the iron oxides was set to 4.0 sites nm^{-2} as per a previous study on Bayoxide E33²²⁵, and 3.0 sites nm^{-2} was chosen for TiO_2 ²⁸⁹. The outer capacitance (C_2) was set to 0.2 F m^{-2} ^{291 288}. The difference between acidity constants ($\log K_{01}$ and $\log K_{02}$), termed ΔpK_n^θ , was set at 5.6 for the iron oxides^{89 291} and 6.3 for TiO_2 ^{448 291} as in previous studies, with this parameter calculated from analysis of titration data and crystal chemistry and Born solvation theory^{449 291}.

Acidity constants (K_0) for the surface reactions were calculated as follows:

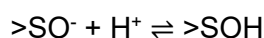
Equation 6.2



$$\log K_{01} = \text{pH}_{\text{pzc}} - \frac{\Delta pK_n^\theta}{2}$$

$$\log K_{01} = \log K_{01} - \log \left(\frac{N_S A_S}{N^\ddagger A^\ddagger} \right)$$

Equation 6.3



$$\log K_{02} = \text{pH}_{\text{pzc}} + \frac{\Delta pK_n^\theta}{2}$$

$$\log K_{02} = \log K_{02} + \log \left(\frac{N_S A_S}{N^\ddagger A^\ddagger} \right)$$

where $>\text{SOH}$ denotes a surface hydroxyl, pH_{pzc} is the point of zero charge (set as pzse), K_0 denotes equilibrium constants for the site-occupancy standard state, and K_0 denotes the hypothetical 1.0 M standard state equilibrium constants entered into FITEQL²⁹¹. N_S and A_S are the site densities (nm^{-2}) and BET-specific surface areas ($\text{m}^2 \text{ g}^{-1}$) used in FITEQL, whilst N^\ddagger and A^\ddagger refer to the site density and surface area of the site-occupancy standard state (10 sites nm^{-2} and 10 $\text{m}^2 \text{ g}^{-1}$)²⁹¹.

Surface charge parameters (inner capacitance, C₁, and electrolyte adsorption constants) were determined by optimising the SCM to potentiometric titration data using FITEQL. Titrations were ell described by the optimised ETLM for the iron oxides (Figure 6.9a, b). The model provided a worse fit for meso-TiO₂, owing to some curvature in the experimental data, most notably at 0.1 M NaCl (Figure 6.9c).

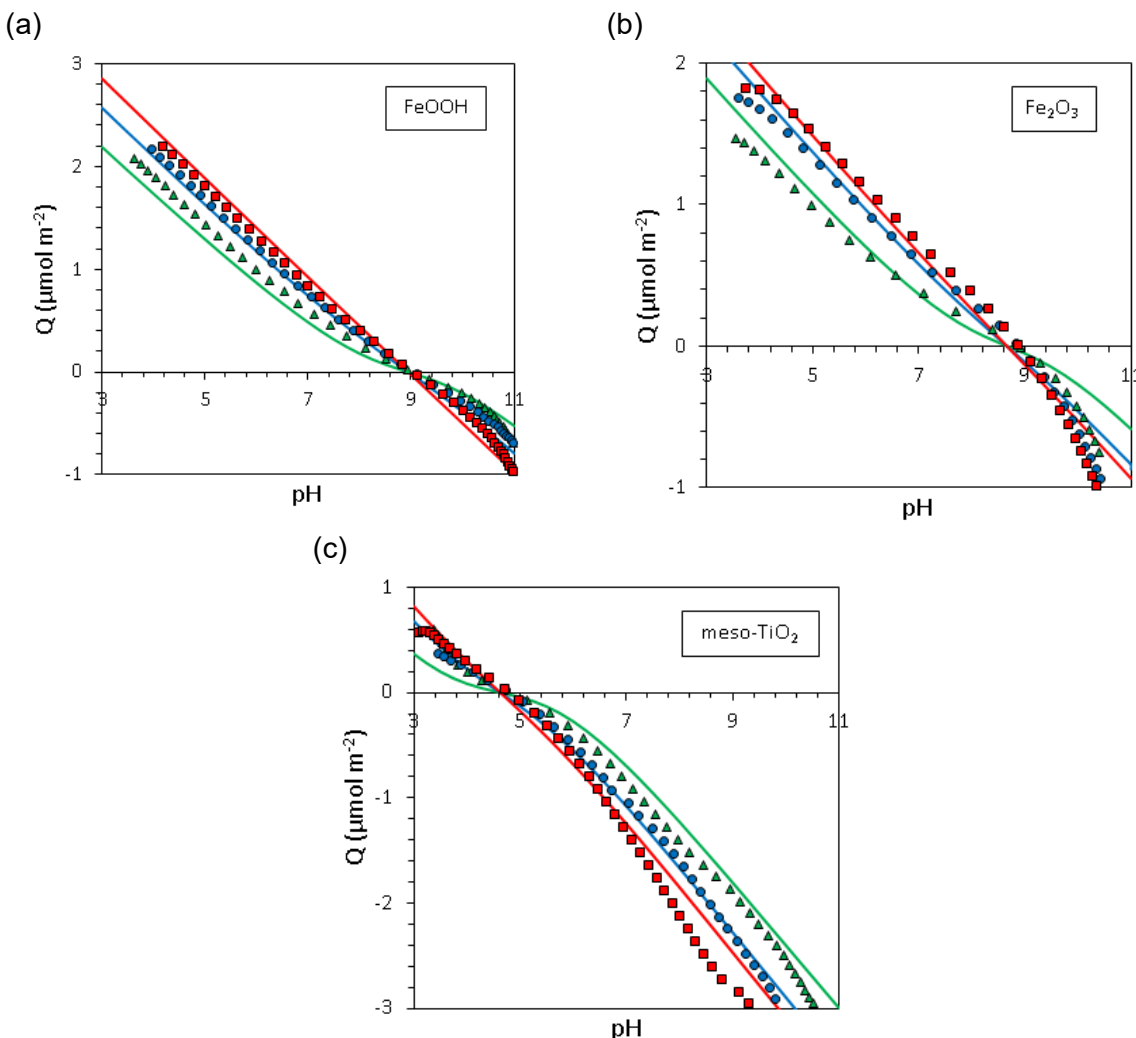


Figure 6.9: ETLM parameter determination using potentiometric titration surface charge curves. The modelled titration curves in 0.1 M NaCl (red squares), 0.05 M NaCl (blue circles) and 0.01 M NaCl (green triangles) are presented for (a) FeOOH, (b) Fe₂O₃, and (c) meso-TiO₂. Lines indicate the fitted SCM (using equilibrium constants averaged from the optimised fit of each of the three titration curves). Experimental conditions were 1 g L⁻¹ sorbent, and only forwards titrations with NaOH were used.

Surface charge titration curves were best modelled with C₁ set to 0.9 F m⁻² for FeOOH (Figure 6.10a) and 0.8 F m⁻² for Fe₂O₃ (Figure 6.10b). These are close to the 1.0 F m⁻² and determined by Kanematsu et al. (FeOOH in 0.01 to 0.1 M NaNO₃) ⁸⁹ and the 0.9 F m⁻² predicted by Sverjensky (Fe₂O₃ in NaCl) ²⁹¹ respectively. Using the 0.01 M NaCl titration, meso-TiO₂ was modelled best with 1.3 F m⁻², which is close to the 1.31 F m⁻² for TiO₂ in (0.01 M NaCl) determined by Sverjensky et al. ⁴⁵⁰ and 1.2 F m⁻² for rutile (in 0.01-0.1 M NaCl) determined by Jonsson et al. ⁴⁴⁸ (Figure 6.10c-d).

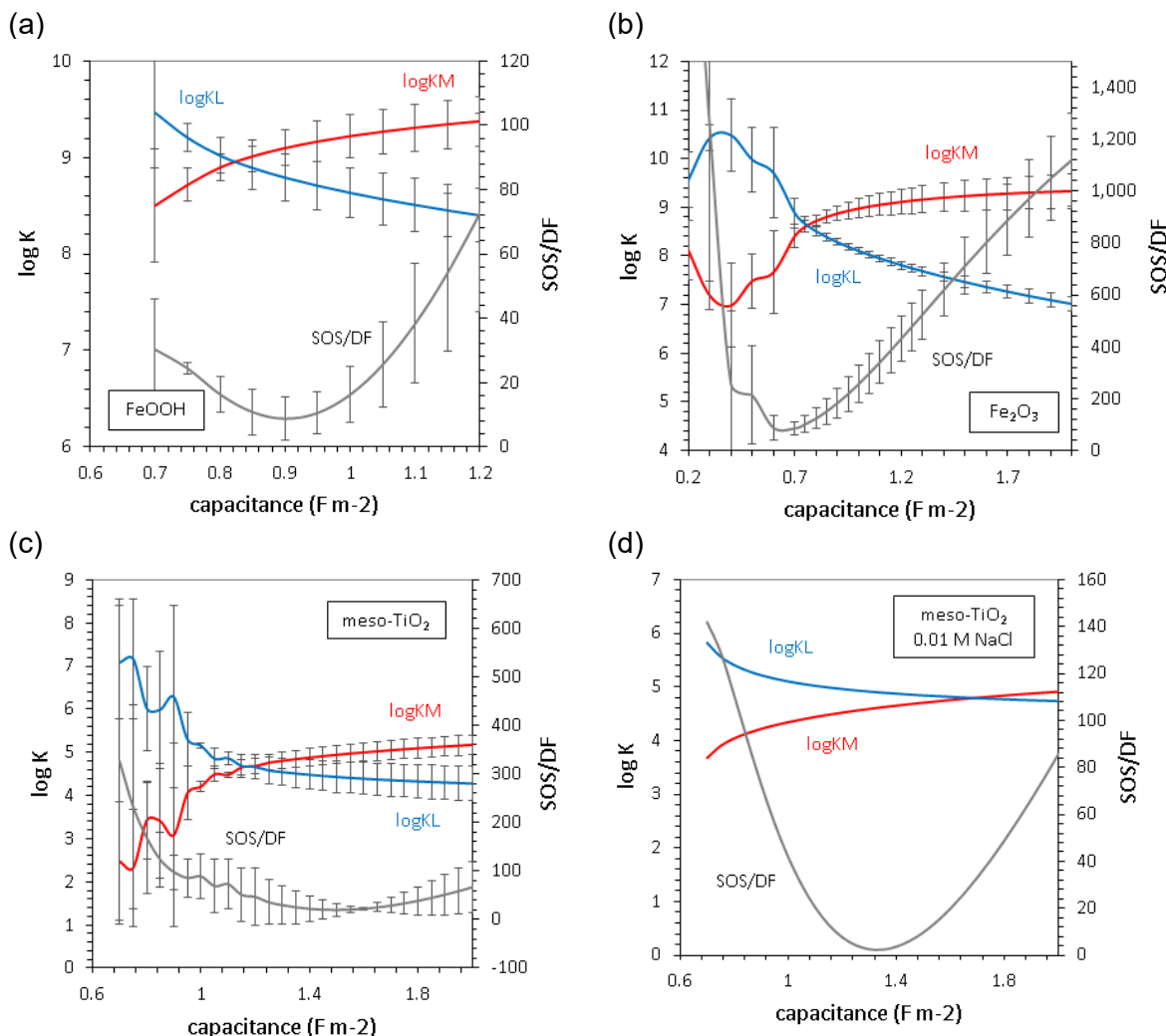


Figure 6.10: Determination of C_1 and optimisation of $\log K_{0M}$ and $\log K_{0L}$ for (a) FeOOH , (b) Fe_2O_3 , and (c) meso- TiO_2 . Lines plotted show post-optimisation values for $-\log K_{0M}$ (red), $\log K_{0L}$ (blue) and the error function $V(Y)$ (SOS/DF) as determined by FITEQL (grey). Titrations of meso- TiO_2 at 0.01, 0.05 and 0.1 M didn't give a clear optimal inner capacitance, and 1.6 F m^{-2} is very high compared to the literature. For meso- TiO_2 the inner capacitance was set to 1.3 F m^{-2} as this gave a very good fit for the 0.01 M NaCl titration (d). Error bars indicate the standard deviation in results obtained from fitting titration curves at three different ionic strengths.

6.4.2. Modelling arsenic surface complexation with pH adsorption edges

Surface complexation constants were determined by fitting pH adsorption edges, with values reported in Table 6.4. The experimental FeOOH pH adsorption edge was described well by the optimised ETLM (Figure 6.11a). As(V) adsorption was greatest at acidic pH, owing both (a) to the electrostatic attraction between the positive mineral surface and negative As(V) oxyanion and (b) to the abundance of protons needed to form bidentate $(>\text{SO})_2\text{HAsO}_2$ and $(>\text{SO})_2\text{AsO}_2^-$ from H_2AsO_4^- and HAsO_4^{2-} . Fe_2O_3 gave similar results, with the experimental data fit very well above pH 4 (Figure 6.11b). Between pH 3 and 4, the high removal of As(V) by Fe_2O_3 observed (up to 99%) could not be described by the ETLM. This discrepancy is possibly

due to As(V) surface precipitation at acidic pH, as discussed in section 6.2.2.1. Compared with FeOOH, the $(>\text{SO})_2\text{HAsO}_2$ complex was more significant and $>\text{SOAsO}_3^{2-}$ was less significant when fitting the Fe₂O₃ pH adsorption edge. For meso-TiO₂, addition of the $(>\text{SO})_2\text{HAsO}_2$ complex had no significant improvement on the fit, and so was not included in order to reduce the number of fitted parameters (Figure 6.11c). The negative surface complexes were increasingly important in the total concentration of adsorbed As(V) in the order Fe₃O₄<FeOOH<meso-TiO₂. This matches the order of increasing inner-capacitance, C₁: with the greatest capacitance, meso-TiO₂ is best able to accommodate the negative charge of $(>\text{SO})_2\text{AsO}_2^-$ and $>\text{SOAsO}_3^{2-}$.

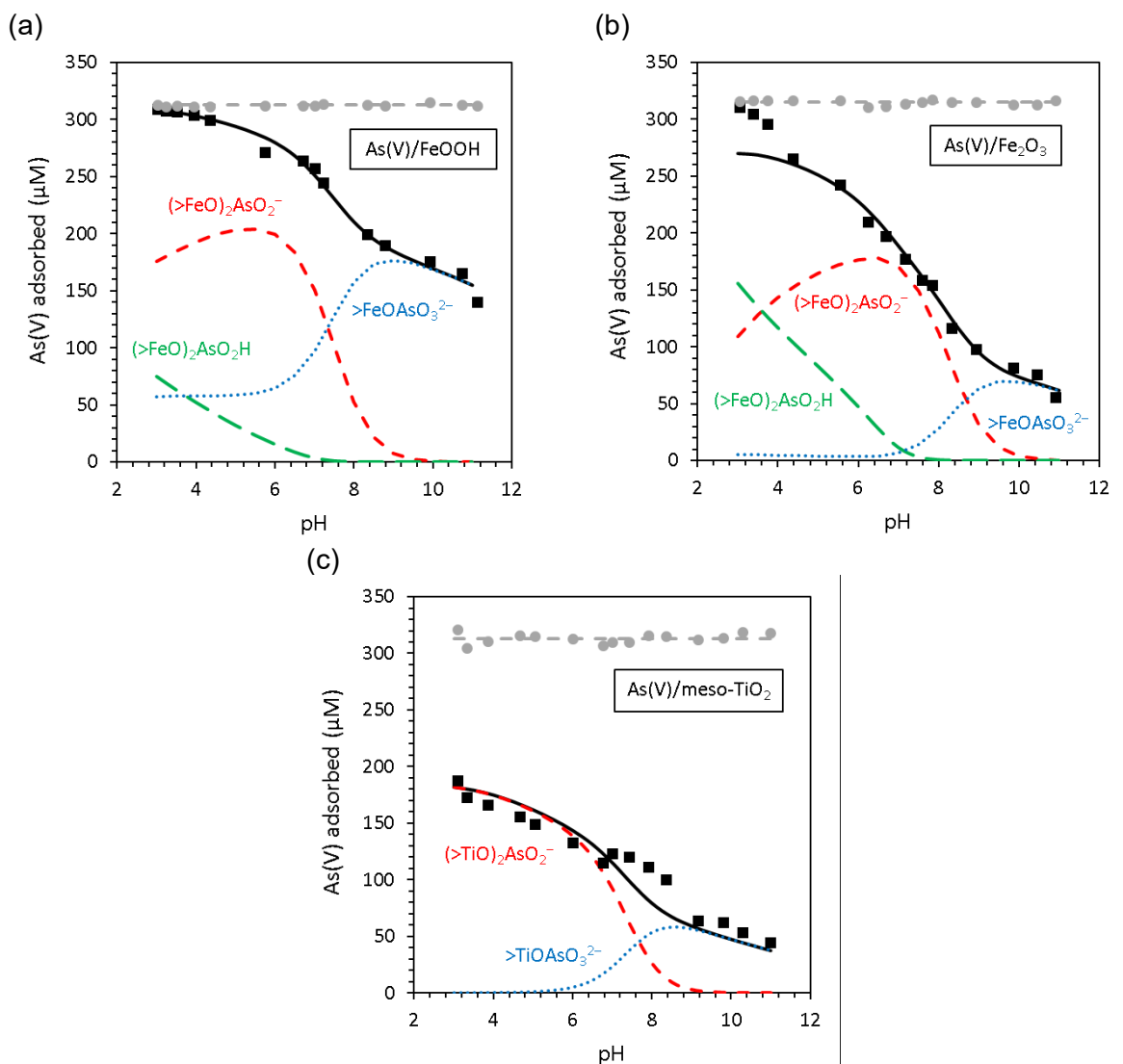


Figure 6.11: Determination of As(V) surface complexation constants using the pH adsorption edges of (a) FeOOH, (b) Fe₂O₃, and (c) meso-TiO₂. Experimental data is presented with total As added (grey circles) and As adsorbed (black squares). The fitted model is presented with total As adsorbed (black solid lines), bidentate protonated complexes (green long dashed lines), bidentate deprotonated complexes (red short dashed lines) and monodentate complexes (blue dotted lines), and total As (grey dashed lines). Experimental conditions were 0.3 mM As(V), 1 g L⁻¹ sorbent, and 0.01 M NaCl.

For the pH adsorption edges of As(III), FeOOH was described well with $(>\text{SO})_2\text{AsO}^-$ as the major complex (Figure 6.12a). In contrast, for Fe_2O_3 the $(>\text{SO})_2\text{AsO}^-$ complex was less important than the $(>\text{SO})_2\text{AsOH}$ and $>\text{SOH}_2^+---\text{AsO}(\text{OH})_2^-$ surface complexes (Figure 6.12b). This again correlates with FeOOH having a higher capacitance than Fe_2O_3 and better accommodating negatively charged surface complexes. The hydrogen-bonded $>\text{SOH}_2^+---\text{AsO}(\text{OH})_2^-$ complex was most significant for meso-TiO₂, where the innersphere $(>\text{SO})_2\text{AsO}^-$ complex only dominated below pH 7 (Figure 6.12c). As with the As(V) adsorption edge, meso-TiO₂ did not require a protonated bidentate complex, i.e. $(>\text{SO})_2\text{AsOH}$, to achieve the best possible fit, and therefore this complex was omitted. The ability to fit meso-TiO₂ pH adsorption edges without protonated surface complexes can be explained by the higher inner capacitance, C_1 , of TiO₂ compared with the iron oxides, accommodating the extra surface charge.

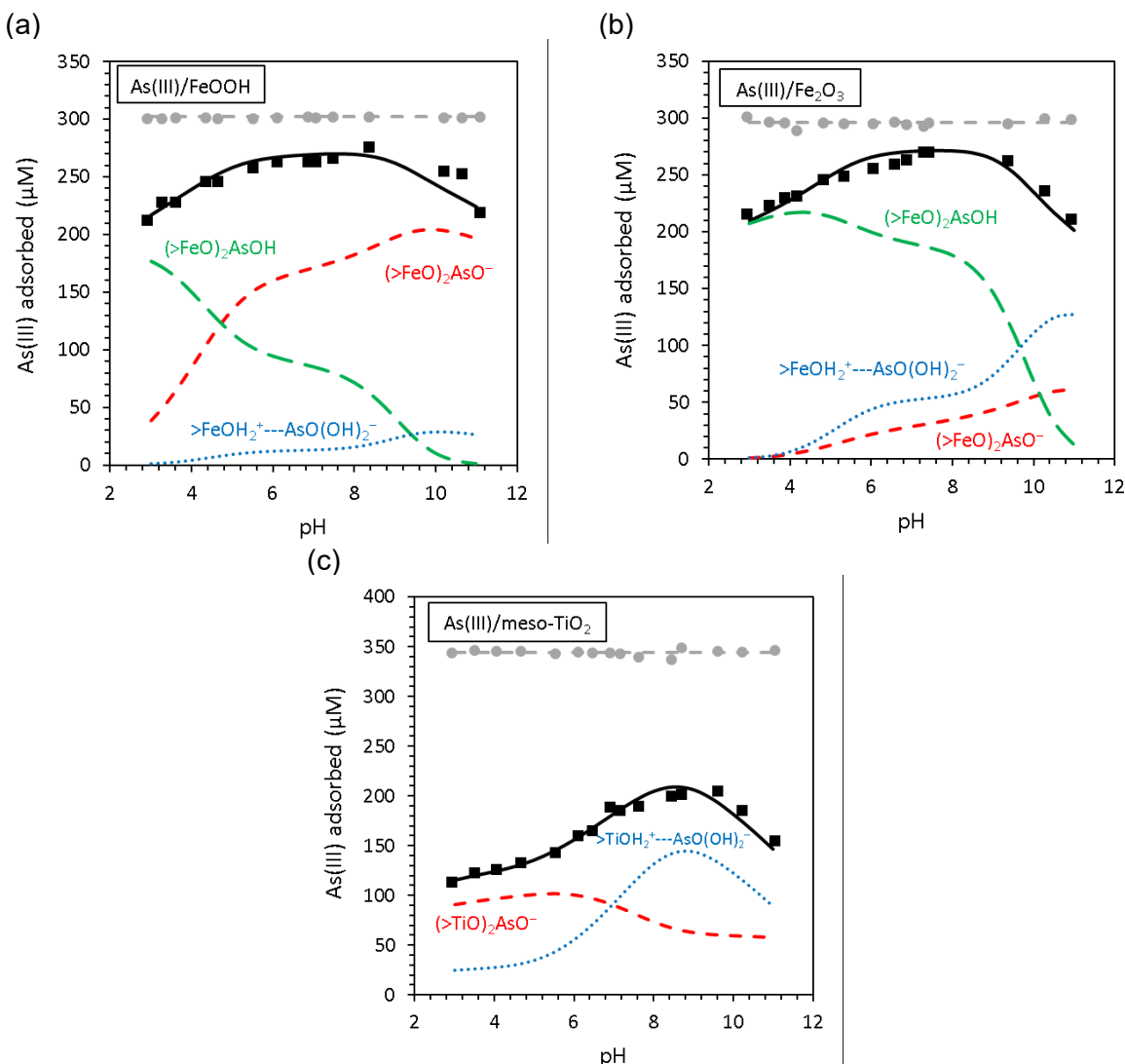


Figure 6.12: Determination of As(III) surface complexation constants using the pH adsorption edges of (a) FeOOH, (b) Fe_2O_3 , and (c) meso-TiO₂. Experimental data is presented with total As added (grey circles) and As adsorbed (black squares). The fitted model is presented with total As adsorbed (black solid lines), bidentate protonated complexes (green long dashed lines), bidentate deprotonated complexes (red short dashed lines) and monodentate complexes (blue dotted lines), and total As (grey dashed lines). Experimental conditions were 0.3 mM As(III), 1 g L⁻¹ sorbent, and 0.01 M NaCl.

Adsorption isotherms were then calculated using the optimised SCM parameters and compared with the experimental adsorption isotherms to validate the model. The ETLM accurately reproduced the experimental As(V) adsorption isotherms (Figure 6.13). This verified that the equilibrium constants determined by fitting pH adsorption edges can be used for quantitative predictions. However, the ETLM failed to predict the full extent of the experimentally observed As(III) adsorption at high sorbate concentrations (Figure 6.14). This was due to multilayer adsorption behaviour not being included within the SCM. Since the CA-SCM requires accurate single-component SCMs, the As(III) model was expanded to include multilayer sorption, as discussed in the following section.

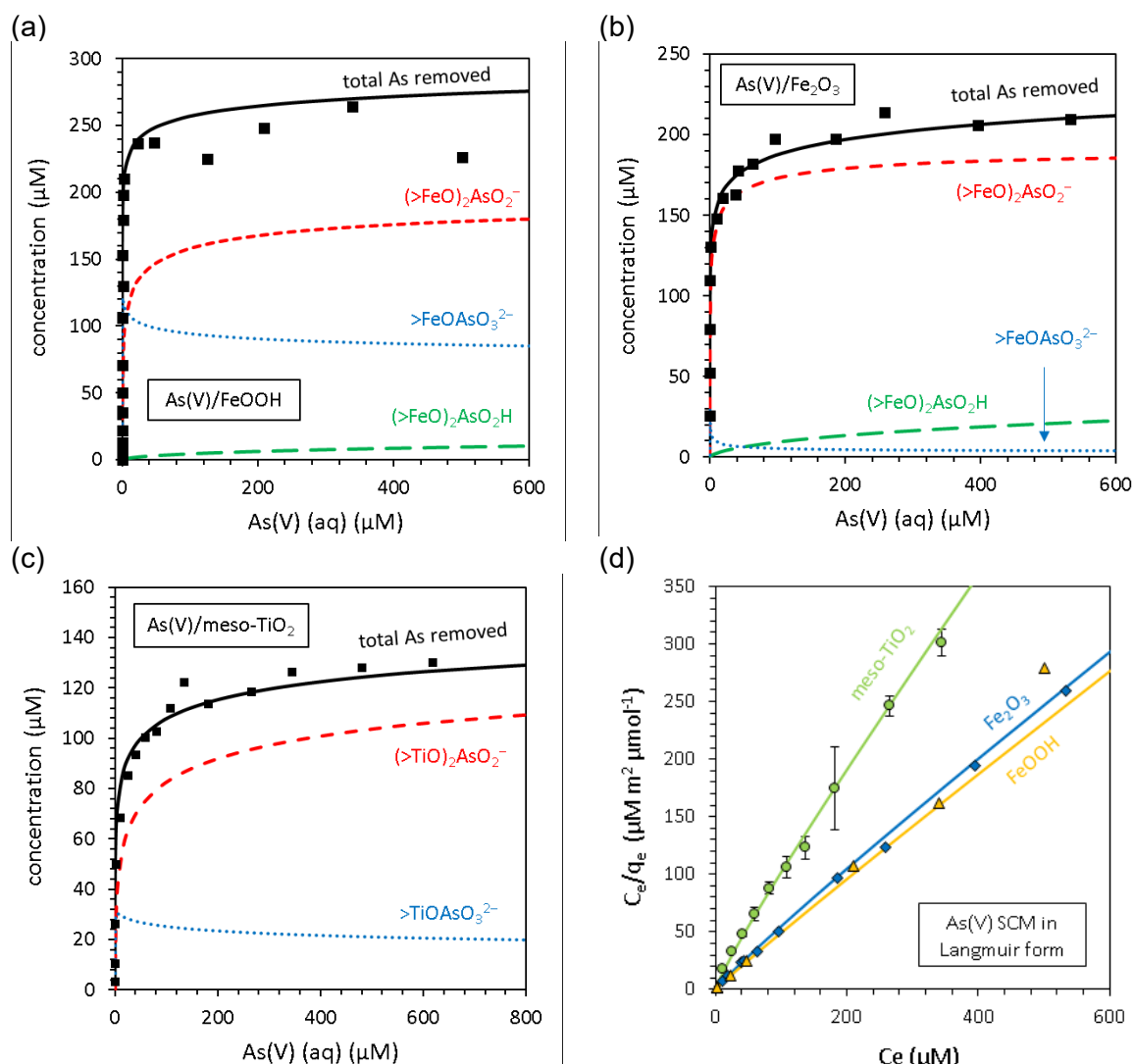


Figure 6.13: Validation of the As(V) surface complexation model. As(V) adsorption isotherms were predicted by the SCM (black lines) and validated against experimental results (black squares) for (a) FeOOH, (b) Fe_2O_3 , and (c) meso-TiO₂. Also presented are the predicted concentrations of bidentate protonated complexes (green long dashed lines), bidentate deprotonated complexes (red short dashed lines) and monodentate complexes (blue dotted lines). (d) shows that the SCM reconstructs the linearised Langmuir adsorption isotherm. Experimental conditions were 1 g L⁻¹ sorbent loading, 0.01 M NaCl, pH 7.0 ± 0.1.

6.4.3. Modelling multilayer As(III) adsorption

The SCM successfully predicted the experimental As(V) adsorption isotherms for all single-component materials. In contrast, the extent of As(III) adsorption was significantly underestimated: the SCM approximated the form of a Langmuir adsorption isotherm, failing to capture the observed Freundlich behaviour, especially at high As(III) concentrations (Figure 6.14). Whilst SCMs are normally mechanistically limited to monolayer adsorption, several studies have identified As(III) surface precipitation on minerals including Fe₂O₃, as discussed in section 6.2.2^{257 256 245 257}. This discrepancy between the ETLM prediction of As(III) adsorption and experimental observations can be seen in other examples of the ETLM, such as Sverjensky and Fukushi, 2006 (see their figures 3b, 4b and 5c)²⁴⁵. Consequently, to develop an accurate CA-SCM for adsorption of arsenic onto meso-TiO₂/Fe₂O₃, the single-component reference samples require a description of multilayer As(III) adsorption (Equation 3.9).

Farley et al. and Lützenkirchen and Behra previously showed how a surface precipitation model modifies the SCM so that instead of reducing to the Langmuir adsorption isotherm, the Freundlich or BET isotherms are approximated^{451 424}. In the surface precipitation model, formation of each surface complex generates a new surface site for further sorbate binding. These studies described the mineral surface as a solid solution, transitioning from a pure sorbent surface to a pure sorbate precipitate as adsorption proceeds. In the solid solution model, precipitation and dissolution of both sorbate and sorbent surface are allowed. The activities of each component within the solid solution are a function of their mass fraction within the solid solution.

Sorbent dissolution was considered unlikely in this work. Previous studies have shown that at pH 3, 40 m² L⁻¹ TiO₂ suspensions release <10 nM Ti into solution⁴⁵², at pH 5, 10 g L⁻¹ FeOOH suspensions release <1 nM Fe per hour⁴⁵³, and at pH 2.4, 5 g L⁻¹ hematite releases <20 µM Fe after 20 hours⁴⁵⁴. These quantities are all far lower than the 100-600 µM concentrations of As(III) used in this work. Therefore, rather than modelling the system as a solid solution, multilayer sorption was include using a simpler reaction:



Equation 6.4

where X is either a proton or a single negative charge; the mass action is equal to the product of the activity of aqueous As(OH)₃ and the sum of the activities of (>SO)₂AsO⁻ and (>SO)₂AsOH surface complexes; and the mass balance is equal to aqueous As(OH)₃ only (i.e.

there is no net consumption of surface complexes, they act to catalyse the process of precipitation). A surface precipitation equilibrium constant was obtained for each reference material by fitting the corresponding adsorption isotherm. This successfully reproduced the observed adsorption isotherm for all reference samples (Figure 6.14).

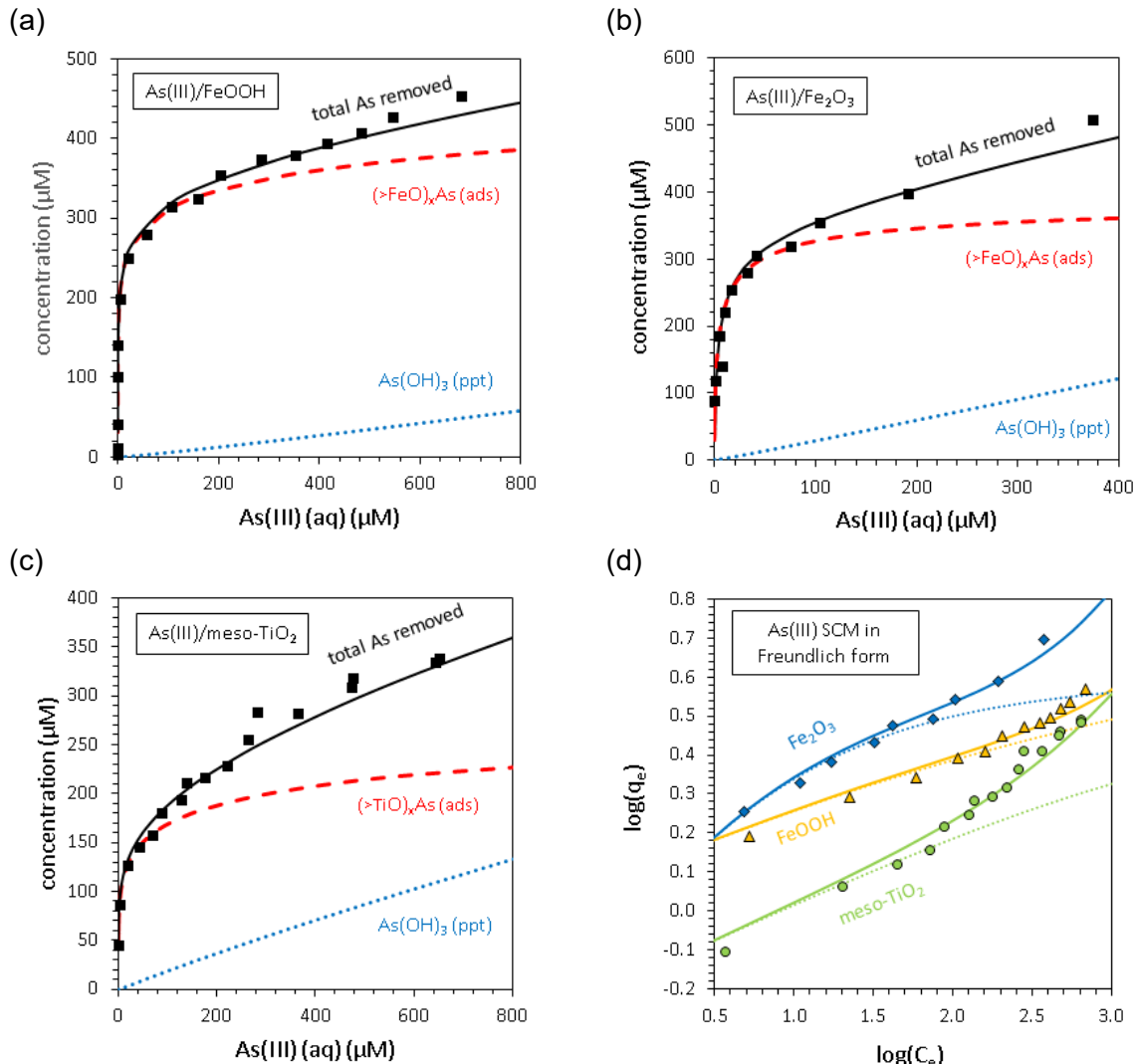


Figure 6.14: Fitting multilayer As(III) adsorption constants to adsorption isotherms. Presented are the experimental adsorption isotherms (black squares) and the optimised SCM (black lines) for (a) FeOOH, (b) Fe₂O₃, and (c) meso-TiO₂. The monolayer surface complexes (red dashed lines) are calculated using the surface complexation constants calculated from the pH adsorption edges, whilst the surface precipitates (blue dashed lines) are calculated after fitting the surface precipitation constant to the adsorption isotherm. (d) presents the SCM in the linearised Freundlich form, with the monolayer-only SCM presented as dashed lines, and the improved multilayer SCM given as solid lines. Experimental conditions were 0.3 mM As(III), 1 g L⁻¹ sorbent, 0.01 M NaCl, pH 7.0 ± 0.1.

The optimised surface precipitation equilibrium constants increased in the order FeOOH<Fe₂O₃<meso-TiO₂ (Table 6.4). This corresponds to the steepness of the Freundlich isotherms. This is explained by considering differences in surface morphology and pore size, since pore sizes decreased in the order FeOOH>Fe₂O₃>meso-TiO₂ (21, 9 and 8 nm respectively, section 5.2.3) and smaller pores provide more concaved surfaces with a smaller contact angles promoting adsorption ¹⁴⁷.

Fe_2O_3 and TiO_2 have low solubility at pH 7, and whilst karibibite, $\text{Fe}(\text{III})_2\text{As}(\text{III})_4(\text{O},\text{OH})_9$, both contains Fe(III) and As(III) and can crystallise on hematite surfaces^{455 456}, no Ti-As minerals were identified in the literature. In line with the amorphous As(III) surface precipitate on hematite identified by Morin et al., in this thesis the surface precipitate was provisionally labelled as “ As_2O_3 ”²⁵⁷. However, surface precipitates were not directly observed in this work (e.g. using spectroscopic techniques) and the principal purpose of including a surface precipitation reaction within the SCM was to provide accurate single-component SCMs that satisfy the experimental adsorption isotherms for use in the final CA model.

The final SCM parameters for all single-component reference samples are presented in Table 6.4.

Table 6.4: Surface complexation modelling parameters for the ETLM. Presented are the hypothetical 1.0 M standard state equilibrium constants ($\log K_0$). Parentheses indicate values of the hypothetical standard state equilibrium constants ($\log K_\theta$).

* aqueous speciation constants are taken from from Dixit and Hering²³⁰, which in turn are referenced elsewhere⁴⁵⁷. Electrolyte adsorption constants were calculated from the average of 3 titrations. Arsenic surface complexation constants were calculated from pH adsorption edges with 14 or 15 experimental data points each. As(III) surface precipitation constants were calculated from adsorption isotherms with 11 to 17 data points. Uncertainties in $\log K_M$ and $\log K_L$ were calculated as the standard deviation between three potentiometric titrations at different ionic strength. Values of FITEQL's error function, V_y , were calculated in the fitting of the SCM to experimental data, and are presented and discussed in the Appendix.

Aqueous phase reactions *	$\log \beta$	+H ⁺	+2H ⁺	+3H ⁺
AsO ₄ ⁻³	11.60	18.35	20.60	
AsO ₃ ⁻³	13.41	25.52	34.74	
---	---	---	---	---
Surface reactions	Material	FeOOH	Fe ₂ O ₃	meso-TiO ₂
Physical properties	BET-specific surface area (m ² g ⁻¹)	127	103	110
	Site density (sites nm ⁻²)	4.0	4.0	3.0
Capacitance	C ₁ (F m ⁻²)	0.9	0.8	1.3
	C ₂ (F m ⁻²)	0.2	0.2	0.2
Surface charge and electrolyte adsorption	$\log K_{a1}$	5.59 (6.3)	5.48 (6.09)	1.13 (1.65)
	$\log K_{a2}$	-12.6 (11.9)	-12.3 (11.7)	-8.47 (7.95)
	$\log K_M$	-8.79 ±0.24 (3.82)	-8.81 ±0.08 (3.50)	-4.88 ±0.19 (3.59)
	$\log K_L$	9.10 ±0.19 (3.51)	8.51 ±0.05 (3.02)	4.37 ±0.32 (3.24)
As(V) surface complexation	$\log K_{(>\text{SO})2\text{AsO}_2^-}$	11.9 (2.71)	10.3 (1.33)	11.0 (10.74)
	$\log K_{(>\text{SO})2\text{HAsO}_2^-}$	11.8 (2.61)	11.8 (2.83)	---
	$\log K_{>\text{SOAsO}_3^{2-}}$	6.12 (0.53)	2.20 (-3.29)	5.00 (3.87)
As(III) surface complexation	$\log K_{(>\text{SO})2\text{AsO}_2^-}$	4.67 (-4.52)	2.41 (-6.56)	6.20 (5.94)
	$\log K_{(>\text{SO})2\text{HAsO}_2^-}$	7.93 (-1.26)	8.40 (-0.57)	---
	$\log K_{>\text{SOH}_2+---\text{H}_2\text{AsO}_3^-}$	5.49 (-0.104)	5.44 (-0.045)	3.75 (2.62)
As(III) surface precipitation	$\log K_{\text{ppt}}$	2.28	3.05	3.32

6.4.4. Site-occupancy standard state parameters

The following tables present the ETLM parameters calculated in this work alongside previously published data.

Table 6.5: Comparison of ETLM parameters for surface protonation and electrolyte adsorption.

Solid	Electrolyte	N _s (nm ⁻²)	A _s (m ² g ⁻¹)	pH _{pzc}	ΔpKnθ	log Kθ1	log Kθ2	log K01	log K02	log KθM	log KθL	log K0M	log K0L	C ₁ (F m ⁻²)	Adsorption data	ETLM parameter estimation
FeOOH	NaCl	4.0	127	9.1	5.6	6.3	11.89	5.59	-12.6	3.82	3.51	-8.79	9.1	0.9	This work	This work
FeOOH	NaNO ₃	4.0	158.1	8.5	5.6	5.7	11.3	4.9	-12.1	3.4	3.1	-8.7	8.0	1.0	Kanematsu et al. (2010) ⁸⁹	Kanematsu et al. (2010) ⁸⁹
FeOOH	NaClO ₄	3.5	-	9.2	5.6	6.4	12	6.1	-12.4	3.4	2.4	-8.9	8.5	1.2	Dixit and Hering (2003) ²³⁰	Fukushi and Sverjensky (2007) ⁴⁴⁶
FeOOH	NaCl	4.5	-	8.5	5.6	5.6	11.4	5.5	-11.5	2.4	2.3	-9	7.9	1.2	Gao and Mucci (2001) ⁴⁵⁸	Fukushi and Sverjensky (2007) ⁴⁴⁶
FeOOH	NaCl	3.9	-	8.7	5.6	5.9	11.5	5.7	-11.7	3.4	3.2	-8.3	8.9	1.4	Manning and Goldberg (1996) ⁴⁵⁹	Fukushi and Sverjensky (2007) ⁴⁴⁶
Fe₂O₃	NaCl	4.0	103	8.9	5.6	6.09	11.71	5.48	-12.32	3.5	3.02	-8.81	8.51	0.8	This work	This work
Fe ₂ O ₃	NaClO ₄	3.0	83	9.17	5.7	6.42	11.92	6.02	-12.32	-	-	-8.63	9.59	0.58	Hwang and Lenhart (2008) ⁴⁶⁰	Hwang and Lenhart (2008) ⁴⁶⁰
Fe ₂ O ₃	NaCl	22.0	-	8.5	5.6	5.7	11.3	-	-	1.6	2.0	-9.7	7.7	0.90	Liang (1988) ⁴⁶¹	Sahai and Sverjensky (1997) ²⁸⁸
TiO₂	NaCl	3.0	110	4.8	6.3	1.65	7.95	1.13	-8.47	3.59	3.24	-4.88	4.37	1.3	This work	This work
TiO ₂ (rutile)	NaCl	3.0	18.1	-	-	-	-	2.52	8.28	-	-	-5.6	5.0	1.2	Jonsson et al. (2009) ⁴⁴⁸	Jonsson et al. (2009) ⁴⁴⁸
TiO ₂ (anatase)	NaCl	12.5	-	6.0	6.4	2.80	9.20	-	-	2.9	2.9	-6.3	5.7	1.3	Sprycha (1984) ⁴⁶²	Sahai and Sverjensky (1997) ²⁸⁸

Table 6.6: Comparison of ETLM parameters for the adsorption of As(V).

Solid	Electrolyte	N_s (nm ⁻²)	C_s (g L ⁻¹)	$\log K_0_{(>SO)2AsO2^-}$	$\log K_\theta_{(>SO)2AsO2^-}$	$\log K_\theta_{(>SO)2AsO2H}$	$\log K_\theta_{(>SO)2AsO2H}$	$\log K_\theta_{>SOAsO3-2}$	$\log K_0_{>SOAsO3-2}$	Adsorption data	ETLM parameter estimation
FeOOH	NaCl	4.0	1.0	11.9	2.71	11.8	2.61	6.12	0.53	This work	This work
FeOOH	NaNO ₃	4.0	1.0	10.7	2.9	10.2	2.4	4.7	-0.2	Kanematsu et al. (2010) ⁸⁹	Kanematsu et al. (2010) ⁸⁹
FeOOH	NaNO ₃	4.0	0.025	12.3	2.9	11.8	2.4	4.7	-0.1	Kanematsu et al. (2010) ⁸⁹	Kanematsu et al. (2010) ⁸⁹
FeOOH	-	-	-	$\log K_\theta_{(>SO)2AsO2^-} = 0.81$ $\log K_\theta_{(>SO)2AsO2H} = 3.4$ $\log K_\theta_{>SOAsO3-2} = -4.3$						-	Fukushi and Sverjensky (2007) ⁴⁴⁶
Fe₂O₃	NaCl	4.0	1.0	10.3	1.33	11.8	2.83	2.2	-3.29	This work	This work
Fe ₂ O ₃	-	-	-	$\log K_\theta_{(>SO)2AsO2^-} = -0.33$ $\log K_\theta_{(>SO)2AsO2H} = 2.5$ $\log K_\theta_{>SOAsO3-2} = -5.7$						-	Fukushi and Sverjensky (2007) ⁴⁴⁶
TiO₂	NaCl	3.0	1.0	11.0	10.74	(not used)	(not used)	5.0	3.87	This work	This work

Table 6.7: Comparison of ETLM parameters for the adsorption of As(III).

Solid	Electrolyte	N _s (nm ⁻²)	C _s (g L ⁻¹)	logK ₀ >SO)2AsO-	logK _θ >(SO)2AsO-	logK ₀ >(SO)2AsOH	logK _θ >(SO)2AsOH	logK ₀ >SOH2+--- H2AsO3-	logK _θ >SOH2+--- H2AsO3-	logK _{0,ppt}	logK _{θ,ppt}	Adsorption data	ETLM parameter estimation
FeOOH	NaCl	4.0	1.0	4.67	-4.52	7.93	-1.26	5.49	-0.104	2.28		This work	This work
FeOOH	NaNO ₃	4.0	1.0	5.0	-5.5	7.2	-0.6	4.2	-0.7	(not used)	(not used)	Kanematsu et al. (2013) ²²⁵	Kanematsu et al. (2013) ²²⁵
FeOOH	NaClO ₄	3.5	0.5	3.7	-4.1	8.9	-1.6	5.8	-0.3	(not used)	(not used)	Dixit and Hering (2003) ²³⁰	Kanematsu et al. (2013) ²²⁵
FeOOH	NaClO ₄	3.5	0.5	(not used)	(not used)	9.3	-1.2	3.8	-2.3	(not used)	(not used)	Dixit and Hering (2003) ²³⁰	Sverjensky and Fukushi (2006) ²⁴⁵
Fe₂O₃	NaCl	4.0	1.0	2.41	-6.56	8.40	-0.57	5.44	-0.045	3.05		This work	This work
Fe ₃ O ₄	NaClO ₄	3.0	0.5	(not used)	(not used)	7.5	2.0	4.4	0.8	(not used)	(not used)	Dixit and Hering (2003) ²³⁰	Sverjensky and Fukushi (2006) ²⁴⁵
TiO ₂	NaCl	3.0	1.0	6.2	5.94	(not used)	(not used)	3.75	2.62	3.32		This work	This work

6.4.5. Accuracy of the component additive surface complexation model

To assess the accuracy of the CA-SCM, adsorption isotherms were modelled and compared against experimental observations. The CA-SCM was modelled by dividing the total surface area of meso-TiO₂/Fe₂O₃ (100 m² g⁻¹) between meso-TiO₂ and Fe₂O₃ surface components, according to the mass ratios calculated using XRF, XPS, and LEIS analysis. The density of surface sites was maintained as 3.0 sites nm⁻² for meso-TiO₂ and 4.0 sites nm⁻² for Fe₂O₃, i.e. assuming that the concentrations of surface hydroxyls per unit area in the reference samples and the composite are equivalent. The CA-SCM was modelled using separate electrical double layers for meso-TiO₂ and Fe₂O₃ surface components, as overlap is not considered to be significant ²⁵³. For completeness, a comparison of results obtained using discrete and shared electrical double layers is given in section 6.4.5.1.

The adsorption isotherms predicted by the final CA-SCM are presented in Figure 6.15. Both the goodness of fit and the errors between experimental and calculated results are presented in Table 6.8. The accuracy of the CA-SCM towards modelling As(V) adsorption improved with surface-sensitive component weighting, in the order XRF<XPS<LEIS (Figure 6.15a). In the LEIS-weighted CA-SCM, the root-mean-square error (RMSE) was 0.12 µmol m⁻², or 8.3%. As(V) adsorption was over estimated when [As(V) (aq)]<60 µM, and overestimated when [As(V) (aq)]>60 µM. When compared with XRF (representing the bulk mass ratios used in most previous CA-SCM studies), using LEIS to weight the CA-SCM reduced the average absolute error by 82%, the average relative error by 96%, and the RMSE by 42%. These results indicate that CA-SCM accuracy is improved when components are weighted according to surface-sensitive analysis (ideally the outermost surface, i.e. using LEIS). The speciation and partitioning of adsorbed As(V) in the CA-SCM is presented in Figure 6.15b.

Much like the linear combination of Freundlich adsorption isotherms, LEIS weighting failed to provide the most accurate CA-SCM for As(III) adsorption, systematically overestimating the experimental results (Figure 6.15c). Consequently, the accuracy of the CA-SCM decreased when using LEIS, instead of XRF, to weight components (Table 6.8). Section 6.4.3 discussed how the equilibrium constant for the As(III) surface precipitation reaction was correlated with sorbent morphology: larger pore sizes resulted in smaller equilibrium constants. Some of the porosity of meso-TiO₂ is lost in the composite material, due to pore filling by Fe₂O₃ (section 5.2.3). This implies that the equilibrium constants obtained for the adsorption of As(III) using the reference samples are too large for the composite sorbent, resulting in the positive error that was observed in the CA-SCM predictions. This is an important finding, as it suggests that

when the morphology and porosity of composite and reference samples are different, CA models are likely to fail in their description of multilayer adsorption processes.

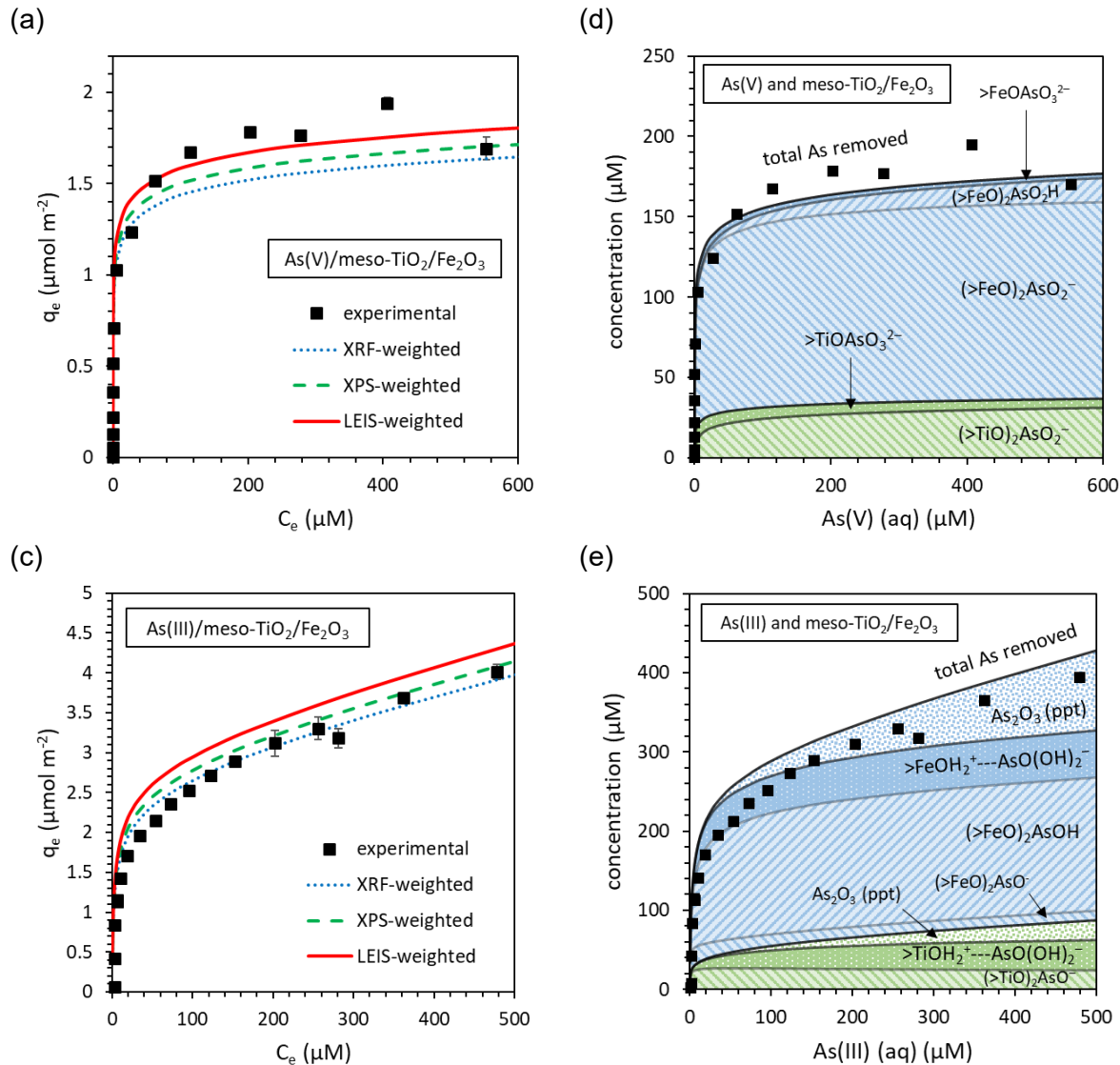


Figure 6.15: A comparison of adsorption isotherms predicted by the component additive surface complexation model (CA-SCM) with experimental results. (a) A comparison of the As(V) adsorption isotherms predicted by the XRF, XPS and LEIS-weighted CA-SCM, and (b) the partitioning and speciation of adsorbed As(V) (in the LEIS-weighted model). (c) A comparison of the As(III) adsorption isotherms predicted by the XRF, XPS and LEIS-weighted CA-SCM, and (d) the partitioning and speciation of adsorbed As(V) (in the LEIS-weighted model). Experimental conditions were 1 g L⁻¹ sorbent, 0.01 M NaCl, and pH 7.0 ± 0.1.

Table 6.8: A comparison of the accuracy of the CA-SCM when components are weighted by XRF (bulk), XPS (near surface) and LEIS (outermost surface) analysis. Errors represent the difference between predicted results and the experimentally determined adsorption isotherms. The root mean square error (RMSE) was calculated using the formula $RMSE = \sqrt{\sum_{i=1}^n \frac{(y_i - \hat{y}_i)^2}{n}}$, where y_i is the experimental observation, \hat{y}_i is the predicted result, n is the number of data points (8 for As(V) and 10 for As(III)), and i is the unique index assigned to each data point.

Sorbate	Property	XRF	XPS	LEIS	% change in error (LEIS-weighting vs. XRF)
As(V)	R ²	0.6706	0.8005	0.8886	-
	average absolute error ($\mu\text{mol m}^{-2}$)	-0.16 \pm 0.13	-0.10 \pm 0.13	-0.029 \pm 0.12	-82
	average relative error (%)	-9.4 \pm 7.5	-5.5 \pm 8.1	-0.4 \pm 8.9	-96
	RMSE ($\mu\text{mol m}^{-2}$)	0.20	0.16	0.12	-42
	RMSE (%)	12	9.3	8.3	-29
As(III)	R ²	0.9767	0.9553	0.9013	-
	average absolute error ($\mu\text{mol m}^{-2}$)	0.11 \pm 0.16	0.22 \pm 0.14	0.37 \pm 0.12	230
	average relative error (%)	7.9 \pm 11	13 \pm 11	20 \pm 12	150
	RMSE ($\mu\text{mol m}^{-2}$)	0.19	0.26	0.38	106
	RMSE (%)	13	17	23	79

6.4.5.1. Describing the electrical double layer in a composite sorbent

Electrostatics are considered an essential component in many SCMs and were modelled in this work through the fitting of potentiometric titrations. Whilst previous authors have suggested that the overlap between electrical double layers (EDL) in heterogeneous sorbents is unlikely to be significant²⁵³, this thesis did not find any systematic studies identifying the nature of the EDL in composite sorbents. The discrete EDL CA-SCM presented in Figure 6.15 was thus compared to a second model, where the meso-TiO₂ and Fe₂O₃ surface components shared a single electrical double layer. The shared EDL model is presented in Figure 6.16 (with all calculations using the LEIS-weighting of surface components).

In the adsorption of As(V), both models overestimate adsorption at low As(V) concentrations. However, the error is more significant in the shared EDL model. The most dramatic difference between the two models is in the partitioning of As(V) across the two surface components, and the speciation of adsorbed As(V). In the discrete EDL model, where each surface component (meso-TiO₂ or Fe₂O₃) has its own EDL, the partitioning of As(V) between the two surface components matches CA predictions calculated using Langmuir adsorption isotherms. Furthermore, the speciation of adsorbed As(V) on each surface component matches the speciation of adsorbed As(V) in the single-component reference SCMs presented in section

6.4.2. In the shared EDL model, however, the TiO₂ surface component adsorbs nearly as much As(V) as the Fe₂O₃ component. This is unlikely, based on the known affinity of arsenic towards Fe₂O₃ versus TiO₂. Furthermore, the speciation of TiO₂-sorbed As(V) in the shared-EDL model was significantly different to the single-component reference SCMs: TiO₂-sorbed As(V) is now present as monodentate >TiOAsO_3^{2-} , rather than bidentate $(\text{>TiO})_2\text{HAsO}_2^-$. The behaviour of the shared EDL model makes sense, given that if surface charge is shared between the majority Fe₂O₃ component (with a positive surface charge) and the minority TiO₂ component (with a negative surface charge), then the electrostatic work done in forming the negative >TiOAsO_3^{2-} surface complex changes from a repulsive force to an attractive force.

The differences between the shared and discrete EDL models were less pronounced in the adsorption of As(III), since neutral surface complexes form a much larger proportion of the As(III) speciation. The partitioning of adsorbed As(III) between meso-TiO₂ and Fe₂O₃ surfaces was similar in each model. However, much like As(V) adsorption, the speciation of TiO₂-sorbed As(III) changes when a shared EDL is used. In this case, the majority of the H-bonded $\text{>TiOH}_2^+ \cdots \text{AsO(OH)}_2^-$ surface complexes are replaced with $(\text{>TiO})_2\text{AsO}^-$. The situation is different in the case of Fe₂O₃-sorbed As(III), where the H-bonded $\text{>FeOH}_2^+ \cdots \text{AsO(OH)}_2^-$ becomes more prevalent and $(\text{>FeO})_2\text{AsOH}$ becomes less prevalent.

Ultimately, using a shared EDL was a poor choice for this CA-SCM. The most significant problems are (a) the partitioning of adsorbed As(V) across the surface components, with an unrealistically high proportion of TiO₂-sorbed As(V), and (b) the high proportion of H-bonded $\text{>FeOH}_2^+ \cdots \text{AsO(OH)}_2^-$ surface complexes, given that As(III) is known to form predominantly inner-sphere complexes with iron oxides^{234 235 239 241}. The ATR-FTIR spectra of meso-TiO₂/Fe₂O₃ produced new peaks after adsorption of arsenic that best resembled the Fe₂O₃ reference sample, rather than meso-TiO₂ (section 6.3.2). The implication is that adsorption of arsenic onto the composite material is likely controlled by the Fe₂O₃ surface, rather than meso-TiO₂. Finally, for both As(V) and As(III), the discrete EDL model, where surface charge was separated between the two surface components, gave a statistically better fit than the shared EDL model. R² values of 0.827 and 0.840 for As(V), and 0.584 and 0.772 for As(III), using the shared and discrete EDL models respectively.

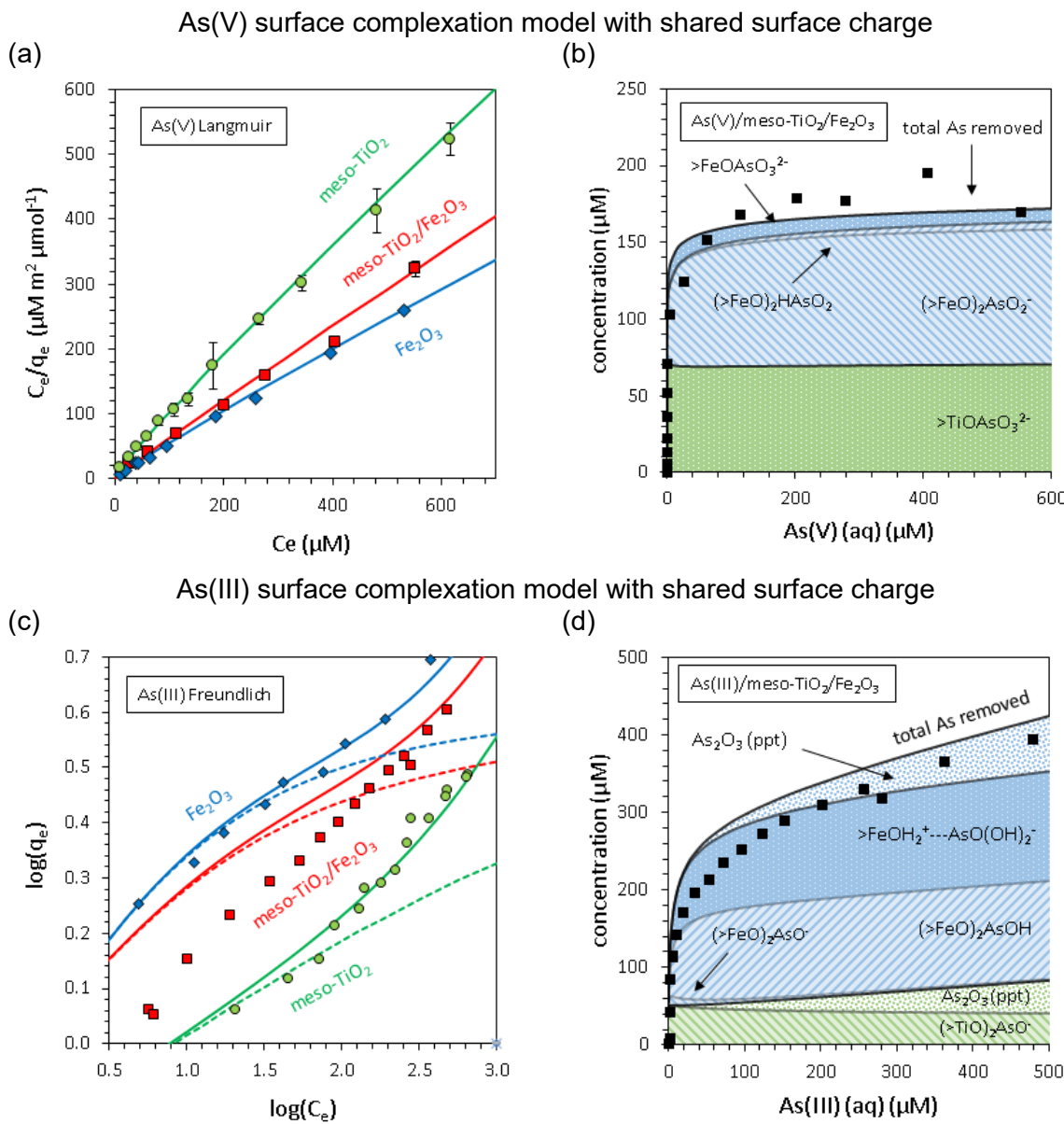


Figure 6.16: The shared EDL CA-SCM, where a single electrical double layer is used to calculate the electrostatic work done in the adsorption of arsenic to both Fe_2O_3 and meso- TiO_2 surface components. (a) As(V) adsorption isotherms in the linearised Langmuir form, and (b) the partitioning of As(V) between meso- TiO_2 and Fe_2O_3 surface components. (c) As(III) adsorption isotherms in the linearised Freundlich form, and (d) the partitioning of As(III) between meso- TiO_2 and Fe_2O_3 surface components. Linearised adsorption isotherms present the experimental data for meso- TiO_2 (green circles), Fe_2O_3 (blue diamonds) and meso- $\text{TiO}_2/\text{Fe}_2\text{O}_3$ (red squares), and SCM predictions are given as solid lines. Dashed lines indicate the SCM prediction with monolayer adsorption only (i.e. without the surface precipitation term). Figures (c) and (d) indicate the experimentally observed adsorption isotherms of meso- $\text{TiO}_2/\text{Fe}_2\text{O}_3$ (black squares) and the SCM predicted adsorption isotherm (black lines), with total adsorption split into constituent species across each mineral surface. The experimental conditions were 1 g L⁻¹ sorbent, 0.01 M NaCl and pH 7.0 ± 0.1.

6.5. Conclusions

A component additive surface complexation model (CA-SCM) was developed, with the aim of better understanding adsorption of arsenic onto meso-TiO₂/Fe₂O₃, and with the aim of providing a tool capable of predicting the influence of surface composition on the adsorption of arsenic onto composite titania-iron oxide sorbents. This chapter considered low energy ion scattering (LEIS) as a novel approach towards determining material composition at the outermost surface, to weight each component more accurately than in previous CA-SCM studies.

The findings of this chapter are that:

- Quantification of material composition at the outermost surface using LEIS provided accurate data for component additive modelling. LEIS-weighted linear combinations of end-member reference samples successfully predicted the monolayer adsorption behaviour of both As(V) adsorption and surface acidity.
- Due to high penetration depths, XRF overestimated the significance of the fine iron oxide surface coating, whilst quantification of material at the near surface using XPS gave intermediate results, between those obtained using XRF and LEIS.
- When using (a) Langmuir and Freundlich adsorption models and (b) the extended triple layer model (ETLM), experimental data was best fit by considering monolayer As(V) adsorption and multilayer As(III) adsorption, at pH 7, 0.01 M NaCl. (Figure 6.17).
- The extent of As(III) adsorption was overestimated by the LEIS-weighted component additivity approach in both Freundlich and CA-SCM models. This was likely caused by changes in surface morphology, witnessed in the decrease of porosity and increase in average pore size, leading to a reduction in surface precipitation effects.
- The ETLM was able to fit As(V) and As(III) pH adsorption edges across Fe₂O₃ and meso-TiO₂ well, successfully reconstructing experimental adsorption isotherms (though an As(III) surface precipitation term was needed).
- This work demonstrates that accurate quantification of the surface composition is an essential prerequisite for component additive modelling, and techniques such as LEIS offer a promising route to resolving this problem which has remained largely unanswered since first identified by Davis et al. in 1998¹⁵.

Surface-sensitive analytical techniques offer a number of key improvements over previous approaches to CA-SCM weighting. Firstly, unlike mass ratios, the significance of fine

precipitates and surface coatings is captured. This solves significant historical problems^{15 253 410}. Secondly, unlike chemical extractions, the technique is precise, and the surface depth probed is known^{15 410}. Thirdly, LEIS provides a route towards modelling ternary sorbent systems, which cannot be characterised using adsorption isotherms alone⁴¹¹. Whilst LEIS is known to provide excellent surface sensitivity, other techniques not considered in this study such as angle-resolved XPS (ARXPS) and secondary ion mass spectrometry (SIMS) may also prove interesting for similar applications in CA-SCM.

Future work should use surface-sensitive analytical techniques to develop increasingly accurate component additive adsorption models. These accurate CA models should be used as a tool (i) to investigate the adsorption chemistry of coupled materials (e.g. whether new behaviour arises), and (ii) to engineer high performing multifunctional sorbents.

It is also worth noting that the adsorption isotherms determined in this work are useful to compare the adsorption capacity of meso-TiO₂/Fe₂O₃ with the commercial benchmark, Bayoxide E33. Meso-TiO₂/Fe₂O₃ showed a slightly lower maximum adsorption capacity for As(V) on a mass basis compared with the Bayoxide E33 goethite (14 mg g⁻¹ to 19 mg g⁻¹), but when normalised to surface area the As(V) capacities were very similar (1.8 to 2.0 μmol m⁻²). Meso-TiO₂/Fe₂O₃ did not adsorb more As(III) than Bayoxide E33 on a per mass basis (mg g⁻¹) within the experimental range of this study (0–500 μM), however it surpassed Bayoxide E33 when normalised to surface area when the concentration of aqueous As(III) was greater than 50 μM (ca. 2.25 μmol m⁻² adsorption). The meso-TiO₂/Fe₂O₃ composite is therefore a competitive arsenic sorbent, comparing well against the commercial Bayoxide E33.

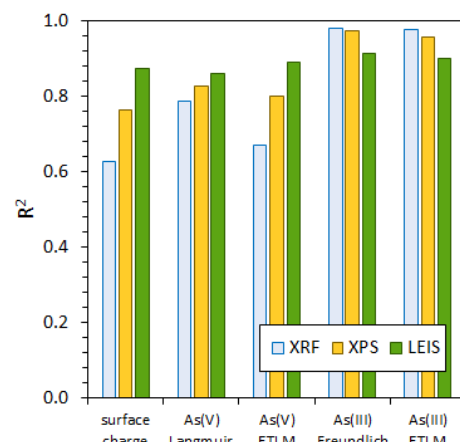


Figure 6.17: Values of the coefficient of determination (R^2) calculated to determine the goodness of fit between meso-TiO₂/Fe₂O₃ experimental data and the component additive predictions, using components weighting according to XRF, XPS and LEIS analysis. Values of R^2 were calculated for surface charge (potentiometric titration), As(V) adsorption isotherms (modelled with both the Langmuir adsorption isotherm and the CA-SCM), and As(III) adsorption isotherms (both the Freundlich adsorption isotherm and the CA-SCM).

7. A mechanistic explanation for different arsenic(III) oxidation rates using single-component TiO_2 and composite $\text{TiO}_2/\text{Fe}_2\text{O}_3$ photocatalysts

7.1. Introduction

As highlighted in chapter 2, composite photocatalysts are being increasingly investigated and developed for water treatment applications. However, despite the attention that titania-iron oxide composites have received so far, we know little about how the photocatalytic oxidation of As(III) is affected when TiO_2 is coupled with an iron oxide sorbent phase such as Fe_2O_3 . Does each component continue to work independently or does new behaviour arise?

Iron oxides can both enhance and suppress the photocatalytic activity of TiO_2 through a variety of mechanisms. Firstly, whilst pure iron oxides are poor photocatalysts due to fast electron-hole recombination kinetics²⁶³, coupling photocatalysts with iron oxides can improve photocatalytic performance through enhanced charge carrier separation (through formation of a heterojunction, as discussed in section 2.6.4)^{183 247 295}. The TiO_2 and Fe_2O_3 conduction and valence bands are positioned such that the transfer of both (a) conduction band electrons and (b) valence band holes from TiO_2 to Fe_2O_3 is energetically favoured. However, when the transfer of electrons and holes from TiO_2 to Fe_2O_3 is unequal, electron-hole recombination is suppressed and charge carrier lifetimes are extended, increasing photocatalytic activity²⁴.

Alternatively, parasitic absorption of incident photons by iron oxides can reduce the photoexcitation of the more active titania phase, decreasing reaction rates¹⁷¹. This is a particularly important consideration, given that the bandgap of Fe_2O_3 is smaller than that of TiO_2 . A third potential behaviour is that sorbent phases such as Fe_2O_3 may prevent photocatalyst deactivation. Adsorption of competitor ions, such as phosphate or the As(V)

produced during As(III) oxidation, is known to suppress the photocatalytic activity of TiO₂^{170 171}. Vaiano et al. reported that deactivation of their pure TiO₂ photocatalyst due to the presence of As(V) was prevented by incorporating a molybdenum oxide sorbent phase¹⁷⁰. If this is true, then Fe₂O₃-coupling should similarly prevent deactivation of meso-TiO₂. A fourth potential effect of Fe₂O₃-coupling is that since high surface areas increase photocatalytic activity^{463 464} the iron oxide surface coating identified in section 5.2 might suppress the photocatalytic oxidation of As(III) by (a) reducing the surface area of exposed meso-TiO₂ and (b) acting as a barrier at the TiO₂-solution interface.

This chapter therefore hypothesised that the kinetics of As(III) photocatalytic oxidation would be significantly altered after meso-TiO₂ is coupled with Fe₂O₃. To date, no study has investigated how photocatalyst-sorbent coupling influences the chemistry of As(III) photocatalytic oxidation^{11 20 21 22}. The aim of this chapter was therefore to identify the major mechanisms by which Fe₂O₃-coupling influences the photocatalytic oxidation of As(III) in the presence of meso-TiO₂. Characterisation of the ultraviolet absorption of meso-TiO₂/Fe₂O₃ was used to determine (a) the extent of parasitic ultraviolet absorption by the Fe₂O₃ component, and (b) whether a heterojunction was formed at the TiO₂/Fe₂O₃ interface. Secondly, kinetic analysis was used to identify reaction mechanisms, considering (a) As(III) adsorption-controlled kinetics, (b) As(V) deactivation control of the kinetics, and (c) the possibility that the iron oxide coating acts as a barrier to photocatalysis using meso-TiO₂.

Chapter 6 demonstrated that the adsorption of As(V) onto meso-TiO₂/Fe₂O₃ can be accurately predicted using component additive modelling. On the other hand, deviations from component additivity in the adsorption of As(III) onto meso-TiO₂/Fe₂O₃ provided insights into how the chemistry of meso-TiO₂/Fe₂O₃ differs from the single-component meso-TiO₂ and Fe₂O₃ reference samples (in this case, the influence of sorbent morphology/porosity on multilayer As(III) adsorption was identified). Component additive modelling is similarly used in this chapter as an approach towards investigating how Fe₂O₃-coupling influences the photocatalytic oxidation of As(III). Firstly, component additivity offers a method for estimating the proportion of available photons lost due to Fe₂O₃ parasitic absorption, by considering the weighted sum of the absorbance of meso-TiO₂ and Fe₂O₃ reference samples.

Secondly, when a favourable heterojunction is formed at the interface between meso-TiO₂ and Fe₂O₃, electron-hole recombination rates are reduced, and photocatalytic activity is enhanced. Photocatalytic oxidation of As(III) using mixed semi-conductors has been reported in several studies, e.g. the improved removal of As(III) by graphitic carbon nitride (g-C₃N₄) when coupled with either Fe₂O₃¹⁸⁷ or Fe₃O₄¹⁵³ has been assigned to the heterojunction effect. However, this effect has not been isolated from other influences, for instance g-C₃N₄/Fe₂O₃ composites may

show improved As(III) removal simply thanks to the combination of the high surface area of g-C₃N₄ and the high adsorption capacity (per unit area) of Fe₂O₃. Heterojunction behaviour is better identified by measuring charge carrier lifetimes, since this is the mechanism by which heterojunctions improve photocatalytic performance. Transient absorption spectroscopy (TAS) can be used to identify charge carrier lifetimes^{184–466}, and any beneficial heterojunction between meso-TiO₂ and Fe₂O₃ components will lead to the experimental transient absorption lifetimes of meso-TiO₂/Fe₂O₃ being longer than the lifetimes predicted by component additivity (using single-component meso-TiO₂ and Fe₂O₃ samples)¹⁸⁴.

Kinetic analysis is used to identify the remaining mechanisms by which Fe₂O₃-coupling influences the photocatalytic oxidation of As(III), such as As(V) deactivation. Previous studies have identified both zero-order²⁸ and first-order¹³⁹ relationships between the concentration of aqueous As(III) and the rate of photocatalytic oxidation in the presence of TiO₂. Zero-order kinetics indicate that the generation of charge carriers or reactive intermediates is the rate determining step, whilst pseudo-first order kinetics indicate that aqueous oxidation of As(III) is the rate determining step. The adsorption of As(III) to both meso-TiO₂ and Fe₂O₃ surfaces is significant (chapter 6) and adsorption was considered likely to play a role in the kinetics of As(III) photocatalytic oxidation. Langmuir-Hinshelwood (LH) kinetics are often used to describe surface-controlled photocatalytic reactions. In the LH model, the reaction rate is first-order with respect to the concentration of adsorbed substrate, which is estimated using the Langmuir adsorption isotherm³⁰⁰. A few papers have successfully used surface-controlled LH kinetics to describe the photocatalytic oxidation of As(III)^{153–467}. Adsorption-controlled photocatalytic oxidation kinetics can also be identified by addition of competitor sorbates, such as phosphate, which will block access of As(III) to the catalyst surface and consequently suppress oxidation rates if adsorbed As(III) is involved in the rate determining step¹⁷¹.

The method of initial rates is recommended as the superior approach towards identifying the order of a reaction compared with the integral analysis of serial data¹⁹⁵. This is because serial data can disguise the true order of a reaction^{195–468}. Disguised kinetics can be identified when the rate constant is conditional (e.g. when the rate constant changes with changing substrate concentrations), since the rate constant of the true rate law is independent of experimental conditions¹⁹⁵. Consequently, experimental data was first analysed using the method of initial rates to establish the order of reaction and serial data was then analysed for verification of results, with any differences resolved through the development of new rate equations.

Deactivation of TiO₂ due to the presence of As(V) can be modelled using a kinetic model where the rate decreases with increasing [As(V)]. This chapter develops two rate equations based upon As(V) deactivation to help explain the differences between meso-TiO₂ and meso-

TiO₂/Fe₂O₃ photocatalytic oxidation kinetics. This chapter also develops an adsorption-controlled rate law, where for the first time, a surface complexation model (SCM) is used to calculate the concentration of adsorbed As(III) at each point in time, providing a more nuanced description of adsorption than the single sorbate Langmuir-Hinshelwood kinetic model.

7.1.1. Aims and objectives

The aim of this chapter was to determine mechanistically how coupling the meso-TiO₂ photocatalyst with a Fe₂O₃ sorbent phase affects the photocatalytic oxidation of As(III). To achieve this aim, the objectives were: (1) to verify that the UV-Vis absorption of meso-TiO₂/Fe₂O₃ is component additive; (2) to use the component additive approach to identify whether heterojunctions were formed after coupling meso-TiO₂ with Fe₂O₃; (3) to compare arsenic removal via adsorption under environmentally relevant conditions for both meso-TiO₂ and meso-TiO₂/Fe₂O₃, with and without photocatalytic oxidation; (4) to determine the order of reaction using the method of initial rates; (5) to verify the order of reaction using the integral analysis of serial data; (6) to establish reaction mechanisms explaining discrepancies between initial rates and serial data; and (7) to establish a mechanistic rationale to explain observed differences between the kinetics of As(III) photocatalytic oxidation using meso-TiO₂ and meso-TiO₂/Fe₂O₃.

7.2. Optical characterisation to understand the ultraviolet absorption of meso-TiO₂/Fe₂O₃

A combination of UV-Vis absorption (and reflectance) spectroscopy and transient absorption spectroscopy (TAS) were used to identify and quantify how coupling meso-TiO₂ and Fe₂O₃ influences ultraviolet absorption (i.e. parasitic absorption) and charge carrier lifetimes (i.e. heterojunction formation). The results were used to explain the observed differences in the rates of As(III) photocatalytic oxidation.

7.2.1. Parasitic ultraviolet absorption and determination of band gaps

The UV-Vis absorption spectra of powders suspended in water are presented in Figure 7.1a. Fe₂O₃ showed a characteristic absorption band edge from 600 nm to lower wavelengths. Meso-TiO₂ showed a sharper band edge, characteristic of this material, from around 380 nm to lower wavelengths. The UV-Vis absorbance spectra of meso-TiO₂/Fe₂O₃ was dominated by the influence of Fe₂O₃, with a similar band edge observed. The single-component Fe₂O₃ sample was more scattering than both other samples, showing a broad absorption from 600 nm to 1200 nm, indicative of larger particles being present in this sample ⁴⁶⁹.

A linear combination of meso-TiO₂ and Fe₂O₃ UV-Vis absorbance spectra (weighted 44% and 56% respectively as per XRF analysis, using Equation 3.13) successfully predicted the absorbance of meso-TiO₂/Fe₂O₃ at wavelengths shorter than 580 nm (Figure 7.1a), suggesting component additivity. (The meso-TiO₂:Fe₂O₃ mass ratio of the bulk material (as determined by XRF analysis) was used for component weighting, since $\lambda=368$ nm photons penetrate $\sim 1 \mu\text{m}$ into TiO₂ anatase ⁴⁷⁰. LEIS and XPS component weighting was not used). The ultraviolet absorption of composite meso-TiO₂/Fe₂O₃ can therefore be treated as the mass-weighted linear combination of non-interacting meso-TiO₂ and Fe₂O₃ components. The deviation from component additivity at wavelengths above 580 nm was attributed to differences in particle size influencing the intensity of scattering. Chapter 5 discusses the different particle sizes and crystallite sizes of each powder.

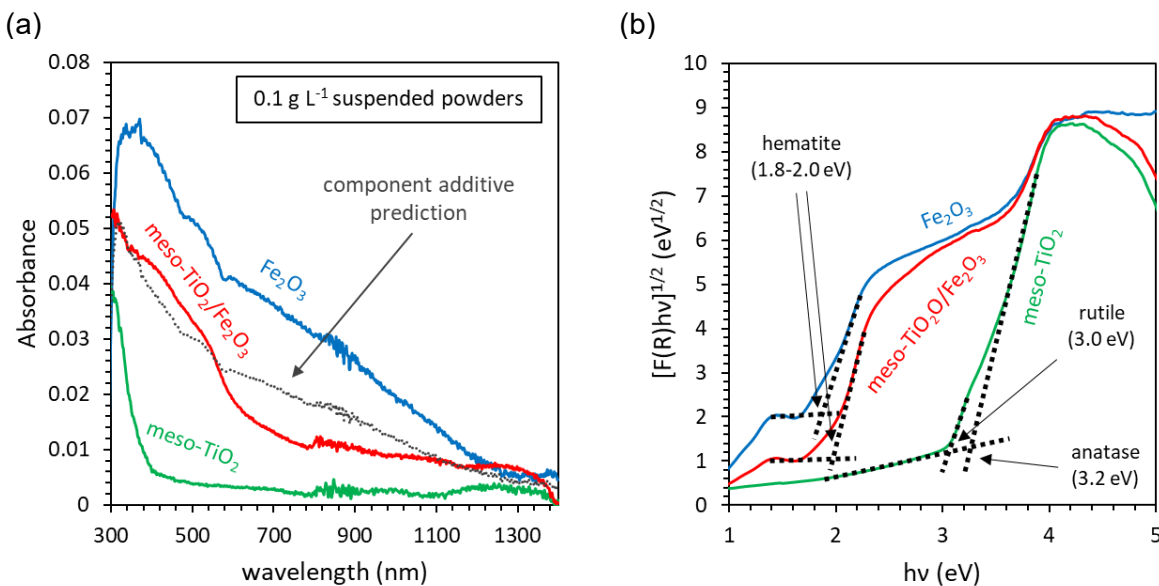


Figure 7.1: Characterisation of UV-Vis absorption. (a) UV-Vis absorbance of meso-TiO₂, meso-TiO₂/Fe₂O₃, and Fe₂O₃ powders (0.1 g L⁻¹ suspended in Milli-Q water). The dashed grey-line indicates the component additive prediction (using meso-TiO₂ and Fe₂O₃ spectra as end-members, weighted according to the XRF mass ratio). The thickness of the cuvette was 2 mm. (b) Bandgap determination using diffuse reflectance spectra of dry powders and the Kubelka-Munk function. The bandgap was identified from the position where the steep linear regions of the Tauc plot intercept the background absorption.

A component additive prediction (Equation 3.13) of the absorption coefficient, ϵ , gave a value of 2.2 L g⁻¹ cm⁻¹ for meso-TiO₂/Fe₂O₃ (at $\lambda=368$ nm), which was only 9% greater than the experimentally observed 2.0 L g⁻¹ cm⁻¹ (Appendix Figure 10.16). Component additive calculations (Equation 3.15) predicted that only 12% of the photons absorbed by meso-TiO₂/Fe₂O₃ (at $\lambda=368$ nm) are absorbed by the meso-TiO₂ component. The remaining 88% of photons are parasitically absorbed by the Fe₂O₃ component. This is an important finding, given that single-component Fe₂O₃ has negligible activity towards the photocatalytic oxidation of As(III) compared with TiO₂¹⁸⁷.

The bandgaps of meso-TiO₂, meso-TiO₂/Fe₂O₃ and Fe₂O₃ powder samples were estimated using a Tauc plot²⁹³. Since absorption could not be determined from the dry powders, the Kubelka-Munk function was used to obtain F(R), a parameter that is proportional to the absorption coefficient, using diffuse reflectance data²⁹⁴. The bandgap of the majority anatase phase within meso-TiO₂ was 3.2 eV, though a weaker absorbance, corresponding to the minority rutile phase at 3.0 eV, can also be seen (Figure 7.1b). The only bandgap that could be identified in the Tauc plot of composite meso-TiO₂/Fe₂O₃ was that of Fe₂O₃ at 2.0 eV. The bandgap of the TiO₂ component within the meso-TiO₂/Fe₂O₃ composite could not be determined.

7.2.2. Probing heterojunction behaviour using component additivity and transient absorption lifetimes

The transient absorption decay of dry powder samples at $\lambda=600$ nm is presented in Figure 7.2a, with the full spectrum of wavelengths presented in the Appendix. The raw data was fit using a power-law decay function²⁹⁷ to calculate the transient absorption half-life more accurately. The distribution of the absorbed laser pulse ($\lambda=355$ nm) between the meso-TiO₂ and Fe₂O₃ phases of the composite meso-TiO₂/Fe₂O₃ photocatalyst was calculated using the product of the optical density and mass fraction of each component (Equation 3.15). This calculation estimated that 37% of the absorbed laser pulse is absorbed by the meso-TiO₂ component, and the remaining 63% is absorbed by Fe₂O₃. The linear combination of normalised transient absorption decays, weighted according to these results (Equation 3.22), closely predicted the experimentally observed transient absorption decay of meso-TiO₂/Fe₂O₃ across all wavelengths (Figure 7.2b). The charge carrier life-times within the dry powder meso-TiO₂/Fe₂O₃ photocatalyst were therefore no different than would be expected for a mixture of non-interacting meso-TiO₂ and Fe₂O₃ powders.

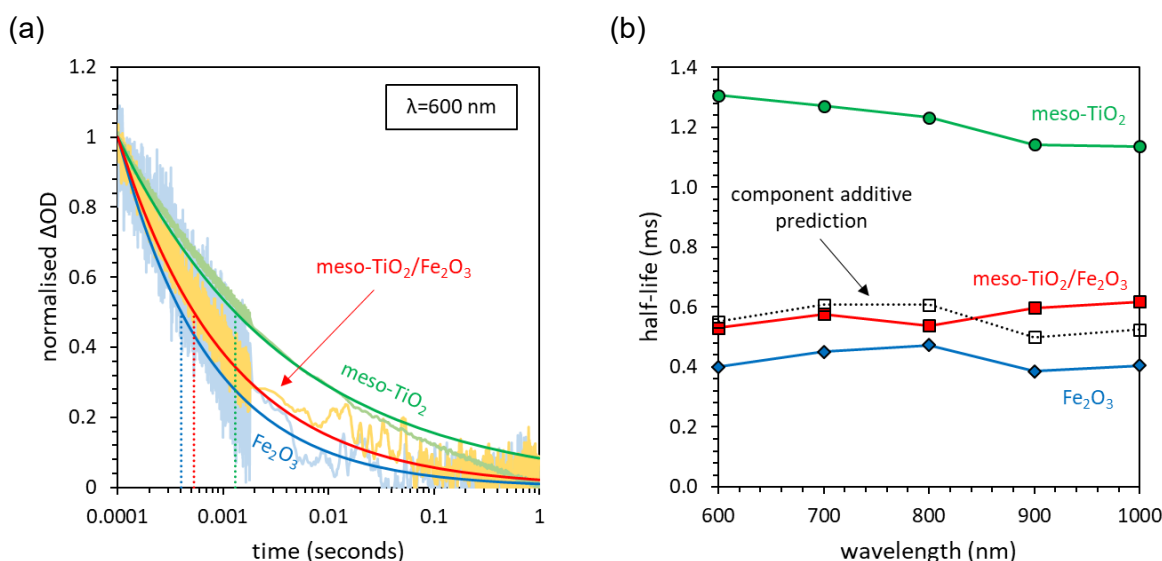


Figure 7.2: Probing heterojunction effects in the composite meso-TiO₂/Fe₂O₃ photocatalyst using transient absorption spectroscopy (TAS). (a) Power-law decay functions were fit to experimental data for all three samples at $\lambda=600$, 700, 800, 900 and 1000 nm, and then used to calculate the transient absorption half-lives. (b) A comparison between the experimentally observed transient absorption lifetimes of meso-TiO₂/Fe₂O₃ and the component additive prediction, using meso-TiO₂ and Fe₂O₃ as end-member reference samples.

These results indicate that either (a) there is no transfer of charge carriers between the two semiconductors, or that (b) both charge carriers are transferred equally from one semi-

conductor phase to the other (the type-I staggered heterojunction indicates favourable energetics for the transfer of both electrons and holes from TiO₂ to Fe₂O₃)²⁴. Since no significant increase in charge carrier lifetimes was observed, meso-TiO₂/Fe₂O₃ does not appear to contain a favourable heterojunction at the TiO₂/Fe₂O₃ interface. The absence of heterojunction behaviour may be due to a poorly-defined TiO₂/Fe₂O₃ interface, given that meso-TiO₂/Fe₂O₃ particles are highly heterogeneous and the Fe₂O₃ precipitates are often particulate and discrete from the meso-TiO₂ core (section 5.2). These findings are in contrast to previous studies reporting increased photocatalytic activity after TiO₂ is coupled with Fe₂O₃. Examples include composite powders formed by precipitation of TiO₂ over Fe₂O₃ nanoparticles⁴⁷¹, and precipitation of TiO₂ over Fe₂O₃ nanorods⁴⁷², and iron oxide deposition onto Degussa P25 TiO₂²⁴⁷. It is worth noting that none of these studies assessed the influence of Fe₂O₃-coupling on charge carrier lifetimes using TAS (instead determining photocatalytic activity by monitoring As(III) oxidation kinetics).

7.3. Verifying that composite photocatalyst-sorbents improve total arsenic removal under environmentally relevant conditions

Before considering oxidation kinetics, this chapter compares the removal of As(III) using meso-TiO₂ and meso-TiO₂/Fe₂O₃ to verify that (a) coupling meso-TiO₂ with Fe₂O₃ improves total arsenic removal under environmentally-relevant conditions, and (b) photocatalytic oxidation improves the removal of arsenic under environmentally-relevant conditions. This experiment was important since all sorbent samples investigated in chapter 6 adsorbed more As(III) than As(V) due to the multilayer adsorption of As(III) at high aqueous arsenic concentrations. The total concentration of arsenic removed at lower As concentrations, with and without ultraviolet radiation, was compared, ignoring kinetics for the time being.

Despite most studies of composite photocatalyst-sorbents working with initial As(III) concentrations in the 10-100 mg L⁻¹ range^{189 249}, the concentrations of arsenic in the groundwaters of South Asia rarely exceed 1 mg L⁻¹^{40 86}. The meso-TiO₂/Fe₂O₃ composite used within this thesis was previously tested in solutions of ≥ 5 mg L⁻¹ As(III)¹¹. Additionally, these natural groundwaters are typically rich in competitor ions, such as phosphate (which is ten times more prevalent than arsenic). Adsorption experiments were thus conducted with 1 mg L⁻¹ initial As(III), in three media at pH 7.3 \pm 0.1 (10 mM HEPES, 10 mM HEPES spiked with

10 mg L^{-1} phosphate, and a natural groundwater sample collected in West Bengal, India), both with and without ultraviolet irradiation. The natural groundwater is characterised in Table 3.2, where it is labelled “STN2”. As(III) removal using the single-phase Fe_2O_3 reference sample was not investigated in this chapter, given that previous studies have shown that Fe_2O_3 has negligible photocatalytic activity towards the oxidation of As(III) when compared with TiO_2 ¹⁸⁷.

The results are presented in Figure 7.3. In all cases, meso- $\text{TiO}_2/\text{Fe}_2\text{O}_3$ removed more arsenic by adsorption than meso- TiO_2 , despite having a smaller surface area ($116 \text{ and } 146 \text{ m}^2 \text{ g}^{-1}$ respectively). Additionally, in all cases photocatalytic oxidation improved arsenic removal. Arsenic removal in the natural groundwater was similar to arsenic removal in HEPES buffer, however addition of 10 mg L^{-1} phosphate (a strong competitor ion, found in natural groundwaters at this concentration) led to a notable reduction in arsenic removal. The influence of phosphate on arsenic adsorption appears to be most pronounced before oxidation, since As(III) surface complexes are weaker than As(V), and thus more easily displaced by phosphate ions. This highlights the importance of oxidation when aiming to remove As(III) from phosphate-rich waters.

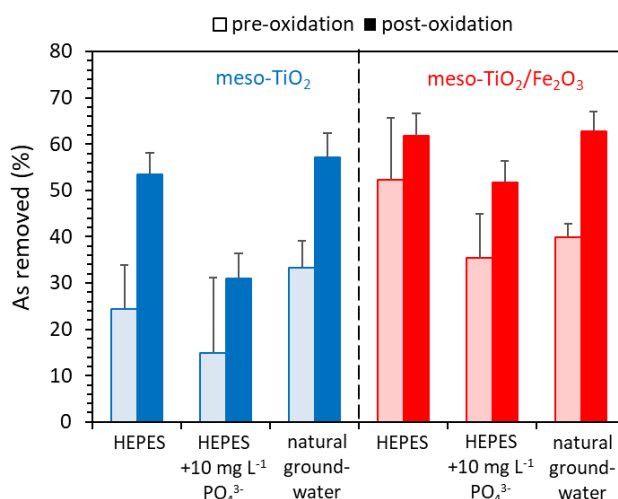


Figure 7.3: A comparison of total arsenic removed before (lightly shaded bars) and after (heavily shaded bars) photooxidation using meso- TiO_2 and meso- $\text{TiO}_2/\text{Fe}_2\text{O}_3$ as photocatalyst-sorbents in a variety of media. The experimental conditions were 1 mg L^{-1} initial As(III) adsorbed in the dark overnight, 0.1 g L^{-1} catalyst, and pH 7.3 ± 0.1 . The amount of arsenic removed from solution was calculated by subtracting the total As remaining in solution after adsorption/photocatalytic oxidation from the initial concentration of As (both determined by ASV). Error bars indicate uncertainties calculated from the standard deviation between repeat measurements.

Much literature, as well as chapter 6 in this thesis, demonstrates that TiO_2 and Fe_2O_3 have higher adsorption capacities for As(III) than As(V) at high equilibrium concentrations of arsenic (C_e). At neutral pH, As(III) adsorption isotherms often follow the Freundlich adsorption isotherm model, rather than the Langmuir model, due to multilayer adsorption: surface precipitation or surface polymerisation²⁵⁷. In this experiment, however, adsorption was

greatest after photooxidation. This is explained by the experimental conditions: with only 1 mg L⁻¹ total arsenic, multilayer adsorption is insignificant and therefore As(V) adsorption is greater than As(III) adsorption due to the strong surface complexes that As(V) forms with Fe₂O₃ and TiO₂ surfaces.

This experiment thus identified that Fe₂O₃-coupling and a combined photocatalytic oxidation-adsorption approach does indeed improve arsenic(III) removal compared with (a) single-component TiO₂ photocatalysts, and (b) adsorption without oxidation. The experiment also showed that the lost adsorption capacity due to the presence of phosphate competitor ions is reduced when meso-TiO₂ is coupled with Fe₂O₃, indicating the importance of coupling TiO₂ with an effective sorbent phase when working in the phosphate-rich groundwaters of South Asia.

Having verified that removal of As(III) is improved by coupling TiO₂ with Fe₂O₃ and using ultraviolet radiation, the kinetics of photocatalytic oxidation were investigated. Initial As(III) concentrations were increased to 10 mg L⁻¹ to minimise uncertainties in the calculated oxidation kinetics due to changes in the concentration of adsorbed arsenic (discussed in the Appendix).

7.4. Establishing the order of reaction: Analysis of initial rates

Analysis of initial rates was used to establish the influence of (a) light intensity, (b) As(III) concentrations, and (c) the presence of phosphate, upon the photocatalytic oxidation of As(III). Light intensity was investigated to ensure that meso-TiO₂ and meso-TiO₂/Fe₂O₃ were compared within the linear range, before different electron-hole pairs begin to interact and increase recombination rates (see section 7.4.1). The influence of As(III) and phosphate was investigated to establish whether As(III) is required in the rate determining step, and whether As(III) must be adsorbed to the photocatalyst surface for the rate determining step.

A full characterisation of the experimental set-up is provided in the Appendix. This includes (1) a comparison between the spectral output of the ultraviolet lamp and the band edges of each sample, (2) the calculated photon flux absorbed by the photoreactor, (3) a total arsenic mass balance throughout the course of the experiment, and (4) control experiments (a) in the dark and (b) without addition of the photocatalyst.

7.4.1. Electron-hole recombination kinetics: The influence of light intensity on the initial rate of As(III) photocatalytic oxidation

It is well established that above a threshold light power, the relationship between reaction rates and light intensity changes from first-order to half-order and then zero-order ^{141 473}. The linear region indicates fast charge transfer kinetics, with slow charge recombination ⁴⁷⁴, whilst half-order and zero-order kinetics reflect the increased rates of electron-hole recombination, and mass transport limitations ¹⁴¹. As identified in section 7.2.1, a significant proportion of ultraviolet photons (88% at $\lambda=368$ nm) are absorbed by the photocatalytically inactive Fe₂O₃ phase. The reduced availability of photons to excite the meso-TiO₂ phase will lead to increased electron-hole recombination rates becoming a problem at higher light intensities for the composite photocatalyst compared with single-component meso-TiO₂. It was therefore important to identify the relationship between light intensity and As(III) oxidation rates for each material, so that the two materials could be compared within the linear range.

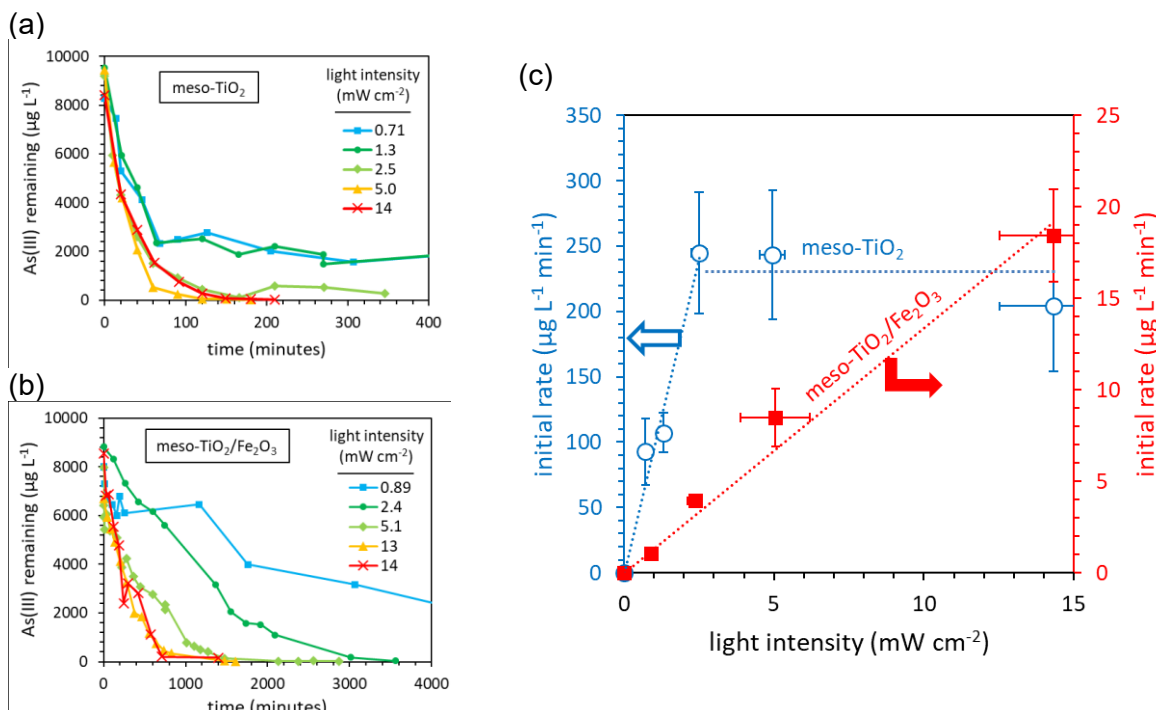


Figure 7.4: The influence of light intensity on the initial rate of As(III) photocatalytic oxidation in the presence of (a) meso-TiO₂ and (b) meso-TiO₂/Fe₂O₃ photocatalysts. (c) The comparison of initial rates. The light intensity was varied by increasing and decreasing the distance between the UV lamp ($\lambda=368\text{ nm}$) and the photoreactor surface. The experimental conditions were 10 mg L^{-1} initial As(III), 0.1 g L^{-1} photocatalyst, 10 mM HEPES ($\text{pH }7.3 \pm 0.1$), and 100 mL total volume. Error bars indicate the standard deviation in the slope of the linear regression used to calculate the initial rates.

Single-component meso-TiO₂ and composite meso-TiO₂/Fe₂O₃ showed differences in the response of photocatalytic oxidation to changes in light intensity (Figure 7.4). A linear relationship between initial rate and light intensity was observed for meso-TiO₂/Fe₂O₃. The meso-TiO₂ system initially showed a first-order relationship between light intensity and initial rate. However, after 2.5 mW cm^{-2} the initial rates became independent of light intensity. This is similar to the change in the order of reaction at 6 mW cm^{-2} observed by Dutta et al. for photocatalytic oxidation of As(III) using Degussa P25 TiO₂²⁸. Dutta et al. found that overall, the rate of reaction was proportional to $I^{0.23}$, where I is the light intensity.

The quantum yield (Φ) indicates the number of reactions completed per incident photon (Equation 3.34). At 2.5 mW cm^{-2} , the quantum yield of As(III) oxidation in the presence of meso-TiO₂ ($\Phi=0.39 \pm 0.09$) was greater than the quantum yield using the meso-TiO₂/Fe₂O₃ composite ($\Phi=0.00057 \pm 0.00017$) by a factor of 68. Beyond the linear region, the quantum efficiency of meso-TiO₂ decreases with increasing light intensity (e.g. $\Phi=0.0057 \pm 0.006$ at 14.3 mW cm^{-2}). In contrast, the quantum efficiency of meso-TiO₂/Fe₂O₃ was maintained at high light intensity (e.g. $\Phi=0.00051 \pm 0.00010$ at 14.3 mW cm^{-2}). High quantum yields have been previously observed in the homogeneous photooxidation of As(III): Ryu et al. reported a quantum yield as high as 2.1 in the absence of a heterogeneous photocatalyst¹⁴³. Ryu et al.

used a harder UV light source ($\lambda = 254$ nm), which often increases quantum efficiency, and the authors attributed the observation that Φ was greater than unity to the regeneration of reactive oxygen species (ROS) during the oxidation of the As(IV) intermediate product to As(V)¹⁴³.

UV-Vis absorption spectroscopy showed that due to parasitic absorption by Fe_2O_3 , the meso- TiO_2 component of the composite photocatalyst only absorbs 12% of the total ultraviolet photons absorbed by meso- $\text{TiO}_2/\text{Fe}_2\text{O}_3$. Consequently, the photocatalytic rate observed at 14 mW cm⁻² in the composite is analogous to irradiating pure meso- TiO_2 with 1.7 mW cm⁻², which is within the linear range of meso- TiO_2 . The linear relationship between light intensity and initial rates therefore extends to higher values of light intensity for the composite photocatalyst.

It is also important to note that with ≤ 1.3 mW cm⁻², complete oxidation of As(III) in the presence of meso- TiO_2 was not achieved, with ~ 2 mg L⁻¹ (20% of the initial As(III)) remaining. In contrast, meso- $\text{TiO}_2/\text{Fe}_2\text{O}_3$ always reached complete oxidation. Stalled photooxidation of As(III) has been reported elsewhere, for instance the study of Vaiano et al. who also used a TiO_2 photocatalyst (0.1-0.5 g L⁻¹ TiO_2 (70 m² g⁻¹), 5 mg L⁻¹ initial As(III) and 0.75 mW cm⁻² UV irradiation)¹⁷⁰. The authors hypothesised that the failure of TiO_2 to oxidise all As(III) was due to surface deactivation caused by the As(V) product acting as a competitor ion and occupying TiO_2 surface sites. Following this explanation, meso- $\text{TiO}_2/\text{Fe}_2\text{O}_3$ potentially achieves complete oxidation where meso- TiO_2 fails thanks to the Fe_2O_3 component adsorbing As(V) and freeing the TiO_2 surface to continue photocatalysis.

7.4.2. Order of reaction with respect to As(III): The influence of As(III) concentration on the initial rate of As(III) photocatalytic oxidation

The influence of the initial concentration of As(III) upon reaction rates was investigated, since both zero-²⁸ and first-order¹³⁹ kinetics have been observed in the photooxidation of As(III) in the presence of TiO_2 photocatalysts. Meso- TiO_2 and meso- $\text{TiO}_2/\text{Fe}_2\text{O}_3$ systems differed in how the initial rates responded to changes in the concentration of As(III) (Figure 7.5). In the presence of meso- TiO_2 , the initial rate was independent of As(III) concentrations (0.5-10 mg L⁻¹ As(III) added) (Figure 7.5c). Zero-order kinetics were also observed by Dutta et al. using TiO_2 ²⁸. Zero-order kinetics may be observed when the photocatalyst surface is saturated with the substrate. However, the As(III) adsorption isotherms and surface complexation model (SCM) calculations presented in chapter 6 indicate that at pH 7.0±0.1 monolayer coverage is incomplete with less than 7.5 mg L⁻¹ aqueous As(III), whilst multilayer As(III) adsorption results in adsorption continuing after monolayer coverage. Therefore, the zero-order kinetics observed indicate that the reaction rate is independent of both aqueous and adsorbed As(III).

concentrations, and that the rate determining step should be linked to another process, such as the generation of holes, electrons or intermediates, such as reactive oxygen species (ROS).

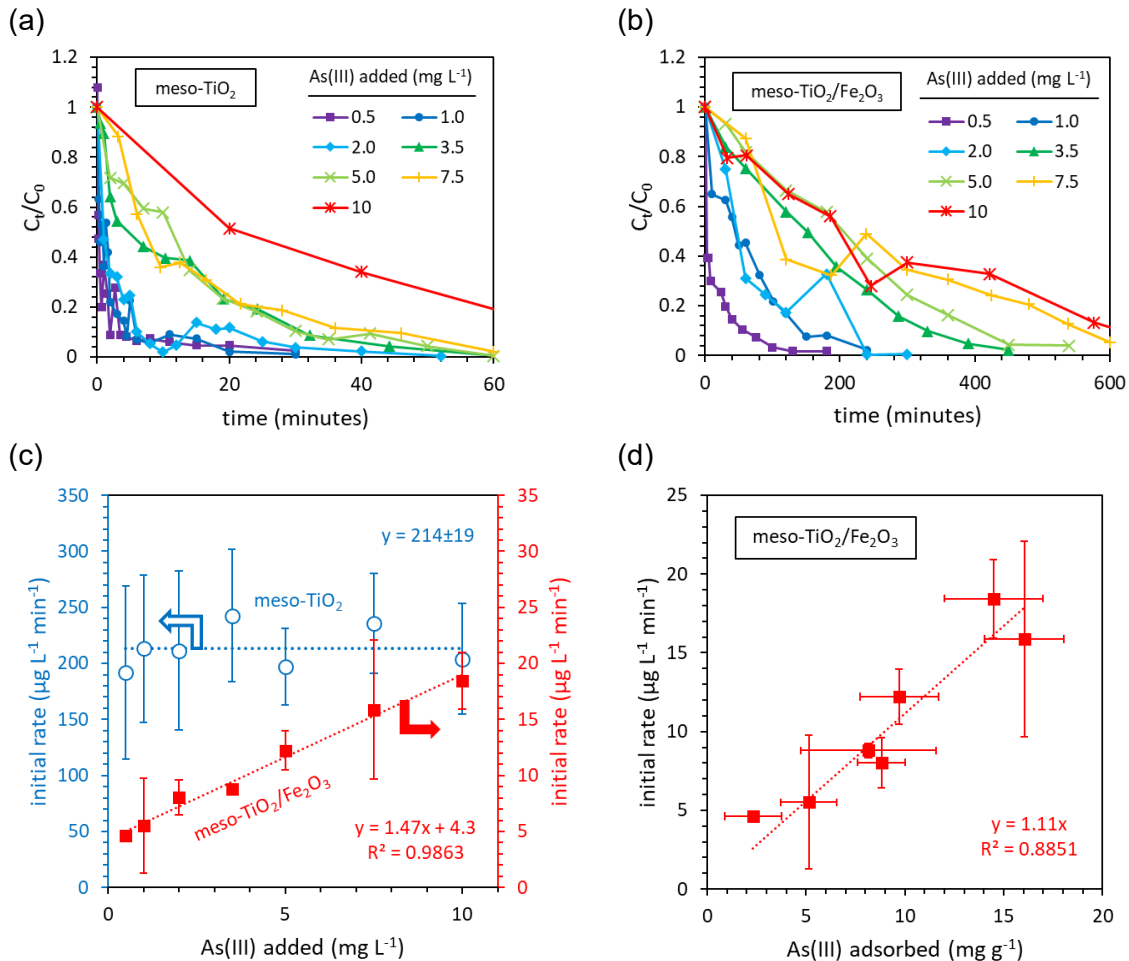


Figure 7.5: The influence of As(III) concentration on the rate of photocatalytic oxidation in the presence of (a) meso-TiO₂ and (b) meso-TiO₂/Fe₂O₃ photocatalysts. (c) The influence of the As(III) concentration on the initial rate. (d) The influence of adsorbed As(III) on the initial rate. Experimental conditions were 0.5–10 mg L⁻¹ As(III), 0.1 g L⁻¹ photocatalyst and 10 mM HEPES (pH 7.3±0.1), 14 mW cm⁻² light intensity ($\lambda=368$ nm), and 100 mL total volume. Error bars indicate the uncertainty in the initial rate determined as the standard deviation of the slope in the linear regression fitted to the initial experimental kinetics (linear region).

In contrast, a linear relationship was observed between the initial rate and the concentration of As(III) in the presence of meso-TiO₂/Fe₂O₃, albeit offset from the origin by a positive y-intercept (Figure 7.5c). Pseudo first-order kinetics are therefore approximated at high As(III) concentrations, but not at low concentrations. A more significant first-order relationship (passing through the origin) was observed between initial rate and the concentration of adsorbed As(III) (Figure 7.5d). This indicates that unlike meso-TiO₂, the kinetics of As(III) oxidation in the presence of meso-TiO₂/Fe₂O₃ are determined by the concentration of adsorbed As(III).

7.4.3. Adsorption-control versus intermediate oxidants: The influence of phosphate on the initial rate of As(III) photocatalytic oxidation

Addition of phosphate was used to further probe the mechanism of As(III) photocatalytic oxidation using the two photocatalysts. Phosphate is known to suppress arsenic adsorption through competitive adsorption to mineral surfaces^{225 228}, and 10 mg L⁻¹ is sufficient to achieve monolayer coverage at pH 7²³. By blocking access to the photocatalyst surface, phosphate should suppress the photocatalytic oxidation of As(III) when adsorbed As(III) is involved in the rate determining step¹⁷¹.

Addition of 10 mg L⁻¹ phosphate decreased adsorption of As(III) onto meso-TiO₂ by 19% (Figure 7.6a), however since only a small proportion of the initial 10 mg L⁻¹ As(III) was adsorbed by 0.1 g L⁻¹ meso-TiO₂, the uncertainty is large. Surface complexation modelling (SCM) was therefore used to confirm the result, predicting a 5% decrease in [As(III) (ads)]. Presence of phosphate had a more significant effect on the adsorption of As(III) onto meso-TiO₂/Fe₂O₃, with [As(III) (ads)] decreasing by 62% and 36% when calculated using experimental data and the SCM respectively.

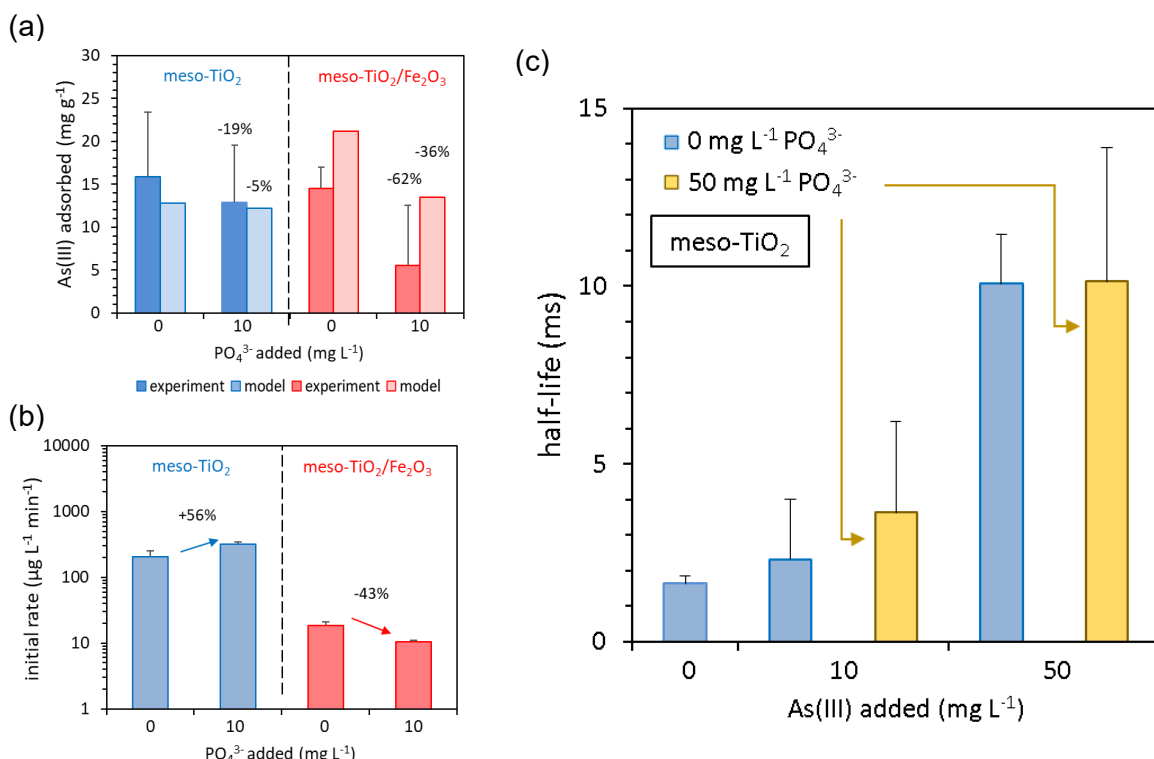


Figure 7.6: The influence of phosphate (10 mg L⁻¹) on the photocatalytic oxidation of As(III). The influence of phosphate on (a) the adsorption of As(III), and (b) initial rates in the photocatalytic oxidation of As(III) is presented. The experimental conditions were 10 mg L⁻¹ As(III), 0.1 g L⁻¹ photocatalyst, 10 mM HEPES (pH 7.3±0.1), 14 mW cm⁻² light intensity ($\lambda=368\text{ nm}$), and 100 mL total volume. (c) The influence of phosphate (10 mg L⁻¹) on the transient absorption half-lives of suspensions of 10 and 50 mg L⁻¹ As(III) in the presence of meso-TiO₂ (1 g L⁻¹) in 10 mM HEPES (pH 7.3±0.1). The results presented are averages of measurements taken at $\lambda=600, 700, 800, 900$ and 1000 nm and error bars indicate the standard deviation.

The initial rate of As(III) photooxidation in the presence of meso-TiO₂/Fe₂O₃ decreased by 43% when 10 mg L⁻¹ phosphate was added (Figure 7.6b). This is similar in magnitude to the 62% decrease in As(III) adsorption, suggesting that the rate of reaction is controlled by the concentration of As(III) adsorbed onto the photocatalyst surface, in agreement with section 7.4.2. The opposite effect was observed for meso-TiO₂: the initial rate of As(III) photooxidation increased by 56% upon addition of 10 mg L⁻¹ phosphate (Figure 7.6b), despite the 19% decrease in adsorbed As(III). This suggests that the rate of photocatalytic oxidation is not controlled by the concentration of adsorbed As(III) under these experimental conditions, in agreement with the zero-order kinetics identified in section 7.4.2. It is reported that under certain conditions phosphate can enhance photocatalysis, either (a) by the formation of hydrogen-bonded complexes between adsorbed phosphate and H₂O facilitating charge transfer and the subsequent generation of intermediate reactive oxygen species (ROS), such as ·OH and H₂O₂, or (b) by the attraction between adsorbed phosphate (which is negatively charged at pH 7) and positive holes, improving charge extraction ¹⁷¹.

TAS data showed that As(III) scavenges charge carriers from meso-TiO₂, increasing transient absorption lifetimes (Appendix). The half-lives of transient absorption did not decrease after addition of phosphate, indicating that As(III) scavenged charge carriers just as effectively (Figure 7.6c). These results provide additional evidence that site-blocking does not suppress the photocatalytic oxidation of As(III) using meso-TiO₂, and therefore suggest that the rate depends on charge extraction and the generation of ROS intermediates, rather than the concentration of adsorbed As(III). A reaction mechanism where the generation of ROS intermediates is the rate determining step would explain the zero-order relationship between initial rates and As(III) concentrations that was identified in section 7.4.2. Suspensions of meso-TiO₂/Fe₂O₃ were not analysed using TAS since changes in optical density after laser excitation were small compared with the total optical density of meso-TiO₂/Fe₂O₃ suspensions, and the transient decays of meso-TiO₂/Fe₂O₃ could not be sufficiently resolved.

7.5. New rate equations reconcile discrepancies between initial rates and serial data

Section 7.4 established zero-order kinetics for meso-TiO₂ and surface-controlled kinetics, (approaching pseudo first-order kinetics at high As(III) concentrations) for meso-TiO₂/Fe₂O₃ using the method of initial rates. In this section, kinetic analysis of serial data was used to confirm the results. However, serial data presented challenges in the kinetic description of both photocatalysts, which were resolved by the development of new rate equations.

7.5.1. Contradictions between analysis of initial rates and serial data

Analysis of initial rates established a zero-order relationship between As(III) concentrations and meso-TiO₂ photocatalytic oxidation rates (section 7.4.2). However, the serial data obtained in each individual kinetics experiment could not be described by zero-order kinetics, as in all cases the reaction rate slowed as As(III) was depleted (Figure 7.5a). Serial data was better described using pseudo first-order (PFO) kinetics, and serial data was successfully linearised by plotting $\ln(C_t/C_0)$ as a function of time (Figure 7.7a). Whilst the method of initial rates had demonstrated zero-order kinetics, integral analysis of serial data suggested pseudo first-order kinetics.

A different phenomenon was observed in the kinetic analysis of meso-TiO₂/Fe₂O₃ serial data. Initial rate analysis indicated a first-order dependence upon [As(III) (ads)], approximating PFO kinetics (first-order with respect to [As(III) (aq)]) at high concentrations of As(III) (section 7.4.2). Plots of C_t/C_0 as a function of time began to overlap when at least 3.5 mg L⁻¹ As(III) was added (Figure 7.5b), in line with the PFO approximation at high As(III) concentrations. Whilst serial data was successfully linearised when less than 2 mg L⁻¹ As(III) was added (Figure 7.7b), linearisation was less successful with more than 2 mg L⁻¹ As(III), with the slope of $\ln(C_t/C_0)$ versus time increasing when $\ln(C_t/C_0) \approx -1.5$ (Figure 7.7c). Whilst initial rates indicated that PFO kinetics were approximated at high As(III) concentrations, integral analysis gave a PFO rate constant, k_1 , that appeared to *speed up* towards the end of each experiment. PFO kinetics were therefore insufficient to explain the full range of experimental observations. The curvature in $\ln(C_t/C_0)$ as a function of time can be seen elsewhere, for instance in the study of Ferguson et al. (3.2 mg L⁻¹ initial As(III) and Degussa P25 TiO₂)²⁰³. In their study, no curvature was observed at lower initial As(III) concentrations of 190 µg L⁻¹²⁰³, similar to the results here.

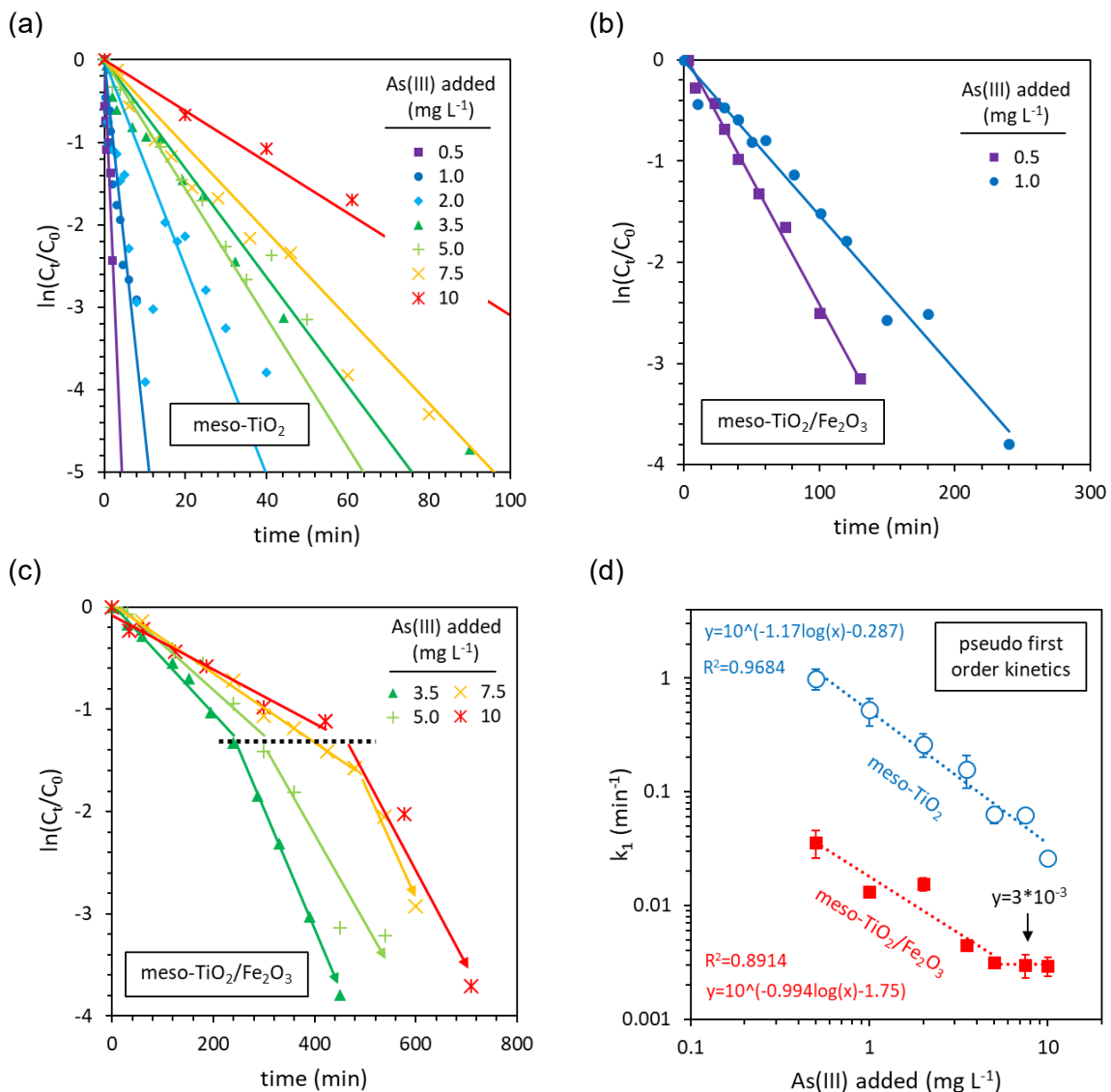


Figure 7.7: Linearisation of serial data using pseudo first-order kinetics. (a) Linearisation of meso-TiO₂ serial data. (b) Linearisation of meso-TiO₂/Fe₂O₃ serial data with 0.5 and 1 mg L⁻¹ initial As(III). (c) Failed linearisation of meso-TiO₂/Fe₂O₃ serial data with ≥ 3.5 mg L⁻¹ As(III). (d) The influence of As(III) concentrations on the calculated values of the PFO rate constant k_1 .

The influence of As(III) concentrations on the PFO rate constant k_1 is presented in Figure 7.7d. For the meso-TiO₂ system, k_1 decreases exponentially with increasing As(III) concentrations. The rate constant of the true rate law will be independent of the experimental conditions and therefore this conditionality of k_1 indicates that the meso-TiO₂ system does not truly follow PFO kinetics, but rather 'disguised' zero-order kinetics¹⁹⁵ explored later (section 7.5.2). For the meso-TiO₂/Fe₂O₃ system, k_1 decreases exponentially with increasing As(III) concentrations until 5 mg L⁻¹ is reached, whereupon k_1 stabilises. This indicates that PFO kinetics are approximated at high As(III) concentrations, in agreement with section 7.4.2. The following sections investigate the causes behind the behaviour observed in the serial data and develop rate equations that provide rate constants that are stable (i.e. less conditional) across the entire 0.5–10 mg L⁻¹ As(III) concentration range.

7.5.2. The disguised zero-order kinetics of meso-TiO₂ are explained by photocatalyst deactivation

The method of initial rates is considered to show the true reaction order, whilst serial data can sometimes disguise the true kinetic law ¹⁹⁵. This section considers how disguised zero-order kinetics might arise in the meso-TiO₂ system. The true rate law should satisfy two conditions: (1) the initial rate is not influenced by the concentration of As(III) (between 0.5 and 10 mg L⁻¹), in-line with section 7.4.2, and (2) serial data follows the behaviour of pseudo first-order kinetics, with the absolute reaction rate decreasing as oxidation progresses, in-line with section 7.5. Vaiano et al. observed deactivation of TiO₂ due to the presence of As(V) ¹⁷⁰. Incomplete oxidation of As(III) using meso-TiO₂ with low light intensities was similarly identified in section 7.4.1. This section therefore considered whether deactivation of meso-TiO₂ due to the presence of As(V) would explain the experimental data.

Two rate equations that depend on the concentration of As(V) were explored. If we construct a rate law where the rate depends on the concentration of As(V) present, rather than the concentration of As(III), it is evident that initial rate analysis will show zero-order kinetics, but serial data will not. This is because (1) at t=0, there is no As(V), and (2) the concentration of As(V) continually increases during each experiment. If the rate is suppressed by the presence of As(V), then the reaction rate will slow as oxidation of As(III) progresses, and the shape of PFO kinetics observed in the serial data can be emulated.

For instance, in the first example of an As(V) deactivation model, we can consider a scenario where the absolute rate decreases linearly with increasing concentrations of As(V). The reaction would cease once all arsenic is present as As(V). Since the fraction of total As converted to As(V) at time *t* is equal to $1 - \frac{C_t}{C_0}$, we arrive at the following rate equation:

$$\frac{dC}{dt} = k^\ddagger \left(1 - \left(1 - \frac{C_t}{C_0} \right) \right)$$

Equation 7.1

where C is the concentration of aqueous As(III) (μg L⁻¹), k[†] is the rate constant (μg L⁻¹ min⁻¹), and C_t and C₀ are the concentrations of aqueous As(III) at time *t* and t=0 respectively (μg L⁻¹). This equation reduces to:

$$\frac{dC}{dt} = k^\ddagger \left(\frac{C_t}{C_0} \right)$$

Equation 7.2

and consequently, relates to the pseudo-first order rate equation through the expression:

$$k^\dagger = k_1 C_0$$

Equation 7.3

This simple rate law therefore satisfies both conditions needed to reconstruct the observed disguised zero-order kinetics: (1) the rate constant is independent of the concentration of As(III), since the term $\frac{C_t}{C_0}$ in Equation 7.2 is always 1 at t=0, regardless of the concentration of As(III) added, and (2) the shape of pseudo-first order kinetics will be observed in the serial data, since the rate is proportional to C_t .

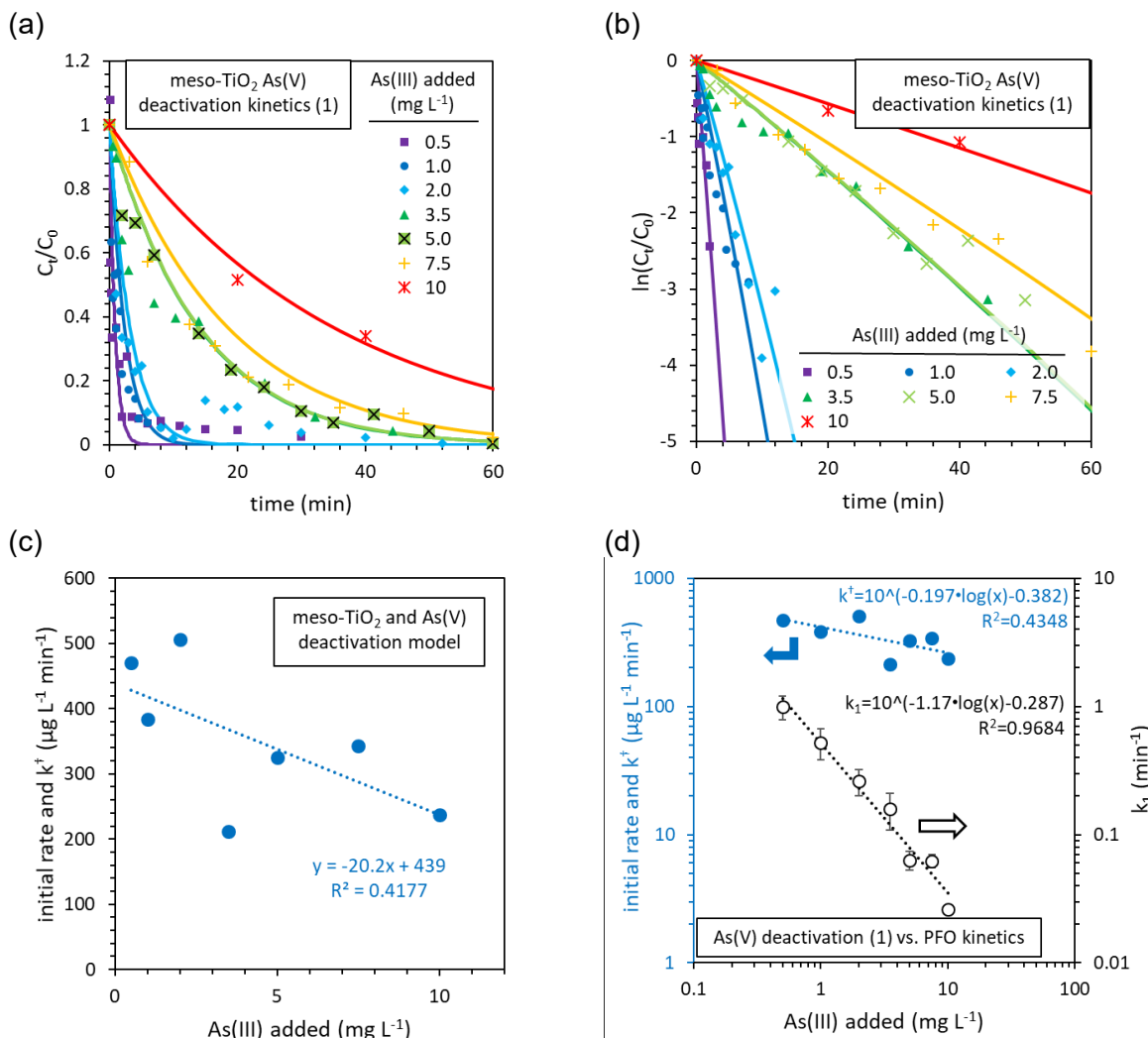


Figure 7.8: Application of the As(V) deactivation kinetics given in Equation 3.29 to explain the disguised zero-order kinetics of meso-TiO₂. The rate constant k^\dagger was obtained by minimising the sum of squares between the model and experimental observations of $\ln(C_t/C_0)$. The goodness of fit was calculated with $R^2 = 0.8991, 0.7964, 0.9155, 0.9641, 0.9513, 0.9708, 0.9957$ for the 0.5, 1, 2, 3.5, 5, 7.5 and 10 mg L^{-1} initial As(III) data sets.

Application of this rate law to the experimental data is presented in Figure 7.8. The rate law successfully reconstructed the pseudo-first order behaviour observed in the serial data, with

reaction rates decreasing as time increases (Figure 7.8a, b). This model also reduces the conditionality of the rate constant upon the concentration of As(III) added, compared with the PFO model (Figure 7.8d). Firstly, the trend for an exponential decrease in the rate constant with increasing As(III) concentrations is a lot weaker ($R^2=0.4348$ versus $R^2=0.9648$ in the PFO model). Secondly and more importantly, the slope of $\log(k^\ddagger)$ versus $\log([\text{As(III)} \text{ added}])$ (-0.197) is shallower than the slope of $\log(k_1)$ versus $\log([\text{As(III)} \text{ added}])$ (-1.17). This suggests that photocatalyst deactivation due to the presence of As(V) is a reasonable explanation for the disguised zero-order kinetics identified in sections 7.4.2 and 7.5.1.

Whilst helping to explain the disguised zero-order kinetics, this rate equation uses only C_0 and C_t parameters, i.e. only aqueous phase data was used. However, photocatalyst deactivation due to the presence of As(V) is likely to occur through surface effects, e.g. site blocking¹⁷¹. We can therefore consider a rate law where only adsorbed As(V) leads to reductions in the reaction rate. For a linear relationship between the concentration of adsorbed As(V) and the reduction in the absolute rate of oxidation, we arrive at the following rate equation:

$$\frac{d[\text{As(III)} \text{ (total)}]}{dt} = k^\ddagger(1 - j[\text{As(V)} \text{ (ads)}]_t)$$

Equation 7.4

where k^\ddagger is the rate constant ($\mu\text{g L}^{-1} \text{ min}^{-1}$), j is a sensitivity factor reflecting the extent to which the presence of As(V) suppresses the reaction (g mg^{-1}), and $[\text{As(V)} \text{ (ads)}]_t$ is the concentration of adsorbed As(V) at time t (mg g^{-1}). The concentration of adsorbed As(V) at each point in time was calculated using the surface complexation model (SCM) developed in chapter 6. The concentration of aqueous phase As(III) was also calculated using the SCM and used to calculate $\frac{C_t}{C_0}$. This model is named the *SCM-constrained As(V) model*.

The results are presented in Figure 7.9. This rate equation satisfied both conditions (1) and (2) of the disguised zero-order kinetics that were observed experimentally. Firstly, the PFO behaviour of serial data was emulated by the model (Figure 7.9a), with the data linearised as $\ln(C_t/C_0)$ (Figure 7.9b). It is only at the end of each reaction that the model deviates from the form of linearised PFO kinetics. This is because once $[\text{As(V)} \text{ (ads)}]$ reaches $\frac{1}{j}$, the term in the brackets of Equation 7.4 falls to zero and the reaction ceases. Secondly, with 3.5 mg L^{-1} or greater initial As(III), the initial rate is independent of the As(III) concentration (Figure 7.9c), emulating the zero-order behaviour identified using the method of initial rates. Within this concentration range, the sensitivity parameter, j , is also constant ($0.131 \pm 0.009 \text{ g mg}^{-1}$, with the reaction ceasing once $[\text{As(V)} \text{ (ads)}]$ is $7.6 \pm 0.5 \text{ mg g}^{-1}$). In this model, the presence of As(V) therefore has a similar influence on the reaction rate regardless of the concentration of As(III).

This model failed below 3.5 mg L⁻¹ initial As(III), where the rate increased exponentially with decreasing As(III) concentrations.

The inverse exponential relationship between the concentration of As(III) added and the rate constant was significantly weaker in this SCM-constrained As(V) deactivation model compared with the PFO model (Figure 7.9d). The reduced conditionality of the rate constant provides strong evidence that the disguised zero-order kinetics of meso-TiO₂ are caused by As(V) deactivation of the catalyst. Since initial rates were independent of As(III) concentrations (section 7.4.2), and the presence of phosphate enhanced reaction rates (section 7.4.3), any deactivation of meso-TiO₂ due to the presence of As(V) should derive from interference of As(V) with the generation of reactive oxygen species (ROS) intermediates, rather than from As(V) blocking access of As(III) to the catalyst surface.

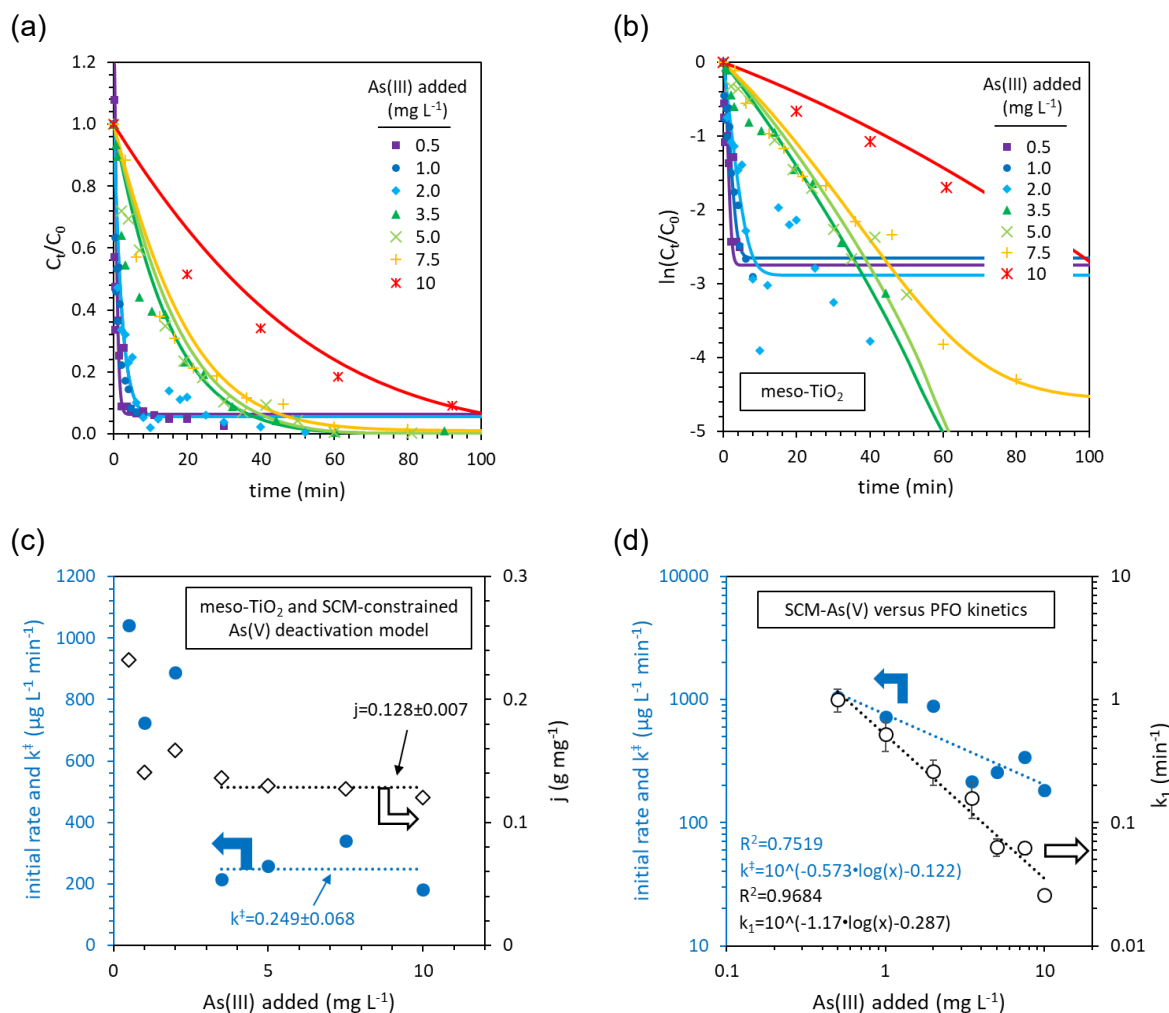


Figure 7.9: The SCM-constrained As(V) deactivation model for the photocatalytic oxidation of As(III) in the presence of meso-TiO₂. (a) and (b) present a comparison of the fitted model with experimental data. (c) The influence of As(III) concentration on the initial rate, the rate constant k^\ddagger , and the sensitivity factor j . (d) Values of k^\ddagger calculated from experimental data are less dependent upon the concentration of As(III) added than PFO rate constant k_1 .

7.5.3. Changes in the apparent pseudo first-order rate constant of meso-TiO₂/Fe₂O₃ are explained by late stage partitioning of As(III) onto the catalyst surface

Analysis of initial rate indicated that the rate of As(III) photocatalytic oxidation in the presence of meso-TiO₂/Fe₂O₃ is first-order with respect to the concentration of adsorbed As(III) (section 7.4.2). This approximated PFO kinetics at high As(III) concentrations, however the apparent PFO rate constant, k_1 , was observed to *speed up* in the later stages of each experiment.

The Langmuir-Hinshelwood (LH) kinetic model (Equation 3.25) is the most popular method used to describe kinetics controlled by the concentration of substrate adsorbed on the catalyst surface. LH kinetics were used to analyse the experimental data set, attempting both linearisation of initial rates, and fitting the LH model to serial data. The results are presented in detail within the Appendix. Briefly, linearisation of initial rates failed for meso-TiO₂ in line with section 7.4.2. Linearisation of initial rates for meso-TiO₂/Fe₂O₃ was partially successfully, however the slope of linearised initial rates changes by a factor of four when [As(III) added]=3.5 mg L⁻¹. Non-linear fitting of LH kinetics to meso-TiO₂/Fe₂O₃ serial data introduced some of the curvature in $\ln(C_t/C_0)$ versus time that was observed in the experimental data but could not be captured when using the PFO model. However, non-linearised LH kinetics failed when considering that like the PFO rate constant, k_1 , the Langmuir-Hinshelwood rate constant, k_{LH} , decreases exponentially with increasing As(III) concentrations (Figure 7.13b). This conditionality of the rate constant k_{LH} indicates that the accuracy of Langmuir-Hinshelwood kinetics applied to describe the meso-TiO₂/Fe₂O₃ system is limited.

Langmuir-Hinshelwood kinetics do not consider interference by competitor ions, such as the As(V) that appears to deactivate meso-TiO₂ (section 7.5.2). The single-sorbate Langmuir adsorption isotherm was therefore replaced with the As(V)-sensitive SCM developed in chapter 6, in order to better estimate how the concentration of adsorbed As(III) changes as photocatalytic oxidation progresses.

SCM calculations demonstrated that the distribution of As(III) between the aqueous and adsorbed phases during photocatalytic oxidation in the presence of meso-TiO₂ remained relatively constant during the reaction, at all concentrations of initial As(III) (Figure 7.10a). In contrast, a significant increase was observed in the partitioning of As(III) to the adsorbed phase in the final 20% of the oxidation reaction when using meso-TiO₂/Fe₂O₃ as the catalyst (Figure 7.10b). Whilst TiO₂-sorbed As(III) was rapidly displaced with As(V), the SCM predicted that Fe₂O₃ retains As(III) until the very last stages of photooxidation. This effect becomes more

pronounced as As(III) concentrations are increased, correlating with the observed non-linearity of $\ln(C_t/C_0)$ versus time at high values of C_0 . The increase in the slope of the linearised PFO plots of meso-TiO₂/Fe₂O₃-catalysed As(III) oxidation occurred at $\ln(C_t/C_0) \approx -1.5$, which is equivalent to 78% of aqueous As(III) being oxidised. The SCM predicted that the increased partitioning of As(III) from solution to the surface begins close to this point (Figure 7.10b), suggesting that this effect is responsible for the observed kinetics. Further analysis of As(III) partitioning during photocatalytic oxidation using the SCM is presented in the Appendix.

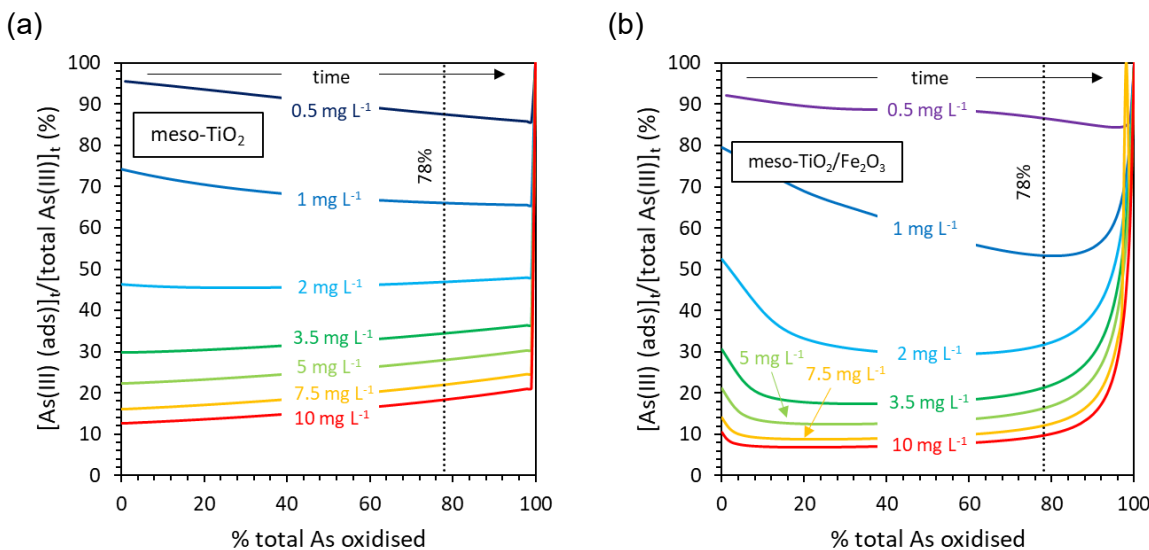


Figure 7.10: The SCM-predicted partitioning of As(III) between adsorbed and aqueous phases for (a) meso-TiO₂ and (b) meso-TiO₂/Fe₂O₃, with different total arsenic concentrations, as photocatalytic oxidation progresses. The y-axis indicates the percentage of total As(III) that is adsorbed, and the x-axis indicates the increasing progress of photooxidation. The 78% line is approximately equivalent to $\ln(C_t/C_0) = -1.5$. The catalyst concentration was 0.1 g L⁻¹, and the SCM methodology is described in chapter 3.

Increased partitioning of total As(III) to the adsorbed phase was also predicted by the Langmuir adsorption isotherm (agreeing with the SCM) (Figure 7.11). However, the transition from low to high partitioning of As(III) from the aqueous phase to the adsorbed phase is relatively gentle, and no significant feature appears around the 78% mark. There was also little significant difference between the calculations for meso-TiO₂ and meso-TiO₂/Fe₂O₃. Consequently, if the rate equation is first-order with respect to the concentration of adsorbed As(III), the SCM would predict faster kinetics after $\ln(C_t/C_0) = -1.5$ than the Langmuir-Hinshelwood model.

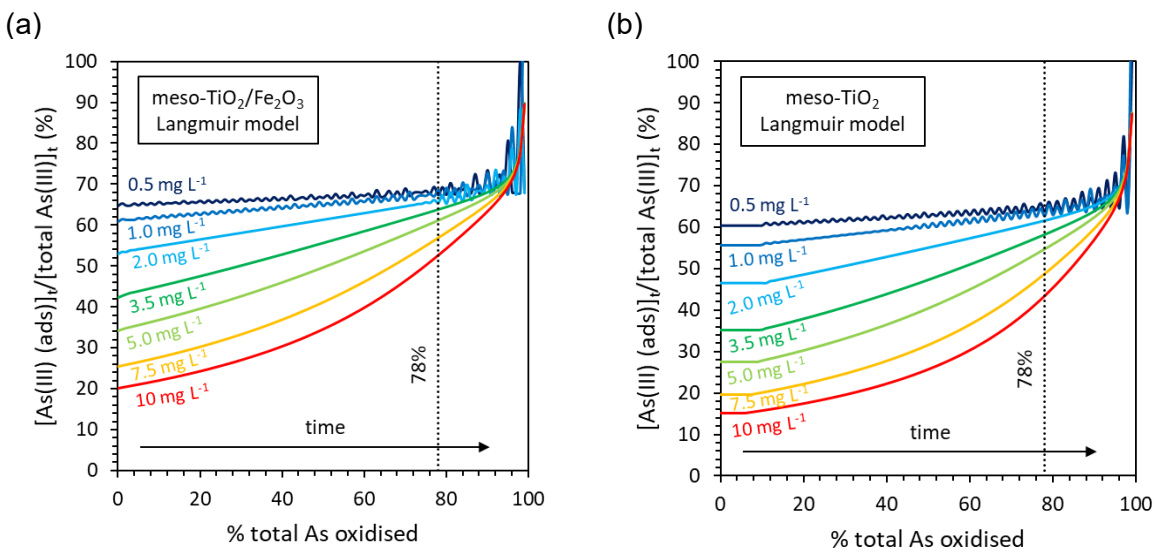


Figure 7.11: The partitioning of As(III) between aqueous and adsorbed phases predicted by the Langmuir adsorption isotherm as photocatalytic oxidation of As(III) increases, with (a) meso-TiO₂ and (b) meso-TiO₂/Fe₂O₃. The y-axis indicates the percentage of total As(III) that is adsorbed, and the x-axis indicates the increasing progress of photooxidation. Results were modelled using the Langmuir adsorption isotherm with K_L and Q_{max} parameters calculated from the experimental adsorption isotherms presented in chapter 6, as explained in the Appendix.

A new rate equation was subsequently constructed, being first-order with respect to the concentration of adsorbed As(III) calculated by the SCM (Equation 3.33). This model was fit to the experimental serial data. This model gave the linear form of $\ln(C_t/C_0)$ versus time for meso-TiO₂ since the SCM predicted no significant change in the relative distribution of As(III) between aqueous and adsorbed phases during the experiment (Figure 7.10a). However, the SCM-constrained model successfully captured the curvature in $\ln(C_t/C_0)$ versus time that is observed after $\ln(C_t/C_0) = -1.5$ (Figure 7.12b), owing to the increased partitioning of As(III) to the photocatalyst surface in the late stages of each experiment (Figure 7.10b).

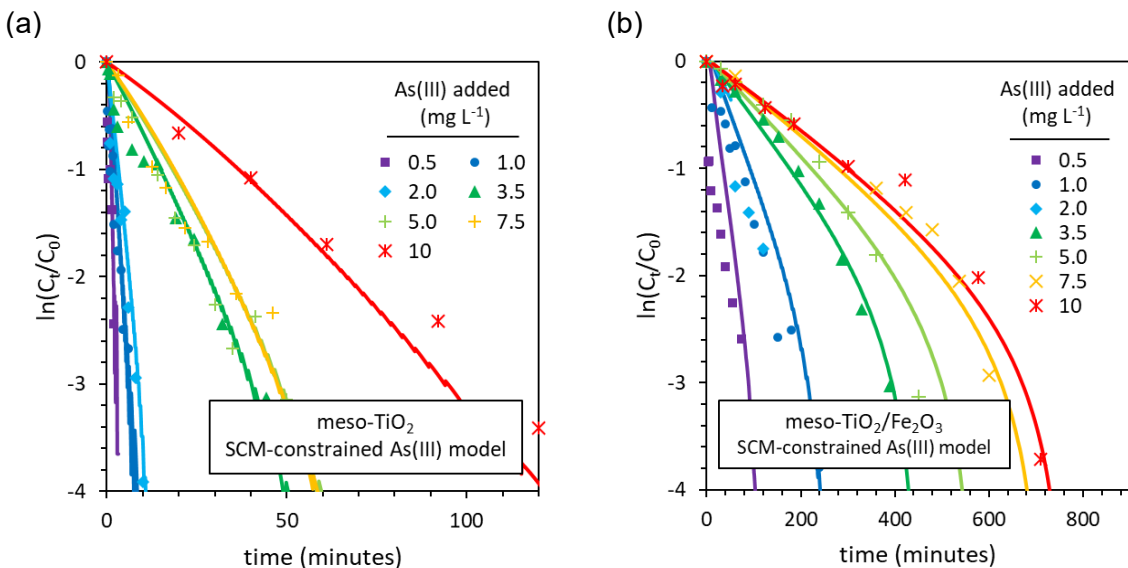


Figure 7.12: The SCM-constrained As(III) kinetic model, fitted to serial data in the form $\ln(C_t/C_0)$.

The curvature observed in plots of $\ln(C_t/C_0)$ versus time for meso-TiO₂/Fe₂O₃ was best described using this SCM-constrained model, compared with PFO and LH kinetics (Figure 7.13a). PFO kinetics provided no curvature, whilst LH kinetics provided an intermediate amount of curvature, since the Langmuir adsorption isotherm predicted gently increased surface-partitioning of As(III) as oxidation progresses, but without the sharp feature after 78% oxidation predicted by the SCM (Figure 7.11b versus Figure 7.12b). The SCM-constrained model also greatly reduced the dependency of rate constants on initial As(III) concentrations, compared with PFO and LH kinetics (Figure 7.13b). This provides further evidence, alongside phosphate deactivation (section 7.4.3), that adsorbed As(III) is needed in the rate determining step for the meso-TiO₂/Fe₂O₃ system.

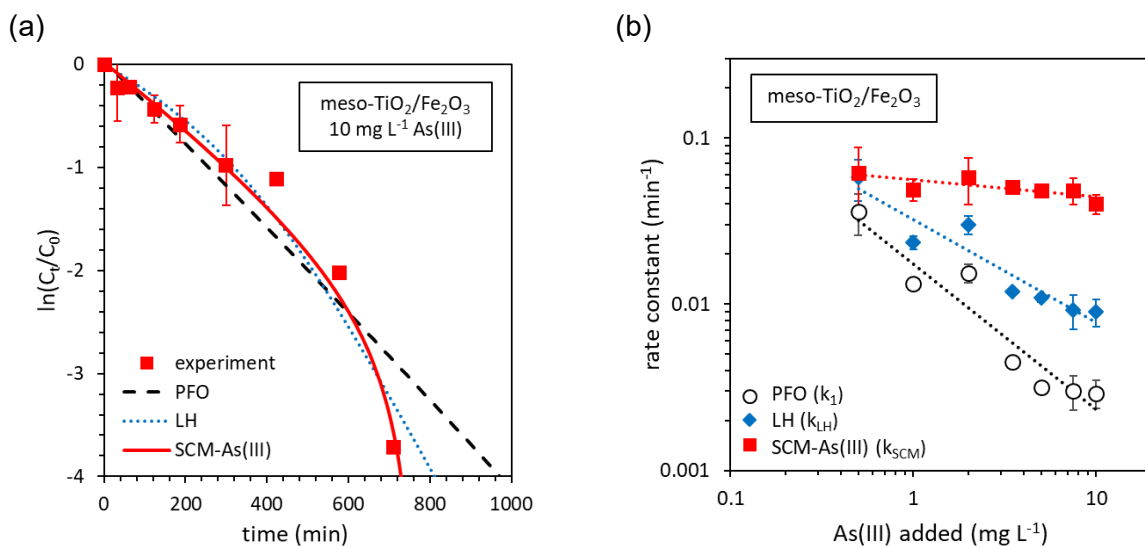


Figure 7.13: A comparison of the SCM-constrained As(III) kinetic model with pseudo first-order (PFO) and Langmuir-Hinshelwood (LH) kinetics. (a) A comparison of models fitted to serial data in the form $\ln(C_t/C_0)$. (b) The influence of As(III) concentration on the rate constants calculated for each model.

7.6. A mechanistic account for changes in photocatalytic oxidation kinetics after coupling meso-TiO₂ with Fe₂O₃

This section aims to provide a mechanistic explanation for the observed differences in the rates of As(III) photocatalytic oxidation using the composite meso-TiO₂/Fe₂O₃ versus the single-component meso-TiO₂. First, all kinetic models are compared and the most appropriate description of each photocatalyst is identified. Then the characterisation of optical absorbance presented in section Figure 7.2 and the kinetic analysis in sections Figure 7.4 and Figure 7.5 are combined to provide the final mechanistic explanation of how Fe₂O₃-coupling has influenced the photocatalytic oxidation of As(III) using meso-TiO₂.

An accurate rate equation must yield a rate constant that is independent of experimental conditions, e.g. the concentration of As(III). This comparison of rate equations is given in Figure 7.14a, where rate constants that are independent of [As(III) added] are given by

$$\frac{\Delta \log(k)}{\Delta \log([As(III)_{\text{added}}])} = 0. \text{ PFO kinetics failed to describe both meso-TiO}_2 \text{ and meso-TiO}_2/\text{Fe}_2\text{O}_3.$$

The most stable rate constants for meso-TiO₂ were achieved using As(V) deactivation kinetics. The kinetics of meso-TiO₂ were independent of aqueous and adsorbed As(III) concentrations (sections 7.4.2 and 7.4.3) and the disguised zero-order kinetics were predicted using As(V) deactivation models (Figure 7.14a). Kinetic analysis (section 7.5.2) and the enhanced oxidation rates in the presence of phosphate (section 7.4.3) suggest that photocatalytic oxidation of As(III) in the presence of meso-TiO₂ proceeds via ROS intermediates ¹⁷¹.

In contrast, the kinetics of meso-TiO₂/Fe₂O₃ depended on the concentration of adsorbed As(III) (sections 7.4.2, 7.4.3 and 7.5.3) and the most stable rate constants for meso-TiO₂/Fe₂O₃ were achieved using the SCM-constrained [As(V) (ads)] and [As(III) (ads)] models (Figure 7.14a). Of these, only the [As(III) (ads)] rate equation gives the first order relationship between [As(III) (ads)]₀ and initial rates that was observed experimentally (section 7.4.2). The evidence suggests that generation of ROS intermediates does not determine the reaction rate.

Fe₂O₃ has a less positive valence band potential (2.4–2.7 V) than TiO₂ (2.9–3.1 V) ⁴⁷⁵. Subsequently, holes within Fe₂O₃ are less oxidising and less able to generate hydroxyl radicals via water splitting (+2.73 V for the •OH + H⁺/H₂O redox couple ⁴⁷⁶). Fe₂O₃ holes may be able to directly oxidise As(III) (+2.4 V for the As(IV)/As(III) redox couple) ⁴⁷⁷. Whilst Fe₂O₃ holes are sufficiently oxidising to generate hydroxyl radicals from hydroxide ions (+1.9 V for the •OH/-OH redox couple) ⁴⁷⁶, at pH 7, 10 mg L⁻¹ As(III) (0.133 mM) is one thousand times

more prevalent than the hydroxide ion. The [As(III)] (ads)-dependent kinetics of meso-TiO₂/Fe₂O₃ are therefore explained by the iron oxide coating preventing generation of ROS, or trapping ROS at the catalyst surface, and photocatalytic oxidation of As(III) proceeding via direct hole oxidation.

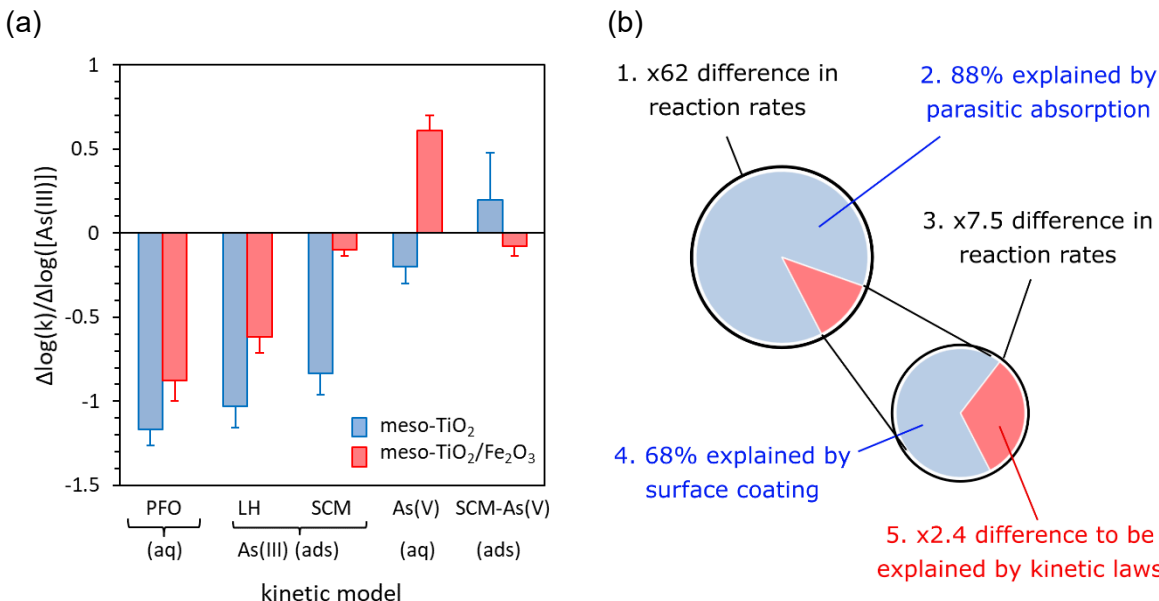


Figure 7.14: A mechanistic account for the observed differences between the rates of photocatalytic oxidation of As(III) in the presence of meso-TiO₂ and meso-TiO₂/Fe₂O₃. (a) A comparison of how initial As(III) concentrations influence the rate constants calculated by fitting serial data. Accurate rate equations will provide a rate constant that is independent of [As(III)], and therefore, the closer to zero that $\frac{\Delta \log(k)}{\Delta \log([As(III)])}$ is, the more valid the kinetic model is. (b) A graphical representation of how the observed difference in rates between meso-TiO₂ and meso-TiO₂/Fe₂O₃ can be rationalised, by considering both the physical properties of the material, and the different reaction mechanisms.

The greatest difference between the photocatalytic rates of meso-TiO₂ and meso-TiO₂/Fe₂O₃ was observed within the light intensity linear range. By using the end-point of this linear range (2.5 mW cm⁻²), we can assume that recombination between different electron-hole pairs is insignificant. With 2.5 mW cm⁻², the photocatalytic oxidation of As(III) was 62±12 times faster in the meso-TiO₂ system compared with meso-TiO₂/Fe₂O₃.

UV-Vis absorbance spectra suggested that only 12% of the 368 nm photons absorbed by meso-TiO₂ would be absorbed by the titania component of meso-TiO₂/Fe₂O₃ (section 7.2.1). Assuming that the photocatalytic activity of Fe₂O₃ is negligible compared with TiO₂¹⁸⁷, parasitic absorption explains 88% of the observed difference in rates. After factoring in parasitic light absorption, a factor of 7.5±1.4 difference in rates needs to be explained (Figure 7.14b). No heterojunction effect was observed for meso-TiO₂/Fe₂O₃ (section 7.2.2) so we can assume that charge extraction from the meso-TiO₂ component is similar in both photocatalysts (i.e. 0% of the difference in reaction rates is explained by heterojunction effects).

Chapter 5 identified that Fe_2O_3 coats most of the surface of this material, with only $32.0 \pm 0.3\%$ of the surface being TiO_2 (in the batch 2 product). Assuming a linear relationship between photocatalytic activity and the surface area of exposed TiO_2 , the Fe_2O_3 surface area can account for 68% of the observed difference in rates. Considering both parasitic light absorption and reduced exposure of TiO_2 to solution, the difference in rates that remains unaccounted for is a factor of 2.4 ± 0.5 (Figure 7.14b). The remaining difference between observed and anticipated reaction rates is explained by considering that meso- TiO_2 and meso- $\text{TiO}_2/\text{Fe}_2\text{O}_3$ show different kinetic laws and different reaction mechanisms. This chapter found evidence that meso- $\text{TiO}_2/\text{Fe}_2\text{O}_3$ is less able to promote the oxidation of As(III) through ROS intermediates compared with meso- TiO_2 , and the loss of this pathway would explain the remaining difference between the rates of As(III) oxidation using meso- TiO_2 and meso- $\text{TiO}_2/\text{Fe}_2\text{O}_3$ photocatalysts.

7.7. Conclusions

The aim of this chapter was to determine the mechanisms by which coupling meso- TiO_2 with Fe_2O_3 influences the kinetics of the photocatalytic oxidation of As(III). Meso- $\text{TiO}_2/\text{Fe}_2\text{O}_3$ was characterised using UV-Vis spectroscopy and TAS to probe parasitic ultraviolet absorption (by the Fe_2O_3 phase) and heterojunction behaviour. Photocatalytic oxidation kinetics were determined and used to identify the different mechanisms of As(III) photocatalytic oxidation using single-component meso- TiO_2 and composite meso- $\text{TiO}_2/\text{Fe}_2\text{O}_3$ photocatalysts. The key findings are that:

- Under environmentally relevant conditions, meso- $\text{TiO}_2/\text{Fe}_2\text{O}_3$ provides superior removal of As(III) both with and without ultraviolet irradiation, compared with uncoupled meso- TiO_2 . Coupling TiO_2 with Fe_2O_3 also reduces adsorption capacity loss due to the presence of phosphate at low As.
- Fe_2O_3 parasitically absorbs the majority of incident photons in the meso- $\text{TiO}_2/\text{Fe}_2\text{O}_3$ system, limiting the rates at which charge carriers are generated.
- No beneficial heterojunction was formed between TiO_2 and Fe_2O_3 using the precipitation route outlined in chapter 3.
- Meso- TiO_2 photocatalytic oxidation kinetics are zero-order with respect to As(III) concentrations, however the reaction order is disguised in the serial data, due to As(V) deactivation of the catalyst. Photocatalytic oxidation of As(III) using meso- TiO_2 appears to proceed via reactive oxygen species (ROS) intermediates.

- Coupling meso-TiO₂ with Fe₂O₃ changes the kinetic law from zero-order to first-order (depending on the concentration of adsorbed As(III)). This is explained by considering that the less oxidising Fe₂O₃ holes generate fewer ROS intermediates than the holes within TiO₂, and potentially limit the system to a direct hole oxidation mechanism.
- The surface-controlled kinetics of meso-TiO₂/Fe₂O₃ were best modelled when As(III) adsorption was calculated using surface complexation modelling (SCM), since unlike Langmuir-Hinshelwood kinetics, the SCM incorporates competitive adsorption of the As(V) product.
- Whilst coupling TiO₂ with Fe₂O₃ improves the adsorption capacity by as much as a factor of two (chapter 6), oxidation rates are decreased up to sixty times. This material is therefore not appropriate when the cost or availability of ultraviolet radiation is an important consideration, or when high throughput is needed. However, as a multifunctional photocatalyst-sorbent, meso-TiO₂/Fe₂O₃ offers an all-in-one approach towards the remediation of As(III) contaminated waters and will be useful when a single-reactor design is required.

This chapter provides the first mechanistic account for different rates between single-component and composite photocatalysts for the oxidation of As(III). This study demonstrated that composite materials can exhibit photocatalytic chemistry that is significantly different to their individual components. This chapter showed for the first time how surface complexation modelling (SCM) can be incorporated into photocatalysis kinetic models to provide sensitivity towards other sorbates, which is lacking in the Langmuir-Hinshelwood kinetic model. This is important for the photocatalytic oxidation of As(III), given that As(V) adsorbs strongly to the TiO₂ surface. This chapter also identified that further work is needed to characterise the mechanism for As(V) deactivation of TiO₂, and to include such effects in future kinetic models.

These findings have several implications. Future work on composite photocatalyst-sorbents for the remediation of As(III) must consider that reaction rates will be suppressed when small band gap sorbent phases are used, such as iron oxides, due to parasitic light absorption. Efforts to improve As(III) remediation using composite photocatalysts should consider alternative synthetic routes, such as epitaxial film growth, in order to maximise the interface between different semi-conductor phases and promote heterojunction behaviour ²⁹⁵.

The As(V) deactivation models found that the disguised zero-order kinetics of meso-TiO₂ can be at least partially captured by considering As(V) deactivation of the catalyst. These models made an arbitrary assumption of a linear relationship between the decrease in the absolute reaction rate and the increasing concentrations of As(V). Further experimental work is needed to identify how As(V) really influences the photocatalytic oxidation of As(III), as both the

mechanism and rate laws governing As(V) deactivation of TiO₂ are unknown. The results also indicate that future studies must consider the possible influence of As(V) when determining the kinetics of As(III) photocatalytic oxidation, and should ensure that the analysis of initial rates agrees with any analysis of serial data.

Additional experiments identifying the influence of media on the photocatalytic oxidation of As(III) (i.e. enhanced rates in the presence of chlorine and carbonate, and mixed effects in the presence of phosphate), as well as experiments in natural groundwater, are presented and discussed in the Appendix.

8. Design of an arsenic treatment plant: Insights from a kinetic adsorption model

8.1. Introduction

Photocatalyst-sorbent materials remain untested for real-life applications in the remediation of arsenic(III). An important yet unanswered question when engineering this system is how much material should be used. Low concentrations of suspended photocatalysts ($<1\text{ g L}^{-1}$) are typically used for As(III) photooxidation to achieve effective light penetration through the system^{25 26 26 27 28 29}. Whilst linear relationships between TiO_2 concentrations and reaction rates are often observed at low catalyst concentrations, at high catalyst concentrations reaction rates become limited by the supply of photons or by light scattering effects²⁷. Reaction rates may even decrease with excess concentrations of the photocatalyst²⁶⁴. However, low sorbent concentrations lead to low adsorption capacities and thus limited filter life-times, before spent sorbent media (i.e. with no adsorption capacity left) must be replaced or regenerated. Sorbent life-time is a major factor determining the success or failure of arsenic mitigation schemes in South Asia: users often fail to replace sorbent media when spent, due to lack of expertise³⁰, lack of confidence³¹.

Another reason for the limited success of arsenic mitigation programs is the cost of replacing spent sorbent media³⁰. Economical use of the sorbent means achieving the highest degree of arsenic removal before breakthrough (i.e. when the material is saturated, and arsenic emerges in the effluent). Factors affecting the sorbent economy include not just the amount of sorbent used, but also how it is used, e.g. the choice between batch treatments and continuous-flow treatments²⁷⁰. In a batch treatment, discrete volumes of water are treated sequentially, for a designated time, after which the effluent hopefully meets safety guidelines. For continuous-flow treatments, influent and effluent are continuously pumped into and out of

the reactor and flow-rate becomes another parameter that requires optimisation. The best sorbent efficiencies are achieved with slow flow rates, but users of household arsenic filtration systems have previously complained that the flow-rates of these devices are too slow³¹.

The efficiency of treatments using adsorption can be defined both by their sorbent economy and by the volume of water treated before the effluent exceeds the maximum contaminant level (MCL, commonly set to 10 µg L⁻¹ as per the WHO). Most household and community-scale solutions for the treatment of arsenic-contaminated water use sorbent media in a continuous-flow, column arrangement^{1 478}. It is commonly believed that continuous-flow treatments are more efficient than batch treatments, but under certain conditions batch treatments can prove superior²⁷⁰, and despite many papers reporting novel sorbents investigated using both batch and column studies, few papers provide a direct comparison between each treatment. When applied towards environmental remediation, photocatalysts are also deployed in both batch and continuous-flow devices⁴⁷⁹. Photocatalytic performance also varies between the two processes, e.g. Colombo and Ashokkumar (2017) reported a 110% increase in the efficiency of the photocatalytic degradation of dyes when using continuous-flow conditions compared with batch treatment²⁶⁴. It is non-trivial to compare the efficiency of batch and continuous-flow treatments, since batch treatments are defined by the duration of the treatment (minutes per unit volume) whilst continuous-flow treatments are defined by the flow rate (volume per minute) and bed volumes treated before breakthrough. The lack of substantial cross-evaluation between the two techniques is therefore not surprising⁴⁸⁰.

Previous work on the relative merits of batch and continuous-flow design includes the study of Dichiara et al. (2015) where a ‘critical concentration’ parameter was calculated from experimentally determined coefficients (pertaining to the fixed-bed sorbate removal efficiency, and incorporating effects such as pore channelling)²⁷⁰. When the target effluent concentration (e.g. the MCL) exceeds this critical concentration, batch treatment should give a better sorbent economy than fixed bed column treatments, and vice versa. Secondly, Lekić et al. (2013) compared the efficiencies of their sorbent for As(III) and As(V) remediation in batch and column configurations by comparing the amount of arsenic removed per gram of sorbent⁴⁸¹. The authors found that the amount of arsenic removed per gram of sorbent was greater when treated using continuous-flow columns compared with batch treatment, which they posited as being due to non-adsorption processes such as coagulation, flocculation and filtration⁴⁸¹.

The meso-TiO₂/Fe₂O₃ arsenic treatment plant should therefore be modelled, to establish the lowest concentration of material needed to provide sufficient adsorption, and thus provide an indication of the concentration range that needs to be tested in future engineering studies. For example, whilst we may wish to minimise material concentrations to ensure effective light

penetration, it is illogical to conduct engineering tests with 0.1 g L^{-1} meso-TiO₂/Fe₂O₃ if the material is instantly saturated. This model should be a kinetic model, given that batch and continuous-flow treatments often perform differently, and given that at high flow rates the continuous-flow system provides treated water outside of equilibrium adsorption.

The ideal model would combine both adsorption and oxidation kinetics. Whilst kinetic laws for the photocatalytic oxidation of As(III) in the presence of meso-TiO₂ and meso-TiO₂/Fe₂O₃ were experimentally determined in chapter 7, integration of oxidation kinetics with adsorption kinetics is challenging, since most kinetic adsorption models such as the PSO are in fact a convolution of adsorption and desorption reactions²⁷¹. Deconvolution of experimental data to obtain separate adsorption and desorption rate constants is necessary if the competitive adsorption between As(III) and As(V) during photocatalytic oxidation is to be modelled. Adsorption of As(V) is important given that chapter 7 demonstrated the significant influence of As(V) on the deactivation of meso-TiO₂ and on the [As(III) (ads)] controlled kinetics of meso-TiO₂/Fe₂O₃. Unfortunately, literature data on desorption kinetics is limited and experimental procedures have not been standardised^{303 482 483 484}.

The risk of exposure to arsenic contaminated water in South Asia is greatest amongst the rural poor^{105 110}. Rural communities often lack access to replacement parts and lack expertise in maintaining filter systems, two major reasons for the short-lifetimes of arsenic mitigation schemes³⁰. Electrical outages⁴⁸⁵ and the challenge of maintaining equipment³¹ mean that a system based on multifunctional photocatalyst-sorbent materials needs a fail-safe option: the device should provide reasonable removal of As(III) in the absence of photooxidation. This chapter therefore develops an initial model of the arsenic treatment plant by considering adsorption of As(III) only. This chapter then considers how desorption kinetics might be estimated from experimental adsorption kinetics and integrated into future models, to allow simultaneous photocatalytic oxidation and adsorption reactions to be modelled.

8.1.1. Aims and objectives

The aim of this chapter was thus to determine the minimum concentration of meso-TiO₂/Fe₂O₃ needed for an arsenic treatment plant, considering the worst-case scenario that the material is operated as a sorbent only, and not photocatalyst. To achieve this aim, the objectives were: (1) to develop a model describing adsorption kinetics that is sensitive to changes in sorbent concentration, and arsenic concentration; (2) to implement experimentally determined adsorption capacity and adsorption kinetic data from the As(III)/meso-TiO₂/Fe₃ system into

this model; (3) to investigate the influence of sorbent concentration on batch and continuous-flow treatments; (4) to investigate sorbent life-times in both systems, simulating a single household's clean water requirement over a 365-day period; (5) to recommend a reactor design for use in subsequent experimental work; and (6) to explore how a combined photocatalytic oxidation-adsorption arsenic treatment plant can be modelled in future work.

8.2. Developing a kinetic model sensitive to changes in the initial sorbate and sorbent concentration

8.2.1. The need for a new kinetic rate equation

In most models of adsorption kinetics, kinetic parameters are conditional to the specific experimental conditions used (Table 8.1). These models therefore lack sensitivity to changes in sorbate and sorbent concentration and cannot be used in a predictive capacity. This section describes how the popular pseudo-second order (PSO) model was adjusted to offer the sensitivity needed to model an arsenic treatment plant.

There are two main classes of kinetic adsorption models, differing in their mechanistic description: diffusion-controlled and adsorption-controlled. For diffusion-controlled models, external diffusion is rarely considered rate limiting²⁷². Instead, adsorption rates are controlled by intraparticle diffusion, with a diffusivity parameter reflecting the rate at which sorbate diffuses through the porous spaces within sorbent particles²⁷². This category includes the Crank model (1956)⁴⁸⁶ which approximates the sorbent as spherical particles and where the concentration of sorbate at the surface is constant²⁷². Adsorption kinetics can often be linearised using the Weber-Morris model (1963)⁴⁸⁷, where q_t (the concentrations of adsorbed analyte at time t) is proportional to $t^{1/2}$ ⁴⁸⁸.

Adsorption-controlled kinetic models consider formation of the surface complex to be the rate determining step. The original adsorption-controlled model was the Lagergren, or pseudo-first order model (PFO, 1898)⁴⁸⁹, with a reaction rate that is first order with respect to $(q_e - q_t)$, where q_e is the concentration of sorbate adsorbed at equilibrium⁴⁸⁸. The Elovich equation (1934)⁴⁹⁰ is another adsorption-control kinetic model, where the reaction rate decreases exponentially with the increasing progress of adsorption⁴⁸⁸.

The pseudo-second order (PSO) rate equation, popularised by Ho and McKay (1999)²⁷¹, is probably the model mostly widely at present used to describe adsorption kinetics⁴⁹¹, especially for new and novel sorbent materials. The PSO rate equation is the same as the earlier Lagergren model, save that the dependence of reaction rate upon ($q_e - q_t$) is second-order rather than first-order. The PSO rate equation takes the form:

$$\frac{dq}{dt} = k_2(q_e - q_t)^2$$

Equation 8.1

where t is time (minutes), q_t is the amount of sorbate adsorbed at time t (mg g⁻¹), k_2 is the pseudo-second order rate constant (g mg⁻¹ min⁻¹), and q_e is the amount of sorbate adsorbed at equilibrium (mg g⁻¹)²⁷¹.

The vital limitation of PSO kinetics is that the variables C_0 and C_s are not included (the initial concentrations of sorbate and sorbent, respectively) and this model therefore lacks sensitivity to changes in C_0 and C_s . Consequently, the PSO model does not allow us to identify appropriate sorbent concentrations for water remediation under different contaminant concentrations. Table 8.1 demonstrates that this lack of sensitivity towards sorbate and sorbent concentrations is common to most kinetic adsorption models. These models are without predictive capacity, and their parameters are only valid for the particular experimental conditions under which they were calculated. Furthermore, since k_2 is only valid for the experimental conditions under which it was determined, the comparison of rate constants between literature studies with different experimental values of C_0 and C_s can lead to false conclusions⁴⁹². The ability to normalise rate constants to account for differences in C_0 and C_s would be a major advantage, allowing improvements in sorbent engineering to be better identified and validated.

The first objective was to develop a kinetic adsorption model that could be used to predict changes in adsorption kinetics as a function of sorbate and sorbent concentrations. The PSO model was used as a starting point, due to it being (a) well-known and widely used, and (b) capable of describing most kinetic data, despite doubts over whether adsorption or diffusion-controlled models are more mechanistically appropriate⁴⁹³. To develop the new model, the following steps were carried out: (1) a wide range of literature, where the influence of C_0 and C_s on adsorption kinetics was investigated, was collected; (2) the relationship between C_0 and C_s on adsorption kinetics within this data set was determined; (3) the observed C_0 and C_s dependence was built into a modified form of the PSO model; (4) it was verified that the rate constants of this new model are less conditional than the PSO rate constant k_2 ; and (5) the new model was validated by fitting experimental serial data from the literature.

Table 8.1: A selection of kinetic models used to describe adsorption. The table illustrates that in most of these kinetic models $\frac{dq}{dt}$ is sensitive to neither (i) changes in C_0 or C_t nor (ii) changes in C_s and are thus limited in predictive capability. C_0 is the initial concentration of aqueous sorbate, C_t is the concentration of aqueous sorbate at time t , C_e is the concentration of aqueous sorbate at equilibrium, q_t is the quantity of sorbate adsorbed at time t , q_e is the quantity of sorbate adsorbed at equilibrium, k is the rate constant, a is the desorption constant, a is the initial adsorption rate, D is molecular diffusion coefficient of the sorbate in solution, r is the radial coordinate, ρ is particle density, ε_r is particle porosity, N is the local concentration of sorbate in the adsorbed phase (presumably equivalent to q_t), D_s is surface diffusivity (assumed constant), θ_t is surface coverage at time t , θ_e is surface coverage at equilibrium, u_e is the relative sorbate uptake at equilibrium, with $u_e = 1 - \frac{C_e}{C_0}$, k_a is a rate constant for adsorption. q_e^{t2} and C_0^t denote the values of q_e and C_0 under the experimental conditions used to determine k_2 .

Model	Equation	Is the rate equation sensitive to changes in C_t or C_0 ?	Is the rate equation sensitive to changes in C_s ?	Reference
Intraparticle diffusion-controlled models				
Crank model	$\frac{\partial C}{\partial t} = \frac{D}{T} \left(\frac{\partial^2 C_t}{\partial r^2} + 2 \frac{\partial C_t}{r \partial r} \right) - \frac{\rho}{\varepsilon_r} \frac{\partial N}{\partial t}$	Yes	No	494
Simplified Crank model	$\frac{\partial q}{\partial t} = \frac{D_s}{r^2} \frac{\partial}{\partial r} \left(r^2 \frac{\partial q_t}{\partial r} \right)$	No (model assumes a constant surface concentration of sorbate)	No	272
Web and Morris	$q_t = kt^{\frac{1}{2}}$	No	No	272
Adsorption-controlled models				
Pseudo-first order	$\frac{dq}{dt} = k(q_e - q_t)$	No	No (unless q_e is replaced with a variable term)	488
Pseudo-second order	$\frac{dq}{dt} = k(q_e - q_t)^2$	No	No (unless q_e is replaced with a variable term)	488
Elovich equation	$\frac{dq}{dt} = ae^{-\alpha q_t}$	No	No	488
Second-order rate equation (aqueous phase)	$\frac{dC}{dt} = -k_2 C_t^2$	Yes (second order)	No	488
Integrated Kinetic Langmuir model	$\frac{d\theta}{dt} = k_a C_0 [(1 - \theta_e u_e) \left(1 - \frac{q_t}{q_e} \right) + \theta_e u_e \left(1 - \frac{q_t}{q_e} \right)^2]$	Yes (but only C_0 and not C_t)	Yes (θ_e and u_e will change with C_s)	273
This work	$\frac{dq}{dt} = k' C_t \left(1 - \frac{q_t}{q_e} \right)^2$ where $k' = \frac{k_2 q_e^{t2}}{C_0^t}$	Yes (1 st order)	Yes (q_e is calculated at each time interval using adsorption isotherms)	This work

8.2.2. The influence of C_0 and C_s upon initial rates

The first objective was to establish the influence that the initial sorbate concentration, C_0 , and the sorbent concentration, C_s , have on adsorption kinetics. A range of experimental data was collected, with oxyanions, metal cations and organic dyes all represented as sorbates, and single-component minerals, composite sorbents and activated carbon represented as sorbents. The data set was deliberately broad, to provide generalised findings. The initial rate of reaction (interpolated from the linearised PSO plot) was calculated for each kinetic experiment. The order of reaction with respect to C_0 and C_s was then calculated from the slope of the linear regression when plotting $\log(\text{initial rate})$ as a function of $\log(C_0 \text{ or } C_s)$ for all kinetic experiments within a single data set (where a data set is defined as all kinetic experiments using the same sorbate-sorbent combination). In total, 11 data sets with a combined 43 kinetic experiments were collected to investigate the influence of C_0 . 11 data sets with a combined 43 kinetic experiments were also collected to determine the influence of C_s .

The data compiled from the literature generally showed a linear relationship between the initial sorbate concentration and the initial rate (normalised to mass, $\text{mg g}^{-1} \text{ min}^{-1}$). This is shown in Figure 8.1a where the average result for the gradient between $\log(\text{initial rate})$ and $\log(C_0)$ was $\bar{x}=0.829\pm0.417$, $\tilde{x}=0.801$ (where \bar{x} and \tilde{x} are the mean and median results respectively). Despite a large deviation of ± 0.417 , the average and median results were significantly closer to 1, indicating a first-order relationship, compared with 0 or 2, which would indicate a zero-order or second-order relationship respectively. This is intuitive for both diffusion and adsorption-controlled mechanisms, as doubling the sorbate concentration should (a) double the flux of the sorbate from the sorbent surface into the sorbent pores, and (b) double the frequency of sorbate collisions with the sorbent surface.

Similarly, a first order dependence of reaction rate upon C_s was observed in the compiled data sets. This is shown in Figure 8.1b, where the average gradient was $\bar{x}=1.18\pm0.61$, $\tilde{x}=1.15$. This is also intuitive for both diffusion and adsorption-controlled mechanisms, as when C_s is doubled, the total surface area is doubled, and (a) the overall flux of sorbate entering the sorbent pores is doubled, whilst (b) the rate of collisions between the sorbate and the sorbent surface is also doubled. When normalised to mass ($\text{mg g}^{-1} \text{ min}^{-1}$) the initial rate was zero-order with respect to C_s , as expected. Again, despite a large deviation in the calculated order of reaction, the relationship between initial rate and C_s was significantly closer to first-order (when rate is normalised to $\text{mg L}^{-1} \text{ min}^{-1}$) than both zero-order and second-order. The median result was very close to the average for both C_0 and C_s , indicating that the analysis was not significantly skewed by any outlying data sets.

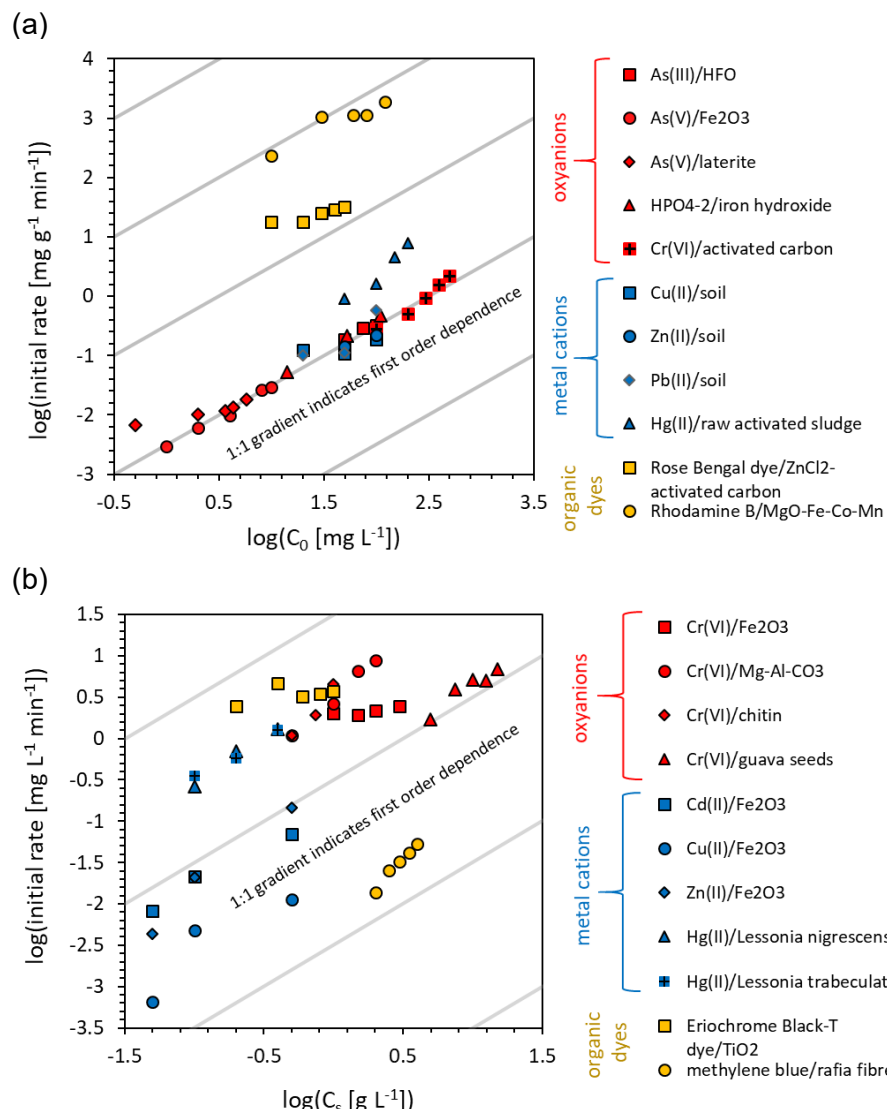


Figure 8.1: The initial rate of adsorption as a function of (a) initial sorbate concentration (C_0) and (b) sorbent concentration (C_s). Each data point represents a single kinetic experiment. Each experiment was fitted with the pseudo-second order (PSO) model and the rate at time $t=0$ was calculated as discussed in chapter 3. Kinetic experiments are grouped into data sets, where all conditions except for (a) C_0 or (b) C_s were kept constant. The gradients of most data sets align with the 1:1 gradient (grey guidelines given for visual reference) indicating that the adsorption reaction is first order with respect to the independent variables C_0 and C_s .

8.2.3. Conditionality of k_2 and the absence of predictive capabilities in the pseudo-second order kinetic model

To predict the sensitivity of adsorption kinetics as a function of changes to C_0 and C_s , and to facilitate comparison of adsorption kinetics within the literature, it is necessary that the rate constant determined under one set of experimental conditions can be used to model further experiments with different values of C_0 and C_s . Having identified the first-order dependence of

the reaction rate upon C_0 and C_s , the influence that the independent variables C_0 and C_s have on the pseudo-second order (PSO) rate constant k_2 was identified, using the same data sets.

Whilst section 8.2.2 demonstrated that adsorption kinetics are approximately first-order with respect to C_0 (Figure 8.1a), the PSO rate constant, k_2 , is inversely proportional to C_0 , i.e. doubling initial sorbate concentration results in the rate constant k_2 decreasing by a factor of two (Figure 8.2a). This inverse relationship between k_2 and C_0 is explained by the second-order dependence that PSO kinetics have upon the **absolute** concentration of available surface sites, ($q_e - q_t$). This is demonstrated mathematically in the following discussion.

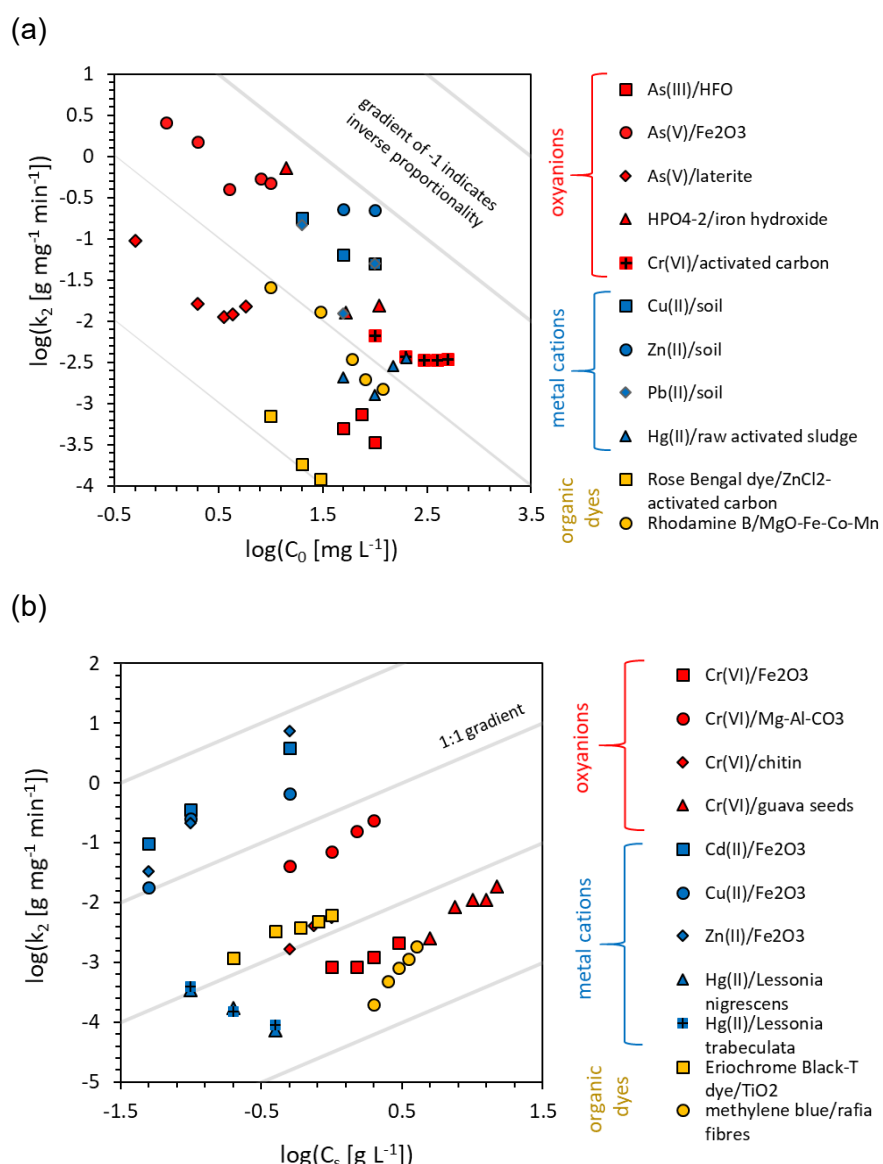


Figure 8.2: Pseudo-second order (PSO) rate constant k_2 as a function of (a) initial sorbate concentration (C_0) and (b) sorbent concentration (C_s). Grey lines indicate gradients and thus reaction orders of (a) -1 and (b) +1.

Many studies of adsorption kinetics operate under conditions where the sorbent remains unsaturated at equilibrium. This is natural since the authors wish to investigate the conditions under which their sorbent successfully removes contaminants. Under these conditions, C_e is low compared with q_e. At low values of C_e, a linear relationship is observed between C_e and q_e (this is known as Henry's adsorption isotherm ⁴¹⁹). If we approximate the adsorption isotherm as a linear relationship between C_e and q_e, and let coefficient a represent the factor increase in C₀ between experiments (1) and (2), we get the following:

$$a = \frac{\text{reaction rate (2)}}{\text{reaction rate (1)}} = \frac{C_{0(2)}}{C_{0(1)}} \approx \frac{C_{e(2)}}{C_{e(1)}} \approx \frac{q_{e(2)}}{q_{e(1)}}$$

Equation 8.2

where coefficient a is equal not just to the quotient of C₀₍₂₎ and C₀₍₁₎, but also the quotient of reaction rates, given the first-order dependence of the reaction rate upon C₀ observed in section 8.2.2. q_{e(2)} can thus be substituted for the product of coefficient a and the old q_{e(1)}:

$$q_{e(2)} \approx aq_{e(1)}$$

Equation 8.3

Rearrangement of Equation 8.1 gives the following:

$$k_2 = \frac{\text{reaction rate}}{(q_e - q_t)^2}$$

Equation 8.4

which at time t=0 reduces to:

$$k_2 = \frac{\text{initial rate}}{q_e^2}$$

Equation 8.5

Substitution of q_{e(2)} with a • q_{e(1)} as per Equation 8.3 gives:

$$k_{2(2)} = \frac{\text{initial rate (2)}}{q_{e(2)}^2} \approx \frac{\text{initial rate (2)}}{(aq_{e(1)})^2}$$

Equation 8.6

Substituting initial rate (2) for the product of a and initial rate (1) as per Equation 8.2 gives:

$$k_{2(2)} \approx \frac{\text{initial rate (2)}}{(aq_{e(1)})^2} = \frac{a \cdot \text{initial rate (1)}}{a^2 q_{e(1)}^2} = \frac{ak_{2(1)}}{a^2} = \frac{k_{2(1)}}{a}$$

Equation 8.7

This mathematically demonstrates that k_2 is inversely proportional to C_0 , to a first approximation, when the sorbent is unsaturated and adsorption can be represented by a linear adsorption isotherm. This was observed experimentally, as whilst the reaction rate only doubles with a doubling of C_0 (Figure 8.1a), the PSO rate constant, k_2 , conditional to the value of C_0 used, typically decreases by a factor of two (Figure 8.2a). The average slope of $\log(k_2)$ as a function of $\log(C_0)$ was $\bar{x}=-0.761 \pm 0.663$, $\bar{x}=-0.765$, $N=11$ data sets and 43 kinetic experiments, confirming this inverse first-order relationship. However, the deviation in this result was large, and nearly includes $x=0$ for a zero-order relationship between k_2 and C_0 .

Most data sets showed a first-order dependence of k_2 upon C_s (Figure 8.2b). This can also be explained by considering adsorption isotherms and the term $(q_e - q_t)^2$. If coefficient b indicates the factor increase in C_s between two experiments, then:

$$b = \frac{C_{s(2)}}{C_{s(1)}}$$

Equation 8.8

When the sorbent is saturated and $C_e \gg (C_s \cdot q_e)$, the adsorption isotherm approaches a plateau and increasing C_s has limited effect on q_e . Therefore:

$$q_{e(2)} \approx q_{e(1)}$$

Equation 8.9

If we consider reaction rates normalised to mass (e.g. $\text{mg g}^{-1} \text{ min}^{-1}$) then the zero-order dependence of the reaction rate upon C_s , identified in section 8.2.2, leads to:

$$\text{initial rate (2)} \approx \text{initial rate (1)}$$

Equation 8.10

From Equation 8.5, we subsequently obtain:

$$k_{2(2)} = \frac{\text{initial rate (2)}}{q_{e(2)}^2} \approx \frac{\text{initial rate (1)}}{q_{e(1)}^2} \approx k_{2(1)}$$

Equation 8.11

C_s does not enter the equations, and thus k_2 is predicted to have a zero-order dependence upon C_s at high values of C_e where the adsorption isotherm reaches a plateau.

We can also consider the opposite case, being the low C_e region of the adsorption isotherm. When $C_e \ll (C_s \cdot q_e)$, the majority of the sorbate is removed by adsorption regardless of the sorbent concentration, and increasing C_s therefore causes a decrease in q_e (mg g^{-1}) since a limited amount of sorbate is divided across a larger surface area. In this case:

$$q_{e(2)} \approx \frac{q_{e(1)}}{b}$$

Equation 8.12

If Equation 8.10 (based upon our observations from section 8.2.2) is still valid, then:

$$k_{2(2)} = \frac{\text{initial rate (2)}}{q_{e(2)}^2} \approx \frac{\text{initial rate (1)}}{\left(\frac{q_{e(1)}}{b}\right)^2} \approx \frac{b^2 \cdot \text{initial rate (1)}}{q_{e(1)}^2} \approx b^2 k_{2(1)}$$

Equation 8.13

This gives a second-order dependence of k_2 upon C_s .

It therefore follows that the low and upper bounds of k_2 dependence upon C_s are zero and second-order respectively. These bounds fit the majority of data sets, as shown in Figure 8.2b. The final results for the dependency of k_2 with respect to C_s were $\bar{x}=1.16 \pm 1.28$, $\hat{x}=1.39$, $N=11$ data sets and 43 kinetic experiments. Zero, first and second-order dependencies between k_2 and C_s are all included within the standard deviation. Out of 11 data sets, three showed a relationship between k_2 and C_s outside of the predicted constraints: methylene blue/raffia fibres demonstrated a dependency of 3.1 ± 0.2 , and the two Hg(II)/biosorbent data sets gave a dependency of -1.1 ± 0.2 .

Having determined the typical conditionality of the PSO rate constant k_2 with respect to C_0 and C_s , the implications of this conditionality with regards to the possibility of using the PSO model to predict adsorption kinetics as C_0 and C_s are varied was investigated. For predictive modelling, a single rate constant should be able to model experiments with different values of C_0 and C_s . The data sets were thus simulated using PSO kinetics, with a single value of k_2 used to model all of the kinetic experiments in a given data set. This value of k_2 was set as the average value of k_2 for all kinetic experiments within the particular data set. However, each kinetic experiment was modelled using a unique value of q_e , which was determined by fitting the given kinetic experiment with linearised PSO kinetics. All parameters are tabulated in the Appendix. Figure 8.3 shows that the resulting PSO model cannot accurately describe data sets differing in C_0 or C_s when the rate constant k_2 is fixed. The implication is that (a) the PSO model cannot be used to accurately predict changes in adsorption kinetics as a function of C_0 and C_s , and (b) comparison of the PSO rate constant k_2 between different literature studies is only valid if PSO parameters were determined under the same experimental conditions (i.e. identical values of C_0 and C_s).

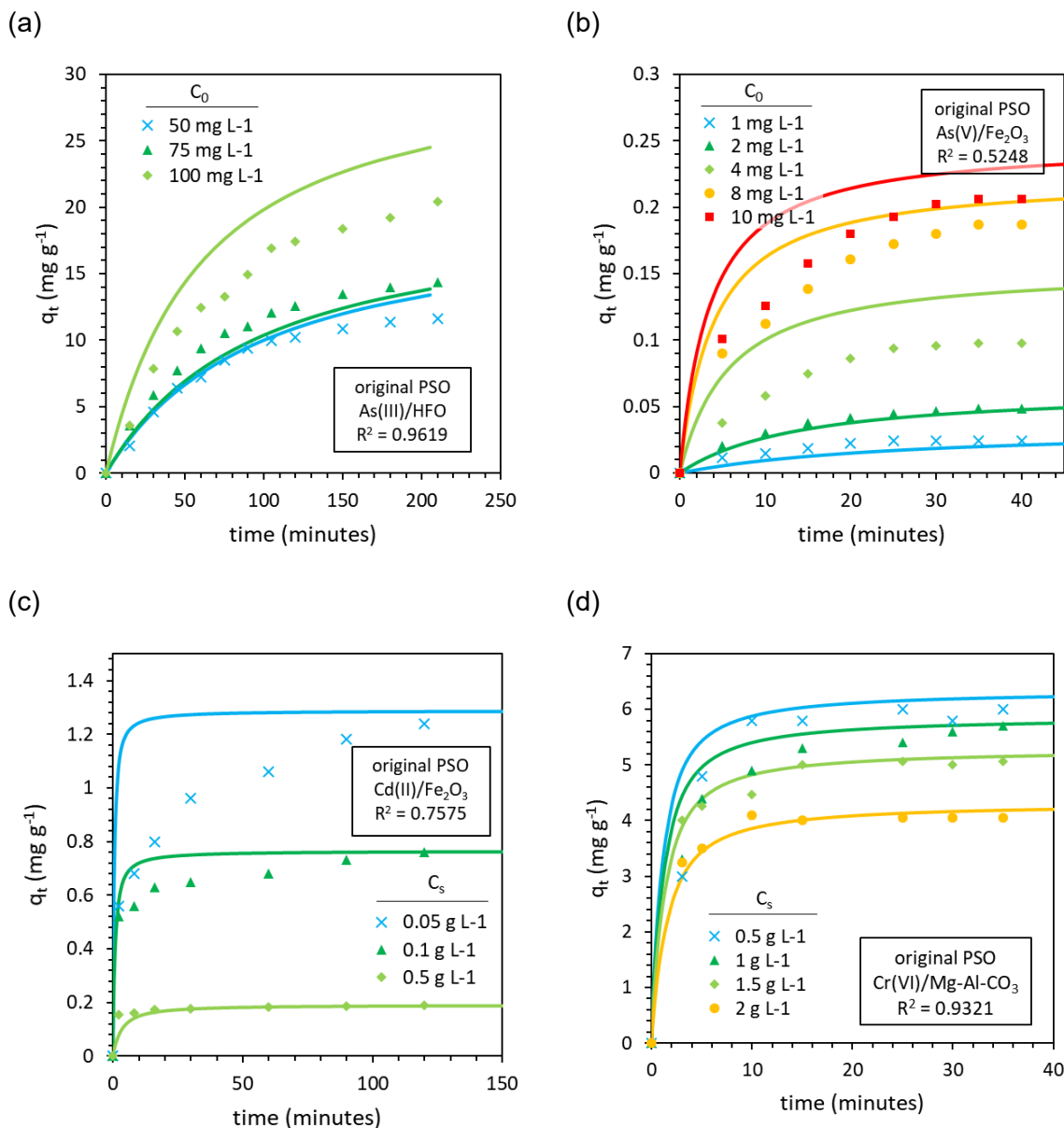


Figure 8.3: Demonstrating the lack of predictive capability in the PSO model due to the C_0 and C_s conditionality of k_2 . A selection of literature data sets were modelled using PSO kinetics with a single value of k_2 , calculated as the average value of the PSO rate constant k_2 across all kinetic experiments within the given data set. Each kinetic experiment was modelled using its own unique value of q_e . (a) and (b) are data sets wherein C_0 is varied whilst (c) and (d) are data sets where C_s is varied. Experimental data is from the literature ^{495 496 497 303}.

8.2.4. Development of a kinetic model sensitive to changes in C_0 and C_s

To provide sensitivity when predicting changes in adsorption kinetics due to changes in C_0 and C_s , the PSO rate equation was modified, resulting in a new pseudo-second order kinetic model. Firstly, to remove the inverse relationship between the rate constant upon C_0 (Figure 8.2a), the right-hand side of the rate equation must be made proportional to C_0 (Figure 8.1a) and not proportional to C_0^2 , which the unmodified PSO rate equation approximates to through

the term $(q_e - q_t)^2$ (Equation 8.1). This problem is solved by replacing $(q_e - q_t)^2$, which provides second order dependence on the **absolute amount** of adsorption capacity remaining, with a new term that provides a second order dependence on the **relative amount** of adsorption capacity remaining. The term used herein is of the form $\left(1 - \frac{q_t}{q_e}\right)^2$. This modification of Equation 8.1 gives the following:

$$\frac{dq}{dt} = k' \left(1 - \frac{q_t}{q_e}\right)^2$$

Equation 8.14

where $k' = k_2 q_e^{\dagger 2}$ and q_e^{\dagger} denotes the equilibrium concentration of adsorbed sorbate in the specific kinetic experiment that was used to calculate k_2 . At time $t=0$, this new term $\left(1 - \frac{q_t}{q_e}\right)^2$ always returns a value of 1, independent of the initial sorbate concentration.

The first-order dependence of the reaction rate upon the sorbate concentration can then be explicitly defined, giving the final equation:

$$\frac{dq}{dt} = k' C_t \left(1 - \frac{q_t}{q_e}\right)^2$$

Equation 8.15

where $k' = \frac{k_2 q_e^{\dagger 2}}{C_0^{\dagger}}$ and C_0^{\dagger} denotes the initial sorbate concentration in the specific kinetic experiment that was used to calculate k_2 . Modification of the PSO rate equation to this new form, with second-order dependence on the **relative** concentration of unused adsorption capacity rather than the **absolute** concentration, results in no change to the calculated adsorption kinetics when simulated under the same experimental conditions.

Figure 8.1b demonstrated a first-order dependence of the initial rate upon C_s when normalised to volume ($\text{mg L}^{-1} \text{ min}^{-1}$) and a zero-order dependence when normalised to sorbent mass ($\text{mg g}^{-1} \text{ min}^{-1}$). The current modified equation is dependent on the relative availability of adsorption capacity rather than the absolute availability. Any changes in q_e due to varying C_s do not affect the term $(1 - \frac{q_t}{q_e})^2$ at $t=0$, as it continues to reduce to unity. Therefore, when the rate equation is normalised to $\text{mg g}^{-1} \text{ min}^{-1}$ (i.e. $\frac{dq}{dt}$ rather than $\frac{dC}{dt}$) no modification of the rate equation to account for variations in C_s is required. The modified rate equation, Equation 8.15, is similar to the adsorption-only form of the Kinetic Langmuir Model (kLm), which at high surface coverage is first-order with respect to C_t and second-order towards $(1 - \frac{q_t}{q_e})^{498/273}$.

8.2.5. Confirming that k' is less conditional than k_2

A predictive kinetic adsorption model, sensitive to changes in C_0 and C_s , requires a rate constant that is unaffected by either independent variable. Since the ideal rate constant is therefore entirely unaffected by changes to C_0 and C_s , the slope of $\log(\text{initial rate})$ as a function of $\log(C_0)$ or $\log(C_s)$ should return a gradient of zero, indicating a zero-order dependence. The dependency of k' upon C_0 and C_s was calculated identically as for k_2 in section 8.2.3. The hypothesis that k' is less conditional than k_2 was then validated by identifying whether $\Delta\log(k')/\Delta\log(C_0 \text{ or } C_s)$ or $\Delta\log(k_2)/\Delta\log(C_0 \text{ or } C_s)$ returns the gradient closest to zero.

The visual comparison of k_2 and k' dependencies upon C_0 and C_s is given in Figure 8.4. k_2 displayed an inverse relationship with C_0 , with $\bar{x}=-0.761\pm 0.663$, $\tilde{x}=-0.765$, and an approximately first-order dependence on C_s with $\bar{x}=1.16 \pm 1.28$, $\tilde{x}=1.39$. The new rate constant k' was significantly closer to zero-order than any other dependency with regards to both C_0 and C_s . The results were $\bar{x}=-0.28\pm 0.53$, $\tilde{x}=-0.38$ for C_0 dependency, and $\bar{x}=0.04\pm 0.61$, $\tilde{x}=-0.02$ for C_s dependency. Additionally, the standard deviation in these results was smaller for k' than for k_2 , indicating that the relationship between each independent variable and the rate constants k' and k_2 was most consistent between data sets for k' than k_2 . These results suggest that the new rate constant k' is less conditional than k_2 , and that the dependency of adsorption kinetics upon C_0 and C_s has been captured by the new rate equation, at least in part, if not fully.

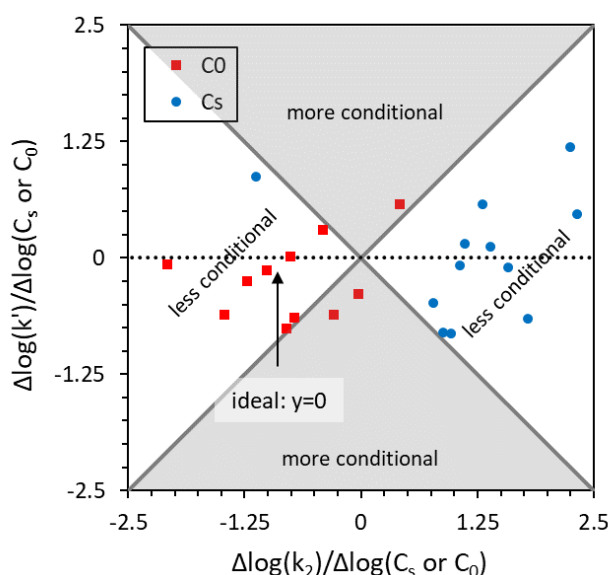


Figure 8.4: Mathematical demonstration of the reduced sensitivity towards C_0 and C_s in the new rate constant k' compared with k_2 . Where the rate constant is not influenced by changes in C_0 and C_s , a gradient of $\log(\text{rate constant})$ versus either $\log(C_0)$ or $\log(C_s)$ will return a value of zero (indicating that the rate constant does not change). A value of +1 indicates a first-order relationship, -1 indicates an inverse relationship and so on. The white shaded area of the plot indicates experimental data sets where k' was less sensitive to changes in C_0 and C_s than k_2 . The grey shaded area indicates data sets where k' varied more with changes in C_0 and C_s than k_2 .

8.2.6. Using adsorption isotherms in a kinetic adsorption model

The PSO model traditionally uses a unique, fixed value of q_e to model the entire duration of any given adsorption kinetic experiment. However, q_e is sensitive to both C_0 and C_s , and therefore the single value of q_e obtained under one set of experimental conditions cannot be used to predict adsorption kinetics once C_0 and C_s are changed. To provide appropriate sensitivity, the modified kinetic model must therefore have a q_e term that is sensitive to sorbate concentration. This can be achieved by replacing q_e with adsorption isotherms such as the Langmuir or Freundlich models ⁴¹⁹. Using adsorption isotherms, q_e can either be set as the concentration of adsorbed sorbate at equilibrium (as per convention), or q_e can be recalculated at each point in time, giving an out-of-equilibrium value of q_e which decreases throughout the kinetic experiment as the progress of adsorption increases. In this second case, the term C_e within the adsorption isotherm is replaced with C_t . Huang et al. previously demonstrated that this second case actually gives better account of the true driving force of the reaction during the early stages of adsorption ³⁰⁵. Recalculating ' q_e ' using C_t in this way is also more appropriate when modelling column systems, where $C_t \ll C_e$ for the majority of the experiment. Langmuir and Freundlich adsorption isotherm parameters were obtained for the data sets selected in section 8.2.3 (Figure 8.5). The isotherms were incorporated into the modified rate equation (Equation 8.15), and these data sets were modelled, as presented in section 8.2.7.

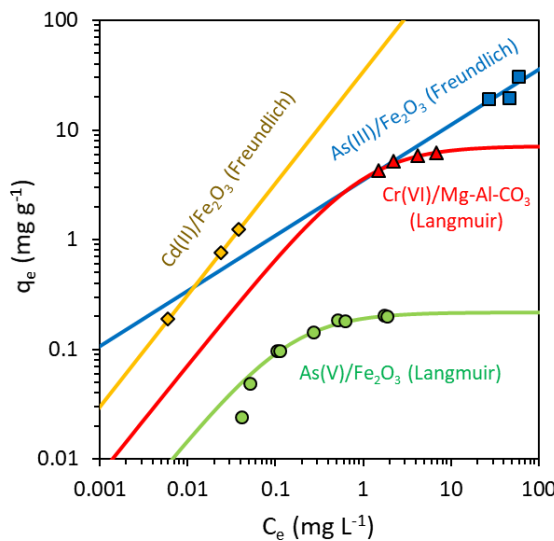


Figure 8.5: Adsorption isotherms were fit using experimental data and then used to recalculate q_e at each point in time when modelling kinetic experiments using the modified form of the pseudo-second order rate equation.

8.2.7. Validating improvements in the modified equation

In order to validate the modified model, Equation 8.15 was used to model the same data sets that were modelled using the PSO model with an average value of k_2 (section 8.2.3). A single value of k' was used to model all kinetic experiments within each data set (k' was calculated for each kinetic experiment using $k' = k_2 q_e^{+2}$ and an average was taken). The value of q_e at

each point in time was calculated using the adsorption isotherms presented in Figure 8.5, for which all parameters are tabulated in Table 8.2.

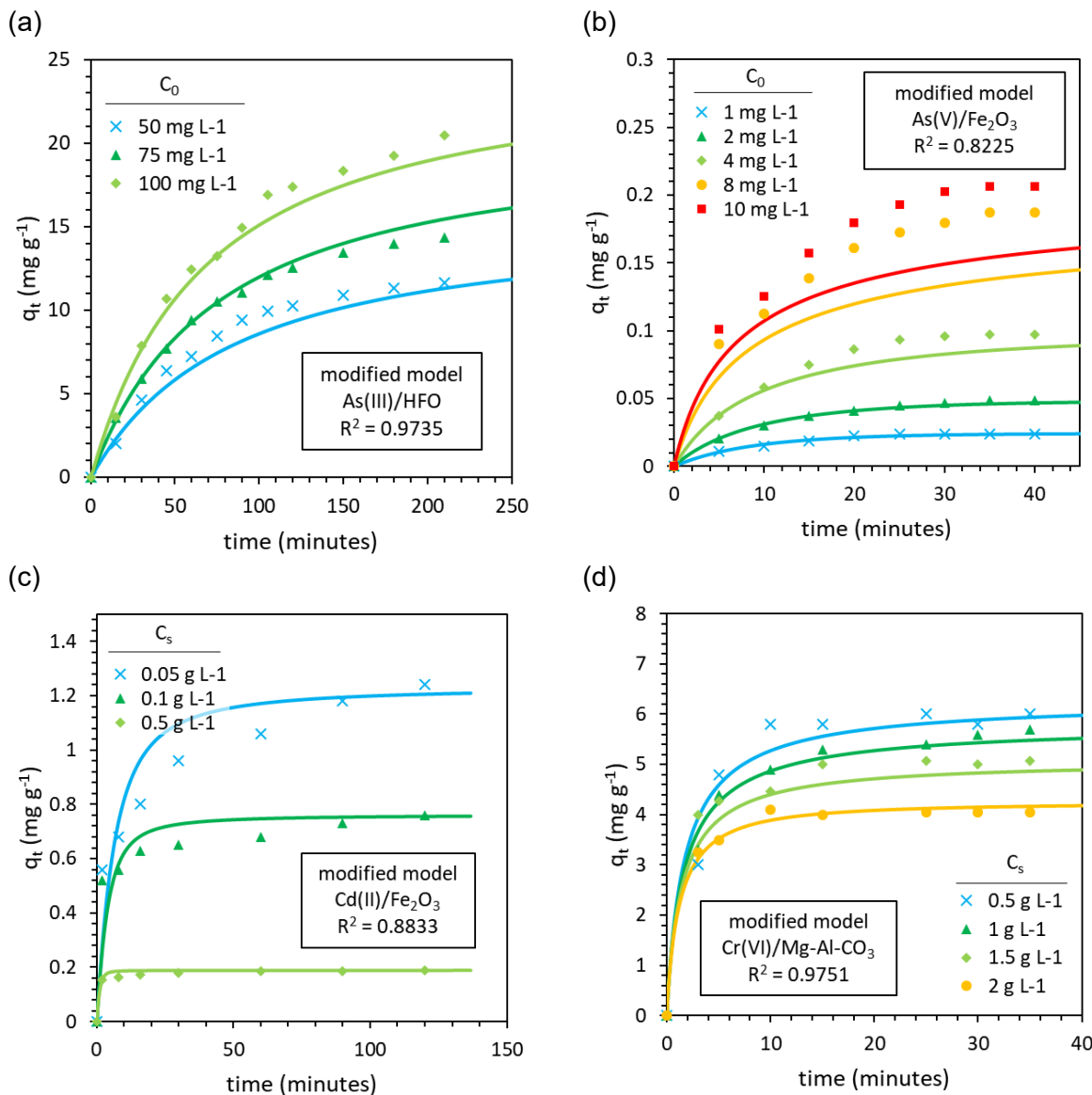


Figure 8.6: Modelling adsorption kinetics using the new kinetic model. For each data set, a single value of rate constant k' was used and q_e was determined for all points in time using the same adsorption isotherm, for all kinetic experiments within a given data set. The kinetic model was used to model experiments differing in C_0 (a and b) and C_s (c and d). The Freundlich adsorption isotherm was used for all experiments in (a) and (d), and the Langmuir adsorption isotherm for all experiments in (c) and (d). Experimental data is from the literature 495 496 497 303.

The results are presented in Figure 8.6, and in all cases the goodness of fit (represented by R^2) was improved compared with section 8.2.3, where PSO kinetics were simulated using a single value of k_2 . The results were $R^2=0.9735$ vs. 0.9619 for As(III)/HFO (with C_0 varied), $R^2=0.8225$ vs. 0.5248 for As(V)/Fe₂O₃ (C_0 varied), $R^2=0.8833$ vs. 0.7575 for Cd/Fe₂O₃ (C_s varied) and $R^2=0.9751$ vs. 0.9321 for Cr(VI)/Mg-Al-CO₃ (C_s varied) for the new rate equation versus the unmodified PSO model respectively. This is especially significant given that in section 8.2.3, every individual kinetic experiment was given its own value of q_e (determined by experimental fitting) in the PSO simulations, whilst for the new rate equation, a single

adsorption isotherm (Langmuir or Freundlich) was used to calculate values of q_e for all kinetic experiments within a given data set. The new model thus not only provided simulations that were more accurate than the unmodified PSO model, but also used fewer fitting parameters when providing the more accurate simulations, as presented in Table 8.2.

The q_t values predicted by the PSO model and the new model were cross-calibrated against the values of q_t observed experimentally (Figure 8.7). Using the unmodified PSO model with a single value of k_2 but unique experimentally-fitted values of q_e gave a cross-calibration slope of 1.0770 ± 0.0186 ($R^2 = 0.9638$), i.e. an error of 7.7% and an uncertainty of 1.7% (Figure 8.7a). The agreement between experiment and model was improved when using the new model, with a slope of 0.9598 ± 0.0061 ($R^2 = 0.9949$), i.e. an error of 4.0% and an uncertainty of 0.6%. In the logarithmic form (Figure 8.7b) the cross-calibration slope of the new model was closer to unity with a gradient of 1.0117 ± 0.0063 and $R^2 = 0.9957$, indicating that the linear regression in Figure 8.7a is skewed by the few data points at high q_t values. Again, there is a better goodness of fit in the new model than the original PSO model (where $R^2 = 0.9880$). The modified rate equation therefore goes some way towards providing realistic sensitivity towards changes in C_0 and C_s .

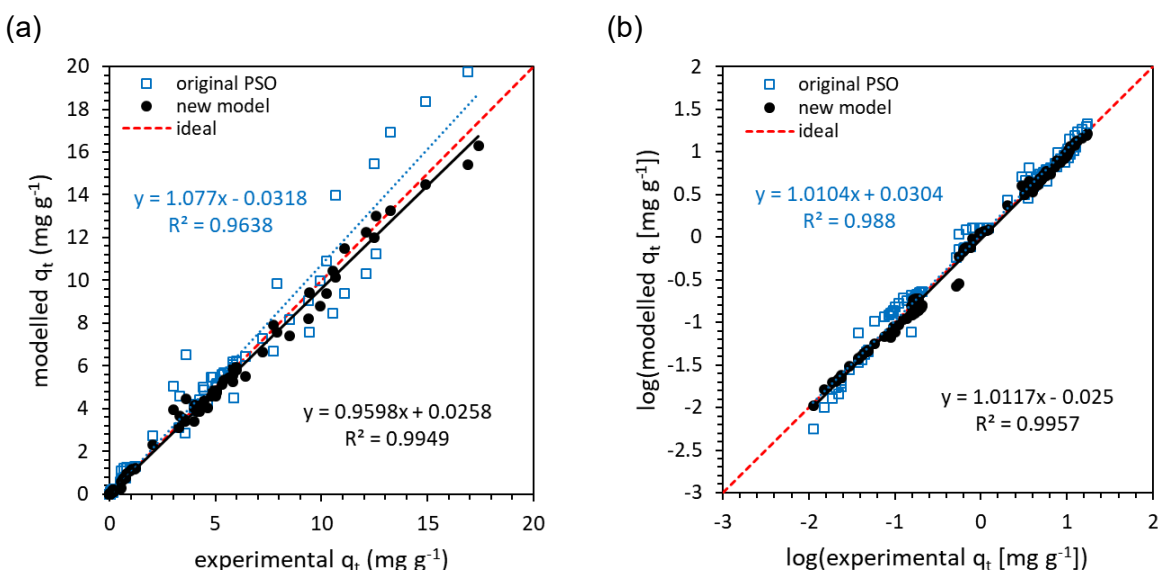


Figure 8.7: Calibration curves between the experimentally observed q_t and q_t values predicted by the original PSO and modified kinetic models in (a) absolute form and (b) logarithmic form. A single rate constant was used to model all kinetic experiments within a given data set. $N = 132$ data points are shown, with the original PSO model (blue open squares) and the new rate equation (black filled circles) along with their linear regressions (blue dotted and black solid lines respectively). The red dashed line indicates the one-to-one slope for a perfect model.

Using the original PSO model, two unique parameters (k_2 and q_e) were required for each kinetic experiment within each data set, and no predictive capability was offered. In the new model, one kinetic parameter (k') along with two adsorption isotherm parameters (K_L and q_{\max} for Langmuir or K_F and n for Freundlich) can be used to model multiple kinetic experiments, offering improved, though imperfect, predictive capability.

Table 8.2: Parameters used to model selected data sets using the PSO model and the new rate equation, using a single rate constant to model all kinetic experiments in a given data set, where C_0 or C_s was varied.

8.3. Modelling an arsenic treatment plant to inform the design of photocatalyst-sorbent remediation

Having developed a kinetic adsorption model with improved predictive capabilities, this chapter now models an arsenic treatment plant, aiming to identify the minimum mass of meso-TiO₂/Fe₂O₃ required to provide sufficient adsorption, and to identify the best reactor design for future engineering studies (i.e. batch or continuous-flow).

8.3.1. Experimental parameters

This modified kinetic adsorption model required (a) an adsorption isotherm to calculate q_e at each point in time, and (b) a rate constant (k'), re-normalised from the PSO rate constant k_2 . Adsorption isotherm and PSO parameters were experimentally determined for the adsorption of As(III) onto meso-TiO₂/Fe₂O₃ elsewhere²⁵¹. Adsorption isotherms were fit best when using the Freundlich adsorption isotherm model, compared with the Langmuir adsorption isotherm (agreeing with chapter 6), whilst adsorption kinetics were fit better by the PSO model compared with pseudo-first order (PFO) kinetics. The experimentally determined parameters are presented in Table 8.3.

Table 8.3: Experimentally determined parameters for the adsorption capacity and kinetics of the As(III)/TiO₂-Fe₂O₃ system at pH 7 (10 mM HEPES buffer) using experimental data from Lapinee²⁵¹. The sorbent concentration was always 1 g L⁻¹, and for adsorption kinetic experiments, the initial sorbate concentration was 39 mg L⁻¹ As(III).

Property	Adsorption capacity	Adsorption kinetics
Model	Freundlich isotherm	Pseudo-second order
Parameter 1	$K_F = 4.06 \pm 1.15 \text{ mg g}^{-1} (\text{mg L}^{-1})^{-1/n}$	$k_2 = 0.020 \pm 0.010 \text{ g mg}^{-1} \text{ min}^{-1}$
Parameter 2	$n = 2.63 \pm 0.14$	$q_e = 17.6 \pm 0.6 \text{ mg g}^{-1}$
R ²	0.773 (0.880 in linearised form)	(linearised form)

8.3.2. Validation of the new kinetic model with the integrated experimental parameters

This chapter demonstrated that the PSO model can be modified to provide better sensitivity towards changes in C_0 and C_s . In this model, the rate constant k' is readily calculated from experimental PSO parameters via Equation 3.42. The original PSO model provides no sensitivity towards C_0 and C_s , whilst the new model is first-order towards C_t and incorporates sensitivity to C_s through the use of adsorption isotherms to determine q_e ³⁰⁴. Despite these differences, the new model (using the Freundlich adsorption isotherm to determine q_e) successfully reconstructed the adsorption kinetics of the original PSO model from which it was derived (Figure 8.8). It is consequently evident that whilst providing sensitivity towards changes in C_0 and C_s that were lacking in the original PSO, the modified rate equation successfully reduces to the original PSO model under the same initial conditions.

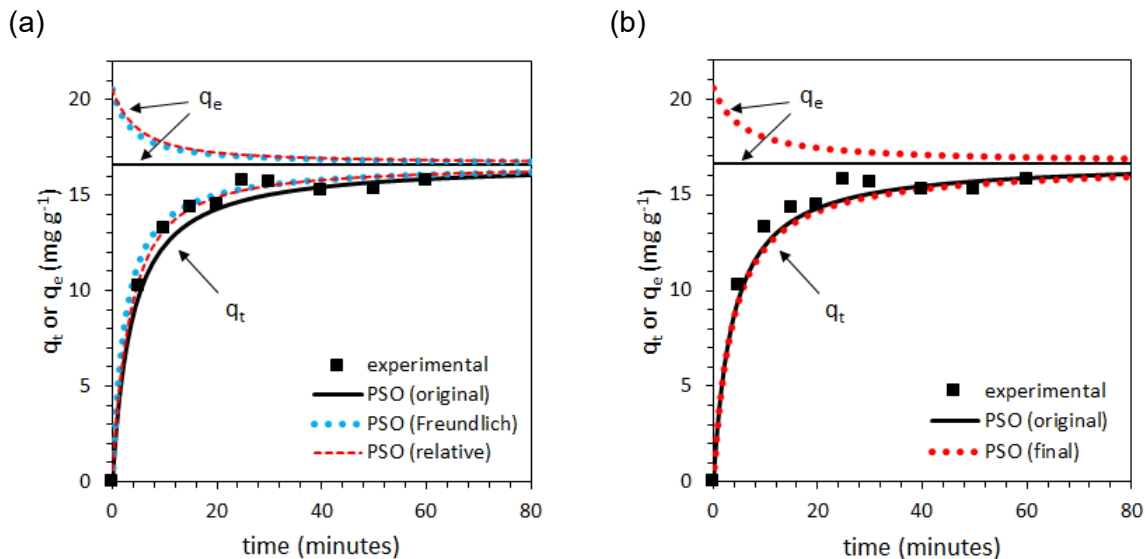


Figure 8.8: Comparison of the modified adsorption kinetic model with the unmodified PSO. (a) Comparison of the original PSO model with (i) calculating q_e at each point in time using the Freundlich adsorption isotherm, and (ii) modification to provide second-order dependence on the relative amount of remaining adsorption capacity, rather than the absolute amount of remaining adsorption capacity. (b) Comparison of the original PSO model with the new model, which incorporates both modifications (i) and (ii). The labels ‘ q_t ’ and ‘ q_e ’ indicate the quantity of adsorbed As(III) and the fixed or calculated value of q_e at each time point respectively. Note that the magnitude of the Freundlich constant K_F has been increased (from 4.06 to 5.10) to account for the 26% difference in q_e observed between the adsorption isotherm and kinetic experiments when $C_e = 22.5 \text{ mg L}^{-1}$ (in the Freundlich adsorption isotherm when $C_e = 22.4 \text{ mg L}^{-1}$, $q_e = 13.3 \text{ mg g}^{-1}$, whilst in the kinetic experiments when $C_e = 22.4 \text{ mg L}^{-1}$, $q_e = 16.7 \text{ mg g}^{-1}$).

The four models presented are labelled as follows: PSO (original): $\frac{dq}{dt} = k_2(q_e - q_t)^2$, PSO (Freundlich): $\frac{dq}{dt} = k_2(K_F C_t^{-1/n} - q_t)^2$, PSO (relative): $\frac{dq}{dt} = k'(1 - \frac{q_t}{K_F C_t^{-1/n}})^2$ where $k' = k_2 q_e^{1/2}$, PSO (final): $\frac{dq}{dt} = k' C_t (1 - \frac{q_t}{q_e})^2$ where $k' = \frac{k_2 q_e^{1/2}}{C_0}$.

8.3.3. Modelling an arsenic treatment plant

The input parameters for the arsenic treatment plant model reported in Table 8.3 were calculated from adsorption isotherms at pH 7, $C_e = 20\text{-}100 \text{ mg L}^{-1}$ and $C_s=1 \text{ g L}^{-1}$, and adsorption kinetics at pH 7, $C_0=39 \text{ mg L}^{-1}$ and $C_s=1 \text{ g L}^{-1}$. This neutral pH is representative of the typical groundwaters of South Asia and matches the point of zero charge for meso-TiO₂/Fe₂O₃ ($\text{pH } 7.0 \pm 0.3$) and is thus appropriate for modelling small scale treatment systems where the pH is not optimised. The value of C_0 used in the experimental data is over an order of magnitude greater than the C_0 values being modelled and the experimental sorbent loading (1 g L^{-1}) is (a) at the upper-end of typical photocatalyst concentrations and (b) at the bottom-end of typical sorbent concentrations. This work therefore extrapolates outside the conditions used to experimentally determine the model parameters, and the results should be considered as giving a semi-quantitative or qualitative comparison of different reactor designs only, based on identifying appropriate orders of magnitude in (a) the amount of sorbent required and (b) flow-rates and treatment times.

Table 8.4: Parameters used for modelling an arsenic treatment plant. The rate constant k' was calculated from experimental adsorption kinetics reported elsewhere²⁵¹. Freundlich isotherm parameters were determined from the equilibrium adsorption studies reported elsewhere²⁵¹, with K_F rescaled to account for the difference in q_e obtained in the adsorption isotherm and adsorption kinetic studies.

Parameter	Label and units	Value
Rate constant	$k' (\text{L g}^{-1} \text{ min}^{-1})$	0.111
Initial sorbate concentration	$C_0 (\mu\text{g L}^{-1})$	10-2000 (batch) 0 (continuous flow)
Initial sorbent concentration	$C_s (\text{g L}^{-1})$	0.01-10 000
Influent concentration	$C_{\text{influent}} (\mu\text{g L}^{-1})$	0 (batch) 500, 1000 and 2000 (continuous flow)
Turnover rate	$j (\text{L L}^{-1} \text{ min}^{-1})$	0 (batch) 0.001-1 (continuous flow)
Adsorption capacity $q_e (\text{mg g}^{-1})$	$K_F (\text{mg g}^{-1} (\text{mg L}^{-1})^{-1/n})$	5.10
	$n (\text{unitless})$	2.63

8.3.3.1. Batch reactor design

Batch reactors treat a single volume of water until contaminant concentrations are within safety limits. The user must wait for treatment before water is collected, however longer treatments allow for more complete removal of contaminants. The results from the batch treatment model are presented in Figure 8.9, with kinetic profiles in Figure 8.9a, and the time required to provide safe drinking water within the $10 \mu\text{g L}^{-1}$ WHO limit in Figure 8.9b. The model predicted that 0.1 g L^{-1} $\text{TiO}_2\text{-Fe}_2\text{O}_3$ could only treat water contaminated with $<100 \mu\text{g L}^{-1}$ As(III), and then only with long treatment times on the hour timescale. At least 1 g L^{-1} $\text{TiO}_2\text{-Fe}_2\text{O}_3$ was needed to treat As(III) contaminated water within 1 hour, and even then, above $400 \mu\text{g L}^{-1}$ As(III) several hours treatment was needed). At $\geq 10 \text{ g L}^{-1}$, water contaminated with up to $2000 \mu\text{g L}^{-1}$ As(III) was rapidly remediated within a matter of minutes. This model suggests that in batch treatments using multi-functional sorbents combining adsorption and photocatalytic properties, more than the typical $0.01\text{--}0.1 \text{ g L}^{-1}$ photocatalyst loading is required for the sorbent to perform sufficiently. Furthermore, below 1 g L^{-1} kinetic limitations will be important, adding constraints on treatment time.

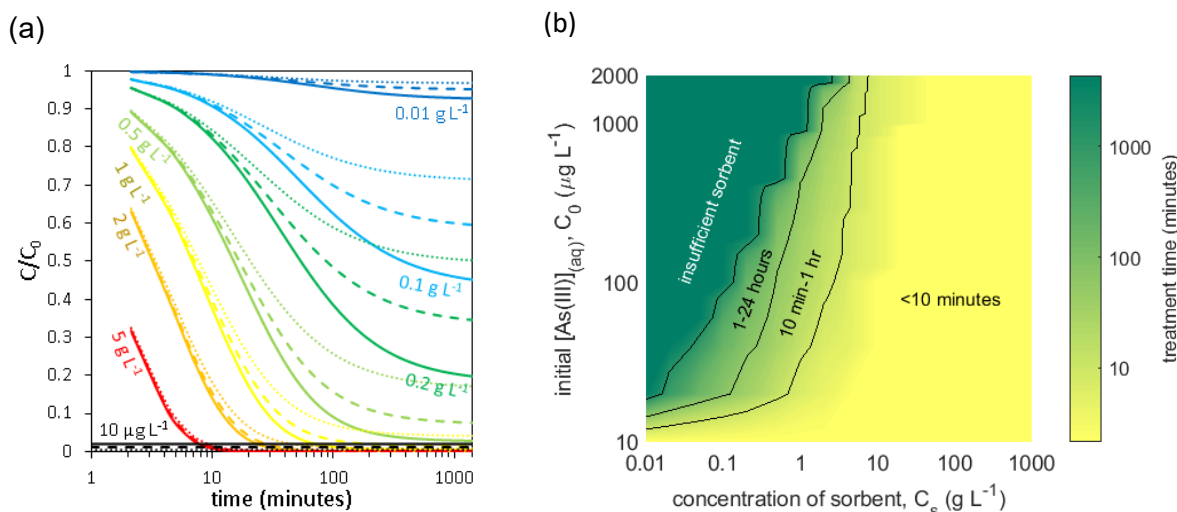


Figure 8.9: Modelling batch treatments. (a) Batch kinetics predicted for As(III) adsorption using different sorbent loadings of $\text{TiO}_2\text{/Fe}_2\text{O}_3$. The simulated kinetics are shown for initial As(III) concentrations of $500 \mu\text{g L}^{-1}$ (solid lines), $1000 \mu\text{g L}^{-1}$ (dashed lines) and $2000 \mu\text{g L}^{-1}$ (dotted lines). The black lines close to the x-axis indicate the $10 \mu\text{g L}^{-1}$ WHO arsenic guideline limit. (b) The time taken to remove arsenic below the $10 \mu\text{g L}^{-1}$ WHO limit, as a function of both initial As(III) concentration and sorbent loading. C_s refers to sorbent loading and $[\text{As(III)}]_0$ to the initial concentration of aqueous As(III), C_0 .

8.3.3.2. Continuous-flow reactor design

In a continuous-flow system, contaminated influent is continuously pumped into the reactor whilst treated effluent is extracted. Breakthrough curves for the continuous-flow model are given in Figure 8.10a and Figure 8.10b. At high sorbent concentrations ($\geq 100 \text{ g L}^{-1}$), varying the turnover rate (the rate at which a volume of effluent equivalent to the reactor volume is collected) between 0.001 and 0.1 min⁻¹ had little effect on the shape of the simulated breakthrough curve: the sorbent removed As(III) sufficiently fast that no build-up of aqueous As(III) in the reactor occurred prior to sorbent saturation. For more dilute meso-TiO₂/Fe₂O₃ suspensions ($\leq 10 \text{ g L}^{-1}$) however, the shape of the simulated breakthrough curve was strongly influenced by the turnover rate. For instance, when modelling suspensions of 10 g L⁻¹ sorbent, under a slow turnover rate of 0.001 min⁻¹, breakthrough only occurred once the sorbent was saturated. With an influent of 500 µg L⁻¹ As(III) this corresponds to breakthrough (above the WHO limit of 10 µg L⁻¹) at 14 bed volumes (Figure 8.10c).

When turn over frequency was increased to 0.01 min⁻¹, fewer bed volumes were treated before breakthrough due to kinetic limitations to adsorption: breakthrough was reached at just 6 bed volumes. Formation of a steady-state before breakthrough was also observed, with a temporarily stable effluent concentration of 4.5 µg L⁻¹ As(III). Here, $jC_{\text{influent}} = \text{rate of adsorption} - jC_t$. When turnover frequency was increased to 0.1 min⁻¹, breakthrough was reached after just 2.6 bed volumes. Here, the model predicted a steady state scenario with approximately 43 µg L⁻¹ As(III), already exceeding the WHO limit. Since breakthrough occurred with an unsaturated sorbent, due to the As(III) steady-state, this scenario is an inefficient and uneconomical use of the sorbent. Similar results are observed with an influent concentration of 2000 µg L⁻¹ As(III) (Figure 8.10d), however the higher influent concentration leads to As(III) steady-states surpassing the guideline limits at lower turnover rates.

The simulated results match experimental observations of similar systems: breakthrough at undersaturated conditions at high flow-rates in the adsorption of As(V) onto laterite ⁴⁹⁹, and steady-state breakthrough during the adsorption of As(V) onto both two-line ferrihydrite (an iron oxide) ⁵⁰⁰ and anion exchange beads ⁵⁰¹. Ideally, the sorbent is saturated at breakthrough, since this is a more economical use of material, with the sorbent requiring replacement less frequently. The simulated results suggested that aiming to achieve (i) at least 50% saturation before breakthrough, (ii) potable water with <10 µg L⁻¹ As(III), and (iii) a turnover rate of 0.01–0.1 min⁻¹ (i.e. between 10 and 100 minutes treatment time), sorbent concentrations in the order of 100 and 1000 g L⁻¹ are needed to treat influent concentrations of 500 and 2000 µg L⁻¹ As(III) respectively.

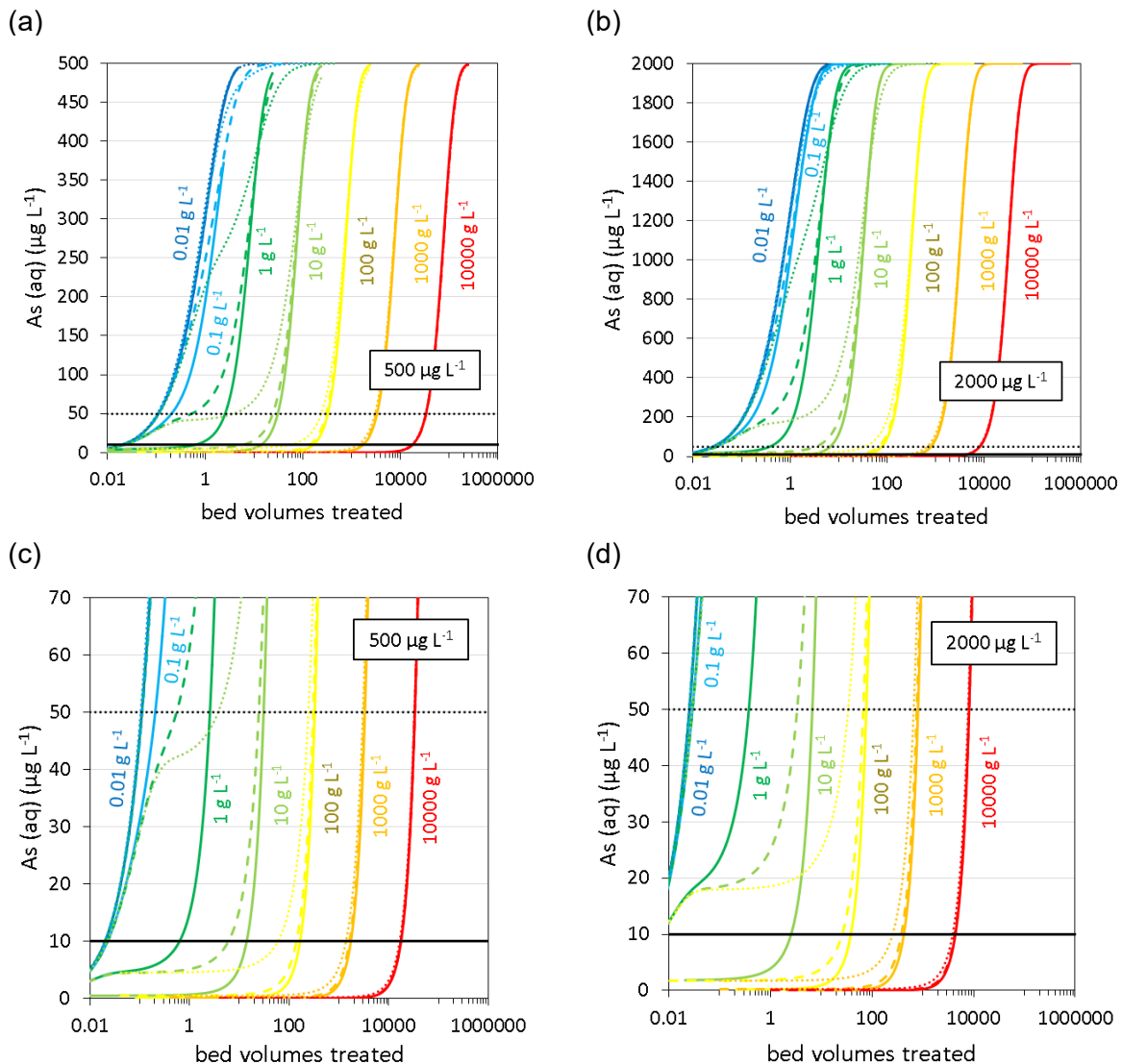


Figure 8.10: Modelling continuous-flow treatment. Simulated As(III) breakthrough curves as a function of sorbent loading are presented with influent concentrations of (a) $500 \mu\text{g L}^{-1}$ and (b) $2000 \mu\text{g L}^{-1}$ As(III). (c) and (d) provide close ups of arsenic breakthrough and the presence of steady-states. Breakthrough curves were simulated at turnover rates of 0.001 (solid lines), 0.01 (dashed lines) and 0.1 (dotted lines) min^{-1} . The WHO $10 \mu\text{g L}^{-1}$ guideline limit is indicated as the solid black line, and the higher $50 \mu\text{g L}^{-1}$ guideline limit is indicated as the dashed black line.

8.3.3.3. Comparison of reactor designs

A comparison between simulated results using the batch treatment and continuous-flow models is given in Figure 8.11, showing both turnover rate (the reciprocal of treatment time, on the left-hand y-axis) and sorbent efficiency (as the quantity of sorbate adsorbed after treatment, or at breakthrough, on the right-hand y-axis) as a function of sorbent concentration. For the continuous-flow system the reported data was selected to give the best combination of turnover rate and sorbent efficiency (calculated as the product between the two).

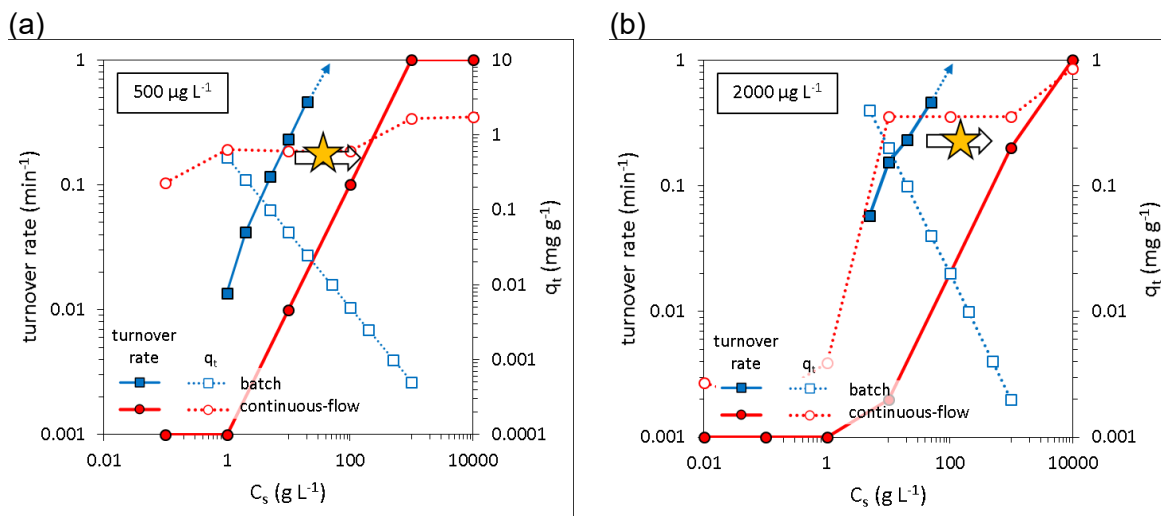


Figure 8.11: Comparison of simulated results for the batch (blue squares) and continuous-flow (red circles) models. Turnover rate (filled shapes and solid lines) and sorbent efficiency (open shapes, dotted lines) are given as a function of sorbent concentration. For the continuous-flow system, a two-dimensional matrix of C_s and turnover rate values was simulated. To reduce the two independent variables to just one (C_s), the data shown corresponds to the 'optimum' turnover rate identified at each value of C_s , determined as the value of turnover rate that gives the highest product $j \cdot q_t$, i.e. an equal priority weighting for turnover rate and sorbent efficiency. The arrow labelled with a star denotes the shift in sorbent concentration required to achieve similar performance (turnover and sorbent efficiencies) between continuous-flow and batch treatment systems.

For the batch treatment, the model gives a linear relationship between increasing C_s and turnover rate, since the rate of As(III) removal in the model is first-order with respect to C_s . The sorbent efficiency linearly decreases with increasing C_s , as the same quantity of arsenic in the reactor is distributed across an increasingly large sorbent mass. Above the minimum ~ 1 g L⁻¹ sorbent required to remove As(III), any further increase in C_s decreases sorbent economy.

The continuous-flow system also shows a linear increase between C_s and turnover rate, again due to the first-order dependence upon C_s . However, unlike the batch system, the sorbent efficiency of the continuous-flow treatment increases with C_s . This is due to breakthrough occurring with undersaturated sorbent due to the slow kinetics of arsenic adsorption when C_s is small. At high values of C_s , kinetic limitations become less significant and the sorbent achieves a higher degree of saturation before breakthrough.

The batch system has a minimum concentration of sorbent required to provide any volume of safe water, since the influent is treated as a single, discrete volume. On the other hand, the continuous-flow system does not treat the influent in discrete volumes and therefore there is theoretically no minimum threshold value of C_s needed before potable water is extracted in the effluent. Of course, at low values of C_s , the continuous-flow system requires long treatment times (low turnover rates) to avoid undersaturated breakthrough.

As indicated by the stars in Figure 8.11, the continuous-flow system is predicted to require between one and two orders of magnitude more sorbent (g L⁻¹) than the batch system to

achieve the same sorbent efficiencies (mg g^{-1}) with similar turnover rates (min^{-1}). For example, in the batch treatment, 10 g L^{-1} sorbent was sufficient to treat water contaminated with up to $2000 \mu\text{g L}^{-1}$ As(III) in less than ten minutes (i.e. a turnover rate of 0.1 minute^{-1}). This was a much lower concentration of sorbent than in the continuous-flow model, where 1000 g L^{-1} sorbent was necessary to treat water contaminated with up to $2000 \mu\text{g L}^{-1}$ As(III) at a turnover rate of 0.1 minute^{-1} . This is logical since in the batch treatment, the entire quantity of sorbate is introduced to the sorbent at once, leading to much faster early adsorption kinetics (due to the first-order dependency upon C_t). The continuous-flow scenario is different, as C_t can never exceed $10 \mu\text{g L}^{-1}$ As(III) without breakthrough having been reached. The difference between batch and continuous-flow systems becomes more pronounced at higher sorbate concentrations, as the difference in C_t at $t=0$ for batch and continuous-flow systems becomes more significant. The implication is that batch treatment may be more appropriate for scenarios requiring low sorbent concentrations (such as in a simultaneous photocatalytic oxidation-adsorption treatment) and requiring a very large reduction in the relative concentration of contaminants (e.g. reducing $2000 \mu\text{g L}^{-1}$ As(III) to just $10 \mu\text{g L}^{-1}$).

These results suggest that for one-off remediation, batch treatment is more appropriate than continuous-flow, with faster treatment times and the same sorbent efficiencies, but only as long as the appropriate mass of sorbent can be identified to achieve sufficient sorbent economies (due to the need to minimise surplus sorbent). The implication for the photocatalyst-sorbent system is that batch treatment may be more appropriate, given that low material concentrations may be needed to achieve sufficient penetration of light through the reactor.

8.3.4. Modelling a 365-day deployment

8.3.4.1. Daily household water requirements and boundary conditions

As indicated above, one historic failing of the arsenic mitigation schemes in South Asia designed around sorbent filters has been the difficulty users find when cleaning saturated media³⁰, and the limited market availability of replacement media^{110 31}. This section therefore aimed to explore how batch and continuous-flow treatments would compare if the sorbent was used for an entire year before replenishment. The best solution would provide safe, potable water ($<10 \mu\text{g L}^{-1}$ arsenic) for 365 days, using the least sorbent due to the need for cost efficiency³⁰.

As boundary conditions for the volume of potable water required, the needs of a rural family in West Bengal, India were considered, with an average of 5.7 people per household⁵⁰². The WHO South-East Asia Technical Office reports that 7 litres of water is required per person per day (4 L per capita per day (Lpcd) for drinking and 3 Lpcd for food preparation)⁵⁰³. These two figures give a requirement for 40 L day⁻¹ potable water per household. This is equivalent to 14,600 L per year per household. At an influent concentration of 500 µg L⁻¹ As(III), this equates to the removal of 7.3 grams of arsenic per year. Flow rate was not considered an essential parameter, as whilst the WHO specifies that the flow rate at each collection point should be at least 0.125 litres per second⁵⁰³, in cases where treatment is slow, the effluent can be collected in a storage tank prior to distribution, as is in current treatment plants⁴⁷⁸.

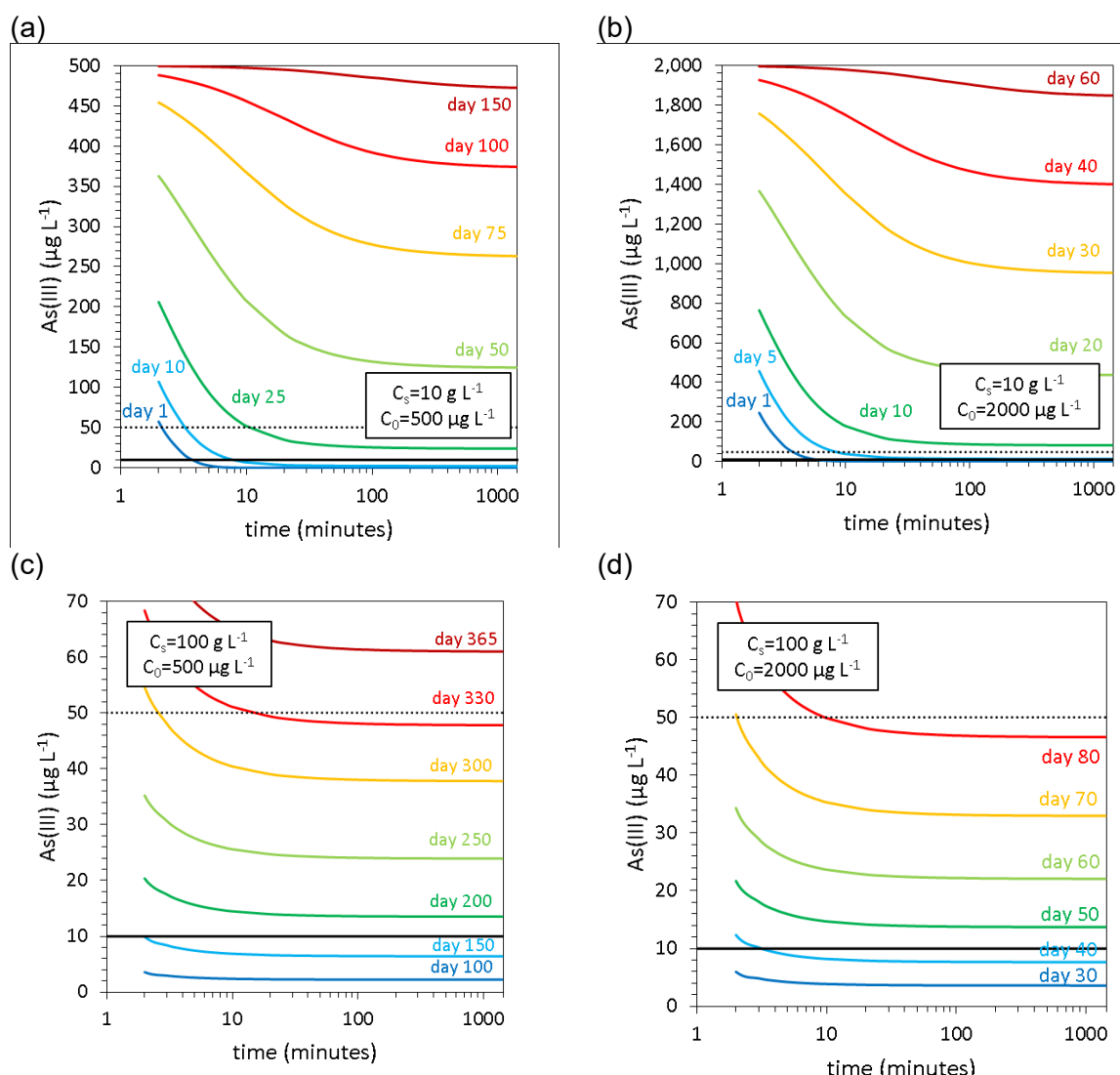


Figure 8.12: Kinetic adsorption modelling: batch treatment using the same sorbent for 365 days. Shown are kinetic profiles for simulations with 500 (a and c) and 2000 (b and d) µg L⁻¹ initial As(III) (C_0), and with 10 (a and b) and 100 (c and d) g L⁻¹ sorbent concentration (C_s). For each simulation after day 1, the initial amount of adsorbed As(III) (q_t) was set as the final value of q_t for the simulation corresponding to the previous day, reflecting the sorbent becoming increasingly saturated through repeat use. The solid black line corresponds to the WHO 10 µg L⁻¹ guideline limit, and the dotted black line corresponds to 50 µg L⁻¹ arsenic.

8.3.4.2. Modelling sequential batch treatments

To model a 365-day deployment, the continuous-flow MATLAB code was used without modification. For the batch treatment system, however, codes were modified to represent gradual saturation of the media during 365 sequential treatments (as illustrated by Figure 8.12).

8.3.4.3. Comparison of batch and continuous-flow treatments

The models predicted that the batch reactor design provides safe water for at least as many days as the continuous-flow design under all combinations of C_s and treatment time (Figure 8.13). For the batch reactor, the number of days per year successfully treated depended primarily on the sorbent concentration and was not significantly affected by the treatment time: batch treatment was rapid due to the fast kinetics during initial mixing, resulting from the high initial concentration of As(III) and first order dependence on C_t . However, for the continuous-flow reactor, sorbent concentrations and flow rate (turnover rate) were equally important. For instance, reducing the flow rate by a factor of 10 had the same effect on the number of days successfully treated as multiplying the sorbent concentration by a factor of 10. This was due to high turnover rates (short residence times) leading to breakthrough before the sorbent was saturated: adsorption kinetics were limited by the first order dependence on C_t since during operation the concentration of As(III) in the continuous-flow reactor is always $<10 \mu\text{g L}^{-1}$.

The model also suggested that the batch reactor can run for more days than the continuous-flow reactor when treatment times are shortened. For instance, in the batch model, 100 g L^{-1} sorbent successfully removed $500 \mu\text{g L}^{-1}$ As(III) for 175 days with a treatment time of just 20 minutes per day (Figure 8.13a). In contrast, 100 g L^{-1} sorbent in the continuous-flow system failed to treat water contaminated with $500 \mu\text{g L}^{-1}$ As(III) with an average residence time of 20 minutes after just one day (Figure 8.13b). The implications here are that batch reactor designs may be more economical: shorter treatment times in a batch reactor mean that energy intensive processes such as pumping, mixing and ultraviolet irradiation might be performed for shorter durations.

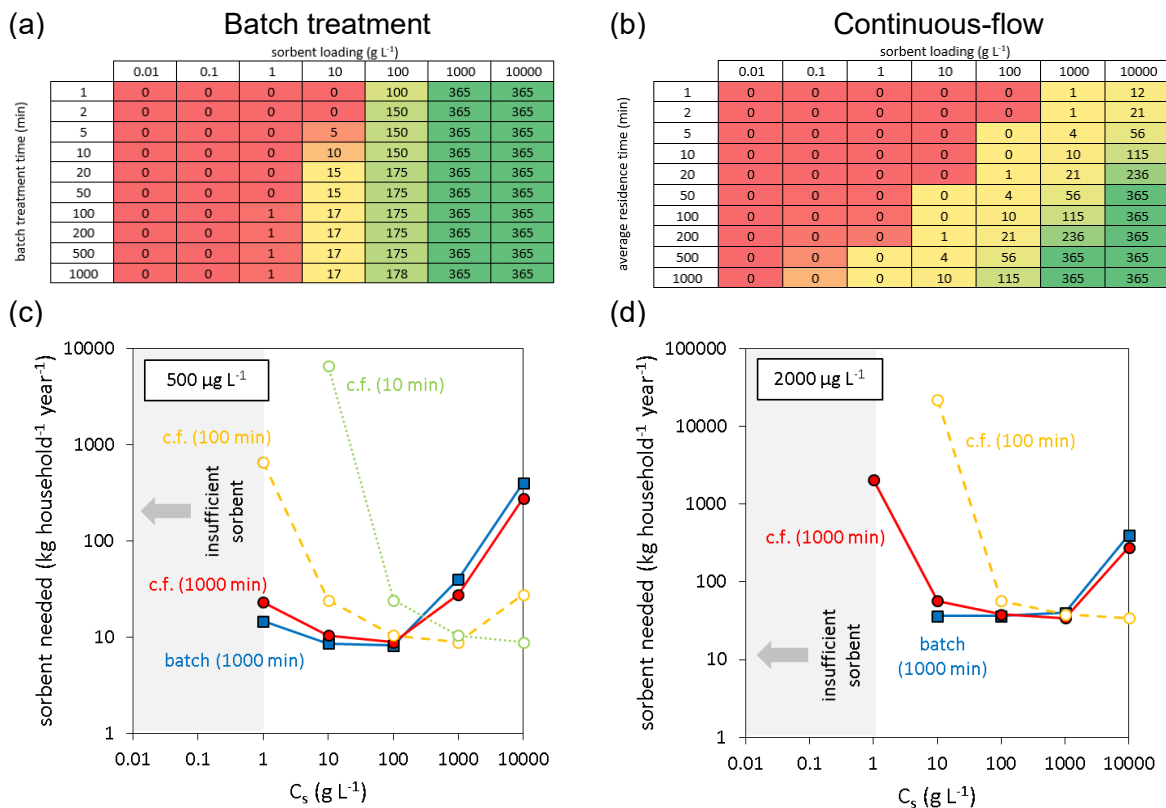


Figure 8.13: Comparison of 365-day sorbent deployments simulated using batch and continuous-flow configurations. Presented are the number of days during which water was successfully treated for (a) batch and (b) continuous-flow systems as a function of sorbent concentration and average residence time, with 500 µg L⁻¹ initial As(III). The colour transition between red, yellow and green reflects increasing life-times of the reactor before breakthrough (with a maximum of 365 days simulated). Sorbent efficiency (kg sorbent required per household per year) is presented as a function of sorbent concentration, and with different treatment times, where initial As(III) concentrations are (c) 500 µg L⁻¹ and (d) 2000 µg L⁻¹. Note that some data points presented in (c) and (d) correspond with scenarios wherein the sorbent has failed to provide 365 days of safe water. Continuous-flow is abbreviated as 'c.f.', the batch model is given as blue squares, and continuous-flow is given as (i) red circles-solid lines (1000 minutes average residence time), (ii) open circles-yellow dashed lines (100 minutes) and (iii) open circles-green dotted lines (10 minutes).

8.3.4.4. Economising sorbent use

A minimum sorbent concentration of 1 kg L⁻¹ was required to safely remove As(III) for an entire year in both reactor designs. This is much higher than normal photocatalyst concentrations. Whilst treatments in the hours timescale were needed for the continuous-flow configuration, batch treatment was successful in just minutes. However, the best sorbent economies were achieved under conditions wherein the sorbent needed replacing during the 365-day deployment (Figure 8.13c, d). At the slowest treatment times (1000 minutes, i.e. a reactor operated continuously all day), batch treatments gave the best sorbent economy when C_s<100 g L⁻¹, and continuous-flow treatments gave a better sorbent economy when C_s>100 g L⁻¹ (Figure 8.13c, d). More detailed results on sorbent economy are presented in Figure 8.14.

	batch							continuous-flow							
	sorbent loading (g L ⁻¹)							sorbent loading (g L ⁻¹)							
batch treatment time (min)	0.01	0.1	1	10	100	1000	10000	average residence time (min)	0.01	0.1	1	10	100	1000	10000
1	0.00	0.00	0.00	0.00	0.50	0.18	0.02	1	0.00	0.00	0.00	0.00	0.83	0.87	
2	0.00	0.00	0.00	0.00	0.75	0.18	0.02	2	0.00	0.00	0.00	0.00	0.47	0.76	
5	0.00	0.00	0.00	0.25	0.75	0.18	0.02	5	0.00	0.00	0.00	0.00	0.06	0.63	0.81
10	0.00	0.00	0.00	0.50	0.75	0.18	0.02	10	0.00	0.00	0.00	0.00	0.30	0.70	0.83
20	0.00	0.00	0.00	0.75	0.88	0.18	0.02	20	0.00	0.00	0.00	0.00	0.47	0.76	0.85
50	0.00	0.00	0.00	0.75	0.88	0.18	0.02	50	0.00	0.00	0.00	0.06	0.63	0.81	0.53
100	0.00	0.00	0.50	0.85	0.88	0.18	0.02	100	0.00	0.00	0.01	0.30	0.70	0.83	0.26
200	0.00	0.00	0.50	0.85	0.88	0.18	0.02	200	0.00	0.00	0.01	0.47	0.76	0.85	0.13
500	0.00	0.00	0.50	0.85	0.88	0.18	0.02	500	0.00	0.00	0.07	0.63	0.81	0.53	0.05
1000	0.00	0.00	0.50	0.85	0.89	0.18	0.02	1000	0.00	0.00	0.32	0.70	0.83	0.26	0.03

Figure 8.14: Sorbent efficiency (mg g⁻¹ adsorbed at the end of year or at breakthrough, whichever occurs soonest). The initial As(III) concentration was 500 µg L⁻¹ in all simulations.

The minimum mass of sorbent required was similar between batch and continuous-flow models, with 8.2 and 8.4 kg sorbent household⁻¹ year⁻¹ respectively (when initial As(III) was 500 µg L⁻¹). However, the conditions under which optimal sorbent economies were obtained varied between the two systems. Sorbent economy was best in the batch model when using 100 g L⁻¹ sorbent and treatment times of 1000 minutes (8.2 kg sorbent household⁻¹ year⁻¹), however similar results were achieved with less sorbent and faster treatment times: 10 g L⁻¹ sorbent and 100 minutes treatment times gave a sorbent requirement of 8.6 kg household⁻¹ year⁻¹. When C_s = 10 g L⁻¹ and 100 g L⁻¹, the sorbent required replacing every 17 and 175 days respectively. In the continuous-flow model, the best sorbent economy was achieved with much higher sorbent concentrations: C_s = 1 and 10 kg L⁻¹, and average residence times of 200 and 20 minutes respectively. Under these conditions, 8.6 kg sorbent household⁻¹ year⁻¹ was needed and the sorbent required replacing every 236 days. The batch model therefore provided better sorbent economies at low sorbent concentrations, again suggesting that this is the more appropriate reactor design for photocatalyst-sorbent systems.

The ~8 kg of sorbent per household per year is only an estimation, as a number of factors will affect the true amount of sorbent needed. For instance, As(III) has been considered in the absence of competitor ions which suppress adsorption. Secondly, multilayer surface precipitation effects are important for both As(III) and As(V), increasing arsenic removal^{257 423}. Surface precipitation is a much slower process than adsorption and is thus unlikely to have been captured in our experimental determination of As(III) adsorption kinetics.

	sorbent loading (g L ⁻¹)						
batch treatment time (min)	0.01	0.1	1	10	100	1000	
1	-	-	-	-	-	0.22	0.02
2	-	-	-	-	-	0.38	0.02
5	-	-	-	288.35	13.61	0.29	0.02
10	-	-	-	455.37	2.49	0.26	0.02
20	-	-	-	561.80	1.84	0.24	0.02
50	-	-	-	13.20	1.40	0.23	0.03
100	-	-	44.88	2.80	1.24	0.22	0.07
200	-	-	37.65	1.79	1.16	0.21	0.14
500	-	-	6.78	1.35	1.09	0.35	0.35
1000	-	-	1.57	1.21	1.07	0.69	0.69

Figure 8.15: The mass of sorbent required per household per year using the continuous-flow configuration divided by the mass of sorbent required in the batch treatment, with an initial concentration of 500 µg L⁻¹ As(III). Blank cells indicate conditions under which the continuous-flow model was unable to provide at least 1 day of safe water (<10 µg L⁻¹ As(III)).

8.3.5. Implications for engineering photocatalyst-sorbent systems

The simulated models suggested that batch treatments are more efficient than continuous-flow when the sorbent concentration is limited (i.e. <10 g L⁻¹), for both single use and long-term deployments. Since most applications of photocatalysts for water remediation use low catalyst concentrations, the batch reactor design appears most promising for the application of bifunctional composite-sorbents such as TiO₂-Fe₂O₃. The model also suggested that more than 100 g L⁻¹ of the sorbent is required for successful treatment without changing media for an entire year. This is much higher than typical photocatalyst concentrations. To operate at 1 g L⁻¹ and under, media would thus need to be replenished several times per year.

The batch reactor design is ‘safer’ in the sense that there is less dependency on the treatment time (due to fast adsorption in the initial minutes of treatment thanks to high C_t values), with sorbent loading being the principal parameter. By using excess concentrations of sorbent, water can be treated rapidly without breakthrough. Our results contrast with Lekić et al. who observed experimentally that As(III) and As(V) removal per gram of sorbent was superior in a column (continuous-flow) configuration, which they suggested was due to non-adsorption processes such as coagulation, flocculation and filtration, that are not captured in the present model ⁴⁸¹. This chapter indicates that photooxidation kinetics in the photocatalyst-sorbent system need to be studied at high material concentrations (\geq 10 g L⁻¹), and with different reactor dimensions, to verify that suspensions can be sufficiently irradiated to provide effective photooxidation kinetics at the high sorbent concentrations needed to achieve sufficient device lifetimes. This information is currently lacking from all previous studies on the remediation of As(III) using multifunctional photocatalyst-sorbent materials.

8.4. Future work: Integrating desorption rates

The next step in the development of this arsenic treatment plant model is the introduction of rate equations for the photocatalytic oxidation of As(III), to provide a mathematical description of how photocatalyst-sorbent systems might outperform the sorbent-only filter devices. Such a model requires additional levels of complexity besides photocatalytic oxidation rate constants. Firstly, rate equations for the desorption of As(III) and As(V) are needed to model the balance between adsorbed As(III) and As(V) at equilibrium, especially given that chapter 6 identified that (a) photooxidation using meso-TiO₂ suffers from As(V) photocatalyst deactivation and (b) photooxidation using meso-TiO₂/Fe₂O₃ is better modelled using the As(V)-sensitive surface complexation model (SCM) compared with the single-sorbate Langmuir-Hinshelwood model. Secondly, the rational for the oxidative pretreatment is that As(V) binds more strongly to the mineral surface than As(III), and so removal capacity in the presence of competitor ions is improved after oxidation. The model therefore requires adsorption and desorption constants for competitor ions such as phosphate and sulphate. Thirdly, rate constants for the adsorption of all aqueous species onto each surface component (i.e. meso-TiO₂ and Fe₂O₃) will need to be calculated, if this model is going to be used for composites prepared under different synthetic conditions with different surface compositions.

Desorption kinetics are infrequently studied, with just a handful of relevant examples, including As(III)/FeOOH ⁴⁸², As(III)/laterite and As(V)/laterite ⁴⁸³, Cr(VI)/Mg-Al-CO₃ ³⁰³, and Pb(II)/γ-Al₂O₃ ⁴⁸⁴. Experimental techniques include drying minerals after adsorption of the analyte, and then re-suspending powders in either the same electrolyte ⁴⁸⁴, in NaOH ⁴⁸³, in the presence of a competitor ion (e.g. CaCO₃ ³⁰³ or SO₄²⁻ ⁴⁸²), or in the presence of an ion-exchange resin ⁴⁸⁴. Desorption studies are thus not only rare, but they also lack standardised experimental techniques. In the lack of sufficient literature data, adsorption-desorption kinetics could be estimated by fitting experimental adsorption data, as will be shown in this preliminary proof.

8.4.1. A method to determine desorption constants

Serial adsorption data obtained by experiment is in reality a convolution of adsorption and desorption reactions: the observed rate of adsorption is equal to the real rate of adsorption minus the rate of desorption. The rate constants governing the true rate of adsorption r can be determined from the initial rate ($t=0$), where the rate of desorption is zero. The rate of

desorption can then be determined by subtracting the observed rate of adsorption from the calculated true rate of adsorption at each point in time.

As a preliminary investigation, this method was studied using the As(III)/meso-TiO₂/Fe₂O₃ adsorption kinetics data set²⁵¹. The PSO model developed in this work was used to ‘smooth’ the experimental data and generate the appropriate curvature through interpolation between experimental data points. In the adsorption-only PSO model, adsorption and desorption reactions are convoluted, and so the driving force for the forwards reaction (adsorption) is governed by the concentration of available adsorption capacity remaining. This is calculated by subtracting q_t from q_e , where q_e defines the upper limit to adsorption. In an adsorption-desorption model, however, adsorption and desorption reactions are not convoluted, and so the upper limit to adsorption (which defines the driving force of the forwards reaction) is not the equilibrium capacity, q_e , but rather the total concentration of available binding sites.

Accurate quantification of the total concentration of adsorption sites is challenging, given that the range of characterisation techniques available provides numbers differing by whole orders of magnitude^{504 290}. For a first approximation, the concentration of surface sites might be assigned to a somewhat arbitrary number, such as the concentration of surface hydroxyls in the extended triple layer model (ETLM). This can be rationalised on the basis that parameters for the rate of desorption are to be fitted from the experimental data and the site density, so the influence of the chosen site density upon the final adsorption-desorption model should be limited.

If the site density of the meso-TiO₂/Fe₂O₃ sorbent is fixed at 4.0 sites nm⁻² as per the Fe₂O₃ surface phase in the SCM developed in chapter 6, then a 1 g L⁻¹ suspension (with a surface area of 63 m² g⁻¹) gives a surface hydroxyl concentration of 0.419 mM. This is equivalent to 31.4 mg g⁻¹ arsenic, a significantly greater number than the 13.8 mg g⁻¹ As(III) removed at the end of the adsorption kinetic experiment (q_e). By replacing q_e with 31.4 mg g⁻¹ (q_{\max}) in the modified PSO rate equation, the ‘true’ rate of adsorption is estimated, using the new equation:

$$\text{rate of adsorption (mg g}^{-1} \text{ min}^{-1}\text{)} = k_{\text{ads}} C_t \left(1 - \frac{q_t}{q_{\max}}\right)^2$$

Equation 8.16

The calculated rate of adsorption is shown in Figure 8.16a. By subtracting the observed reaction rate from this ‘true’ rate of adsorption, the rate of desorption is determined. Application of a rate law to this data allows us to determine the desorption rate constant. For instance, if we describe the rate of desorption as being first-order with respect to the concentration of adsorbed As(III), then we arrive at the following:

$$\text{rate of desorption (mg g}^{-1} \text{ min}^{-1}) = k_{\text{des}} q_t$$

Equation 8.17

Using this first-order rate equation and plotting the rate of desorption as a function of the concentration of adsorbed As(III), q_t , should yield a straight line, of which the gradient is equal to the rate constant k_{des} .

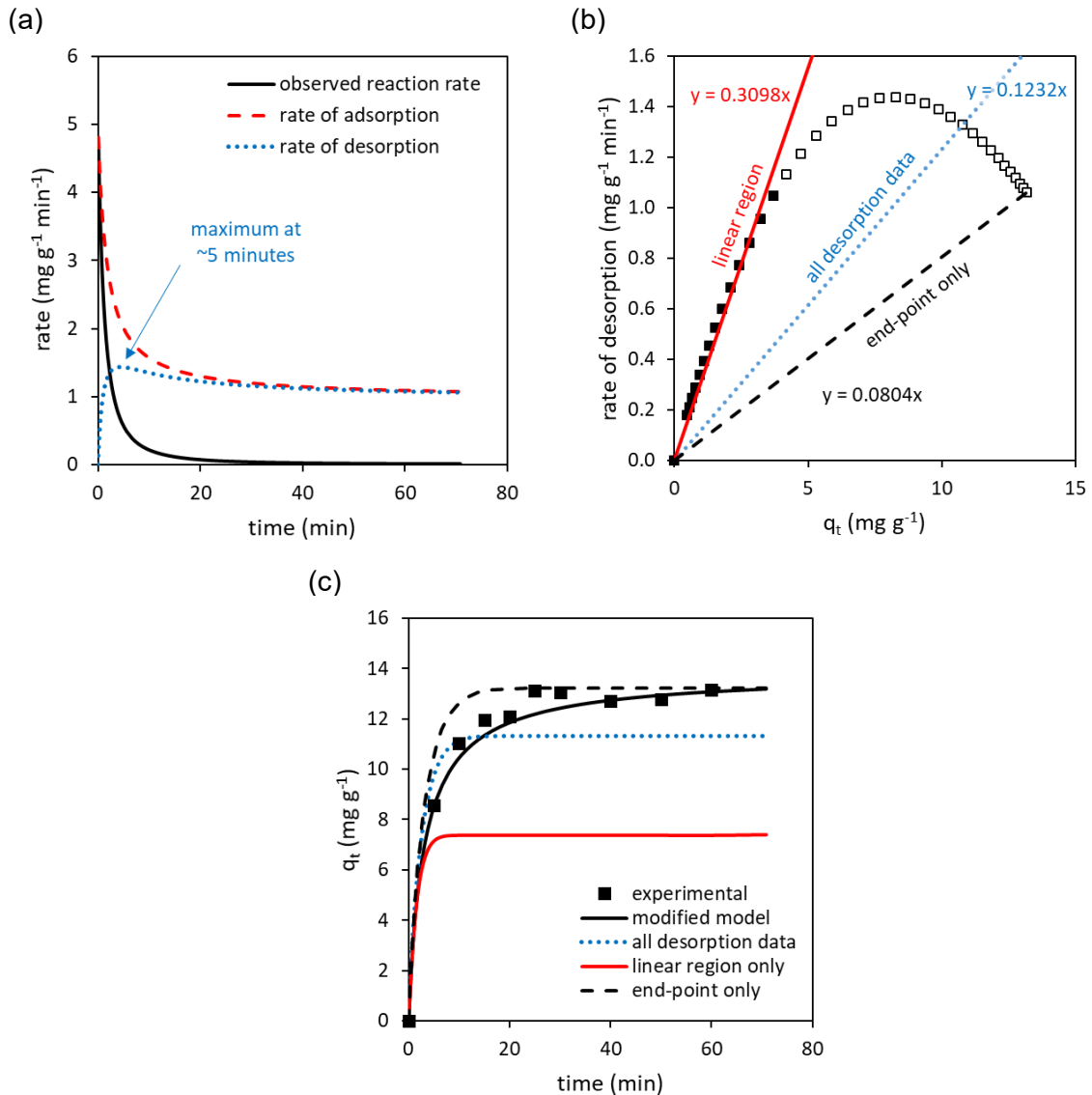


Figure 8.16: An adsorption-desorption model using a single type of surface complex. (a) shows how the rate of desorption is calculated at each point in time by subtracting the observed rate of reaction (in this case smoothed from the experimental data using the unmodified PSO model) from the 'true' rate of adsorption, which was calculated using the new rate equation in chapter 8 with a theoretical maximum adsorption capacity, $q_{\text{max}} = 31.4 \text{ mg g}^{-1}$ (4.0 sites nm^{-2} and $63 \text{ m}^2 \text{ g}^{-1}$). Initial sorbate concentration, $C_0 = 39 \text{ mg L}^{-1}$ and sorbent concentration, $C_s = 1 \text{ g L}^{-1}$. $k_{\text{ads}} = 0.123 \text{ L g}^{-1} \text{ min}^{-1}$ and was calculated from the initial rate using the PSO model. (b) shows how the desorption rate constant, k_{des} , was calculated from the linear regression of desorption rates as a function of q_t , which was only linear between $q_t = 0$ and 3 mg g^{-1} , corresponding to $t = \sim 5 \text{ minutes}$ in figure (a). (c) shows the results of this adsorption-desorption model (with a single surface complex), where the desorption rate constant was determined using a linear regression fitted to different data points within figure (b).

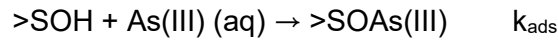
This was not the case in this preliminary study, as indicated by Figure 8.16b, as the initial linear relationship between the rate of desorption and q_t reached a point of inversion. The highest rate of desorption at $q_t=8 \text{ mg g}^{-1}$ corresponds with $t \approx 5$ minutes in Figure 8.16a. Using the shallow gradient calculated from the linear regression the end-point only ($k_{des}=0.08 \text{ min}^{-1}$), the correct final value of q_t (i.e. q_e) was returned (Figure 8.16c), however adsorption in the initial stages of the experiment was over estimated. Using the steeper gradient of the linear regression in the initial linear region only ($k_{des}=0.31 \text{ min}^{-1}$) gave the opposite results: a model that gives the correct adsorption kinetics in the early stages of the experiment but reached equilibrium with a much lower value of q_e than was experimentally observed (Figure 8.16c).

This is logical as equilibrium is reached when the rate of desorption equals the rate of adsorption. When k_{des} is increased, then the rate of desorption becomes equal in magnitude to the rate of desorption at lower concentrations of adsorbed analyte. When using a value of k_{des} determined as the gradient in the linear regression between all calculated data points, a result lying between the ‘linear region’ and ‘end-point only’ scenarios was observed (Figure 8.16c).

8.4.2. Improving the experimental fit using monodentate and bidentate complexes

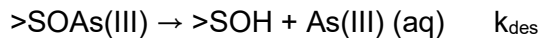
The linear region of Figure 8.16b, at low q_t , in the early stages of the reaction, suggests that a first-order desorption rate equation is appropriate for an adsorption-desorption model, at least in the initial stages of reaction. However, the model clearly requires refinement. As discussed in chapter 6, As(III) may bind to mineral sorbents including Fe₂O₃ and TiO₂ through both monodentate and bidentate binding modes.

The limited success of first-order desorption kinetics to describe the rate of desorption in Figure 8.16b can be explained by the presence of multiple surface species contributing to the overall value of q_t , e.g. one monodentate and one bidentate surface complex. We can imagine a mechanism wherein As(III) adsorption proceeds via (a) initial formation of a monodentate surface complex, which may then either (b) desorb back into solution or (c) transform into a bidentate complex. We may wish to allow the bidentate complex to (d) change back into the original monodentate complex, and not allow direct desorption: such a mechanism would explain why the calculated results gave the greatest rate of desorption at $t=5$ minutes rather than at equilibrium (Figure 8.16a). The reactions in this model would be:

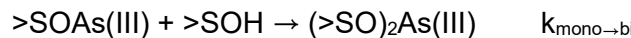


Equation 8.18

(e.g. $>\text{SOH} + \text{H}_3\text{AsO}_3 \text{ (aq)} \rightarrow >\text{SOH}_2\text{AsO}_3 + \text{H}_2\text{O}$, or $>\text{SOH} + \text{H}_3\text{AsO}_3 \text{ (aq)} \rightarrow >\text{SOH}_2^+ - \text{H}_2\text{AsO}_3^-$).

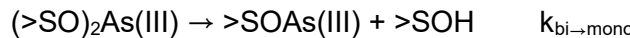


Equation 8.19



Equation 8.20

where $(>\text{SO})_2\text{As(III)}$ represents $(>\text{SO})_2\text{AsOH}$ or $(>\text{SO})_2\text{AsO}^-$.



Equation 8.21

In this model, the parameter q_t is the sum of q_{mono} and q_{bi} , reflecting the concentrations of monodentate and bidentate surface complexes respectively, giving $q_t = q_{\text{mono}} + q_{\text{bi}}$. For the purpose of this demonstration, we will keep k_{ads} as second-order with respect to $\left(1 - \frac{q_t}{q_e}\right)$, and we will also set $k_{\text{mono} \rightarrow \text{bi}}$ as second-order with respect to $\left(1 - \frac{q_t}{q_e}\right)$. Desorption rate equations are first-order. This gives the following rate equations:

$$\text{rate of adsorption} = k_{\text{ads}} C_t \left(1 - \frac{q_t}{q_{\text{max}}}\right)^2$$

Equation 8.22

$$\text{rate of desorption} = k_{\text{des}} q_{\text{mono}}$$

Equation 8.23

$$\text{rate of bidentate complex formation} = k_{\text{mono} \rightarrow \text{bi}} q_{\text{mono}} \left(1 - \frac{q_t}{q_{\text{max}}}\right)^2$$

Equation 8.24

$$\text{rate of bidentate to monodentate transformation} = k_{\text{bi} \rightarrow \text{mono}} q_{\text{bi}}$$

Equation 8.25

This model (a) reconstructs the observation that the rate of desorption is at its maximum after ~5 minutes (Figure 8.17a); (b) better fits experimental data than the previous model with only

one type of surface complex (Figure 8.17a versus Figure 8.16c); (c) reconstructs the observation in the SCM that monodentate surface complexes only account for between one quarter and one third of total adsorbed As(III) on mesoTiO₂/Fe₂O₃ (chapter 6); and (d) matches experimental observations that the prevalence of bidentate over monodentate surface complexes increases as surface coverage is increased⁵⁰⁵.

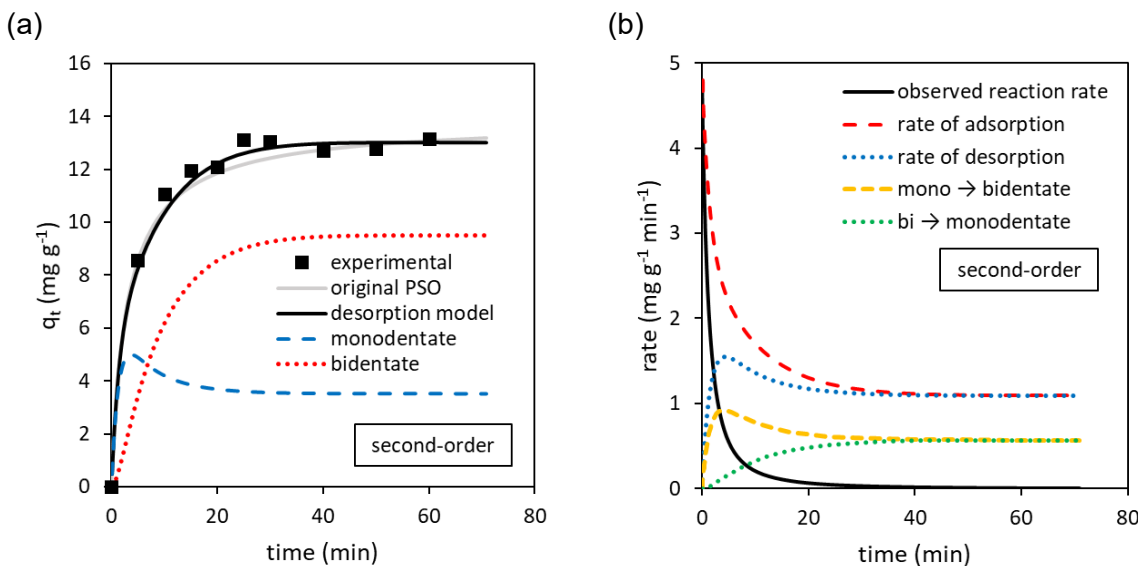


Figure 8.17: Demonstration of adsorption kinetic data fitting using an adsorption-desorption model with monodentate and bidentate surface complexes. A better fit to experimental data is observed compared with Figure 8.16. In this model, the rates of (i) adsorption and (ii) bidentate surface complexation were both given second order dependency upon the proportion of available sorbent capacity remaining. $k_{ads} = 0.123 \text{ L g}^{-1} \text{ min}^{-1}$; $k_{des} = 0.31 \text{ min}^{-1}$, $k_{bi \rightarrow mono} = 0.2$ (unitless); $k_{mono \rightarrow bi} = 0.06$ (min⁻¹). k_{ads} was calculated using the initial rate determined by the unmodified PSO model; k_{des} was calculated from the initial linear region in the plot of the desorption rate versus q_t , where the rate of desorption was calculated as the difference between the calculated 'true' rate of adsorption using the theoretical maximum adsorption capacity (31.4 mg g⁻¹) and the observed rate of adsorption (where $q_e = 13.8 \text{ mg g}^{-1}$); $k_{bi \rightarrow mono}$ and $k_{mono \rightarrow bi}$ were both estimated by fitting the model against the experimental data. Maximum adsorption capacity $q_{max} = 31.4 \text{ mg g}^{-1}$, sorbent concentration $C_s = 1 \text{ mg L}^{-1}$ and initial sorbate concentration $C_0 = 39 \text{ mg L}^{-1}$.

In this example, a second-order dependency was used between the proportion of available adsorption capacity remaining, $\left(1 - \frac{q_t}{q_{max}}\right)$, and the rates of (a) adsorption and (b) bidentate complex formation. Azizian reported that both experimentally observed PSO and PFO adsorption kinetics are predicted using adsorption-desorption kinetic models, when the rate of adsorption is first-order with respect to both C_t and $\left(1 - \frac{q_t}{q_{max}}\right)$, and the rate of desorption is first-order with respect to q_t ⁴⁹⁸. Azizian's model reduces to PSO kinetics at low values of C_0 and PFO kinetics at high values of C_0 . Following from Azizian's study, we can change the dependency between $\left(1 - \frac{q_t}{q_{max}}\right)$ and the rates of (a) adsorption and (b) bidentate complex formation to first-order, and again reconstruct the observed PSO adsorption kinetics (Figure 8.18).

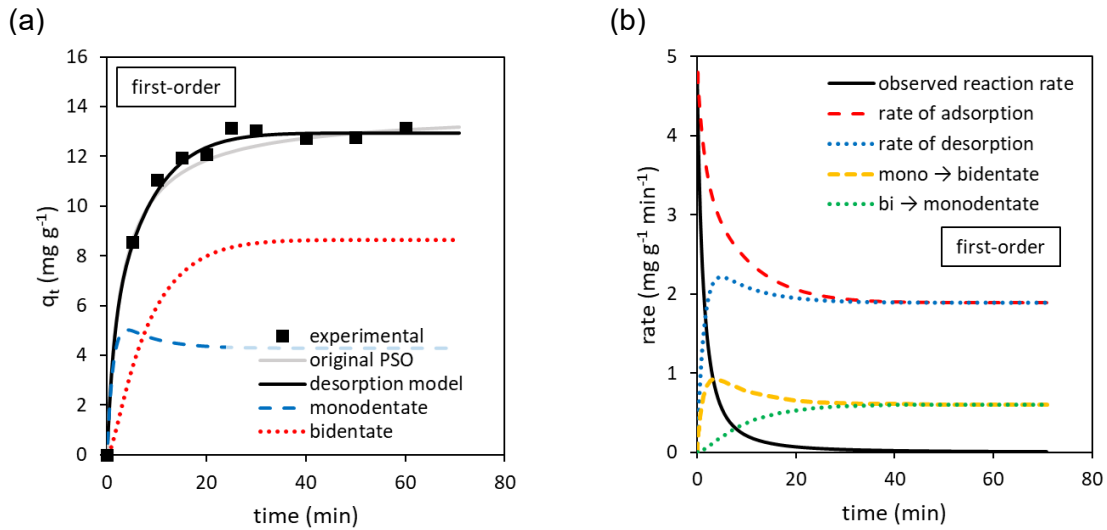


Figure 8.18: Recreating PSO kinetics using first-order adsorption and desorption rates, with monodentate and bidentate surface complexes. $k_{ads} = 0.123 \text{ L g}^{-1} \text{ min}^{-1}$; $k_{des} = 0.44 \text{ min}^{-1}$, $k_{bi \rightarrow mono} = 0.24$ (unitless); $k_{mono \rightarrow bi} = 0.07 \text{ (min}^{-1})$. Maximum adsorption capacity $q_{max} = 31.4 \text{ mg g}^{-1}$, sorbent concentration $C_s = 1 \text{ mg L}^{-1}$ and initial sorbate concentration $C_0 = 39 \text{ mg L}^{-1}$.

In the simulations so far, the proportion of surface sites remaining was calculated as $\left(1 - \frac{q_t}{q_e}\right)$, where $q_t = q_{\text{mono}} + q_{\text{bi}}$. However, bidentate surface complexes require twice as many surface hydroxyls as monodentate surface complexes. Given that bidentate surface complexation is considered the dominant binding mode (see chapter 6), we may wish to replace q_t with the expression $q_{\text{weighted}} = \frac{q_{\text{mono}}}{2} + q_{\text{bi}}$, and set the proportion of available surface sites remaining used in the rate equations as $\left(1 - \frac{q_{\text{weighted}}}{q_e}\right)$. Again, this modification also successfully reconstructs the observed PSO kinetics (Figure 8.19).

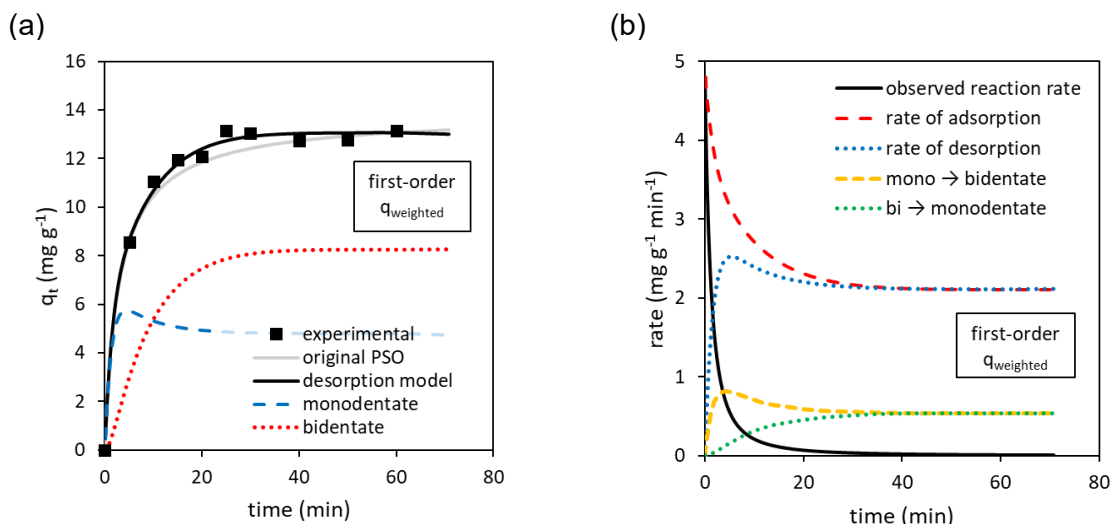


Figure 8.19: Recreating PSO kinetics using first-order adsorption and desorption rates, with monodentate and bidentate surface complexes, where the proportion of available adsorption capacity remaining is weighted via $q_{\text{weighted}} = \frac{q_{\text{mono}}}{2} + q_{\text{bi}}$. $k_{ads} = 0.123 \text{ L g}^{-1} \text{ min}^{-1}$; $k_{des} = 0.44 \text{ min}^{-1}$, $k_{bi \rightarrow mono} = 0.17$ (unitless); $k_{mono \rightarrow bi} = 0.065 \text{ (min}^{-1})$. Maximum adsorption capacity $q_{max} = 31.4 \text{ mg g}^{-1}$, sorbent concentration $C_s = 1 \text{ mg L}^{-1}$ and initial sorbate concentration $C_0 = 39 \text{ mg L}^{-1}$.

Table 8.5: Parameters used to model experimental adsorption kinetic data, using a combination of monodentate and bidentate surface complexes. Simulations were modelled using $(1 - \frac{q_t}{max})$ and $(1 - \frac{q_{weighted}}{max})$ to determine the proportion of available surface sites remaining, for the simulations labelled 'q_t' and 'weighted q_t' respectively. k_{ads} was calculated using the initial rate determined by the unmodified PSO model; k_{des} was calculated from the initial linear region in the plot of the desorption rate versus q_t, where the rate of desorption was calculated as the difference between the calculated 'true' rate of adsorption using the theoretical maximum adsorption capacity (31.4 mg g⁻¹) and the observed rate of adsorption (where q_e=13.8 mg g⁻¹); k_{bi→mono} and k_{mono→bi} were both estimated by fitting kinetic adsorption models against the experimental data. Sorbent concentration C_s = 1 mg L⁻¹ and initial sorbate concentration C₀ = 39 mg L⁻¹.

	k _{ads} (L g ⁻¹ min ⁻¹)	k _{des} (min ⁻¹)	k _{mono→bi} (min ⁻¹)	k _{bi→mono} (min ⁻¹)
First-order (q _t)	0.123	0.44	0.24	0.07
First-order (with weighted q _t)	0.123	0.44	0.17	0.065
Second-order (q _t)	0.123	0.31	0.2	0.06
Second-order (with weighted q _t)	0.123	0.31	0.1	0.04

The different simulations provide a nearly identical fit to the experimental data, with a similar goodness of fit in each case. The implication is that mechanistic details cannot be revealed using this analytical approach, since multiple parameters are fit simultaneously (i.e. k_{mono→bi} and k_{bi→mono}). Nonetheless, this work demonstrates both (a) how parameters for desorption kinetics can be estimated from experimental adsorption data, and (b) how the description of experimental data for the adsorption of As(III) onto meso-TiO₂/Fe₂O₃ can be improved by separating adsorbed As(III) into multiple species, e.g. monodentate and bidentate surface complexes.

Non-equilibrium surface complexation is important for determining the transport of water contaminants ⁵⁰⁶, and as explained earlier, is essential for the further development of an arsenic treatment plant model. Non-equilibrium modelling is essential to describe the adsorption kinetics of As(III) and As(V) in the presence of one another (especially when modelling advanced oxidation processes), and in the presence of competitor ions. A new 'kinetic surface complexation model' would reduce to the conventional surface complexation model at equilibrium, yet it would also enable time-sensitive processes such as water remediation and reactive transport ⁵⁰⁶ to be better understood and engineered. The future generation of surface complexation models might thereby be kinetic models, rather than equilibrium models, and might offer a similar treatment of electrostatic forces.

8.5. Conclusions

This chapter aimed to develop a kinetic adsorption model to address the overlooked problem of how we reconcile low photocatalyst concentrations with high sorbent concentrations for an As(III) remediation based upon composite photocatalyst-sorbents, considering the meso-TiO₂/Fe₂O₃ system. To meet this aim, PSO kinetics were modified to provide a less conditional rate equation, and an arsenic treatment plant was modelled in both batch and continuous-flow reactor designs. It was demonstrated how the desorption kinetics needed to model the competitive adsorption between As(III) and As(V) can be estimated so that As(III) oxidation kinetics can be integrated into the arsenic treatment plant model. This chapter found that:

- Material concentrations significantly greater than the 0.01-0.1 g L⁻¹ typically used in photocatalyst studies are needed for meso-TiO₂/Fe₂O₃ to effectively remove As(III) from contaminated waters through adsorption.
- Kinetic modelling predicts that batch treatment processes are preferred over continuous-flow for the adsorption of As(III) at sorbent concentrations <100 g L⁻¹. Batch processes should be considered in preference to continuous-flow, given that sorbent concentrations should be <100 g L⁻¹ to provide sufficient penetration of light through the photocatalyst-sorbent suspension.
- With 10 g L⁻¹ meso-TiO₂/Fe₂O₃ or less, the media would need to be replenished multiple times throughout the year to maintain effective treatment.
- Continuous-flow only offers more economical use of sorbent at high sorbent concentrations (>100 g L⁻¹).
- Desorption rate constants can be estimated from experimental adsorption kinetic data, with the quality of fit improved by distinguishing between monodentate and bidentate surface complexes. However, under this approach, the rate laws governing each reaction cannot be determined due to the number of fitting parameters.

On the basis of this study, subsequent experimental work on multifunctional photocatalyst-sorbent materials is recommended, to investigate the influence of material concentration on the kinetics of photocatalysis, given that concentrations of ≥ 10 g L⁻¹ is required for effective removal of arsenic, and likely most other contaminants. This kinetic adsorption model should be further advanced through introduction of experimental photooxidation rates to provide further insights into how photocatalyst-sorbent materials can be applied in engineered applications towards the remediation of As(III) contaminated waters.

9. Conclusions and evaluation

9.1. Summary of key findings

This thesis investigated meso-TiO₂/Fe₂O₃, a multifunctional photocatalyst-sorbent material, for the remediation of arsenic(III) contaminated waters. The central focus was on determining how coupling meso-TiO₂ with Fe₂O₃ influences the chemistry of arsenic adsorption and the photocatalytic oxidation of As(III).

The three primary experimental objectives were as follows:

- To develop the use of surface-sensitive analytical techniques for the accurate weighting of components within component additive surface complexation models (CA-SCM), so that the adsorption of arsenic onto meso-TiO₂/Fe₂O₃ can be accurately modelled.
- To determine the effects of Fe₂O₃-coupling on the photocatalytic oxidation of As(III) using meso-TiO₂/Fe₂O₃, to inform the design of future composite photocatalyst-sorbents and so that treatments can be better engineered.
- To develop a kinetic adsorption model and determine the minimum concentration of meso-TiO₂/Fe₂O₃ needed for an arsenic treatment plant, to inform future engineering studies.

The component additive surface complexation model (CA-SCM) developed in this work highlighted how it is essential to choose appropriate characterisation techniques to weight the contribution of each component within a CA model. CA-SCM accuracy was improved when low energy ion scattering (LEIS) characterisation of the outermost surface was used to constrain the relative abundance of the meso-TiO₂ and Fe₂O₃ sorbent surfaces. The CA-SCM gave accurate predictions in the adsorption of As(V) and the surface proton excess. Component additive predictions of As(III) adsorption were inaccurate, due to the influence of

sorbent morphology upon the multilayer adsorption of As(III): the reference samples and the meso-TiO₂/Fe₂O₃ composite had different pore structures, and therefore the surface complexation constants for multilayer As(III) adsorption obtained from the single-component reference samples were not valid for the composite sorbent system. The CA-SCM offers a tool that can be used to quickly predict the adsorption of arsenic onto other titania-iron oxide composites. This can be achieved for each new synthetic product, by characterising the surface of the sample, ideally using LEIS, and adjusting the weighting of the CA-SCM correspondingly. This may prove useful in the optimisation of future multifunctional sorbents.

The photocatalytic oxidation of As(III) was significantly suppressed when meso-TiO₂ was coupled with Fe₂O₃. This was primarily due to the parasitic absorption of ultraviolet photons by the Fe₂O₃ phase. It was also found that the rate law changed after Fe₂O₃-coupling from disguised zero-order kinetics, where As(III) is oxidised by intermediate reactive oxygen species (ROS, most likely the hydroxyl radical), to first-order kinetics, depending upon the concentration of adsorbed As(III). Compared with the Langmuir-Hinshelwood kinetic model, the surface-controlled first-order kinetics were better described when using the CA-SCM to calculate the concentration of adsorbed As(III) at each point in time. This is due to the competitive adsorption between As(III) and As(V) and the surface enrichment of As(III) towards the end of each experiment, which are both described by the SCM but are not predicted by the Langmuir-Hinshelwood model.

A kinetic adsorption model was used to assess the design of arsenic treatment plants based upon a simultaneous photocatalytic oxidation-adsorption approach. This model was used to address the question of how much media should be used in such a treatment plant. The study found that with 1 g L⁻¹ meso-TiO₂/Fe₂O₃, the media would need replacing once every day. Concentrations of at least 10 and 100 g L⁻¹ are needed if the reactor is to run interrupted for 17 and 170 days respectively. This presents an engineering challenge, to achieve effective oxidation of As(III) in such optically dense suspensions, where ultraviolet light cannot penetrate deeply. This challenge is particularly significant for TiO₂/Fe₂O₃ composites, given that Fe₂O₃ parasitically absorbs incident photons. Engineering studies are clearly needed to investigate how such a system would operate in real-life.

A central theme of this thesis was the identification of how coupling TiO₂ and Fe₂O₃ into new composite forms affects the adsorptive and photocatalytic properties of each component. Meso-TiO₂/Fe₂O₃ retains most of the adsorption capacity of Fe₂O₃. For instance, when [As(III) (aq)] = 27 mg L⁻¹, Fe₂O₃ and meso-TiO₂/Fe₂O₃ adsorb 38.3±0.6 and 27.7±0.3 mg g⁻¹ As(III) respectively. Consequently, meso-TiO₂/Fe₂O₃ compares very favourably with Bayoxide E33, the commercially established arsenic sorbent, which adsorbs 28.8±0.3 mg g⁻¹ As(III) under the

same conditions. (All data is presented in section 6.2.2). In contrast, when compared with meso-TiO₂, the photocatalytic activity of the TiO₂ phase was drastically reduced after Fe₂O₃-coupling, primarily due to parasitic light absorption by the Fe₂O₃ phase. Meso-TiO₂/Fe₂O₃ is thus best considered as a sorbent material with the added bonus of photocatalytic activity, rather than as a photocatalyst with improved adsorption capabilities. Substituting current sorbent media with meso-TiO₂/Fe₂O₃ should prove advantageous, since oxidation improves total As removal (section 7.3), and engineered applications should be investigated.

9.2. New concepts and innovations

This thesis proposed several innovations for modelling both adsorption and photocatalytic oxidation. Firstly, this work showed how the accuracy of component additive (CA) adsorption models is improved by choosing appropriate surface-sensitive techniques when weighting the contribution of each surface component towards the total composite sorbent surface. The best results are achieved using low energy ion scattering (LEIS), a technique that is sensitive to the outermost atomic surface. XPS is less surface-sensitive than LEIS, but still offers improved constraints for component additive adsorption modelling compared with the bulk mass ratio. These techniques were all fully quantitative, with good precision (<3% uncertainty in this work), and fast results (on the hours timescale).

Accurate CA models are important for a number of reasons. Firstly, if a composite system deviates from the results predicted by a well-constrained CA model, then this indicates that the structure of the composite is influencing the chemical properties of the material (e.g. the sorbent morphology control of multilayer As(III) adsorption/surface precipitation that was identified in chapter 6). Accurate, well-constrained CA models thus provide new insights into adsorption mechanisms. Secondly, accurate CA models can be used to engineer optimised multifunctional sorbents. Since the favourability of multilayer As(III) adsorption was inversely correlated with the pore size, one could optimise synthetic conditions to introduce a higher volume of small nanopores, aiming to maximise arsenic surface precipitation and thus increase adsorption capacities. Alternatively, one may be able to optimise the ratio of surface components to provide the best balance between adsorption and photocatalysis (as TiO₂ needs an exposed surface to generate intermediate oxidants). The CA-SCM could also be used to identify the relative abundance of Fe₂O₃ (or another sorbent phase) needed to mitigate the impact of photocatalyst deactivation (e.g. through the adsorption of As(V) onto TiO₂).

Secondly, this thesis showed how surface complexation modelling (SCM) can be integrated into photocatalytic oxidation kinetic models. Compared with Langmuir-Hinshelwood kinetics, the SCM provides a more nuanced description of adsorption of the substrate onto the photocatalyst (e.g. through the inclusion of competitor ions). This is especially true for systems where the product of photocatalysis adsorbs to the catalyst surface and causes photocatalyst deactivation (e.g. the adsorption of As(V) onto TiO₂). Whilst a SCM-constrained kinetic model can include competitive adsorption and thus photocatalyst deactivation, Langmuir-Hinshelwood kinetics do not, as only a single sorbate is included in the Langmuir adsorption isotherm equation. Furthermore, the Langmuir adsorption isotherm kinetic parameters are conditional to the experimental conditions used, e.g. pH and ionic strength, whereas the SCM is not, allowing SCM kinetics to be better used in a predictive capacity. This may prove useful for separating the contribution of pH-dependent surface charge towards photocatalysis kinetics from aqueous pH effects, e.g. the dependence of rate constants upon the availability of hydroxide ions as precursors for generation of the hydroxyl radical intermediate. This thesis also demonstrated non-SCM kinetic models that reconstruct the disguised zero-order kinetics of meso-TiO₂ through a description of As(V) deactivation. However, further experimental work is needed to (a) characterise the mechanism for As(V) deactivation of TiO₂, and (b) determine appropriate rate laws.

Thirdly, this thesis showed how the popular pseudo-second order (PSO) kinetic adsorption model can be modified to give a new rate equation with a rate constant that is less conditional towards initial sorbate and sorbent concentrations. This modified rate equation reproduces the PSO model when the same parameters are used (e.g. initial sorbate and sorbent concentration). This new model will ideally replace the current PSO rate equation, as it provides all the same benefits (a simple equation that fits a wide range of data) with fewer disadvantages (i.e. the conditionality of the PSO rate constant, k_2). Advantages include, firstly, that rate constants are normalised (at least to a degree) to sorbate concentration, and the irrational inverse relationship between the initial sorbate concentration and k_2 is removed. This facilitates the comparison of kinetic data between different studies using different sorbate and sorbent concentrations. Secondly, this model offers predictive capabilities (at least to a degree) and can thus be used to identify how the influence of sorbent and sorbate concentrations may affect the performance of new multifunctional materials.

It is hoped that the kinetic model of the arsenic treatment plant will be further developed, as outlined in chapter 8. The future arsenic treatment plant model will introduce oxidation kinetics, and the necessary adsorption-desorption reactions, allowing the design of a reactor using a combined photocatalytic oxidation-adsorption approach to be explored in more detail. Such a model is important not just to understand TiO₂/Fe₂O₃ composites, but to understand the

photocatalytic remediation of any substrate where the adsorption of reactants and products is significant. The photocatalytic oxidation-adsorption kinetic model should therefore be advanced not just for composite materials, but also for the photocatalytic oxidation of As(III) using pure, single-phase TiO₂.

9.3. The future of the TiO₂/Fe₂O₃ multifunctional sorbent

Meso-TiO₂/Fe₂O₃ offers similar adsorption capacities to commercial arsenic sorbents (section 9.1), whilst the photocatalytic capabilities of this material can further improve total arsenic removal (e.g. with 1 mg L⁻¹ initial As(III), as per section 7.3). The evidence suggests that current adsorption-based remediation can be improved by replacing the sorbent media with TiO₂/Fe₂O₃ composite sorbents. Adsorption capacities would remain similar, whilst oxidation of As(III) would improve total As removal. These titania-iron oxide composites offer promise when the engineered treatment must be simple, e.g. single-reactor systems with a single sorbent media. As highlighted in chapter 8, engineering studies are required to identify what a treatment based on photocatalyst-sorbent technology would actually look like: the reactor design, the media concentrations, the size and scale of the treatment etc.

Unlike adsorption technology, light-driven remediation of arsenic remains uncommercialised. Current challenges in commercialising water remediation using heterogeneous photocatalysis include (a) the high energy input needed for ultraviolet-driven photocatalysis, and (b) the large land footprints needed for sunlight-driven photocatalysis⁵⁰⁷. These both present an economic challenge, which is exacerbated in the meso-TiO₂/Fe₂O₃ system given that the photocatalytically inactive Fe₂O₃-phase absorbs the majority of ultraviolet photons.

Consequently, future development of TiO₂/Fe₂O₃ composites should aim to improve the quantum efficiency of As(III) photooxidation by minimising the parasitic absorption of the Fe₂O₃-phase. In the meso-TiO₂/Fe₂O₃ system, iron oxide was present both as a thin coating and as larger aggregate particles (section 5.2). The larger iron oxide particles are not advantageous: they provide less adsorption capacity than the small particles (normalised to mass, mg g⁻¹), yet parasitically absorb the same proportion of ultraviolet photons (since absorption is proportional to mass, with the absorption coefficient (ϵ) taking the units L g⁻¹ cm⁻¹). To reduce the size of Fe₂O₃ particles in the meso-TiO₂/Fe₂O₃ composite, the simplest adjustment would be to increase the temperature when meso-TiO₂ is mixed with ethanolic iron

nitrate and ethanol is evaporated, thereby limiting iron oxide crystal growth. However, the thin iron oxide coating appears to suppress photocatalytic rates, by forming a barrier, as hydroxyl radicals cannot be generated at the Fe₂O₃ surface (as discussed in chapter 7). Consequently, it may also be worth optimising the synthesis to expose more TiO₂ at the composite surface, considering that LEIS analysis identified that only 32% of the exposed surface is TiO₂.

Optimisation of the synthetic procedure should also aim to form a clean interface between TiO₂ and Fe₂O₃ so that heterojunction effects may be achieved. This could be realised by replacing the solution-phase iron oxide precipitation with epitaxial film growth using techniques such as chemical vapour deposition (CVD)²⁹⁵. Alternatively, a Janus particle synthesis could be used, where one side of each particle is TiO₂ and the other side is Fe₂O₃. Photocatalytic activity can be improved by an order of magnitude when using the Janus structure⁵⁰⁸. If the photocatalytic oxidation kinetics of meso-TiO₂/Fe₂O₃ prove too slow for use in the provision of drinking water, then this material might find better applications in less time-constrained processes, such as the decontamination of irrigation water.

9.4. The future for the combined photocatalytic oxidation-adsorption approach towards the remediation of arsenic(III)

Whilst meso-TiO₂/Fe₂O₃ offers adsorption capacities to rival commercial arsenic sorbents (section 9.1), slow oxidation kinetics may limit the performance of a practical As(III) treatment based upon a combined oxidation-adsorption approach. The principal factor limiting the photocatalytic oxidation kinetics of meso-TiO₂/Fe₂O₃ is the parasitic absorption of light by the Fe₂O₃-phase (chapter 7). This problem can be overcome by replacing iron oxides with a high band gap sorbent phase. Aluminium oxides (Al₂O₃) typically have bandgaps greater than 6 eV (<207 nm)^{509 510 511} (decreasing for thin films⁵¹²) and therefore should not suppress the excitation of TiO₂ using ultraviolet A or ultraviolet B radiation (in this thesis a 368 nm lamp was used, an example of ultraviolet A). Al₂O₃ has already been used as a sorbent in arsenic treatment plants¹, and can offer similar adsorption capacities to iron oxides such as Fe₂O₃¹⁶⁶. TiO₂ composites have been prepared with Al₂O₃ and other high bandgap mineral oxides, such as ZnO (band gap 3.2-3.3 eV^{475 513}), and investigated for arsenic removal¹⁶⁵. Future work may wish to provide a systematic comparison of TiO₂/Fe₂O₃ with these other TiO₂ composites, considering both photocatalytic oxidation rates and adsorption performance.

This thesis worked with TiO_2 since it is the benchmark photocatalyst, however As(III) remediation might be improved using alternative photocatalyst phases. In particular, organic photocatalysts such as graphitic carbon nitride ($\text{g-C}_3\text{N}_4$) should be examined more closely, as (a) they have smaller band gaps (2.7 eV) than TiO_2 and can therefore better harness solar energy¹⁵³, and (b) they are poor arsenic sorbents and therefore should not suffer from photocatalyst deactivation, due to adsorption of the As(V) produced^{514 153 187}. There are comparatively few examples of studies demonstrating the photooxidation of As(III) in the presence of non- TiO_2 photocatalysts^{154 514 515}. A comprehensive screening study of single-phase photocatalysts, with TiO_2 used as the baseline catalyst, should be used before investigating new mixed mineral composites.

Engineering studies might find that the quantum efficiency of meso- $\text{TiO}_2/\text{Fe}_2\text{O}_3$ is a limiting factor in the practical application of a simultaneous photocatalytic oxidation-adsorption treatment (e.g. the energy cost for ultraviolet irradiation is too expensive, or treatments using solar light are too slow). In this case, a two-reactor, sequential treatment consisting of photocatalytic oxidation in the first reactor and adsorption in the second reactor will be more suitable, since greater quantum efficiencies can be achieved using single-component meso- TiO_2 and other TiO_2 photocatalysts such as commercial Degussa P25. For example, the quantum yield of As(III) photocatalytic oxidation using single-component meso- TiO_2 was up to 60 times greater than the quantum yield using the composite photocatalyst (chapter 7). A single-component sorbent such as Fe_2O_3 or Bayoxide E33 (FeOOH) could be used in the second reactor. The shorter treatment times would not only save on the electricity costs of ultraviolet irradiation, but also save on the costs of pumping and mixing. An exception to this is the case where a $\text{TiO}_2/\text{Fe}_2\text{O}_3$ composite is synthesised with a heterojunction effect powerful enough to overcome the suppression in photocatalysis that results from the parasitic absorption of photons by the Fe_2O_3 component.

Acknowledgements

I would like to thank the following people for their support:

- First and foremost, Prof Dominik Weiss for his supervision and guidance. I am grateful for the opportunity to have worked on such an interesting topic.
- My co-supervisors: Prof Ramon Vilar, Dr Andreas Kafizas, and Prof Stephen Skinner, who all provided invaluable feedback, informing the direction of this work.
- Dr Pascal Salaün from the University of Liverpool, who offered expert knowledge in the electrochemical detection of arsenic and took part in the field work.
- My colleagues in the Environmental Geochemistry group: particularly Dr Chaipat Lapinee for his earlier work on $\text{TiO}_2/\text{Fe}_2\text{O}_3$ composites, and Dr Aaron Torres-Huerta who synthesised the ImpAs chemisorbent.
- My UROP and Nuffield Trust summer students who tested out some of my experimental procedures and prepared samples for DLS analysis.
- Dr Jon Watson for his help running the ICP-MS, and Swachchha Majumdar and Dr Priyanka Mondal for their coordination of the field work component.
- My colleagues in the CDT ACM, especially Alexis Belessiotis and Epameinondas Skountzos.
- My friends and family, including but not limited to: Helen Bullen, Paul Terry, Shem Bullen, Mikyung, Mik Oliver, my grandparents, Lilith, Shaun, Clio, and Domenico.

I was very fortunate to receive training in a wide range of techniques, and therefore thank: Dr Sarah Fearn (low energy ion scattering); Dr Jorge Gonzalez Garcia (potentiometric titration); Dr Andreas Kafizas (transient absorption spectroscopy); Dr Pascal Salaün (electrochemistry); Dr Mahmoud Ardkani and Dr Ecaterina Ware (electron microscopy); Richard Sweeney (X-ray diffraction); Dr Alessandra Pinna (BET analysis); Dr Janice Kenney (surface complexation modelling); Dr Ahu Parry (dynamic light scattering); and Dr Gwilherm Kerheve (X-ray photoelectron spectroscopy).

List of publications

Peer reviewed

- Bullen, J. C. et al. (2020). Portable and rapid arsenic speciation in synthetic and natural waters by an As(V)-selective chemisorbent, validated against anodic stripping voltammetry. *Water Research*. <https://doi.org/10.1016/j.watres.2020.115650>
 - Based upon chapter 4.
- Bullen, J. C. et al. (2020). Improved Accuracy in the Surface Complexation Modelling of Arsenic on Multicomponent Sorbents Using Low Energy Ion Scattering. *Journal of Colloid and Interface Science*. <https://doi.org/10.1016/j.jcis.2020.06.119>
 - Based upon chapter 6.
- Bullen, J. C. et al (2020). On the application of photocatalyst-sorbent composite materials for arsenic(III) remediation: insights from kinetic adsorption modelling. *Journal of Environmental Chemical Engineering*. <https://doi.org/10.1016/j.jece.2020.104033>
 - Based upon the middle of chapter 8.
- Bullen, J. C. et al. (2020). TiO₂/Fe₂O composites for the oxidation and removal of arsenic(III): How does coupling TiO₂ with Fe₂O₃ influence photocatalytic oxidation kinetics? *In review*.
 - Based upon chapter 7.
- Kirby, M. et al. (2019). Determining the Effect of pH on Iron Oxidation Kinetics in Aquatic Environments: Exploring a Fundamental Chemical Reaction to Grasp the Significant Ecosystem Implications of Iron Bioavailability. *Journal of Chemical Education*.
<https://doi.org/10.1021/acs.jchemed.8b01036>

Non-peer reviewed

- Bullen, J. C. et al. (2020). A revised pseudo-second order kinetic model for adsorption, sensitive to changes in sorbate and sorbent concentrations. *ChemRxiv Preprint*.
<https://doi.org/10.26434/chemrxiv.12008799>
 - Based upon the first part of chapter 8.
- Weiss, D. J. et al. (2019). Arsenic contaminated groundwater - A problem in India and the UK. *Royal Society of Chemistry - Environmental Chemistry Group Bulletin*.

Selected presentations

- “Towards accurate modelling of arsenic adsorption over multicomponent sorbents.” #EnvChem2019: Advances in Environmental Chemistry at the Royal Society of Chemistry, London, UK. 15th October 2019. *Talk*.
- “High frequency water monitoring for developing countries.” Department for International Development, Her Majesty's Government, UK. 1st October 2019. *Talk*.
- “Modelling composite materials for arsenic adsorption with incorporation of Low Energy Ion Scattering (LEIS).” Joliot Conference, Royal Society of Chemistry at the University of Nottingham, UK. 11th-12th September 2019. *Poster*.
- “Arsenic remediation using TiO₂/Fe₂O₃ composites: investigating mixed mineral adsorption via SCM and LEIS.” Geochemistry Group Research in Progress Meeting 2019 (GGriP 2019) at the University of Portsmouth, UK. 16th April 2019. *Talk*.
- “Bifunctional Photocatalyst-Sorbents For Remediation Of Arsenic Contaminated Groundwaters.” Materials for Clean Energy Conference 2019 (MCEC 2019) at the National Physical Laboratory, Teddington, UK. 10th April 2019. *Talk*.
- “Arsenic speciation in the field – comparison of Anodic Stripping Voltammetry and As(V)-selective chemisorbent resin.” Environmental Chemistry of Water, Sediment, Soil and Air at the Royal Society of Chemistry. 14th December 2018. *Talk*.
- “Bifunctional Materials for Remediation of As(III) Contaminated Waters: mesoscale TiO₂/Fe₂O₃ photocatalyst-sorbents.” *Towards a new generation of arsenic removal plants in India*, a Newton-Bhabha funded workshop in Kolkata, India. 27th-29th September 2018. *Talk*.
- “Surface Complexation Modelling of a Synthetic Mineral Composite: Adsorption of arsenic over meso-TiO₂/Fe₂O₃.” NanoScience@Surfaces at the Cavendish Laboratory, University of Cambridge, UK. 30th July – 2nd August 2018. *Poster*.
- “Surface Complexation Modelling of Arsenic adsorption over composite minerals for remediation of contaminated groundwater.” Environmental Chemistry of Water, Sediment, Soil and Air: Early careers meeting at the Royal Society of Chemistry, UK. 14th December 2017. *Poster*.

References

1. Kumar, A., Roy, M. B., Roy, P. K. & Wallace, J. M. Assessment of Arsenic Removal Units in Arsenic-Prone Rural Area in Uttar Pradesh, India. *J. Inst. Eng. Ser. A* **100**, 253–259 (2019).
2. Nickson, R. T., McArthur, J. M., Ravenscroft, P., Burgess, W. G. & Ahmed, K. M. Mechanism of arsenic release to groundwater, Bangladesh and West Bengal. *Appl. Geochemistry* **15**, 403–413 (2000).
3. Singh, R. *et al.* Arsenic contamination, consequences and remediation techniques: A review. *Ecotoxicol. Environ. Saf.* **112**, 247–270 (2015).
4. Hering, J. G., Katsoyiannis, I. A., Theoduloz, G. A., Berg, M. & Hug, S. J. Arsenic removal from drinking water: Experiences with technologies and constraints in practice. *J. Environ. Eng. (United States)* **143**, 1–9 (2017).
5. Sorlini, S. & Gialdini, F. Conventional oxidation treatments for the removal of arsenic with chlorine dioxide, hypochlorite, potassium permanganate and monochloramine. *Water Res.* **44**, 5653–5659 (2010).
6. Sharma, V. K. & Sohn, M. Aquatic arsenic: Toxicity, speciation, transformations, and remediation. *Environ. Int.* **35**, 743–759 (2009).
7. Krichevskaya, M., Klauson, D., Portjanskaja, E. & Preis, S. The cost evaluation of advanced oxidation processes in laboratory and pilot-scale experiments. *Ozone Sci. Eng.* **33**, 211–223 (2011).
8. Barndök, H., Hermosilla, D., Negro, C. & Blanco, Á. Comparison and Predesign Cost Assessment of Different Advanced Oxidation Processes for the Treatment of 1,4-Dioxane-Containing Wastewater from the Chemical Industry. *ACS Sustain. Chem. Eng.* **6**, 5888–5894 (2018).
9. Lavonen, E. E., Gonsior, M., Tranvik, L. J., Schmitt-Kopplin, P. & Köhler, S. J. Selective chlorination of natural organic matter: Identification of previously unknown disinfection byproducts. *Environ. Sci. Technol.* **47**, 2264–2271 (2013).
10. Gamage, J. & Zhang, Z. Applications of photocatalytic disinfection. *Int. J. Photoenergy* **2010**, (2010).
11. Zhou, W. *et al.* Mesoporous TiO₂/α-Fe₂O₃: Bifunctional Composites for Effective Elimination of Arsenite Contamination through Simultaneous Photocatalytic Oxidation and Adsorption. *J Phys Chem* **112**, 19584–19589 (2008).
12. Yu, L. *et al.* Arsenite removal from aqueous solutions by γ-Fe₂O₃-TiO₂ magnetic nanoparticles through simultaneous photocatalytic oxidation and adsorption. *J. Hazard. Mater.* **246–247**, 10–17 (2013).
13. Su, H., Lv, X., Zhang, Z., Yu, J. & Wang, T. Arsenic removal from water by photocatalytic functional Fe₂O₃-TiO₂ porous ceramic. *J. Porous Mater.* **24**, 1227–1235 (2017).
14. Jeppu, G. P. & Clement, T. P. A modified Langmuir-Freundlich isotherm model for simulating pH-dependent adsorption effects. *J. Contam. Hydrol.* **129–130**, 46–53 (2012).
15. Davis, J. A., Coston, J. A., Kent, D. B. & Fuller, C. C. Application of the Surface Complexation Concept to Complex Mineral Assemblages. *Environ. Sci. Technol.* **32**, 2820–2828 (1998).
16. Arnold, T., Zorn, T., Zänker, H., Bernhard, G. & Nitsche, H. Sorption behavior of U(VI) on phyllite: Experiments and modeling. in *Journal of Contaminant Hydrology* vol. 47 219–231 (2001).
17. Qu, C., Ma, M., Chen, W., Cai, P. & Huang, Q. Surface complexation modeling of Cu(II) sorption to montmorillonite–bacteria composites. *Sci. Total Environ.* **607–608**, 1408–1418 (2017).
18. Moon, E. M. & Peacock, C. L. Modelling Cu(II) adsorption to ferrihydrite and ferrihydrite-bacteria composites: Deviation from additive adsorption in the composite sorption system. *Geochim. Cosmochim. Acta* **104**, 148–164 (2013).
19. Vaca-Escobar, K. & Villalobos, M. Modeling the additive effects of Pb(II) and Cu(II) on the competitive attenuation of As(V) through solid precipitation versus adsorption to goethite. *Bol. la Soc. Geol. Mex.* **67**, 457–465 (2015).
20. Fu, W. *et al.* Simultaneous roxarsone photocatalytic degradation and arsenic adsorption removal by TiO₂/FeOOH hybrid. *Environ. Sci. Pollut. Res.* **27**, 18434–18442 (2020).

21. Li, Y. *et al.* Fabrication of α -Fe₂O₃/TiO₂ bi-functional composites with hierarchical and hollow structures and their application in water treatment. *J. Nanoparticle Res.* **18**, 1–8 (2016).
22. Mohan, C. *et al.* Characterization of reduced graphene oxide supported mesoporous Fe₂O₃/TiO₂ nanoparticles and adsorption of As(III) and As(V) from potable water. *J. Taiwan Inst. Chem. Eng.* **62**, 199–208 (2016).
23. D'Arcy, M., Weiss, D., Bluck, M. & Vilar, R. Adsorption kinetics, capacity and mechanism of arsenate and phosphate on a bifunctional TiO₂-Fe₂O₃ bi-composite. *J. Colloid Interface Sci.* **364**, 205–212 (2011).
24. Low, J., Yu, J., Jaroniec, M., Wageh, S. & Al-Ghamdi, A. A. Heterojunction Photocatalysts. *Adv. Mater.* **29**, (2017).
25. Bickley, R. I., Slater, M. J. & Wang, W. J. Engineering development of a photocatalytic reactor for waste water treatment. *Process Saf. Environ. Prot.* **83**, 205–216 (2005).
26. Yerkinova, A., Balbayeva, G., Inglezakis, V. J. & Poulopoulos, S. G. Photocatalytic Treatment of a Synthetic Wastewater. *IOP Conf. Ser. Mater. Sci. Eng.* **301**, (2018).
27. Ferreiro, C. *et al.* Analysis of a hybrid suspended-supported photocatalytic reactor for the treatment of wastewater containing benzothiazole and aniline. *Water (Switzerland)* **11**, (2019).
28. Dutta, P. K., Pehkonen, S. O., Sharma, V. K. & Ray, A. K. Photocatalytic oxidation of arsenic(III): Evidence of hydroxyl radicals. *Environ. Sci. Technol.* **39**, 1827–1834 (2005).
29. Vaiano, V. *et al.* Enhanced photocatalytic oxidation of arsenite to arsenate in water solutions by a new catalyst based on MoO_x supported on TiO₂. *Appl. Catal. B Environ.* **160–161**, 247–253 (2014).
30. Johnston, R. B., Hanchett, S. & Khan, M. H. The socio-economics of arsenic removal. *Nat. Geosci.* **3**, 2–3 (2010).
31. Shafiquzzaman, M., Azam, M. S., Moshima, I. & Nakajima, J. Technical and Social evaluation of arsenic mitigation in rural bangladesh. *J. Heal. Popul. Nutr.* **27**, 674–683 (2009).
32. USGS. Where is Earth's Water? https://www.usgs.gov/special-topic/water-science-school/science/where-earths-water?qt-science_center_objects=0#qt-science_center_objects [Accessed: 8 June 2020].
33. Shiklomanov, I. World fresh water resources. in *Water in crisis a guide to the world's fresh water resources* (Oxford University Press, 1993).
34. de Graaf, I. E. M., Gleeson, T., (Rens) van Beek, L. P. H., Sutanudjaja, E. H. & Bierkens, M. F. P. Environmental flow limits to global groundwater pumping. *Nature* **574**, 90–94 (2019).
35. Margat, J. & Gun, J. van der. *Groundwater Around the World: A Geographic Synopsis*. (CRC Press, 2013). doi:10.1201/b13977.
36. Naujokas, M. F. *et al.* The broad scope of health effects from chronic arsenic exposure: Update on a worldwide public health problem. *Environ. Health Perspect.* **121**, 295–302 (2013).
37. Ravenscroft, P., Brammer, H. & Richards, K. . *Arsenic pollution: a global synthesis*. (Wiley-Blackwell, 2009). doi:10.1002/9781444308785.
38. Kavanagh, P. *et al.* Urinary arsenic species in Devon and Cornwall residents, UK. A pilot study. *Analyst* **123**, 27–29 (1998).
39. Ratnaike, R. N. Acute and chronic arsenic toxicity. *Postgrad. Med. J.* **79**, 391–396 (2003).
40. Hug, S. J., Leupin, O. X. & Berg, M. Bangladesh and Vietnam: Different groundwater compositions require different approaches to arsenic mitigation. *Environ. Sci. Technol.* **42**, 6318–6323 (2008).
41. George, C. M. *et al.* Arsenic exposure in drinking water: an unrecognized health threat in Peru. *Bull. World Health Organ.* **92**, 565–572 (2014).
42. Cheng, Y. Y. *et al.* Associations between arsenic in drinking water and the progression of chronic kidney disease: A nationwide study in Taiwan. *J. Hazard. Mater.* **321**, 432–439 (2017).
43. Smith, A. H., Lingas, E. O. & Rahman, M. Contamination of drinking-water by arsenic in Bangladesh: a public health emergency. *Bull. World Health Organ.* **78**, (2000).
44. Alaerts, G. J. & Khouri, N. Arsenic contamination of groundwater: Mitigation strategies and policies. *Hydrogeol. J.* **12**, 103–114 (2004).
45. Silent killer: Arsenic. *WaterAid Bangladesh* (2007).
46. Fatmi, Z. *et al.* Health burden of skin lesions at low arsenic exposure through groundwater in Pakistan. Is river the source? *Environ. Res.* **109**, 575–581 (2009).
47. DeSimone, L., Hamilton, P. & Gilliom, R. *The quality of our nation's waters—Quality of water*

- from domestic wells in principal aquifers of the United States, 1991–2004—Overview of major findings: U.S. Geological Survey Circular 1332.* (2009).
- 48. Thomas, M. A. *The Association of Arsenic With Redox Conditions, Depth, and Ground-Water Age in the Glacial Aquifer System of the Northern United States. U.S. Geological Survey Scientific Investigations Report 2007-5036* (2007).
 - 49. Smedley, P. & Kinniburgh, D. G. Chapter 11: Arsenic in Groundwater and the Environment. in *Essentials of Medical Geology* (eds. Selinus, O. et al.) 263–299 (Elsevier Academic Press, 2005).
 - 50. Smedley, P. L. Sources and distribution of arsenic in groundwater and aquifers. in *Arsenic in Groundwater: a World Problem*. (ed. Appelo, T.) 1–34 (International Association of Hydrogeologists Publication, 2008).
 - 51. Cullen, W. R. & Reimer, K. J. Arsenic Speciation in the Environment. *Chem. Rev.* **89**, 713–764 (1989).
 - 52. Smedley, P. L. & Kinniburgh, D. G. *Chapter 1. Source and behaviour of arsenic in natural waters Importance of arsenic in drinking water. United Nations Synthesis Report on Arsenic in Drinking-Water* <https://www.ircwash.org/resources/united-nations-synthesis-report-arsenic-drinking-water> (2001).
 - 53. Sahu, P. & Sikdar, P. K. Threat of land subsidence in and around Kolkata City and East Kolkata Wetlands, West Bengal, India. *J. Earth Syst. Sci.* **120**, 435–446 (2011).
 - 54. *Integrated groundwater management: Concepts, approaches and challenges*. (Springer International Publishing, 2016). doi:10.1007/978-3-319-23576-9.
 - 55. Smith, R., Knight, R. & Fendorf, S. Overpumping leads to California groundwater arsenic threat. *Nat. Commun.* **9**, 2089 (2018).
 - 56. Sikdar, P. K. & Sahu, P. Security of groundwater based water supply of Kolkata city. *Indian Groundw.* **II**, (2014).
 - 57. Armienta, M. A. & Segovia, N. Arsenic and fluoride in the groundwater of Mexico. *Environ. Geochem. Health* **30**, 345–353 (2008).
 - 58. Warner, K. L. & Ayotte, J. D. *Water Quality in the Glacial Aquifer System, Northern United States, 1993–2009: U.S. Geological Survey Circular 1352*. (2014) doi:doi.org/10.3133/cir1352.
 - 59. Priority List of Hazardous Substances | ATSDR. <https://www.atsdr.cdc.gov/spl/index.html> [Accessed: 15 June 2017].
 - 60. *Toxicological Profile for Arsenic. U.S Public Health Service, Agency for Toxic Substances and Disease Registry (ATSDR)* <http://dx.doi.org/10.1155/2013/286524> (2007) doi:<http://dx.doi.org/10.1155/2013/286524>.
 - 61. Peripheral neuropathy - NHS Choices. *NHS choices* <http://www.nhs.uk/conditions/Peripheral-neuropathy/Pages/Introduction.aspx> [Accessed: 18 September 2017].
 - 62. Coping, M. Death in the beer glass: the Manchester arsenic-in-beer epidemic of 1900–1 and the long-term poisoning of beer. *J Brew. Hist Soc* **132**, 31–57 (2009).
 - 63. Moe, B. *et al.* Comparative cytotoxicity of fourteen trivalent and pentavalent arsenic species determined using real-time cell sensing. *Jes* **49**, 1–12 (2016).
 - 64. Petrick, J. S., Ayala-Fierro, F., Cullen, W. R., Carter, D. E. & Vasken Aposhian, H. Monomethylarsonous Acid (MMAIII) Is More Toxic Than Arsenite in Chang Human Hepatocytes. *Toxicol. Appl. Pharmacol.* **163**, 203–207 (2000).
 - 65. Finnegan, P. M. & Chen, W. Arsenic toxicity: The effects on plant metabolism. *Front. Physiol.* **3**, 1–18 (2012).
 - 66. Liu, X. *et al.* Impaired autophagic flux and p62-mediated EMT are involved in arsenite-induced transformation of L-02 cells. *Toxicol. Appl. Pharmacol.* **334**, 75–87 (2017).
 - 67. EFSA Panel on Contaminants in the Food Chain (CONTAM). Scientific Opinion on Arsenic in Food. *ESFA J.* **7**, 1–199 (2009).
 - 68. Vahter, M. E. Interactions between Arsenic-Induced Toxicity and Nutrition in Early Life. *J. Nutr.* **137**, 2798–2804 (2007).
 - 69. Sun, H. J. *et al.* Arsenic and selenium toxicity and their interactive effects in humans. *Environ. Int.* **69**, 148–158 (2014).
 - 70. Watanabe, T. & Hirano, S. Metabolism of arsenic and its toxicological relevance. *Arch. Toxicol.* **87**, 969–979 (2013).
 - 71. Buncombe, A. How the West poisoned Bangladesh | The Independent. <http://www.independent.co.uk/news/world/asia/how-the-west-poisoned-bangladesh->

- 1924631.html [Accessed: 15 June 2017].
72. Akbar, A. Arsenic-tainted water from Unicef wells is poisoning half of Bangladesh | The Independent. <http://www.independent.co.uk/news/arsenic-tainted-water-from-unicef-wells-is-poisoning-half-of-bangladesh-1196091.html> [Accessed: 15 June 2017].
73. Uddin, R. & Huda, N. H. Arsenic poisoning in Bangladesh. *Oman Med. J.* **26**, 207 (2011).
74. Flanagan, S., Johnston, R. & Zheng, Y. Arsenic in tube well water in Bangladesh: health and economic impacts and implications for arsenic mitigation. *Bull. World Health Organ.* **90**, 839–846 (2012).
75. Infant Mortality Rate for Bangladesh. <https://fred.stlouisfed.org/series/SPDYNIMRTINBGD> (2015) [Accessed: 15 June 2017].
76. Mortality rate, infant (per 1,000 live births) | Data. <http://data.worldbank.org/indicator/SP.DYN.IMRT.IN?locations=BD> [Accessed: 15 June 2017].
77. Anawar, H. M. et al. Arsenic Contamination in Groundwater of Bangladesh: Perspectives on Geochemical, Microbial and Anthropogenic Issues. *Water* **3**, 1050–1076 (2011).
78. Guillot, S. & Charlet, L. Bengal arsenic, an archive of Himalaya orogeny and paleohydrology. *J. Environ. Sci. Heal. - Part A Toxic/Hazardous Subst. Environ. Eng.* **42**, 1785–1794 (2007).
79. Thakur, J. K., Thakur, R. K., Ramanathan, A., Kumar, M. & Singh, S. K. Arsenic Contamination of Groundwater in Nepal—An Overview. *Water* **3**, 1–20 (2010).
80. Li, S. et al. Enrichment of Arsenic in Surface Water, Stream Sediments and Soils in Tibet. *J. Geochemical Explor.* **135**, (2013).
81. Mukherjee, A. et al. Arsenic contamination in groundwater: A global perspective with emphasis on the Asian scenario. *J. Heal. Popul. Nutr.* **24**, 142–163 (2006).
82. Berg, M. et al. Magnitude of arsenic pollution in the Mekong and Red River Deltas - Cambodia and Vietnam. *Sci. Total Environ.* **372**, 413–425 (2007).
83. Mukherjee, A. et al. Groundwater systems of the Indian Sub-Continent. *J. Hydrol. Reg. Stud.* **4**, 1–14 (2015).
84. Tuinhof, A. et al. Groundwater Resource Management: an introduction to its scope and practice. *Sustainable Groundwater Groundwater Management: Concepts and Tools* 1–6 (2006).
85. Ayers, J. C. et al. Sources of salinity and arsenic in groundwater in southwest Bangladesh. *Geochem. Trans.* **17**, 4 (2016).
86. McArthur, J. M. et al. Natural organic matter in sedimentary basins and its relation to arsenic in anoxic ground water: The example of West Bengal and its worldwide implications. *Appl. Geochemistry* **19**, 1255–1293 (2004).
87. Aggarwal, P. K. et al. *Isotope Hydrology of Groundwater in Bangladesh: Implications for characterization and mitigation of arsenic in groundwater*. IAEA-TC project (BGD/8/016). (2000).
88. Xu, R., Wang, Y., Tiwari, D. & Wang, H. Effect of ionic strength on adsorption of As(III) and As(V) on variable charge soils. *J. Environ. Sci.* **21**, 927–932 (2009).
89. Kanematsu, M., Young, T. M., Fukushi, K., Green, P. G. & Darby, J. L. Extended Triple Layer Modeling of Arsenate and Phosphate Adsorption on a Goethite-based Granular Porous Adsorbent. *Environ. Sci. Technol.* **44**, 3388–3394 (2010).
90. Pakzadeh, B. & Batista, J. R. Impacts of cocontaminants on the performances of perchlorate and nitrate specialty ion-exchange resins. *Ind. Eng. Chem. Res.* **50**, 7484–7493 (2011).
91. Gibbon-Walsh, K. et al. Voltammetric determination of arsenic in high iron and manganese groundwaters. *Talanta* **85**, 1404–1411 (2011).
92. Bissen, M. & Frimmel, F. H. Arsenic - A review. Part II: Oxidation of arsenic and its removal in water treatment. *Acta Hydrochim. Hydrobiol.* **31**, 97–107 (2003).
93. Dodd, M. C. et al. Kinetics and mechanistic aspects of As(III) oxidation by aqueous chlorine, chloramines, and ozone: Relevance to drinking water treatment. *Environ. Sci. Technol.* **40**, 3285–3292 (2006).
94. WHO | Arsenic - Mass poisoning on an unprecedented scale. WHO <http://www.who.int/features/archives/feature206/en/> (2010) [Accessed: 15 June 2017].
95. Nordstrom, D. K. An Overview of Arsenic Mass-Poisoning in Bangladesh and West Bengal, India. in *Minor elements 2000; processing and environmental aspects of As, Sb, Se, Te, and Bi* 21–30 (Society for Mining, Metallurgy, and Exploration, 2000).
96. Sen, P. & Biswas, T. Arsenic: the largest mass poisoning of a population in history. *Bmj* **346**, f3625 (2013).

97. Ahmed, M. F. An Overview of Arsenic Removal Technologies in Bangladesh and India. in *Proceedings of BUET-UNU international workshop on technologies for arsenic removal from drinking water, Dhaka* 251–269 (Bangladesh University of Engineering and Technology, 2001).
98. Rahman, M. A., Rahman, A., Khan, M. Z. K. & Renzaho, A. M. N. Human health risks and socio-economic perspectives of arsenic exposure in Bangladesh: A scoping review. *Ecotoxicol. Environ. Saf.* **150**, 335–343 (2018).
99. Nepotism and Neglect: The Failing Response to Arsenic in the Drinking Water of Bangladesh's Rural Poor. <https://www.hrw.org/report/2016/04/06/nepotism-and-neglect/failing-response-arsenic-drinking-water-bangladesh-rural> [Accessed: 15 June 2017].
100. Kinniburgh, D. G. & Smedley, P. L. *Arsenic contamination of groundwater in Bangladesh, Vol 2: Final Report. British Geological Survey Report WC/00/19, Volume 2* vol. 2 (2001).
101. Munir, A. et al. Evaluation of performance of Sono 3-Kolshi filter for arsenic removal from groundwater using zero valent iron through laboratory and field studies. in *Proceedings International Workshop on Technology for Arsenic Removal from Drinking Water, Bangladesh University of Engineering and Technology and United Nations University, Japan* 171–189 (2001).
102. Bangladesh: DPHE/BGS National Hydrochemical Survey | British Geological Survey (BGS). <http://www.bgs.ac.uk/research/groundwater/health/arsenic/Bangladesh/mapsnhs.html> [Accessed: 15 June 2017].
103. Kinniburgh, D. & Smedley, P. *Arsenic contamination of groundwater in Bangladesh, Vol 1: Summary. British Geological Survey Report WC/00/19* vol. 1 <http://nora.nerc.ac.uk/id/eprint/11986> (2001).
104. Balasubramanya, S. & Horbulyk, T. M. Groundwater arsenic in Bangladesh: What's new for policy research? *Water Policy* **20**, 461–474 (2018).
105. The Failing Response to Arsenic in the Drinking Water of Bangladesh's Rural Poor | HRW. <https://www.hrw.org/report/2016/04/06/nepotism-and-neglect/failing-response-arsenic-drinking-water-bangladesh-rural> [Accessed: 15 June 2017].
106. van Geen, A. et al. Inequitable allocation of deep community wells for reducing arsenic exposure in Bangladesh. *J. Water, Sanit. Hyg. Dev.* **6**, 142–150 (2016).
107. McArthur, J. M., Ghosal, U., Sikdar, P. K. & Ball, J. D. Arsenic in Groundwater: The Deep Late Pleistocene Aquifers of the Western Bengal Basin. *Environ. Sci. Technol.* **50**, 3469–3476 (2016).
108. Winston, J. J. et al. Protective benefits of deep tube wells against childhood diarrhea in Matlab, Bangladesh. *Am. J. Public Health* **103**, 1287–1291 (2013).
109. Neumann, A. et al. Arsenic removal with composite iron matrix filters in Bangladesh: A field and laboratory study. *Environ. Sci. Technol.* **47**, 4544–4554 (2013).
110. Kundu, D. K., Mola, A. P. J. & Gupta, A. Failing arsenic mitigation technology in rural Bangladesh: Explaining stagnation in niche formation of the Sono filter. *Water Policy* **18**, 1490–1507 (2016).
111. Chan, N. W., Roy, R. & Chaffin, B. C. Water governance in Bangladesh: An evaluation of institutional and political context. *Water (Switzerland)* **8**, 1–18 (2016).
112. Harvey, C. F. et al. Arsenic mobility and groundwater extraction in Bangladesh. *Science (80-.)* **298**, 1602–1606 (2002).
113. Nicomel, N. R., Leus, K., Folens, K., Van Der Voort, P. & Du Laing, G. Technologies for arsenic removal from water: Current status and future perspectives. *Int. J. Environ. Res. Public Health* **13**, 1–24 (2015).
114. Singh, R., Singh, S., Parihar, P. & Pratap, V. Arsenic contamination, consequences and remediation techniques: A review. *Ecotoxicol. Environ. Saf.* **112**, 247–270 (2015).
115. Mondal, P., Bhowmick, S., Chatterjee, D., Figoli, A. & Van der Bruggen, B. Remediation of inorganic arsenic in groundwater for safe water supply: A critical assessment of technological solutions. *Chemosphere* **92**, 157–170 (2013).
116. Mohan, D. & Pittman, C. U. Arsenic removal from water/wastewater using adsorbents-A critical review. *Journal of Hazardous Materials* vol. 142 1–53 (2007).
117. Robins, R. G., Nishimura, T. & Singh, P. Removal of Arsenic from Drinking Water by Precipitation, Adsorption or Cementation. in *Technologies for arsenic removal from drinking water: compilation of papers presented at the International Workshop on Technologies for Arsenic Removal from Drinking Water, Dhaka, Bangladesh, 5-7 May 2001* 31–42 (Bangladesh University of Engineering and Technology, 2001).
118. Jia, Y. & Demopoulos, G. P. Coprecipitation of arsenate with iron(III) in aqueous sulfate media: Effect of time, lime as base and co-ions on arsenic retention. *Water Res.* **42**, 661–668 (2008).

119. Ungureanu, G., Santos, S., Boaventura, R. & Botelho, C. Arsenic and antimony in water and wastewater: Overview of removal techniques with special reference to latest advances in adsorption. *Journal of Environmental Management* vol. 151 326–342 (2015).
120. Otter, P. et al. Arsenic removal from groundwater by solar driven inline-electrolytic induced co-precipitation and filtration-a long term field test conducted in West Bengal. *Int. J. Environ. Res. Public Health* **14**, 22 (2017).
121. Karima, A. & Shafiu Islam, K. M. Drinking water desalination using low-cost Tubular Solar Still. *Appl. Water Sci.* **10**, (2020).
122. Sarkar, M. N. I., Sifat, A. I., Reza, S. M. S. & Sadique, M. S. A review of optimum parameter values of a passive solar still and a design for southern Bangladesh. *Renewables Wind. Water, Sol.* **4**, 1–13 (2017).
123. Winecki, S. Selected environmental applications of nanocrystalline metal oxides. *ACS Symposium Series* vol. 1045 77–95 (2010).
124. Agrawal, V. K. & Bhalwar, R. Household water purification: Low-cost interventions. *Med. J. Armed Forces India* **65**, 260–263 (2009).
125. Bernal, V., Giraldo, L., Moreno-Piraján, J. C., Balsamo, M. & Erto, A. Mechanisms of methylparaben adsorption onto activated carbons: Removal tests supported by a calorimetric study of the adsorbent–adsorbate interactions. *Molecules* **24**, 413 (2019).
126. Gallios, G. P. et al. Adsorption of arsenate by nano scaled activated carbon modified by iron and manganese oxides. *Sustainability* **9**, 1–18 (2017).
127. Velazquez-jimenez, L. H., Arcibar-orozco, J. A. & Rangel-mendez, J. R. Overview of As(V) adsorption on Zr-functionalized activated carbon for aqueous streams remediation. *J. Environ. Manage.* **212**, 121–130 (2018).
128. Chuang, C. L. et al. Adsorption of arsenic(V) by activated carbon prepared from oat hulls. *Chemosphere* **61**, 478–483 (2005).
129. Di Iorio, E. et al. Arsenate retention mechanisms on hematite with different morphologies evaluated using AFM, TEM measurements and vibrational spectroscopy. *Geochim. Cosmochim. Acta* **237**, 155–170 (2018).
130. Yazdani, M. R., Tuutijärvi, T., Bhatnagar, A. & Vahala, R. Adsorptive removal of arsenic(V) from aqueous phase by feldspars: Kinetics, mechanism, and thermodynamic aspects of adsorption. *J. Mol. Liq.* **214**, 149–156 (2016).
131. Fendorf, S., Michael, H. A. & van Geen, A. Spatial and Temporal Variations of Groundwater Arsenic in South and Southeast Asia. *Science (80-.).* **328**, 1123–1127 (2010).
132. Lescano, M., Zalazar, C. & Brandi, R. Arsenic removal from water employing a combined system: photooxidation and adsorption. *Environ. Sci. Pollut. Res.* **22**, 3865–3875 (2015).
133. Kong, S. et al. Adsorption/Oxidation of Arsenic in Groundwater by Nanoscale Fe-Mn Binary Oxides Loaded on Zeolite. *Water Environ. Res.* **86**, 147–155 (2014).
134. Gupta, B. Sen et al. New initiative A simple chemical free arsenic removal method for community water supply – A case study from West Bengal , India. *Environ. Pollut.* **157**, 3351–3353 (2009).
135. Brunsting, J. H. & Mcbean, E. A. In situ treatment of arsenic-contaminated groundwater by air sparging peristaltic pump. *J. Contam. Hydrol.* **159**, 20–35 (2014).
136. Zhao, J., Matsune, H., Takenaka, S. & Kishida, M. Rapid and efficient catalytic oxidation of As(III) with oxygen over a Pt catalyst at increased temperature. *Chem. Eng. J.* **325**, 270–278 (2017).
137. Jasudkar, D., Rakhunde, R., Deshpande, L., Labhsetwar, P. & Juneja, H. D. Arsenic remediation from drinking water using fenton's reagent with slow sand filter. *Bull. Environ. Contam. Toxicol.* **89**, 1231–1234 (2012).
138. Wang, Z., Bush, R. T. & Liu, J. Arsenic(III) and iron(II) co-oxidation by oxygen and hydrogen peroxide: Divergent reactions in the presence of organic ligands. *Chemosphere* **93**, 1936–1941 (2013).
139. Bissen, M., Vieillard-Baron, M. M., Schindelin, A. J. & Frimmel, F. H. TiO₂-catalyzed photooxidation of arsenite to arsenate in aqueous samples. *Chemosphere* **44**, 751–757 (2001).
140. Pickering, A. J. et al. Effect of in-line drinking water chlorination at the point of collection on child diarrhoea in urban Bangladesh: a double-blind, cluster-randomised controlled trial. *Lancet Glob. Heal.* **7**, e1247–e1256 (2019).
141. Marinho, B. A., Cristóvão, R. O., Boaventura, R. A. R. & Vilar, V. J. P. As(III) and Cr(VI) oxyanion removal from water by advanced oxidation/reduction processes—a review. *Environ. Sci. Pollut.*

- Res. **26**, 2203–2227 (2019).
142. UV Waterworks: Reliable, Inexpensive Water Disinfection for the World. https://eta.lbl.gov/newsletter/cbs_nl/nl09/cbs-nl9-waterworks.html [Accessed: 15 June 2017].
143. Ryu, J., Monllor-Satoca, D., Kim, D. H., Yeo, J. & Choi, W. Photooxidation of arsenite under 254 nm irradiation with a quantum yield higher than unity. *Environ. Sci. Technol.* **47**, 9381–9387 (2013).
144. Chai, L. *et al.* Kinetics and molecular mechanism of arsenite photochemical oxidation based on sulfate radical. *Mol. Catal.* **438**, 113–120 (2017).
145. Goodeve, C. F. & Kitchener, J. A. Photosensitisation by titanium dioxide. *Trans. Faraday Soc.* **34**, 570–579 (1938).
146. Hashimoto, K., Irie, H. & Fujishima, A. TiO₂ photocatalysis: A historical overview and future prospects. *Jpn. J. Appl. Phys.* **44**, 8269–8285 (2005).
147. Atkins, P. & Paula, J. De. *Atkins' Physical Chemistry. Chemistry* (Oxford University Press, 2009). doi:10.1021/ed056pA260.1.
148. Zhao, D., Budhi, S. & Koodali, R. T. Mesoporous titanium dioxide. *ACS Symposium Series* vol. 1045 97–123 (2010).
149. Dong, S. *et al.* Recent developments in heterogeneous photocatalytic water treatment using visible light-responsive photocatalysts: A review. *RSC Adv.* **5**, 14610–14630 (2015).
150. Foster, A. L., Brown, G. E. & Parks, G. A. X-ray absorption fine-structure spectroscopy study of photocatalyzed, heterogeneous As(III) oxidation on kaolin and anatase. *Environ. Sci. Technol.* **32**, 1444–1452 (1998).
151. Yang, H., Lin, W.-Y. & Rajeshwar, K. Homogeneous and heterogeneous photocatalytic reactions involving As(III) and As(V) species in aqueous media. *J. Photochem. Photobiol. A Chem.* **123**, 137–143 (1999).
152. Kim, D. H., Bokare, A. D., Koo, M. S. & Choi, W. Heterogeneous catalytic oxidation of As(III) on nonferrous metal oxides in the presence of H₂O₂. *Environ. Sci. Technol.* **49**, 3506–3513 (2015).
153. Chi, S. *et al.* Magnetically Separated meso-g-C₃N₄/Fe₃O₄: Bifunctional Composites for Removal of Arsenite by Simultaneous Visible-Light Catalysis and Adsorption. *Ind. Eng. Chem. Res.* **55**, 12060–12067 (2016).
154. Samad, A., Furukawa, M., Katsumata, H., Suzuki, T. & Kaneko, S. Photocatalytic oxidation and simultaneous removal of arsenite with CuO/ZnO photocatalyst. *J. Photochem. Photobiol. A Chem.* **325**, (2016).
155. Iervolino, G., Vaiano, V. & Matarangolo, M. Photocatalytic Oxidation of Arsenite to Arsenate Using a Continuous Packed Bed Photoreactor. *73*, 253–258 (2019).
156. Wong, W., Wong, H. Y., Badruzzaman, A. B. M., Goh, H. H. & Zaman, M. Recent advances in exploitation of nanomaterial for arsenic removal from water: A review. *Nanotechnology* **28**, (2017).
157. Liu, K. *et al.* Preparation of large-pore mesoporous nanocrystalline TiO₂ thin films with tailored pore diameters. *J. Phys. Chem. B* **109**, 18719–18722 (2005).
158. Ji, Y. *et al.* Recent developments in nano filtration membranes based on nanomaterials. *Chinese J. Chem. Eng.* **25**, 1639–1652 (2017).
159. Muntha, S. T., Kausar, A. & Siddiq, M. Advances in Polymeric Nanofiltration Membrane : A Review. *Polym. Plast. Technol. Eng.* **56**, 841–856 (2017).
160. León, A. *et al.* FTIR and raman characterization of TiO₂ nanoparticles coated with polyethylene glycol as carrier for 2-methoxyestradiol. *Appl. Sci.* **7**, 1–9 (2017).
161. Gehrke, I., Geiser, A. & Somborn-Schulz, A. Innovations in nanotechnology for water treatment. *Nanotechnol. Sci. Appl.* **8**, 1–17 (2015).
162. Luo, H. *et al.* 2D-Fe₃O₄ Nanosheets for Effective Arsenic Removal. *J. Contemp. Water Res. Educ.* **160**, 132–143 (2017).
163. Pincus, L. N., Lounsbury, A. W. & Zimmerman, J. B. Toward Realizing Multifunctionality: Photoactive and Selective Adsorbents for the Removal of Inorganics in Water Treatment. *Acc. Chem. Res.* **52**, 1206–1214 (2019).
164. Narayana, K. J. & Gupta Burela, R. A review of recent research on multifunctional composite materials and structures with their applications. *Mater. Today Proc.* **5**, 5580–5590 (2018).
165. Ashraf, S., Siddiq, A., Shahida, S. & Qaisar, S. Titanium-based nanocomposite materials for arsenic removal from water: A review. *Heliyon* **5**, e01577 (2019).

166. PARK, J. *et al.* Adsorption of Arsenic by Fe₃O₄, TiO₂, and Al₂O₃ Adsorbents. *J. Ion Exch.* **23**, 82–87 (2012).
167. Wei, Z. *et al.* The effect of pH on the adsorption of arsenic(III) and arsenic(V) at the TiO₂ anatase [101] surface. *J. Colloid Interface Sci.* **462**, 252–259 (2016).
168. Lee, S. H. *et al.* Adsorption properties of arsenic on sulfated TiO₂ adsorbents. *J. Ind. Eng. Chem.* **80**, 444–449 (2019).
169. Hu, S., Shi, Q. & Jing, C. Groundwater Arsenic Adsorption on Granular TiO₂: Integrating Atomic Structure, Filtration, and Health Impact. *Environ. Sci. Technol.* **49**, 9707–9713 (2015).
170. Vaiano, V. *et al.* Enhanced photocatalytic oxidation of arsenite to arsenate in water solutions by a new catalyst based on MoO_x supported on TiO₂. *Appl. Catal. B Environ.* **160–161**, 247–253 (2014).
171. Katz, A., Mcdonagh, A., Tijing, L. & Shon, H. K. Technology Fouling and Inactivation of Titanium Dioxide- Based Photocatalytic Systems Fouling and Inactivation of Titanium. *Crit. Rev. Environ. Sci. Technol.* **3389**, (2015).
172. Upadhyay, R. K., Soin, N. & Roy, S. S. Role of graphene/metal oxide composites as photocatalysts, adsorbents and disinfectants in water treatment: A review. *RSC Adv.* **4**, 3823–3851 (2014).
173. Miller, S. M. & Zimmerman, J. B. Novel, bio-based, photoactive arsenic sorbent: TiO₂-impregnated chitosan bead. *Water Res.* **44**, 5722–5729 (2010).
174. Joshi, A. & Chaudhuri, M. Removal of Arsenic from Ground Water by Iron Oxide-Coated Sand. *J. Environ. Eng.* **769**, (1996).
175. Gupta, V. K., Saini, V. K. & Jain, N. Adsorption of As(III) from aqueous solutions by iron oxide-coated sand. *J. Colloid Interface Sci.* **288**, 55–60 (2005).
176. Callegari, A., Ferronato, N., Rada, E. C., Capodaglio, A. G. & Torretta, V. Assessment of arsenic removal efficiency by an iron oxide-coated sand filter process. *Environ. Sci. Pollut. Res.* **25**, 26135–26143 (2018).
177. Boddu, V. M., Abburi, K., Randolph, A. J. & Smith, E. D. Removal of copper(II) and nickel(II) ions from aqueous solutions by a composite chitosan biosorbent. *Sep. Sci. Technol.* **43**, 1365–1381 (2008).
178. Egodawatte, S., Datt, A., Burns, E. A. & Larsen, S. C. Chemical Insight into the Adsorption of Chromium(III) on Iron Oxide/Mesoporous Silica Nanocomposites. *Langmuir* **31**, 7553–7562 (2015).
179. Mohammad, A. M., Salah Eldin, T. A., Hassan, M. A. & El-Anadouli, B. E. Efficient treatment of lead-containing wastewater by hydroxyapatite/chitosan nanostructures. *Arab. J. Chem.* **10**, 683–690 (2017).
180. Daikopoulos, C. *et al.* A functionalized phosphonate-rich organosilica layered hybrid material (PSLM) fabricated through a mild process for heavy metal uptake. *J. Hazard. Mater.* **270**, 118–126 (2014).
181. Baybaş, D. & Ulusoy, U. The use of polyacrylamide-aluminosilicate composites for thorium adsorption. *Appl. Clay Sci.* **51**, 138–146 (2011).
182. Sato, S. *et al.* Band bending and dipole effect at interface of metal-nanoparticles and TiO₂ directly observed by angular-resolved hard X-ray photoemission spectroscopy. *Phys. Chem. Chem. Phys.* **20**, 11342–11346 (2018).
183. Wang, H. *et al.* Semiconductor heterojunction photocatalysts: design, construction, and photocatalytic performances. *Chem. Soc. Rev.* **43**, 5234 (2014).
184. Kafizas, A. *et al.* Where Do Photogenerated Holes Go in Anatase:Rutile TiO₂? A Transient Absorption Spectroscopy Study of Charge Transfer and Lifetime. *J. Phys. Chem. A* **120**, 715–723 (2016).
185. Beydoun, D., Amal, R., Low, G. K.-C. & McEvoy, S. Novel Photocatalyst: Titania-Coated Magnetite. Activity and Photodissolution. *J. Phys. Chem. B* **104**, 4387–4396 (2000).
186. Fausey, C. L., Zucker, I., Shaulsky, E., Zimmerman, J. B. & Elimelech, M. Removal of arsenic with reduced graphene oxide-TiO₂-enabled nanofibrous mats. *Chem. Eng. J.* **375**, 122040 (2019).
187. Sun, S. *et al.* Facile one-pot construction of α -Fe₂O₃/g-C₃N₄ heterojunction for arsenic removal by synchronous visible light catalysis oxidation and adsorption. *Mater. Chem. Phys.* **194**, 1–8 (2017).

188. Yahya, N. *et al.* A review of integrated photocatalyst adsorbents for wastewater treatment. *J. Environ. Chem. Eng.* **6**, 7411–7425 (2018).
189. Pincus, L. N., Melnikov, F., Yamani, J. S. & Zimmerman, J. B. Multifunctional photoactive and selective adsorbent for arsenite and arsenate: Evaluation of nano titanium dioxide-enabled chitosan cross-linked with copper. *J. Hazard. Mater.* **358**, 145–154 (2018).
190. Yoon, S. H. *et al.* TiO₂ photocatalytic oxidation mechanism of As(III). *Environ. Sci. Technol.* **43**, 864–869 (2009).
191. Lee, H. & Choi, W. Photocatalytic Oxidation of Arsenite in TiO₂ Suspension: Kinetics and Mechanisms. *Environ. Sci. Technol.* **36**, 3872–3878 (2002).
192. Choi, W., Yeo, J., Ryu, J., Tachikawa, T. & Majima, T. Photocatalytic oxidation mechanism of As(III) on TiO₂: Unique role of As(III) as a charge recombinant species. *Environ. Sci. Technol.* **44**, 9099–9104 (2010).
193. Zhang, F. S. & Itoh, H. Photocatalytic oxidation and removal of arsenite from water using slag-iron oxide-TiO₂ adsorbent. *Chemosphere* **65**, 125–131 (2006).
194. Nguyen, T. V., Vigneswaran, S., Ngo, H. H., Kandasamy, J. & Choi, H. C. Arsenic removal by photo-catalysis hybrid system. *Sep. Purif. Technol.* **61**, 44–50 (2008).
195. Ollis, D. F. Kinetics of Photocatalyzed Reactions: Five Lessons Learned. *6*, 1–7 (2018).
196. Buschmann, J., Canonica, S., Lindauer, U., Hug, S. J. & Sigg, L. Photoirradiation of dissolved humic acid induces arsenic(III) oxidation. *Environ. Sci. Technol.* **39**, 9541–9546 (2005).
197. Yan, M., Korshin, G., Wang, D. & Cai, Z. Characterization of dissolved organic matter using high-performance liquid chromatography (HPLC)-size exclusion chromatography (SEC) with a multiple wavelength absorbance detector. *Chemosphere* **87**, 879–885 (2012).
198. Mandal, P. C., Bardhan, D. K., Sarkar, S. & Bhattacharyya, S. N. Oxidation of nickel(II) ethylenediaminetetraacetate by carbonate radical. *J. Chem. Soc. Dalton Trans.* 1457–1461 (1991) doi:10.1039/DT9910001457.
199. Cheng, X., Kong, D. S., Wang, Z., Feng, Y. Y. & Li, W. J. Inhibiting effect of carbonate on the photoinduced flatband potential shifts during water photooxidation at TiO₂/solution interface. *J. Solid State Electrochem.* **21**, 1467–1475 (2017).
200. Guan, X. *et al.* Application of titanium dioxide in arsenic removal from water: A review. *J. Hazard. Mater.* **215–216**, 1–16 (2012).
201. Tsimas, E. S. *et al.* Simultaneous photocatalytic oxidation of As(III) and humic acid in aqueous TiO₂ suspensions. *J. Hazard. Mater.* **169**, 376–385 (2009).
202. Xu, Z., Jing, C., Li, F. & Meng, X. Mechanisms of photocatalytical degradation of monomethylarsonic and dimethylarsinic acids using nanocrystalline titanium dioxide. *Environ. Sci. Technol.* **42**, 2349–2354 (2008).
203. Ferguson, M. A., Hoffmann, M. R. & Hering, J. G. TiO₂-photocatalyzed As(III) oxidation in aqueous suspensions: Reaction kinetics and effects of adsorption. *Environ. Sci. Technol.* **39**, 1880–1886 (2005).
204. Scanlon, D. O. *et al.* Band alignment of rutile and anatase TiO₂. *Nat. Mater.* **12**, 798–801 (2013).
205. Odling, G. & Robertson, N. Why is anatase a better photocatalyst than rutile? the importance of free hydroxyl radicals. *ChemSusChem* **8**, 1838–1840 (2015).
206. Nosaka, Y. & Nosaka, A. Understanding Hydroxyl Radical (\cdot OH) Generation Processes in Photocatalysis. *ACS Energy Lett.* **1**, 356–359 (2016).
207. Sarkar, R. A. D. & Datta, K. R. B. R. Adsorption of arsenic(V) from aqueous solutions by goethite/silica nanocomposite. *Int. J. Environ. Sci. Technol.* **12**, 3905–3914 (2015).
208. BAYOXIDE® E 33 - Liquid Purification Technologies. <http://lpt.lanxess.com/en/products-lpt/product-groups/iron-oxide-adsorber/bayoxide-product-detail/bayoxider-e-33/> [Accessed: 15 June 2017].
209. Stanish, F. Arsenic Removal with Bayoxide® E33 Ferric Oxide Media & SORB 33® As Adsorption. in *AWWA New York Conference, Saratoga Springs, NY* (Severn Trent Services, 2015).
210. Bayoxide® E33 Adsorption Media – Arsenic Reduction. *AdEdge Technologies*.
211. Kanematsu, M. *et al.* Quantification of the effects of organic and carbonate buffers on arsenate and phosphate adsorption on a goethite-based granular porous adsorbent. *Environ. Sci. Technol.* **45**, 561–568 (2011).
212. Moffat, C. D. *et al.* Molecular recognition and scavenging of arsenate from aqueous solution

- using dimetallic receptors. *Chem. - A Eur. J.* **20**, 17168–17177 (2014).
213. Hao, L., Liu, M., Wang, N. & Li, G. A critical review on arsenic removal from water using iron-based adsorbents. *RSC Adv.* **3**, 39545–39560 (2018).
214. Giménez, J., Martínez, M., de Pablo, J., Rovira, M. & Duro, L. Arsenic sorption onto natural hematite, magnetite, and goethite. *J. Hazard. Mater.* **141**, 575–580 (2007).
215. Das, S., Essilfie-Dughan, J. & Hendry, M. J. Arsenate adsorption onto hematite nanoparticles under alkaline conditions: Effects of aging. *J. Nanoparticle Res.* **16**, (2014).
216. Tang, W., Li, Q., Gao, S. & Shang, J. K. Arsenic (III,V) removal from aqueous solution by ultrafine α -Fe₂O₃ nanoparticles synthesized from solvent thermal method. *J. Hazard. Mater.* **192**, 131–138 (2011).
217. Liu, R., Liu, J. F., Zhang, L. Q., Sun, J. F. & Jiang, G. Bin. Low temperature synthesized ultrathin γ -Fe₂O₃ nanosheets show similar adsorption behaviour for As(III) and As(V). *J. Mater. Chem. A* **4**, 7606–7614 (2016).
218. Chowdhury, S. R. & Yanful, E. K. Arsenic and chromium removal by mixed magnetite-maghemite nanoparticles and the effect of phosphate on removal. *J. Environ. Manage.* **91**, 2238–2247 (2010).
219. Vourlias, G. *et al.* Magnetic separation of hematite-coated Fe₃O₄ particles used as arsenic adsorbents. *Chem. Eng. J.* **168**, 1008–1015 (2011).
220. Iconaru, S. L. *et al.* Magnetite (Fe₃O₄) nanoparticles as adsorbents for As and Cu removal. *Appl. Clay Sci.* **134**, 128–135 (2016).
221. Zhang, J. & Stanforth, R. Slow adsorption reaction between arsenic species and goethite (α -FeOOH): Diffusion or heterogeneous surface reaction control. *Langmuir* **21**, 2895–2901 (2005).
222. Jacobson, A. T. & Fan, M. Evaluation of natural goethite on the removal of arsenate and selenite from water. *J. Environ. Sci. (China)* **76**, 133–141 (2019).
223. Grafe, M., Eick, M. J. & Grossl, P. R. Adsorption of Arsenate (V) and Arsenite (III) on Goethite in the Presence and Absence of Dissolved Organic Carbon. *Soil Sci. Soc. Am. J.* **65**, 1680 (2010).
224. Manning, B. A., Fendorf, S. E. & Goldberg, S. Surface structures and stability of arsenic(III) on goethite: Spectroscopic evidence for inner-sphere complexes. *Environ. Sci. Technol.* **32**, 2383–2388 (1998).
225. Kanematsu, M., Young, T. M., Fukushi, K., Green, P. G. & Darby, J. L. Arsenic(III, V) adsorption on a goethite-based adsorbent in the presence of major co-existing ions: Modeling competitive adsorption consistent with spectroscopic and molecular evidence. *Geochim. Cosmochim. Acta* **106**, 404–428 (2013).
226. Das, S., Essilfie-Dughan, J. & Hendry, M. J. Arsenate partitioning from ferrihydrite to hematite: Spectroscopic evidence. *Am. Mineral.* **99**, 749–754 (2014).
227. Qi, P. & Pichler, T. Competitive Adsorption of As(III) and As(V) by Ferrihydrite: Equilibrium, Kinetics, and Surface Complexation. *Water. Air. Soil Pollut.* **227**, (2016).
228. Frau, F. *et al.* Influence of major anions on As(V) adsorption by synthetic 2-line Ferrihydrite. Kinetic investigation and XPS study of the competitive effect of bicarbonate. *Water. Air. Soil Pollut.* **205**, 25–41 (2010).
229. Goldberg, S. & Johnston, C. T. Mechanisms of Arsenic Adsorption on Amorphous Oxides Evaluated Using Macroscopic Measurements , Vibrational Spectroscopy , and Surface Complexation Modeling. *216*, 204–216 (2001).
230. Dixit, S. & Hering, J. Comparison of arsenic(V) and arsenic(III) sorption onto iron oxide minerals: Implications for arsenic mobility. *Environ. Sci. Technol.* **37**, 4182–4189 (2003).
231. Kumar, A. Arsenic removal effectiveness of iron oxide-based fibrous adsorbents and stability of granular iron oxide media. (Doctoral dissertation or master's thesis). (Drexel University, 2008).
232. Nguyen, V. L., Chen, W. H., Young, T. & Darby, J. Effect of interferences on the breakthrough of arsenic: Rapid small scale column tests. *Water Res.* **45**, 4069–4080 (2011).
233. Yang, X. *et al.* Adsorption of As(III) on porous hematite synthesized from goethite concentrate. *Chemosphere* **169**, 188–193 (2017).
234. Arai, Y., Sparks, D. L. & Davis, J. A. Effects of Dissolved Carbonate on Arsenate Adsorption and Surface Speciation at the Hematite-Water Interface. *Environ. Sci. Technol.* **38**, 817–824 (2004).
235. Ona-Nguema, G., Morin, G., Juillot, F., Calas, G. & Brown, G. E. EXAFS analysis of arsenite adsorption onto two-line ferrihydrite, hematite, goethite, and lepidocrocite. *Environ. Sci. Technol.* **39**, 9147–9155 (2005).

236. Gräfe, M., Beattie, D. A., Smith, E., Skinner, W. M. & Singh, B. Copper and arsenate co-sorption at the mineral-water interfaces of goethite and jarosite. *J. Colloid Interface Sci.* **322**, 399–413 (2008).
237. Manning, B. A., Hunt, M. L., Amrhein, C. & Yarmoff, J. A. Arsenic(III) and arsenic(V) reactions with zerovalent iron corrosion products. *Environ. Sci. Technol.* **36**, 5455–5461 (2002).
238. Adra, A., Morin, G., Ona-Nguema, G. & Brest, J. Arsenate and arsenite adsorption onto Al-containing ferrihydrites. Implications for arsenic immobilization after neutralization of acid mine drainage. *Appl. Geochemistry* **64**, 2–9 (2015).
239. Zhang, M., He, G. & Pan, G. Binding mechanism of arsenate on rutile (110) and (001) planes studied using grazing-incidence EXAFS measurement and DFT calculation. *Chemosphere* **122**, 199–205 (2015).
240. Pena, M., Meng, X., Jing, C., Korfiatis, G. & Jing, C. Adsorption Mechanism of Arsenic on Nanocrystalline Titanium Dioxide. *Environ. Sci. Technol.* **40**, 1257–1262 (2006).
241. Dzade, N. Y. & De Leeuw, N. H. Density functional theory characterization of the structures of H₃AsO₃ and H₃AsO₄ adsorption complexes on ferrihydrite. *Environ. Sci. Process. Impacts* **20**, 977–987 (2018).
242. Brechbühl, Y., Christl, I., Elzinga, E. J. & Kretzschmar, R. Competitive sorption of carbonate and arsenic to hematite: Combined ATR-FTIR and batch experiments. *J. Colloid Interface Sci.* **377**, 313–321 (2012).
243. Müller, K., Ciminelli, V. S. T., Dantas, M. S. S. & Willscher, S. A comparative study of As(III) and As(V) in aqueous solutions and adsorbed on iron oxy-hydroxides by Raman spectroscopy. *Water Res.* **44**, 5660–5672 (2010).
244. Loring, J. S., Sandström, M. H., Norén, K. & Persson, P. Rethinking arsenate coordination at the surface of goethite. *Chem. - A Eur. J.* **15**, 5063–5072 (2009).
245. Sverjensky, D. A. & Fukushima, K. A predictive model (ETLM) for As(III) adsorption and surface speciation on oxides consistent with spectroscopic data. *Geochim. Cosmochim. Acta* **70**, 3778–3802 (2006).
246. Coronado, J. M. & Hernández-Alonso, M. D. The Keys of Success: TiO₂ as a Benchmark Photocatalyst. in *Design of Advanced Photocatalytic Materials for Energy and Environmental Applications* (eds. Coronado, J. M., Fresno, F., Hernández-Alonso, M. D. & Portela, R.) 85–101 (Springer London, 2013). doi:10.1007/978-1-4471-5061-9_5.
247. Moniz, S. J. A., Shevlin, S. A., An, X., Guo, Z. X. & Tang, J. Fe₂O₃-TiO₂ nanocomposites for enhanced charge separation and photocatalytic activity. *Chem. - A Eur. J.* **20**, 15571–15579 (2014).
248. Beduk, F. Superparamagnetic nanomaterial Fe₃O₄-TiO₂ for the removal of As(V) and As(III) from aqueous solutions. *Environ. Technol. (United Kingdom)* **37**, 1790–1801 (2016).
249. Deng, M., Wu, X., Zhu, A., Zhang, Q. & Liu, Q. Well-dispersed TiO₂ nanoparticles anchored on Fe₃O₄ magnetic nanosheets for efficient arsenic removal. *J. Environ. Manage.* **237**, 63–74 (2019).
250. Bullough, F. Towards a new Arsenic remediation technique - A bi-functional TiO₂-Fe₂O₃ adsorbent for the photooxidation of As(III) and adsorption of As(V). (Doctoral dissertation or master's thesis). (Imperial College London).
251. Lapinee, C. Mesoporous TiO₂/Fe₂O₃ bicomposites: synthesis and mechanistic studies of arsenic scavenging. (Doctoral dissertation or master's thesis). (Imperial College London, 2016). doi:10.25560/57029.
252. Stumm, W. & Morgan, J. J. *Aquatic Chemistry*. (John Wiley & Sons, Inc., 1996).
253. Davis, J. A., Meece, D. E., Kohler, M. & Curtis, G. P. Approaches to surface complexation modeling of Uranium(VI) adsorption on aquifer sediments. *Geochim. Cosmochim. Acta* **68**, 3621–3641 (2004).
254. Hafeznezami, S. *et al.* Arsenic mobilization in an oxidizing alkaline groundwater: Experimental studies, comparison and optimization of geochemical modeling parameters. *Appl. Geochemistry* **72**, 97–112 (2016).
255. Zhang, F. S. & Itoh, H. Iron oxide-loaded slag for arsenic removal from aqueous system. *Chemosphere* **60**, 319–325 (2005).
256. Raven, K. P., Jain, A. & Loepert, R. H. Arsenite and Arsenate Adsorption on Ferrihydrite: Kinetics, Equilibrium, and Adsorption Envelopes. *Env. Sci. Technol.* **32**, 344–349 (1998).
257. Morin, G. *et al.* EXAFS and HRTEM evidence for As(III)-containing surface precipitates on

- nanocrystalline magnetite: Implications for arsenic sequestration. *Langmuir* **25**, 9119–9128 (2009).
258. Casanova, F., Chiang, C. E., Ruminski, A. M., Sailor, M. J. & Schuller, I. K. Controlling the role of nanopore morphology in capillary condensation. *Langmuir* **28**, 6832–6838 (2012).
259. David, R. *et al.* The Role of Contact Angle and Pore Width on Pore Condensation and Freezing. *Atmos. Chem. Phys. Discuss.* 1–33 (2019) doi:10.5194/acp-2019-1019.
260. Pandey, S. & Tiwari, S. Facile approach to synthesize chitosan based composite - Characterization and cadmium(II) ion adsorption studies. *Carbohydr. Polym.* **134**, 646–656 (2015).
261. Zhang, Y., Hou, X., Sun, T. & Zhao, X. Calcination of reduced graphene oxide decorated TiO₂ composites for recovery and reuse in photocatalytic applications. *Ceram. Int.* **43**, 1150–1159 (2017).
262. Zemskova, L. A., Voit, A. V., Barinov, N. N., Nikolenko, Y. M. & Shlyk, D. K. Composite sorbents based on synthetic manganese oxide and carbon fiber. *Russ. J. Inorg. Chem.* **61**, 1567–1572 (2016).
263. Carneiro, L. M. *et al.* Excitation-wavelength-dependent small polaron trapping of photoexcited carriers in α-Fe₂O₃. *Nat. Mater.* **16**, 819–825 (2017).
264. Colombo, E. & Ashokkumar, M. Comparison of the photocatalytic efficiencies of continuous stirred tank reactor (CSTR) and batch systems using a dispersed micron sized photocatalyst. *RSC Adv.* **7**, 48222–48229 (2017).
265. Qu, C. *et al.* Pb sorption on montmorillonite-bacteria composites: A combination study by XAFS, ITC and SCM. *Chemosphere* **200**, 427–436 (2018).
266. Wang, N. *et al.* Surface complexation modeling of Cd(II) sorption to montmorillonite, bacteria, and their composite. *Biogeosciences* **13**, 5557–5566 (2016).
267. Mayordomo, N., Alonso, U. & Missana, T. Effects of γ-alumina nanoparticles on strontium sorption in smectite: Additive model approach. *Appl. Geochemistry* **100**, 121–130 (2019).
268. Lei, M. *et al.* Binding of Sb(III) by Sb-tolerant *Bacillus cereus* cell and cell-goethite composite: implications for Sb mobility and fate in soils and sediments. *J. Soils Sediments* **19**, 2850–2858 (2019).
269. Otero, A., Peacock, C. L., Fiol, S., Antelo, J. & Carvin, B. A universal adsorption behaviour for Cu uptake by iron (hydr)oxide organo-mineral composites. *Chem. Geol.* **479**, 22–35 (2018).
270. Dichiara, A. B., Weinstein, S. J. & Rogers, R. E. On the Choice of Batch or Fixed Bed Adsorption Processes for Wastewater Treatment. *Ind. Eng. Chem. Res.* **54**, 8579–8586 (2015).
271. Ho, Y. S. & McKay, G. Pseudo-second order model for sorption processes. *Process Biochem.* **34**, 451–465 (1999).
272. Largitte, L. & Pasquier, R. A review of the kinetics adsorption models and their application to the adsorption of lead by an activated carbon. *Chem. Eng. Res. Des.* **109**, 495–504 (2016).
273. Marczewski, A. W. Analysis of kinetic langmuir model. Part I: Integrated kinetic langmuir equation (IKL): A new complete analytical solution of the langmuir rate equation. *Langmuir* **26**, 15229–15238 (2010).
274. Mouelhi, M., Giraudet, S., Amrane, A. & Hamrouni, B. Competitive adsorption of fluoride and natural organic matter onto activated alumina. *Environ. Technol. (United Kingdom)* **37**, (2016).
275. Luttrell, T. *et al.* Why is anatase a better photocatalyst than rutile? - Model studies on epitaxial TiO₂ films. *Sci. Rep.* **4**, 4043 (2015).
276. Cornell, R. M. & Schwertmann, U. *The Iron Oxides: Structure, Properties, Reactions, Occurrences and Uses*. vol. 6 (Wiley, 1996).
277. Scherrer, P. Bestimmung der Grösse und der inneren Struktur von Kolloidteilchen mittels Röntgentränen. in *Kolloidchemie Ein Lehrbuch. Chemische Technologie in Einzeldarstellungen* 387–409 (Springer, 1912).
278. Holzwarth, U. & Gibson, N. The Scherrer equation versus the ‘Debye-Scherrer equation’. *Nat. Nanotechnol.* **6**, 534–534 (2011).
279. Lützenkirchen, J. *et al.* Potentiometric titrations as a tool for surface charge determination. *Croat. Chem. Acta* **85**, 391–417 (2012).
280. Cheng, A. *et al.* Investigating Arsenic Contents in Surface and Drinking Water by Voltammetry and the Method of Standard Additions. *J. Chem. Educ.* **93**, 1945–1950 (2016).
281. Salaün, P., Gibbon-Walsh, K. B., Alves, G. M. S., Soares, H. M. V. M. & van den Berg, C. M. G. Determination of arsenic and antimony in seawater by voltammetric and chronopotentiometric

- stripping using a vibrated gold microwire electrode. *Anal. Chim. Acta* **746**, 53–62 (2012).
282. Harris, D. C. *Quantitative Chemical Analysis*. W.H. Freeman & Company vol. 53 (2010).
283. Salaün, P., Planer-Friedrich, B. & van den Berg, C. M. G. Inorganic arsenic speciation in water and seawater by anodic stripping voltammetry with a gold microelectrode. *Anal. Chim. Acta* **585**, 312–322 (2007).
284. Kanematsu, M., Young, T. M., Fukushi, K., Green, P. G. & Darby, J. L. Extended triple layer modeling arsenate adsorption on a nanostructured goethite-based granular porous adsorbent in the presence of major co-existing ions. *Abstr. Pap. Am. Chem. Soc.* **241**, 3388–3394 (2011).
285. Westall, J. *FITEQL: A Computer Program for Determination of Chemical Equilibrium Constants from Empirical Data*. (1982).
286. Marchi, G. *et al.* Surface Complexation Modeling in Variable Charge Soils: Prediction of Cadmium Adsorption. *Rev. Bras. Ciéncia do Solo* **39**, 1395–1405 (2015).
287. Righetto, L., Azimonti, G., Missana, T. & Bidoglio, G. The triple layer model revised. *Colloids Surfaces A Physicochem. Eng. Asp.* **95**, 141–157 (1995).
288. Sahai, N. & Sverjensky, D. A. Evaluation of internally consistent parameters for the triple-layer model by the systematic analysis of oxide surface titration data. *Geochim. Cosmochim. Acta* **61**, 2801–2826 (1997).
289. Jonsson, C. M. *et al.* Adsorption of L-aspartate to rutile (α -TiO₂): Experimental and theoretical surface complexation studies. *Geochim. Cosmochim. Acta* **74**, 2356–2367 (2010).
290. Sverjensky, D. a. A Predictive Model of Surface Charge on Oxides in Aqueous Electrolyte Solutions: The Extended Triple Layer Model (ETLM). *Mineral. Mag.* **62A**, 1483–1484 (1998).
291. Sverjensky, D. A. Prediction of surface charge on oxides in salt solutions: Revisions for 1:1 (M+L-) electrolytes. *Geochim. Cosmochim. Acta* **69**, 225–257 (2005).
292. Bullen, J. C. Arsenic adsorption modelling: TiO₂, Fe₂O₃ and composite TiO₂-Fe₂O₃ sorbents - detailed characterisation and adsorption data sets. <http://www.doi.org/10.5281/zenodo.3689692> (2020) doi:10.5281/zenodo.3689692.
293. Tauc, J. Optical properties and electronic structure of amorphous Ge and Si. *Mater. Res. Bull.* **3**, 37–46 (1968).
294. Tunc, I., Bruns, M., Gliemann, H., Grunze, M. & Koelsch, P. Bandgap determination and charge separation in Ag@TiO₂ core shell nanoparticle films. *Surf. Interface Anal.* **42**, 835–841 (2010).
295. Jiamprasertboon, A. *et al.* Heterojunction α -Fe₂O₃/ZnO Films with Enhanced Photocatalytic Properties Grown by Aerosol-Assisted Chemical Vapour Deposition. *Chem. - A Eur. J.* **25**, 11337–11345 (2019).
296. Ernest, P. H. Transient spectroscopic studies of photocatalysts for CO₂ and proton reduction. (Doctoral dissertation or master's thesis). (Imperial College London, 2015).
297. Nelson, J. & Chandler, R. E. Random walk models of charge transfer and transport in dye sensitized systems. *Coord. Chem. Rev.* **248**, 1181–1194 (2004).
298. Vallance, C. & Vallance, C. Determining the rate law and obtaining mechanistic information from experimental data. in *An Introduction to Chemical Kinetics* (Morgan and Claypool, 2017). doi:10.1088/978-1-6817-4664-7ch4.
299. Kirby, M. E. *et al.* Determining the Effect of pH on Iron Oxidation Kinetics in Aquatic Environments: Exploring a Fundamental Chemical Reaction to Grasp the Significant Ecosystem Implications of Iron Bioavailability. *J. Chem. Educ.* (2019) doi:10.1021/acs.jchemed.8b01036.
300. Ohtani, B. Chapter 10 - Photocatalysis by inorganic solid materials: Revisiting its definition, concepts, and experimental procedures. in *Advances in Inorganic Chemistry* vol. 63 395–430 (2011).
301. Kang, S. A., Li, W., Lee, H. E., Phillips, B. L. & Lee, Y. J. Phosphate uptake by TiO₂: Batch studies and NMR spectroscopic evidence for multisite adsorption. *J. Colloid Interface Sci.* **364**, 455–461 (2011).
302. Huang, X., Foster, G. D., Honeychuck, R. V. & Schreibels, J. A. The maximum of phosphate adsorption at pH 4.0: Why it appears on aluminum oxides but not on iron oxides. *Langmuir* **25**, 4450–4461 (2009).
303. Lazaridis, N. K., Pandi, T. A. & Matis, K. A. Chromium(VI) Removal from Aqueous Solutions by Mg-Al-CO₃ Hydrotalcite: Sorption-Desorption Kinetic and Equilibrium Studies. *Ind. Eng. Chem. Res.* **43**, 2209–2215 (2004).
304. Bullen, J. C., Saleesongsom, S. & Weiss, D. J. A revised pseudo-second order kinetic model for

- adsorption, sensitive to changes in sorbate and sorbent concentrations. *ChemRxiv Prepr.* (2020) doi:10.26434/chemrxiv.12008799.
305. Huang, Y. *et al.* Model fitting of sorption kinetics data: Misapplications overlooked and their rectifications. *AIChE J.* **64**, 1793–1805 (2018).
306. Bullen, J. C. MATLAB codes - A kinetic adsorption model for modelling Arsenic Treatment Plant (ATP) lifetimes. <http://www.doi.org/10.5281/zenodo.3690170> (2020) doi:10.5281/zenodo.3690170.
307. Chakraborti, D. *et al.* Groundwater arsenic contamination in Bangladesh-21 Years of research. *J. Trace Elem. Med. Biol.* **31**, 237–248 (2015).
308. Steinmaus, C. M., George, C. M., Kalman, D. A. & Smith, A. H. Evaluation of two new arsenic field test kits capable of detecting arsenic water concentrations close to 10 µg/L. *Environ. Sci. Technol.* **40**, 3362–3366 (2006).
309. Lambrou, T. P., Anastasiou, C. C., Panayiotou, C. G. & Polycarpou, M. M. A low-cost sensor network for real-time monitoring and contamination detection in drinking water distribution systems. *IEEE Sens. J.* **14**, (2014).
310. Stefan, M. I. *Advanced Oxidation Processes for Water Treatment - Fundamentals and Applications.* (IWA Publishing, 2017). doi:10.2166/9781780407197.
311. Shahid, M. *et al.* A meta-analysis of the distribution, sources and health risks of arsenic-contaminated groundwater in Pakistan. *Environ. Pollut.* **242**, 307–319 (2018).
312. Markley, C. T. & Herbert, B. E. Arsenic risk assessment: The importance of speciation in different hydrologic systems. *Water. Air. Soil Pollut.* **204**, 385–398 (2009).
313. Shankar, S., Shanker, U. & Shikha. Arsenic contamination of groundwater: A review of sources, prevalence, health risks, and strategies for mitigation. *Sci. World J.* **2014**, (2014).
314. Qi, P. & Pichler, T. Competitive adsorption of As(III), As(V), Sb(III) and Sb(V) onto ferrihydrite in multi-component systems: Implications for mobility and distribution. *J. Hazard. Mater.* **330**, 142–148 (2017).
315. Bednar, A. J., Garbarino, J. R., Burkhardt, M. R., Ranville, J. F. & Wildeman, T. R. Field and laboratory arsenic speciation methods and their application to natural-water analysis. *Water Res.* **38**, 355–364 (2004).
316. Yogarajah, N. & Tsai, S. S. H. Detection of trace arsenic in drinking water: Challenges and opportunities for microfluidics. *Environ. Sci. Water Res. Technol.* **4**, (2015).
317. Agilent Technologies. A comparison of the relative cost and productivity of traditional metals analysis techniques versus ICP-MS in high throughput commercial laboratories.
318. Johnston, R. B. & Sarker, M. H. Arsenic mitigation in Bangladesh: National screening data and case studies in three upazilas. *J. Environ. Sci. Heal. Part A* **42**, 1889–1896 (2007).
319. McGrory, E. R. *et al.* Arsenic contamination of drinking water in Ireland: A spatial analysis of occurrence and potential risk. *Sci. Total Environ.* **579**, 1863–1875 (2017).
320. Rabbani, U., Mahar, G., Siddique, A. & Fatmi, Z. Risk assessment for arsenic-contaminated groundwater along River Indus in Pakistan. *Environ. Geochem. Health* **39**, 179–190 (2017).
321. Liang, C. P., Chen, J. S., Chien, Y. C. & Chen, C. F. Spatial analysis of the risk to human health from exposure to arsenic contaminated groundwater: A kriging approach. *Sci. Total Environ.* **627**, 1048–1057 (2018).
322. Bird, F. C. J. The Gutzeit Test for Arsenic. *Analyst July*, (1901).
323. Sanger, C. R. & Black, O. F. The Quantitative Determination of Arsenic by the Gutzeit Method. *Proc. Am. Acad. Arts Sci.* **43**, 297–324 (1907).
324. Okazaki, T. *et al.* Visual colorimetry for determination of trace arsenic in groundwater based on improved molybdenum blue spectrophotometry. *Anal. Methods* **7**, 2794–2799 (2015).
325. Okazaki, T., Wang, W., Kuramitz, H., Hata, N. & Taguchi, S. Molybdenum blue spectrophotometry for trace arsenic in ground water using a soluble membrane filter and calcium carbonate column. *Anal. Sci.* **29**, 67–72 (2013).
326. Emerman, S. H. *et al.* Arsenic and other heavy metals in the Sunkoshi and Saptakoshi Rivers , eastern Nepal. *J. Nepal Geol. Soc.* **43**, 241–254 (2011).
327. Tsang, S., Phu, F., Baum, M. M. & Poskrebyshev, G. A. Determination of phosphate/arsenate by a modified molybdenum blue method and reduction of arsenate by S₂O₄2-. *Talanta* **71**, 1560–1568 (2007).
328. Forsberg, G., O'Laughlin, J. W., Megargle, R. G., Koirtyohann, S. R. & Koirtyohann, S. R.

- Determination of arsenic by anodic stripping voltammetry and differential pulse anodic stripping voltammetry. *Anal. Chem.* **47**, 1586–1592 (1975).
329. Fabricant, D. Arsenic in herbal kelp supplements: concentration, regulations, and labeling. *Environ. Health Perspect.* **115**, 574–577 (2007).
330. Brainina, K. Z., Malakhova, N. A. & Stojko, N. Y. Stripping voltammetry in environmental and food analysis. *Fresenius. J. Anal. Chem.* **368**, 307–325 (2000).
331. Borrill, A. J., Reily, N. E. & Macpherson, J. V. Addressing the practicalities of anodic stripping voltammetry for heavy metal detection: A tutorial review. *Analyst* **144**, 6834–6849 (2019).
332. Gibbon-Walsh, K., Salaün, P. & van den Berg, C. M. G. Arsenic speciation in natural waters by cathodic stripping voltammetry. *Anal. Chim. Acta* **662**, 1–8 (2010).
333. Luong, J. H. T., Lam, E. & Male, K. B. Recent advances in electrochemical detection of arsenic in drinking and ground waters. *Anal. Methods* **6**, 6157 (2014).
334. Shoog, D. A. & West, D. M. *Fundamentals of analytical chemistry*. (Holt, Rinehart, and Winston, 1976). doi:10.1201/9781420056716.ch25.
335. Holak, W. Determination of arsenic by cathodic stripping voltammetry with a hanging mercury drop electrode. *Anal. Chem.* **52**, 2189–2192 (1980).
336. Sadana, R. S. Determination of arsenic in the presence of copper by differential pulse cathodic stripping voltammetry at a hanging mercury drop electrode. *Anal. Chem.* **55**, 304–307 (1983).
337. Vyskočil, V. & Barek, J. Mercury Electrodes—Possibilities and Limitations in Environmental Electroanalysis. *Crit. Rev. Anal. Chem.* **39**, 173–188 (2009).
338. Huang, H. & Dasgupta, P. K. A field-deployable instrument for the measurement and speciation of arsenic in potable water. *Anal. Chim. Acta* **380**, 27–37 (1999).
339. Simm, A. O., Banks, C. E. & Compton, R. G. The electrochemical detection of arsenic(III) at a silver electrode. *Electroanalysis* **17**, 1727–1733 (2005).
340. Chen, Y.-W., Yu, X. & Belzile, N. Arsenic speciation in surface waters and lake sediments in an abandoned mine site and field observations of arsenic eco-toxicity. *J. Geochemical Explor.* **205**, 106349 (2019).
341. O'Reilly, J., Watts, M. J., Shaw, R. A., Marcilla, A. L. & Ward, N. I. Arsenic contamination of natural waters in San Juan and La Pampa, Argentina. *Environ. Geochem. Health* **32**, 491–515 (2010).
342. Watts, M. J., O'Reilly, J., Marcilla, A. L., Shaw, R. A. & Ward, N. I. Field based speciation of arsenic in UK and Argentinean water samples. *Environ. Geochem. Health* **32**, 479–490 (2010).
343. Mihucz, V. G. et al. A simple method for monitoring of removal of arsenic species from drinking water applying on-site separation with solid phase extraction and detection by atomic absorption and X-ray fluorescence based techniques. *Microchem. J.* **135**, 105–113 (2017).
344. Bednar, A. J., Garbarino, J. R., Burkhardt, M. R., Ranville, J. F. & Wildeman, T. R. Field and laboratory arsenic speciation methods and their application to natural-water analysis. *Water Res.* **38**, 355–364 (2004).
345. Voice, T. C., Flores del Pino, L. V., Havezov, I. & Long, D. T. Field deployable method for arsenic speciation in water. *Phys. Chem. Earth* **36**, 436–441 (2011).
346. Benramdane, L., Bressolle, F. & Vallon, J. J. Arsenic speciation in humans and food products: A review. *J. Chromatogr. Sci.* **37**, 330–344 (1999).
347. An, J., Lee, J., Lee, G., Nam, K. & Yoon, H. O. Combined use of collision cell technique and methanol addition for the analysis of arsenic in a high-chloride-containing sample by ICP-MS. *Microchem. J.* **120**, 77–81 (2015).
348. Zhao, L. yu et al. Preparation of thiol- and amine-bifunctionalized hybrid monolithic column via “one-pot” and applications in speciation of inorganic arsenic. *Talanta* **192**, 339–346 (2019).
349. Montoro Leal, P. et al. Speciation analysis of inorganic arsenic by magnetic solid phase extraction on-line with inductively coupled mass spectrometry determination. *Talanta* **184**, 251–259 (2018).
350. Chen, S., Li, J., Lu, D. & Zhang, Y. Dual extraction based on solid phase extraction and solidified floating organic drop microextraction for speciation of arsenic and its distribution in tea leaves and tea infusion by electrothermal vaporization ICP-MS. *Food Chem.* **211**, 741–747 (2016).
351. Gupta, A. & Singh, E. J. Arsenic–Iron Relationships in Aquifers of North East India: Implications for Public Health and the Environment. *Environ. Manage.* **63**, 437–443 (2018).
352. Rasul, S. B. et al. Electrochemical measurement and speciation of inorganic arsenic in

- groundwater of Bangladesh. *Talanta* **58**, 33–43 (2002).
353. Paul, S. C., Rahman, M. A., Siddique, N. & Alam, a M. S. Voltammetric Study of Arsenic(III) and Arsenic(V) in Ground Water of Hajigonj and Kalkini in Bangladesh. *Pak. J. Anal. Environ. Chem.* **9**, 49–55 (2008).
354. The NSF Joint Committee on Drinking Water Treatment Units. *NSF/ANSI 53 - 2016 Drinking Water Treatment Units - Health Effects*. <https://blog.ansi.org/2017/03/nsfansi-53-2016-drinking-water-treatment-units-health/#gref> (2016).
355. Miller, W. S., Castagna, C. J. & Pieper, A. W. Understanding ion-exchange resins for water treatment systems. *GE Water Process Technol.* 1–13 (2009).
356. Gönder, Z. B., Kaya, Y., Vergili, I. & Barlas, H. Capacity loss in an organically fouled anion exchanger. *Desalination* **189**, 303–307 (2006).
357. Cvetkovic, T. *et al.* Interaction of cobalt(II), nickel(II) and zinc(II) with humic-like ligands studied by ESI-MS and ion-exchange method. *J. Serbian Chem. Soc.* **81**, 255–270 (2015).
358. Hirata, S. Stability constants for the complexes of transition-metal ions with fulvic and humic acids in sediments measured by gel filtration. *Talanta* **28**, 809–815 (1981).
359. Hansen, A. M. *et al.* Optical properties of dissolved organic matter (DOM): Effects of biological and photolytic degradation. *Limnol. Oceanogr.* **61**, 1015–1032 (2016).
360. Boija, S. *et al.* Determination of conditional stability constants for some divalent transition metal ion-EDTA complexes by electrospray ionization mass spectrometry. *J. Mass Spectrom.* **49**, 550–556 (2014).
361. Mladenov, N. *et al.* Dissolved Organic Matter Quality in a Shallow Aquifer of Bangladesh: Implications for Arsenic Mobility. *Environ. Sci. Technol.* **49**, 10815–10824 (2015).
362. Tsutsuki, K. & Kuwatsuka, S. Determination of molecular weights of humic acids by osmotic pressure measurement and by permeation chromatography on controlled pore glass. *Soil Sci. Plant Nutr.* **35**, 393–403 (1989).
363. Status of Trace & Toxic Metals in Indian Rivers. (2019).
364. Spurr, R. A. & Myers, H. Quantitative Analysis of Anatase-Rutile Mixtures with an X-Ray Diffractometer. *Anal. Chem.* **29**, 760–762 (1957).
365. Gupta, K. K. *et al.* Effect of Anatase/Rutile TiO₂ Phase Composition on Arsenic Adsorption. *J. Dispers. Sci. Technol.* **34**, 1043–1052 (2013).
366. Lin, Z. & Puls, R. W. Effect of impurities associated with aluminosilicates on arsenic sorption and oxidation. *Hydrol. Sci. Technol.* **15**, 130–137 (1999).
367. Thommes, M. *et al.* Physisorption of gases, with special reference to the evaluation of surface area and pore size distribution (IUPAC Technical Report). *Pure Appl. Chem.* **87**, 1051–1069 (2015).
368. Sotomayor, F. J., Cychosz, K. A. & Thommes, M. Characterization of Micro/Mesoporous Materials by Physisorption: Concepts and Case Studies. *Acc. Mater. Surf. Res* **3**, 34–50 (2018).
369. Sekiya, T., Ichimura, K., Igarashi, M. & Kurita, S. Absorption spectra of anatase TiO₂ single crystals heat-treated under oxygen atmosphere. *J. Phys. Chem. Solids* **61**, 1237–1242 (2000).
370. Randorn, C. & Irvine, J. T. S. Synthesis and visible light photoactivity of a high temperature stable yellow TiO₂ photocatalyst. *J. Mater. Chem.* **20**, 8700–8704 (2010).
371. Dette, C. *et al.* TiO₂ anatase with a bandgap in the visible region. *Nano Lett.* **14**, 6533–6538 (2014).
372. Luo, H. *et al.* Photocatalytic Activity Enhancing for Titanium Dioxide by Co-doping with Bromine and Chlorine. *Chem. Mater.* **16**, 846–849 (2004).
373. Vickerman, J. S. & Gilmore, I. S. *Surface Analysis – The Principal Techniques*, 2nd Edition. (John Wiley & Sons, Inc., 2009). doi:10.1002/9780470721582.
374. Serrano, S., O'Day, P. A., Vlassopoulos, D., García-González, M. T. & Garrido, F. A surface complexation and ion exchange model of Pb and Cd competitive sorption on natural soils. *Geochim. Cosmochim. Acta* **73**, 543–558 (2009).
375. Lewis, T. M. Sorption of Metals to Clay Minerals in the Presence of Complexing Organic Ligands. (Doctoral dissertation or master's thesis). (Loughborough University, 2008).
376. Ebong, F. S. & Evans, N. Modelling the Sorption of 63 Ni to Granitic Materials: Application of the Component Additive Model. *J. Environ. Sci. Eng. B* **1** 281–292 (2012).
377. Gunnarsson, M. Surface Complexation at the Iron Oxide/Water Interface. (Doctoral dissertation or master's thesis). (University of Gothenberg, 2002).

378. Kosmulski, M. Isoelectric points and points of zero charge of metal (hydr)oxides: 50 years after Parks' review. *Adv. Colloid Interface Sci.* **238**, 1–61 (2016).
379. Vakros, J., Kordulis, C. & Lycourghiotis, A. Potentiometric mass titrations: a quick scan for determining the point of zero charge. *Chem. Commun. (Camb)*. 1980–1981 (2002) doi:10.1039/b205398e.
380. Bourikas, K., Vakros, J., Kordulis, C. & Lycourghiotis, A. Potentiometric Mass Titrations: Experimental and Theoretical Establishment of a New Technique for Determining the Point of Zero Charge (PZC) of Metal (Hydr)Oxides. *J. Phys. Chem. B* **107**, 9441–9451 (2003).
381. Hasani Bijarbooneh, F. *et al.* Aqueous colloidal stability evaluated by zeta potential measurement and resultant TiO₂ for superior photovoltaic performance. *J. Am. Ceram. Soc.* **96**, 2636–2643 (2013).
382. Song, J. *et al.* Surface complexation modeling of calcite zeta potential measurements in brines with mixed potential determining ions (Ca²⁺, CO₃²⁻, Mg²⁺, SO₄²⁻) for characterizing carbonate wettability. *J. Colloid Interface Sci.* **506**, 169–179 (2017).
383. Bargar, J. R., Kubicki, J. D., Reitmeyer, R. & Davis, J. A. ATR-FTIR spectroscopic characterization of coexisting carbonate surface complexes on hematite. *Geochim. Cosmochim. Acta* **69**, 1527–1542 (2005).
384. Rahnemaie, R., Hiemstra, T. & van Riemsdijk, W. H. Carbonate adsorption on goethite in competition with phosphate. *J. Colloid Interface Sci.* **315**, 415–425 (2007).
385. Kosmulski, M. The significance of the difference in the point of zero charge between rutile and anatase. *Adv. Colloid Interface Sci.* **99**, 255–264 (2002).
386. Prasad, P. S. R. *et al.* In situ FTIR study on the dehydration of natural goethite. *J. Asian Earth Sci.* **27**, 503–511 (2006).
387. Ruan, H. D., Frost, R. L., Kloprogge, J. T. & Duong, L. Infrared spectroscopy of goethite dehydroxylation: III. FT-IR microscopy of in situ study of the thermal transformation of goethite to hematite. *Spectrochim. Acta - Part A Mol. Biomol. Spectrosc.* **58**, 967–981 (2002).
388. Karkare, M. M. Choice of precursor not affecting the size of anatase TiO₂ nanoparticles but affecting morphology under broader view. *Int. Nano Lett.* **4**, 111 (2014).
389. Belhadj, H., Hakki, A., Robertson, P. K. J. & Bahnemann, D. W. In situ ATR-FTIR study of H₂O and D₂O adsorption on TiO₂ under UV irradiation. *Phys. Chem. Chem. Phys.* **17**, 22940–22946 (2015).
390. Kauffman, K. L., Culp, J. T., Goodman, A. & Matranga, C. FT-IR study of CO₂ adsorption in a dynamic copper(II) benzoate-pyrazine host with CO₂-CO₂ interactions in the adsorbed state. *J. Phys. Chem. C* **115**, 1857–1866 (2011).
391. Rother, G. *et al.* FT-IR study of CO₂ interaction with Na⁺ exchanged montmorillonite. *Appl. Clay Sci.* **114**, 61–68 (2015).
392. Mino, L., Spoto, G. & Ferrari, A. M. CO₂ capture by TiO₂ anatase surfaces: A combined DFT and FTIR study. *J. Phys. Chem. C* **118**, 25016–25026 (2014).
393. Genge, M. J., Jones, A. P. & Price, G. D. An infrared and Raman study of carbonate glasses : Implications for the structure of carbonatite magmas. *59*, 927–937 (1995).
394. Propylene Carbonate. <https://webbook.nist.gov/cgi/cbook.cgi?ID=C108327&Units=SI&Type=IR-SPEC&Index=1#IR-SPEC> [Accessed: 6 May 2019].
395. Diphenyl carbonate. <https://webbook.nist.gov/cgi/cbook.cgi?ID=C102090&Units=SI&Type=IR-SPEC&Index=0#IR-SPEC> [Accessed: 6 May 2019].
396. Tso, T.-L., Diem, M. & Lee, E. K. C. Oxidation of formyl radical in solid O₂ at 13 K: formation of formic acid and formylperoxy radical, HC(O)OO. *Chem. Phys. Lett.* **91**, 339–342 (1982).
397. Yang, R., Yu, L., Zeng, A. & Zhou, M. Infrared Spectrum of the Formylperoxy Radical in Solid Argon. *J. Phys. Chem. A* **108**, 4228–4231 (2004).
398. Bruckman, V. J. & Wriessnig, K. Improved soil carbonate determination by FT-IR and X-ray analysis. *Environ. Chem. Lett.* **11**, 65–70 (2013).
399. Zhao, D., Wang, X., Yang, S., Guo, Z. & Sheng, G. Impact of water quality parameters on the sorption of U(VI) onto hematite. *J. Environ. Radioact.* **103**, 20–29 (2012).
400. Behrad, F., Helmi Rashid Farimani, M., Shahtahmasebi, N., Rezaee Roknabadi, M. & Karimipour, M. Synthesis and characterization of Fe₃O₄/TiO₂ magnetic and photocatalyst bifunctional core-shell with superparamagnetic performance. *Eur. Phys. J. Plus* **130**, 144 (2015).

401. Yu, J. G. *et al.* The Effect of Calcination Temperature on the Surface Microstructure and Photocatalytic Activity of TiO₂ Thin Films Prepared by Liquid Phase Deposition. *J. Phys. Chem. B* **107**, 13871–13879 (2003).
402. Villalobos, M. & Leckie, J. O. Surface Complexation Modeling and FTIR Study of Carbonate Adsorption to Goethite. *J. Colloid Interface Sci.* **235**, 15–32 (2001).
403. Roonasi, P. & Holmgren, A. An ATR-FTIR study of carbonate sorption onto magnetite. in *Surface and Interface Analysis* vol. 42 1118–1121 (2010).
404. Bhattacharyya, K., Wu, W., Weitz, E., Vijayan, B. K. & Gray, K. A. Probing water and CO₂ interactions at the surface of collapsed titania nanotubes using IR spectroscopy. *Molecules* **20**, 15469–15487 (2015).
405. Su, C. & Suarez, D. L. In situ infrared speciation of adsorbed carbonate on aluminium and iron oxides. *Clays Clay Miner.* **45**, 814–825 (1997).
406. Lefèvre, G. In situ Fourier-transform infrared spectroscopy studies of inorganic ions adsorption on metal oxides and hydroxides. *Adv. Colloid Interface Sci.* **107**, 109–123 (2004).
407. Zhao, K. & Guo, H. Behavior and mechanism of arsenate adsorption on activated natural siderite: Evidences from FTIR and XANES analysis. *Environ. Sci. Pollut. Res.* **21**, 1944–1953 (2014).
408. Ding, C., Cheng, W., Jin, Z. & Sun, Y. Plasma synthesis of β-cyclodextrin/Al(OH)₃ composites as adsorbents for removal of UO₂⁺² from aqueous solutions. *J. Mol. Liq.* **207**, 224–230 (2015).
409. Alessi, D. S. & Fein, J. B. Cadmium adsorption to mixtures of soil components: Testing the component additivity approach. *Chem. Geol.* **270**, 186–195 (2010).
410. Gustafsson, J. P. Modelling competitive anion adsorption on oxide minerals and an allophane-containing soil. *Eur. J. Soil Sci.* **52**, 639–653 (2001).
411. Dong, W. & Wan, J. Additive surface complexation modeling of uranium(VI) adsorption onto quartz-sand dominated sediments. *Environ. Sci. Technol.* **48**, 6569–6577 (2014).
412. Mourdikoudis, S., Pallares, R. M. & Thanh, N. T. K. Characterization techniques for nanoparticles: Comparison and complementarity upon studying nanoparticle properties. *Nanoscale* **10**, 12871–12934 (2018).
413. Motuzas, A., Vaisvalavicius, R. & Prosyčevas, I. Application of new physical chemical methods in soil ecological investigations. *Environ. Sci. Pollut. Res.* **9**, 55–62 (2002).
414. Goebel, D., Bruckner, B., Roth, D., Ahamer, C. & Bauer, P. Low-energy ion scattering: A quantitative method? *Nucl. Instruments Methods Phys. Res. Sect. B Beam Interact. with Mater. Atoms* **354**, 3–8 (2015).
415. Cushman, C. V. *et al.* Low energy ion scattering (LEIS). A practical introduction to its theory, instrumentation, and applications. *Anal. Methods* **8**, 3419–3439 (2016).
416. van Leerdam, G. C. Surface analysis of catalysts by low-energy ion scattering. (Doctoral dissertation or master's thesis). (Eindhoven University of Technology, 1991). doi:10.6100/IR345264.
417. Almeida, R. M., Jain, H. & Pantano, C. G. Low-Energy Ion-Scattering Spectroscopy of Modified Silicate Glasses. *J. Am. Ceram. Soc.* **99**, 1259–1265 (2016).
418. ter Veen, H. R. J., Kim, T., Wachs, I. E. & Brongersma, H. H. Applications of High Sensitivity-Low Energy Ion Scattering (HS-LEIS) in heterogeneous catalysis. *Catal. Today* **140**, 197–201 (2009).
419. Ayawei, N., Ebelegi, A. N. & Wankasi, D. Modelling and Interpretation of Adsorption Isotherms. *J. Chem.* **2017**, (2017).
420. Batool, F., Akbar, J., Iqbal, S., Noreen, S. & Bukhari, S. N. A. Study of Isothermal, Kinetic, and Thermodynamic Parameters for Adsorption of Cadmium: An Overview of Linear and Nonlinear Approach and Error Analysis. *Bioinorg. Chem. Appl.* **2018**, (2018).
421. Mamidy-Pajany, Y., Hurel, C., Marmier, N. & Roméo, M. Arsenic(V) adsorption from aqueous solution onto goethite, hematite, magnetite and zero-valent iron: Effects of pH, concentration and reversibility. *Desalination* **281**, 93–99 (2011).
422. Jeong, Y. *et al.* Evaluation of iron oxide and aluminum oxide as potential arsenic(V) adsorbents. *Chem. Eng. Process.* **46**, 1030–1039 (2007).
423. Jia, Y., Xu, L., Fang, Z. & Demopoulos, G. P. Observation of surface precipitation of arsenate on ferrihydrite. *Environ. Sci. Technol.* **40**, 3248–3253 (2006).
424. Lützenkirchen, J. & Behra, P. On the surface precipitation model for cation sorption at the (hydr)oxide water interface. *Aquat. Geochemistry* **1**, 375–397 (1995).

425. Hu, W., Xie, J., Chau, H. W. & Si, B. C. Evaluation of parameter uncertainties in nonlinear regression using Microsoft Excel Spreadsheet. *Environ. Syst. Res.* **4**, (2015).
426. Zhu, H. Y., Ni, L. A. & Lu, G. Q. Pore-size-dependent equation of state for multilayer adsorption in cylindrical mesopores. *Langmuir* **15**, 3632–3641 (1999).
427. Fripiat, J. J., Gatineau, L. & van Damme, H. Multilayer Physical Adsorption on Fractal Surfaces. *Langmuir* **2**, 562–567 (1986).
428. S. Pantuso, F., L. Gómez Castro, M., C. Larregain, C., Coscarello, E. & J. Aguerre, R. Kinetic Approach to Multilayer Sorption: Equations of Isotherm and Applications. in *Food Engineering* (IntechOpen, 2019). doi:10.5772/intechopen.82669.
429. Kitadai, N., Nishiuchi, K. & Tanaka, M. ScienceDirect A comprehensive predictive model for sulfate adsorption on oxide minerals. *Geochim. Cosmochim. Acta* **238**, 150–168 (2018).
430. Wang, Y., Liu, W., Wang, T. & Ni, J. Arsenate adsorption onto Fe-TNTs prepared by a novel water-ethanol hydrothermal method: Mechanism and synergistic effect. *J. Colloid Interface Sci.* **440**, 253–262 (2015).
431. Myneni, S. C. B., Traina, S. J., Waychunas, G. A. & Logan, T. J. Experimental and theoretical vibrational spectroscopic evaluation of arsenate coordination in aqueous solutions, solids, and at mineral-water interfaces. *Geochim. Cosmochim. Acta* **62**, 3285–3300 (1998).
432. Ela, W., Farrell, J., Root, R. A., Chorover, J. & Gao, X. Effect of silicic acid on arsenate and arsenite retention mechanisms on 6-L ferrihydrite: A spectroscopic and batch adsorption approach. *Appl. Geochemistry* **38**, 110–120 (2013).
433. Myneni, S. A. C. B. M., Raina, S. A. J. T., Aychunas, G. L. A. W. & Ogan, T. E. J. L. Vibrational spectroscopy of functional group chemistry and arsenate coordination in ettringite. **62**, 3499–3514 (1998).
434. Sumin de Portilla, V. I. The nature of hydrogen bonds and water legrandite by IR spectroscopy. *Am. Mineral.* **61**, 95–99 (1976).
435. Li, Z. *et al.* Characterization on arsenic sorption and mobility of the sediments of Chia-Nan Plain, where Blackfoot disease occurred. *Environ. Earth Sci.* **64**, 823–831 (2011).
436. Bahfenne, S. & Frost, R. L. A review of the vibrational spectroscopic studies of arsenite, antimonite, and antimonate minerals. *Appl. Spectrosc. Rev.* **45**, 101–129 (2010).
437. Makreski, P., Todorov, J., Makrievski, V., Pejov, L. & Jovanovski, G. Vibrational spectra of the rare-occurring complex hydrogen arsenate minerals pharmacolite, picropharmacolite, and vladimirite. *J. Raman Spectrosc.* **49**, 747–763 (2017).
438. Miller, F. A. & Wilkins, C. H. Infrared spectra and characteristic frequencies of inorganic ions. *Anal. Chem.* **24**, 1253–1294 (1952).
439. Mahanta, N. & Chen, J. P. A novel route to the engineering of zirconium immobilized nano-scale carbon for arsenate removal from water. *J. Mater. Chem. A* **1**, 8636–8644 (2013).
440. Perez, J. *et al.* Arsenic sorption onto an aluminum oxyhydroxide-poly[(4-vinylbenzyl)trimethylammonium chloride] hybrid sorbent. *RSC Adv.* **6**, 28379–28387 (2016).
441. Feldhoff, R., Huth-Fehre, T. & Cammann, K. Detection of inorganic wood preservatives on timber by near infrared spectroscopy. *J. Near Infrared Spectrosc.* **6**, 171–173 (1998).
442. Szymanski, H. A., Marabella, L., Hoke, J. & Harter, J. Infrared and Raman Studies of Arsenic Compounds. *Appl. Spectrosc.* **22**, 297–304 (1968).
443. Frost, R. L., Lopes, A., Scholz, R. & Xi, Y. Infrared and Raman spectroscopic characterization of the arsenate mineral ceruleite Cu₂Al₇(AsO₄)₄(OH)₁₃·11.5(H₂O). *Spectrochim. Acta - Part A Mol. Biomol. Spectrosc.* **116**, 518–523 (2013).
444. Frost, R. L., Kloprogge, J. T. & Martens, W. N. Raman spectroscopy of the arsenates and sulphates of the tsumcorite mineral group. *J. Raman Spectrosc.* **35**, 28–35 (2004).
445. León-Pimentel, C. I. *et al.* On the aqueous solvation of AsO(OH)₃ vs. As(OH)₃. Born-Oppenheimer molecular dynamics density functional theory cluster studies. *Phys. Chem. Chem. Phys.* **20**, 16568–16578 (2018).
446. Fukushi, K. & Sverjensky, D. A. A predictive model (ETLM) for arsenate adsorption and surface speciation on oxides consistent with spectroscopic and theoretical molecular evidence. *Geochim. Cosmochim. Acta* **71**, 3717–3745 (2007).
447. Sverjensky, D. A. & Fukushi, K. Anion Adsorption on Oxide Surfaces: Inclusion of the Water Dipole in Modeling the Electrostatics of Ligand Exchange. **40**, 263–271 (2006).
448. Jonsson, C. M., Jonsson, C. L., Sverjensky, D. A., Cleaves, H. J. & Hazen, R. M. Attachment of

- L-Glutamate to Rutile (r-TiO₂): A Potentiometric, Adsorption, and Surface Complexation Study. *Langmuir* **25**, 12127–12135 (2009).
449. Sverjensky Sahai, N., D. A. Theoretical predicton of single-site surface protonation equilibrium constants for oxides and silicates in water. *Geochim. Cosmochim. Acta* **60**, 3773–3798 (1996).
450. Sverjensky, D. A. Interpretation and prediction of triple-layer model capacitances and the structure of the oxide-electrolyte-water interface. *Geochim. Cosmochim. Acta* **65**, 3643–3655 (2001).
451. Farley, K. J., Dzombak, D. A. & Morel, F. M. M. A surface precipitation model for the sorption of cations on metal oxides. *J. Colloid Interface Sci.* **106**, 226–242 (1985).
452. Schmidt, J. & Vogelsberger, W. Dissolution kinetics of titanium dioxide nanoparticles: The observation of an unusual kinetic size effect. *J. Phys. Chem. B* **110**, 3955–3963 (2006).
453. Cheah, S. F., Kraemer, S. M., Cervini-Silva, J. & Sposito, G. Steady-state dissolution kinetics of goethite in the presence of desferrioxamine B and oxalate ligands: Implications for the microbial acquisition of iron. *Chem. Geol.* **198**, 63–75 (2003).
454. Xu, N. & Gao, Y. Characterization of hematite dissolution affected by oxalate coating, kinetics and pH. *Appl. Geochemistry* **23**, 783–793 (2008).
455. Knorring, O. V., Sahama, T. G. & Rehtijärvi, P. Karibibite, a new FeAs mineral from South West Africa. *Lithos* **6**, 265–271 (1973).
456. Colombo, F. et al. Crystal structure determination of karibibite, an Fe³⁺ arsenite, using electron diffraction tomography. *Mineral. Mag.* **81**, 1191–1202 (2017).
457. Schecher, W. D. & McAvoy, D. C. *MINEQL+ V.4.5 Users Manual*. (Hallowell, 1998).
458. Gao, Y. & Mucci, A. Acid base reactions, phosphate and arsenate complexation, and their competitive adsorption at the surface of goethite in 0.7 M NaCl solution. *Geochim. Cosmochim. Acta* **65**, 2361–2378 (2001).
459. Manning, B. A. & Goldberg, S. Modeling Arsenate Competitive Adsorption on Kaolinite, Montmorillonite and Illite. *Clays Clay Miner.* **44**, (1996).
460. Hwang, Y. S. & Lenhart, J. J. The dependence of hematite site-occupancy standard state triple-layer model parameters on inner-layer capacitance. *J. Colloid Interface Sci.* **319**, 206–213 (2008).
461. Liang, L. Effects of Surface Chemistry on Kinetics of Coagulation of Submicron Iron Oxide Particles (α -Fe₂O₃) in Water. (Doctoral dissertation or master's thesis). (California Institute of Technology, 1988). doi:10.7907/4XGW-4G55.
462. Sprycha, R. Surface charge and adsorption of background electrolyte ions at anatase/electrolyte interface. *J. Colloid Interface Sci.* **102**, 173–185 (1984).
463. Mazinani, B., Masrom, A. K., Beitollahi, A. & Luque, R. Photocatalytic activity, surface area and phase modification of mesoporous SiO₂-TiO₂ prepared by a one-step hydrothermal procedure. *Ceram. Int.* **40**, 11525–11532 (2014).
464. Amano, F., Nogami, K., Tanaka, M. & Ohtani, B. Correlation between surface area and photocatalytic activity for acetaldehyde decomposition over bismuth tungstate particles with a hierarchical structure. *Langmuir* **26**, 7174–7180 (2010).
465. Jain, A. & Vaya, D. Photocatalytic activity of TiO₂ nanomaterial. *J. Chil. Chem. Soc.* **62**, (2017).
466. Moss, B. et al. Comparing photoelectrochemical water oxidation, recombination kinetics and charge trapping in the three polymorphs of TiO₂. *Sci. Rep.* **7**, 1–7 (2017).
467. Xu, T., Kamat, P. V. & O'Shea, K. E. Mechanistic evaluation of arsenite oxidation in TiO₂ assisted photocatalysis. *J. Phys. Chem. A* **109**, 9070–9075 (2005).
468. Ollis, D. Kinetics of photocatalyzed film removal on self-cleaning surfaces: Simple configurations and useful models. *Appl. Catal. B Environ.* **99**, 478–484 (2010).
469. Seinfeld, J. H. & Pandis, S. N. *Atmospheric Chemistry and Physics: From Air Pollution to Climate Change*. (Wiley-Blackwell, 2006). doi:10.5194/acp-5-139-2005.
470. Kafizas, A. et al. Water Oxidation Kinetics of Accumulated Holes on the Surface of a TiO₂ Photoanode: A Rate Law Analysis. *ACS Catal.* **7**, 4896–4903 (2017).
471. Mohamed, H. H., Alomair, N. A., Akhtar, S. & Youssef, T. E. Eco-friendly synthesized α -Fe₂O₃/TiO₂ heterojunction with enhanced visible light photocatalytic activity. *J. Photochem. Photobiol. A Chem.* **382**, (2019).
472. Fu, H. et al. A facile coating method to construct uniform porous α -Fe₂O₃@TiO₂ core-shell nanostructures with enhanced solar light photocatalytic activity. *Powder Technol.* **328**, 389–396

- (2018).
473. Wang, H. & Turner, J. A. Photoelectrochemistry of Hematite Thin Films. *ECS Trans.* **25**, 49–62 (2010).
474. Ward, M. D., White, J. R. & Bard, A. J. Electrochemical Investigation of the Energetics of Particulate Titanium Dioxide Photocatalysts. The Methyl Viologen-Acetate System. *J. Am. Chem. Soc.* **105**, 27–31 (1983).
475. Tamirat, A. G., Rick, J., Dubale, A. & Su, W. Nanoscale Horizons Using hematite for photoelectrochemical water splitting: a review of current progress and challenges. *Nanoscale Horizons* **1**, 243–267 (2016).
476. Kornweitz, H. & Meyerstein, D. The plausible role of carbonate in photo-catalytic water oxidation processes. *Phys. Chem. Chem. Phys.* **18**, 11069–11072 (2016).
477. Kláning, U. K., Bielski, B. H. J. & Sehested, K. Arsenic(IV). A Pulse-Radiolysis Study. *Inorg. Chem.* **28**, 2717–2724 (1989).
478. Bhardwaj, A., Rajput, R. & Misra, K. Status of Arsenic Remediation in India. in *Advances in Water Purification Techniques* 219–258 (Elsevier Inc., 2019). doi:10.1016/b978-0-12-814790-0.00009-0.
479. McCullagh, C., Skillen, N., Adams, M. & Robertson, P. K. J. J. Photocatalytic reactors for environmental remediation: A review. *J. Chem. Technol. Biotechnol.* **86**, 1002–1017 (2011).
480. Ali, I., Al-Othman, Z. A., Alwarthan, A., Asim, M. & Khan, T. A. Removal of arsenic species from water by batch and column operations on bagasse fly ash. *Environ. Sci. Pollut. Res.* **21**, 3218–3229 (2014).
481. Lekić, B. M., Marković, D. D., Rajaković-Ognjanović, V. N., Dukić, A. R. & Rajaković, L. V. Arsenic removal from water using industrial By-products. *J. Chem.* **2013**, (2013).
482. Luxton, T. P., Eick, M. J. & Rimstidt, D. J. The role of silicate in the adsorption/desorption of arsenite on goethite. *Chem. Geol.* **252**, 125–135 (2008).
483. Maiti, A., Basu, J. K. & De, S. Desorption kinetics and leaching study of arsenic from arsenite/arsenate-loaded Natural Laterite. *Int. J. Environ. Technol. Manag.* **12**, 294 (2010).
484. Strawn, D. G., Scheidegger, A. M. & Sparks, D. L. Kinetics and mechanisms of Pb(II) sorption and desorption at the aluminum oxide - Water interface. *Environ. Sci. Technol.* **32**, 2596–2601 (1998).
485. Khandker, S. R., Samad, H. A., Ali, R. & Barnes, D. F. Who benefits most from rural electrification? Evidence in India. *Energy J.* **35**, (2014).
486. Crank, J. *Mathematics of Diffusion*. (Oxford at the Clarendon Press, 1956).
487. Weber, W. Kinetics of Adsorption on Carbon from Solution. *J. Sanit. Eng. Div.* **89**, 31–60 (1963).
488. Qiu, H. *et al.* Critical review in adsorption kinetic models. *J. Zhejiang Univ. Sci. A* **10**, 716–724 (2009).
489. Lagergren, S. Zur theorie der sogenannten adsorption gelöster stoffe. *K. Svens. Vetenskapsakademiens. Handl.* **24**, 1–39 (1898).
490. Zeldowitsch, J. Über den mechanismus der katalytischen oxydation von CO an MnO₂. *Acta Physicochim. U.R.S.S.* **364**–449 (1934).
491. Simonin, J. P. On the comparison of pseudo-first order and pseudo-second order rate laws in the modeling of adsorption kinetics. *Chem. Eng. J.* **300**, 254–263 (2016).
492. Wang, Z. & Giammar, D. E. Tackling Deficiencies in the Presentation and Interpretation of Adsorption Results for New Materials. *Environ. Sci. Technol.* **53**, 5543–5544 (2019).
493. Plazinski, W., Dziuba, J. & Rudzinski, W. Modeling of sorption kinetics: The pseudo-second order equation and the sorbate intraparticle diffusivity. *Adsorption* **19**, 1055–1064 (2013).
494. Plazinski, W. & Rudzinski, W. Kinetics of adsorption at solid/Solution interfaces controlled by intraparticle diffusion: A theoretical analysis. *J. Phys. Chem. C* **113**, 12495–12501 (2009).
495. Manna, B. R., Dey, S., Debnath, S. & Ghosh, U. C. Removal of arsenic from groundwater using crystalline hydrous ferric oxide (CHFO). *Water Qual. Res. J. Canada* **38**, 193–210 (2003).
496. Singh, D. B., Prasad, G. & Rupainwar, D. C. Adsorption technique for the treatment of As(V)-rich effluents. *Colloids Surfaces A Physicochem. Eng. Asp.* **111**, 49–56 (1996).
497. Shipley, H. J., Engates, K. E. & Grover, V. A. Removal of Pb(II), Cd(II), Cu(II), and Zn(II) by hematite nanoparticles: Effect of sorbent concentration, pH, temperature, and exhaustion. *Environ. Sci. Pollut. Res.* **20**, 1727–1736 (2013).
498. Azizian, S. Kinetic models of sorption: A theoretical analysis. *J. Colloid Interface Sci.* **276**, 47–

- 52 (2004).
499. Maiti, A., DasGupta, S., Basu, J. K. & De, S. Batch and column study: Adsorption of arsenate using untreated laterite as adsorbent. *Ind. Eng. Chem. Res.* **47**, 1620–1629 (2008).
500. Zeng, H., Arashiro, M. & Giammar, D. E. Effects of water chemistry and flow rate on arsenate removal by adsorption to an iron oxide-based sorbent. *Water Res.* **42**, 4629–4636 (2008).
501. Dominguez, L., Economy, J., Benak, K. & Mangun, C. L. Anion exchange fibers for arsenate removal derived from a vinylbenzyl chloride precursor. *Polym. Adv. Technol.* **14**, 632–637 (2003).
502. Sarkar, S. Consumption pattern and determinants of nutritional intake among rural households of West Bengal, India. *J. Settlements Spat. Plan.* **6**, 85–94 (2015).
503. WHO Regional Office for South-East Asia. *Minimum water quantity needed for domestic uses. Technical Notes for Emergencies* (2005).
504. Goldberg, S. Sensitivity of surface complexation modeling to the surface site density parameter. *J. Colloid Interface Sci.* **145**, 1–9 (1991).
505. Fendorf, S., Eick, M. J., Grossl, P. & Sparks, D. L. Arsenate and chromate retention mechanisms on goethite. 1. Surface structure. *Environ. Sci. Technol.* **31**, 315–320 (1997).
506. Greskowiak, J., Gwo, J., Jacques, D., Yin, J. & Mayer, K. U. A benchmark for multi-rate surface complexation and 1D dual-domain multi-component reactive transport of U(VI). *Comput. Geosci.* **19**, 585–597 (2015).
507. Cates, E. L. Photocatalytic water treatment: So where are we going with this? *Environ. Sci. Technol.* **51**, 757–758 (2017).
508. Chauhan, A. et al. Janus nanostructures for heterogeneous photocatalysis. *Appl. Phys. Rev.* **5**, (2018).
509. Filatova, E. O. & Konashuk, A. S. Interpretation of the Changing the Band Gap of Al₂O₃ Depending on Its Crystalline Form: Connection with Different Local Symmetries. *J. Phys. Chem. C* **119**, 20755–20761 (2015).
510. French, R. H. Electronic Band Structure of Al₂O₃, with Comparison to Alon and AlN. *J. Am. Ceram. Soc.* **73**, 477–489 (1990).
511. Yazdanmehr, M., Asadabadi, S. J., Nourmohammadi, A., Ghasemzadeh, M. & Rezvanian, M. Electronic structure and bandgap of γ-Al₂O₃ compound using mBJ exchange potential. *Nanoscale Res. Lett.* **7**, (2012).
512. Costina, I. & Franchy, R. Band gap of amorphous and well-ordered Al₂O₃ on Ni₃Al(100). *Appl. Phys. Lett.* **78**, (2001).
513. Srikant, V. & Clarke, D. R. On the optical band gap of zinc oxide. *J. Appl. Phys.* **83**, (1998).
514. Daikopoulos, C. et al. Arsenite remediation by an amine-rich graphitic carbon nitride synthesized by a novel low-temperature method. *Chem. Eng. J.* **256**, 347–355 (2014).
515. Cui, H., Su, Y., Li, Q., Gao, S. & Shang, J. K. Exceptional arsenic (III,V) removal performance of highly porous, nanostructured ZrO₂ spheres for fixed bed reactors and the full-scale system modeling. *Water Res.* **47**, 6258–6268 (2013).
516. Hua, C., Jagner, D. & Renman, L. Automated determination of total arsenic in sea water by flow constant-current stripping analysis with gold fibre electrodes. *Anal. Chim. Acta* **201**, 263–268 (1987).
517. Greulach, U. & Henze, G. Analysis of arsenic(V) by cathodic stripping voltammetry. *Anal. Chim. Acta* **306**, 217–223 (1995).
518. Sun, Y. C., Mierzwa, J. & Yang, M. H. New method of gold-film electrode preparation for anodic stripping voltammetric determination of arsenic (III and V) in seawater. *Talanta* **44**, 1379–1387 (1997).
519. Kopanica, M. & Novotný, L. Determination of traces of arsenic(III) by anodic stripping voltammetry in solutions, natural waters and biological material. *Anal. Chim. Acta* **368**, 211–218 (1998).
520. Sancho, D., Vega, M., Debán, L., Pardo, R. & González, G. Determination of copper and arsenic in refined beet sugar by stripping voltammetry without sample pretreatment. *Analyst* **123**, 743–7 (1998).
521. Laschi, S., Bagni, G., Palchetti, I. & Mascini, M. As(III) Voltammetric Detection by Means of Disposable Screen-Printed Gold Electrochemical Sensors. *Anal. Lett.* **40**, 3002–3013 (2007).
522. Shimada, K. A. and K. Anodic Stripping Voltammetry of Arsenic(III) in the Presence of Copper(II) at a Mechanical Pencil Lead Electrode as a Screening Tool in Environmental Water. *61*, 411–

- 418 (2012).
523. Yang, M. *et al.* Electrochemical Detection of Trace Arsenic(III) by Nanocomposite of Nanorod-Like α -MnO₂Decorated with ~5 nm Au Nanoparticles: Considering the Change of Arsenic Speciation. *Anal. Chem.* **88**, 9720–9728 (2016).
524. Marei, M. M., Kaht, K. L., Roussel, T. J., Keynton, R. S. & Baldwin, R. P. Measurement of As(III) with in situ subtraction of background and interferent signals by double potential step-anodic stripping coulometry. *Sensors Actuators B Chem.* **301**, 127005 (2019).
525. Ullattil, S. G. & Periyat, P. A 'one pot' gel combustion strategy towards Ti ³⁺ self-doped 'black' anatase TiO_{2-x} solar photocatalyst. *J. Mater. Chem. A* **4**, 5854–5858 (2016).
526. Byrne, C., Fagan, R., Hinder, S., McCormack, D. E. & Pillai, S. C. New approach of modifying the anatase to rutile transition temperature in TiO₂ photocatalysts. *RSC Adv.* **6**, (2016).
527. Krivtsov, I. *et al.* Exceptional thermal stability of undoped anatase TiO₂ photocatalysts prepared by a solvent-exchange method. *RSC Adv.* **5**, (2015).
528. Baltrusaitis, J., Cwiertny, D. M. & Grassian, V. H. Adsorption of sulfur dioxide on hematite and goethite particle surfaces. *Phys. Chem. Chem. Phys.* **9**, 5542–5554 (2007).
529. Preocanin, T. & Kallay, N. Point of zero charge and surface charge density of TiO₂ in aqueous electrolyte solution as obtained by potentiometric mass titration. *Croat. Chem. Acta* **79**, 95–106 (2006).
530. Somasundaran, P. *Encyclopedia of surface and colloid science*. (Taylor & Francis, 2006).
531. Sahai, N. & Sverjensky, D. A. GEOSURF: A computer program for modeling adsorption on mineral surfaces from aqueous solution. *Comput. Geosci.* **24**, 853–873 (1998).
532. Brown, M. A., Goel, A. & Abbas, Z. Effect of Electrolyte Concentration on the Stern Layer Thickness at a Charged Interface. *Angew. Chemie - Int. Ed.* **55**, 3790–3794 (2016).
533. Lu, J. The Constant Capacitance Model and Variable Ionic Strength : An Evaluation of Possible Applications and Applicability. *18*, 8–18 (1999).
534. Goldberg, S. Adsorption models incorporated into chemical equilibrium models. in *Chemical Equilibrium and Reaction Models* 75–95 (Wiley, 1995). doi:10.2136/sssaspecpub42.c5.
535. Goldberg, S. Constant Capacitance Model: Chemical Surface Complexation Model for Describing Adsorption of Toxic Trace Elements on Soil Minerals. in *Emerging Technologies in Hazardous Waste Management III* (eds. Tedder, D. W. & Pohland, F. G.) (American Chemical Society, 1993).
536. Gouy, M. Sur la constitution de la charge électrique à la surface d'un électrolyte. *J. Phys. Théorique Appliquée* **9**, 457–468 (1910).
537. Chapman, D. L. LI. A contribution to the theory of electrocapillarity. *London, Edinburgh, Dublin Philos. Mag. J. Sci.* **25**, 475–481 (1913).
538. Shaw, D. J. *Introduction to Colloid and Surface Chemistry*. (Butterworth & Co. Limited, 1966).
539. Butt, H., Graf, K. & Kappl, M. *Physics and Chemistry of Interfaces*. (Wiley, 2003). doi:10.1002/3527602313.
540. Hiemstra, T. Surface complexation at mineral interfaces : Multisite and Charge Distribution approach. (Doctoral dissertation or master's thesis). (Wageningen University, 2010).
541. Hiemstra, T. & van Riemsdijk, W. H. A Surface Structural Approach to Ion Adsorption: The Charge Distribution (CD) Model. *J. Colloid Interface Sci.* **179**, 488–508 (1996).
542. Vieira, A. R. Surface Complexation Modeling of Pb(II), Cd(II) and Se(IV) onto Iron Hydroxides in Single and Bisolute Systems. (Doctoral dissertation or master's thesis). (The University of Texas at Austin, 2006).
543. Visual MINTEQ – a free equilibrium speciation model. <https://vminteq.lwr.kth.se/> [Accessed: 7 June 2020].
544. PHREEQC Version 3. <https://www.usgs.gov/software/phreeqc-version-3> [Accessed: 7 June 2020].
545. Basic Stern Model in PHREEQC. <https://phreeqcusers.org/index.php?topic=959.0> (2017).
546. Dzombak, DA, Morel, F. *Surface Complexation Modeling: Hydrous Ferric Oxide*. (Wiley, 1990). doi:10.1016/S1573-4285(06)80052-9.
547. Kriaa, A., Hamdi, N., Goncalves, M. A. & Srasra, E. Acid-base properties of tunisian glauconite in aqueous suspensions. *Int. J. Electrochem. Sci.* **4**, 535–550 (2009).
548. Gligorovski, S., Strekowski, R., Barbat, S. & Vione, D. Environmental Implications of Hydroxyl Radicals (\bullet OH). *Chem. Rev.* **115**, 13051–13092 (2015).

549. Giraldo-Aguirre, A. L., Erazo-Erazo, E. D., Flórez-Acosta, O. A., Serna-Galvis, E. A. & Torres-Palma, R. A. TiO₂ photocatalysis applied to the degradation and antimicrobial activity removal of oxacillin: Evaluation of matrix components, experimental parameters, degradation pathways and identification of organics by-products. *J. Photochem. Photobiol. A Chem.* **311**, 95–103 (2015).
550. Iguchi, S., Teramura, K., Hosokawa, S. & Tanaka, T. Effect of the chloride ion as a hole scavenger on the photocatalytic conversion of CO₂ in an aqueous solution over Ni-Al layered double hydroxides. *Phys. Chem. Chem. Phys.* **17**, 17995–18003 (2015).
551. Giraldo, A. L., Erazo-Erazo, E. D., Flórez-Acosta, O. A., Serna-Galvis, E. A. & Torres-Palma, R. A. Degradation of the antibiotic oxacillin in water by anodic oxidation with Ti/IrO₂ anodes: Evaluation of degradation routes, organic by-products and effects of water matrix components. *Chem. Eng. J.* **279**, 103–114 (2015).
552. Ajmal, A., Majeed, I., Malik, R. N., Idriss, H. & Nadeem, M. A. Principles and mechanisms of photocatalytic dye degradation on TiO₂ based photocatalysts: A comparative overview. *RSC Advances* vol. 4 37003–37026 (2014).
553. Sayama, K. & Arakawa, H. Effect of carbonate addition on the photocatalytic decomposition of liquid water over a ZrO₂ catalyst. *J. Photochem. Photobiol. A Chem.* **6030**, (1996).
554. Copeland, A. R. I. & Lytle, D. A. Measuring the oxidation – reduction potential of important oxidants in drinking water. *J. AWWA* (2014) doi:10.5942/jawwa.2014.106.0002.
555. Zilberg, S., Mizrahi, A., Meyerstein, D. & Kornweitz, H. Carbonate and carbonate anion radicals in aqueous solutions exist as CO₃(H₂O)⁶²⁻ and CO₃(H₂O)⁶⁻ respectively: The crucial role of the inner hydration sphere of anions in explaining their properties. *Phys. Chem. Chem. Phys.* **20**, 9429–9435 (2018).
556. Vanýsek, P. Electrochemical Series. in *Handbook of Chemistry and Physics* 5–80 (Chemical Rubber Company, 2012).
557. Burnside, S., Moser, J. E., Brooks, K., Grätzel, M. & Cahen, D. Nanocrystalline mesoporous strontium titanate as photoelectrode material for photosensitized solar devices: Increasing photovoltage through flatband potential engineering. *J. Phys. Chem. B* **103**, 9328–9332 (1999).
558. Kim, W., Tachikawa, T., Moon, G. H., Majima, T. & Choi, W. Molecular-level understanding of the photocatalytic activity difference between anatase and rutile nanoparticles. *Angew. Chemie - Int. Ed.* **53**, 14036–14041 (2014).
559. Kirsch, M., Lomonosova, E. E., Korth, H. G., Sustmann, R. & De Groot, H. Hydrogen peroxide formation by reaction of peroxy nitrite with HEPES and related tertiary amines: Implications for a general mechanism. *J. Biol. Chem.* **273**, 12716–12724 (1998).
560. Xiao, X. et al. Zwitterionic buffer-induced visible light excitation of TiO₂ for efficient pollutant photodegradation. *RSC Adv.* **6**, 35449–35454 (2016).
561. Mezenner, N. Y. & Bensmaili, A. Kinetics and thermodynamic study of phosphate adsorption on iron hydroxide-eggshell waste. *Chem. Eng. J.* **147**, 87–96 (2009).
562. Lim, S. F. & Lee, A. Y. W. Kinetic study on removal of heavy metal ions from aqueous solution by using soil. *Environ. Sci. Pollut. Res.* **22**, 10144–58 (2015).
563. Rahdar, S., Rahdar, A., Zafar, M. N., Shafqat, S. S. & Ahmadi, S. Synthesis and characterization of MgO supported Fe-Co-Mn nanoparticles with exceptionally high adsorption capacity for Rhodamine B dye. *J. Mater. Res. Technol.* **8**, 3800–3810 (2019).
564. Natarajan, R. & Manivasagan, R. Biosorptive Removal of Heavy Metal onto Raw Activated Sludge: Parametric, Equilibrium, and Kinetic Studies. *J. Environ. Eng. (United States)* **142**, (2016).
565. Aworanti, A. & Agarry, S. E. Kinetics, Isothermal and Thermodynamic Modelling Studies of Hexavalent Chromium Ions Adsorption from Simulated Wastewater onto Parkia biglobosa - Sawdust Derived Acid-Steam Activated. *Appl. J. Environ. Eng. Sci.* **3**, 58–76 (2017).
566. Nandhakumar, V. Adsorption of Rose Bengal Dye from Aqueous Solution onto Zinc Chloride Activated Carbon. *SOJ Mater. Sci. Eng.* **3**, 1–9 (2015).
567. Debnath, A., Bera, A., Chattopadhyay, K. K. & Saha, B. Facile additive-free synthesis of hematite nanoparticles for enhanced adsorption of hexavalent chromium from aqueous media: Kinetic, isotherm, and thermodynamic study. *Inorg. Nano-Metal Chem.* **47**, 1605–1613 (2017).
568. Sağ, Y. & Aktay, Y. Mass transfer and equilibrium studies for the sorption of chromium ions onto chitin. *Process Biochem.* **36**, 157–173 (2000).
569. Robalds, A., Dreijalte, L., Bikovens, O. & Klavins, M. A novel peat-based biosorbent for the

- removal of phosphate from synthetic and real wastewater and possible utilization of spent sorbent in land application. *Desalin. Water Treat.* **57**, 13285–13294 (2016).
570. Abdelwahab, O., El Sikaily, A., Khaled, A. & El Nemr, A. Mass-transfer processes of chromium(VI) adsorption onto guava seeds. *Chem. Ecol.* **23**, 73–85 (2007).
571. Reategui, M., Maldonado, H., Ly, M. & Guibal, E. Mercury(II) biosorption using *Lessonia* sp. kelp. *Appl. Biochem. Biotechnol.* **162**, 805–822 (2010).
572. Priyadarshini, B. et al. Kinetics, Thermodynamics and Isotherm studies on Adsorption of Eriochrome Black-T from aqueous solution using Rutile TiO₂. *IOP Conf. Ser. Mater. Sci. Eng.* **310**, (2018).
573. Staroń, P., Chwastowski, J. & Banach, M. Sorption behavior of methylene blue from aqueous solution by raphia fibers. *Int. J. Environ. Sci. Technol.* **16**, 8449–8460 (2019).
574. Di, E., Goo, H., Liu, Y. & Cheng, Z. Arsenate retention mechanisms on hematite with different morphologies evaluated using AFM, TEM measurements and vibrational spectroscopy ScienceDirect Arsenate retention mechanisms on hematite with different morphologies evaluated using AFM , TEM measure. *Geochim. Cosmochim. Acta* **237**, 155–170 (2018).
575. Suresh Kumar, P., Korving, L., Keesman, K. J., van Loosdrecht, M. C. M. & Witkamp, G. J. Effect of pore size distribution and particle size of porous metal oxides on phosphate adsorption capacity and kinetics. *Chem. Eng. J.* **358**, 160–169 (2019).
576. Tsai, W. T., Lai, C. W. & Hsien, K. J. Effect of particle size of activated clay on the adsorption of paraquat from aqueous solution. *J. Colloid Interface Sci.* **263**, 29–34 (2003).
577. Sun, X. et al. Phenol adsorption kinetics and isotherms on coal: effect of particle size. *Energy Sources, Part A Recover. Util. Environ. Eff.* 1–14 (2019) doi:10.1080/15567036.2019.1628130.
578. Xu, H. et al. Removal of quinoline using various particle sizes anthracite: Adsorption kinetics and adsorption isotherms. *Physicochem. Probl. Miner. Process.* **55**, 196–207 (2019).
579. Benavente, M. Adsorption of Metallic Ions onto Chitosan: Equilibrium and Kinetic Studies. (Doctoral dissertation or master's thesis). (KTH Royal Institute of Technology, 2008).
580. Gupta, G. S., Prasad, G., Panday, K. K. & Singh, V. N. Removal of chrome dye from aqueous solutions by fly ash. *Water. Air. Soil Pollut.* **37**, 13–24 (1988).
581. Dickson, D., Liu, G. & Cai, Y. Adsorption kinetics and isotherms of arsenite and arsenate on hematite nanoparticles and aggregates. *J. Environ. Manage.* **186**, 261–267 (2017).
582. Cheng, W. et al. Etching synthesis of iron oxide nanoparticles for adsorption of arsenic from water. *RSC Adv.* **6**, 15900–15910 (2016).
583. Monárez-Cordero, B. E., Amézaga-Madrid, P., Leyva-Porras, C. C., Pizá-Ruiz, P. & Miki-Yoshida, M. Study of the adsorption of arsenic (III and V) by magnetite nanoparticles synthetized via AACVD. *Mater. Res.* **19**, 103–112 (2016).
584. Baig, S. A. et al. Arsenic Removal from Aqueous Solutions Using Fe₃O₄-HBC Composite: Effect of Calcination on Adsorbents Performance. *PLoS One* **9**, (2014).
585. Roy, P. K., Choudhury, M. R. & Ali, M. A. As (III) and As (V) Adsorption on Magnetite Nanoparticles: Adsorption Isotherms, Effect of pH and phosphate, and Adsorption Kinetics. *Int. J. Chem. Environ. Eng.* **4**, (2013).
586. Wei, Y. et al. Efficient removal of arsenic from groundwater using iron oxide nanoneedle array-decorated biochar fibers with high Fe utilization and fast adsorption kinetics. *Water Res.* **167**, 115107 (2019).
587. Simsek, E. B. & Beker, U. Kinetic Performance of Aluminum and Iron Oxides in the Removal of Arsenate from Aqueous Environment. *J. Clean Energy Technol.* **2**, 206–209 (2014).
588. Jain, M. et al. Development of iron oxide/activated carbon nanoparticle composite for the removal of Cr(VI), Cu(II) and Cd(II) ions from aqueous solution. *Water Resour. Ind.* **20**, 54–74 (2018).
589. Liu, F., Zhou, K., Chen, Q., Wang, A. & Chen, W. Comparative study on the synthesis of magnetic ferrite adsorbent for the removal of Cd(II) from wastewater. *Adsorpt. Sci. Technol.* **36**, 1456–1469 (2018).
590. Hosseinzadeh, M., Ali Seyyed Ebrahimi, S., Raygan, S. & Morteza Masoudpanah, S. Removal of Cadmium and Lead Ions from Aqueous Solution by Nanocrystalline Magnetite Through Mechanochemical Activation. *J. Ultrafine Grained Nanostructured Mater.* **49**, 72–79 (2016).
591. Naeem, M. A. et al. Batch and column scale removal of cadmium from water using raw and acid activated wheat straw biochar. *Water (Switzerland)* **11**, (2019).

592. Özer, A., Tanyildizi, M. S. & Tümen, F. Study of Cadmium Adsorption from Aqueous Solution on Activated Carbon from Sugar Beet Pulp. *Environ. Technol.* **19**, 1119–1125 (1998).
593. Liu, X., Xu, X., Dong, X. & Park, J. Competitive Adsorption of Heavy Metal Ions from Aqueous Solutions onto Activated Carbon and Agricultural Waste Materials. *Polish J. Environ. Stud.* **29**, 749–761 (2020).
594. Asuquo, E., Martin, A., Nzerem, P., Siperstein, F. & Fan, X. Adsorption of Cd(II) and Pb(II) ions from aqueous solutions using mesoporous activated carbon adsorbent: Equilibrium, kinetics and characterisation studies. *J. Environ. Chem. Eng.* **5**, 679–698 (2017).
595. Madala, S., Nadavala, S. K., Vudagandla, S., Boddu, V. M. & Abburi, K. Equilibrium, kinetics and thermodynamics of Cadmium (II) biosorption on to composite chitosan biosorbent. *Arab. J. Chem.* **10**, S1883–S1893 (2017).
596. Park, S., Gomez-Flores, A., Chung, Y. S. & Kim, H. Removal of Cadmium and Lead from Aqueous Solution by Hydroxyapatite/Chitosan Hybrid Fibrous Sorbent: Kinetics and Equilibrium Studies. *J. Chem.* **2015**, 396290 (2015).
597. Kelesoglu, S. Comparative adsorption studies of heavy metal ions on chitin and chitosan biopolymers. (Doctoral dissertation or master's thesis). (Izmir Institute of Technology, 2007).
598. Unagolla, J. M. & Adikary, S. U. Adsorption of cadmium and lead heavy metals by chitosan biopolymer: A study on equilibrium isotherms and kinetics. in *MERCon 2015 - Moratuwa Engineering Research Conference* 234–239 (IEEE, 2015). doi:10.1109/MERCon.2015.7112351.
599. Jia, P., Tan, H., Liu, K. & Gao, W. Removal of methylene blue from aqueous solution by bone char. *Appl. Sci.* **8**, (2018).
600. Geçgel, Ü., Özcan, G. & Gürpnar, G. Ç. Removal of methylene blue from aqueous solution by activated carbon prepared from pea shells (*Pisum sativum*). *J. Chem.* **2013**, (2013).
601. Dural, M. U., Cavas, L., Papageorgiou, S. K. & Katsaros, F. K. Methylene blue adsorption on activated carbon prepared from *Posidonia oceanica* (L.) dead leaves: Kinetics and equilibrium studies. *Chem. Eng. J.* **168**, 77–85 (2011).
602. Gao, J. J. et al. Adsorption of methylene blue onto activated carbon produced from tea (*Camellia sinensis* L.) seed shells: Kinetics, equilibrium, and thermodynamics studies. *J. Zhejiang Univ. Sci. B* **14**, 650–658 (2013).
603. Bello, O. S., Adeogun, I. A., Ajaelu, J. C. & Fehintola, E. O. Adsorption of methylene blue onto activated carbon derived from periwinkle shells: Kinetics and equilibrium studies. *Chem. Ecol.* **24**, 285–295 (2008).
604. Mahmoudi, K., Hamdi, N. & Srasra, E. Study of adsorption of methylene blue onto activated carbon from lignite. *Surf. Eng. Appl. Electrochem.* **51**, 427–433 (2015).
605. Li, D., Yan, J., Liu, Z. & Liu, Z. Adsorption kinetic studies for removal of methylene blue using activated carbon prepared from sugar beet pulp. *Int. J. Environ. Sci. Technol.* **13**, 1815–1822 (2016).
606. Liu, L., Lin, Y., Liu, Y., Zhu, H. & He, Q. Removal of Methylene Blue from Aqueous Solutions by Sewage Sludge Based Granular Activated Carbon: Adsorption Equilibrium, Kinetics, and Thermodynamics. *J. Chem. Eng. Data* **58**, 2248–2253 (2013).
607. Gherbia, A., Chergui, A., Yeddou, A. R., Selatnia Ammar, S. & Boubekeur, N. Removal of methylene blue using activated carbon prepared from date stones activated with NaOH. *Glob. Nest J.* **21**, 374–380 (2019).
608. Matos, J. et al. C-doped anatase TiO₂: Adsorption kinetics and photocatalytic degradation of methylene blue and phenol, and correlations with DFT estimations. *J. Colloid Interface Sci.* **547**, 14–29 (2019).
609. Makama, A. B., Salmiaton, A., Saion, E. B., Choong, T. S. Y. & Abdullah, N. Synthesis of CdS Sensitized TiO₂ Photocatalysts: Methylene Blue Adsorption and Enhanced Photocatalytic Activities. *Int. J. Photoenergy* **2016**, (2016).
610. Mohammadi, A. & Aliakbarzadeh Karimi, A. Methylene Blue Removal Using Surface-Modified TiO₂ Nanoparticles: A Comparative Study on Adsorption and Photocatalytic Degradation. *J. Water Environ. Nanotechnol.* **2**, 118–128 (2017).
611. Kurajica, S., Minga, I., Blazic, R., Muzina, K. & Tominac, P. Adsorption and Degradation Kinetics of Methylene Blue on As-prepared and Calcined Titanate Nanotubes. *Athens J. Sci.* **5**, 7–22 (2018).
612. Geng, Y., Zhang, J., Zhou, J. & Lei, J. Study on adsorption of methylene blue by a novel composite material of TiO₂ and alum sludge. *RSC Adv.* **8**, (2018).

613. Chinnakoti, P., Chunduri, A. L. A., Vankayala, R. K., Patnaik, S. & Kamisetti, V. Enhanced fluoride adsorption by nano crystalline γ -alumina: adsorption kinetics, isotherm modeling and thermodynamic studies. *Appl. Water Sci.* **7**, 2413–2423 (2017).
614. Camacho, L. M., Torres, A., Saha, D. & Deng, S. Adsorption equilibrium and kinetics of fluoride on sol-gel-derived activated alumina adsorbents. *J. Colloid Interface Sci.* **349**, 307–313 (2010).
615. Ahamad, K. U., Singh, R., Baruah, I., Choudhury, H. & Sharma, M. R. Equilibrium and kinetics modeling of fluoride adsorption onto activated alumina, alum and brick powder. *Groundw. Sustain. Dev.* **7**, 452–458 (2018).
616. Lanas, S. G. *et al.* Efficient fluoride adsorption by mesoporous hierarchical alumina microspheres. *RSC Adv.* **6**, (2016).
617. Dhawane, S. H. *et al.* Insight into Optimization, isotherm, kinetics, and thermodynamics of fluoride adsorption onto activated alumina. *Environ. Prog. Sustain. Energy* **37**, 766–776 (2018).
618. Duan, Y., Wang, C., Li, X. & Xu, W. Fluoride adsorption properties of three modified forms of activated alumina in drinking water. *J. Water Health* **12**, 715–21 (2014).
619. Bakkal Gula, C., Bilgin Simsek, E., Duranoglu, D. & Beker, U. An experimental design approach for modeling As(V) adsorption from aqueous solution by activated carbon. *Water Sci. Technol.* **71**, 203–210 (2015).
620. Matović, L. L. *et al.* Mechanochemically improved surface properties of activated carbon cloth for the removal of As(V) from aqueous solutions. *Arab. J. Chem.* **12**, 4446–4457 (2019).
621. Mondal, S., Aikat, K. & Halder, G. Biosorptive uptake of arsenic(V) by steam activated carbon from mung bean husk: equilibrium, kinetics, thermodynamics and modeling. *Appl. Water Sci.* **7**, 4479–4495 (2017).
622. Yang, L., Wu, S. & Chen, J. P. Modification of activated carbon by polyaniline for enhanced adsorption of aqueous arsenate. *Ind. Eng. Chem. Res.* **46**, 2133–2140 (2007).
623. Bhat, A. *et al.* Adsorption and optimization studies of lead from aqueous solution using γ -Alumina. *J. Environ. Chem. Eng.* **3**, 30–39 (2015).
624. Zulmajdi, S. L. N. *et al.* Comparative study on the adsorption, kinetics, and thermodynamics of the photocatalytic degradation of six different synthetic dyes on TiO₂ nanoparticles. *React. Kinet. Mech. Catal.* **129**, 1–16 (2019).

10. Appendix

10.1. Literature search

To understand the historical and contemporary levels of research interest paid towards different technologies for the remediation of arsenic, data was collected using the advanced search feature in Web of Science. The key words used to find papers are given in Table 10.1.

Table 10.1: Search terms used in Web of Science's advanced search feature to identify literature.

Label in main text	Label in appendix	Advanced search terms in Web of Science
Water treatment		
Water treatment (general)	water+treatment	TI=(water OR *water) AND TI=(treatment OR remediation)
Water treatment (adsorption)	+sorbent	TI=(water OR *water) AND TI=(treatment OR remediation) AND TI=(sorbent OR adsorbent OR adsorption OR sorbents OR adsorbents)
Water treatment (photocatalysis)	+photocatalyst	TI=(water OR *water) AND TI=(treatment OR remediation) AND TI=(photocataly*)
-	+nano	TI=(water OR *water) AND TI=(treatment OR remediation) AND TI=(nano OR nano*)
-	+sorbent+composite	TI=(water OR *water) AND TI=(treatment OR remediation) AND TI=(sorbent OR adsorbent OR adsorption OR sorbents OR adsorbents) AND TI=(composite OR composites)
-	+photocatalyst+composite	TI=(water OR *water) AND TI=(treatment OR remediation) AND TI=(photocataly*) AND TI=(composite OR composites)
-	+sorbent+photocatalyst	TI=(water OR *water) AND TI=(treatment OR remediation) AND TI=(sorbent OR adsorbent OR adsorption OR sorbents OR adsorbents) AND TI=(photocataly*)

Label in main text	Label in appendix	Advanced search terms in Web of Science
Arsenic remediation		
Arsenic remediation (general)	arsenic	TI=(arsenic OR arsenite OR arsenate OR "As(III)" OR "As(V)" NOT soil) AND TI=(treatment OR remediation)
Arsenic adsorption	+sorbent	TI=(arsenic OR arsenite OR arsenate OR "As(III)" OR "As(V)" NOT soil) AND TI=(sorbent OR adsorbent OR adsorption OR sorbents OR adsorbents)
Arsenic and photocatalysis	+photocatalyst	TI=(arsenic OR arsenite OR arsenate OR "As(III)" OR "As(V)" NOT soil) AND TI=(photocataly*)
Composite sorbents	+sorbent+composite	TI=(arsenic OR arsenite OR arsenate OR "As(III)" OR "As(V)" NOT soil) AND TI=(sorbent OR adsorbent OR adsorption OR sorbents OR adsorbents) AND TI=(composite OR composites)
Composite photocatalysts	+photocatalyst+sorbent	TI=(arsenic OR arsenite OR arsenate OR "As(III)" OR "As(V)" NOT soil) AND TI=(photocataly*) AND TI=(composite OR composites)
Composite photocatalyst-sorbents	+sorbent+photocatalyst	TI=(arsenic OR arsenite OR arsenate OR "As(III)" OR "As(V)" NOT soil) AND TI=(sorbent OR adsorbent OR adsorption OR sorbents OR adsorbents) AND TI=(photocataly*)
-	+oxidation	TI=(arsenic OR arsenite OR arsenate OR "As(III)" OR "As(V)" NOT soil) AND TI=(treatment OR remediation)+(oxidation NOT photocataly*)
-	+membrane	TI=(arsenic OR arsenite OR arsenate OR "As(III)" OR "As(V)" NOT soil) AND TI=(treatment OR remediation)+(membrane OR "reverse osmosis" OR filtration OR *filtration)
-	+F/C/P	TI=(arsenic OR arsenite OR arsenate OR "As(III)" OR "As(V)" NOT soil) AND TI=(treatment OR remediation)+(flocculatio* OR coagulation OR precipitation)

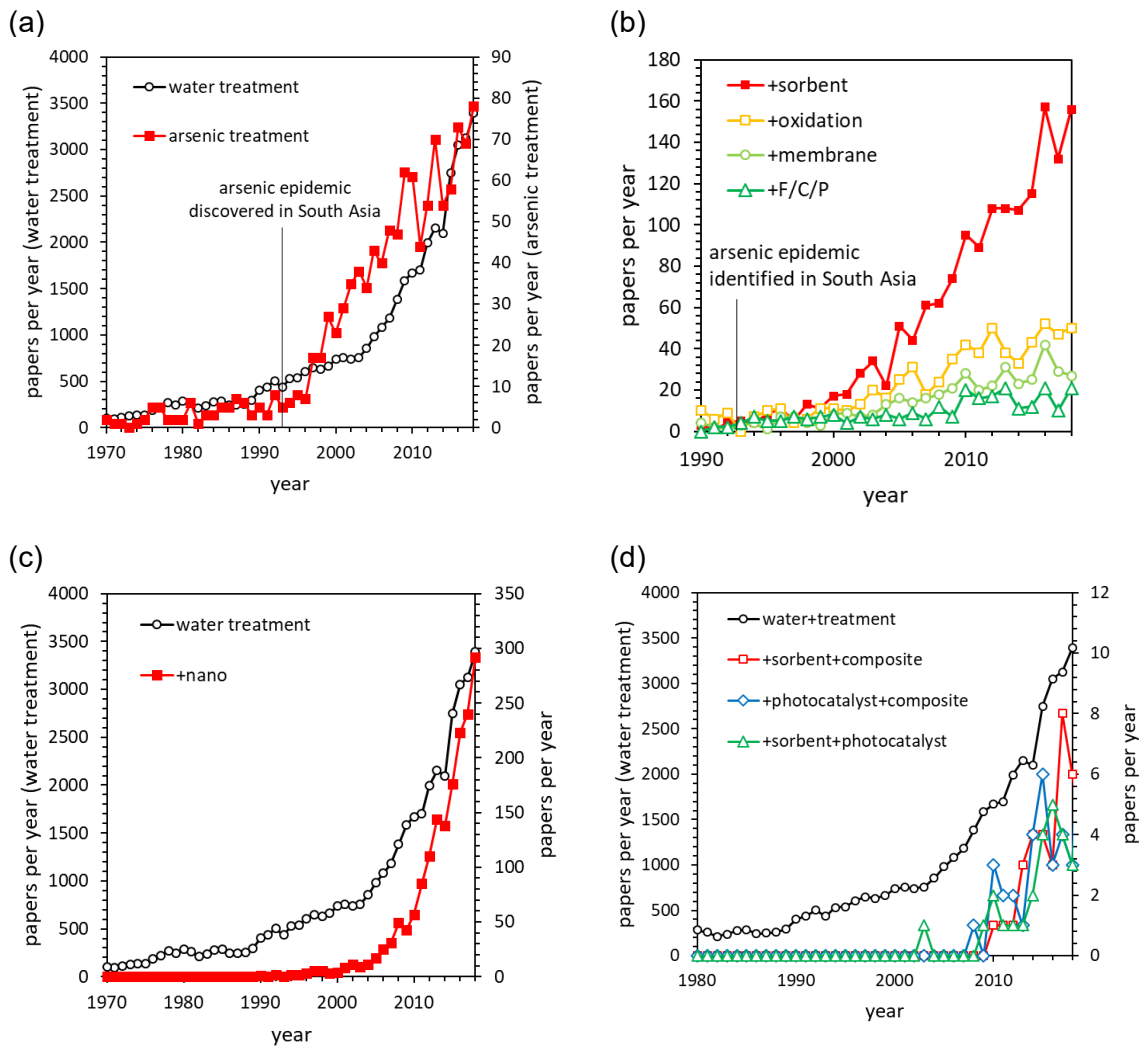


Figure 10.1: Publications published each year on water treatment and arsenic remediation. (a) presents a comparison between research interest in water treatment generally versus research specific towards arsenic remediation. (b) presents a comparison of arsenic remediation treatments: adsorption, oxidation (without heterogeneous photocatalysts), membrane technology, and flocculation-coagulation or precipitation. (c) presents the interest in using nano materials to treat contaminated water. (d) shows the research published on composite sorbents, composite photocatalysts, and photocatalyst-sorbent materials for water treatment.

10.2. Reagents

Table 10.2: Chemical reagents used in this work.

Reagent	Name	Manufacturer	Grade/purity	CAS #
Na ₂ HAsO ₄ ·7H ₂ O	Sodium arsenate dibasic heptahydrate	Sigma	ACS reagent	10048-95-0
As ₂ O ₃	Arsenic trioxide	Aldrich	99%	1327-53-3
As (aq)	Arsenic standard	Fluka	1000 ± 4 mg L ⁻¹ traceCERT	-
N ₂ H ₄ .H ₂ O	Hydrazine hydrate	Fisher	Analytical reagent	7803-57-8
N ₂ H ₆ SO ₄	Hydrazinium sulphate	Fluka, Aldrich	ACS reagent ≥ 99.0%	10034-93-2
C ₁₀ H ₂₀ N ₂ Na ₄ O ₁₀	EDTA tetrasodium salt, dihydrate	Fisher	BioReagent	10378-23-1
FeSO ₄ ·7H ₂ O	Iron(II) sulphate heptahydrate	Fluka, Sigma Aldrich	ACS reagent ≥ 99.0%	7782-63-0
MnCl ₂ .4H ₂ O	Manganese(II) chloride tetrahydrate	Sigma Aldrich	ACS reagent ≥ 98.0%	13446-34-9
C ₈ H ₁₈ N ₂ O ₄ S	HEPES free acid	Amresco	High purity grade	7365-45-9
1.0 M NaOH	Sodium hydroxide	Honeywell Fluka	-	1310-73-2
Na ₂ SiO ₃	Sodium metasilicate	Aldrich	SiO ₂ , 50-53%	6834-92-0
NaHCO ₃	Sodium bicarbonate	BDH	99 to 101% assay	144-55-8
1.0 M HCl	Hydrochloric acid	Honeywell Fluka	-	7647-01-0
NaNO ₃	Sodium nitrate	VWR	AnalaR NORMAPUR ACS reagent	7631-99-4
NaF	Sodium fluoride	Alfa Aesar	99% min ACS reagent	7681-49-4
HNa ₂ PO ₄ .7H ₂ O	Sodium phosphate dibasic heptahydrate	Acros organics	99+% for analysis	7782-85-6
CaCl ₂ .2H ₂ O	Calcium chloride dihydrate	BDH	AnalaR, 99.5% minimum assay	10035-04-8
MgSO ₄ .7H ₂ O	Magnesium sulphate hexahydrate	Sigma	BioReagent	10034-99-8
KHCO ₃	Potassium hydrogen carbonate	Merck	EMSURE, ACS	298-14-6
MgCl ₂ .6H ₂ O	Magnesium chloride hexahydrate	Sigma	BioReagent	7791-18-6
KH ₂ PO ₄	Potassium dihydrogen phosphate	Riedel-de-Haë	98-100.5% assay	7778-77-0
Ca(NO ₃) ₂ .4H ₂ O	Calcium Nitrate Tetrahydrate	Fluka Analytical	ACS ≥ 99.0%	13477-34-4
NH ₄ Cl	Ammonium chloride	Fisher	Analytical reagent grade	12125-02-9
-	Multi-element standard (10 µg mL ⁻¹) Ag, Al, As, B, Ba, Be, Ca, Cd, Ce, Co, Cr(3), Cs, Cu, Dy, Er, Eu, Fe, Ga, Gd, Ho, K, La, Lu, Mg, Mn, Na, Nd, Ni, P, Pb, Pr, Rb, S, Se, Sm, Sr, Th, Tl, Tm, U, V, Yb, Zn	Inorganic Ventures	NIST-traceable standard	-

10.3. Removal of arsenic(V) using ImpAs and shaking by hand

Before implementing ImpAs in a plastic syringe device, the potential application of ImpAs by mixing with contaminated waters and shaking by hand (i.e. a batch reaction) was investigated for the portable and rapid speciation of inorganic arsenic (Figure 10.2). Shaking by hand was too slow for any practical application, with only 90% of the As(V) removed after 10 minutes.

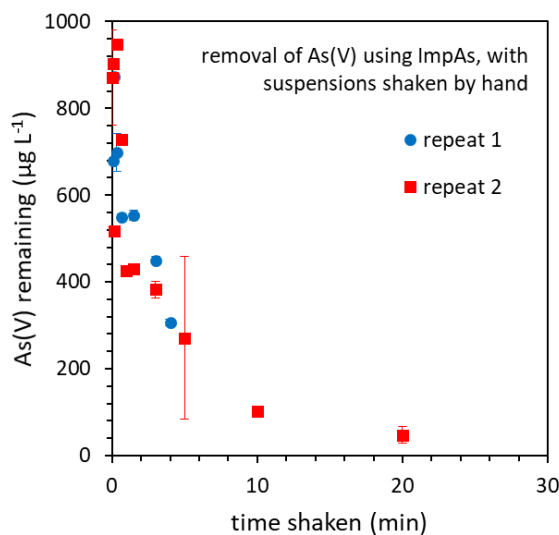


Figure 10.2: Removal of As(V) using ImpAs, with suspensions shaken by hand. The experimental conditions were 1 mg L⁻¹ initial As(V), 1 g L⁻¹ ImpAs, 10 mM HEPES buffered to pH 7.4, total volume 50 mL. Aliquots of approximately 1 mL were sequentially extracted from the initial 50 mL suspension at each time point sampled. Arsenic concentrations were determined by ICP-MS. The experiment was repeated twice. Error bars indicate the uncertainty propagated from the root-square-deviation of the total As determined using ICP-MS.

10.4. Anodic stripping voltammetry

Table 10.3: Various procedures and detection limits reported for the electrochemical detection of arsenic. Abbreviations: HDME: hanging drop mercury electrode, CSV: cathodic stripping voltammetry, ASV: anodic stripping voltammetry, SC: (anodic) stripping chronopotentiometry, DP: differential pulse, SW: square wave.

Electrode	Method	Analyte	Electrolyte	Deposition potential (V) and time	Peak potential (V)	LoD (nM)	LoD ($\mu\text{g L}^{-1}$)	Year and ref.
HDME	DPCSV	As(III)	2.5 g L ⁻¹ hydrazinium chloride 5 mg L ⁻¹ Cu(II) 0.75 M HCl	unclear (120 s)	-0.8	13	1	1983 ³³⁶
Gold ultramicro-electrode (25 μm fibre)	Constant current stripping analysis	Total As	5 M HCl 0.01 M KI	N/A (240 s, continuous flow system)	+0.2	2	0.15	1986 ⁵¹⁶
HDME	DPCSV	As(V)	2 M NaClO ₄ pH 1.7 2 mM CuSO ₄ 0.5 M mannitol 0.3 M NaCl	-0.55 (60-140 s)	-0.88	~130 (60 s) ~13 (140 s)	~10 (60 s) ~1 (140 s)	1995 ⁵¹⁷
Gold ultra-micro-electrode array	SWASV	As(III)	2 M HCl	-0.3 (270 s)	+0.1	2.5	0.19	1997 ⁵¹⁸
	SWASV	As(V) (total As)	2 M HCl (SO ₂ gas to reduce As(V)) 5 mg L ⁻¹ hydrazine	-0.3 (270 s)	presumably as above	not given	not given	
Gold disc	Linear sweep ASV DPASV	As(III)	1 M H ₂ SO ₄ 0.1 M HCl (10 mg L ⁻¹ Triton X-100)	-0.3 (30 s)	+0.07 (+0.14)	2.0	0.15 (300 s)	1998 ⁵¹⁹
HDME	DPSCV	As (sugar beet)	0.3 M HCl 8 mM CuCl ₂ 40 μM hydrazine sulphate	-0.4 (60 s)	-0.78	26	2	1998 ⁵²⁰
Silver macroelectrode	SWASV	As(III)	0.1 M HNO ₃	-0.6 (120 s)	~0	630 (or 14 when using ultrasound)	47 (or 1)	2005 ³³⁹
Gold micro-electrode (5 μm x 0.5mm)	SC	As(III)	natural pH	-1.2 (30 s)	-0.35	0.2	0.015	2007 ²⁸³
	ASV	Total As	pH 1 0.01 M HNO ₃ 0.1 H ₂ SO ₄	-1 (30 s)	-0.05	0.3	0.022	
Gold (screen printed)	SWASV	As(III)	6 M LiCl 0.1 M H ₂ SO ₄	-0.5 (60 s)	+0.25	33	2.5	2007 ⁵²¹
Gold microwire (25 μm diameter)	CV	As(III)	pH 9, 10 mM H ₃ BO ₃ , 0.01 M NaCl	N/A	-0.75	not given	not given	2010 ³³²
	CSV		natural groundwaters	0 (60 s)	-1.1	0.5	0.04	

Electrode	Method	Analyte	Electrolyte	Deposition potential (V) and time	Peak potential (V)	LoD (nM)	LoD ($\mu\text{g L}^{-1}$)	Year and ref.
Gold microwire (25 μm x 2mm)	CSV	As(III)	No electrolyte Natural pH (good for high Fe(II) solutions with EDTA)	0 (60-90 s)	-0.2	0.5 (model solutions) 3 (ground-waters)	0.037 0.22	2011 ⁹¹
	ASV	As(III)	0.1 M HCl 10 mM EDTA	-0.4 (60s)	-0.2	not given	not given	
	ASV	Total As	0.1 M HCl	-1.2 (60s)	-0.2	not given	not given	
Graphite (pencil lead)	ASV	As(III)	3 M NaCl 1 M HNO ₃ 5 mg L ⁻¹ Cu(II)	-0.8 (600 s)	+0.13	21	1.6	2012 ⁵²²
Nanorod-Like α -MnO ₂ /Au nanoparticle composite electrode	SWASV	As(III)	pH 9, 0.1 M sodium carbonate buffer	-1 (150 s)	-0.3	0.25	0.019	2016 ⁵²³
Gold	Anodic stripping coulometry	As(III)	0.01 M HNO ₃ 0.01 M NaCl	-0.5 (60.1 s)	+0.5 (stepped, not swept)	1000	75	2019 ⁵²⁴

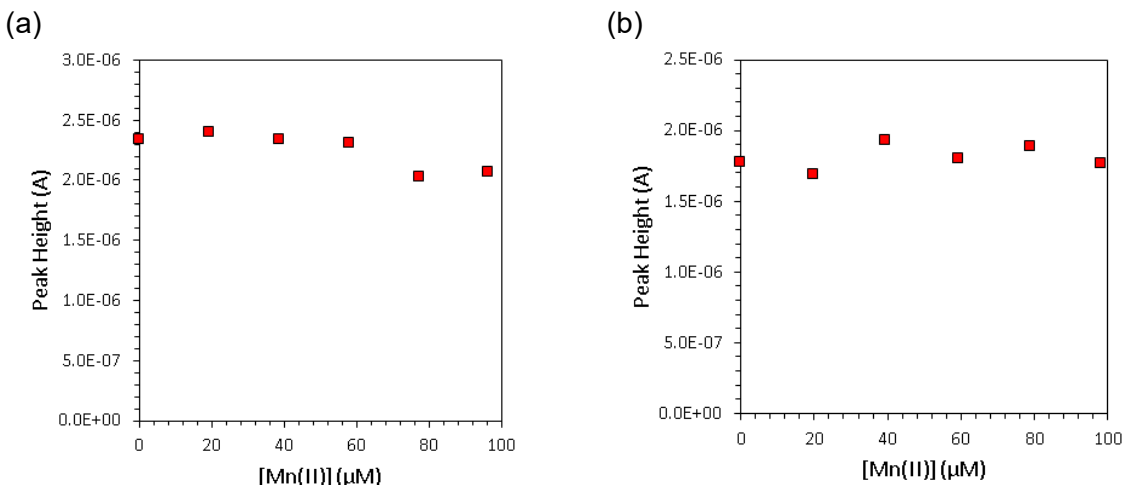


Figure 10.3: The (lack of) influence of Mn(II) upon As stripping peaks for (a) 5 $\mu\text{g L}^{-1}$ As(V), pH 1, and (b) 5 $\mu\text{g L}^{-1}$ As(III), pH 2, 20 μM hydrazine. In South Asia groundwaters, Mn(II) can be found in concentrations of 4-40 μM (220 $\mu\text{g L}^{-1}$ to 2.2 mg L⁻¹)^{86 40 85}. LSASV conditions: 15s at -1.3 V (total As) or -0.7V (As(III)), 10s hold at -0.4 V, stripping from -0.4 V to +0.7 V at 4 V s⁻¹. Detection was made at pH 2 with 20 μM hydrazine for As(III), and at pH 1 with no hydrazine for total As.

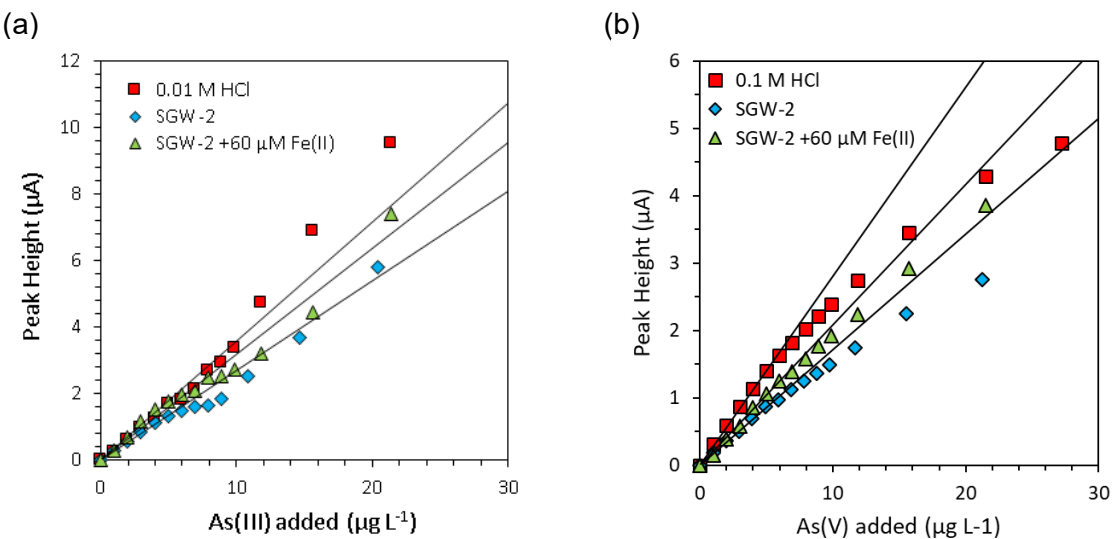


Figure 10.4: Upper limits to the linear range of (a) As(III) (with 10 µM hydrazine) and (b) total As determinations. LSASV conditions: 15s at -1.3 V (total As) or -0.7 V (As(III)), 10s hold at -0.4 V, stripping from -0.4 V to +0.7 V at 4 V s⁻¹. Detection was made at pH 2 with 20 µM hydrazine for As(III), and at pH 1 with no hydrazine for total As.

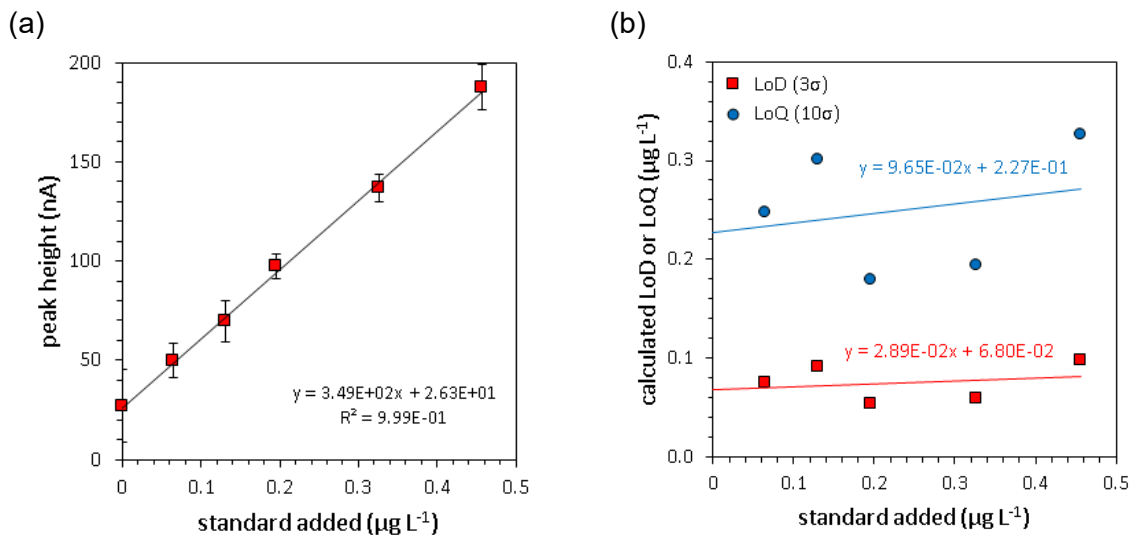


Figure 10.5: Determining the limit of detection (LoD) and limit of quantification (LoQ) for total As determination in 0.1 M HCl. The LoD and LoQ were calculated respectively as 3 and 10 times the standard deviation (σ) of seven repeat scans at the lowest concentration of standard added (the standard deviation is shown as the error bars in (a)). (a) Standard additions show the linear calibration, and (b) the LoD is between 0.05 and 0.1 µg L⁻¹ whether calculated within this range. LSASV conditions: 15s at -1.3 V, 10s hold at -0.4 V, stripping from -0.4 V to +0.7 V at 8 V s⁻¹. The 'peak height' at 0 µg L⁻¹ standard added corresponds to the noise in the voltammogram owing to background current. This noise was not corrected for, as when extrapolated, this error (26 nA) contributes no more than 1.6% of the signal when 5 µg L⁻¹ As is present in the cell. The background signal was insignificant compared with the arsenic standard additions.

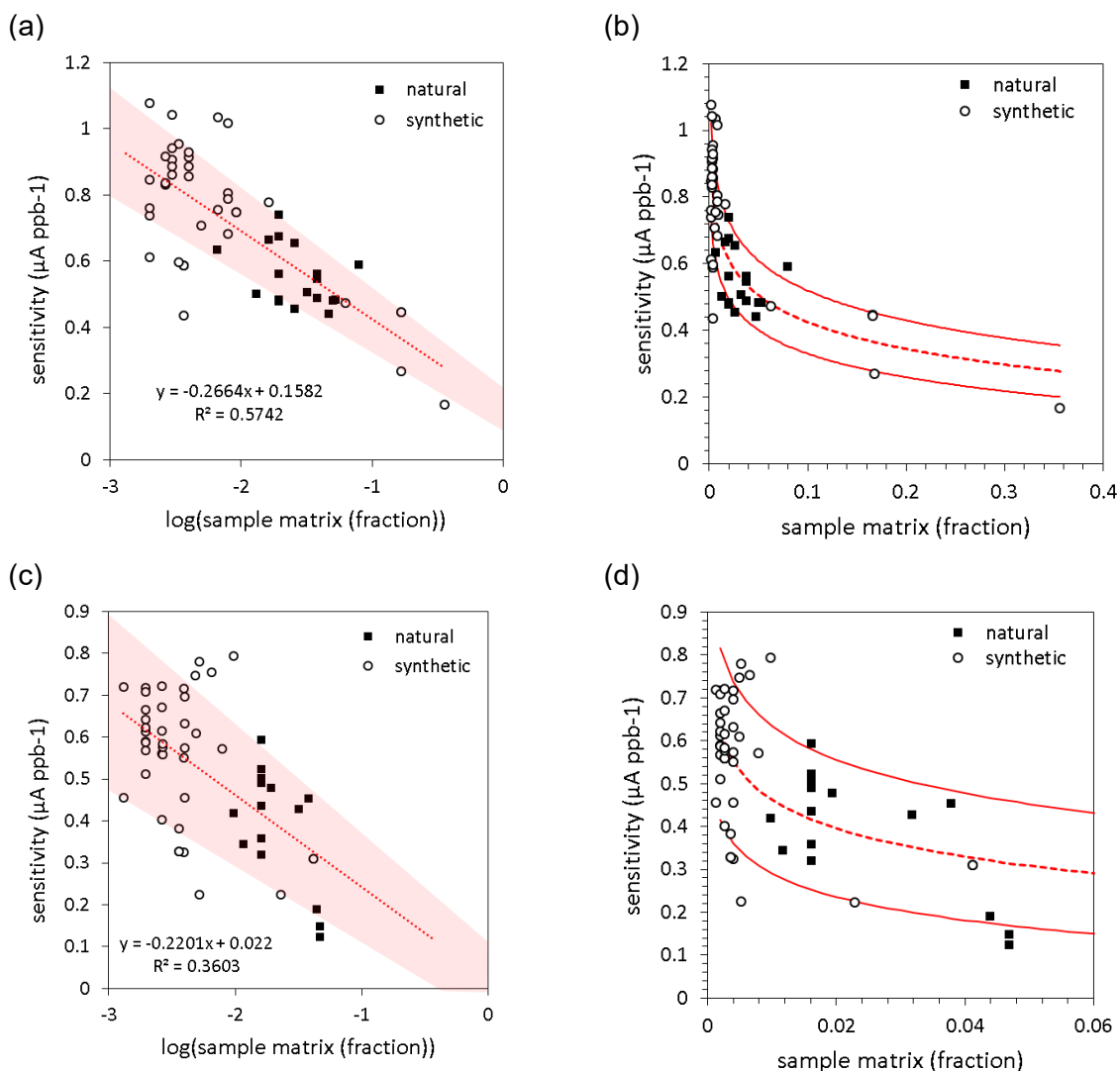


Figure 10.6: The loss of electrode sensitivity during determination of (a,b) As(III) and (c,d) total As in synthetic and natural waters due to matrix effects. ‘Synthetic’ data points are all measurements recorded during the speciation of arsenic in SGW-2 and CW (i.e. the control samples prepared during the ImpAs batch experiments). ‘Natural’ data points are measurements recorded during the speciation of arsenic using West Bengal groundwaters as the matrix (i.e. during the As(V) spike experiment), where EDTA was used for sample preservation. A linear regression was fit to the plot between electrode sensitivity and the logarithm of the fraction of sample in the overall cell volume (dashed red line). The shaded area and solid red lines indicate the error bounds of the linear fit, based on the standard error in the linear regression.

10.5. Differences between synthetic batches of meso-TiO₂/Fe₂O₃

Application of the Spurr and Myers equation to the XRD patterns of meso-TiO₂/Fe₂O₃ revealed that the meso-TiO₂ components of the two batches meso-TiO₂/Fe₂O₃ were significantly different to one another, with an anatase:rutile ratio of 86:14 in the first batch, and just 28:72 in the second batch (discussed in chapter 5). This thesis did not intend to optimise the synthesis of TiO₂/Fe₂O₃ materials, however the causes for the inconsistent TiO₂ crystal phase were investigated. The possibility that different sol-gel products were collected in the two batch syntheses was investigated by considering the colour of the product and the mass loss during calcination. The possibility that anatase transformed into rutile in the second batch during calcination was investigated using high temperature XRD.

10.5.1. Colour and mass loss during calcination

A range of visibly different sol-gel products were obtained within each beaker before calcination in the first synthetic stage. Around one third of beakers demonstrated a white solid foam as the majority product; one third of beakers showed a yellow-esque translucent gel, similar in colour to the Ti(OBu)₄ precursor, as the primary product; and the final third of beakers contained a mixture of product and reactants, often in patches. Whilst a brittle aerogel film was often formed on the top surface, this proved too thin and low in mass to isolate. This thin film appeared to prevent further evaporation of the solvent, since the resulting gel was more liquid and less viscous than that of other beakers. Evaporation of the solvent and formation of the gel took anywhere between a few days and over a week.

With just 0.75 g of meso-TiO₂ obtained per batch synthesis in a single beaker, synthesis of many separate batches was needed to prepare a sufficient quantity of product for adsorption experiments (batch 2). The sol-gel products were all calcined simultaneously to constant calcination conditions. Consequently, the aging of the gel product varied from between 10 (typical) and 79 days (the oldest sol-gel product from batch 2). Scaling up reagent quantities by a factor of two or three was attempted, however the product was more heterogeneous than in the small-scale synthesis. Consequently, synthesis was continued with the original quantities of reagents.

After calcination distinct coloured regions of product were observed, with black, white, grey and brown areas (Figure 10.7). The colour significantly varied not just within each crucible, but also between crucibles. A homogeneous powder with a constant colour was obtained after crushing. Possible causes for dark colour in TiO_2 include (a) Ti(III) centres⁵²⁵ (however the reduction of Ti(IV) during calcination in an oxygenated environment is unlikely) and (b) carbon residues from burnt Pluronic P123. Washing and filtering powders with ethanol did not remove this colouration. SEM-EDS showed significant carbon peaks in meso- TiO_2 and meso- $\text{TiO}_2/\text{Fe}_2\text{O}_3$ products that were not observed in the Fe_2O_3 reference sample, indicating residual carbon content. Small Cl peaks are also observed in SEM-EDS (and identified as a major impurity using XRF, chapter 5), which indicate residual chlorine from the hydrochloric acid that is used as the solvent for Ti(IV) -butoxide. Thermal gravimetric analysis (TGA) would likely reveal further information about the nature of any impurities.

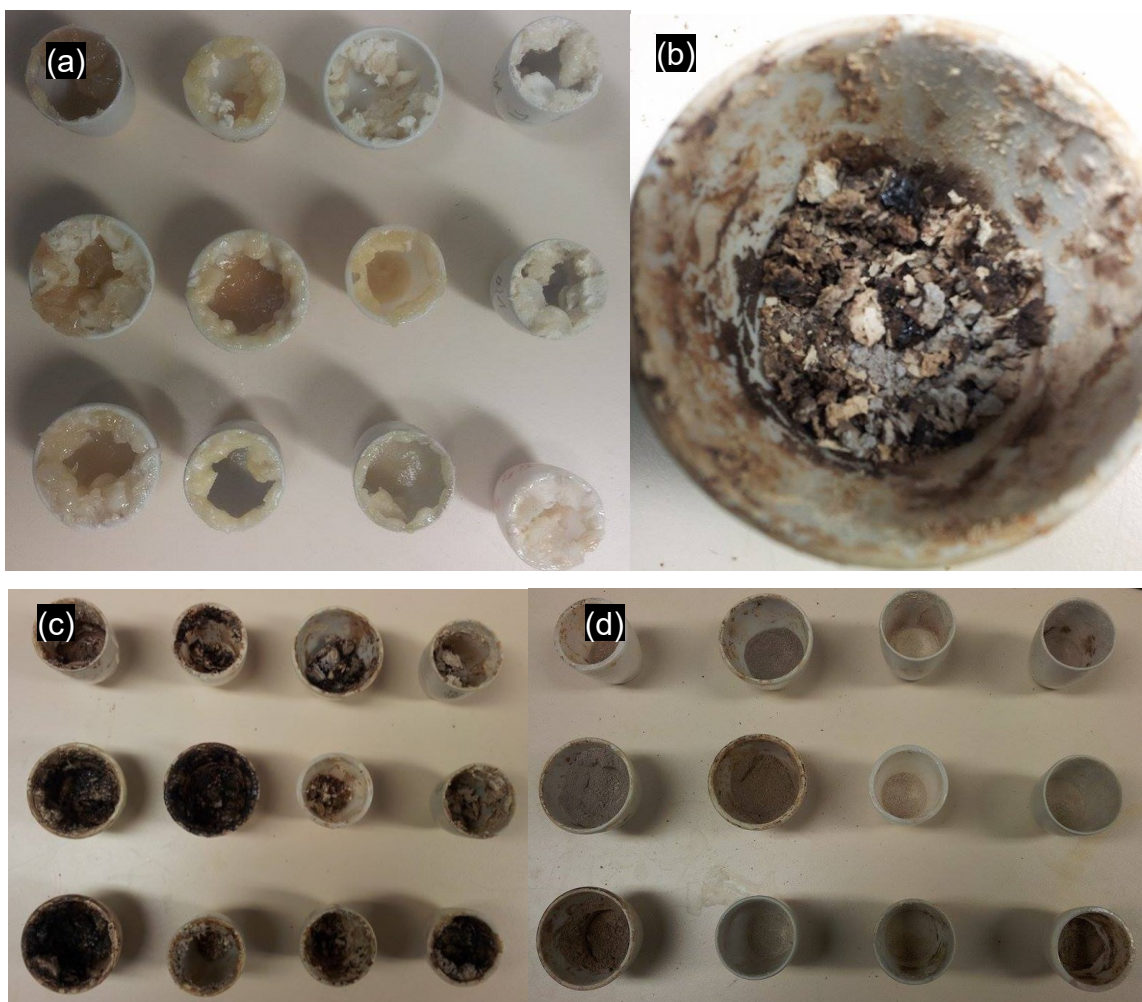


Figure 10.7: Meso- TiO_2 batch 2: (a) the sol-gel product, and the calcination product (b, c) before, and (d) after crushing.

All crucibles were given a qualitative colour index to denote how strongly coloured each sample was. The colour grading index used was as follows: (1) sand, (2) pale grey, (3) grey/brown, (4) brown, (5) grey. This colour grading is demonstrated in Figure 10.8.



Figure 10.8: Meso-TiO₂ batch 2: rough classification of products according to the after calcination and crushing. The green label in the top left hand denotes the arbitrary ID assigned to each crucible.

Samples from three crucibles (chosen to represent the observed range of colours) were analysed using XRD, and differences in the anatase:rutile ratio were observed between each. A consistent correlation was not observed: whilst the colour grading followed the order o1<c9<c8, the anatase:rutile ratio followed the order c9<o1<c8. Anatase peaks were significantly strongest for sample c8, with a dark grey colour.

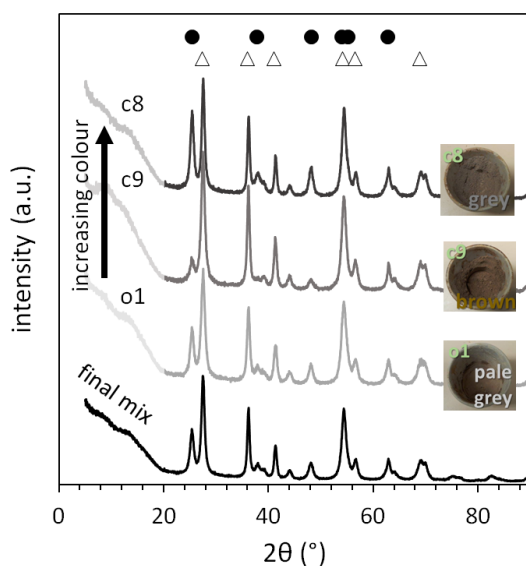


Figure 10.9: Different coloured meso-TiO₂ samples analysed with powder-XRD. Representative rutile peaks highlighted. First spectrum is the mixed sample of all crucibles used in subsequent synthesis of meso-TiO₂/Fe₂O₃. Black circles denote anatase and white triangles denote rutile crystal phases.

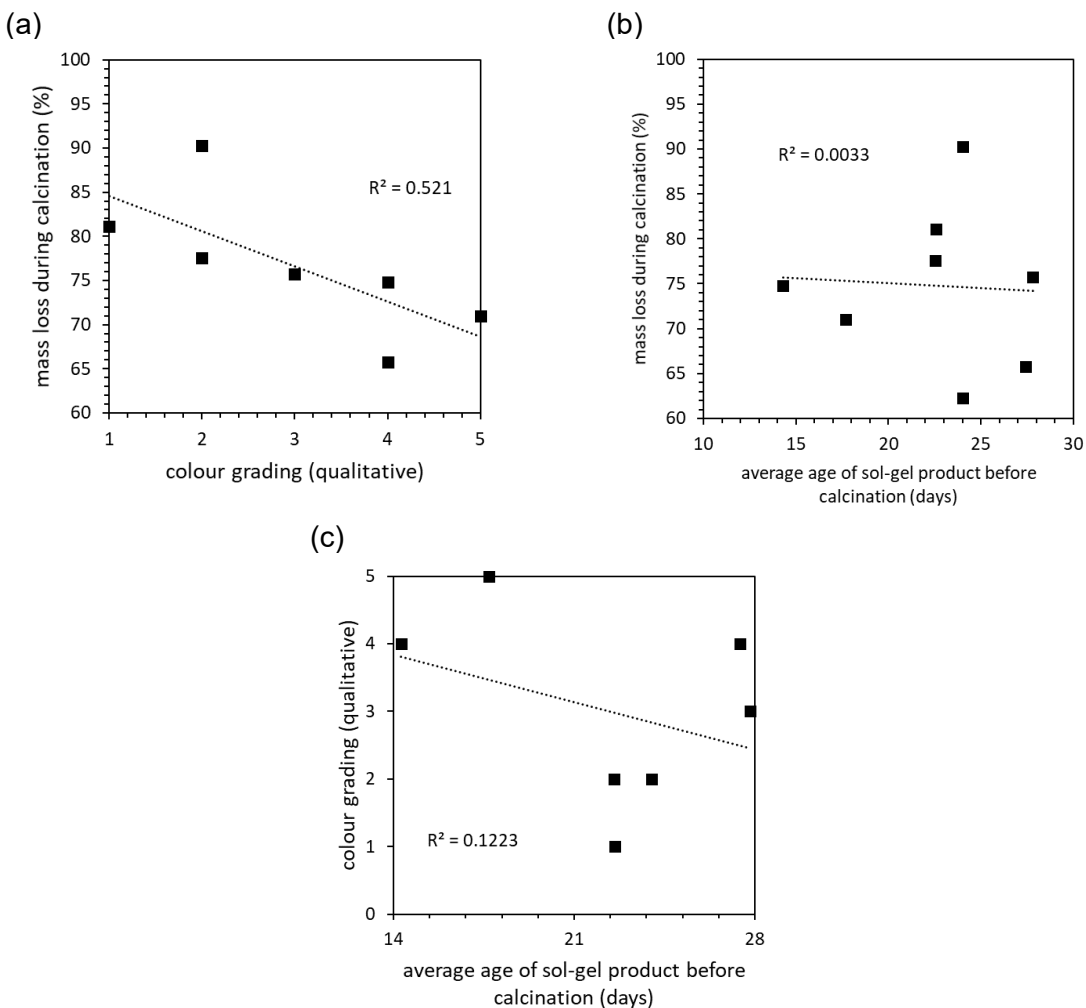


Figure 10.10: Meso-TiO₂ batch 2: (a) colour grading and mass loss during calcination, (b) average duration of sol-gel product aging and colour grading, and (c) mass loss during calcination and sol-gel product aging.

A more convincing correlation was found between colour grading and sample mass loss during calcination, with darker samples losing less mass (Figure 10.10a). No correlation was identified between the age of the sol-gel product before calcination and colour (Figure 10.10b) or between the age of the sol-gel product and the mass lost during calcination (Figure 10.10c). Mass loss during calcination corresponds to the evaporation of volatile substances, of which the principal sources would be residual solvent (H₂O, HCl and EtOH), butoxide from the Ti(IV)-butoxide precursor, and the combustion of P123. Of these, the Ti(IV)-butoxide precursor is green-yellow, whilst residual carbon from combustion of P123 would darken the TiO₂. The low mass loss observed for the darker samples therefore indicates incomplete evaporation of the Ti(IV)-butoxide and P123 precursors.

10.5.2. High temperature X-ray diffraction

Rutile is the most thermodynamically stable crystal phase of the TiO₂ polymorphs, and anatase normally transforms into rutile at temperatures of 600-700 °C⁵²⁶. High temperature XRD was used to investigate the possibility that the intense rutile peak in the XRD patterns of the second batch of products was due to a transformation of anatase to rutile during the calcination process. XRD patterns were recorded up to 800 °C, which is in excess both of the typical anatase to rutile transition temperature (600-700 °C⁵²⁶) and the calcination temperature used in this work (350 °C).

XRD patterns did not show anatase peaks shrinking and rutile peaks increasing as the temperature is increased. Instead, both anatase and rutile peaks increased in height. However, the areas of anatase and rutile peaks did not substantially change. Changes in the XRD patterns as the sample is heated were therefore primarily due to increasing crystallinity, rather than due to any crystal phase transformation.

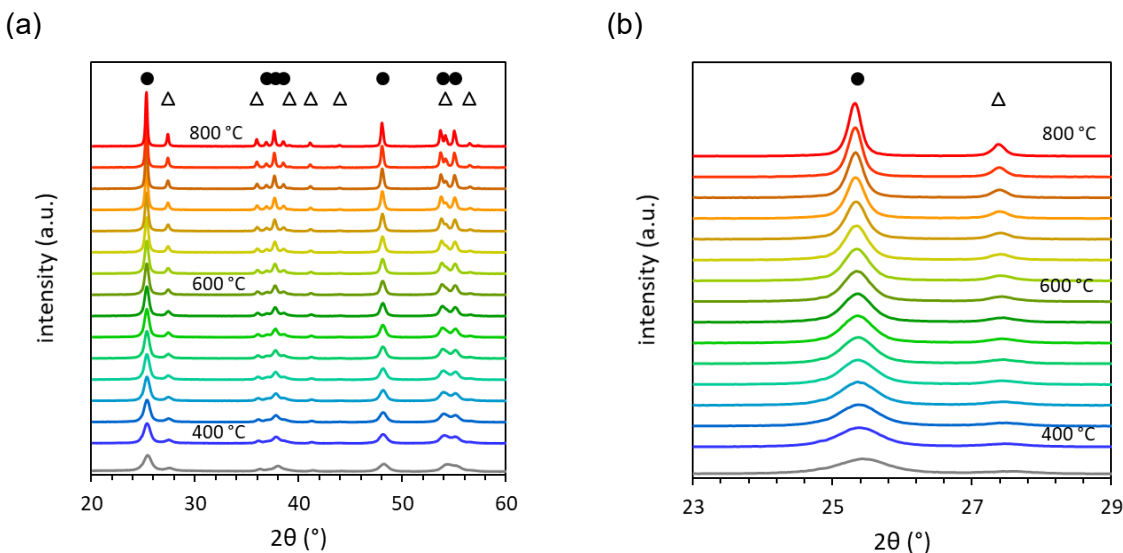


Figure 10.11: High temperature XRD of meso-TiO₂ (batch 1). (a) XRD patterns for meso-TiO₂ (batch 1) as temperature is increased in 25°C intervals between 400 and 800 °C. The initial XRD pattern at room temperature is given as the grey line at the bottom of the figure. Filled circles denote peaks assigned to anatase whilst open triangles denote peaks assigned to rutile. XRD patterns are shifted in the y-axis for clarity. (b) A close up of the most intense anatase and rutile peaks. The filled circle corresponds to the peak caused by diffraction from the anatase 101 plane, whilst the open triangle corresponds to the rutile 110 plane.

In fact, the anatase {101} peak increased in height at a faster rate than the rutile {110} peak, until approximately 700 °C was reached. It is only from around 750 °C that the rutile {110} was observed to increase in height more rapidly than the anatase {101} peak (Figure 10.12). These temperatures are notably higher than the temperature of the anatase-to-rutile transformations reported in the literature (600–700 °C⁵²⁶) and therefore raise the possibility that the anatase phase of this meso-TiO₂ product is metastable. Elsewhere, mesoporous anatase stable up to 1000 °C has been reported⁵²⁷. This suggests that the difference in anatase:rutile ratios in the two batches of products was not due to a thermal transformation from anatase to rutile in the second batch.

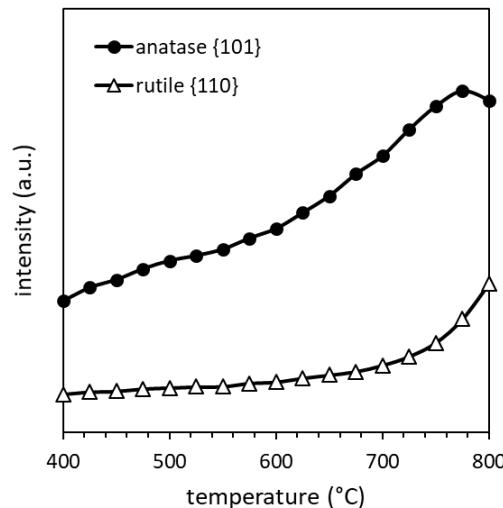


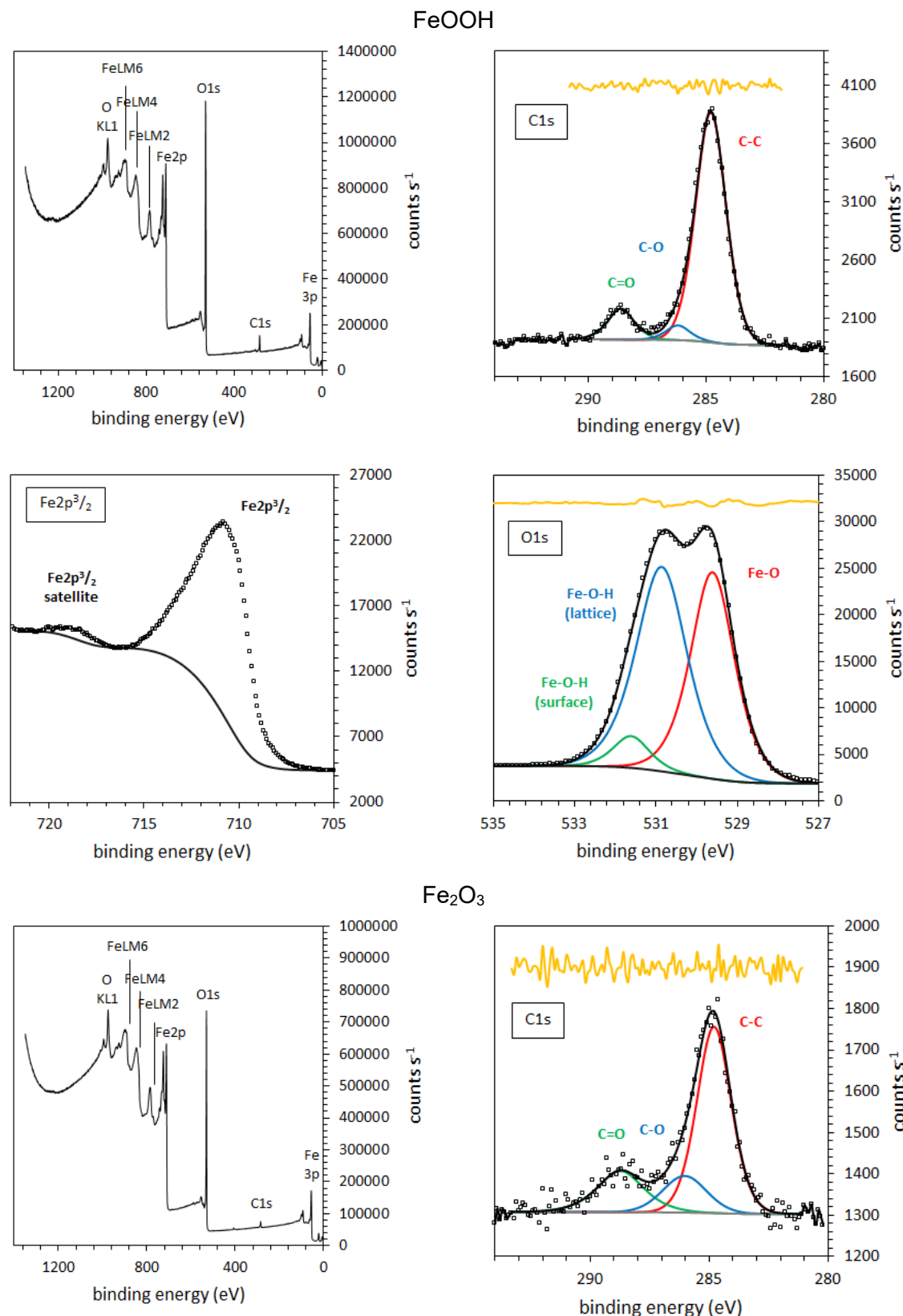
Figure 10.12: The increasing intensity of anatase {101} and rutile {110} peaks with increasing temperature.

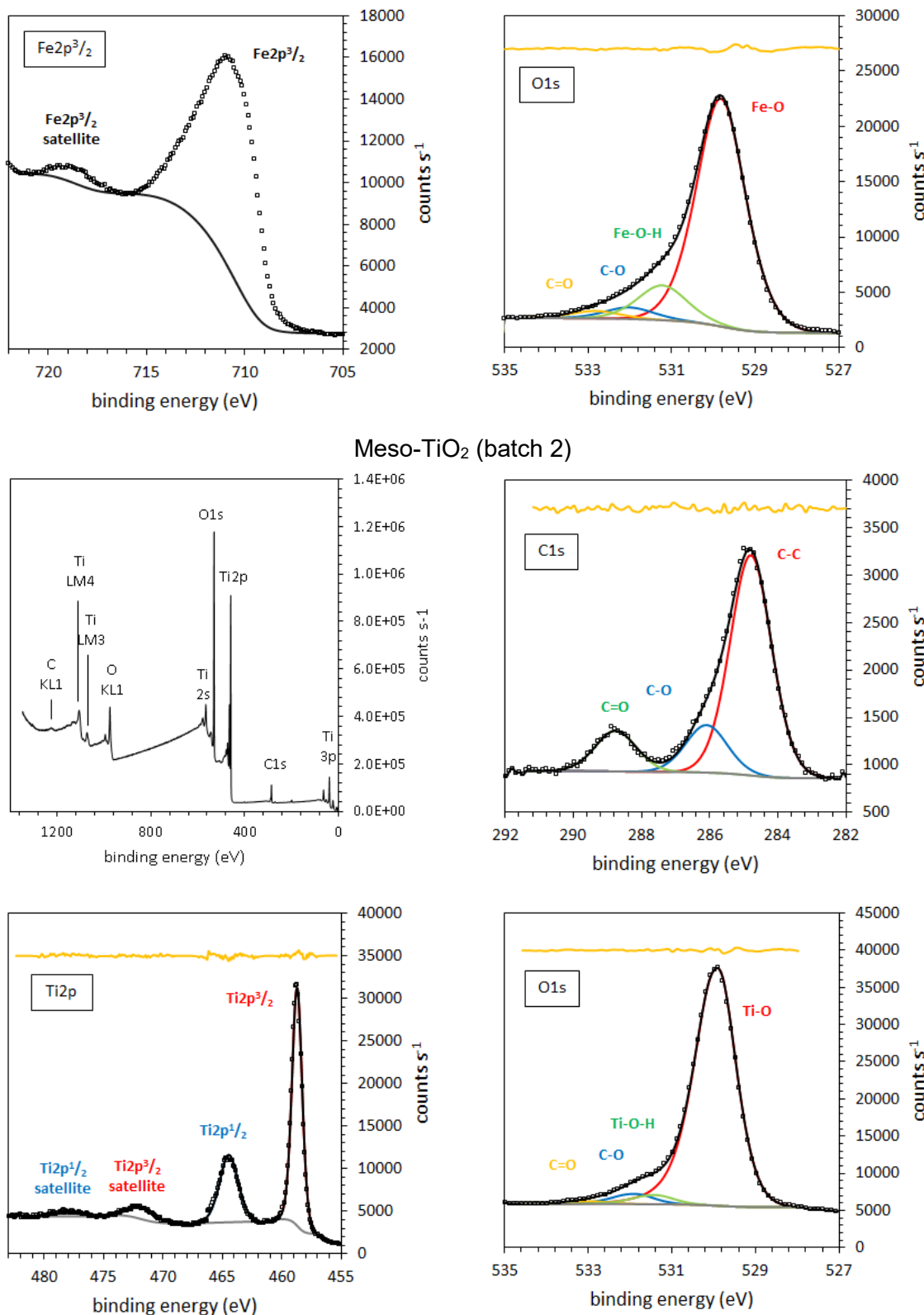
10.5.3. Incomplete sol-gel reactions as the cause of high rutile content

High temperature XRD indicated that there was probably no significant transformation of anatase to rutile during calcination in the second batch synthesis of meso-TiO₂. However, it was identified that meso-TiO₂ samples with intense colour were associated with low mass loss during calcination, and therefore the presence of residual reagents (either Ti(IV)-butoxide or P123). Optical microscopy (chapter 5) identified both white particles and larger green particles in meso-TiO₂ batch 2. The white particles likely correspond to mesoporous anatase, and the rutile component likely corresponds to the larger green particles, formed by the calcination of Ti(IV)-butoxide that has failed to undergo the sol-gel reaction.

To ensure sample consistency, future studies must better characterise the differences between (i) the solid white foam, (ii) the thin and brittle aerogel and (iii) the green-yellow gels produced by the sol-gel procedure, and to ensure that the same material is collected and calcinated in each synthesis.

10.6. XPS spectra of samples before adsorption of arsenic





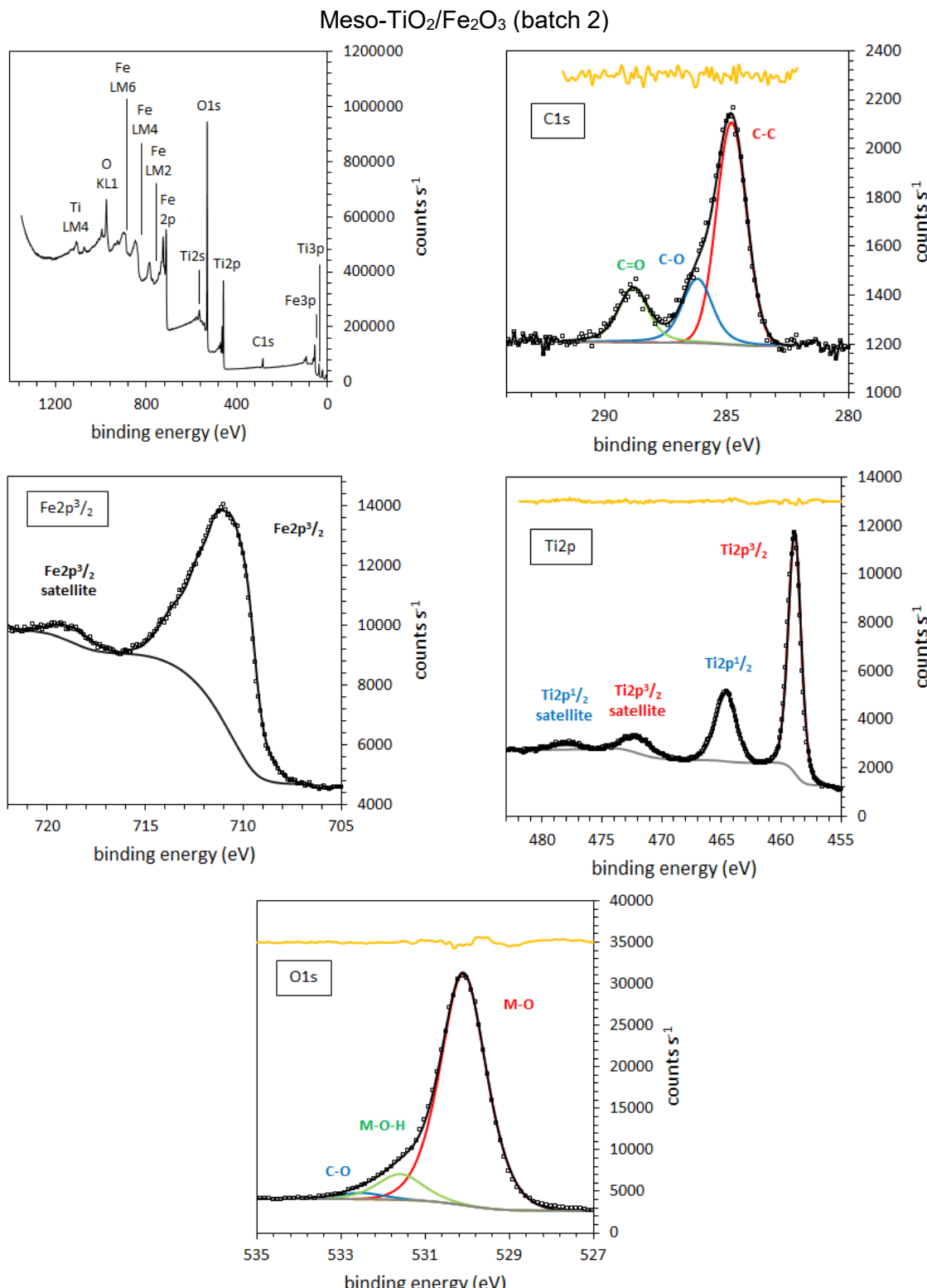


Figure 10.13: XPS spectra of minerals used in this work. Squares indicate experimental data, and the black line indicates the fit. The residual of the peak fitting is shown in yellow. Survey scans, C1s, Fe2p3/2, Ti2p and O1s spectra are presented. The magnitudes of O1s C-O and C=O peaks were constrained to the atomic % returned for C1s C-O and C=O peaks, allowing for the fitting of O1s M-O-H peaks. The peaks fitted to O1s for FeOOH agree very closely in both position and intensity with Baltrusaitis et al. (2007)⁵²⁸. Atomic % was determined using C1s, O1s, Fe2p3/2 and Ti2p3/2 peaks only (and the trace amounts of N1s and Cl2p). Spectra were normalised to the adventitious carbon peak (C-C) at 248.8 eV. Metal oxide O1s peaks are designated as M-O, corresponding to O1s bulk lattice peaks, and M-O-H, corresponding to surface hydroxyl O1s peaks. Goethite is an exception, with both surface and bulk lattice M-O-H peaks fit to the spectra and labelled separately.

10.7. Unsuccessful application of the potentiometric mass titration technique

To validate the point of zero charge (pzc), potentiometric mass titrations (PMT) were used. PMT has been suggested as a quick and easy approach to determining the pzc^{379 380}. This technique involves varying the concentration of the sorbent, rather than the ionic strength. Since the sorbent has no net charge at the pzc, increasing sorbent concentration should have no influence on the position of the titration curve at this point. The pzc is obtained as either (a) the intersection point of titrations at different sorbent concentrations, or (b) the intersection point of a sorbent titration with a blank electrolyte titration (i.e. zero mass). This was labelled as the 'point of zero mass effect' (pzme).

The results are presented in Figure 10.14. In this work, PMT had limited success in the precise determination of the pzc for three reasons. Firstly, all materials except for FeOOH retained significant acidic impurities even after washing. The concentration of acidic impurities scales linearly with increasing sorbent mass, and so unlike the ionic strength titrations used to determine the pzse (where the influence of acidic impurities is cancelled out), acidic/basic impurities remain a source of error in PMT as noted in the literature^{380 529}. Secondly, meso-TiO₂ and FeOOH titration curves intersected one another and the blank electrolyte curve at pH extremes, increasing uncertainty as [H⁺] and [OH] become significant when compared with surface charge, Q. Thirdly, the resolution and precision in the intersection points of these titration curves was limited.

10.7.1. Comparison of potentiometric titrations and PMT

Kosmulski provides a thorough review of mineral oxide pzc values in the literature, focusing on studies where the pzc was determined using both the pzse and iep for verification³⁷⁸. PMT gave values of the pzc that were the furthest from the literature, differing by 1.4, 2.3 and 0.9 pH units for samples meso-TiO₂, Fe₂O₃ and FeOOH respectively (Table 10.4). In contrast, the pzc values determined from ionic strength titrations (the pzse) were within the range of reported literature values for Fe₂O₃ and FeOOH. (However, the pzse of 4.8 for meso-TiO₂ was 0.6 pH units more acidic than the minimum pzc of 5.4 reported in Kosmulski's review³⁷⁸).

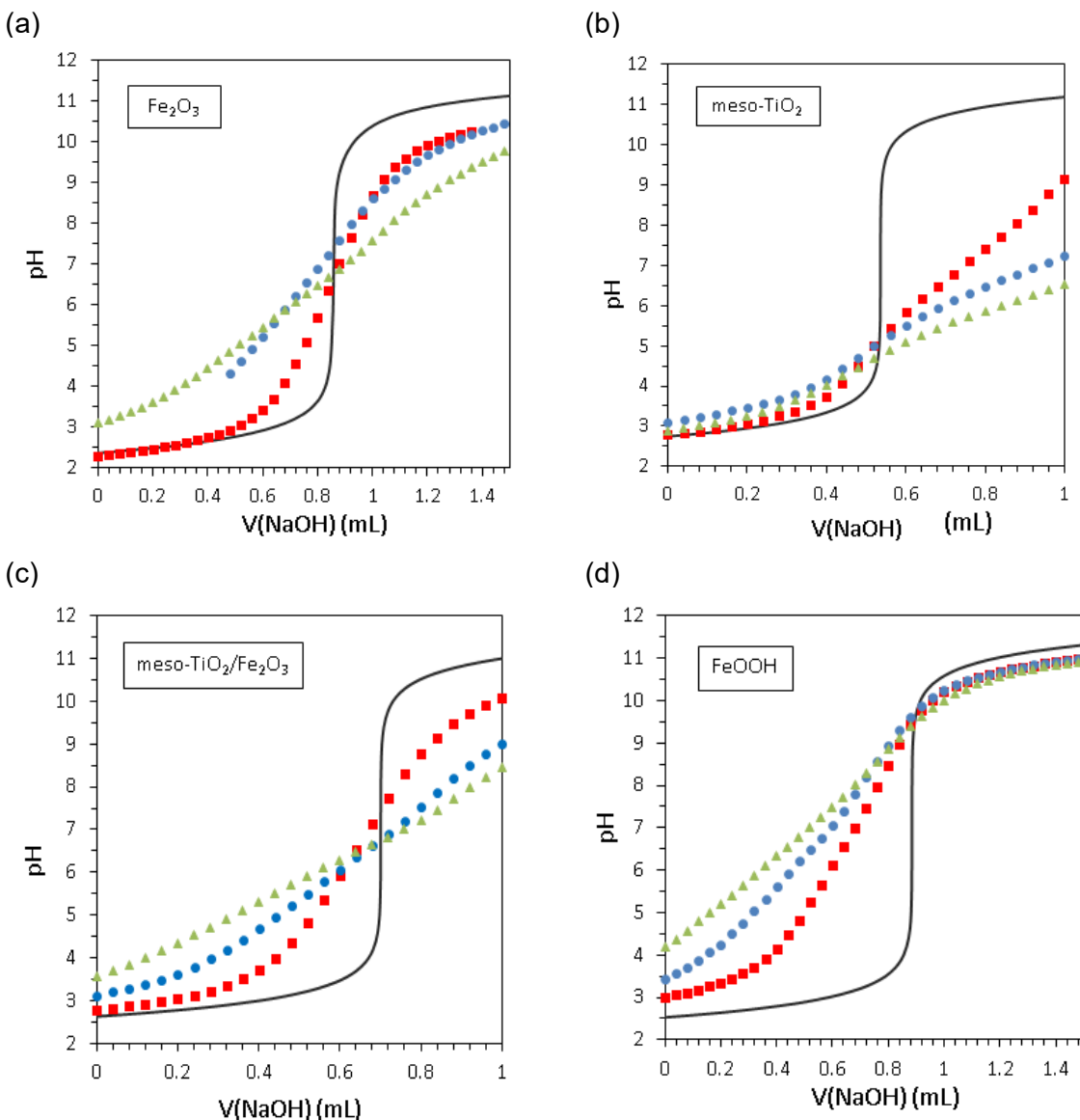


Figure 10.14: Potentiometric mass titration curves for (a) Fe₂O₃, (b) meso-TiO₂, (c) meso-TiO₂/Fe₂O₃, and (d) FeOOH. All titrations shown used washed samples. Titrations were carried out with 5 g L⁻¹ sorbent (green triangles), 10 (Fe₂O₃, meso-TiO₂ and meso-TiO₂/Fe₂O₃) and 7.5 (FeOOH) g L⁻¹ sorbent (blue circles), and 15 (Fe₂O₃, meso-TiO₂ and meso-TiO₂/Fe₂O₃) and 10 (FeOOH) g L⁻¹ sorbent (red squares). All titrations were carried out in 0.01 M NaCl using 0.1 M HCl and 0.1 M NaOH.

10.7.2. Reverse titrations

It is common practice to follow the forwards potentiometric titration (in this case the addition of NaOH to the acidified mineral suspension) with a reverse titration (in this case addition of HCl) to check for hysteresis. Ideally the two titrations provide the same surface charge profile. However, dissolution of CO₂ at high pH provides (i) carbonate anions, which block surface sites through adsorption, and (ii) acidic protons which cause an error in c(a)-c(b). The hysteresis observed in this work was limited (chapter 3). For all titrations except meso-TiO₂/Fe₂O₃, the pzse values obtained using forwards and reverse titrations were within error

of one another (Table 10.4). However, reverse titrations were not used as a final measure of the pzc as in all cases they gave poorer resolution in the pzse (i.e. the intersection point between titration curves at the three ionic strengths was less clear).

Table 10.4: A comparison of the point of zero charge as determined by the potentiometric titration and potentiometric mass titrations techniques. Green-shaded cells indicate the values then used to normalised surface charge for surface complexation modelling within chapter 6.

sample		meso-TiO ₂		Fe ₂ O ₃		meso-TiO ₂ /Fe ₂ O ₃		FeOOH	
condition		unwashed	washed	unwashed	washed	unwashed	washed	unwashed	washed
pzse	minimum	4.4	4.7	8.6	7.7	6.9	6.7	8.5	8.9
	mid-point	4.7	4.9	9	8.9	7.3	7.3	8.6	9.3
	maximum	5.0	5.1	9.4	9.7	7.5	8.2	9.3	9.7
	average	4.7	4.9	9.0	8.8	7.2	7.4	8.8	9.3
	σ	0.3	0.2	0.4	1.0	0.3	0.8	0.4	0.4
	combined	4.80		8.88		7.32		9.05	
pzse (using reverse titration)	\pm	0.14		0.16		0.12		0.35	
	minimum	3.9	4.3	9.3	7.4	4.4	4	8.9	7
	mid-point	4	5.5	9.8	8	6.9	7.7	9.3	7.3
	maximum	4.8	6.3	10.3	9.4	7.6	8.3	9.9	7.4
	average	4.2	5.4	9.8	8.3	6.3	6.7	9.4	7.2
	σ	0.5	1.0	0.5	1.0	1.7	2.3	0.5	0.2
pzme	combined	4.80		9.03		6.48		8.30	
	\pm	0.80		1.08		0.26		1.51	
	minimum	3	4.5	4.5	6.8	5.1	6.3	9.8	8.6
	mid-point	3.3	4.5	4.7	6.9	5.3	6.5	9.8	9.2
	maximum	3.4	5.1	4.8	8.3	5.4	7.5	10.3	9.7
	average	3.2	4.7	4.7	7.3	5.3	6.8	10.0	9.2
literature pH _{pzc}	σ	0.2	0.3	0.2	0.8	0.2	0.6	0.3	0.6
	combined	3.97		6.00		6.02		9.57	
	\pm	1.04		1.89		1.06		0.57	
		5.4-5.9 (or 5.2-6.8) ^{385 378}		8.3-9.5 ³⁷⁸		not available		7.9-8.7 for synthetic goethite ³⁷⁸	

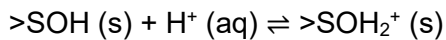
10.8. Surface complexation modelling

The following section provides a brief explanation of surface complexation modelling theory, followed by a discussion of the extended triple layer model (ETLM) used in this thesis.

10.8.1. The influence of electrostatics

The local density of ligands at the mineral surface (i.e. surface hydroxyl groups) is many times greater than the local density of aqueous phase ligands. Consequently, surface complexation reactions occur under the influence of neighbouring surface species and their surface charge. For instance, an aqueous metal cation will adsorb more favourably to a negatively charged solid surface than a positive one, due to the electrostatic interaction.

The major processes that induce mineral oxide surface charge are the acid-base base reactions of the surface hydroxyls, and specific electrolyte adsorption. Surface hydroxyls are protonated or deprotonated under the following reactions:

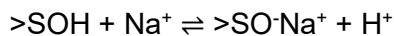


Equation 10.1



Equation 10.2

where $>\text{SOH}$ designates a surface hydroxyl. Specific electrolyte adsorption signifies the following reactions:



Equation 10.3



Equation 10.4

These reactions are obviously pH dependent, but also depend on the ionic strength (discussed in the following section). Consequently, dividing the activities of the products by the activities of the reactants will result in an equilibrium constant that is conditional to the experimental conditions (i.e. pH and ionic strength). If we consider the simplest model, where all surface

charge is located within a two-dimensional plane, then this apparent equilibrium constant, K_{app} , is related to a non-conditional intrinsic equilibrium constant, K_{intr} , using the equation:

$$K_{app} = K_{intr} \cdot e^{-\Delta Z F \Psi_0 / RT}$$

Equation 10.5

where ΔZ is the change in the surface charge⁵³⁰, F is the Faraday constant (96 485 C mol⁻¹), Ψ_0 is the surface potential (V), R is the gas constant (J mol⁻¹ K⁻¹) and T is temperature (K)⁵³¹. The exponential term is an electrostatic correct factor.

10.8.2. The electrical double layer

SCMs differ primarily in their description of the electrical double layer (EDL). The EDL consists of the charged surface and the nearby solution that becomes enriched in counter ions (relative to the bulk solution phase) to provide overall charge neutrality. The thickness of this EDL depends on the ability of the solution to counter the surface charge: as ionic strength is increased the surface charge is neutralised by a smaller volume of solution and the EDL becomes compacted⁵³². In contrast, at low ionic strength, thermal motion limits the concentration of counter ions bound at the surface⁵³³.

In the Helmholtz model of the EDL, the surface charge is neutralised by a single, two-dimensional plane of counterions (the 0-plane). This is the description used in the constant capacitance SCM (CCM), where the surface potential, Ψ_0 , is related to the surface charge, σ , using the following equation:

$$\sigma = \frac{CS\Psi_0}{F}$$

Equation 10.6

where C is the capacitance (F m⁻²), S is the surface area (m² L⁻¹), and F is the Faraday constant (96 485 C mol⁻¹)^{504 534}. In the simplest form of the CCM, adsorption is described using inner-sphere complexes, positioned at the 0-plane, only. Inner-sphere complexation refers to sorbate species that are bound directly to the sorbent surface, with no solvation sphere⁵³⁵. Whilst the CCM can successfully describe many high ionic strength systems (i.e. >0.1 M), this compacted EDL provides a poor description of systems at low ionic strength. This is important given that arsenic contaminated groundwaters in South Asia typically have an ionic strength of 0.03-0.07 M^{87 85}.

The diffuse double layer (DDL) model has more success in describing experimental results at low ionic strength ⁵³³. Again, the DDL positions inner-sphere surface complexes in the 0-plane, however the DDL uses the exponential decay given by the Gouy-Chapman equation ^{536 537} to describe the concentration of counterions as a function of distance from the charged surface. The Gouy-Chapman equation for cations and anions respectively is:

$$n^+_r = n_0 e^{-ze\Psi_r/kT}$$

Equation 10.7

$$n^-_r = n_0 e^{+ze\Psi_r/kT}$$

Equation 10.8

where n^+_r and n^-_r are the concentrations of cations and anions at distance r from the surface (M), n_0 is the electrolyte concentration in the bulk solution (M), z is the valency of the electrolyte ion, e is the elementary charge constant (1.60×10^{-19} C), Ψ_r is the potential at distance r from the surface (V), k is the Boltzmann constant (1.38 J K^{-1}) and T is temperature (K) ⁵³⁸.

The DDL then relates the surface potential to surface charge using the Grahame equation ⁵³⁹, which is as follows:

$$\sigma = \sqrt{8RT\varepsilon\varepsilon_0} I \sinh\left(\frac{z\Psi_0 F}{RT}\right)$$

Equation 10.9

where σ is surface charge ($C \text{ m}^{-2}$), ε is the dielectric constant of water ($F \text{ m}^{-2}$) and ε_0 is the permittivity of vacuum ($F \text{ m}^{-2}$), I is the ionic strength (M) and z is the valency of the electrolyte (for a symmetrical electrolyte, where cations and anions are in a 1:1 ratio) ^{252 538}. Whilst the CCM relates σ to Ψ_0 linearly, in the DDL a hyperbolic sine function reflects the exponential decay of potential towards the bulk of the solution.

The DDL description of the electrical double layer leads to unreasonably high concentrations of counter ions at small distances from the surface. This was corrected in the basic Stern layer (BSL) model, where 0-plane is separated from the surface by some appropriate atomic distance ⁵³⁸. The BSL also adds a δ -plane for the positioning of outer-sphere surface complexes (e.g. where the sorbate retains its solvation sphere but binds with the surface through electrostatic interactions and van der Waals forces). The surface potential experienced by the outer-sphere complexes (Ψ_δ) is different to the potential experienced by the inner-sphere complexes (Ψ_0). This difference is determined using the capacitance between 0 and δ -planes and the CCM equations.

The triple layer model (TLM) goes one step further, adding a β -plane between the 0-plane and δ -plane. Typically, the charge of protonated and deprotonated surface hydroxyls is positioned in the 0-plane, inner-sphere complexes are positioned in the β -plane, and outer-sphere complexes are positioned in the δ -plane. The change in potential between the 0-plane and β -plane is calculated using an inner capacitance parameter, C_1 , and the change in potential between the β -plane and δ -plane is calculated using an outer capacitance parameter, C_2 . The remaining potential is countered by the diffuse double layer. In the TLM, a single surface complex may have charge distributed across multiple planes. The charge is normally assigned to each plane in integer values, however the charge distribution (CD) model attempts to describe the distribution of charge between the planes more realistically, by dividing charge into non-integer values⁵⁴⁰.

Considering the multiple potential planes, Equation 10.5 is modified to give:

$$K_{\text{intr}} = \frac{a_{\text{products}}}{a_{\text{reactants}}} \cdot e^{-F\Delta\Psi/RT}$$

Equation 10.10

where a_{products} and $a_{\text{reactants}}$ represent the product of the activities of all products and all reactants respectively, and $\Delta\Psi$ is the overall change in potential after formation of the surface complex ($\Delta\Psi = \Delta\Psi_0 + \Delta\Psi_\beta + \Delta\Psi_\delta$).

10.8.3. The extended triple layer model (ETLM)

The extended triple layer model (ETLM) is a variant of the TLM developed principally by Sverjensky and Fukushi^{290 245}. The ETLM was chosen for the work in this thesis since (a) it has been proven to be consistent with spectroscopic data⁴⁴⁶, and (b) it provides very agreeable fits for the adsorption of arsenic onto mineral oxides including Bayoxide E33, a commercial goethite (FeOOH) arsenic sorbent²²⁵. This allowed Bayoxide E33 to be used as the benchmark sorbent within this thesis, allowing the experimental procedure and results to be validated against published data.

The ETLM differs from other triple layer models in that (a) the negative charge of inner-sphere arsenic complexes is located in the β -plane⁴⁴⁷, and (b) the site-occupancy standard state is introduced²⁹¹. In the ETLM, the negative charge of inner-sphere deprotonated arsenic surface complexes is distributed to the β -plane, providing better experimental fits than when this

charge is located in the 0-plane²³⁴. This has been assigned to either charge distribution²³⁴ or the release of water dipoles from the adsorption site⁴⁴⁷.

The ETLM site-occupancy standard state offers a way for SCM equilibrium constants to be normalised to account for differences in the point of zero charge (pzc), surface area, and site densities within previously published surface complexation models⁴⁴⁶. Whilst SCM equations typically take equilibrium constants in the hypothetical 1.0 M standard state, in the ETLM site-occupancy standard state, equilibrium constants are normally expressed as those for a hypothetical sorbent with 10 sites nm⁻² and 10 m² g⁻¹ (arbitrarily chosen)⁴⁴⁶.

The charge distribution multisite complexation model (CD-MUSIC) is another modern TLM, more widely known. The charge distribution (CD) is unique in this model, allowing non-integer values of charge to be assigned across the 0, β and δ -planes of the electric double layer⁵⁴¹. The aim here is to provide a more accurate account of how the charge of surface complexes is distributed across the EDL⁵⁴⁰. Furthermore, the multisite (MUSIC) approach of this model describes how surface hydroxyl groups are distinguished between one another on the basis of how many metal cations in the solid lattice they coordinate to⁵⁴⁰.

The authors of the ETLM claim that their model has advantages over the CD-MUSIC model. Firstly, because the ETLM predicts the ionic strength dependence of the distribution between inner and outer-sphere complexes that is observed experimentally, the authors claim that their model is more spectroscopically consistent⁴⁴⁷. Secondly, the authors suggest that because the charge splitting factor introduced in the CD-MUSIC model introduces another fitting parameter, accurate fits between the CD-MUSIC model and experimental data are less statistically significant than the accurate fits achieved using the ETLM⁴⁴⁷.

10.8.4. Experimental determination of modelling parameters

An SCM requires both intrinsic equilibrium constants, to describe both aqueous speciation and surface complexation, and also surface parameters, namely the surface area exposed to solution and the density of surface sites (i.e. surface hydroxyl groups) across that surface. The surface area can be readily obtained via BET analysis of N₂ adsorption-desorption isotherms. Several techniques exist for obtaining surface site density, including potentiometric titration, tritium exchange, crystallography, infrared spectroscopy and thermal gravimetric analysis⁵⁰⁴⁵⁴². However different techniques may give different results, e.g. with goethite ranging from 4 to 20 sites nm⁻² depending on the technique used⁵⁰⁴²⁹⁰. In the ETLM, an approximate value of the site density is typically estimated from adsorption data, or taken from previously

published work⁸⁹ (application of the site-occupancy standard state allows surface complexation constants to be renormalised later on). In the ETLM, surface acidity constants are normally predicted using Sverjensky's empirical formula²⁹¹ and electrolyte adsorption constants (and the inner-sphere capacitance (C_1) are determined by fitting potentiometric titration data^{284 89}. Surface complexation constants are then determined by fitting pH adsorption edges^{284 89} and the model is normally validated by predicting experimental adsorption isotherms²²⁵.

10.8.5. Software for surface complexation modelling

Several computer programs are available for solving SCM problems. However, not all of these incorporate the algorithms necessary to calculate new equilibrium constants. For instance, FITEQL²⁸⁵ and MINTEQ^{286 543} can be used for both predictive modelling and the optimisation of equilibrium constants, whilst PHREEQC⁵⁴⁴ can be used for modelling only. Furthermore, each software package offers slightly different options for modelling the EDL. For instance, FITEQL can be used with non-electrostatic (NEM), constant capacitance (CCM), diffuse double layer (DDL), basic stern layer (BSL) and triple layer (TLM) electrical double layer models²⁸⁵. On the other hand, PHREEQC only includes the DDL and charge distribution multi-site complexation (CD-MUSIC) models⁵⁴⁴. Whilst the CD-MUSIC model can theoretically be reduced into the TLM and BSL models, when the surface charge of each surface complex is constrained to specific planes and with integer values, this remains unconfirmed⁵⁴⁵.

SCM parameters are normally obtained using programs that optimise equilibrium constants by improving the fit of the model against experimental data^{285 543}. An initial guess is made for unknown equilibrium constants. The program calculates the surface complexation model and compares the difference between each experimental data point and the SCM prediction. Equilibrium constants are then adjusted, and the model is recalculated to see if the error is increased or decreased. This process can be repeated over many iterations, with the aim of producing equilibrium constants which provide a convincing agreement between model and experiment.

Since surface charge influences the adsorption of all charged sorbates, equilibrium constants for the major surface charge generating reactions ((de)protonation of surface hydroxyls and electrolyte adsorption) are normally calculated first, by fitting potentiometric titration data^{291 89}. pH adsorption edges are normally used to obtain equilibrium constants for the formation of surface complexes from sorbates such as arsenic^{230 245 225}. pH adsorption edges plot the total

amount of sorbate removed from solution as a function of pH. This data provides very useful constraints for the optimisation of arsenic surface complexation constants, given the strong pH dependence of arsenic adsorption (especially As(V)) ²³⁰. Since the protonation state of arsenic surface complexes changes as a function of pH ^{230 245 225}, pH adsorption edges present the best adsorption data with which to capture that change.

10.8.6. Goodness of fit in the surface complexation model

FITEQL optimises equilibrium constants by reducing the sum of squares of the weighted residuals ⁵⁴⁶. This error function, V_y, is calculated using:

$$V_y = \frac{SOS}{DF} = \frac{\sum(Y_j/S_j)^2}{N_p N_c - N_u}$$

Equation 10.11

where SOS is the sum of squares of the weighted residuals and DF is the number of degrees of freedom. Y_j is the error between the experimental and calculated mass balance, S_j is the error in Y_j calculated from experimental error estimates, and N_p, N_c and N_u are the number of data points, the number of group II components (where both total and free concentration are known), and the number of fitted parameters respectively ^{285 547}. Values of V_y between 0.1 and 20 are generally considered as representing a good fit between experimental and modelled results ⁵⁴⁶.

The majority of the potentiometric titrations presented in chapter 6 showed a statistically good fit, including when averaged values of logK_M and logK_L were used to model titrations at all three ionic strengths (Table 10.5). The Fe₂O₃ model gave the worst fit to experimental titration data, owing to the steep slope in the experimental titration curves at pH values greater than the point of zero charge, which were not captured by the model. This difference is likely due to non-surface charge effects, i.e. interferences or experimental error ²⁷⁹. The titration of meso-TiO₂ in 0.1 M NaCl also gave a value of V_y greater than 20, in this case owing to the curvature in the experimental titration curve at around pH 8, thought to be experimental error.

All pH adsorption edges gave values of V_y below 20, indicating a good fit. The highest value of V_y was 15.9 for As(V) adsorption onto Fe₂O₃, which is due to the model predicting weaker adsorption at acidic pH values than was observed experimentally. This could be due to multilayer As(V) adsorption at acidic pH, with protonation of As(V) oxyanions promoting surface precipitation.

Table 10.5: Values of V_y (a) for the potentiometric titrations with the final, averaged results of electrolyte adsorption equilibrium constants, and (b) for the pH adsorption edges with the final arsenic surface complexation constants.

		V_y		
Sample		FeOOH	Fe ₂ O ₃	meso-TiO ₂
potentiometric titration	0.01 M NaCl	8.27	169	2.59
	0.05 M NaCl	2.46	74.2	10.7
	0.1 M NaCl	15.6	63.7	76.1
pH adsorption edge	As(V)	1.42	15.9	2.77
	As(III)	5.87	6.72	4.14

10.9. FITEQL codes for surface complexation modelling

10.9.1. Example 1: potentiometric titration of FeOOH

```
1  
1  
1  
1  
1  
50  
6       1       1       1       1  
00160 -1.00  1.00E-3  PSI0  
00161 -0.50  0.00    PSIb  
00162 -0.20  0.00    PSId  
00001 -2.07  8.47E-3 SOH  
00030  0.00  1.00E-1 Na  
00020  0.00  1.00E-1 Cl  
00010  0.00  0.00    H+  
00170  0.00  0.00    ACT  
  
00170  0.00  170   1  
00020  0.00  20    1  
00030  0.00  30    1  
00010  0.00  10    1  
00100 -13.95 10   -1  
00001  0.00   1   1  
00011  5.59   1   1   10   1  160  1  
00012 -12.61   1   1   10  -1  160  -1  
03001 -8.90   1   1   10  -1  160  -1   30  1   161  1  
02001  8.50   1   1   10   1  160  1   20  1   161  -1  
  
00170      170  00  
00020      170  0.5  
00030      170  0.5  
00010      170  0.5
```

00100 170 0.5
00001 170 00
00011 170 00
00012 170 00

00004 127.10 9.99 0.90 0.20
0.10 1.0
 2 0
3001
2001
27 2 1 1
10
2.67E-03
2.53E-03
2.39E-03
2.11E-03
1.98E-03
1.84E-03
1.70E-03
1.56E-03
1.43E-03
1.29E-03
1.16E-03
1.02E-03
8.87E-04
7.53E-04
6.18E-04
4.85E-04
3.51E-04
2.18E-04
8.53E-05
-4.72E-05
-1.79E-04
-3.11E-04
-5.74E-04
-7.04E-04
-1.09E-03
-1.48E-03

-2.12E-03

170

9.85E-02

9.84E-02

9.84E-02

9.83E-02

9.82E-02

9.82E-02

9.81E-02

9.80E-02

9.80E-02

9.79E-02

9.79E-02

9.78E-02

9.77E-02

9.77E-02

9.76E-02

9.76E-02

9.75E-02

9.75E-02

9.74E-02

9.73E-02

9.73E-02

9.72E-02

9.71E-02

9.71E-02

9.69E-02

9.67E-02

9.65E-02

10

-4.263

-4.468

-4.679

-5.090

-5.303

-5.531

-5.761

-5.990

-6.223

-6.443

-6.667

-6.893

-7.127

-7.362

-7.624

-7.900

-8.178

-8.457

-8.737

-9.013

-9.278

-9.518

-9.907

-10.053

-10.372

-10.584

-10.812

0.970

0.969

0.968

0.965

0.964

0.963

0.961

0.960

0.959

0.958

0.956

0.955

0.954

0.953

0.952

0.950

0.949

0.948

0.947

0.946	
0.944	
0.943	
0.941	
0.940	
0.936	
0.933	
0.927	
00	00

10.9.2. Example 2: pH adsorption edge for As(V)/FeOOH

1							
1							
1							
1							
1							
50							
6	1	2	1	1			
00160	-1.00	1.00E-3	PSI0				
00161	-0.50	0.00	PSIb				
00162	-0.20	0.00	PSId				
00001	-4.00	0.00	SOH				
00020	-2.00	1.00E-2	Na+				
00030	-2.00	1.00E-2	Cl-				
00090	-9.00	0.00	AsV				
00010	0.00	0.00	H+				
00170	0.00	1.00E-2	ACT				
00010	0.00	10	1				
00100	-13.95	10	-1				
00001	0.00	1	1				
00011	5.59	1	1	10	1	160	1
00012	-12.61	1	1	10	-1	160	-1
00090	0.00	90	1				
00091	-2.25	90	1	10	-1		
00092	-9.00	90	1	10	-2		
00093	-20.6	90	1	10	-3		

8.49E-04

8.48E-04

8.45E-04

8.42E-04

8.45E-04

8.44E-04

8.47E-04

8.49E-04

8.44E-04

90

3.13E-04

3.12E-04

3.12E-04

3.12E-04

3.12E-04

3.12E-04

3.12E-04

3.12E-04

3.14E-04

3.13E-04

3.12E-04

3.15E-04

3.13E-04

3.12E-04

90

-6.23

-6.36

-6.55

-6.78

-6.97

-7.88

-9.00

-9.39

-9.64

-11.56

-12.40

-14.64

-16.24

-17.04
10
-2.97
-3.19
-3.47
-3.90
-4.30
-5.70
-6.67
-6.96
-7.17
-8.30
-8.74
-9.89
-10.68
-11.08
0.996
0.995
1.009
1.004
1.002
1.006
1.005
1.000
0.998
1.001
0.999
1.003
1.005
1.000
00 00

10.9.3. Example 3: pH adsorption edge for As(III)/FeOOH

1

1

1
1
1
50
6 1 2 1 1
00160 -1.00 1.00E-3 PSI0
00161 -0.50 0.00 PSIb
00162 -0.20 0.00 PSId
00001 -3.00 0.00 SOH
00020 -2.00 1.00E-2 Na+
00030 -2.00 1.00E-2 Cl-
00090 0.00 0.00 As3
00010 0.00 0.00 H+
00170 0.00 1.00E-2 ACT

00010 0.00 10 1
00100 -13.95 10 -1
00001 0.00 1 1
00011 5.59 1 1 10 1 160 1
00012 -12.61 1 1 10 -1 160 -1
00090 0.00 90 1
00091 -9.22 90 1 10 -1 170 -2
00092 -21.33 90 1 10 -2 170 -6
00093 -34.74 90 1 10 -3 170 -12
09001 3.00 1 2 90 1 10 -1 161 -1
09002 7.00 1 2 90 1
09003 5.70 1 1 90 1 160 1 161 -1
00020 0.00 20 1
00030 0.00 30 1
00170 0.0 170 01
03001 -9.10 1 1 10 -1 160 -1 30 1 161 1
02001 8.79 1 1 10 1 160 1 20 1 161 -1

00010 170 0.5
00100 170 0.5
00001 170 00
00011 170 00
00012 170 00

00090 170 0.0
00091 170 0.5
00092 170 2.0
00093 170 4.5
09001 170 00
09002 170 00
09003 170 00
00020 170 0.5
00030 170 0.5
00170 170 00
03001 170 00
02001 170 00

00004 127.10 1.00 0.90 0.20
0.01 1.0
2 0
9001
9002
14 2 2 0
1
8.40E-04
8.47E-04
8.41E-04
8.44E-04
8.41E-04
8.39E-04
8.41E-04
8.45E-04
8.42E-04
8.44E-04
8.39E-04
8.44E-04
8.48E-04
8.47E-04
90
3.01E-04
3.01E-04
3.01E-04

3.01E-04

3.01E-04

3.01E-04

3.01E-04

3.02E-04

3.02E-04

3.02E-04

3.02E-04

3.02E-04

3.02E-04

3.02E-04

3.02E-04

90

-4.06

-4.14

-4.14

-4.26

-4.26

-4.37

-4.42

-4.41

-4.42

-4.45

-4.64

-5.34

-5.77

-5.97

10

-2.89

-3.26

-3.60

-4.34

-4.63

-5.49

-6.10

-6.86

-7.04

-7.47

-8.36

-10.18
-10.64
-11.07
00 00

10.9.4. Example 4: adsorption isotherm for As(V)/FeOOH

1
1
1
1
1
50
6 0 3 1 1
00160 -1.00 1.00E-3 PSI0
00161 -0.50 1.00E-3 PSIb
00162 -0.20 1.00E-3 PSId
00001 -4.00 8.46E-4 SOH
00030 -2.00 1.00E-2 Na
00020 -2.00 1.00E-2 Cl
00170 0.00 1.00E-2 ACT
00090 -7.00 1.00E-9 AsV
00010 -7.00 0.00 H+

00010 0.00 10 1
00100 -13.95 10 -1
00001 0.00 1 1
00011 5.59 1 1 10 1 160 1
00012 -12.61 1 1 10 -1 160 -1
00090 0.00 90 1
00091 -2.25 90 1 10 -1
00092 -9.00 90 1 10 -2
00093 -20.6 90 1 10 -3
09001 11.85 1 2 90 1 10 -1 161 -1
09002 11.82 1 2 90 1
09003 6.12 1 1 90 1 10 -2 161 -2
00020 0.00 20 1

00030 0.00 30 1
00170 0.00 170 1
03001 -9.10 1 1 10 -1 160 -1 30 1 161 1
02001 8.79 1 1 10 1 160 1 20 1 161 -1

00170 170 00
00020 170 0.5
00030 170 0.5
00010 170 0.5
00100 170 0.5
00001 170 00
00011 170 00
00012 170 00
00090 170 4.5
00091 170 2.0
00092 170 0.5
00093 170 00
09001 170 00
09002 170 00
09003 170 00
03001 170 00
02001 170 00

00004 127.10 1.00 0.90 0.20

0.01 1.0

0 0
26 0 1 0

90

-19.00

-18.00

-17.00

-16.00

-15.00

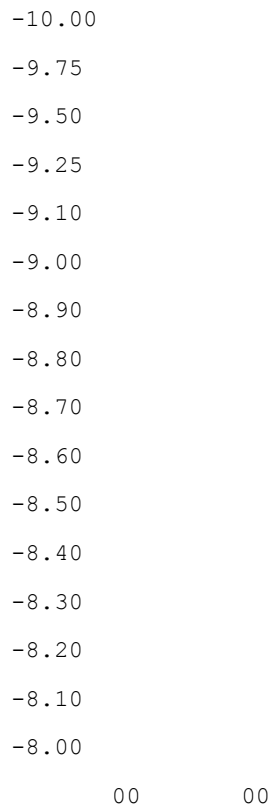
-14.00

-13.00

-12.00

-11.00

-10.50



10.9.5. Example 5: adsorption isotherm for As(III)/FeOOH

1				
1				
1				
1				
1				
50				
7	1	1	1	0
00160	-1.00	1.00E-3	PSI0	
00161	-0.50	1.00E-3	PSIb	
00162	-0.20	1.00E-3	PSId	
00001	-4.00	8.46E-4	SOH	
00030	-2.00	1.00E-2	Na	
00020	-2.00	1.00E-2	Cl	
00998	0.00	1.0E-12	AsOH	
00090	0.00	0.00	As3	
00010	-7.00	0.00	H+	

00010 0.00 10 1
00100 -13.95 10 -1
00001 0.00 1 1
00011 5.59 1 1 10 1 160 1
00012 -12.61 1 1 10 -1 160 -1
00090 0.00 90 1
00091 -9.22 90 1 10 -1
00092 -21.33 90 1 10 -2
00093 -34.74 90 1 10 -3
09001 4.67 1 2 90 1 10 -1 161 -1
09002 7.93 1 2 90 1
09003 5.49 1 1 90 1 160 1 161 -1
00020 0.00 20 1
00030 0.00 30 1
03001 -9.10 1 1 10 -1 160 -1 30 1 161 1
02001 8.79 1 1 10 1 160 1 20 1 161 -1
00998 0.0 998 1
00997 0.00 998 1 90 1

09001 998 -1
09002 998 -1
09003 998 -1
00998 998 1
00997 998 0 90 1

00010
00100
00001
00011
00012
00090
00091
00092
00093
09001
09002
09003
00020
00030

03001
02001

00004 127.10 1.00 0.90 0.20
0.01 1.0
1 0
997
17 1 1 0
90
2.72E-06
9.90E-06
3.99E-05
1.00E-04
1.41E-04
2.02E-04
2.72E-04
3.38E-04
4.22E-04
4.83E-04
5.57E-04
6.57E-04
7.30E-04
8.08E-04
8.90E-04
9.75E-04
1.14E-03
90
-7.21
-7.25
-6.99
-6.36
-5.97
-5.29
-4.65
-4.23
-3.97
-3.80
-3.69

-3.55
-3.46
-3.38
-3.32
-3.26
-3.17

00 00

10.10. Set up of photooxidation kinetic experiments

UV-Vis absorbance data was used to identify an appropriate concentration of powdered photocatalyst to use for oxidation kinetic experiments. The total mass balance of arsenic was monitored during a test experiment using a combination of anodic stripping voltammetry (ASV) and ICP-MS, to verify the experimental set-up. Control experiments were conducted, using aqueous solutions in the dark and under ultraviolet irradiation, and using photocatalyst suspensions in the dark.

10.10.1. Ultraviolet absorbance by powder suspensions

In this work, a soft ultraviolet lamp ("UV-A") was used to irradiate photocatalyst suspensions. The spectral output of this lamp was characterised by a major peak centred at $\lambda=368$ nm. This lies just within the band edge of meso-TiO₂, and significantly within the band edge of meso-TiO₂/Fe₂O₃ (Figure 10.15).

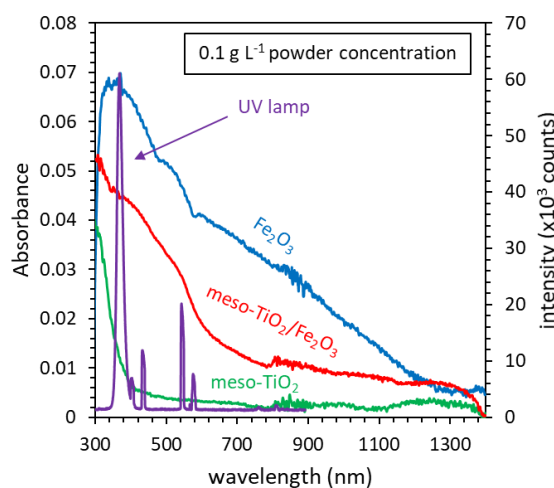


Figure 10.15: UV-Vis absorption spectra of 0.1 g L⁻¹ suspensions of each sample are compared with the spectral output of the 18W ultraviolet lamp used in the kinetic experiments (with the peak centred at $\lambda=368$ nm). 0.1 g L⁻¹ was the photocatalyst concentration used in each kinetic experiment.

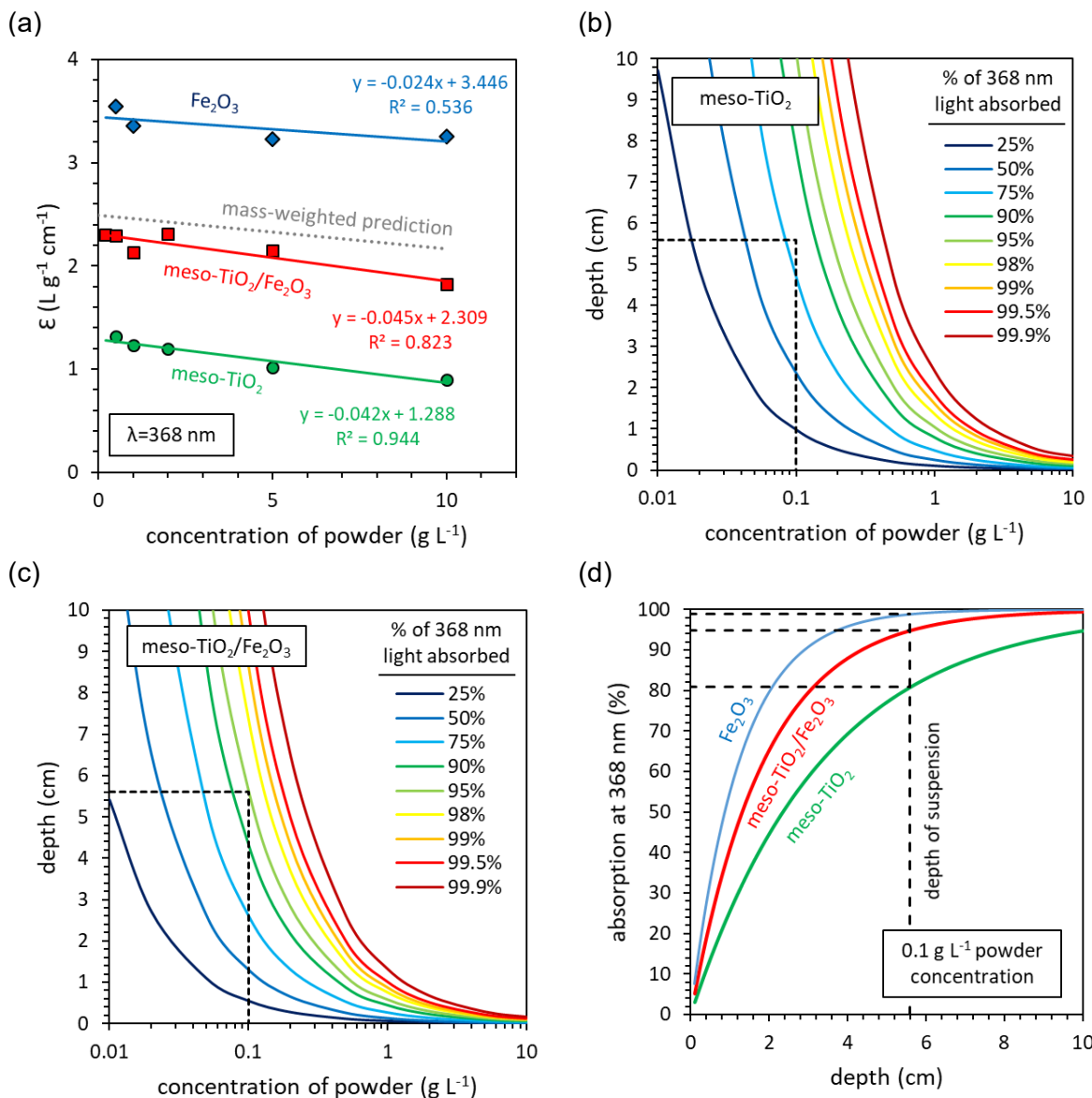


Figure 10.16: UV-Vis spectroscopy of meso-TiO₂, meso-TiO₂/Fe₂O₃ and Fe₂O₃ used to characterise the photoreactor set-up. (a) A comparison of the absorption coefficient (ϵ) at different concentrations of suspended solid. The percentage of incident photons ($\lambda=368\ nm$) absorbed by photocatalyst suspensions as a function of photocatalyst concentration and depth of the reactor vessel is also presented for (b) meso-TiO₂, and (c) meso-TiO₂/Fe₂O₃. A comparison of the percentage of 368 nm radiation absorbed by 0.1 g L⁻¹ suspensions of meso-TiO₂, meso-TiO₂/Fe₂O₃, and Fe₂O₃ is presented in (d). Dashed black lines indicate the depth of the suspension used in the kinetic experiments (with a total volume 100 mL). UV-Vis absorption spectra were obtained using powder samples suspended in Milli-Q water without pH adjustment.

Calculations were made using the Beer-Lambert law to determine an appropriate photocatalyst concentration for subsequent photooxidation kinetic experiments. The wavelength of the ultraviolet lamp was centred at 368 nm. The absorption coefficient, ϵ , was calculated as a function of powder concentration. This data is presented in Figure 10.16a and shows a slight decrease in ϵ with increasing powder concentrations, due to increased diffuse reflectance. This effect was stronger in the meso-TiO₂ containing samples, due to the high

refractive index of titania. The absorption coefficient was used to estimate the percentage of incident photons ($\lambda=368$ nm) absorbed as a function of both the concentration of powder, and the depth of the suspension (Figure 10.16b,c). The average error in ϵ between the mass-weighted combination of meso-TiO₂ and Fe₂O₃ and the experimental data collected for meso-TiO₂/Fe₂O₃ (N=4) was 14% only, indicating that absorbance at 368 nm was approximately component additive. Based on these results, 0.1 g L⁻¹ was chosen as the photocatalyst concentration, and a 100 mL beaker, giving a depth of 5.6 cm once filled, was chosen as the photoreactor vessel, for all kinetic experiments reported in chapter 7.

In this experimental set-up, the results estimated that meso-TiO₂ suspensions absorb 80.9% of incident photons at 368 nm (Figure 10.16d). The true figure may be a little higher, if diffuse reflectance from the magnetic stirrer plate beneath the reactor vessel is included. For meso-TiO₂/Fe₂O₃ this number increases to 94.9%. Fe₂O₃ was predicted to absorb 98.8% of incident photons. It was thus anticipated that the majority of incident photons would be absorbed by the suspension in all cases, and that the photon flux absorbed by each suspension could be assumed as equivalent.

10.10.2. Photooxidation kinetic operating conditions and constraints

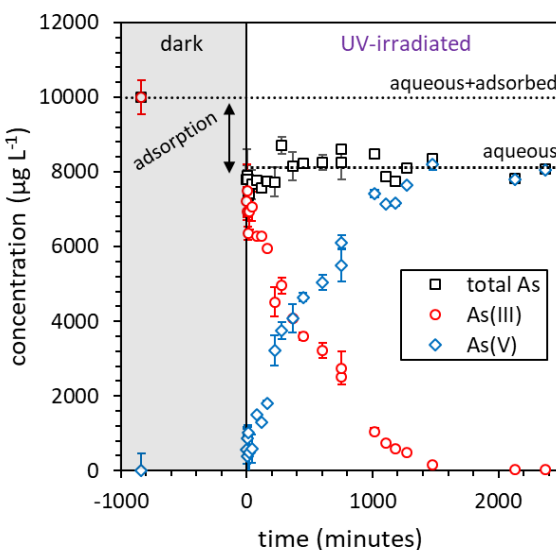


Figure 10.17: Total mass balance during photocatalytic oxidation. As(III) was determined using anodic stripping voltammetry, and total As was determined by ICP-MS. As(V) was calculated by the subtraction of As(III) from As(V). Negative time indicates where the suspension was stirred in the dark to achieve equilibrium adsorption, with t=0 representing when UV irradiation was started. The experimental conditions were 0.1 g L⁻¹ meso-TiO₂/Fe₂O₃, pH 7.4 (10 mM HEPES buffer solution), 10 mg L⁻¹ initial As(III), 368 nm wavelength irradiation, and a photon flux of 5.1 mW cm⁻², or 107 mW L⁻¹.

Chapter 7 demonstrated the improvement in arsenic adsorption after photocatalytic treatment. Experiments at an initial As(III) concentration of 1 mg L⁻¹ indicated that up to 66% of arsenic was removed with just 0.1 g L⁻¹ photocatalyst (section 7.3). Furthermore, adsorption significantly increased after photooxidation (section 7.3). In order to minimise the interference of adsorption in the determination of photooxidation kinetics, the initial concentration of As(III) was therefore increased to 10 mg L⁻¹. Whilst this is around ten times greater than the concentrations of arsenic that occur in the natural environment^{86 40}, test experiments showed that at 10 mg L⁻¹, less than 20% of the total arsenic was adsorbed (Figure 10.17). Furthermore, the proportion of total arsenic adsorbed before and after photooxidation was similar (Figure 10.17) (potentially due to As(III) adsorption being enhanced through multilayer adsorption at high concentrations). Photocatalytic oxidation was thus better separated from adsorption processes by using an initial concentration of 10 mg L⁻¹ As(III). Since the proportion of total arsenic adsorbed showed no significant changes during the course of photooxidation under these conditions, only As(III) was used to monitor the progress of the reaction during subsequent experiments.

10.10.3. Control experiments

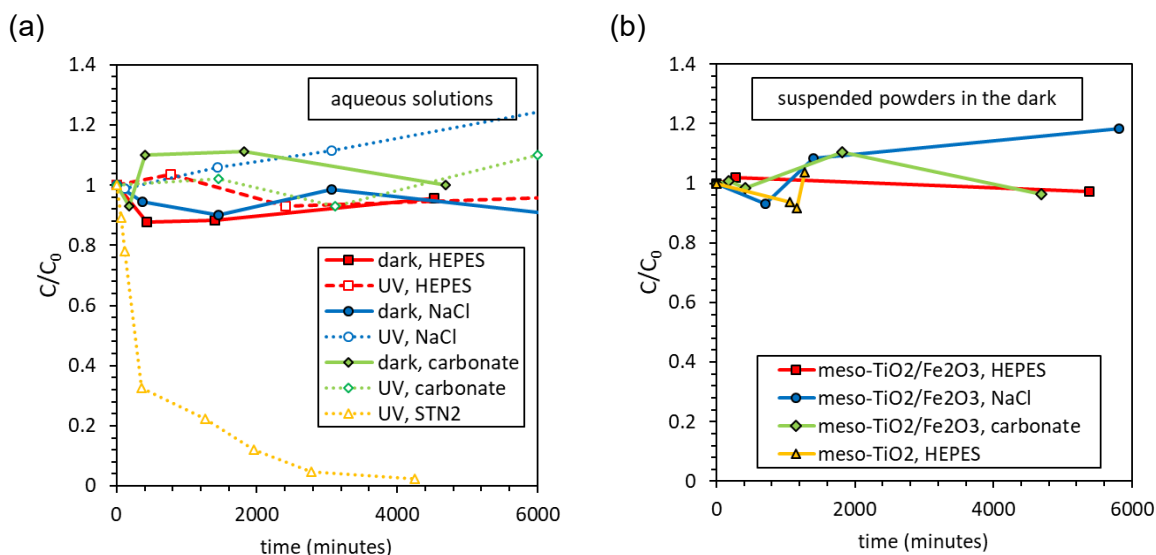


Figure 10.18: Photooxidation kinetic control experiments: (a) aqueous solutions, with and without ultraviolet irradiation, and (b) suspended powders without ultraviolet irradiation. Experimental conditions were 0 or 0.1 g L⁻¹ photocatalyst, and 0.01 M of either HEPES, NaCl, carbonate, or STN2 ($pH 7.2 \pm 0.2$), 368 nm wavelength ultraviolet irradiation, and a photon flux of either 0 or 14.3 mW cm⁻² (0 or 259 mW L⁻¹).

Photooxidation kinetic control experiments are presented in Figure 10.18. In the absence of the heterogeneous photocatalyst, no oxidation of As(III) was observed for solutions of 10 mM HEPES, NaCl or carbonate, both in the dark and when irradiated with 14.3 mW cm⁻¹ ultraviolet radiation ($\lambda=368$ nm) (Figure 10.18a). In fact, the concentration of As(III) in 10 mM NaCl actually increased with ultraviolet radiation, due to evaporation of the solvent. The UV-transparent fused silica lid was used to prevent evaporation in subsequent experiments. Direct, aqueous phase photooxidation of As(III) was therefore eliminated as a potential interference for photocatalytic oxidation kinetics, within the timescale of 0-4000 minutes.

When the natural groundwater *STN2* was spiked with 10 mg L⁻¹ As(III) and irradiated with ultraviolet light, however, the As(III) spike was fully oxidised after approximately 3000 minutes. In natural groundwaters, As(III) concentrations can be reduced through coprecipitation as iron(III) oxides are produced by the oxidation of Fe(II) ions ⁹¹. However, in this work groundwater samples were exposed to air and stirred for two hours after pH neutralisation to induce iron oxidation before spiking with As(III). Additionally, no colour was observed in the final solution after UV irradiation. Loss of As(III) was therefore not likely to be due to iron oxide precipitation. Another possibility is aqueous phase photooxidation of As(III) mediated by dissolved organic matter, e.g. humic acid, which is known to be prevalent in the groundwaters of South Asia ⁸⁶, and which was indicated by the high absorbance of the natural samples given in Table 3.2.

The slow oxidation of As(III) in the natural groundwater sample is therefore anticipated to introduce a small interference on the photocatalytic oxidation kinetics measured for meso-TiO₂/Fe₂O₃ (which reached completion after 1000-1500 minutes, as demonstrated in chapter 7), but should be insignificant for meso-TiO₂ (which reached completion in under 100 minutes). A similar control experiment in the dark was not performed, due to the limited availability of this groundwater sample. No oxidation of As(III) was observed for photocatalyst suspensions in the dark (Figure 10.18b), indicating that no significant oxidation of As(III) occurred during the preparation of each photocatalytic oxidation experiment, where suspensions were stirred in the dark to achieve equilibrium adsorption.

10.11. Langmuir-Hinshelwood kinetics partially capture the adsorption-controlled kinetics of meso-TiO₂/Fe₂O₃

10.11.1. Re-fitting As(III) adsorption isotherms for the Langmuir-Hinshelwood kinetic model

The adsorption isotherms reported in chapter 6 were fit in the range of 0-11 mg L⁻¹ (0-150 µM) [As(III) (aq)] to obtain Langmuir adsorption isotherm parameters (K_L and Q_{max}) before significant multilayer adsorption occurs (Figure 10.19). Values of K_L were 1.18 ± 0.55 L mg⁻¹ and 0.93 ± 0.14 L mg⁻¹ and values of Q_{max} were 15.7 ± 1.0 and 22.8 ± 0.7 mg g⁻¹ for meso-TiO₂ and meso-TiO₂/Fe₂O₃ respectively.

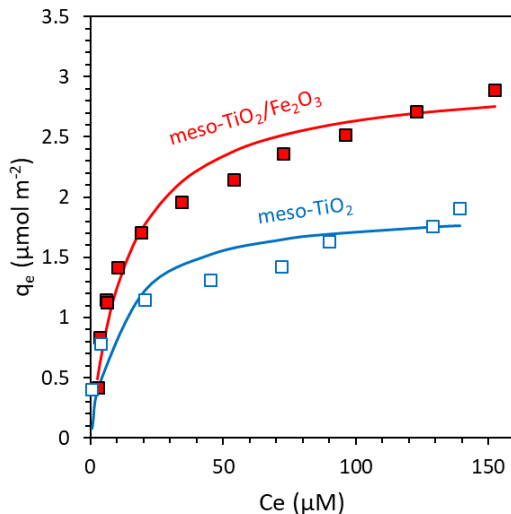


Figure 10.19: Fitting adsorption isotherms to obtain K_L and Q_{max} . C_e denotes the concentration of aqueous As(III) at equilibrium, whilst q_e denotes the concentration of adsorbed As(III) at equilibrium. The experimental conditions were 1 g L⁻¹ photocatalyst, pH 7.0 ± 0.1 and 0.01 M NaCl.

10.11.2. Initial rates analysis using linearised Langmuir-Hinshelwood kinetics fails for both photocatalysts

Analysis of initial rates using Langmuir-Hinshelwood kinetics was performed using the following two linearised equations:

$$\frac{1}{\text{initial rate}} = \frac{1}{K_L k} \cdot \frac{1}{C} + \frac{1}{k}$$

Equation 10.12

$$\frac{C}{\text{initial rate}} = \frac{1}{k} \cdot C + \frac{1}{K_L k}$$

Equation 10.13

where K_L is the Langmuir parameter, reflecting the binding affinity between the substrate and the catalyst surface (L mg^{-1}), and k is the rate constant ($\text{mg L}^{-1} \text{min}^{-1}$)³⁰⁰. These two equations were termed ‘linearisation A’ and ‘linearisation B’ respectively. Rate constant k is a convolution of the Langmuir-Hinshelwood rate constant k_{LH} (min^{-1}) and the monolayer adsorption capacity, Q_{max} (mg g^{-1})³⁰⁰. k_{LH} (min^{-1}) was calculated using the equation:

$$k_{\text{LH}} = \frac{k}{Q_{\text{max}} C_s}$$

Equation 10.14

where C_s is the concentration of suspended photocatalyst (0.1 g L^{-1}).

Analysis of initial rates using linearisation of the Langmuir-Hinshelwood rate equation failed to provide meaningful results for meso-TiO₂, owing to the zero-order dependence previously established in section 7.4.2. Under ‘linearisation A’, the coefficient of determination (R^2) was only 0.2579 (Figure 10.20a). Under ‘linearisation B’, the y-intercept of the linear regression was negative, yielding a physically meaningless negative value of K_L , unless the data point at 0.5 mg L^{-1} As(III) was excluded to alter the slope of the linear regression (Figure 10.20b). Langmuir adsorption constants, K_L , obtained using the two linearisation approaches were much larger than the value obtained from experimental adsorption isotherms (15.2 ± 12.0 and 7.15 ± 21 versus $1.18 \pm 0.55 \text{ L mg}^{-1}$). The large difference between K_L values indicates the failure of the Langmuir-Hinshelwood model to describe photocatalytic oxidation of As(III) using meso-TiO₂³⁰⁰.

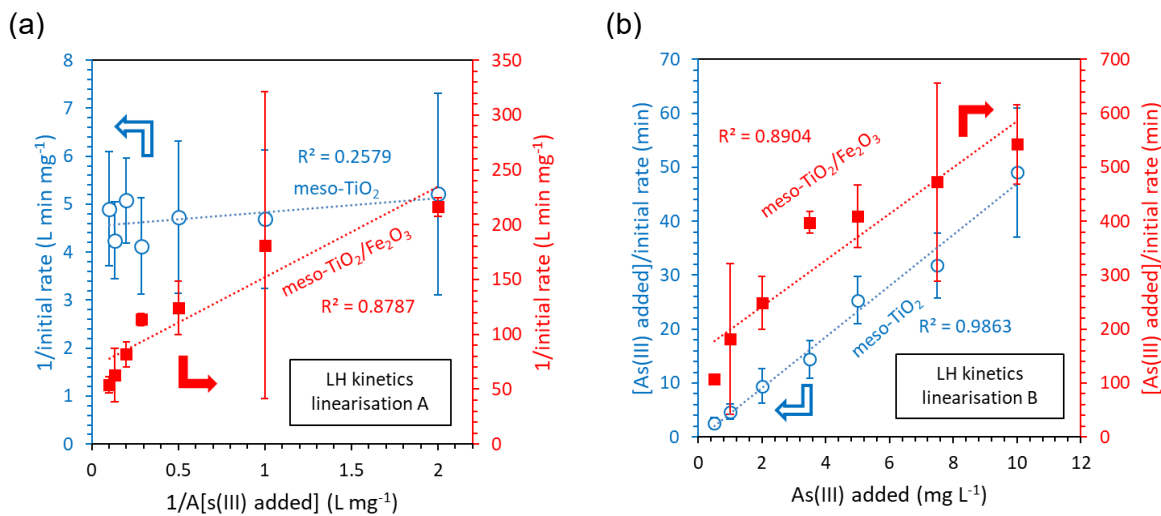


Figure 10.20: Langmuir-Hinshelwood analysis of initial rates. The relationship between initial As(III) concentration and the initial rate of As(III) oxidation kinetics is presented, plotted in two linearised forms of the Langmuir-Hinshelwood kinetic model.³⁰⁰

More physically meaningful results were achieved for meso-TiO₂/Fe₂O₃. The K_L value obtained using ‘linearisation A’ agreed well with the value obtained from adsorption isotherms (0.843 ± 0.2 versus $0.93 \pm 0.14 \text{ L mg}^{-1}$), although K_L was only 0.274 ± 0.089 when calculated using ‘linearisation B’. However, the quality of the linear regression was poor ($R^2 < 0.9$), owing to a change in steepness when more than 3.5 mg L^{-1} As(III) is added. The effect was significant, for instance using ‘linearisation B’, the slope obtained is four times steeper using data in the range $[As(III) \text{ added}] = 0\text{--}3.5 \text{ mg L}^{-1}$, than if using data in the range $[As(III) \text{ added}] \geq 3.5 \text{ mg L}^{-1}$ (Figure 10.20b).

10.11.3. Non-linear Langmuir-Hinshelwood kinetics

Application of Langmuir-Hinshelwood kinetics to kinetic serial data introduced curvature to the plots of $\ln(C_t/C_0)$ versus time. This provided a worse fit for meso-TiO₂ (Figure 10.21a), but a superior fit for meso-TiO₂/Fe₂O₃ (Figure 10.21b), when compared with the PFO model. Despite the superior fit for meso-TiO₂/Fe₂O₃, Langmuir-Hinshelwood rate constants were not constant, with an exponential decrease in k_{LH} as the concentration of As(III) was increased (Figure 7.13). The results suggested (a) that the kinetics of photocatalytic oxidation in the presence of meso-TiO₂/Fe₂O₃ were controlled by the concentration of adsorbed As(III), but also (b) that Langmuir-Hinshelwood kinetics are not sufficient to fully describe the chemistry. One notable feature of LH kinetics is that the adsorption isotherm used to calculate the concentration of adsorbed substrate is independent of competitor ions, such as the As(V) product. As(V)

outcompetes As(III) for adsorption onto minerals such as goethite (FeOOH) at pH 7²²⁵, and it has previously been reported that competitive adsorption of the As(V) product onto TiO_2 photocatalysts leads to catalyst fouling through the blocking of surface sites ($C_0=5 \text{ mg L}^{-1}$, 0.1–0.5 g L⁻¹ photocatalyst)²⁹. It is therefore sensible to anticipate competitive adsorption of the As(V) product, leading to significant deviations from the Langmuir adsorption isotherm as photooxidation proceeds. This was the rational for the SCM-constrained kinetic model presented in chapter 6.

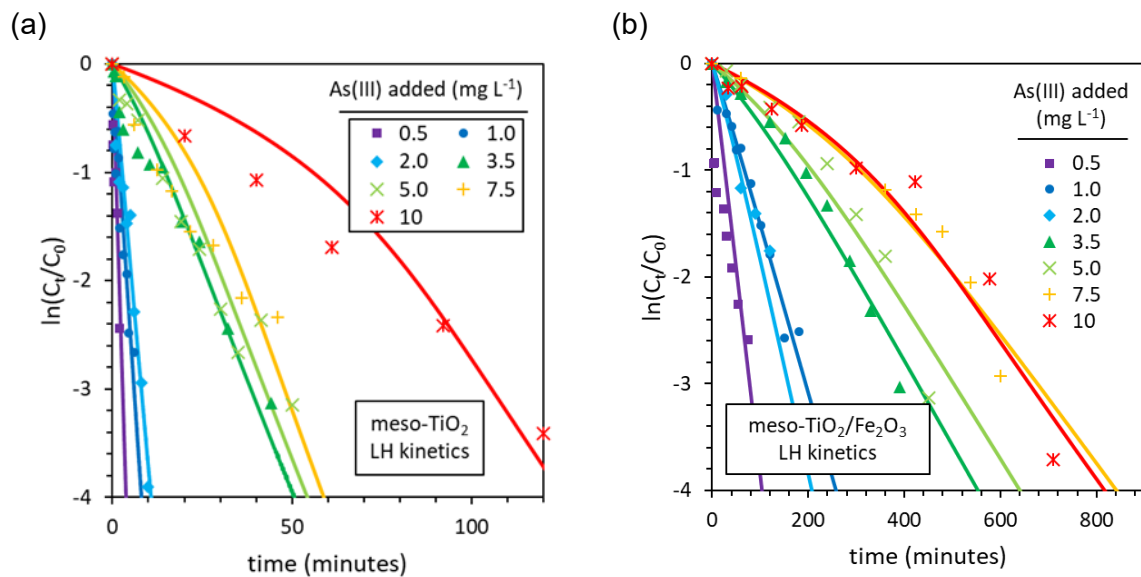


Figure 10.21: Serial data fitted using Langmuir-Hinshelwood kinetics. The Langmuir adsorption constant, K_L , was calculated from experimental adsorption isotherms, using only the data in the range of $C_e = 0\text{--}11 \text{ mg L}^{-1}$ to reduce the error in K_L due to multilayer sorption, whilst covering the full experimental range.

10.12. Surface complexation modelling for the kinetic analysis of As(III) photocatalytic oxidation

Equilibrium constants for the surface complexation of phosphate with Fe₂O₃ and TiO₂ were obtained by fitting experimental data taken from the literature, as presented in Figure 10.22.

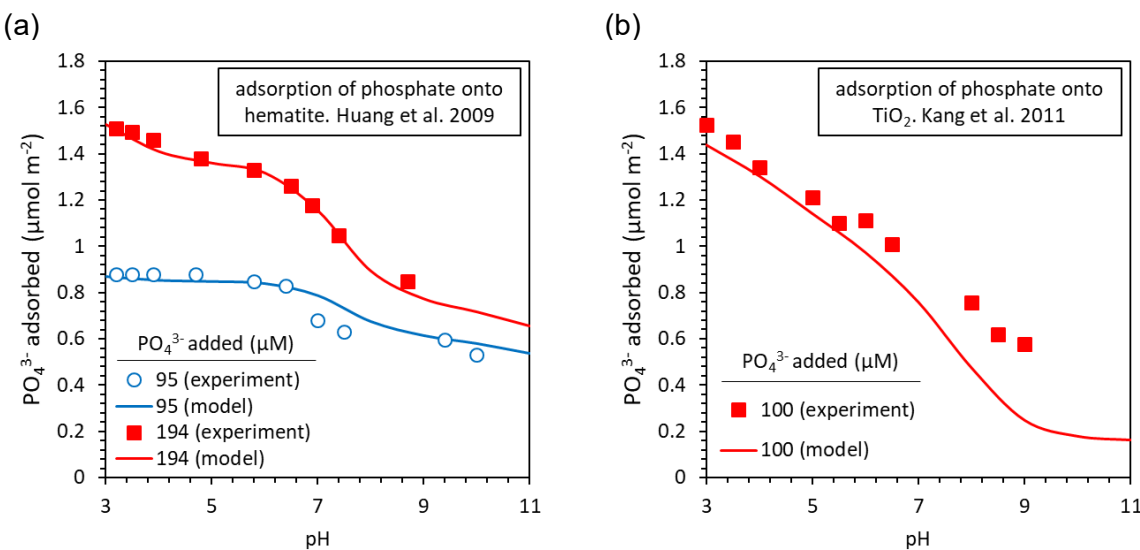


Figure 10.22: Determination of phosphate surface complexation constants. Surface complexation constants for the adsorption of phosphate onto Fe₂O₃ and TiO₂ were obtained by fitting the extended triple layer model (ETLM) to the experimental pH adsorption edges reported by Huang et al.³⁰² and Kang et al.³⁰¹. Adsorption was modelled using Visual MINTEQ and site densities, inner and outer capacitance, surface acidity constants and electrolyte adsorption constants were kept at the values used in chapter 6. The experimental conditions used by Huang et al. were 20 g L⁻¹ Fe₂O₃ (5.3 m² g⁻¹) suspended in 0.1 M NaCl, with the pH adjusted using 0.1 M HCl and 0. M NaOH³⁰². The experimental conditions used by Kang et al. were 1 g L⁻¹ Degussa P25 TiO₂ (50 m² g⁻¹) suspended in 0.01 M NaCl with the pH adjusted using HCl and NaOH³⁰¹.

The SCM predicted an approximately linear decrease in C_t/C₀ (i.e. the decrease in aqueous As(III)) with the progress of total As(III) oxidation for all meso-TiO₂ experiments: with 1 and 10 mg L⁻¹ initial As(III), and both with and without 10 mg L⁻¹ phosphate (Figure 10.23). The SCM prediction signifies that when adsorption-desorption has reached equilibrium, monitoring the concentration of As(III) remaining in the aqueous phase would give an accurate account of the total extent of photooxidation (across aqueous and adsorbed phases) for these experiments using meso-TiO₂.

In contrast, when modelling meso-TiO₂/Fe₂O₃ with an initial As(III) concentration of 10 mg L⁻¹, a highly sigmoidal shape was observed (Figure 10.23): during the first 20% of oxidation progress, [As(III) (ads)] decreased much more quickly than the total concentration of As(III);

during the middle 60% of the reaction, [As(III) (ads)] decreased less quickly than total As(III); and in the final 20% [As(III) (ads)] decreased rapidly again. The implication is that C_t/C_0 (monitored using the concentration of aqueous As(III) remaining) is not equivalent to q_t/q_0 (the relative amount of adsorbed As(III) remaining) and that the relative change in [As(III) (aq)] is not equivalent to the relative change in [As(III) (total)].

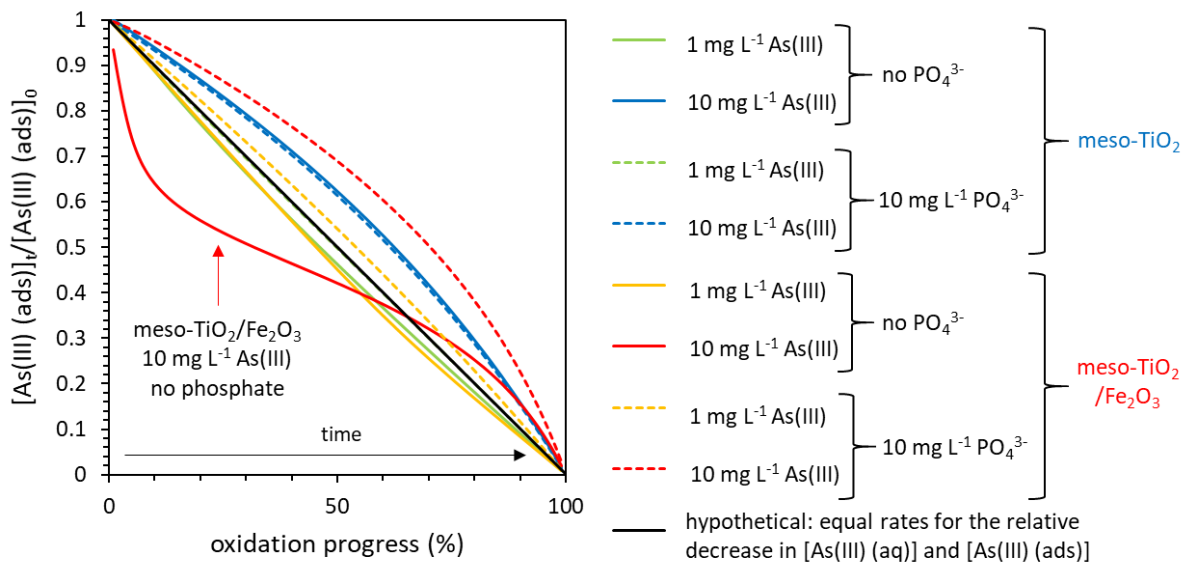


Figure 10.23: Changes in the concentration of adsorbed As(III) with the progress of As(III) oxidation. SCM calculations were made using Visual MINTEQ. All calculations used 0.01 M NaCl as the electrolyte, pH 7, and a photocatalyst concentration of 0.1 g L^{-1} .

These results indicate that monitoring aqueous As(III) would underestimate the total rate of photooxidation in the initial stages of photooxidation, since adsorbed As(III) (unmonitored in the experiment) is depleted at a faster rate than aqueous phase As(III). The rate would be overestimated in later stages of the experiment. The SCM predicted that this effect would become increasingly significant as the initial concentration of As(III) was increased from 0.5 mg L^{-1} to 2 mg L^{-1} . Above 2 mg L^{-1} , this effect reaches its maximum, a behaviour that approximately corresponds with the experimental observation that when $C_0 \leq 1 \text{ mg L}^{-1}$ experimental data can be fitted using the pseudo-first order model for the entire experiment, whilst when $C_0 \geq 5 \text{ mg L}^{-1}$, a steeper slope in the linear plot was observed in the later stages of each experiment, with the rate constant (determined from the slope) appearing to ‘become faster’.

Interestingly, none of these effects were observed in the 10 mg L^{-1} As(III) model when 10 mg L^{-1} phosphate was also added. In this scenario an opposite effect was observed, with the concentration of adsorbed As(III) being slowest to decrease in the initial stages of the reaction. This is explained by the negative surface charge induced by adsorption of phosphate anions reducing the favourability of As(III) substitution by As(V).

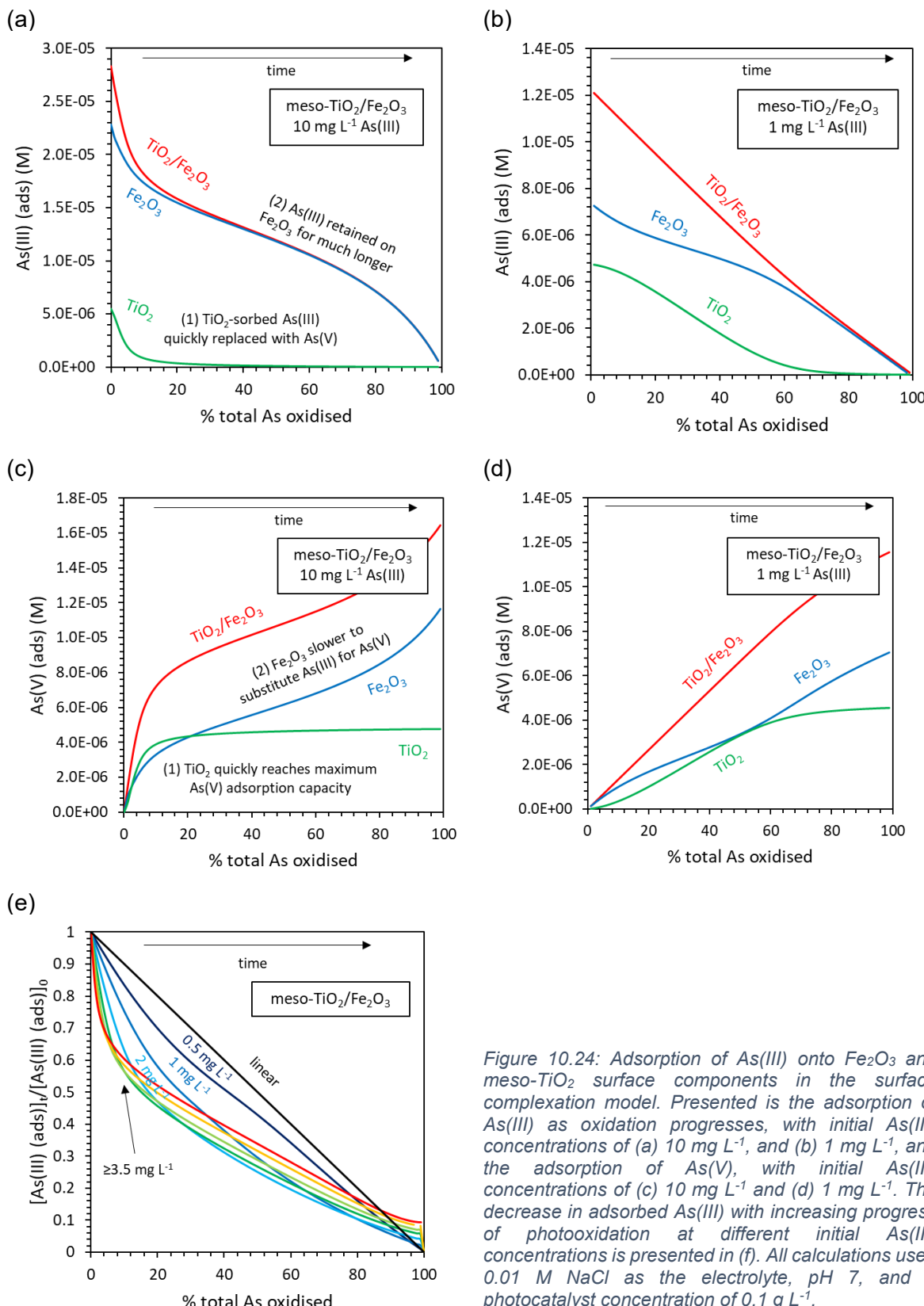


Figure 10.24: Adsorption of As(III) onto Fe_2O_3 and meso- TiO_2 surface components in the surface complexation model. Presented is the adsorption of As(III) as oxidation progresses, with initial As(III) concentrations of (a) 10 mg L^{-1} , and (b) 1 mg L^{-1} , and the adsorption of As(V), with initial As(III) concentrations of (c) 10 mg L^{-1} and (d) 1 mg L^{-1} . The decrease in adsorbed As(III) with increasing progress of photooxidation at different initial As(III) concentrations is presented in (e). All calculations used 0.01 M NaCl as the electrolyte, pH 7, and a photocatalyst concentration of 0.1 g L^{-1} .

The SCM predicted that with an initial concentration of 10 mg L^{-1} , As(III) would be retained on the Fe_2O_3 surface until the very last stages of photooxidation (Figure 10.24a), resulting in the increased ratio of adsorbed-to-aqueous As(III) discussed in chapter 6. This effect was not seen at the lower initial As(III) concentration of 1 mg L^{-1} , with an approximately linear decrease in the concentration of adsorbed As(III) as photooxidation progresses (Figure 10.24b). In this scenario, a similar goodness of fit should be obtained whether constraining kinetics to the concentration of aqueous As(III) or adsorbed As(III). The corresponding speciation of adsorbed As(V) is given in Figure 10.24c and d. The profile of As(III) adsorption as a function of photooxidation transitions from linear to sigmoidal as initial As(III) is increased from 0.5 mg L^{-1} to 3.5 mg L^{-1} (Figure 10.24e).

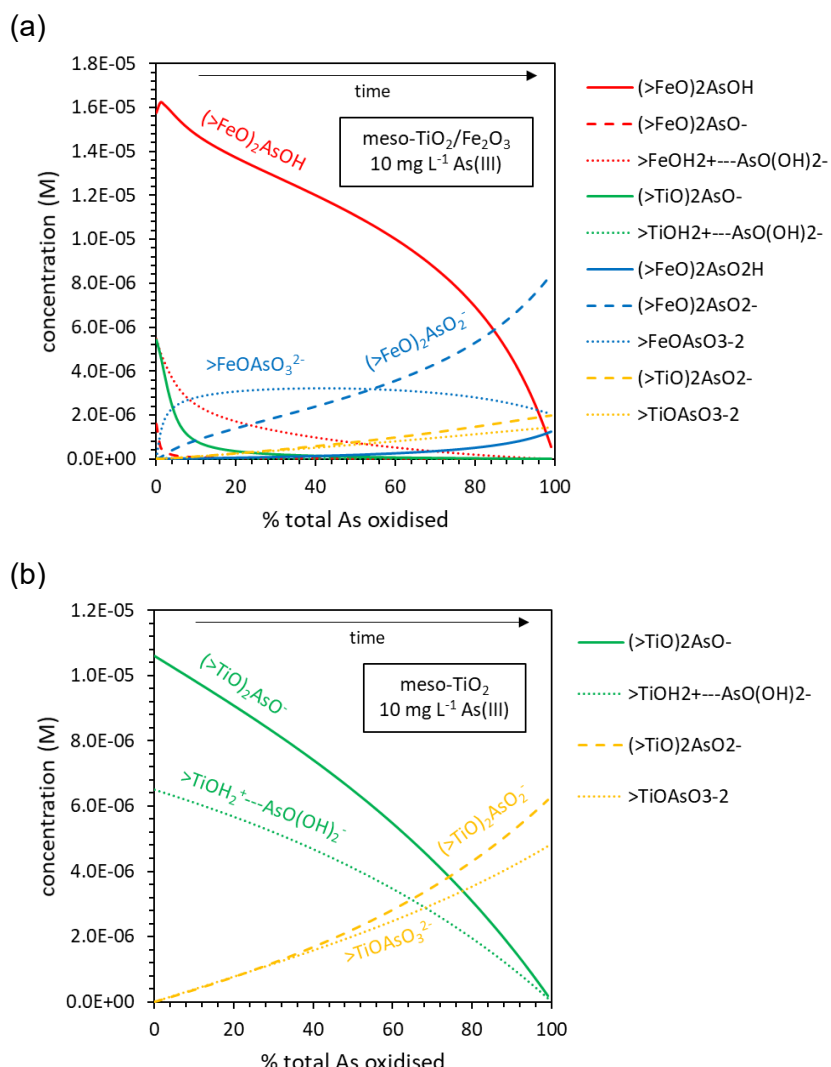


Figure 10.25: The speciation of adsorbed arsenic as a function of photooxidation progress, presented for (a) meso- $\text{TiO}_2/\text{Fe}_2\text{O}_3$, and (b) meso- TiO_2 . All calculations used 0.01 M NaCl as the electrolyte, pH 7, and a photocatalyst concentration of 0.1 g L^{-1} .

In the case of meso-TiO₂/Fe₂O₃, adsorbed As(III) is primarily present as the bidentate surface complex ($>\text{FeO}$)₂AsOH, persisting until the very last stages of photooxidation (Figure 10.25a). A small quantity of As(V) is adsorbed early on as the monodentate $>\text{FeAsO}_3^{2-}$ complex. The concentration of this surface complex remains relatively constant. In later stages of the reaction, As(III) is replaced with the bidentate ($>\text{FeO}$)₂AsO₂⁻ surface complex. The major As(III) complex is thus neutral, whilst As(V) is present as negative surface complexes. The development of negative surface charge as oxidation progresses limits the displacement of adsorbed As(III) with As(V) in this model. On the other hand, both As(III) and As(V) adsorb onto meso-TiO₂ as negatively charged surface complexes, leading to a more even (linear) decrease in the concentration of adsorbed As(III) as photooxidation progresses (Figure 10.25b).

10.13. Natural waters and the influence of media on the photocatalytic oxidation of arsenic(III)

Heterogeneous photocatalysts have still not been deployed in real-life arsenic remediation applications. It is clear that there is much to learn about how the groundwater chemistry of the South Asia will influence photocatalytic oxidation, not just in the composite $\text{TiO}_2/\text{Fe}_2\text{O}_3$ system, but also for the single component TiO_2 photocatalyst^{93 171 198}. This work therefore also investigated the influence that the groundwater chemistry of South Asia will have upon the photocatalytic oxidation of As(III).

The nature of the background media can influence photocatalysis through a variety of mechanisms, including blocking the photocatalyst surface through adsorption, scavenging charge carriers and absorbing incident photons¹⁷¹. The hydroxyl radical, $\cdot\text{OH}$, is one of the most important oxidants in environmental systems⁵⁴⁸, and hydroxyl radical-mediated mechanisms are normally considered to be the major pathway for photooxidation of As(III) (versus the superoxide radical, $\text{O}_2^{\cdot-}$, see chapter 2). The hydroxyl radical is a strong oxidising agent, with redox potentials of +1.90 V versus the SHE (standard hydrogen electrode) for the $\cdot\text{OH}/\text{OH}$ redox couple and +2.73 V for the $\cdot\text{OH} + \text{H}^+/\text{H}_2\text{O}$ redox couple⁴⁷⁶. Holes trapped on the surface produce strongly oxidising hydroxyl radical intermediates (+2.8 eV) through the reactions:

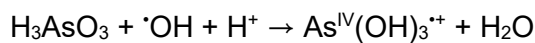


*Equation 10.15*⁵⁴⁹

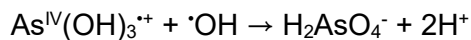


*Equation 10.16*⁵⁴⁹

Hydroxyl radicals may then oxidise As(III) through the following reactions:

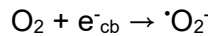


*Equation 10.17*²⁰³

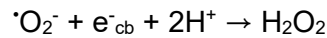


*Equation 10.18*²⁰³

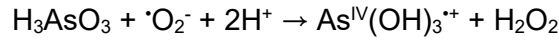
Several studies have considered a super-oxide mediated mechanism to be the major pathway for photocatalytic oxidation of As(III):



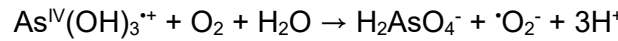
*Equation 10.19*¹⁷¹



*Equation 10.20*¹⁷¹

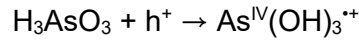


*Equation 10.21*²⁰³

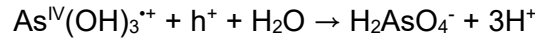


*Equation 10.22*²⁰³

Direct oxidation at the surface by trapped holes is a third possibility:



*Equation 10.23*²⁰³

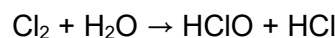


*Equation 10.24*²⁰³

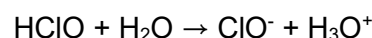
In this study, background media had a strong effect on initial reaction rates, which varied by as much as a factor of three (Figure 10.26). For both photocatalysts, reaction rates were greatest in 0.01 M NaCl and 0.01 M carbonate. This trend is explained by chloride and carbonate anions acting as hole scavengers, facilitating charge extraction and forming intermediate oxidants to oxidise As(III). In the presence of chloride ions, the oxidants hypochlorous acid (HOCl) and ClO⁻ are generated through the reactions:



*Equation 10.25*⁵⁵⁰



*Equation 10.26*⁵⁵¹



*Equation 10.27*⁵⁵¹

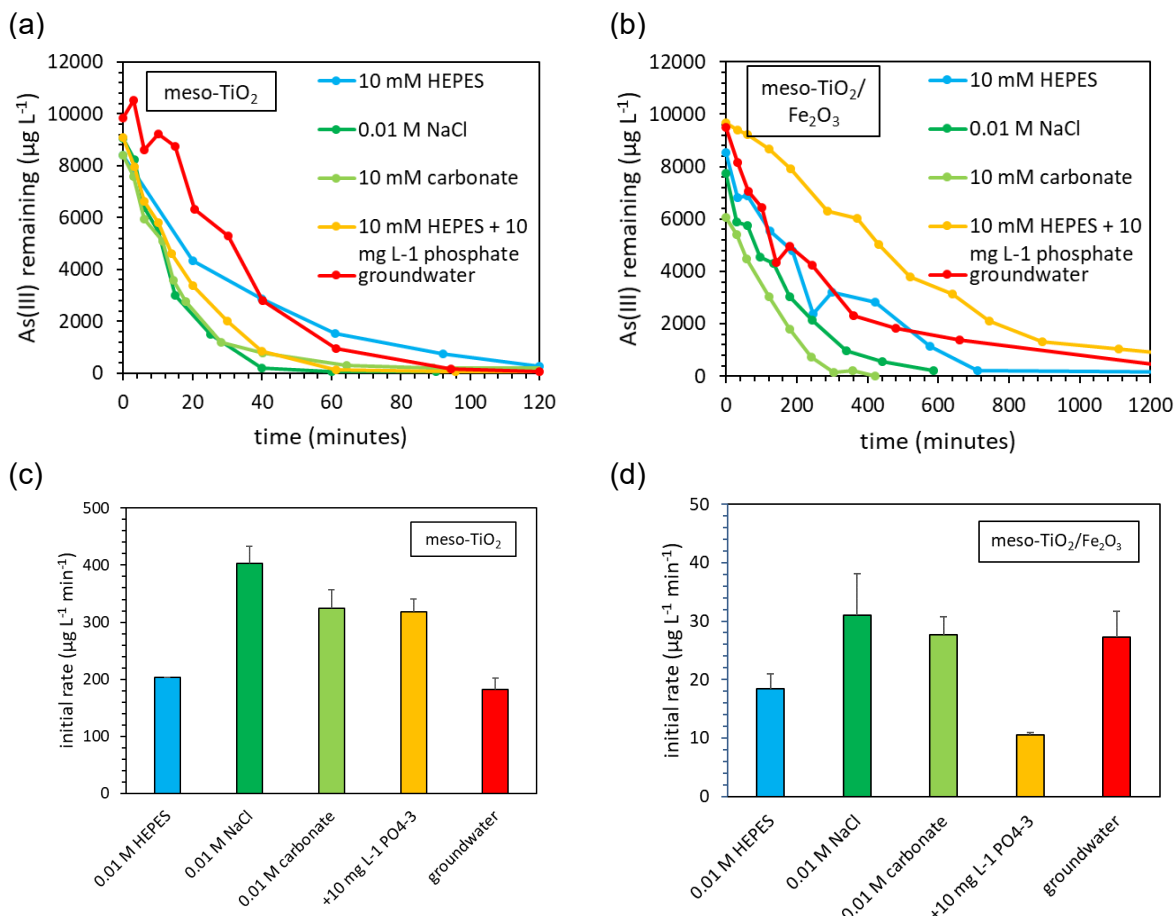
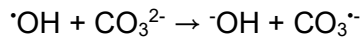


Figure 10.26: The influence of media on the photocatalytic oxidation of As(III). The experimental conditions were 10 mg L⁻¹ initial As(III), 0.1 g L⁻¹ photocatalyst, 368 nm ultraviolet radiation and 14 mW cm⁻² light intensity. The media investigated were 10 mM HEPES, 10 mM NaCl, 10 mM carbonate, 10 mM HEPES with addition of 10 mg L⁻¹ phosphate, and natural groundwater STN2, at pH 7.2±0.2. Error bars denote the uncertainty in the initial rate determined as the standard deviation of the slope in the linear regression fitted to the initial experimental kinetics.

Similarly, carbonate radicals are generated through the reaction:

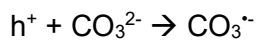


Equation 10.28¹⁹⁸

Both chloride and carbonate radicals can also be produced at the surface, under direct oxidation by trapped holes:



Equation 10.29⁵⁵²



Equation 10.30⁵⁵³

Hypochlorous acid, HOCl, and carbonate radicals are weaker oxidants than the hydroxyl radical, with +1.49 V for the HOCl/Cl⁻ redox couple⁵⁵⁴ and +1.57 V for the CO₃^{·-}/CO₃²⁻ redox

couple ^{555 476}. However, both chloride and carbonate are encountered in high concentrations in the environment.

The initial rate of As(III) photooxidation in the meso-TiO₂/HEPES system was significantly increased with the addition of 10 mg L⁻¹ phosphate. For the meso-TiO₂/Fe₂O₃/HEPES system, however, addition of phosphate significantly decreased the rate of As(III) oxidation. Phosphate can influence photocatalytic oxidation in a number of ways, including supressing oxidation by blocking access to the catalyst surface, or facilitating photooxidation either by drawing positive holes to the surface (H₂PO₄⁻ anions are negatively charged at pH 7), and by forming hydrogen-bonded complexes with H₂O which facilitate charge transfer and the subsequent generation of radical intermediates ¹⁷¹. The H₃PO₄/H₃PO₃ redox couple has a standard electrode potential of -0.276 V ⁵⁵⁶, and is therefore not reduced by the conduction band electrons at -0.25 V ⁵⁵⁷. Phosphate is known as a significant competitor of arsenic for adsorption to mineral surface sites ^{228 225}, and 10 mg L⁻¹ is sufficient to achieve monolayer coverage at pH 7 ²³. Blocking of surface sites should be considered a major mechanism by which presence of phosphate influences the observed photooxidation kinetics in this work.

The rate of As(III) photooxidation in the presence of meso-TiO₂ was similar when HEPES was substituted for the natural groundwater sample. In contrast, rates were faster in groundwater than HEPES in the meso-TiO₂/Fe₂O₃ system. The groundwater was characterised in Table 3.2. Though the dominant anion was not identified, it is likely to be Cl⁻, given that Na⁺ was the dominant cation. Arsenic-contaminated groundwaters in South Asia typically have around ~1 mg L⁻¹ phosphate, ~10 mg L⁻¹ sulphate and ~600 mg L⁻¹ carbonate ⁸⁶. Compared with HEPES, the presence of carbonate anions (and chloride where saline intrusion has occurred) promotes photooxidation through formation of radical intermediates, whilst competitor ions might be expected to supress photooxidation. A conclusion as to the cause of the observed effects of groundwater in the meso-TiO₂ and meso-TiO₂/Fe₂O₃ systems could not be identified.

10.14. Transient absorption spectroscopy (TAS)

10.14.1. Transient absorption decay of dry powders

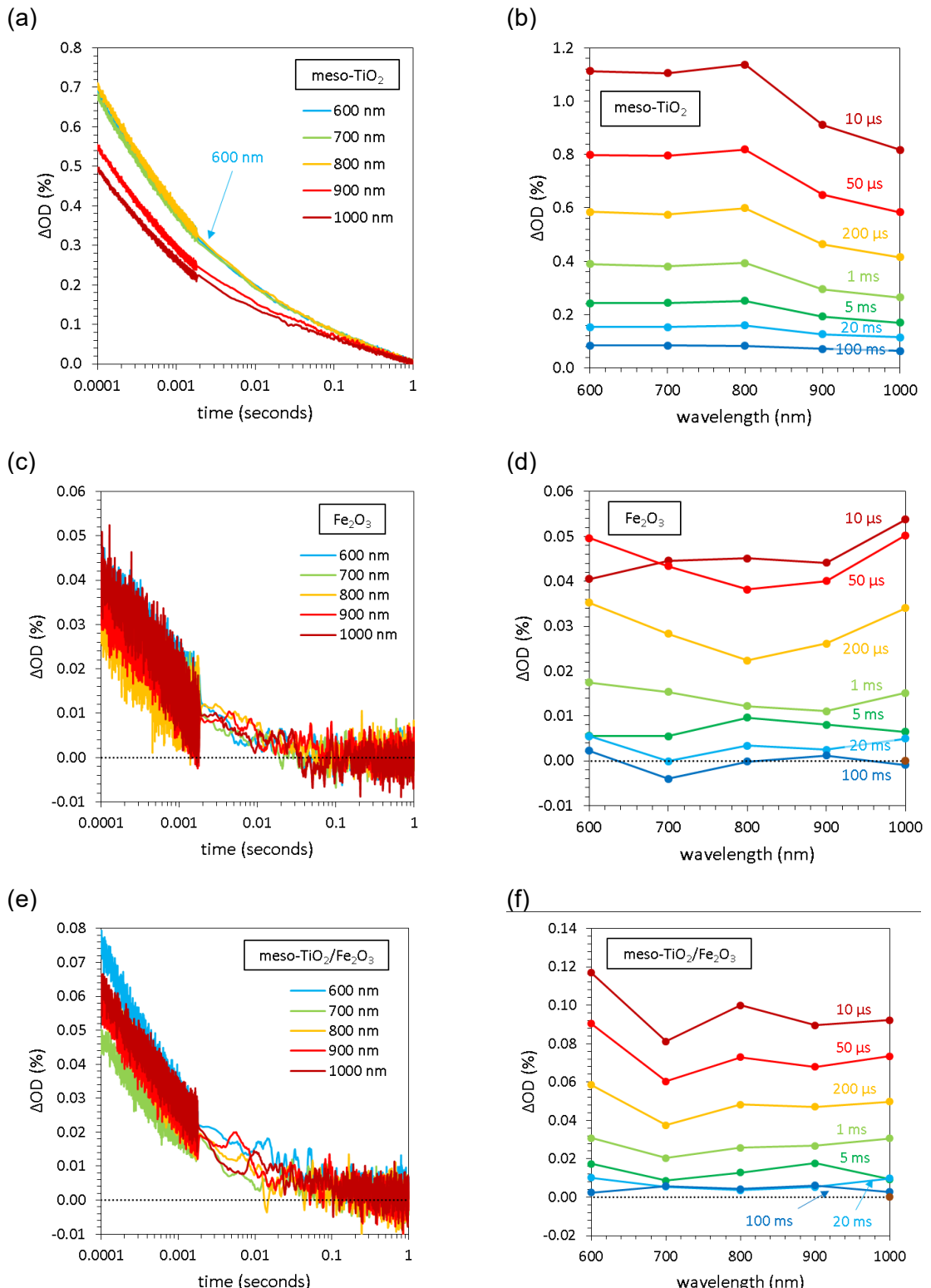


Figure 10.27: Transient absorption spectroscopy of dry powders. (a-b) meso-TiO₂, (c-d) meso-TiO₂/Fe₂O₃, and (e-f) Fe₂O₃.

The transient absorption of meso-TiO₂ decayed after 1 second. The change in optical density decreased when the probe wavelength was greater than 800 nm, as the electron signal in anatase is centred at 850 nm, and the hole signals of anatase and rutile are centred at 460 and 590 nm respectively ¹⁸⁴. The transient absorption of Fe₂O₃ decayed much more quickly, after just 0.1 second. Fe₂O₃ is much less reflecting at all probe wavelengths than meso-TiO₂, with a higher optical density. Therefore, ΔOD was much smaller in magnitude, with more noise in the data. No significant relationship could be observed between the wavelength of the probe and ΔOD. Meso-TiO₂/Fe₂O₃ showed intermediate behaviour. Transient absorption lasted a little over 0.1 second. Again, due to data noise, it was difficult to determine any significant relationship between wavelength and ΔOD.

Table 10.6: Power law decay parameters obtained by fitting the transient absorption decay of dry powders using Origin. The half-life was calculated by rearranging the power law decay function into the form $t = \left(\frac{0.5}{A}\right)^{\frac{1}{\alpha}}$. Data was normalised to give $\Delta O.D.=1$ at $t=0.1$ ms.

sample	wavelength (nm)	A	A (normalised)	α	R^2	half-life (ms)
meso-TiO ₂	600	0.059 ±0.001	0.0834 ±0.0007	0.270 ±0.002	0.9938	1.306
	700	0.0567 ±0.0008	0.0812 ±0.0006	0.273 ±0.002	0.996	1.271
	800	0.0573 ±0.0009	0.0787 ±0.0006	0.276 ±0.002	0.9956	1.232
	900	0.0409 ±0.0004	0.0727 ±0.0003	0.285 ±0.001	0.9982	1.142
	1000	0.0365 ±0.0004	0.0724 ±0.0003	0.285 ±0.001	0.9984	1.137
meso-TiO ₂ /Fe ₂ O ₃	600	0.0017 ±0.0001	0.0218 ±0.0004	0.416 ±0.008	0.9689	0.5301
	700	0.00127 ±0.00009	0.0261 ±0.0006	0.396 ±0.009	0.9635	0.5761
	800	0.00143 ±0.00009	0.0226 ±0.0004	0.412 ±0.008	0.9739	0.5387
	900	0.0017 ±0.0001	0.0282 ±0.0006	0.388 ±0.009	0.9584	0.5981
	1000	0.002 ±0.0001	0.0301 ±0.0005	0.38 ±0.007	0.975	0.6184
Fe ₂ O ₃	600	0.00045 ±0.00007	0.0101 ±0.0004	0.50 ±0.02	0.9065	0.4012
	700	0.00057 ±0.00008	0.0145 ±0.0005	0.46 ±0.02	0.9189	0.4515
	800	0.00049 ±0.0001	0.0164 ±0.0009	0.45 ±0.02	0.8037	0.4724
	900	0.00032 ±0.00006	0.0088 ±0.0004	0.51 ±0.02	0.8821	0.3853
	1000	0.00051 ±0.00008	0.0105 ±0.0004	0.50 ±0.02	0.9164	0.4054

10.14.2. Charge scavenging in meso-TiO₂ suspensions

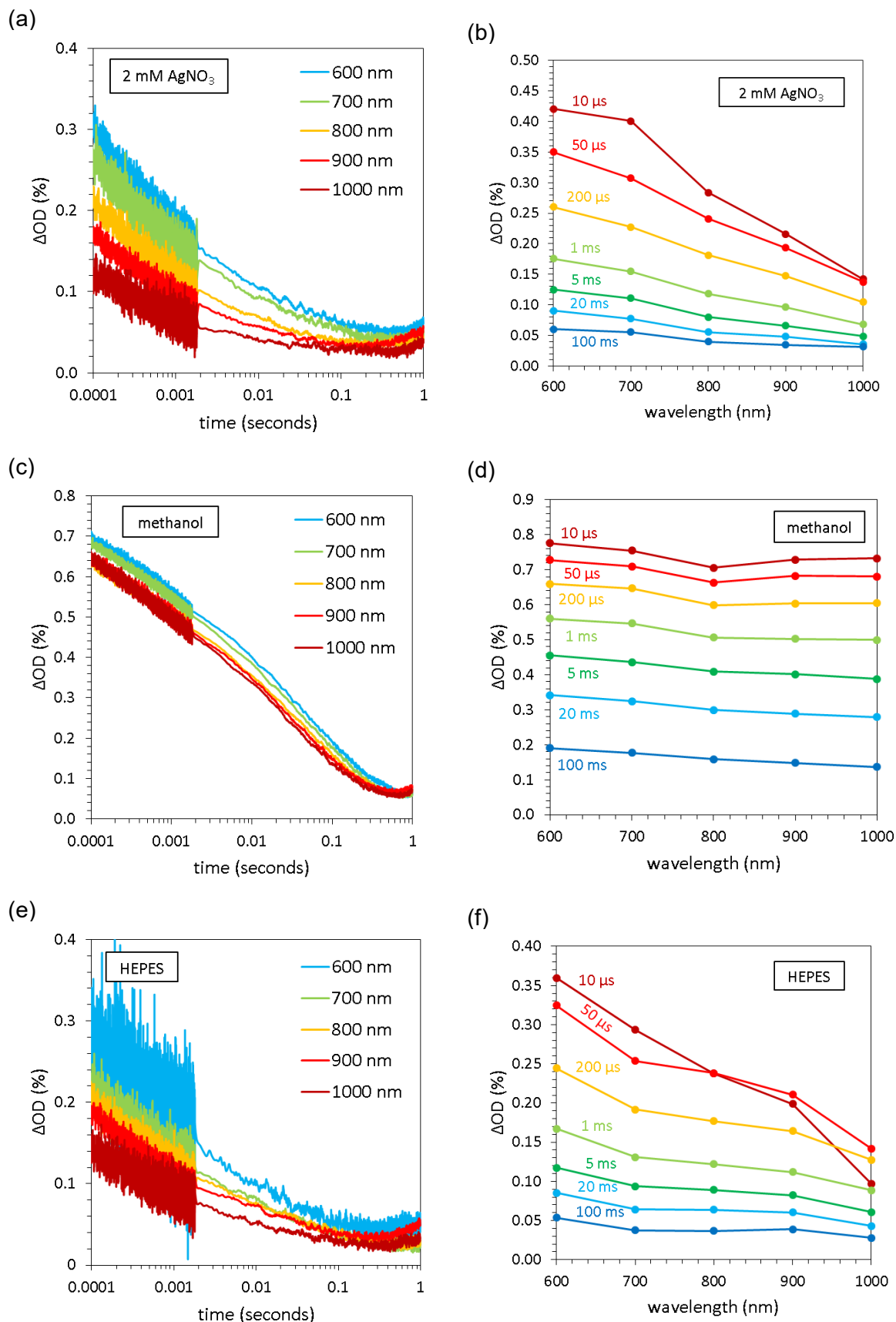
Previous studies on the photocatalytic oxidation of As(III) have reported contradictory mechanisms. On the basis of scavenger studies, authors have suggested both (a) mechanisms mediated by holes or ·OH (hydroxyl) radicals^{28 151 190}, and (b) mechanisms mediated by the ·O₂ (superoxide) radical^{191 192}. According to Marinho et al. (2019) the principle pathway for the As(III)/TiO₂ system has still not been resolved¹⁴¹. Similarly, both first and zero-order kinetics have been observed (with regards to the concentration of aqueous As(III))^{28 139}, whilst no study has determined whether As(III) is oxidised in the aqueous or adsorbed phase. This is important given that superior reaction rates in dye degradation when photocatalysed by anatase versus rutile TiO₂ have been attributed to surface versus solution-controlled reaction mechanisms, i.e. anatase may show superior rates due to the diffusion of hydroxyl radical intermediates into solution, leading to the aqueous phase oxidation of As(III), whilst hydroxyl radicals trapped at the rutile surface are only able to oxidise adsorbed As(III)⁵⁵⁸. The second component in a photocatalyst-sorbent composite (e.g. Fe₂O₃) might also act to trap charge carrier species, reducing reaction rates by limiting As(III) oxidation to the adsorbed phase.

Scavenging studies were conducted, with the aim of identifying the pathway responsible for photocatalytic oxidation of As(III). Only meso-TiO₂ was studied, as Fe₂O₃-containing powders were too optically dense to obtain a resolved transient absorption decay. For dry meso-TiO₂ powders, the magnitude of ΔOD was constant between 600 and 800 nm, before dropping off with increasing wavelength (Figure 10.27). Upon suspension in 2 mM AgNO₃, the magnitude of ΔOD was more wavelength dependent, decreasing as the wavelength was increased past 700 nm, and with a much larger difference between ΔOD at 600 and 1000 nm (Figure 10.28a,b). This is due to the electron scavenging behaviour of AgNO₃, reducing the electron signal, which is centred at 850 nm in anatase, relative to the hole signal (centred at 460 nm in anatase)¹⁸⁴. In contrast, when meso-TiO₂ was suspended in methanol, ΔOD became independent of wavelength (Figure 10.28c,d). This is due to hole scavenging, increasing the electron signal at higher wavelengths.

When suspended in HEPES, the TAS spectra of meso-TiO₂ showed some changes compared with the dry powder, with increased signal loss when the probe wavelength was increased (Figure 10.28e,f). This behaviour was similar, but not as strong, as when meso-TiO₂ was suspended in 2 mM AgNO₃, the electron scavenger. The electron scavenging behaviour of HEPES has been used to explain enhanced rates of H₂O₂ formation from 3-morpholinosydnonimine N-ethylcarbamide when HEPES is added⁵⁵⁹. Enhanced

photocatalytic rates in the presence of HEPES have also been reported in the degradation of methyl orange using TiO_2 as the photocatalyst⁵⁶⁰. The influence of As(III) addition (50 mg L⁻¹) on the transient absorption of meso- TiO_2 suspended in HEPES is presented in Figure 10.28g,h, with a strong increase in ΔOD at 700 nm. However, with 100 scans per wavelength significant photooxidation (induced by the laser pulse) was detected. Consequently, the observed relationship between wavelength and ΔOD was significantly influenced by decreasing concentrations of As(III) during analysis. Consequently, further As(III) experiments were conducted, where suspensions were scanned with 10 laser pulses at each wavelength, with wavelengths investigated in a randomised order, and repeated three times.

Charge carrier life-times were similar for the dry powder, and both 2 mM AgNO_3 and HEPES suspensions, with half-lives of around 1 millisecond in all cases (Figure 10.28i). In contrast, charge carrier lifetimes were significantly increased when meso- TiO_2 was suspended in either methanol or HEPES spiked with 50 mg L⁻¹ As(III) (Figure 10.28i). The half-lives of meso- TiO_2 suspended in 2 mM AgNO_3 , methanol and HEPES without addition of As(III) were all relatively wavelength independent. In contrast, the longest-lived charge carriers in the 50 mg L⁻¹ As(III) HEPES system were centred at 800 nm (Figure 10.28i). Since this is close to the electron signal peak at 850 nm¹⁸⁴, this could indicate scavenging of holes by As(III), indicating either direct hole, or hydroxyl-mediated oxidation of As(III), rather than a superoxide mediated pathway. Further experiments are needed to mitigate the influence of the laser pulse of As(III) concentrations, and therefore assess whether As(III) oxidation proceeds via holes or electrons using transient absorption spectroscopy. Whilst meso- TiO_2 in both 2 mM AgNO_3 and HEPES without As(III) was best described using a power-law decay function, meso- TiO_2 suspended in methanol and HEPES spiked with 50 mg L⁻¹ As(III) was better fit when using the log-linear decay function (Figure 10.28j). This represents a transition in the charge carrier recombination mechanism from thermal transport²⁹⁷ to tunnelling⁴⁶⁶, which is associated with long charge carrier lifetimes.



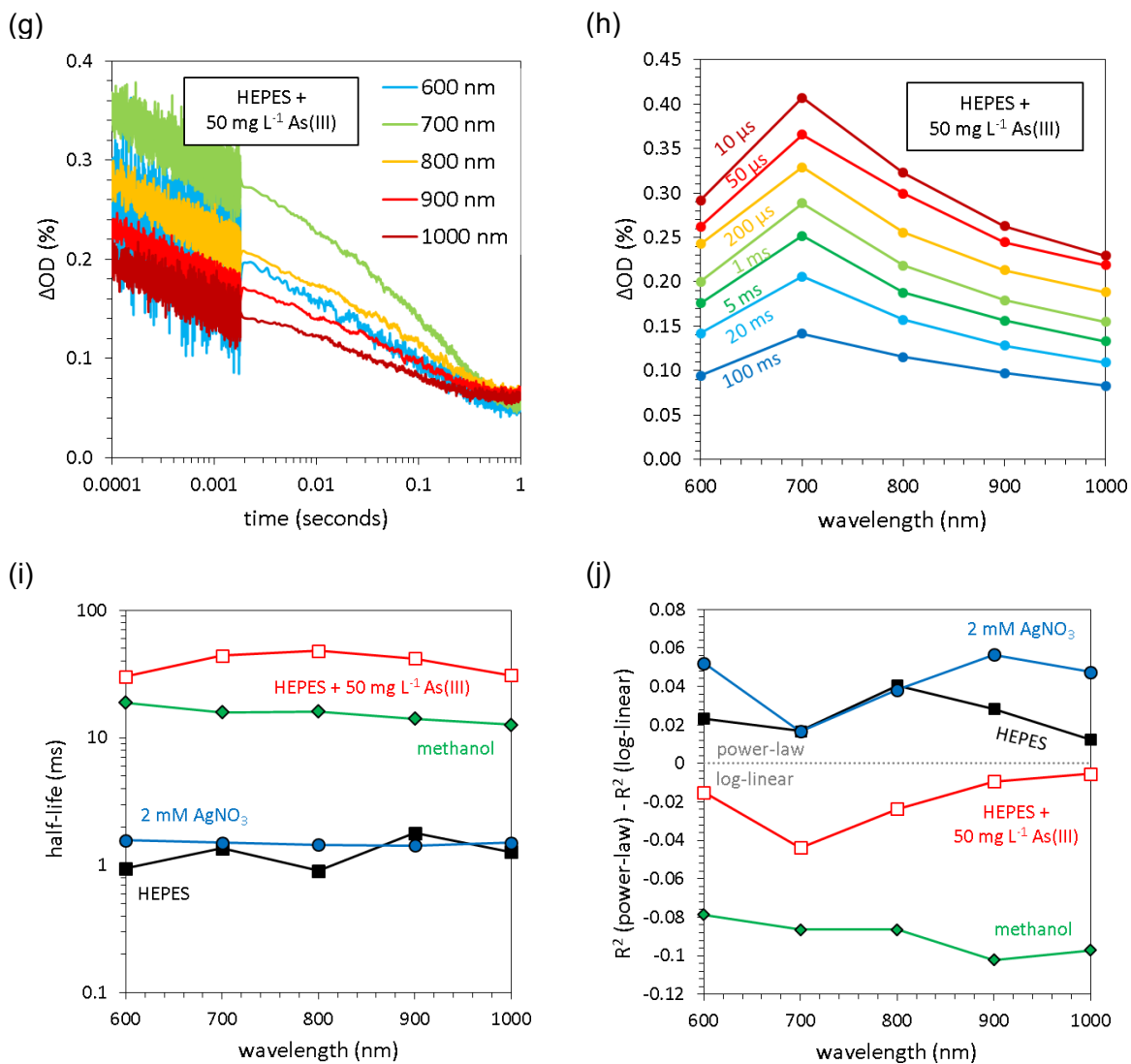


Figure 10.28: Transient absorption decays and spectra of meso- TiO_2 suspensions in various media. TAS spectra were only obtained for meso- TiO_2 , as quality data could not be obtained for the other samples as the change in optical density irradiation by the laser pulse was too small for other samples when compared with the background noise. Each kinetic trace is the average of 100 sequential scans.

10.14.3. The influence of As(III) on transient absorption

Scavenger studies revealed that addition of As(III) led to significantly longer lived transient absorption, however, due to photooxidation of As(III) by the laser pulse, the wavelength dependency of transient absorption could not be resolved to identify the charge carrier responsible for As(III) oxidation. A more detailed study, with reduced scans (10 instead of 100, repeated three times), with wavelengths scanned in a randomised order, was performed, with As(III) varied between 0 and 50 mg L^{-1} .

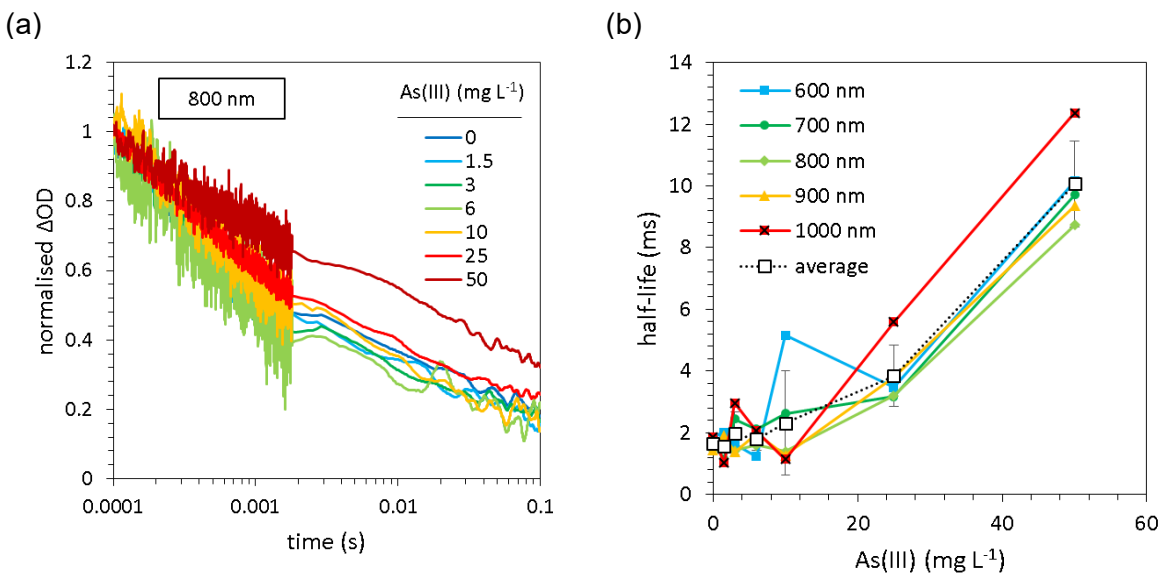
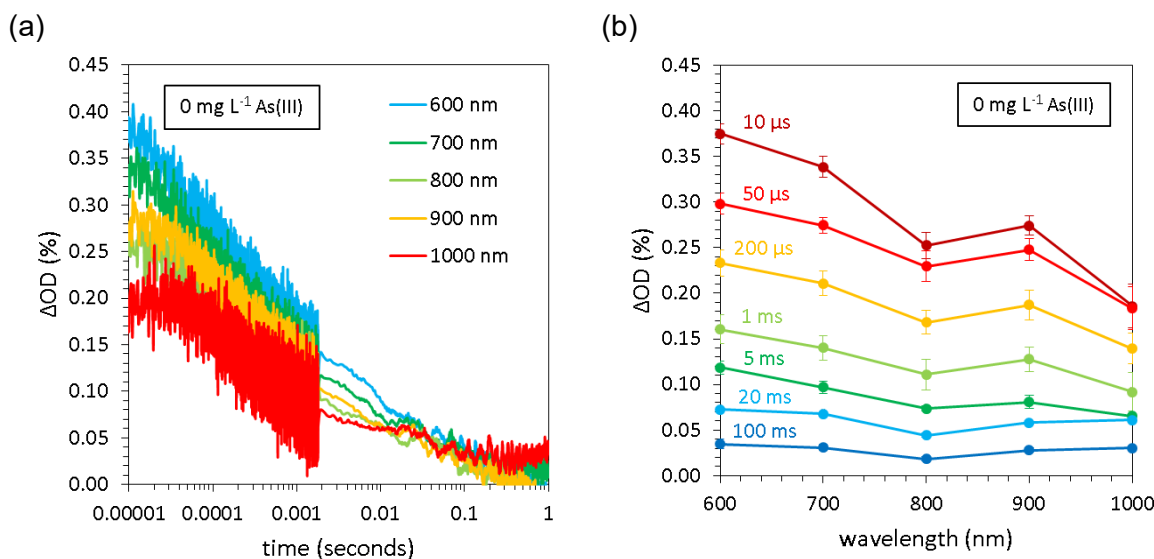
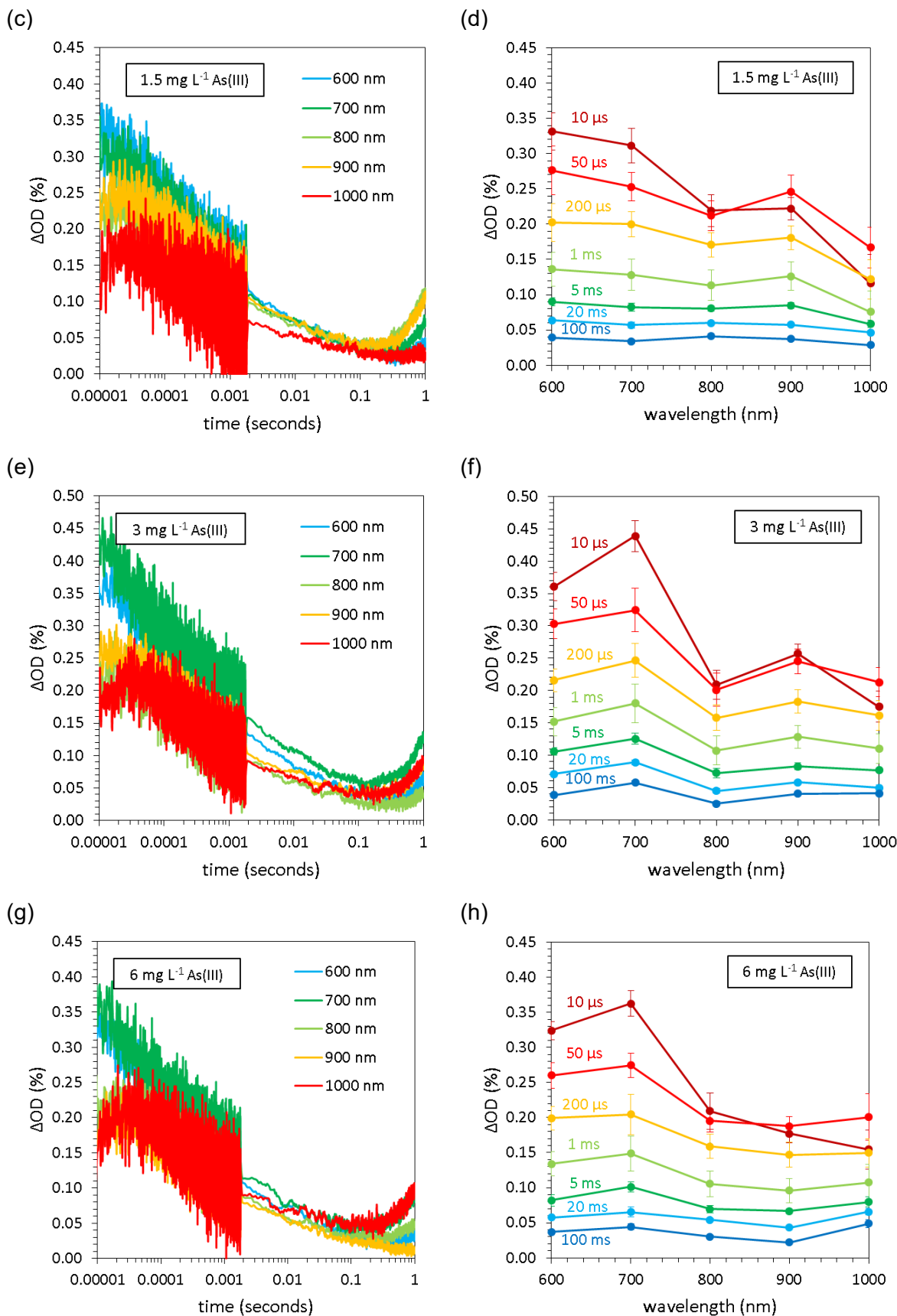


Figure 10.29: The influence of As(III) concentration of charge carrier lifetimes, investigated using TAS.

As As(III) was increased from 0 to 50 mg L⁻¹, a significant increase in charge carrier life-times was observed, with the half live of transient absorption increasing from 2 ms to 10 ms (Figure 10.29a,b). It is unclear whether the relationship is linear or exponential. Increased transient absorption half-lives indicate that one of the charge carriers (the electron or the hole) is long lived, due to scavenging of the other charge carrier. The wavelength dependence of ΔOD was then investigated, with the aim of identifying which charge carrier was longer lived with addition of As(III).





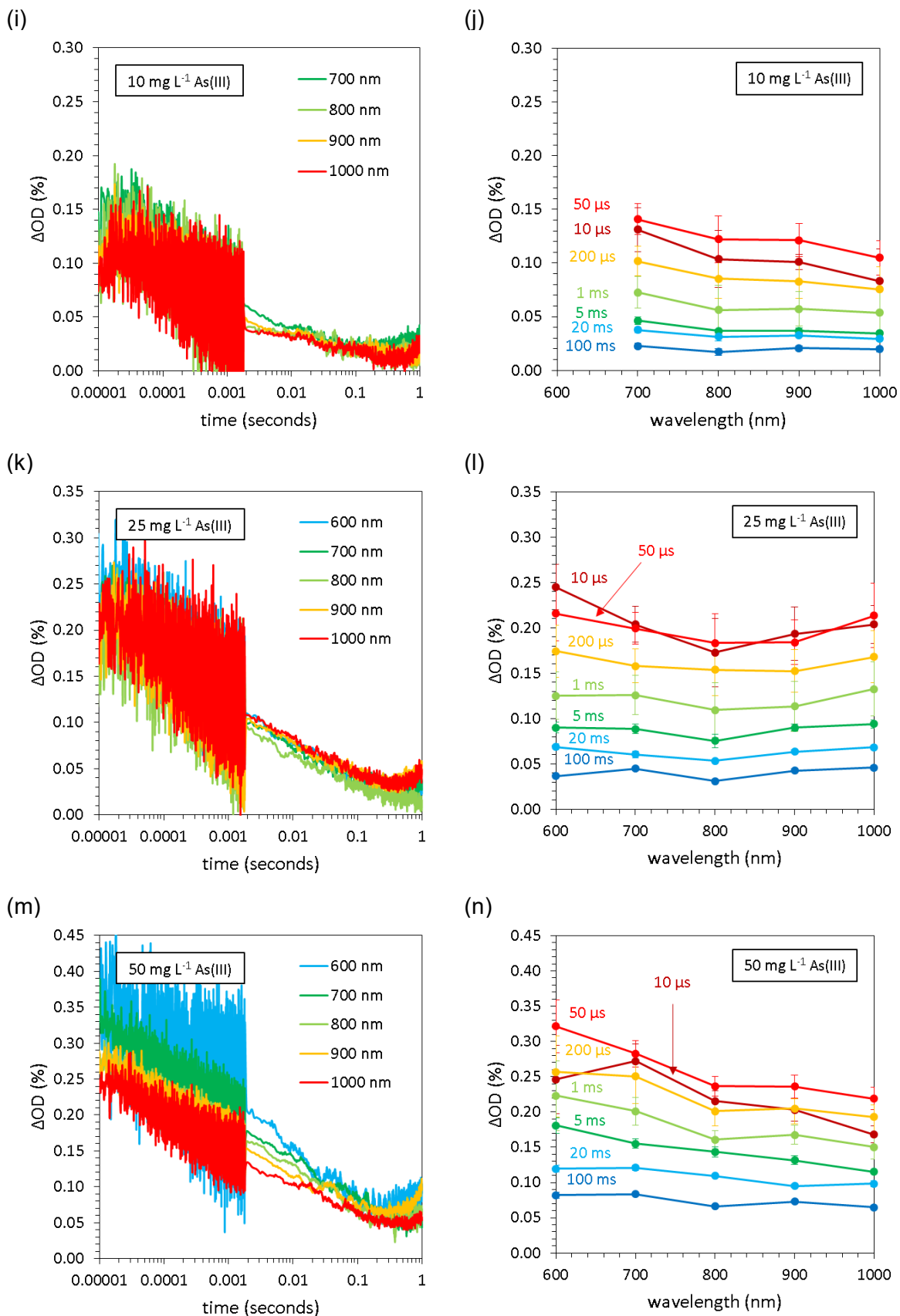


Figure 10.30: Transient absorption decay and TAS spectra for meso-TiO₂ suspensions with different concentrations of As(III). Error bars represent the standard deviation between the average of three repeat measurements, where each measurement was the result of ten scans.

With just 10 scans, transient absorption spectra were considerably noisy, despite combining an average of three repeat measurements. The magnitude of ΔOD across the wavelength series often varied significantly, represented by the error bars in Figure 10.30. In addition to the longer life times at high As(III) concentrations, the difference between ΔOD at 900 and 1000 nm versus 600 nm became smaller as As(III) was increased. The hole signal in anatase is centred at 460 nm and the electron signal is centred at 850 nm¹⁸⁴. This therefore suggests that the electron signal is becoming enhanced relative to the hole signal, a sign that holes are scavenged by addition of As(III). This suggests either direct hole oxidation, or the hydroxyl radical mediated pathway. However, better quality data is needed to prove this hypothesis.

In addition to the noise, challenges involve the mixed crystalline phases of the meso-TiO₂ sample. The TiO₂ phase of both meso-TiO₂ and meso-TiO₂/Fe₂O₃ contained 14-16% rutile (chapter 5). The presence of rutile will influence the observed TAS spectra in a number of ways. Firstly, the hole signal of rutile is centred at a higher wavelength than the hole signal of anatase (590 versus 460 nm), whilst the electron signal may appear at >850 nm¹⁸⁴. A broader spectrum is thus achieved for a mixed-phase TiO₂, making deconvolution of hole and electron signals much more challenging. Secondly, it has been previously reported that photoexcited electrons transfer from anatase to rutile, where they are scavenged less effectively¹⁸⁴. This behaviour increases the amplitude and life-time of the electron signal before any hole scavenger is added, potentially reducing the influence of As(III) addition. To more convincingly determine which charge carrier generated by TiO₂ is preferentially scavenged by As(III), the influence of As(III) on the observed transient absorption must be increased. This could be achieved by improving the quantum yield of As(III) oxidation by improving the nanostructure and surface area of the TiO₂ powder. Using pure anatase TiO₂ would also help deconvolute the electron and hole signals.

10.14.4. The influence of phosphate on transient absorption

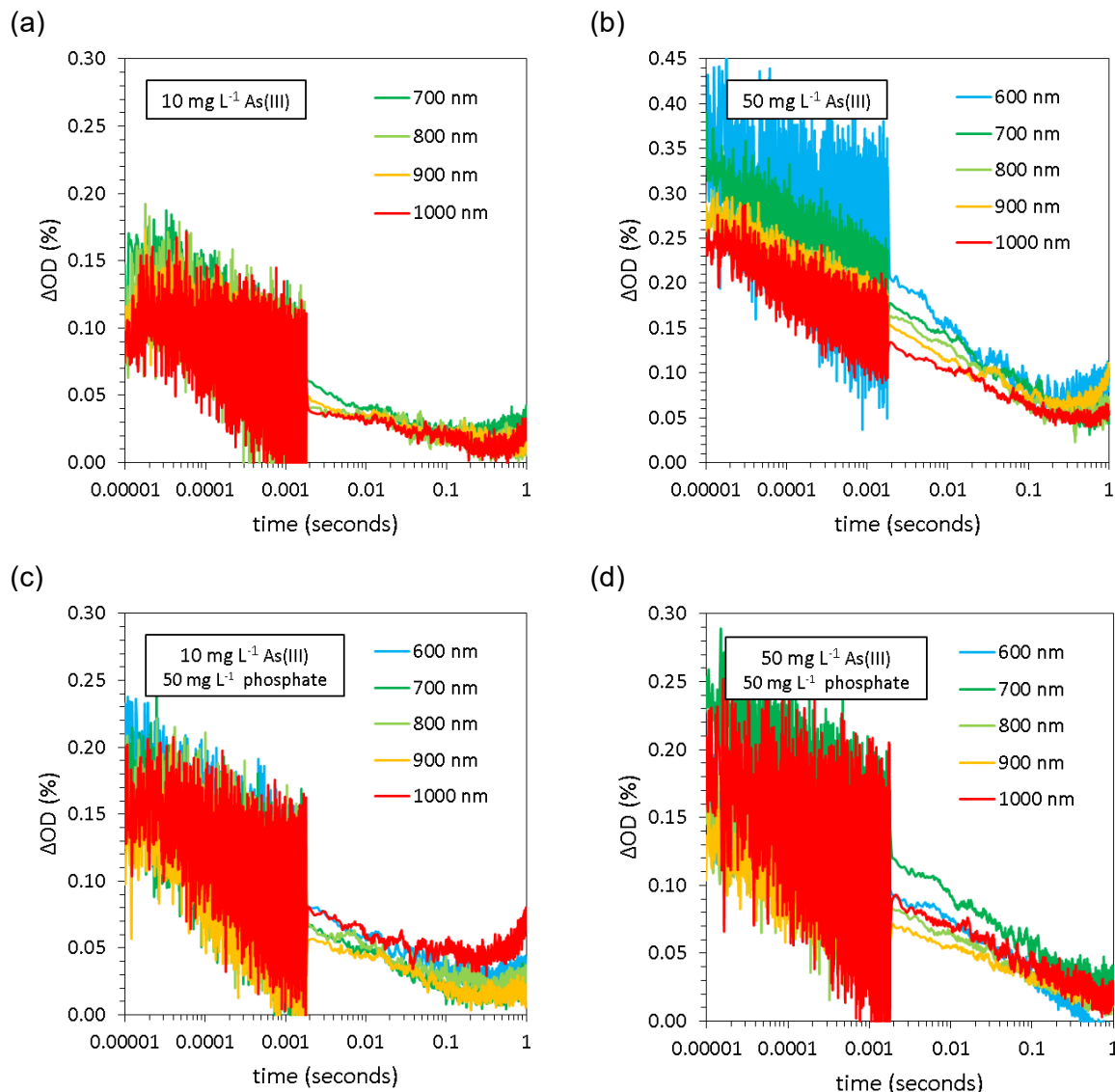


Figure 10.31: The influence of phosphate on the transient absorption of meso-TiO₂. Experiments were conducted with (a) 10 mg L⁻¹ As(III) and (b) 50 mg L⁻¹ As(III) and no phosphate present, and with (c) 10 mg L⁻¹ As(III) and (d) 50 mg L⁻¹ As(III) and 50 mg L⁻¹ phosphate present.

The influence of phosphate on the life-times of transient absorption in suspensions of meso-TiO₂ and As(III) was investigated in order to probe the photocatalytic oxidation mechanism, as discussed in section 7.4.3. The transient absorption decays are presented in Figure 10.31.

10.15. Data used to reduce the conditionality of the pseudo-second order kinetic adsorption model

Table 10.7: Initial sorbate concentration (C_0), sorbent concentration (C_s), surface area and particle size as well as the calculated values of PSO rate constant k_2 , the new rate constant k' , and the initial rate (calculated using the PSO model), for all adsorption kinetic experiments collected from the literature. In most cases, but not all, q_e and k_2 were calculated in this work. In a few other cases these parameters have been pulled directly from the literature.

System	C_0 (mg L ⁻¹)	C_s (g L ⁻¹)	Surface area (m ² g ⁻¹)	Particle size (mm)	q_e (mg g ⁻¹)	k_2 (g mg ⁻¹ min ⁻¹)	k' (L g ⁻¹ min ⁻¹)	Initial rate (mg g ⁻¹ min ⁻¹)	Reference
Varying initial sorbate concentration, C_0									
As(V)/Fe ₂ O ₃	1	40	14.4	0.2	0.0341	2.58	0.003	0.003	496
	2	40	14.4	0.2	0.0629	1.51	0.003	0.00597	
	4	40	14.4	0.2	0.154	0.405	0.00241	0.0096	
	8	40	14.4	0.2	0.222	0.532	0.00329	0.0262	
	10	40	14.4	0.2	0.249	0.480	0.00297	0.030	
As(V)/laterite	1	2	18.05	0.23-0.65	0.267	0.267	0.0136	0.019	483
	2	2	18.05	0.23-0.65	0.789	0.789	0.005	0.491	
	4	2	18.05	0.23-0.65	1	1	0.00317	1	
	8	2	18.05	0.23-0.65	1.05	1.05	0.00309	1.16	
	10	2	18.05	0.23-0.65	1.09	1.09	0.00309	1.3	
As(III)/HFO	50	2		0.14-0.29	19.3	0.000503	0.00376	0.187	495
	75	2		0.14-0.29	19.8	0.000738	0.00384	0.289	
	100	2		0.14-0.29	31.1	0.000335	0.00324	0.324	
HPO ₄ ²⁻ /iron hydroxide	2.8	7.5		0.05-0.315	0.35	0.722	0.0316	0.0884	561

System	C ₀ (mg L ⁻¹)	C _s (g L ⁻¹)	Surface area (m ² g ⁻¹)	Particle size (mm)	q _e (mg g ⁻¹)	k ₂ (g mg ⁻¹ min ⁻¹)	k' (L g ⁻¹ min ⁻¹)	Initial rate (mg g ⁻¹ min ⁻¹)	Reference
	14	7.5		0.05-0.315	2.03	0.0128	0.00374	0.0527	
	53	7.5		0.05-0.315	3.73	0.0156	0.0041	0.217	
	110	7.5		0.05-0.315	9.26	0.00551	0.0043	0.472	
Cu(II)/soil	20	10	287	<1	0.84	0.177	0.00625	0.125	562
	50	10	287	<1	1.29	0.0636	0.00212	0.106	
	100	10	287	<1	1.94	0.0505	0.00189	0.19	
Zn(II)/soil	50	10	287	<1	0.797	0.227	0.00288	0.144	562
	100	10	287	<1	0.995	0.223	0.00221	0.221	
Pb(II)/soil	20	10	287	<1	0.831	0.146	0.00504	0.101	562
	50	10	287	<1	3.04	0.0123	0.00227	0.114	
	100	10	287	<1	3.35	0.0507	0.00569	0.569	
Rhodamine B/MgO-Fe-Co-Mn	10	0.1	59.33		95.4	0.0259	23.6	236	563
	30	0.1	59.33		285	0.013	35.2	1060	
	60	0.1	59.33		568	0.0035	18.8	1130	
	80	0.1	59.33		752	0.002	14.1	1130	
	120	0.1	59.33		1120	0.0015	15.6	1880	
Hg(II)/raw activated sludge	50	2		0.125-0.212	20.7	0.0021	0.018	0.9	564
	100	2		0.125-0.212	35.5	0.00126	0.016	1.59	
	150	2		0.125-0.212	39.5	0.00287	0.0299	4.48	
	200	2		0.125-0.212	46.9	0.00353	0.0389	7.76	
Cr(VI)/activated carbon	100	0.5	38.7	0.15-0.42	6.41	0.00662	0.00272	0.272	565
	200	0.5	38.7	0.15-0.42	11.6	0.00371	0.00252	0.499	
	300	0.5	38.7	0.15-0.42	16.5	0.00336	0.00303	0.915	

System	C_0 (mg L ⁻¹)	C_s (g L ⁻¹)	Surface area (m ² g ⁻¹)	Particle size (mm)	q_e (mg g ⁻¹)	k_2 (g mg ⁻¹ min ⁻¹)	k' (L g ⁻¹ min ⁻¹)	Initial rate (mg g ⁻¹ min ⁻¹)	Reference
	400	0.5	38.7	0.15-0.42	21.2	0.00338	0.00382	1.52	
	500	0.5	38.7	0.15-0.42	25.1	0.0034	0.0043	2.14	
Rose Bengal dye/activated carbon	10	0.05		0.073-0.15	160	0.000706	1.8	18.1	566
	20	0.05		0.073-0.15	312	0.000185	0.903	18	
	30	0.05		0.073-0.15	451	0.000123	0.83	25	
	40	0.05		0.073-0.15	584	0.000083 ₉	0.715	28.6	
	50	0.05		0.073-0.15	709	0.000064 ₃	0.646	32.3	
Varying sorbent concentration, C_s									
Cr(VI)/Fe ₂ O ₃	50	1			49	0.000838	0.0402	2.01	567
	50	1.5			39.4	0.000826	0.0257	1.28	
	50	2			29.9	0.00121	0.0217	1.08	
	50	3			19.6	0.00213	0.0164	0.818	
Cr(VI)/Mg-Al-CO ₃	10	0.5	83.95	0.125-0.25	6.35	0.0812	0.328	3.27	303
	10	1	83.95	0.125-0.25	5.86	0.0879	0.302	3.02	
	10	1.5	83.95	0.125-0.25	5.28	0.157	0.438	4.38	
	10	2	83.95	0.125-0.25	4.32	0.239	0.446	4.46	
Cr(VI)/chitin	100	0.5		0.25-0.42	36.7	0.00164	0.0221	2.21	568
	100	0.75		0.25-0.42	25.4	0.00402	0.026	2.59	
	100	1		0.25-0.42	29	0.00548	0.046	4.61	
	100	1.5		0.25-0.42	8.14	0.0284	0.0188	1.88	
	100	2		0.25-0.42	7.98	0.013	0.00826	0.828	
	100	2.5		0.25-0.42	5.53	0.0205	0.00627	0.627	

System	C ₀ (mg L ⁻¹)	C _s (g L ⁻¹)	Surface area (m ² g ⁻¹)	Particle size (mm)	q _e (mg g ⁻¹)	k ₂ (g mg ⁻¹ min ⁻¹)	k' (L g ⁻¹ min ⁻¹)	Initial rate (mg g ⁻¹ min ⁻¹)	Reference
PO ₄ ³⁻ /peat/amorphous iron(III) hydroxide	25	0.2	43.8		4.72	0.001	0.000891	0.0223	569
	25	1	43.8		2.02	0.037	0.00604	0.151	
Cr(VI)/guava seeds	75	5		0.3-0.8	10	0.0101	0.0136	1.01	570
	75	7.5		0.3-0.8	7.63	0.0136	0.0105	0.792	
	75	10		0.3-0.8	6.63	0.0168	0.00988	0.738	
	75	12.5		0.3-0.8	5.79	0.0169	0.00753	0.567	
	75	15		0.3-0.8	4.88	0.0266	0.00844	0.633	
Cd(II)/Fe ₂ O ₃	0.1	0.05	31.7		1.29	0.0986	1.63	0.164	497
	0.1	0.1	31.7		0.765	0.362	2.12	0.212	
	0.1	0.5	31.7		0.189	3.9	1.4	0.139	
Cu(II)/Fe ₂ O ₃	0.1	0.05	31.7		0.852	0.0181	0.129	0.0131	497
	0.1	0.1	31.7		0.435	0.252	0.47	0.0477	
	0.1	0.5	31.7		0.187	0.656	0.225	0.0229	
Zn(II)/Fe ₂ O ₃	0.1	0.05	31.7		1.61	0.0336	0.894	0.0871	497
	0.1	0.1	31.7		0.983	0.216	2.13	0.209	
	0.1	0.5	31.7		0.197	7.47	2.97	0.29	
Hg(II)/ <i>Lessonia nigrescens</i>	50	0.4		0.125-0.25	97.4	0.00034	0.0645	3.23	571
	50	0.2		0.125-0.25	143	0.000171	0.0695	3.5	
	50	0.1		0.125-0.25	190	0.000073	0.0526	2.64	
Hg(II)/ <i>Lessonia trabeculata</i>	50	0.4		0.125-0.25	90.5	0.00039	0.0639	3.19	571
	50	0.2		0.125-0.25	140	0.000148	0.0579	2.9	
	50	0.1		0.125-0.25	200	0.000089	0.0713	3.56	
Eriochrome Black-T dye/TiO ₂	25	0.2			101	0.0012	0.489	12.2	572

System	C_0 (mg L ⁻¹)	C_s (g L ⁻¹)	Surface area (m ² g ⁻¹)	Particle size (mm)	q_e (mg g ⁻¹)	k_2 (g mg ⁻¹ min ⁻¹)	k' (L g ⁻¹ min ⁻¹)	Initial rate (mg g ⁻¹ min ⁻¹)	Reference
	25	0.4			58.8	0.00335	0.463	11.6	
	25	0.6			37.4	0.0038	0.212	5.32	
	25	0.8			30	0.00484	0.174	4.36	
	25	1			24.7	0.00613	0.15	3.74	
Methylene blue/raffia fibres	11	2	1.08		5.91	0.000198	0.000629	0.00692	573
	11	2.5	1.08		4.55	0.000491	0.000922	0.0102	
	11	3	1.08		3.66	0.000808	0.000985	0.0108	
	11	3.5	1.08		3.21	0.00114	0.00107	0.0117	
	11	4	1.08		2.67	0.00188	0.00122	0.0134	
Varying surface area									
As(V)/Fe ₂ O ₃	35.21	1	20		2.43	0.00295	0.000493	0.0174	574
	35.21	1	29		2.02	0.00245	0.000284	0.01	
	35.21	1	14		2.1	0.0032	0.000402	0.0141	
	35.21	1	24		2.99	0.0027	0.000685	0.0241	
	35.21	1	15		0.911	0.00454	0.000107	0.00377	
	35.21	1	109		75.8	0.000141	0.023	0.81	
Varying particle radius									
PO ₄ ³⁻ /granular ferric oxide	25	2	244	1.13	11.3	0.000028	0.000143	0.00358	575
	25	2	244	0.45	11.8	0.000075	0.000418	0.0104	
	25	2	244	0.1	12.1	0.0038	0.0223	0.556	
PO ₄ ³⁻ /ferrihydrite	25	2	179	1.13	11.8	0.00021	0.00117	0.0292	575
	25	2	179	0.45	11.7	0.00062	0.00339	0.0849	
	25	2	179	0.1	11.6	0.0031	0.0167	0.417	

System	C ₀ (mg L ⁻¹)	C _s (g L ⁻¹)	Surface area (m ² g ⁻¹)	Particle size (mm)	q _e (mg g ⁻¹)	k ₂ (g mg ⁻¹ min ⁻¹)	k' (L g ⁻¹ min ⁻¹)	Initial rate (mg g ⁻¹ min ⁻¹)	Reference
PO ₄ ³⁻ /ferrihydrite	25	2	119	1.13	12.4	0.000034	0.000209	0.00523	575
	25	2	119	0.45	12.6	0.00015	0.000953	0.0238	
	25	2	119	0.1	12.6	0.0031	0.0197	0.492	
PO ₄ ³⁻ /aluminium (hydr)oxide	25	11	235	1.13	11.8	0.00015	0.000835	0.0209	575
	25	12	235	0.45	11.9	0.00044	0.00249	0.0623	
	25	13	235	0.1	11.3	0.0063	0.0322	0.804	
Paraquat ([(C ₆ H ₇ N) ₂]Cl ₂)/activated clay	30	0.25	266.91	0.053	57.8	0.0092	1.02	30.7	576
	30	0.25	266.71	0.037	55.6	0.0166	1.71	51.3	
	30	0.25	229.42	0.0185	45.5	0.082	5.65	170	
Phenol/coal	50	40		0.037	1.16	0.15	0.00404	0.202	577
	50	40		0.074	0.36	0.303	0.000785	0.0393	
	50	40		0.125	0.18	0.353	0.000229	0.0114	
	50	40		0.25	0.11	0.52	0.000126	0.00629	
Quinoline/coal	50	40		0.037	1.24	0.353	0.0108	0.543	578
	50	40		0.074	0.76	0.308	0.00356	0.178	
	50	40		0.125	0.42	0.27	0.000952	0.0476	
Cu(II)/chitosan	20	0.125-0.5		0.11	16.3	0.00407	0.054	1.08	579
	20	0.125-0.5		0.22	16.1	0.00148	0.0191	0.384	
Cu(II)/chitosan (2)	50	0.125-0.5		0.11	36.9	0.000958	0.0261	1.3	579
	50	0.125-0.5		0.22	28.3	0.000707	0.0113	0.566	
Zn(II)/chitosan	20	0.125-0.5		0.11	3.75	0.0436	0.0307	0.613	579
	20	0.125-0.5		0.22	4.13	0.0134	0.0114	0.229	
Zn(II)/chitosan (2)	50	0.125-0.5		0.11	8.98	0.0105	0.0169	0.847	579

System	C_0 (mg L ⁻¹)	C_s (g L ⁻¹)	Surface area (m ² g ⁻¹)	Particle size (mm)	q_e (mg g ⁻¹)	k_2 (g mg ⁻¹ min ⁻¹)	k' (L g ⁻¹ min ⁻¹)	Initial rate (mg g ⁻¹ min ⁻¹)	Reference
	50	0.125-0.5		0.22	8.57	0.00939	0.0138	0.69	
Hg(II)/chitosan	20	0.125-0.5		0.11	2.5	0.546	0.683	3.41	579
	20	0.125-0.5		0.22	2.5	0.263	0.329	1.64	
Hg(II)/chitosan (2)	50	0.125-0.5		0.11	10.1	0.0457	0.232	4.66	579
	50	0.125-0.5		0.22	10.1	0.0248	0.127	2.53	
Omega Chrome Red ME dye/fly ash	10		5.77	0.053	0.496	0.121	0.00298	0.0298	580
	10		5.77	0.075	0.406	0.156	0.00257	0.0257	
	10		5.77	0.125	0.35	0.173	0.00212	0.0212	
Extra data for literature cross-comparison									
As(V)/Fe ₂ O ₃	1.5	4	56	0.0001	7.13	0.116	3.94	5.9	234
As(V)/Fe ₂ O ₃	0.2	0.01	50	6.25E-08	4.31	0.000056 ₇	0.00527	0.00105	581
As(V)/Fe ₂ O ₃	1.5	0.1	0.38	0.000125	0.109	1.58	0.0126	0.0188	214
As(V)/Fe ₂ O ₃	0.01	0.005	162	2.5E-09	8.87	0.004	33.1	0.315	216
	0.01	0.007	162	2.5E-09	8.01	0.006	40.5	0.385	
	0.01	0.01	162	2.5E-09	7.12	0.019	101	0.963	
	0.01	0.02	162	2.5E-09	4.78	0.033	79.4	0.754	
As(V)/Fe ₂ O ₃	10	0.4	317	0.000000002	23.7	0.017	0.955	9.55	582
As(V)/ferrihydrite	2000.36	2.5	202		176	1.29	20	40000	256
	40.01	2.5	202		124	0.000859	0.328	13.2	
	2000.36	2.5	202		19.7	0.458	0.0888	178	
	40.01	2.5	202		19.8	0.989	9.72	388	
As(V)/ferrihydrite	50	1	120		31.5	0.00066	0.0131	0.655	314

System	C ₀ (mg L ⁻¹)	C _s (g L ⁻¹)	Surface area (m ² g ⁻¹)	Particle size (mm)	q _e (mg g ⁻¹)	k ₂ (g mg ⁻¹ min ⁻¹)	k' (L g ⁻¹ min ⁻¹)	Initial rate (mg g ⁻¹ min ⁻¹)	Reference
As(V)/Fe ₃ O ₄	1.5	0.1	0.89	0.00005	0.125	1.29	0.0133	0.0202	214
As(V)/Fe ₃ O ₄	0.04	1	92	0.00000015	0.0364	44.6	1.64	0.0591	583
	0.07	1	92	0.00000015	0.0663	31	2.07	0.136	
As(V)/Fe ₃ O ₄	1	0.2	94.07	0.00000025	4.3	2.75	50.9	50.8	162
As(V)/Fe ₃ O ₄ /γ-Fe ₂ O ₃	1	0.4	49	0.00000015	0.0619	4.15	0.0159	0.0159	218
As(V)/Fe ₃ O ₄ /γ-Fe ₂ O ₃	2	0.4	49	0.00000015	4.97	0.059	0.729	1.46	218
As(V)/Fe ₃ O ₄ -HBC	0.1	0.2	0.03		0.474	0.0162	0.0365	0.00364	584
As(V)/Fe ₃ O ₄	1	0.1	300	1.25E-08	7.89	0.000704	0.0438	0.0438	585
As(V)/FeOOH	8.99	1.98	27	0.00000075	3.34	0.0228	0.0282	0.254	221
As(V)/FeOOH	1.5	0.1	2.01	0.000125	0.205	0.797	0.0224	0.0335	214
As(V)/β-FeOOH	3.36	0.27	9	0.000000145	0.911	0.488	0.121	0.405	586
As(V)/FeOOH	5	1.8	69.62	0.000000145	2.73	0.00496	0.00739	0.037	587
As(V)/FeOOH	5	1.8	69.62	0.000035	2.73	0.009	0.0134	0.0671	587
As(V)/FeOOH	74.92	2.5	103		12.6	0.00984	0.0208	1.56	223
As(III)/Fe ₂ O ₃	0.2	0.01	50	0.00000006	3.02	0.00443	0.202	0.0404	581
As(III)/Fe ₂ O ₃	1.5	0.1	0.38	0.000125	0.112	2.4	0.0201	0.0301	214
As(III)/Fe ₂ O ₃	0.12	0.01	162	2.5E-09	8.92	0.002	1.38	0.159	216
	0.12	0.02	162	2.5E-09	5.46	0.006	1.56	0.179	
	0.12	0.04	162	2.5E-09	2.86	0.027	1.92	0.221	
	0.12	0.06	162	2.5E-09	1.92	0.086	2.76	0.317	
As(III)/Fe ₂ O ₃	10	0.4	317	0.000000002	19.5	0.0036	0.137	1.37	582
As(III)/ferrihydrite	2000.36	2.5	202		306	0.0059	0.277	552	256
	40.01	2.5	202		378	0.00279	9.98	399	

System	C_0 (mg L ⁻¹)	C_s (g L ⁻¹)	Surface area (m ² g ⁻¹)	Particle size (mm)	q_e (mg g ⁻¹)	k_2 (g mg ⁻¹ min ⁻¹)	k' (L g ⁻¹ min ⁻¹)	Initial rate (mg g ⁻¹ min ⁻¹)	Reference
	2000.36	2.5	202		19.7	0.422	0.082	164	
	40.01	2.5	202		20	2.3	22.9	920	
As(III)/ferrihydrite	50	1	120		46.8	0.000913	0.0399	2	314
As(III)/ferrihydrite	50	1	120		48.1	0.00114	0.0529	2.64	
As(III)/Fe ₃ O ₄	1.5	0.1	0.89	0.00005	0.106	2.49	0.0186	0.028	214
As(III)/Fe ₃ O ₄	0.16	1	92	0.00000015	0.155	4.22	0.619	0.101	583
As(III)/Fe ₃ O ₄ /γ-Fe ₂ O ₃	1	0.4	49	0.00000015	0.161	1.17	0.0304	0.0303	218
	2	0.4	49	0.00000015	0.154	1.39	0.0165	0.033	
As(III)/FeOOH	74.92	2.5	103		17.2	0.0413	0.164	12.2	223
As(III)/FeOOH	1.5	0.1	2.01	0.000125	0.212	1.12	0.0334	0.0503	214
Cd(II)/Fe ₃ O ₄	50	5	47.87	0.0000625	0.938	0.139	0.00245	0.122	588
Cd(II)/Fe ₃ O ₄	200	1		0.000000138	174	0.000365	0.0554	11.1	589
	200	1		0.000000138	124	0.000559	0.0433	8.6	
	200	1		0.000000138	133	0.000216	0.0192	3.82	
	200	1		0.000000138	118	0.000469	0.0324	6.53	
Cd(II)/Fe ₃ O ₄	100	5		0.0000002	10.4	0.303	0.328	32.8	590
Cd(II)/activated carbon	50	1	471.67	0.000005	17.3	0.00248	0.0148	0.742	591
Cd(II)/activated carbon	495.61	2.5		0.0000185	131	0.000323	0.0111	5.54	592
Cd(II)/activated carbon	60	0.4	560	0.000425	5.41	0.00709	0.00346	0.208	593
Cd(II)/activated carbon	500	20	4273	0.000213	18.7	0.00716	0.00499	2.5	594
Cd(II)/activated carbon	100	0.05		0.00005	20.4	0.0099	0.041	4.12	420
Cu(II)/activated carbon	60	0.4	560	0.000425	5.64	0.00872	0.00462	0.277	593
Pb(II)/activated carbon	500	20	4273	0.000213	19.6	0.00452	0.00349	1.74	594

System	C ₀ (mg L ⁻¹)	C _s (g L ⁻¹)	Surface area (m ² g ⁻¹)	Particle size (mm)	q _e (mg g ⁻¹)	k ₂ (g mg ⁻¹ min ⁻¹)	k' (L g ⁻¹ min ⁻¹)	Initial rate (mg g ⁻¹ min ⁻¹)	Reference
Cd(II)/chitosan	100	1	125.24	0.000125	81.3	0.000405	0.0268	2.68	595
Cd(II)/chitosan	100	5		0.00005	25	0.000525	0.00328	0.328	596
Cd(II)/chitosan	100	0	4.45	0.00005	8.08	0.00398	0.00259	0.26	597
Cd(II)/chitosan	50	4	20.06	0.000005	24.5	0.00189	0.0227	1.13	260
Cd(II)/chitosan	50	1.72		0.0000315	10.5	0.0363	0.0805	4	598
Pb(II)/chitosan	100	5		0.00005	19.6	0.00618	0.0237	2.37	596
Pb(II)/chitosan	50	1.72		0.0000315	18.9	0.00504	0.0359	1.8	598
Pb(II)/Fe ₃ O ₄	100	5		0.0000002	11.9	0.0564	0.0801	7.99	590
Cu(II)/Fe ₃ O ₄	50	5	47.87	0.0000625	2.6	0.108	0.0146	0.73	588
Methylene blue/activated carbon	4.48	4	116	0.000325	0.682	0.508	0.0528	0.236	599
Methylene blue/activated carbon	200	1		0.000106	203	0.000468	0.0968	19.3	600
Methylene blue/activated carbon	750	10	1483	0.00025	157	0.00151	0.0492	37.2	601
Methylene blue/activated carbon	250	1	1531	0.000045	250	0.00109	0.273	68.1	602
Methylene blue/activated carbon	500	1	1894	0.000075	455	0.000026	0.0107	5.38	603
Methylene blue/activated carbon	1000	0.5	600	0.00025	205	0.000059 ₃	0.00249	2.49	604
Methylene blue/activated carbon	600	1.333	1029	0.000106	280	0.000201	0.0262	15.8	605
Methylene blue/activated carbon	200	1.8	14.27	0.0005	47.2	0.00019	0.00212	0.423	606
Methylene blue/activated carbon	500	1.6	248	0.000158	169	0.00047	0.027	13.4	607
Methylene blue/TiO ₂	12.5	0.5	13	0.0000017	0.647	0.642	0.0215	0.269	608
Methylene blue/TiO ₂	100	2	29.6	0.0000005	12.4	0.0179	0.0274	2.75	609
Methylene blue/TiO ₂	200	0.8		0.0000003	80.3	0.00145	0.0467	9.35	610
Methylene blue/TiO ₂	20	0.2	335	0.0000005	49	0.00321	0.386	7.71	611

System	C_0 (mg L ⁻¹)	C_s (g L ⁻¹)	Surface area (m ² g ⁻¹)	Particle size (mm)	q_e (mg g ⁻¹)	k_2 (g mg ⁻¹ min ⁻¹)	k' (L g ⁻¹ min ⁻¹)	Initial rate (mg g ⁻¹ min ⁻¹)	Reference
Methylene blue/TiO ₂	10	2		0.000005	4.06	0.0462	0.0762	0.762	612
Fluoride/Al ₂ O ₃	10	1	221	0.0000001	8.8	0.0268	0.207	2.08	613
Fluoride/Al ₂ O ₃	10	6.667	118.6	0.001	1.93	0.00115	0.000426	0.00428	614
Fluoride/Al ₂ O ₃	5	1		0.0000315	169	0.0002	1.15	5.71	615
Fluoride/Al ₂ O ₃	304	0.5	254.1	0.00000045	600	0.000040 4	0.0479	14.5	616
Fluoride/Al ₂ O ₃	10	10	185.6	0.00005	0.522	0.137	0.00372	0.0373	617
Fluoride/Al ₂ O ₃	5	4	117.4	0.000125	0.944	0.0762	0.0136	0.0679	618
Fluoride/Al ₂ O ₃	5	2.2	198	0.00005	1.81	0.00949	0.00623	0.0311	274
As(V)/Fe ₂ O ₃	0.1	0.005	162	2.5E-09	8.77	0.00487	3.95	0.375	216
As(III)/Fe ₂ O ₃	0.1	0.005	162	2.5E-09	18	0.00138	4.71	0.447	216
As(V)/activated carbon	4.5	1		0.001	0.0231	2.99	0.000354	0.0016	619
As(V)/activated carbon	10	1	1470	0.000012	6.05	0.00707	0.0258	0.259	620
As(V)/activated carbon	2	1	405	0.0005	0.303	0.376	0.0172	0.0345	621
As(V)/activated carbon	0.1	0.03	520	0.00018	2.87	0.00122	0.101	0.01	128
As(V)/activated carbon	0.15	5	660	0.00025	0.014	10.2	0.0133	0.002	622
Pb(II)/Al ₂ O ₃	414.4	13.3	100		0.000591	93.9	7.92E-08	0.0000328	484
Pb(II)/A ₂ O ₃	20	5	243	0.0000005	4.27	0.0109	0.00992	0.199	623
Methylene blue/TiO ₂	10	0.5	51	0.00001	21.1	0.0333	1.49	14.8	624

10.16. MATLAB codes used to model an arsenic treatment plant

MATLAB codes used to simulate the arsenic treat models (batch and continuous-flow) are also provided at <http://doi.org/10.5281/zenodo.3690170>³⁰⁶.

10.16.1. Simulating a single batch treatment

```
%This code runs a two-dimensional matrix of separate kinetic experiments,  
%each experiment with a unique combination of sorbent concentration (Cs)  
%and initial sorbate concentration (C0).
```

```
%Adsorption kinetics are modelled using the modified pseudo-second order  
%rate equation, being (a) second order with respect to the relative  
%proportion of adsorption capacity remaining (with maximum adsorption  
%capacity determined using the Freundlich adsorption isotherm), (b) first  
%order with respect to sorbate concentration, and (c) zero-/first- order  
%with respect to sorbent concentration when the rate is normalised to  
%sorbent concentration and total volume, respectively.%
```

```
function main
```

```
%this section of code tells MATLAB to run the kinetic model with a  
%different value for the sorbent concentration, Cs, each time  
run('batch_001.txt',0.01);  
run('batch_002.txt',0.02);  
run('batch_005.txt',0.05);  
run('batch_01.txt',0.1);  
run('batch_02.txt',0.2);  
run('batch_05.txt',0.5);  
run('batch_1.txt',1.0);  
run('batch_2.txt',2);  
run('batch_5.txt',5);  
run('batch_10.txt',10);  
run('batch_20.txt',20);
```

```
run('batch_50.txt',50);
run('batch_100.txt',100);
run('batch_200.txt',200);
run('batch_500.txt',500);
run('batch_1000.txt',1000);

end

function run(filename,Cs0)
number_of_experiments=54; %each experiment will have a different initial sorbate concentration (C0)

number_of_variables = 8; %counting how many rows in the array we need to store the input parameters for each kinetic plot

experiments = zeros(number_of_experiments,number_of_variables); %each experiment refers to a single kinetic plot

%creating the input variables for each kinetic plot

C_init = 0; %ppb or ug L-1 - this is the initial concentration of aqueous sorbate in the ssuspension

q_init = 0; %ppb or ug L-1 - this is the initial concentration of adsorbed sorbate in the suspension

Cs = Cs0; %g L-1 - this is the concentration of sorbent

Cinfluent = 0; %ppb or ug L-1 - this is the concentration of sorbate in the influent (for continuous-flow modelling)

j = 0; %this the turn-over frequency, i.e. bed volumes per minute

k = 0.1111; %this is the value of normalised k' (L g-1 min-1)

KF = 5.10; %this is the Freundlich constant (mg g-1) used to determine 'qe' at each time step

n = 2.63; %this is the second parameter for the Freundlich adsorption isotherm (g L-1) used to determine 'qe' at each time step

%setting the time intervals upon which data is recorded

t_end = 4320; %1440 = 1 day

t_steps = 2000;

t_step = t_end/t_steps;

bv_end = t_end*j;

%setting up the arrays where calculated data is to be stored

global results_t;

results_t = zeros(number_of_experiments,t_steps+1);

global results_Ct;
```

```
results_Ct = zeros(number_of_experiments,t_steps+1);
global results_qt;
results_qt = zeros(number_of_experiments,t_steps+1);
global exp;

%we make an array listing all the input parameters for each kinetic plot we
%wish to model. The different values of Cs are automatically plugged in
for i = 1:number_of_experiments
    experiments(i,1) = C_init;
    experiments(i,2) = q_init;
    experiments(i,3) = j;
    experiments(i,4) = Cinfluent;
    experiments(i,5) = k;
    experiments(i,6) = Cs;
    experiments(i,7) = KF;
    experiments(i,8) = n;
end

%here we overwrite the initial aqueous sorbate concentration, C0, with a
%concentration ranging from 10 ug L-1 to 2000 ug L-1, representing the
%arsenic levels in natural water that we are interested in treating
experiments(1,1) = 10;
experiments(2,1) = 20;
experiments(3,1) = 40;
experiments(4,1) = 60;
experiments(5,1) = 80;
experiments(6,1) = 100;
experiments(7,1) = 125;
experiments(8,1) = 150;
experiments(9,1) = 175;
for i=10:46
    experiments(i,1) = ((i-9)*50)+150;
end
for i=47:number_of_experiments
    experiments(i,1) = ((i-46)*500)+2000;
end
```

```
%setting up the formatting for printing results
results_table=[];
formatSpec = '';
formatSpec2 = '';
formatHeader = '';

for i = 1:number_of_experiments
    exp = zeros(1,number_of_variables) ;
    exp(1,:) = experiments(i,:);

    exp_C_init = exp(1,1);
    exp_q_init = exp(1,2);

    %run the ode45 function which will solve the differential rate equation
    [t,C]=ode45(@DiffEq,[0:t_step:t_end],[exp_C_init exp_q_init]);    %call the ODE
    %function

    results_t(i,:) = t;
    results_bv(i,:) = results_t(i,:)*exp(1,3);
    results_Ct(i,:) = C(:,1);
    results_qt(i,:) = C(:,2);
    results_theta(i,:) = C(:,2)/(1000*exp(1,7));

    results_table =
    [results_table,results_t(i,:)',results_bv(i,:)',results_Ct(i,:)',results_qt(i,:)
    ',results_theta(i,:)']

%print the results
%formatSpec = strcat(formatSpec,'\r\n')
fileID = fopen(filename,'w');
%formatSpec = '%10.3f %10.5f %10.3f %10.3f %10.8f\r\n';
fprintf(fileID,'%10s %10s %10s %10s %10s %10s\r\n','C0,ppb','q0,ppb','j,BV
min-1','C_inf,ppb','k','Cs,g L-1','qm,mg g-1');
%formatHeader = strcat(formatHeader,'\r\n');

formatHeader = '';
for i = 1:number_of_experiments
    formatHeader = strcat(formatHeader,'%-50.4f ');
end
%formatHeader = strcat(formatHeader,'%-50.4f ');
```

```
fprintf(fileID,strcat(formatHeader,'\\r\\n'),experiments(:, :, :));

formatSpec2 = strcat(formatSpec2,'%10s %10s %10s %10s %10s\\r\\n');

fprintf(fileID,formatSpec2,'t','BV','Ct','qt','theta');

%formatSpec = strcat(formatSpec,'%10.3f %10.5f %10.3f %10.3f %10.8f');

formatSpec = strcat(formatSpec,'%.5E %.5E %.5E %.5E %.5E');

fprintf(fileID,strcat(formatSpec,'\\r\\n'),results_table.');

fclose(fileID);

end

end

function dCdt = DiffEq(t,conditions)
global exp;

time=t;

j = exp(1,3);
Cinfluent = exp(1,4);
k = exp(1,5);
Cs = exp(1,6);
KF = exp(1,7);
n = exp(1,8);

Ct = conditions(1);      %ppb
qt = conditions(2);      %ppb
Ct_mgL = Ct/1000;        %mg L-1
qt_mgg = qt/(Cs*1000);    %mg g-1

%the rate equation we are using is
%dqt/dt = k' * Ct * (1-(qt/(Kf * Ce^(1/n))))^2
%please see our manuscript for derivation and further information

rate_ads = 1000*k*Ct_mgL*Cs*((1-(qt_mgg/(KF*(Ct_mgL^(1/n))))))^2; %calculate dq/dt
in ppb L-1 min-1

rate_influx = j*Cinfluent; %calculate the rate of sorbate influx (continuous-flow
systems only)

rate_outflux = j*Ct; %calculate the rate of sorbate outflux (continuous-flow
systems only)
```

```
dCdt = [-rate_ads+rate_influx-rate_outflux;rate_ads]; %adjust the concentration of  
aqueous sorbate and adsorbed sorbate, respectively  
end
```

10.16.2. Simulating continuous-flow

```
%This code runs a series of kinetic models in a continuous-flow simulation.  
  
%Adsorption kinetics are modelled using the modified pseudo-second order  
%rate equation, being (a) second order with respect to the relative  
%proportion of adsorption capacity remaining (with maximum adsorption  
%capacity determined using the Freundlich adsorption isotherm), (b) first  
%order with respect to sorbate concentration, and (c) zero-/first- order  
%with respect to sorbent concentration when the rate is normalised to  
%sorbent concentration and total volume, respectively.%  
  
function main  
  
%this section of code tells MATLAB to run the kinetic model with a  
%unique combinations of sorbent concentration, flow rate, and initial sorbate  
%concentrations. The high sorbent concentration models are run last, as  
%these are the most computationally demanding simulations.  
run('data3.txt',5,0.01,500,0.01);  
run('data4.txt',5,0.02,500,0.01);  
run('data5.txt',5,0.05,500,0.01);  
run('data6.txt',5,0.1,500,0.01);  
run('data7.txt',5,0.2,500,0.01);  
run('data8.txt',5,0.5,500,0.01);  
run('data9.txt',5,1.0,500,0.01);  
  
run('data10.txt',5,0.01,2000,0.01);  
run('data11.txt',5,0.02,2000,0.01);  
run('data12.txt',5,0.05,2000,0.01);  
run('data13.txt',5,0.1,2000,0.01);  
run('data14.txt',5,0.2,2000,0.01);  
run('data15.txt',5,0.5,2000,0.01);  
run('data16.txt',5,1.0,2000,0.01);
```

```
run('data17.txt',5,0.01,1000,0.01);
run('data18.txt',5,0.02,1000,0.01);
run('data19.txt',5,0.05,1000,0.01);
run('data20.txt',5,0.1,1000,0.01);
run('data21.txt',5,0.2,1000,0.01);
run('data22.txt',5,0.5,1000,0.01);
run('data23.txt',5,1.0,1000,0.01);

run('data24.txt',1,0.01,500,1000);
run('data25.txt',1,0.02,500,1000);
run('data26.txt',1,0.05,500,1000);
run('data27.txt',1,0.1,500,1000);
run('data28.txt',1,0.2,500,1000);
run('data29.txt',1,0.5,500,1000);
run('data30.txt',1,1.0,500,1000);

run('data31.txt',1,0.01,2000,1000);
run('data32.txt',1,0.02,2000,1000);
run('data33.txt',1,0.05,2000,1000);
run('data34.txt',1,0.1,2000,1000);
run('data35.txt',1,0.2,2000,1000);
run('data36.txt',1,0.5,2000,1000);
run('data37.txt',1,1.0,2000,1000);

run('data38.txt',1,0.01,1000,1000);
run('data39.txt',1,0.02,1000,1000);
run('data40.txt',1,0.05,1000,1000);
run('data41.txt',1,0.1,1000,1000);
run('data42.txt',1,0.2,1000,1000);
run('data43.txt',1,0.5,1000,1000);
run('data44.txt',1,1.0,1000,1000);

run('data45.txt',1,0.01,500,10000);
run('data52.txt',1,0.01,2000,10000);
run('data48.txt',1,0.1,500,10000);
run('data55.txt',1,0.1,2000,10000);
run('data51.txt',1,1.0,500,10000);
run('data58.txt',1,1.0,2000,10000);
```

```
run('data59.txt',1,0.01,1000,10000);
run('data62.txt',1,0.1,1000,10000);
run('data65.txt',1,1.0,1000,10000);

run('data46.txt',1,0.02,500,10000);
run('data47.txt',1,0.05,500,10000);

run('data49.txt',1,0.2,500,10000);
run('data50.txt',1,0.5,500,10000);

run('data53.txt',1,0.02,2000,10000);
run('data54.txt',1,0.05,2000,10000);

run('data56.txt',1,0.2,2000,10000);
run('data57.txt',1,0.5,2000,10000);

run('data60.txt',1,0.02,1000,10000);
run('data61.txt',1,0.05,1000,10000);

run('data63.txt',1,0.2,1000,10000);
run('data64.txt',1,0.5,1000,10000);

run('data66.txt',5,0.001,500,0.01);
run('data67.txt',5,0.002,500,0.01);
run('data68.txt',5,0.005,500,0.01);
run('data69.txt',5,0.001,2000,0.01);
run('data70.txt',5,0.002,2000,0.01);
run('data71.txt',5,0.005,2000,0.01);
run('data72.txt',5,0.001,1000,0.01);
run('data73.txt',5,0.002,1000,0.01);
run('data74.txt',5,0.005,1000,0.01);

run('data75.txt',1,0.001,500,1000);
run('data76.txt',1,0.002,500,1000);
run('data77.txt',1,0.005,500,1000);
run('data78.txt',1,0.001,2000,1000);
run('data79.txt',1,0.002,2000,1000);
run('data80.txt',1,0.005,2000,1000);
```

```
run('data81.txt',1,0.001,1000,1000);
run('data82.txt',1,0.002,1000,1000);
run('data83.txt',1,0.005,1000,1000);

run('data84.txt',1,0.001,500,10000);
run('data87.txt',1,0.001,2000,10000);
run('data90.txt',1,0.001,1000,10000);

run('data85.txt',1,0.002,500,10000);
run('data86.txt',1,0.005,500,10000);
run('data88.txt',1,0.002,2000,10000);
run('data89.txt',1,0.005,2000,10000);
run('data91.txt',1,0.002,1000,10000);
run('data92.txt',1,0.005,1000,10000);

end

function run(filename,number_exps,j_flow,C_inf,Cs0)
number_of_experiments=number_exps; %each experiment will have a different initial
sorbate concentration (C0)

number_of_variables = 8; %counting how many rows in the array we need to
store the input parameters for each kinetic plot

experiments = zeros(number_of_experiments,number_of_variables); %each experiment
refers to a single kinetic plot

%creating the input variables for each kientic plots

C_init = 0.001; %ppb or ug L-1 - this is the initial concentration of aqueous
sorbate in the ssuspension

q_init = 0; %ppb or ug L-1 - this is the initial concentration of adsorbed
sorbate in the suspension

Cs = Cs0; %g L-1 - this is the concentration of sorbent

Cinfluent = C_inf; %ppb or ug L-1 - this is the concentration of sorbate in the
influent (for continuous-flow modelling)

j = j_flow; %this the turn-over frequency, i.e. bed volumes per minute

k = 0.1111; %this is the value of normalised k' (L g-1 min-1)

KF = 5.10; %this is the Freundlich constant (mg g-1) used to determine 'qe' at
each time step

n = 2.63; %this is the second parameter for the Freundlich adsorption
isotherm (g L-1) used to determine 'qe' at each time step

%setting the time intervals upon which data is recorded. This will be
```

```
%overwritten later to avoid wasting computational time after breakthrough  
%has already occurred.  
  
t_end = 1000000; %1440 = 1 day  
t_steps = 2000;  
t_step = t_end/t_steps;  
bv_end = t_end*j;  
  
%setting up the arrays where calculated data is to be stored  
global results_t;  
results_t = zeros(number_of_experiments,t_steps+1);  
global results_Ct;  
results_Ct = zeros(number_of_experiments,t_steps+1);  
global results_qt;  
results_qt = zeros(number_of_experiments,t_steps+1);  
global exp;  
  
%we make an array listing all the input parameters for each kinetic plot we  
%wish to model. The different values of Cs are automatically plugged in  
for i = 1:number_of_experiments  
    experiments(i,1) = C_init;  
    experiments(i,2) = q_init;  
    experiments(i,3) = j;  
    experiments(i,4) = Cinfluent;  
    experiments(i,5) = k;  
    experiments(i,6) = Cs*10^(i-1); %exponentially increasing sorbent concentration  
    experiments(i,7) = KF;  
    experiments(i,8) = n;  
end  
  
%setting up the formatting for printing results  
results_table=[];  
formatSpec = '';  
formatSpec2 = '';  
formatHeader = '';  
  
%for i = 1:1number_of_experiments  
for i = 1:number_of_experiments  
    exp = zeros(1,number_of_variables);
```

```
exp(1,:) = experiments(i,:);
exp_C_init = exp(1,1);
exp_q_init = exp(1,2);

%making sure that we model an appropriate length of time (duration) with
%appropriate interval lengths for each simulation.

%t_end = 9100 * exp(1,6) / (exp(1,3) * exp(1,4)); % 50000*Cs/(j*Cinf)
t_end = 12000 * exp(1,6) / (exp(1,3) * exp(1,4)); % 50000*Cs/(j*Cinf)

if t_end<1000
    t_end = t_end*20;
end

if t_end<500
    t_end=t_end*5;
end

if j<0.01
    t_end=t_end*10;
end

%t_step = t_end/t_steps;
stepping = [1:1:t_steps+1]; %collect data at shorter time intervals in the
initial stages of the simulation

stepping(1)=0;
gradient_1=1;
gradient_2=60;
for i = 2:(t_steps+1)

    %change the time intervals from being evenly spaced to having a smooth
    %transition from gradient_1 to gradient_2

    stepping(i)=stepping(i-
1)+(gradient_2*(stepping(i)/t_steps))+(gradient_1*((t_steps-stepping(i))/t_steps));
end

for i = 2:(t_steps+1)
    %normalise the time intervals to 1 and then multiply out by the desired
    %final time
    stepping(i)=(stepping(i)/stepping(t_steps+1))*t_end;
    %"i is " + i +" and stepping(i) is " + stepping(i)
end

% %speed up ode15s for simulations with 1000+ g L-1 for shorter processing times
% global speed;
% speed=1
```

```
% if exp(1,6)>100
%     speed=exp(1,6)/100
% end

% [stepping]=[stepping]/speed; %and replace the time steps to be recorded by re-
scaled time intervals

%run the ode15s function which will solve the differential rate equation
options = odeset('RelTol',1e-4,'Stats','on','OutputFcn',@odeplot);    %need to
increase the tolerance to avoid errors, was 1e-5 to begin with, tried changing to
1e-4

[t,C]=ode15s(@DiffEq,[stepping],[exp_C_init exp_q_init],options);    %call the ODE
function

%[t,C]=ode15s(@DiffEq,[stepping],[exp_C_init exp_q_init]);    %call the ODE function
%[t,C]=ode15s(@DiffEq,[0:t_step:t_end],[exp_C_init exp_q_init]);    %call the
%ODE function - original call with equal spacing between time intervals

results_t(i,:)=t;
%results_t(i,:)=t/speed;
results_bv(i,:)=results_t(i,:)*exp(1,3);
results_Ct(i,:)=C(:,1);
results_qt(i,:)=C(:,2);
results_theta(i,:)=C(:,2); %ignore, we are not calculating theta

results_table =
[results_table,results_t(i,:)',results_bv(i,:)',results_Ct(i,:)',results_qt(i,:)
',results_theta(i,:)'];

%print the results
%formatSpec = strcat(formatSpec,'\r\n')
fileID = fopen(filename,'w');
%formatSpec = '%10.3f %10.5f %10.3f %10.3f %10.8f\r\n';
%fprintf(fileID,'%10s %10s %10s %10s %10s %10s\r\n','C0,ppb','q0,ppb','j,BV
min-1','C_inf,ppb','k','Cs,g L-1','qm,mg g-1');
%formatHeader = strcat(formatHeader,'\r\n');

formatHeader = '';
for i = 1:number_of_experiments
formatHeader = strcat(formatHeader,'%-50.4f ');
end
%formatHeader = strcat(formatHeader,'%-50.4f ');
fprintf(fileID,strcat(formatHeader,'\r\n'),experiments(:,:,));
```

```
formatSpec2 = strcat(formatSpec2,'%14s %14s %14s %14s %14s\r\n');

fprintf(fileID,formatSpec2,'t','BV','Ct','qt','theta');

%formatSpec = strcat(formatSpec,'%10.3f %10.5f %10.3f %10.3f %1.0f');

formatSpec = strcat(formatSpec,'% 0.3E % 0.3E % 0.3E % 0.3E % 0.3E');

%formatSpec = strcat(formatSpec,'%0.3E %0.3E %0.3E %0.3E %0.3E ');

%formatSpec = strcat(formatSpec,'%.5E %.5E %.5E %.5E %.5E');

fprintf(fileID,strcat(formatSpec,'\r\n'),results_table.',' %s');

fclose(fileID);

"just completed simulation with: j = " + j_flow + " and C_inf = " + C_inf

end

"just completed file: " + filename

end

function dCdt = DiffEq(t,conditions)
global exp;
%global speed

time=t;

j = exp(1,3);
Cinfluent = exp(1,4);
k = exp(1,5);
Cs = exp(1,6);
KF = exp(1,7);
n = exp(1,8);

Ct = conditions(1);    %ppb
if Ct<0.001
    Ct=0.001;           %set a minimum concentration of sorbate in the reactor to
    prevent the Freundlich adsorption isotherm from running an error.
end
if Ct>Cinfluent
    Ct=Cinfluent;      %control incase ode15s time intervals are too large
end
qt = conditions(2);    %ppb
```

```

Ct_mgL = Ct/1000;           %mg L-1
qt_mgg = qt/(Cs*1000);     %mg g-1

"Ct is " + Ct + " ug L-1 and qt is " + qt + "ug L-1"

%the rate equation we are using is
%dqt/dt = k' * Ct * (1-(qt/(Kf * Ce^(1/n))))^2
%please see our manuscript for derivation and further information

rate_ads = 1000*k*Ct_mgL*Cs*((1-(qt_mgg/(KF*(Ct_mgL^(1/n))))))^2; %calculate dq/dt
in ppb L-1 min-1

rate_influx = j*Cinfluent; %calculate the rate of sorbate influx (continuous-flow
systems only)

rate_outflux = j*Ct; %calculate the rate of sorbate outflux (continuous-flow
systems only)

dCdt = [-rate_ads+rate_influx-rate_outflux;rate_ads]; %adjust the concentration of
aqueous sorbate and adsorbed sorbate, respectively

%dCdt = [speed*(-rate_ads+rate_influx-rate_outflux);speed*(rate_ads)]; %adjust the
concentration of aqueous sorbate and adsorbed sorbate, respectively

end

```

10.16.3. Simulating 365 days sequential batch treatment

```
%This code runs a batch adsorption model, 365 days, representing a single
%mass of sorbent being used for 365 consecutively
```

```
%Adsorption kinetics are modelled using the modified pseudo-second order
%rate equation, being (a) second order with respect to the relative
%proportion of adsorption capacity remaining (with maximum adsorption
%capacity determined using the Freundlich adsorption isotherm), (b) first
%order with respect to sorbate concentration, and (c) zero-/first- order
%with respect to sorbent concentration when the rate is normalised to
%sorbent concentration and total volume, respectively.%
```

```
function main
global day;
global qt; %variable qt will keep track of how much sorbate is
attached to the sorbent at the end of each day
qt = [0 0 0 0 0 0];
for day = 1:365
```

```

run(strcat('500ppb_day_',sprintf('%03d',day),'.txt'),500,10,qt);      %for 365 days,
run the experiment

end

qt = [0 0 0 0 0 0];

for day = 1:365

run(strcat('2000ppb_day_',sprintf('%03d',day),'.txt'),2000,10,qt);      %for 365
days, run the experiment

end

end

function run(filename,C0,Cs0,qt)

global qt;
global i;
number_of_experiments=7;
number_of_variables = 8;

experiments = zeros(number_of_experiments,number_of_variables);

C_init = C0;      %ppb or ug L-1 - this is the initial concentration of aqueous
sorbate in the ssuspension

q_init = qt;      %ppb or ug L-1 - this is the initial concentration of adsorbed
sorbate in the suspension

Cs = Cs0;         %g L-1 - this is the concentration of sorbent

Cinfluent = 0;    %ppb or ug L-1 - this is the concentration of sorbate in the
influent (for continuous-flow modelling)

j = 0;            %this the turn-over frequency, i.e. bed volumes per minute

k = 0.1111;        %this is the value of normalised k' (L g-1 min-1)

KF = 5.10;         %this is the Freundlich constant (mg g-1) used to determine 'qe' at
each time step

n = 2.63;          %this is the second parameter for the Freundlich adsorption
isotherm (g L-1) used to determine 'qe' at each time step

data_collect = [0    1     2     3     4     5     6     7     8     9     10
                20   30   40   50   60   70   80   90   100  110  120  150
                180  210  240  270  300  330  360  390  420  450  480  510
                540  570  600  630  660  690  720  750  780  810  840  870
                900  930  960  990  1020 1050 1080 1110 1140 1170 1200
               1230 1260 1290 1320 1350 1380 1410 1440

];

t_end = 1440; %1440 = 1 day

t_steps = numel(data_collect);

%t_step = t_end/t_steps;

bv_end = t_end*j;

```

```
%setting up the arrays where calculated data is to be stored
global results_t;
results_t = zeros(number_of_experiments,t_steps);
global results_Ct;
results_Ct = zeros(number_of_experiments,t_steps);
global results_qt;
results_qt = zeros(number_of_experiments,t_steps);
global exp;

%we make an array listing all the input parameters for each kinetic plot we
%wish to model. The different values of Cs are automatically plugged in
for i = 1:number_of_experiments
    experiments(i,1) = C_init;
    experiments(i,2) = qt(i);
    experiments(i,3) = j;
    experiments(i,4) = Cinfluent;
    experiments(i,5) = k;
    experiments(i,6) = Cs *10^(i-4); %10^(i-2);
    experiments(i,7) = KF;
    experiments(i,8) = n;
end

%setting up the formatting for printing results
results_table=[];
formatSpec = '';
formatSpec2 = '';
formatHeader = '';

for i = 1:number_of_experiments
    exp = zeros(1,number_of_variables) ;
    exp(1,:) = experiments(i,:);
    exp_C_init = exp(1,1);
    exp_q_init = exp(1,2);

    %increase the tolerance
    options = odeset('RelTol',1e-3); %need to increase the tolerance to avoid errors,
    was 1e-5 to begin with, tried changing to 1e-4

    %run the ode45 function which will solve the differential rate equation
```

```
[t,C]=ode45(@DiffEq,[data_collect],[exp_C_init exp_q_init]); %call the ODE
function

results_t(i,:)=t;
results_bv(i,:)=results_t(i,:)*exp(1,3);
results_Ct(i,:)=C(:,1);
results_qt(i,:)=C(:,2);
results_theta(i,:)=C(:,2)/(1000*exp(1,7)); %now meaningless

results_table =
[results_table,results_t(i,:)',results_bv(i,:)',results_Ct(i,:)',results_qt(i,:)
.',results_theta(i,:)'];

%print here

formatSpec = strcat(formatSpec,'\r\n');
fileID = fopen(filename,'w');
formatSpec = '%10.3f %10.5f %10.3f %10.3f %10.8f\r\n';
fprintf(fileID,'%10s %10s %10s %10s %10s %10s\r\n','C0,ppb','q0,ppb','j,BV
min-1','C_inf,ppb','k','Cs,g L-1','qm,mg g-1');
formatHeader = strcat(formatHeader,'\r\n');

formatHeader = '';
for i = 1:number_of_experiments
formatHeader = strcat(formatHeader,'%-50.4f ');
end
formatHeader = strcat(formatHeader,'%-50.4f ');
fprintf(fileID,strcat(formatHeader,'\r\n'),experiments(:,:,));
formatSpec2 = strcat(formatSpec2,'%10s %10s %10s %10s %10s \r\n');
fprintf(fileID,formatSpec2,'t','BV','Ct','qt','theta');
formatSpec = strcat(formatSpec,'%10.3f %10.5f %10.3f %10.3f %10.8f');
formatSpec = strcat(formatSpec,' %.3E %.3E %.3E %.3E %.3E');
fprintf(fileID,strcat(formatSpec,'\r\n'),results_table.');
fclose(fileID);

end

end
```

```
function dCdt = DiffEq(t,conditions)
global day;
global exp;
global i;
global qt;

time=t;

j = exp(1,3);
Cinfluent = exp(1,4);
k = exp(1,5);
Cs = exp(1,6);
KF = exp(1,7);
n = exp(1,8);

Ct = conditions(1);    %ug L-1
qt(i) = conditions(2);    %ug L-1
Ct_mgL = Ct/1000;        %mg L-1
qt_mgg = qt(i)/(Cs*1000);    %mg g-1

%the rate equation we are using is
%dqt/dt = k' * Ct * (1-(qt/(Kf * Ce^(1/n))))^2
%please see our manuscript for derivation and further information

rate_ads = 1000*k*Ct_mgL*Cs*((1-(qt_mgg/(KF*(Ct_mgL^(1/n))))))^2; %calculate dq/dt
in ppb L-1 min-1

if conditions(1) <0
    conditions(1) = 0.00000001;    %Ct can never be negative, otherwise this seems to
slow down the simulation
    rate_ads=0;
end

rate_influx = j*Cinfluent; %calculate the rate of sorbate influx (continuous-flow
systems only)

rate_outflux = j*Ct; %calculate the rate of sorbate outflux (continuous-flow
systems only)

dCdt = [-rate_ads+rate_influx-rate_outflux;rate_ads]; %adjust the concentration of
aqueous sorbate and adsorbed sorbate, respectively

%finally we need to update qt(i) so that the next day's simulation begins
%with the appropriate amount of sorbate already attached.
```

```
qt(i)=qt(i)+rate_ads;

%print the variables out for debugging
"t is " + t + ", Ct is " + Ct + " ug L-1 and qt is " + qt(i) + "ug L-1, day " + day
+ ", i is " + i

end
```